Physics of Atomic Nuclei, Vol. 65, No. 8, 2002, pp. 1377–1382. Translated from Yadernaya Fizika, Vol. 65, No. 8, 2002, pp. 1411–1416.

NUCLEI
Experiment

Study of ^{201}Tl $\xrightarrow{\varepsilon}$ ^{201}Hg Decay Properties

V. V. Kharitonov and V. N. Gerasimov

Russian Research Centre Kurchatov Institute, pl. Kurchatova 1, Moscow, 123098 Russia

Received April 9, 2001; in final form, August 20, 2001

Abstract—The intensities of the transitions to the ground-state and the first excited level of ^{201}Hg in ^{201}Tl decay and the values of the constant log ft are estimated on the basis of an analysis of the relative intensities of the mercury $M_4N_{6,7}N_{6,7}$ Auger electron line induced by ε capture and the mercury conversion O_3 line caused by the 1.56-keV nuclear transition. © *2002 MAIK "Nauka/Interperiodica".*

1. INTRODUCTION

Four low-lying excited levels in the daughter nucleus ^{201}Hg were revealed experimentally in the decay ^{201}Tl $\xrightarrow{\varepsilon}$ ^{201}Hg [1, 2]. The results of previous studies can be found in the articles quoted in the list of references in [3]. The first excited level has an excitation energy of about 1.56 keV. The properties of the transition in the ^{201}Hg nucleus from the first excited to the ground state were explored in [4], where the values of 1564.8 ± 1.0 eV and $\delta^2_\gamma(E2/M1) = (2.10^{+0.55}_{-0.40}) \times 10^{-4}$ were obtained for the energy of the transition to the ground state and the multipole-mixing parameter, respectively. A close proximity of the first excited level to the ground state generates difficulties in assessing their population in the decay process. At present, only data on the sum of the intensities of the transitions to these two levels are available. It is $(43 \pm 2)\%$ [3].

By using the relative intensities of the mercury conversion O_3 line (caused by the 1.56-keV nuclear transition in the daughter nucleus ^{201}Hg) and the mercury $M_4N_{6,7}N_{6,7}$ Auger electron line (initiated in the ε-capture process), we were able here to obtain information needed for extracting data for estimating the intensities of the transitions to the first excited and the ground-state level of ^{201}Hg in the decay of the parent nucleus ^{201}Tl.

2. DESCRIPTION OF THE EXPERIMENT

The spectrum-measuring apparatus and the procedures used to prepare samples, perform measurements, and process experimental data were similar to those described in [4]. The electron spectra were measured by a Hewlett–Packard HP5950A electrostatic x-ray-electron spectrometer [5]. The instrument is intended for measuring the spectra of electrons excited in the sample under study by the photoeffect process induced by the monochromatic 1486.6-eV Al $K_{\alpha_{1,2}}$ radiation. The parameters of the HP5950A spectrometer suit the investigation of the conversion spectra of soft nuclear transitions (up to 3 keV). At the radioactive-source dimensions of 1×5 mm^2, the spectrometer resolution estimated by the experimental conversion spectra is about 1.1 eV in the mode of conversion measurements.

The calibration of the scale of electron kinetic energies (with respect to the vacuum level for the sample) was performed according to the expression

$$E_i = 1486.6 \text{ eV} - \varepsilon_i + \Delta E_i - \varphi_s, \qquad (1)$$

where 1486.6 eV is the energy of Al x-ray $K_{\alpha_{1,2}}$ photons, ε_i is the electron binding energy in the ith subshell with respect to the Fermi level, ΔE_i is the experimental difference of the kinetic energies of the conversion and x-ray-electron lines corresponding to the ith subshell, and ϕ_s is the work function for electron emission from the sample. The value of ϕ_s was assumed to be equal to 4.0 eV.

In measuring the conversion and Auger electron spectra, it is necessary to fix the sample position. In practice, the sample position was made to be coincident with the standard position of the x-ray-irradiated square (1×5 mm^2) in the x-ray-electron mode of instrument operation, and the fixing of this position ensured a precision, in measuring the relative position of intense lines, not poorer than 0.2 eV. Throughout the measurements, the calibration of the instrument energy scale was monitored by the position of the x-ray-electron C1s line of the oil vapors of a rough-vacuum pump, which were sorbed on the sample surface, and by the x-ray-electron lines of substrate platinum, as well as by the valence-zone edge (Fermi level).

The ^{201}Tl isotope (supplied by the Izotop company) in the form of a water solution of its chloride was used to prepare the working sample. The total amount

1063-7788/02/6508-1377$22.00

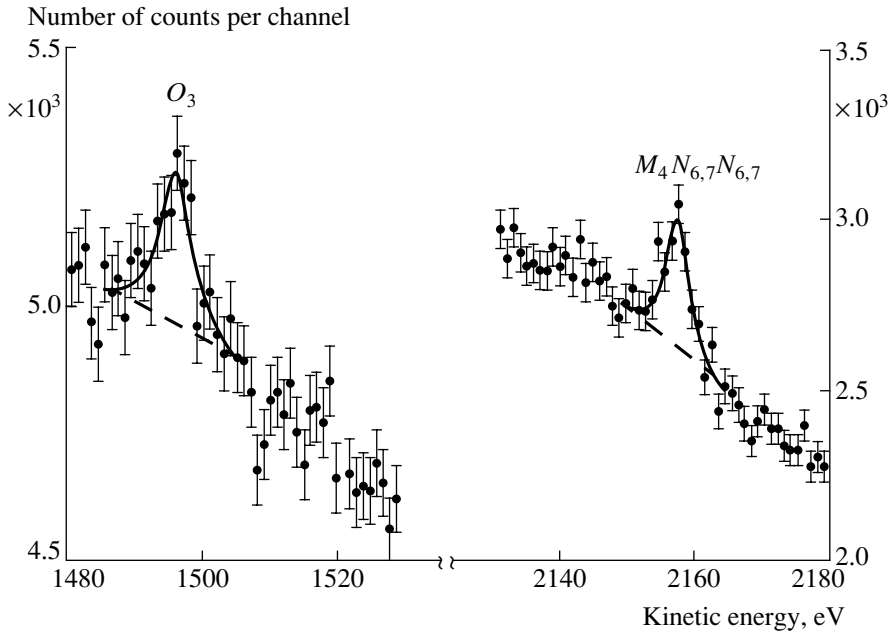

Fig. 1. Spectrum of lines of conversion electrons of the mercury O_3 subshell and mercury $M_4N_{6,7}N_{6,7}$ Auger electrons per single energy window. The thick solid lines represent fits obtained by the maximum-likelihood method. The dashed lines illustrate the behavior of the background under the peaks.

of provided activity was 3600 MBq. Radionuclide admixtures in the solution, like ^{200}Tl, ^{202}Tl, and ^{203}Pb, had virtually no effect on the results of the measurements, since there are no low-energy transitions in their decay chains. The admixtures can influence the chemical state of the sample and reduce the rate of spectrum taking because of a decrease in the partial density of the ^{201}Tl isotope in the sample volume.

The working sample was prepared by means of ^{201}Tl electrolytic deposition from the solution onto the platinum substrate. This method appeared to be successful in similar studies with the ^{99m}Tc isomer (see [6–8]). It ensures the accumulation of the deposited substance on the substrate; its purification from admixtures, which were contained in the original product; and its uniform distribution over the substrate in accordance with the requested geometry. The actual amount of the substance deposited on the substrate is between a few tens of nanograms and a few micrograms. Therefore, it is necessary to monitor the chemical purity of the equipment and the reagents.

The electrolytic cell was a polytetrafluoroethylene (PTFE) cylinder with sealing rings. It was 3.5 cm high, and its inner diameter was 1.5 cm. The working sample was covered with a PTFE mask having a window of required size cut in it (1×5 mm^2) and was fastened in the lower part of the cylinder by means of a clamping ring. Electrolysis was performed in three steps. The first two steps were used to purify the original solution, and only at the third step was electrolysis performed onto the working substrate. The external voltage applied to the cell was varied between 10 and 20 V. A single electrolysis step took approximately one hour. The thallium content in the electrolyte and on the substrate and thallium losses were monitored by γ radiation with a dose meter. At all stages of the work, measures were taken to reduce the possible contamination of the prepared sample by admixtures. The activity of the prepared samples was about 300 MBq.

The spectra were processed by using the SPRO code [9].

3. RESULTS AND DISCUSSION

The procedure used to determine the intensities of the transitions to the ^{201}Hg ground-state and first excited levels in decay $^{201}\mathrm{Tl} \xrightarrow{\varepsilon} {}^{201}\mathrm{Hg}$ was based on the concurrent detection of the mercury conversion O_3 line (caused by the 1.56-keV nuclear transition in the daughter nucleus ^{201}Hg) and mercury $M_4N_{6,7}N_{6,7}$ Auger electron line (induced by the ε-capture process and subsequent fluorescent transitions). This procedure relates the intensity of the $M_4N_{6,7}N_{6,7}$ line of mercury Auger electrons to the intensity of the decays of the parent nucleus ^{201}Tl, on one hand, and to the intensity of the 1.56-keV conversion transition in ^{201}Hg, on the other hand.

Figure 1 shows the electron spectrum of the lines of the O_3-subshell conversion electrons and

Table 1. Probability of the observed $M_4N_{6,7}N_{6,7}$ Auger transition with respect to conversion in the O_3

$I(M_4N_{6,7}N_{6,7})/I(O_3)$	χ	$\omega(M_4N_{6,7}N_{6,7})/\omega(O_3)$
0.86 ± 0.24	0.718 ± 0.171	0.62 ± 0.23

$M_4N_{6,7}N_{6,7}$ Auger electrons obtained in a single energy window. The curves fitted to the experimental data (thick solid lines in Fig. 1) were obtained by the maximum-likelihood method with the SPRO code [9]. The above lines were chosen for the following reason. On one hand, the $M_4N_{6,7}N_{6,7}$ Auger electron line is one of the most intense Auger electron lines of mercury within the energy range of our instrument; on the other hand, this line is located off the energy range of cascade Auger processes and is the most distinct in the electron spectrum. The mercury conversion O_3 line in the electron spectrum is sufficiently intense for performing a quantitative analysis and is closer in kinetic energy to the mercury $M_4N_{6,7}N_{6,7}$ Auger electron line than other lines. Owing to the latter, both lines can be recorded within a single energy window.

The conversion O_3 line was identified by using the tabular x-ray-electron data from [10] and the results of our measurements of reference samples. The $M_4N_{6,7}N_{6,7}$ Auger electron line was identified by the tabular theoretical and experimental data on Auger transitions from [11, 12].

The first column of Table 1 presents the intensity of the observed Auger electron line with respect to the conversion line. In order to go over from the relative line intensities to the experimental relative probabilities of the processes, it is necessary to introduce some corrections associated with the spectrometer transmission and the elastic and inelastic scattering of electrons in the substrate (in the layer of the radioactive source deposited by electrolysis and in the substrate material) and in the sorbed surface layer of hydrocarbons and oxygen. It is difficult and ambiguous to take into account these corrections if they are introduced directly as an overall quantity, since their values are affected by the effective thickness of the prepared source of conversion electrons and by the thickness of the sorbed layer, these thicknesses being unknown to the required precision. Therefore, a dedicated approach was developed here for introducing such corrections. Let us find the total value of all corrections in the following manner. As follows from the results that our group obtained in [4] by studying the spectrum of conversion electrons of the 1.56-keV nuclear transition in ^{201}Hg [4], $I(O_2)/I(N_2) = 0.247 \pm 0.051$ for the relative intensities in the O_2 and N_2 subshells. Using the relation

$$\frac{\omega(O_2)}{\omega(N_2)} = \frac{I(O_2)}{I(N_2)}\chi(\Delta E), \qquad (2)$$

where ω is the theoretical value of the conversion probability in the corresponding subshell and $\chi(\Delta)$ is the correction factor, which, to a first approximation, depends on the difference ΔE of the kinetic energies of electrons of two subshells ($\Delta E = 597.1$ eV for the O_2 and N_2 subshells [10]), and taking into account the theoretical internal-conversion coefficients for the subshells in question, we obtain $\chi(597.1\ \text{eV}) = 0.745 \pm 0.154$ [13]. Using this value and considering that $\chi(0) = 1$, we introduce the correction factor for the ratio of the intensities of the $M_4N_{6,7}N_{6,7}$ Auger electron line and the conversion O_3 line by the linear-extrapolation method (the use of an exponential extrapolation leads to nearly identical results). Taking into account the value of $\Delta E = 660.1$ eV (the difference of the kinetic energies of the $M_4N_{6,7}N_{6,7}$ Auger electrons and conversion electrons of the O_3 subshell), we obtain the relative probability of these processes (Table 1). Here, we assume that the behavior of $\chi(\Delta E)$ does not change in response to a shift of 700 eV toward higher kinetic energies of electrons.

Let us now estimate the number of holes produced in the mercury M_4 subshell per 100 decays of ^{201}Tl. In doing this, we must take into account only those cases of hole production in the M_4 subshell in which there are no holes in other subshells, because, in the presence of additional holes, the Auger electron lines are shifted and smeared over a wide region. The production of a single hole in the M_4 subshell is due primarily to electron capture from the K and L subshells and internal conversion in these subshells that is followed by fluorescent transitions involving the emission of x-ray photons. The remaining processes that also lead to hole production in the M_4 subshell have a low probability and are insignificant. The production of holes through internal conversion in deep subshells can easily be estimated if the nuclear-transition energies and multipole-mixing parameters are known, along with the populations of three high-lying ^{201}Hg levels (with respect to the first excited level) [3], and if the tables of internal-conversion coefficients [14] are used. The number of holes produced upon ε capture is determined by using the electron-capture tables from [15] and the energy properties of the decay ^{201}Tl $\xrightarrow{\varepsilon}$ ^{201}Hg [3]. Further, we find the number of holes in the M_4 subshell per 100 decays of the parent nucleus by using the available tables of the fluorescent yields and the probabilities of radiative transitions (see [16]). The

Table 2. Number of holes formed in the subshells of a ^{201}Hg atom per 100 decays of the parent nucleus ^{201}Tl

Subshell	N^0	Transition	N^1	Transition	$\sum N(M_4)$
K	97.28	$K-L_2(0.275)^*$ $K-L_3(0.463)$			9.48
L_2	3.42		30.17	$L_2-M_4(0.276)$	
L_3	~ 0.2		45.24	$L_3-M_4(0.0255)$	

Note: Here, N^0 is the total number of primary holes produced as the result of electron capture and subsequent internal conversion in deep inner subshells; N^l is the number of holes in the L subshells with allowance for fluorescent transitions; $\sum N(M_4)$ is the total number of holes in the M_4 subshell; an asterisk labels the type of fluorescent transition; and the values in parentheses stand for the probability of the decay of a single hole through the channel of the indicated fluorescent transition.

second column of Table 2 presents the total numbers of holes produced in the mercury subshells both as the result of electron capture and as the result of subsequent conversion. The types of fluorescent transitions and their probabilities in the total number of decays of primary holes are given in the third and the fifth columns, respectively. The fourth and the last column display, respectively, the total numbers of holes in various subshells upon the corresponding fluorescent transitions and the total number of holes in the M_4 subshell per 100 ^{201}Tl decays. Table 2 gives the numbers of holes only in those mercury subshells from which there occur fluorescent transitions making a noticeable contribution to hole production in the M_4 subshell. It is precisely for this reason that the L_1 subshell is not indicated in Table 2. Finally, we have found that 9.48 holes are produced in the M_4 subshell of mercury per 100 decays of the parent nucleus ^{201}Tl.

It should be noted that, according to our analysis, ε capture produces many more holes in the M_4 subshell than internal conversion does. Moreover, it follows from the theoretical calculations presented in [17] and from a series of experimental studies [18–20] that the kinetic energy of Auger electrons initiated in the ε-capture process is 7–15 eV greater than the kinetic energy of electrons caused by the internal-conversion process. This is because of the presence of an "extra" electron in the valence shell of the daughter atom upon ε capture (the time of Auger electron cascades is much less than the time it takes for an extra electron to leave the daughter atom). Thus, the mercury $M_4N_{6,7}N_{6,7}$ Auger electron line initiated by conversion falls within the region of inelastic losses and processes of multiple ionization for the Auger electrons of the $M_4N_{6,7}N_{6,7}$ line caused by ε capture, the former line being separated from the latter in energy.

Let us proceed to determine the intensities of the transitions to the 1.56-keV level in ^{201}Tl decays. For this purpose, we consider that, according to [21], the filling of holes in the M_4 subshell occurs through the $M_4N_{6,7}N_{6,7}$ Auger transition with a probability of 33.6% of the total number of hole decays in the M_4 subshell. The ratio of the probability of the total conversion of the 1.56-keV nuclear transition to the conversion probability in the mercury O_3 subshell can be straightforwardly assessed by using the theoretical values of the internal-conversion coefficients from [13] and the value of the multipole-mixing parameter for this transition ($\delta^2_\gamma(E2/M1) = 2.10 \times 10^{-4}$) from [4]. The ratio of the probabilities is 15.943. Now, we have the entire body of information needed for obtaining the intensities of the transitions to the first excited level in ^{201}Hg. For this purpose, we use the expression

$$I\varepsilon\,(1.56\ keV) = 9.48K \times 0.336\frac{\omega(O_3)}{\omega(M_4N_{6,7}N_{6,7})}\frac{\sum\omega_e}{\omega(O_3)} - 12.9, \quad (3)$$

where $I\varepsilon$ is the intensity of the transitions to the 1.56-keV level (per 100 ^{201}Tl decays); 9.48 is the total number of holes produced in the M_4 subshell per 100 ^{201}Tl decays due to both ε capture and internal conversion in lower lying subshells; K is the correction coefficient equal to the fraction of vacancies produced in the M_4 subshell due to ε capture ($K = 0.729$); 0.336 is the fraction of those decays of vacancies in the M_4 subshell that are associated with the $M_4N_{6,7}N_{6,7}$ Auger electron line; the next two factors represent, respectively, the relation between the probabilities of conversion in the O_3 subshell and the observed $M_4N_{6,7}N_{6,7}$ Auger transition and the relation between total conversion and conversion in the O_3 subshell; and 12.9 is the number of transitions to the 1.56-keV level from higher lying levels in the ^{201}Hg nucleus [3].

In order to calculate the uncertainty in the total number of holes in the M_4 subshell, we took into account the uncertainty in the production of primary holes via ε capture and subsequent fluorescent transitions. In determining the total uncertainty in the

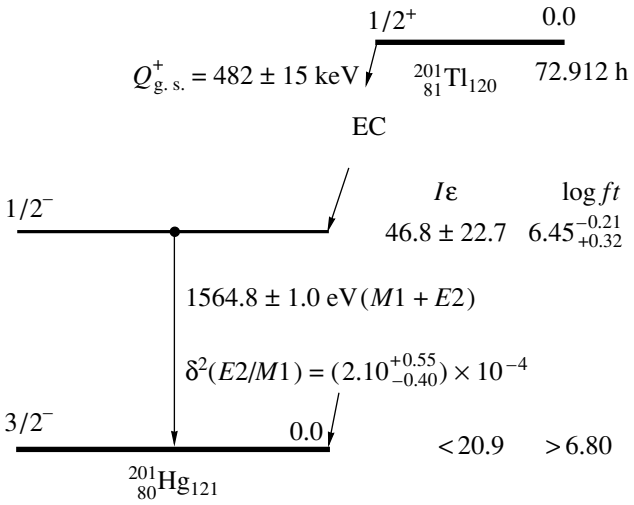

Fig. 2. Section of the $^{201}\mathrm{Tl} \xrightarrow{\varepsilon} {}^{201}\mathrm{Hg}$ decay scheme, along with the values of nuclear features. The quoted intensities are those per 100 decays of the parent nucleus ^{201}Tl.

intensity of the transitions, we took into account the uncertainty in each factor in expression (3).

We have obtained $I\varepsilon(1.56\,\mathrm{keV}) = 46.8 \pm 22.7$ (per 100 primary decays of ^{201}Tl). Using this intensity of ^{201}Tl decays to the first excited level of ^{201}Hg and the tabular data from [15], we find for the constant log ft that $\log ft = 6.45^{-0.21}_{+0.32}$. As was mentioned in the Introduction, only data on the total intensity of the transitions to the ground-state and first-excited levels of ^{201}Hg are available at present. According to [3], it is $(43 \pm 2)\%$, which is less than the value that we obtained for the intensity of the transitions to the first excited level of ^{201}Hg. Using the value of the total intensity of the transitions to the ground-state and first-excited levels (with allowance for the uncertainty indicated in [3]) and our value of the intensity of the transitions to the first-excited level (with the uncertainty indicated above), we can obtain an upper limit on the intensity of the transitions to the ^{201}Hg ground-state level in the decay and a lower limit on the constant log ft. These are $I\varepsilon(0.0\,\mathrm{keV}) < 20.9$ per 100 ^{201}Tl decays and $\log ft > 6.80$.

Figure 2 shows a section of the ^{201}Tl decay scheme, along with the transition energies and the multipole-mixing parameters obtained previously in [4]. Also given in this figure are the estimates obtained here for the intensities of the transitions to the first excited and the ground-state level and for log ft.

The nuclear data obtained in the present study supplement our knowledge of the decay $^{201}\mathrm{Tl} \xrightarrow{\varepsilon} {}^{201}\mathrm{Hg}$.

ACKNOWLEDGMENTS

We are grateful to V.I. Zhudov for stimulating discussions.

REFERENCES

1. C. J. Herrlander, R. Stockendal, and R. K. Gupta, Ark. Fys. **17**, 315 (1960).
2. P. Schüler, K. Hardt, G. Günther, *et al.*, Z. Phys. A **313**, 305 (1983).
3. S. Rab, Nucl. Data Sheets **71**, 421 (1994).
4. V. N. Gerasimov, D. V. Grebennikov, V. M. Kulakov, *et al.*, Yad. Fiz. **60**, 1948 (1997) [Phys. At. Nucl. **60**, 1780 (1997)].
5. M. A. Kelly and C. E. Tyler, Hewlett-Packard J. **24**, 2 (1973).
6. V. N. Gerasimov, A. G. Zelenkov, V. M. Kulakov, *et al.*, Yad. Fiz. **34**, 3 (1981) [Sov. J. Nucl. Phys. **34**, 1 (1981)].
7. V. N. Gerasimov, A. G. Zelenkov, V. M. Kulakov, *et al.*, Zh. Éksp. Teor. Fiz. **86**, 1169 (1984) [Sov. Phys. JETP **59**, 683 (1984)].
8. V. N. Gerasimov and V. M. Kulakov, *Influence of Chemical Environment on Conversion: Conversion Electron Spectroscopy of Technetium Compounds: Review* (TsNIIatominform, Moscow, 1988).
9. A. D. Panov, Preprint No. IAÉ-6019/15, IAÉ (Institute of Atomic Energy, Moscow, 1997).
10. J. C. Fuggle and N. Mårtensson, J. Electron Spectrosc. Relat. Phenom. **21**, 275 (1980).
11. F. P. Larkins, At. Data Nucl. Data Tables **20**, 312 (1977).
12. L. E. Davis, N. C. MacDonald, P. W. Palmberg, *et al.*, *Handbook of Auger Electron Spectroscopy* (Perkin–Elmer Corporation, Minnesota, 1976), p. 253.
13. O. Dragoun, V. Brabec, M. Ryšavý, *et al.*, Z. Phys. A **326**, 279 (1987).

14. F. Rösel, H. M. Fries, K. Alder, and H. C. Pauli, At. Data Nucl. Data Tables **21**, 91 (1978).
15. B. S. Dzhelepov, L. N. Zyryanova, and Yu. P. Suslov, *Beta Processes: Functions for Analysis of Beta Spectra and Electron Capture* (Nauka, Leningrad, 1972).
16. E. Browne and R. B. Firestone, *Table of Radioactive Isotopes* (Wiley, New York, 1986).
17. E. Yu. Remeta and A. I. Lendel, Izv. Akad. Nauk, Ser. Fiz. **58**, 143 (1994).
18. V. V. Bulgakov, V. I. Gavrilyuk, V. I. Kirishchuk, *et al.*, Izv. Akad. Nauk SSSR, Ser. Fiz. **50**, 1944 (1986).
19. V. V. Bulgakov, V. I. Kirishchuk, V. T. Kupryashkin, *et al.*, Izv. Akad. Nauk SSSR, Ser. Fiz. **53**, 2120 (1989).
20. V. V. Bulgakov, A. V. Kaznovetskiĭ, V. I. Kirishchuk, *et al.*, Izv. Akad. Nauk SSSR, Ser. Fiz. **55**, 2147 (1991).
21. C. P. Bhalla, Phys. Rev. A **6**, 1409 (1972).

Translated by E. Kozlovskiĭ

Physics of Atomic Nuclei, Vol. 65, No. 8, 2002, pp. 1383–1389. Translated from Yadernaya Fizika, Vol. 65, No. 8, 2002, pp. 1417–1423.

NUCLEI
Experiment

Cross Sections for ^{209}Bi, ^{232}Th, ^{235}U, ^{238}U, and ^{237}Np Fission Induced by Intermediate-Energy Protons and Deuterons

V. I. Yurevich*, V. A. Nikolaev[1)], R. M. Yakovlev[1)], and A. N. Sosnin

Joint Institute for Nuclear Research, Dubna, Moscow oblast, 141980 Russia

Received April 16, 2001; in final form, October 4, 2001

Abstract—The cross sections for ^{209}Bi, ^{232}Th, ^{235}U, ^{238}U, and ^{237}Np fission induced by protons of energy in the range 1.0–3.7 GeV and by deuterons of energy 1.0 GeV were measured. The results are compared with data from other experiments, with available estimates, and with the predictions of theoretical models.

1. INTRODUCTION

The fission reaction is one of the main channels of inelastic hadron interaction with extremely light nuclei in the energy range 0.1–10 GeV. Despite the long history of experimental and theoretical investigations into the fission process, the problem of obtaining reliable data on the cross sections for the fission of various nuclides at intermediate energies and of constructing their adequate theoretical description remains, however, pressing. As the projectile energy is increased in the region around 1 GeV, there occurs a fast growth of the cross sections for target-fragmentation and target-disintegration reactions resulting in the formation of various nuclear fragments, which is accompanied by the emission of a large number of nucleons. The presence of several competing channels through which the nuclear system formed in a collision process may decay generates severe problems both for experimental and for theoretical investigations into the fission of heavy nuclei in this energy range.

A detailed analysis of data on nuclear fission induced by intermediate-energy protons and neutrons was recently performed in the original studies [1–4] and in the review article of Obukhov [5].

The objective of this study was to measure the fission cross sections for ^{209}Bi, ^{232}Th, ^{235}U, ^{238}U, and ^{237}Np nuclei in an extracted beam of protons and deuterons from the synchrophasotron of the Joint Institute for Nuclear Research (JINR, Dubna) in the energy region $E \geq 1$ GeV, which is the most difficult for investigations. The results obtained in this experiment are compared with the experimental data from [6–17], which are the most reliable in our opinion; with the predictions of existing model calculations; and with the available model estimates of the dependence of the cross sections for nuclear fission on the projectile-proton energy [4, 18].

2. EXPERIMENTAL PROCEDURE

In our experiment, fission fragments were recorded by solid-state nuclear track detectors (SSNTD) based on a 6-μm film from Dupont polyester fiber (its commercial name is Dacron), which were adjacent to fissile layers. After etching in a KOH alkali solution, the tracks from fission framents were counted with the aid of information readout by a spark track counter [19]. The efficiency of the detection of fission fragments escaping from a thin layer and having an isotropic angular distribution was estimated by using a ^{252}Cf source. The resulting efficiency value of $\eta = 0.515$ corresponds to the critical fission-fragment-detection angle of $\theta = 29°$.

Fissile layers of thickness 1 mg/cm^2 were deposited onto an aluminum substrate of diameter 11.3 mm. Actinide layers were prepared by means of coating that was repeated many times and then followed by annealing, whereas bismuth layers were manufactured via the thermal evaporation of bismuth from a tantalum substrate in a vacuum. In either case, the error in determining the mass of a layer was 2 to 3%, while the nonuniformity of the layer thickness did not exceed 10%.

Fission fragments escaping from a thin fissile layer possess optimum features for detecting them with polymer SSNTDs. Our measurements revealed that the threshold of sensitivity to the charge of a nuclear fragment for Dacron is $Z_{\text{thr}} = 5$, which agrees well with data of other authors [20]. The threshold charge value is well below the charges of fission fragments;

[1)]Khlopin Radium Institute, Vtoroi Murinskiĭ proezd 28, St. Petersburg, 194021 Russia.
*e-mail: yurevich@sunhe.jinr.ru

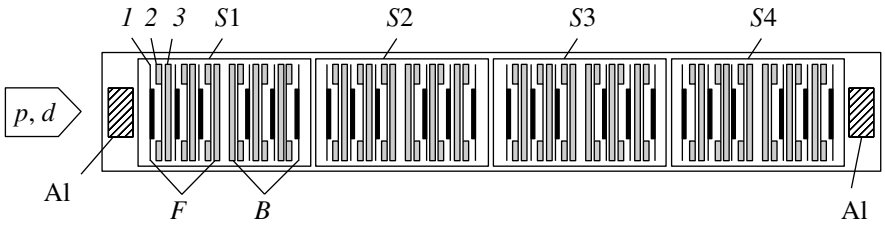

Fig. 1. Layout of irradiation: (*1*) substrate carrying a fissile layer; (*2*) SSNTD; (*3*) polyethylene screen; (Al) aluminum monitoring disk; (F, B) assemblies that contain identical layers and which are oriented, respectively, along and against the beam direction; and ($S1$–$S4$) assemblies for different fissile nuclides.

therefore, it is assumed here that, for all fissile nuclides investigated in our study and for all energies of projectile protons and deuterons, the features of fission fragments remain optimal for detecting them by the method that we use. The total methodological error in determining the number of fission fragments—it is associated with the uncertainty in knowledge of the etching parameters, the uncertainty in film thickness, and the error of the method for track counting—ranges between 6 and 8%.

The reliability of the results of our experiment crucially depends on the estimate of the contribution to the number of tracks from other nuclear fragments of a nonfission origin that emerge from the inelastic interactions of high-energy particles with target nuclei and with nuclei of structural materials and on the minimization of this background effect at the stage of planning the experiment. The majority of light nuclear fragments arising in a thin target layer owing to the fragmentation reaction have kinetic energies such that $dE/dx < (dE/dx)_{\text{thr}}$; therefore, they cannot be recorded by the method used. At the same time, heavy nuclear fragments and residual nuclei formed in the disintegration of target nuclei may possess features required for detection—in particular, their range in the SSNTD may be longer than 5 μm. An analysis of data available in the literature revealed that, in the disintegration of nuclei whose mass numbers lie in the region $A > 200$, residual nuclei possessing kinetic energies sufficient for detection can make a significant contribution to the number of counts at projectile-proton energies higher than approximately 1.5 GeV.

In order to estimate the contribution of nuclear fragments to detector readings and to optimize the design of the irradiated assembly of fissile layers and track detectors with the aim of reducing background effects, we have performed additional investigations in a proton beam from the JINR synchrophasotron. We have studied experimentally the sensitivity of the method to nuclear fragments escaping from the target in the mass-number range $9 < A < 207$, from the aluminum substrate, and from the polyethylene disk and have also measured the number of background counts of the SSNTD itself. The proton-beam energy was varied between 0.2 and 3.7 GeV. The investigations revealed that the number of recorded fragments depends greatly on the target material, the proton energy, and the orientation of the target–SSNTD assembly. By way of example, we indicate that, in the energy region above 1 GeV, the number of recorded fragments originating from the disintegration of $A <$ 200 nuclides in the forward direction (along the beam axis) exceeds the number of fragments escaping in the opposite direction by a factor greater than 10. The maximum contribution of fragments to the total number of recorded tracks from fission fragments (forward and backward) was obtained for a thin bismuth layer at the highest proton energy of 3.7 GeV (it was 15%). The choice of target-substrate material for minimizing background counts depends on the energy region being studied. At proton energies above 600 MeV, it is necessary to use extremely light materials, such as beryllium and aluminum. The number of counts from an aluminum substrate depends only slightly on the proton energy and contributes about 4% for a bismuth target and 0.6–1.0% for actinide targets. The intrinsic background counts of the SSNTD, together with the contribution from the polyethylene disks (screens) arranged on the two sides of the SSNTD, are negligible.

3. MEASUREMENTS

The layout of irradiation and the design of the assemblies consisting of fissile layers, the SSNTD, the polyethylene screens, and the aluminum monitoring disks are shown in Fig. 1. The assemblies containing ^{232}Th, ^{235}U, ^{238}U, and ^{237}Np layers and the assemblies containing ^{209}Bi layers were irradiated with a proton beam in different experimental runs. The isolation of bismuth layers into an individual assembly is explained by the need for ensuring, in order to obtain optimal statistics of about 3000–4000 cm^{-2}, approximately five times more beam protons incident on the target than in the case of the nuclides entering into the composition of the first assembly. In a deuteron

Table 1. Measurements performed in proton and deuteron beams

Beam	Energy, GeV	Target	Uncertainty in monitoring, %
p	1.0	^{232}Th, ^{235}U, ^{238}U, ^{237}Np	10
p	1.0	^{209}Bi	20
p	2.0	^{209}Bi	10
p	2.55	^{232}Th, ^{238}U, ^{237}Np	9
p	2.55	^{209}Bi	9
p	3.17	^{209}Bi	8
p	3.65	^{209}Bi	10
d	1.0	^{209}Bi, ^{232}Th, ^{238}U, ^{237}Np	

beam, we performed only one experiment in which the layers of bismuth and actinides were irradiated simultaneously. In the experiments for each nuclide, we used six targets; in three of these, the fissile layer faced incident beam protons, the remaining three being oriented inversely. In this way, fission fragments were recorded for the angular regions $\theta > 119^\circ$ and $\theta < 61^\circ$ for, respectively, the first and the second case of fissile-layer orientation. The track detectors were positioned between the fissile layers and the polyethylene disks 0.1 mm thick, which were used to screen the SSNTD from other assembly materials capable of producing additional background counts. The list of the irradiation runs performed is given in Table 1.

The number of protons that traversed the fissile layers was determined with the aid of the reaction $^{27}\mathrm{Al}(p, X)^{24}\mathrm{Na}$. In order to ensure beam monitoring, aluminum disks of thickness 3.0 mm and diameter 11.3 mm (which is identical to that of the fissile layers) were arranged at either endface of the irradiated assembly. The monitoring disks and the fissile targets were placed on the same axis coincident with the beam axis. In the energy range under investigation, the cross section for the monitoring reaction is known to a precision not poorer than 5%; it was taken to be 10.8 mb at the proton energy of 1.0 GeV and 10.0 mb for higher energies. Only relative measurements were performed for a deuteron beam of energy 1.0 GeV.

The position and the transverse dimension of the beam were measured by using a doublet of multiwire proportional chambers.

4. RESULTS OF THE MEASUREMENTS

In order to obtain the cross section for the nuclear-fission process, it is necessary to integrate the angular distribution of fission fragments over the entire range of emission angles; at the same time, fission fragments were recorded in our measurements within bounded angular intervals. In the case of an isotropic distribution of fission fragments, the total number of fission reactions per 1 mg of the sample can be determined by the formula

$$N = (N_F + N_B)/2\eta = 0.971(N_F + N_B),$$

where N_F and N_B are the numbers of fragments recorded in the angular regions $\theta < 61^\circ$ and $\theta > 119^\circ$, respectively. The angular dependence of the yield of fission fragments was studied with the aid of the ratio N_F/N_B. The results obtained in a deuteron beam of energy 1.0 GeV and in proton beams of energies 1.0 and 2.55 GeV are given in Table 2. The angular distributions of fragments originating from ^{232}Th fission induced by protons, deuterons, and alpha particles of various energies—in particular, by 1.0-GeV protons and deuterons—were measured directly in [14]. The N_F/N_B values computed on the basis of these data agree with the results of our measurements for either projectile type. It was shown in [14] that, with increasing energy (above about 140 MeV for protons and from about 500 MeV for deuterons), the angular distributions become isotropic in the c.m. frame. This corresponds to an angular distribution that, in the laboratory frame, is slightly stretched in the forward direction; all the aforesaid is direct proof of the applicability of the method used here to go over from a bounded angular interval to a full solid angle by means of the above formula, where, instead of the factor 0.971, we took the value of 0.93 ± 0.04 in order to take into account the angular-anisotropy effect. This procedure for data processing assumes the emission of two fragments in a fission event—this assumption is legitimate by virtue of the smallness of the cross section for ternary fission.

The eventual values of the measured fission cross sections including corrections for the detection of

Table 2. Measured values of the ratios N_F/N_B for fission fragments

Beam	Energy, GeV	^{209}Bi	^{232}Th	^{238}U	^{237}Np
p	1.0	1.36 ± 0.20	1.23 ± 0.10	1.09 ± 0.09	1.00 ± 0.09
p	2.55	1.24 ± 0.20	1.34 ± 0.09	1.21 ± 0.08	1.14 ± 0.08
d	1.0	1.37 ± 0.17	1.24 ± 0.08	1.23 ± 0.08	1.13 ± 0.07

Table 3. Fission cross sections measured in a proton beam (mb)

Energy, GeV	^{209}Bi	^{232}Th	^{235}U	^{238}U	^{237}Np
1.0	216 ± 49	996 ± 110	1282 ± 141	1364 ± 150	1736 ± 195
2.0	219 ± 33				
2.55	215 ± 26	909 ± 131		1213 ± 184	1393 ± 236
3.17	199 ± 24				
3.65	180 ± 24				

nuclear fragments of a nonfission origin are given in Table 3.

5. DISCUSSION OF THE RESULTS

In order to compare the experimental data with theoretical predictions for actinides, we have estimated the cross section for the fission of excited nuclei that arise upon the completion of the cascade stage of high-energy proton–nucleus interactions in the energy range 0.1–5.0 GeV. The cross section for the fission of these nuclei was computed by using the relation

$$\sigma_f = \sigma_{\text{inel}} N_f / N_{\text{inel}},$$

where σ_f and σ_{inel} are the fission cross section and the inelastic-interaction cross section, respectively, and N_f is the number of nuclear-fission events per N_{inel} in inelastic interactions. In order to calculate the inelastic-interaction cross section, we used data from [21]. In these calculations, we did not take into account the trailing effect—that is, a change (decrease) in the number of intranuclear nucleons at the cascade state of interaction. The fission widths were determined by the same method as in [22–25] with the aid of the Cameron formula [26]. We took into account shell-model even–odd corrections. In the calculations, we relied on the model of a nucleus with a diffuse boundary. The nucleon density in a nucleus was described by the Woods–Saxon distribution. In each intranuclear nucleon–nucleon and pion–nucleon collision, we took into account the laws of energy–momentum conservation. For the fission and evaporation processes, the level-density parameter in a nucleus was taken in the form $a_f = a_n = aA$ (MeV^{-1}), where $a = 0.1$ did not include corrections for the shell structure of the decaying nucleus and did not depend on the excitation energy.

The results of our measurements were also compared with experimental data from [6–17], which are the most reliable in our opinion. As can be seen from Figs. 2–4, the fission cross sections found in the present study are in good agreement with those measured at a proton energy of 1.0 GeV for ^{209}Bi, ^{232}Th, ^{235}U, and ^{238}U [12–14,16] and in the region 2.5–3.0 GeV for ^{209}Bi, ^{232}Th, and ^{238}U [8, 9, 12, 15]. We also note that, for ^{235}U, ^{238}U, and ^{237}Np, the results obtained with 1.0-GeV protons agree, to within 10%, with cross sections measured for fission induced by 0.8-GeV neutrons [27, 28]. Data from [6], which were measured at proton energies below 0.66 GeV, comply well with the aforementioned results for all targets, with the exception of ^{232}Th, in which case the fission cross sections seem underestimated. The results of the calculation describe quite satisfactorily the dependence of the fission cross sections on the incident-proton energy and agree, to within 10–20%, both with the results of our measurements and with the majority of other experimental data. The best agreement is observed for ^{237}Np. According to the calculated dependences, the cross sections for the fission of actinide nuclei change only slightly in the energy range 0.1–1.0 GeV.

This character of the theoretical curves complies with the behavior of the cross sections for uranium

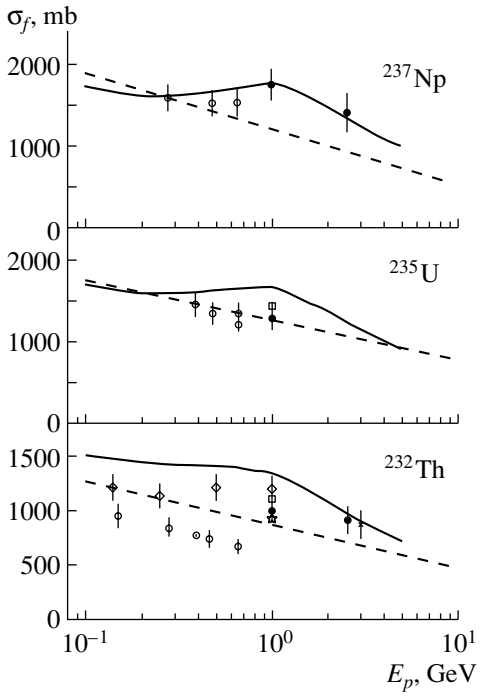

Fig. 2. Cross section for ^{232}Th,^{235}U, and ^{237}Np fission induced by protons of energy above 0.1 GeV: (●) our present data, (solid curves) results of the calculation, and (dashed curves) estimate from [4]; the remaining symbols represent experimental data from (○) [6, 7], (□) [13], (◇) [14], (×) [15], and (⋆) [16].

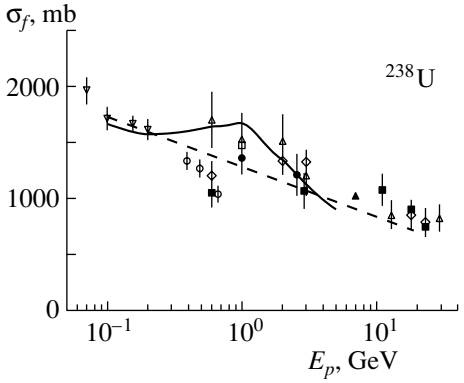

Fig. 3. Cross sections for ^{238}U fission induced by protons of energy above 0.1 GeV: (●) our present data, (solid curve) result of the calculation, and (dashed curve) estimate from [4]; the remaining symbols represent experimental data from (○) [6, 7], (◇) [8], (■) [9], (▽) [10, 11], (△) [12], (□) [13], and (▲) [17].

and neptunium fission induced by neutrons of energies up to 0.8 GeV [27, 28]. In the energy region around 1 GeV, the theoretical model predicts a change in the character of the dependences: the fission cross sections decrease monotonically with increasing proton energy. On the basis of the qualitative pattern of target-nucleus disintegration induced by intermediate-energy protons, where the fragmentation and splitting reactions begin to play an ever more important role with increasing energy, one could expect a reduction of the contribution from the fission reaction. In view of the paucity of reliable data, a large scatter of measured cross sections, and relatively large experimental uncertainties, it does not seem possible to study in greater detail the character of the energy dependence of the fission cross sections for actinide nuclei over the energy region under investigation by relying only on experimental results. However, experiments yield a smoother variation of the fission cross sections in the region around $E_p \sim 1$ GeV than what is predicted by the calculation. All experimental results for thorium and uranium (especially for ^{235}U) fall systematically short of the calculated values at proton energies below 1 GeV; at the same time, there is good agreement between the experimental data and the results of the calculation in the energy region around 2 to 3 GeV. Measurements performed for ^{238}U with $E_p > 5$ GeV protons demonstrate that the decrease in the fission cross section is terminated at higher energies. For all actinides, the estimation performed in [4] on the basis of experimental data yields a smooth decrease in the fission cross section with increasing proton energy (see Figs. 2 and 3). The data were approximated with the aid of a comparatively simple expression that was not intended for describing a detailed energy dependence of the fission cross sections in the range 0.1–10.0 GeV. It can be seen from the figures that, in the range 1–3 GeV, our results and experimental data from other studies lie systematically higher than the estimates from [4]. For ^{209}Bi, Fig. 4 also shows, in addition to our data and the results from [6–13, 17], the estimated proton-energy dependences of the fission cross section from [4, 18]. The cross-section values measured in the present study are in good agreement with data of other authors, showing a slight decrease in the probability of the nuclear-fission process as the energy is increased in the energy region above 2.5 GeV. The cross section for bismuth fission grows as the energy is increased up to about 0.6 GeV, whereupon it reaches a maximum and, as that for actinide nuclei, then decreases smoothly as the energy is increased up to about 5.0 GeV, remaining approximately constant at higher energies. For 1.0-GeV protons, the estimation performed in [18] yields a fission-cross-section value close to that measured in the present study. At the same time, the estimation from [4] led to values of the bismuth-fission cross section in the region $E_p \geq$ 1.0 GeV that are smaller than those determined in our measurements and in other experimental studies discussed here.

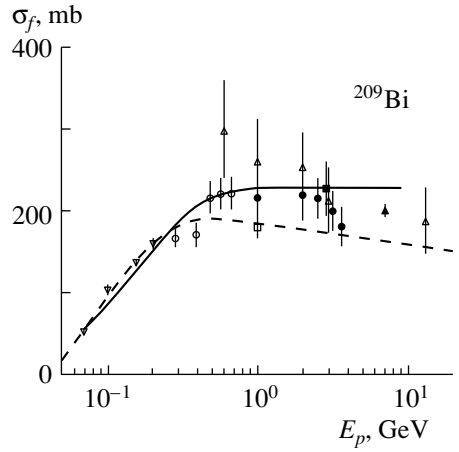

Fig. 4. Cross sections for ^{209}Bi fission induced by protons of energy above 0.1 GeV: (•) our present data and (solid curve) estimate from [18]; the rest of the notation is identical to that in Fig. 3.

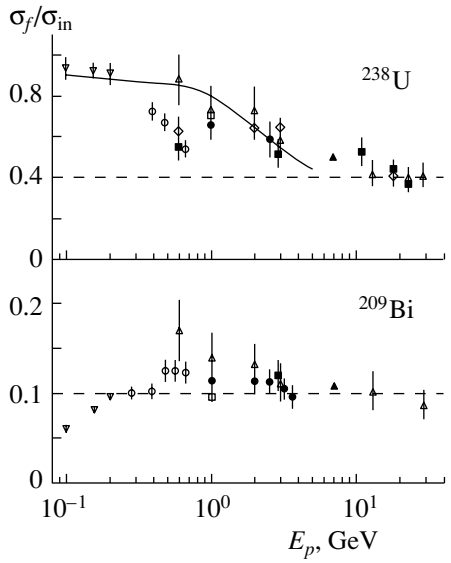

Fig. 5. Ratio of the fission cross section to the total inelastic-interaction cross section for ^{209}Bi and ^{238}U in the region of proton energies above 0.1 GeV: (•) our present data and (solid curve) results of the calculations; the remaining symbols have the same meaning as in Fig. 3.

For collisions of protons with ^{209}Bi and ^{238}U nuclei, Fig. 5 displays the energy dependences of the ratios of the fission cross sections to cross sections for inelastic interactions. For bismuth, this cross-section ratio is about 10% at proton energies above 0.15 GeV, reaching a maximum of about 12% in the region 0.6–2.0 GeV. For uranium, the fission cross section dominates the cross section for inelastic interaction up to an energy of 1.0 GeV. As the energy grows further, the cross-section ratio in question tends to 40%. The calculation predicts approximately the same value of the cross-section ratio $\sigma_f/\sigma_{\text{inel}}$ for other actinide nuclei.

In the measurements performed in a 1.0-GeV deuteron beam, only the relative probabilities of nuclear fission were determined for want of data on the number of beam particles incident on the target throughout the irradiation time. For ^{209}Bi, ^{232}Th, ^{238}U, and ^{237}Np, the resulting numbers of nuclear-fission events per 1 mg of target matter were 803 ± 90, 3622 ± 360, 4410 ± 440, and 4429 ± 440, respectively. For the nuclear species in question, the relative fission probabilities determined from these values are in the ratio 1 : 5.04 : 6.28 : 6.29. In the literature, there are virtually no data on nuclear fission induced by deuterons of energy in the range being investigated. For ^{238}U fission induced by 1.0-GeV deuterons, the calculations performed in [29] yielded the cross section of 1540 mb. If this value is used to normalize our experimental data, the cross section for ^{232}Th fission will be 1236 ± 173 mb, which is in good agreement with the result from [14] (1350 ± 135 mb).

6. CONCLUSION

New data on the cross sections for the proton- and deuteron-induced fission of ^{209}Bi, ^{232}Th, ^{235}U, ^{238}U, and ^{237}Np have been obtained in the energy range 1.0–3.7 GeV. The results are in good agreement with experimental data from [6–17]. The cross-section values calculated on the basis of the theoretical model developed at JINR [22–25, 29] also reproduce satisfactorily our experimental results. An analysis of the character of the energy dependence of the nuclear-fission cross section at proton energies above 0.1 GeV has revealed that, for ^{209}Bi, the ratio of the fission cross section to the cross section for inelastic interaction reaches a maximum of about 12% in the energy range 0.6–2.0 GeV and tends to a constant value of about 10% as the energy is increased further. With increasing proton energy, the fission cross section for actinide nuclei decreases, approaching a level of about 40% of the inelastic interaction cross section at $E_p \sim 10$ GeV.

REFERENCES

1. V. P. Eismont, A. I. Obukhov, A. V. Prokofyev, and A. N. Smirnov, in *Proceedings of the 2nd International Conference on Accelerator-Driven Transmutation Technologies and Applications, Kalmar, Sweden, 1996,* p. 592.
2. H. Conde, V. P. Eismont, K. Elmgren, *et al.*, in *Proceedings of the 2nd International Conference on*

Accelerator-Driven Transmutation Technologies and Applications, Kalmar, Sweden, 1996, p. 599.
3. V. P. Eismont, A. V. Prokofyev, A. N. Smirnov, *et al.*, in *Proceedings of the 9th International Conference on Emerging Nuclear Energy Systems, Tel-Aviv, Israel, 1998,* p. 753.
4. A. V. Prokofiev, Uppsala Univ. Report UU-NF 01#4 (2001).
5. A. I. Obukhov, Fiz. Élem. Chastits At. Yadra **32**, 319 (2001) [Phys. Part. Nucl. **32**, 162 (2001)].
6. V. A. Kon'shin, E. S. Matusevich, and V. I. Regushevskiĭ, Yad. Fiz. **2**, 682 (1965) [Sov. J. Nucl. Phys. **2**, 489 (1966)].
7. V. A. Kon'shin, E. S. Matusevich, and V. I. Regushevskiĭ, Yad. Fiz. **4**, 97 (1966) [Sov. J. Nucl. Phys. **4**, 69 (1967)].
8. G. Remy, J. Ralarosy, R. Stein, *et al.*, Nucl. Phys. A **163**, 583 (1971).
9. R. Brandt, F. Carbonara, E. Cieslak, *et al.*, Rev. Phys. Appl. **7**, 243 (1972).
10. V. S. Bychenkov, M. F. Lomanov, A. I. Obukhov, *et al.*, Preprint ITÉF-965 (Institute of Theoretical and Experimental Physics, Moscow, 1972).
11. O. E. Shigaev, V. S. Bychenkov, M. F. Lomanov, *et al.*, Preprint RI-17 (Leningrad, 1973).
12. J. Hudis and S. Katcoff, Phys. Rev. C **13**, 1961 (1976).
13. B. A. Bochagov, V. S. Bychenkov, V. D. Dmitriev, *et al.*, Yad. Fiz. **28**, 572 (1978) [Sov. J. Nucl. Phys. **28**, 291 (1978)].
14. F. Saint-Laurent, M. Conjeaud, R. Dayras, *et al.*, in *Proceedings of the International Symposium on Nuclear Fission and Related Collective Phenomena and Properties of Heavy Nuclei*, Lect. Notes Phys. **158**, 354 (1982).
15. M. Debeauvais, J. Tripier, and S. Jokic, in *Proceedings of the 9th International Conference on Solid State Nuclear Track Detectors, Neuherburg/Munich, 1978,* Vol. 2, p. 1179.
16. L. A. Vaishnene, L. N. Andronenko, G. G. Kovshevny, *et al.*, Z. Phys. A **302**, 143 (1981).
17. H. A. Khan and N. A. Khan, Phys. Rev. C **29**, 2199 (1984).
18. T. Fukahori and S. Pearlstein, in *Proceedings of the Meeting on Intermediate Energy Nuclear Data for Applications*, INDC(NDS)-245 (IAEA, Vienna, 1991), p. 93.
19. V. A. Nikolaev, B. M. Aleksandrov, V. S. Vedeneev, and A. S. Krivokhatskiĭ, Prib. Tekh. Éksp., No. 4, 57 (1978).
20. A. M. Marennyĭ, *Dielectric Tracking Detectors in Radiophysical and Radiobiological Experiment* (Énergoizdat, Moscow, 1978).
21. V. S. Barashenkov and A. Polanski, JINR Commun. E2-94-17 (Dubna, 1994).
22. V. S. Barashenkov and V. D. Toneev, *Interaction of High-Energy Particles and Nuclei with Nuclei* (Atomizdat, Moscow, 1972).
23. V. S. Barashenkov *et al.*, Nucl. Phys. A **206**, 131 (1973).
24. V. S. Barashenkov *et al.*, Nucl. Phys. A **222**, 204 (1974).
25. V. S. Barashenkov and S. Yu. Shmakov, JINR Commun. E2-12902 (Dubna, 1979).
26. A. G. W. Cameron, Can. J. Phys. **35**, 1021 (1956).
27. P. W. Lisowski, A. Gavron, W. E. Parker, *et al.*, in *Proceedings of the Meeting on Neutron Cross Sections Standards for the Energy Region above 20 MeV, Uppsala, Sweden, 1991,* OECD/NEA Report NEANDC-305"U," p. 177.
28. P. W. Lisowski, J. L. Ullmann, S. J. Balestrini, *et al.*, in *Proceedings of the International Conference on Nuclear Data for Science and Technology, Mito, Japan, 1988,* p. 97.
29. V. S. Barashenkov *et al.*, Preprint No. R2-85-124, OIYaI (Joint Inst. for Nuclear Research, Dubna, 1985).

Translated by A. Isaakyan

Physics of Atomic Nuclei, Vol. 65, No. 8, 2002, pp. 1390–1402. Translated from Yadernaya Fizika, Vol. 65, No. 8, 2002, pp. 1424–1437.

NUCLEI
Theory

Decay and Fission of Oriented Nuclei

S. G. Kadmensky

Voronezh State University, Universitetskaya pl. 1, Voronezh, 394693 Russia

Received April 4, 2001

Abstract—The angular distributions of fragments originating from the binary decay of oriented spherical and deformed nuclei are investigated with allowance for correct transformation properties of wave functions under time inversion. It is shown that, as in the case of protonic decay, the adiabatic approximation for collective rotational degrees of freedom of the systems under investigation is inapplicable in describing the angular distributions of fragments of the deep-subbarrier alpha and cluster decays of nuclei. It is demonstrated that this approximation is justified in describing spontaneous and induced low-energy nuclear fission. The dependence of partial fission widths on the orientation of intrinsic axes, spins, and projections of spins and relative orbital angular momenta of fission fragments is analyzed by using the formalism of the unified theory of nuclear reactions and the theory of open Fermi systems. It is shown that the adiabatic approximation leads to the coherent interference between the wave functions for the relative motion of fragments, whereby the universal angular distributions of fission fragments of oriented nuclei is formed. Deviations from the A. Bohr formula are investigated for these distributions.

1. INTRODUCTION

A number of studies [1–5] based on either the use of the R-matrix theory of nuclear reactions [6] or the non-R-matrix versions of the theory of nuclear decays [4, 7] were devoted to theoretically describing the angular distributions of alpha particles emitted by oriented spherical and deformed nuclei. A method for calculating the angular distributions of fragments originating from the fission of oriented and polarized nuclei was proposed in [8–14] on the basis of the A. Bohr concept [8] of the role of transition states in the nuclear-fission process. In [15, 16], the angular distributions of protons emitted by oriented spherical and deformed nuclei were investigated on the basis of the multiparticle theory of protonic decay [17–19], and the possibility of using the adiabatic and the semiclassical approximation to describe the angular distributions of protons was analyzed in [16] for the case of deformed decaying nuclei. However, the angular distributions of clusters emitted by oriented nuclei undergoing cluster decays have not yet been explored.

A general approach to describing the structure of nuclei and nuclear reactions was formulated in [20] on the basis of the method of nonorthogonal variations. This approach is so general that the authors of [20] also employed it to describe some properties of such a complicated phenomenon as nuclear fission. With the aid of the method of projection operators and the theory of open Fermi systems, the approach proposed in [20] was generalized in [21] in order to take more consistently into account the effects of antisymmetrization and fragmentation in nuclear reactions and was used to describe the decay widths of nuclei.

On the basis of a development of the methods proposed in [16, 20, 21], we analyze here the angular distributions of fragments originating from the alpha and cluster decays and from the fission of oriented nuclei. In this analysis, special attention is given to investigating the problem of oriented-nucleus fission; in doing this, we explicitly consider the coherent properties of this process on the basis of the adiabatic approximation, using directly the quantum-mechanical theory of resonance nuclear reactions [6, 20, 21] and the formalism of fission widths.

2. ANGULAR DISTRIBUTIONS OF FRAGMENTS ORIGINATING FROM THE DECAY AND FISSION OF ORIENTED NUCLEI IN THE LABORATORY FRAME

In order to describe the protonic, alpha, and cluster decays of nuclei and their binary fission, we consider, in the c.m. frame, the general case of the spontaneous decay of an isolated quasistationary state of a parent nucleus having an atomic weight A and a charge Z into two fragments whose atomic weights are A_1 and $A_2 = A - A_1$ ($A_1 \geq A_2$) and whose charges are Z_1 and $Z_2 = Z - Z_1$. The wave function ψ_σ^{JM} describing the decaying parent-nucleus state characterized by the spin J; its projection M onto the Z axis in

1063-7788/02/6508-1390$22.00

the laboratory frame; and other quantum numbers σ, including the parity π, satisfies the Schrödinger equation

$$H_A\psi_\sigma^{JM} = E_\sigma^J\psi_\sigma^{JM}, \quad (1)$$

where H_A is the Hamiltonian for the A nucleus in the c.m. frame, $E_\sigma^J = (\mathrm{Re}E_\sigma^J - i\Gamma_\sigma^J/2)$ is the complex energy, and Γ_σ^J is the total decay width of the nucleus A (it is equal to the sum of the partial decay widths through all open decay channels, including, in general, protonic, alpha-particle, cluster, fission, radiative, and β-decay channels).

That the state of the decaying nucleus is quasistationary and isolated means that the total decay width Γ_σ^J of this state is much less than the energies Q_c of the relative motion of decay fragments in all open channels and than the energy spacings between the neighboring levels of the nucleus characterized by fixed values of the spin J and parity π. Among all channels of nuclear decay, we single out those—we label them with the indices $cIl = \sigma_1 J_1 \sigma_2 J_2 Il$—that correspond to the emergence of the A_1 and A_2 fragments in the states specified by the wave functions $\psi_{\sigma_1}^{J_1M_1}$ and $\psi_{\sigma_2}^{J_2M_2}$, the channel spin I, and the relative orbital angular momentum l. We denote by $\Gamma_{\sigma cIl}^J$ the partial width of the A nucleus with respect to the decay through such a channel. The decay-fragment wave functions $\psi_{\sigma_1}^{J_1M_1}$ and $\psi_{\sigma_2}^{J_2M_2}$ satisfy the Schrödinger Eq. (1), where the Hamiltonian H_A is replaced by the Hamiltonians H_{A_1} and H_{A_2} and the energy E_σ^J is replaced by the energies $E_{\sigma_1}^{J_1}$ and $E_{\sigma_2}^{J_2}$ for the first and the second fragment, respectively. We introduce the energy Q_c, the velocity v_c, and the wave vector k_c of the relative motion of the fragments. We have

$$Q_c = \mathrm{Re}E_\sigma^J - \mathrm{Re}E_{\sigma_1}^{J_1} - \mathrm{Re}E_{\sigma_2}^{J_2} = \frac{\hbar^2k_c^2}{2m} = \frac{mv_c^2}{2}, \quad (2)$$

where $m = (M_{A_1}M_{A_2})/M_A$ is the reduced mass of the fragments. The decay-fragment wave functions $\psi_{\sigma_1}^{J_1M_1}$ and $\psi_{\sigma_2}^{J_2M_2}$ are constructed in such a way that they have correct transformation properties under time inversion [6]; this means that, under the action of the time-inversion operator T, these functions transform as

$$T\psi_{\sigma_1}^{J_1M_1} = (-1)^{J_1+M_1}\psi_{\sigma_1}^{J_1-M_1}. \quad (3)$$

Following [6], we define the orthonormalized channel function U_{cIl}^{JM} possessing correct transformation properties under time inversion as

$$U_{cIl}^{JM} = \left\{\left\{\psi_{\sigma_1}^{J_1M_1}\psi_{\sigma_2}^{J_2M_2}\right\}_{IM_I} i^l Y_{lm_l}(\Omega)\right\}_{JM}, \quad (4)$$

where braces denote the vector coupling of the angular momenta and where the spherical harmonic $Y_{lm_l}(\Omega)$, which corresponds to the relative orbital motion of the decay fragments, depends on the solid angle Ω specifying the direction of the radius vector $\mathbf{R} = \mathbf{R}_{A_2} - \mathbf{R}_{A_1}$ in the laboratory frame, $\mathbf{R}_{A_1}$ and $\mathbf{R}_{A_2}$ being the coordinates of the centers of mass of these fragments. In the external region $R \geq R_{cl}$, where R_{cl} is a point that occurs to the right of the maximum of the potential barrier for the decay fragments (in this region, the interaction of the fragments is determined exclusively by the Coulomb potential $V_0^{\mathrm{C}}(R) = Z_1Z_2e^2/R$ of the respective pointlike charge), the parent-nucleus wave function ψ_σ^{JM} satisfies the Gamow condition [7]

$$\psi_\sigma^{JM} = \sum_{cIl}\hat{A}\left\{U_{cIl}^{JM}\frac{1}{R}(G_{cl}(R) + iF_{cl}(R))\sqrt{\Gamma_{\sigma cIl}^J/\hbar v_c}e^{i\delta_{cl}^{\mathrm{pot}}}\right\}, \quad (5)$$

where $\hat{A}$ is the antisymmetrization operator and $F_{cl}(R)$ and $G_{cl}(R)$ are, respectively, the regular and the irregular radial Coulomb function. For $R \to \infty$, the asymptotic expressions for these functions are

$$F_{cl}(R) \to \sin\left(k_cR - l\pi/2 + \delta_{cl}^{\mathrm{C}}\right), \quad (6)$$
$$G_{cl}(R) \to \cos\left(k_cR - l\pi/2 + \delta_{cl}^{\mathrm{C}}\right),$$

where δ_{cl}^{C} and δ_{cl}^{pot} are the Coulomb and the nuclear phase shift for the potential elastic scattering of the fragments on each other. When used to determine the wave functions possessing correct transformation properties under time inversion, the partial-width amplitude $\sqrt{\Gamma_{\sigma cjl}^J}$ is real-valued and is independent of the projection M of the parent-nucleus spin [6]. By virtue of the law of parity conservation in the decay process, the quantity $\sqrt{\Gamma_{\sigma cIl}^J}$ does not vanish under the condition

$$(-1)^l = \pi\pi_1\pi_2, \quad (7)$$

where π, π_1, and π_2 are the parities of the parent-nucleus and decay-fragment states. We now consider the multiparticle density j_σ^{JM} of the decay-fragment flux in the direction of the radius vector $\mathbf{R}$ for $R \to \infty$:

$$j_\sigma^{JM} = \frac{i\hbar}{2m}\left[\psi_\sigma^{JM}\frac{d}{dR}(\psi_\sigma^{JM})^* - (\psi_\sigma^{JM})^*\frac{d}{dR}\psi_\sigma^{JM}\right]. \quad (8)$$

Let us perform integration in (8) over all coordinates of the parent nucleus, with the exception of the coordinate $\mathbf{R}$, by using the orthonormality of the decay-fragment wave functions and the asymptotic representation (5). For the density $j_\sigma^{JM}(\mathbf{R})$ of the flux of light decay fragments A_2 in the direction specified by the solid angle Ω, we then obtain

$$j_\sigma^{JM}(\mathbf{R}) = \frac{1}{R^2}\sum_c \sum_{M_1M_2}\left|\sum_{IlM_Im_l} C^{IM_I}_{J_1J_2M_1M_2} C^{JM}_{IlM_Im_l} Y_{lm_l}(\Omega)\sqrt{\frac{1}{\hbar}\Gamma^J_{\sigma cIl}}\, e^{i\bar{\delta}_{cl}}\right|^2, \quad (9)$$

where the phase shift $\bar{\delta}_{cl}$ is given by $\bar{\delta}_{cl} = (\delta^{\mathrm{C}}_{cl} + \delta^{\mathrm{pot}}_{cl})$. For the density of the flux of heavy decay fragments A_1, we have a formula of the type in (9), where $\mathbf{R}$ must be replaced by $(-\mathbf{R})$. As will be shown below, expression (9) is invariant under this replacement; therefore, the heavy-fragment-flux density is also given by (9).

Performing summation in (9) with the aid of the orthonormality properties of the Clebsch–Gordan coefficients $C^{IM_I}_{J_1J_2M_1M_2}$, we obtain

$$j_\sigma^{JM}(\mathbf{R}) = \frac{1}{R^2}\sum_c \sum_{I=|J_1-J_2|}^{J_1+J_2}\sum_{M_I}\left|\sum_{lm_l} C^{JM}_{IlM_Im_l} Y_{lm_l}(\Omega)\sqrt{\frac{1}{\hbar}\Gamma^J_{\sigma cIl}}\, e^{i\bar{\delta}_{cl}}\right|^2. \quad (10)$$

Averaging the flux density (10) over the projections M of the parent-nucleus spin J and using the distribution function $S(M)$ satisfying the condition $\sum_M S(M) = 1$, we arrive at

$$j_\sigma^J(\mathbf{R}) = \sum_M S(M) j_\sigma^{JM}(\mathbf{R}). \quad (11)$$

Suppose that decay fragments are recorded by a detector that is arranged orthogonally to the radius vector $\mathbf{R}$, the detector area being $R^2 d\Omega$, and which fixes only the mass A_2 of a fragment, its charge Z_2, and the energy Q_c. The number dN^J_σ of decay fragments A_2 that is recorded by this detector per unit time is then given by

$$dN^J_\sigma(\Omega) = \sum_M S(M) j_\sigma^{JM}(\mathbf{R}) R^2 d(\Omega). \quad (12)$$

Performing integration in (12) over all directions of the radius vector $\mathbf{R}$ by using formula (10), we find, as might have been expected, that the total number $N^J_\sigma(\Omega)$ of A_2 fragments emitted by the parent nucleus per unit time is

$$N^J_\sigma = \frac{1}{\hbar}\Gamma^J_\sigma = \frac{1}{\hbar}\sum_c \Gamma^J_{\sigma c} = \frac{1}{\hbar}\sum_{cIl}\Gamma^J_{\sigma cIl}. \quad (13)$$

The total angular distribution $dP^J_\sigma(\Omega)/d\Omega$ of decay fragments that is normalized to unity can be represented as

$$\frac{dP^J_\sigma(\Omega)}{d\Omega} = \frac{dN^J_\sigma(\Omega)}{d\Omega}\frac{1}{N^J_\sigma} = \sum_c \frac{\Gamma^J_{\sigma c}}{\Gamma^J_\sigma}\frac{dP^J_{\sigma c}(\Omega)}{d\Omega}, \quad (14)$$

where the normalized (to unity) angular distribution $dP^J_{\sigma c}(\Omega)/d\Omega$ of decay fragments in the c channel then has the form

$$\frac{dP^J_{\sigma c}(\Omega)}{d\Omega} = \frac{1}{\Gamma^J_{\sigma c}}\sum_M S(M) \quad (15)$$

$$\times \sum_{I=|J_1-J_2|}^{J_1+J_2}\sum_{M_I}\left|\sum_{lm_l} C^{JM}_{IlM_Im_l} Y_{lm_l}(\Omega) e^{i\bar{\delta}_{cl}}\sqrt{\Gamma^J_{\sigma cIl}}\right|^2.$$

As can be seen from (14), there is no interference between different decay channels in the total angular distributions, so that the angular distributions for the channels are merely summed, the relative weights of these channels being taken into account in this summation. Formula (15) can also be used to describe the angular distributions of fragments in the case where the detectors recording fragments have a poor energy resolution that gives no way to separate specific decay channels c in energies Q_c.

By using the multiplication theorem for spherical harmonics [9],

$$Y_{lm}(\Omega)Y^*_{l'm}(\Omega) = \frac{(-1)^m}{4\pi} \times \sum_L \sqrt{(2l+1)(2l'+1)} C^{L0}_{ll'00} C^{L0}_{ll'm-m} P_L(\cos\theta),$$

where $P_L(\cos\theta)$ is a Legendre polynomial, and the formalism of Racah coefficients [9], we can recast expression (15) into the form

$$\frac{dP^J_{\sigma c}(\Omega)}{d\Omega} = \frac{1}{4\pi}\frac{1}{\Gamma^J_{\sigma c}}\sum_M S(M) \quad (16)$$
$$\times \sum_{ILll'}\sqrt{\Gamma^J_{\sigma cIl}}\sqrt{\Gamma^J_{\sigma cIl'}}(-1)^{J-I} C^{JM}_{JLM0} C^{L0}_{ll'00}$$
$$\times \sqrt{(2l+1)(2l'+1)(2L+1)(2J+1)}$$
$$\times \cos(\bar{\delta}_{cl} - \bar{\delta}_{cl'}) W(lJl'J; Il) P_L(\cos\theta),$$

where $W(lJl'J; Il)$ are Racah coefficients.

From the fact that the orbital angular momenta l and l' in (15) have the same parity by virtue of condition (7) and from the properties of the Clebsch–Gordan coefficient $C^{L0}_{ll'00}$, it follows that L takes only even values, so that the angular distribution (16) is symmetric with respect to the angle $\theta = \pi/2$; that is, it does not change upon the substitution of $(\pi - \theta)$ for θ. The $L = 0$ term in the sum in (16) has the value of $1/4\pi$, which is consistent with the normalization of the angular distribution (15) to unity. For

the parent-nucleus spins of $J = 0$ and $J = 1/2$, the Clebsch–Gordan coefficient C^{JM}_{JLM0} does not vanish only at $L = 0$; therefore, the angular distribution (15) becomes isotropic and takes the value of $1/4\pi$.

If the parent nucleus is not oriented, all the projections M of its spin J are equiprobable, so that the distribution function has the form $S(M) = 1/(2J + 1)$. In this case, the angular distribution (15) again becomes isotropic and equal to $1/4\pi$.

But if the parent nucleus is completely oriented at ultralow temperatures by a strong external magnetic field directed along the Z axis in the laboratory frame, the distribution function $S(M)$ is $S(M) = \delta_{M,J}$ or $S(M) = \delta_{M,-J}$ at, respectively, a positive or a negative value of the gyromagnetic ratio for the parent nucleus. Since the Clebsch–Gordan coefficient C^{JM}_{JLM0}, which specifies the M dependence of angular distribution (16), possesses the property $C^{J-M}_{JL-M0} = C^{JM}_{JLM0}$ at even values of L, the angular distribution (16) for an oriented parent nucleus is independent of the sign of the gyromagnetic ratio and can be represented in the form (16) with the substitution of $\delta_{M,J}$ for $S(M)$.

Formulas (14)–(16) are of a universal character and are valid for decay and fission processes involving both spherical and deformed parent nuclei and daughter nuclear fragments, the shapes of the daughter nuclei not being necessarily coincident with the shapes of the parent nuclei. The structure of the above nuclei affects the angular distributions (14)–(16) through specific values of the partial-width amplitudes. Formulas of the type in (16) were previously used in [1–5] to describe the angular distributions of alpha particles emitted by oriented alpha-decay spherical and deformed nuclei. In a number of studies—for example, in [4]—the phase-shift combination $(\bar{\delta}_{cl} - \bar{\delta}_{cl'})$ in (16) was replaced by the combination $(\bar{\delta}_{cl} - l\pi/2 - \bar{\delta}_{cl'} + l'\pi/2)$, which arises if, in formula (5), one substitutes, for the channel functions U^{JM}_{cIl} (4), the channel functions differing from those in (4) by the absence of the factor i^l and disregards, in calculating the partial widths, the requirements associated with time inversion.

3. STRUCTURE OF WAVE FUNCTIONS, AND PARTIAL WIDTHS WITH RESPECT TO THE DECAY AND FISSION OF NUCLEI

In general, the wave function (5) for a decaying nucleus can be represented in the form [7, 21]

$$\psi^{JM}_{\sigma} = \left(\psi^{JM}_{\sigma}\right)_{\rm sh} + \left(\psi^{JM}_{\sigma}\right)_{\rm clust}, \qquad (17)$$

where the function $\left(\psi^{JM}_{\sigma}\right)_{\rm sh}$ differs from zero in that region of the parent nucleus where the decay fragments have not yet been formed and is constructed on the basis of the multiparticle shell model with allowance for normal and superfluid nucleon–nucleon correlations and for both rotational and collective modes of motion that are associated with variations in nuclear-deformation parameters, for example, in describing the nuclear-fission process. The cluster wave-function component $\left(\psi^{JM}_{\sigma}\right)_{\rm clust}$ in (17) corresponds to the fully formed nuclear-decay fragments and can be written as [21]

$$\left(\psi^{JM}_{\sigma}\right)_{\rm clust} = \sum_{cIl} \frac{\hbar^2 k_c}{2m_c} U^{JM}_{cIl} \qquad (18)$$
$$\times \int R' dR' \left[g_{cl}(R_>) + i f_{cl}(R_>)\right]$$
$$\times f_{cl}(R_<) \left\langle U^{JM}_{cIl} \left| V_{A_1A_2} \right| \left(\psi^{JM}_{\sigma}\right)_{\rm sh} \right\rangle,$$

where the operators $\hat{A}$ of antisymmetrization between decay fragments are omitted to simplify the presentation, $R_>$ ($R_<$) is the larger (smaller) value of R and R', and $V_{A_1A_2}$ is the multiparticle potential of the interaction between the fragments. The functions $f_{cl}(R)$ and $g_{cl}(R)$ are, respectively, the regular and the irregular solution to the radial Schrödinger equation describing the relative motion of the fragments with the energy Q_c. In combinations of the form $\hat{A}\left\{U^{JM}_{cIl} f_{cl}(R)/R\right\}$, these functions are orthogonal to the basis shell-model functions used in constructing the wave functions $(\psi^{JM}_{\sigma})_{\rm sh}$; for $R \to \infty$, their asymptotic expressions are

$$f_{cl}(R) \to \sin(k_c R - l\pi/2 + \delta^{\rm C}_{cl} + \delta^{\rm pot}_{cl}), \qquad (19)$$
$$g_{cl}(R) \to \cos(k_c R - l\pi/2 + \delta^{\rm C}_{cl} + \delta^{\rm pot}_{cl}).$$

In the external region $R \geq R_{cl}$, the function $\left(\psi^{JM}_{\sigma}\right)_{\rm clust}$ then has the behavior corresponding to the correct asymptotic expression (5) for the function $\left(\psi^{JM}_{\sigma}\right)$ (17) with the partial-decay-width amplitude given by [21]

$$\sqrt{\Gamma^{J}_{\sigma cIl}} \qquad (20)$$
$$= \sqrt{2\pi} \left\langle \hat{A} \left\{ \frac{\tilde{f}_{cl}(R)}{R} U^{JM}_{cIl} \middle| V_{A_1A_2} \right\} \middle| \left(\psi^{JM}_{\sigma}\right)_{\rm sh} \right\rangle,$$

where the function $\tilde{f}_{cl}(R)$ differs from the functions $f_{cl}(R)$ (19) by the fact that it is normalized to a δ function of energy.

For deep-subbarrier protonic, alpha, and cluster decays, in which case the condition $|F_{cl}(R)| \ll |G_{cl}(R)|$, under which the process is of a subbarrier character, is satisfied for $R > R_{cl}$, we can neglect the

function $F_{cl}(R)$ and the potential phase shift $\delta_{\rm cl}^{\rm pot}$ in formula (5) and represent the asymptotic condition (5) in the form

$$\left(\psi_\sigma^{JM}\right)^0 = \sum_{cIl} \hat{A}\left\{U_{cIl}^{JM}\frac{G_{cl}(R)}{R}\sqrt{\Gamma_{\sigma cIl}^J/\hbar\upsilon_c}\right\}. \tag{21}$$

Over the entire internal region $R \le R_{cl}$, the quasistationary wave function ψ_σ^{JM} for the parent nucleus then reduces to the time-independent function $\left(\psi_\sigma^{JM}\right)^0$, which obeys the Schrödinger Eq. (1) with the real-valued energy $\mathrm{Re}E_\sigma^J$ and satisfies the boundary condition (21).

In this case, the set of functions $\left(\psi_\sigma^{JM}\right)_0$ can be used in the internal region $R \le R_{cl}$ as the R-matrix basis of functions X_σ^{JM} [6], for which the boundary condition (21) coincides with the natural boundary condition requiring that the shift of the resonance energy in the S matrix with respect to the energy $\mathrm{Re}E_\sigma^J$ be zero and that the phase shift $\delta_{cl}^{\rm pot} = -\arctan(F_{cl}(R_{cl})/G_{cl}(R_{cl}))$ for potential nuclear scattering at $|F_{cl}(R_{cl})| \ll |G_{cl}(R_{cl})|$ be much less than unity. As was shown by considering the examples of deep-subbarrier protonic [17], alpha [7], and cluster [22] decays of nuclei, the amplitude of the partial-decay width can then be represented in a form that is different from that in (20), but which is equivalent to it and which can be used in concrete calculations; specifically,

$$\sqrt{\Gamma_{\sigma cIl}^J} = \sqrt{2\pi}\left\langle \hat{A}\left\{\frac{\tilde{F}_{cl}(R)}{R}U_{cIl}^{JM}\middle|(V_{A_1A_2} - V_0^{\rm C}(R))\right\}\middle|\left(\psi_\sigma^{JM}\right)^0\right\rangle, \tag{22}$$

where $\tilde{F}_{cl}(R)$ is the regular radial Coulomb function normalized to a δ function of energy.

It was shown in [17] that, for deep-subbarrier protonic decay, the main contribution to the partial-width amplitude (22) comes from the shell-model component $\left(\psi_\sigma^{JM}\right)_{\rm sh}$ of the wave function (17) for the decaying nucleus. As to the case of deep-subbarrier alpha and cluster decays, it was shown in [7, 22] that the cluster component $\left(\psi_\sigma^{JM}\right)_{\rm clust}$ of the wave function (17) makes a dominant contribution to the amplitude in (22). For this reason, it is more appropriate to use formula (20) for alpha and cluster decays.

In the case of an isolated quasistationary state of a decaying nucleus, one can also use, for the amplitude of the partial-decay width, the R-matrix formula, which has the form [6]

$$\sqrt{\Gamma_{\sigma cIl}^J} = \sqrt{\frac{\hbar^2 k_c}{2m_c}P_{cl}} \times \left\langle \hat{A}\left\{U_{cIl}^{JM}R\delta(R-R_{cl})\right\}\middle|X_\sigma^{JM}\right\rangle, \tag{23}$$

where $P_{cl} = \left[F_{cl}^2(R_{cl}) + G_{cl}^2(R_{cl})\right]^{-1}$ is the penetrability factor and the function X_σ^{JM} is the R-matrix basis time-independent wave function for the parent nucleus in the internal region $R \le R_{cl}$. It obeys the Schrödinger Eq. (1) with the real energy E_σ^J and, at $R \approx R_{cl}$, satisfies the natural boundary condition obtained by replacing the function $[G_{cl}(R) + iF_{cl}(R)]\,e^{i\delta_{cl}^{pot}}$ in (5) by its modulus $|G_{cl}(R) + iF_{cl}(R)|$.

If a representation similar to that in (17) is used for the function X_σ^{JM}, it can be seen that, in order to find the partial width (23), one must know the cluster component $\left(X_\sigma^{JM}\right)_{\rm clust}$ of this function. Although formula (23) is equivalent to formulas (20) and (22), it is therefore preferable to use (20) and (22) to describe nuclear decay, because, in these formulas, there is no problem of defining specific values of the channel radii R_{cl}. This is especially important in the case of deformed decaying nuclei.

4. ADIABATIC APPROXIMATION AND DESCRIPTION OF ALPHA AND CLUSTER DECAYS OF DEFORMED NUCLEI

In order to understand the structure of the angular distributions of protons in the protonic decay of oriented deformed nuclei, use was made in [16] of the adiabatic approximation [9]. This approximation is widely employed to describe collective modes of motion in spherical and deformed nuclei in their interior region and is based on the fact that the characteristic times of nucleon motion in nuclei are much shorter than the characteristic times associated with the above collective modes. This means that the characteristic energy spacing ΔE_N between single-nucleon levels having identical values of good quantum numbers is considerably greater than the characteristic energy spacing between neighboring collective rotational and vibrational levels of a nucleus. The strong-coupling model and the potential describing the deformation of nuclei are constructed in the adiabatic approximation [9].

Let us consider the possibility of using the adiabatic approximation to describe the widths and the angular distributions of decay fragments of oriented deformed nuclei. Our consideration will be restricted

to the case where fragments arising from the decay of an axisymmetric nucleus also have axially symmetric shapes. This means that, in the scission of the parent nucleus into fragments, torsion [23], which is a form of motion where the emerging fragments can acquire nonaxial shapes with nonzero values of the γ deformation, is insignificant. For the adiabatic approximation to be applicable, it is then required that the following conditions be satisfied.

(i) It is necessary that, up to the instant of the scission of a nucleus into two fragments A_1 and A_2, the shell-model component $\left(\psi_\sigma^{JM}\right)_{\rm sh}$ of the decaying-nucleus wave function (17) have fixed values of the Euler angles $\{\alpha, \beta, \gamma\} = \omega$ specifying the orientation of the intrinsic coordinate axes of the nucleus with respect to the axes of the laboratory frame. It was indicated in [8] that, in the case of fission, this condition is satisfied if the time it takes for the nucleus to go over from a compact bound state at the saddle point to the state corresponding to its scission into two fragments is much shorter than the characteristic times of nuclear rotations determining time variations of the Euler angles ω.

(ii) At all attainable values of the fragment spin J_1 for a fixed value of its projection K_1 onto the intrinsic fragment symmetry axis, the excitation energies $\left(E_{K_1}^{J_1}\right)^*$ of the levels of the rotational band of the heavy fragment A_1 must be negligible in relation to the kinetic energy $E_c^{\rm kin}$ of the relative motion of the fragments A_1 and A_2 for the observed channels c over the entire region where these fragments exist. The analogous condition must be satisfied for the second decay fragment A_2 as well if this fragment is a sufficiently heavy axisymmetric deformed nucleus. In this case, we can neglect the effect of the energies $(E_{K_1}^{J_1})^*$ and $(E_{K_2}^{J_2})^*$ on the radial wave functions $f_{cl}(R)$ and $g_{cl}(R)$ for the relative motion of the fragments and, hence, on the partial widths (20) and the potential phase shifts $\bar{\delta}_{cl}$.

(iii) It is necessary that detectors recording decay fragments not fix the fragment spins J_1 and J_2, and, at the same time, have a poor energy resolution ΔE_d [$(\Delta E_d \gg (E_{K_1}^{J_1})^*(E_{K_2}^{J_2})^*)$], which gives no way to separate fragments in their spins J_1 and J_2 if the energy scale is used. In this case, one can observe the interference between the wave functions for the relative motion of the fragments for the decay channels c, with the result that there can arise coherent effects in the fragment angular distributions.

The angular distributions of protons emitted by oriented spherical and deformed nuclei undergoing protonic decay were analyzed in [15, 16], and it was demonstrated in [16] that, because of the deep-subbarrier character of protonic decay, the second condition is not realized in this case; therefore, the adiabatic approximation is not applicable to describing the above angular distributions.

The results obtained in [16] for protonic decay are generalized to the case of the deep-subbarrier alpha and cluster decays of spherical and deformed nuclei, where the adiabatic approximation is also inapplicable. In order to describe the angular distributions of alpha particles and clusters emitted by oriented spherical and deformed nuclei, we can therefore use formulas (14)–(16), which were obtained above. It should be noted that these formulas remain in force if there are distinctions between the shapes of the parent and daughter nuclei; this is characteristic of cluster nuclear decays, which are considered here.

5. ADIABATIC APPROXIMATION FOR NUCLEAR FISSION

The spontaneous and low-energy induced fission of axisymmetric deformed parent nuclei is described on the basis of the mechanism proposed in [8]. This mechanism employs the concept of fission channels or transition states. We will describe these transition states in terms of the wave functions ψ_t^{JM}, which include not only the initial multiparticle shell-model functions $\left(\psi_t^{JM}\right)^0$ specified by the symmetry and deformation parameters of the parent nucleus at the saddle points of the nuclear-deformation potential but also the shell-model wave functions corresponding to different values of the nuclear deformation parameters and describing the evolution of the nucleus from the saddle points to the point of its scission into two fission fragments. If, in (20), the function ψ_t^{JM} is used instead of the nuclear shell-model wave function $\left(\psi_\sigma^{JM}\right)_{\rm sh}$, the partial-fission-width amplitudes $\sqrt{\Gamma_{tcIL}^J}$ can be obtained in considering the evolution of the nucleus from its initial transition state specified by the function $\left(\psi_t^{JM}\right)^0$. If we assume that the functions $\left(\psi_t^{JM}\right)^0$ orthonormalized for different values of the quantum numbers JMt appear with the amplitudes $\alpha_{\sigma t}^J$ in the total shell-model wave function $\left(\psi_\sigma^{JM}\right)_{\rm sh}$ of the parent nucleus, the partial fission width for the fission channel cIl is given by

$$\Gamma_{\sigma cIl}^J = \sum_t \left(\alpha_{\sigma t}^J\right)^2 \Gamma_{tcIl}^J, \qquad (24)$$

where Γ_{tcIl}^J is the partial fission width for the JMt transition state.

In order to simplify the calculations, we go over from the channel function U_{cIl}^{JM} (4) to the channel function U_{cjl}^{JM} that is defined as

$$U_{cjl}^{JM} = \left\{ \psi_{\sigma_1}^{J_1 M_1} \left\{ \psi_{\sigma_2}^{J_2 M_2} Y_{lm_l}(\Omega) \right\}_{jm_j} \right\}_{JM} \cdot i^l \quad (25)$$

and which is related to the channel function U_{cIl}^{JM} (4) by the Racah transformation as [9]

$$U_{cIl}^{JM} = \sum_j \sqrt{(2j+1)(2I+1)} W(J_1 J_2 J l; I j) U_{cjl}^{JM}. \quad (26)$$

The asymptotic expression (5) for the parent-nucleus wave function then remains unchanged upon replacing the sum over I by the sum over j, the channel function U_{cIl}^{JM} by the function U_{cjl}^{JM}, and the partial-width amplitude $\sqrt{\Gamma_{\sigma cIl}^{J}}$ by the amplitude $\sqrt{\Gamma_{\sigma cjl}^{J}}$. In this case, the amplitude $\sqrt{\Gamma_{tK_i cjl}^{J}}$ of the partial width with respect to nuclear decay from the JMt transition state through the channel cjl is given by the formula

$$\sqrt{\Gamma_{tcjl}^{J}} = \sqrt{2\pi} \left\langle \hat{A} \left\{ U_{cjl}^{JM} \frac{\tilde{f}_{lc}(R)}{R} \middle| V_{A_1 A_2} \right\} \middle| \psi_t^{JM} \right\rangle, \quad (27)$$

which follows from (20).

All the above three conditions necessary for the adiabatic approximation to be valid in describing the angular distributions of fission fragments are satisfied, in all probability, for the spontaneous or induced low-energy fission of deformed axisymmetric nuclei.

Prior to considering in detail these conditions, we will dwell upon yet another condition, the fourth one, relevant to the efficiency of the adiabatic approximation in describing the nuclear-fission process. We require that, in all observable fission channels c, the centrifugal potential $V_{cl}^{cf}(R) = \hbar^2 l(l+1)/(2mR^2)$ for the relative motion of fission fragments be much less than the kinetic energy $E_c^{\mathrm{kin}}(\mathbf{R}) = \hbar^2 k_c(\mathbf{R})/(2m)$ of the relative motion of the fragments in the region $R \geq |\mathbf{R}_{scl}|$, where the radius vector $\mathbf{R}_{scl}$ specifies the nonspherical surface of scission of a parent nucleus into two fragments. If this condition is satisfied, we can eliminate the centrifugal potential from the equations for the radial functions $f_{cl}(R)$, thereby making the function $f_{cl}(R)$ and, hence, the partial fission width (27), along with the potential phase shift $\bar{\delta}_{cl}$, independent of the orbital angular momentum l. It is clear that this condition is always satisfied at large values of R, in which case the centrifugal potential $V_{cl}^{cf}(R)$ tends to zero and $E_c^{\mathrm{kin}}(R) \to Q_c$. Therefore, it is necessary to ensure fulfillment of this condition at $R \approx |\mathbf{R}_{scl}|$ in the vicinity of the point of scission of the parent nucleus into fission fragments. The semiclassical estimate $l_m \approx k_c(\mathbf{R}_{scl})d$, where d is the diameter of the neck that arises before the scission of the parent nucleus into fragments, was used in [13] for the maximum value l_m of l. In this case, the ratio of the maximum value of the centrifugal potential $V_{cl}^{cf}(|\mathbf{R}_{scl}|)$ to the kinetic energy $E_c^{\mathrm{kin}}(\mathbf{R}_{scl})$ is equal to $(d/|\mathbf{R}_{scl}|)^2$. If the quantity $|\mathbf{R}_{scl}|$ is estimated at 20 fm and if the neck diameter d is set to 2 fm, this ratio proves to be $(1/100)$, which immediately ensures fulfillment of the fourth condition.

Let us dwell at some length on corollaries from the second condition of applicability of the adiabatic approximation. This condition implies that, at all values of $\mathbf{R}$ corresponding to the region where fission fragments exist, the kinetic energy $E_c^{\mathrm{kin}}(\mathbf{R})$ of the relative motion of these fragments must satisfy the condition $E_c^{\mathrm{kin}}(\mathbf{R}) \gg (E_{K_1}^{J_1})^*, (E_{K_2}^{J_2})^*$; that is, it must be positive and sufficiently large in magnitude. If $E_c^{\mathrm{kin}}(\mathbf{R})$ is expressed through the energy-conservation law as $E_c^{\mathrm{kin}}(\mathbf{R}) = Q_c - V_c^{\mathrm{C}}(\mathbf{R}) - V_c^{\mathrm{nucl}}(\mathbf{R})$, where $V_c^{\mathrm{C}}(\mathbf{R})$ and $V_c^{\mathrm{nucl}}(\mathbf{R})$ are the nonspherical Coulomb and nuclear (with allowance for effects associated with the fragment polarizability) potentials of the interaction of fission fragments, then the second condition means that, at all points $\mathbf{R}$ of the region where the fragments exist, the quantity Q_c exceeds the sum $V_c^{\mathrm{C}}(\mathbf{R}) + V_c^{\mathrm{nucl}}(\mathbf{R})$; that is, the fission process is of the above-barrier character with respect to these potentials. This statement corresponds to a physically clear pattern of fission, where an axisymmetric parent nucleus in the space of the deformation variables $\beta_\lambda (\lambda = 2, 4, ...)$ evolves, undergoing shape variations, up to the instant of the scission of the nucleus into two fragments, in which case the deformation parameter β_2 develops very large values of $(\beta_2 \approx 0, 8)$; in the space of the variables $\mathbf{R}$, they correspond to the above-barrier motion of the fragments.

Before final fragments find their way to detectors recording them, primary fragments arising at the first stage of the fission process undergo rearrangement, deexcite completely via the emission of prompt neutrons and photons, and go over to the ground states or long-lived isomeric states of final fission fragments. Therefore, the above detectors are unable in principle to resolve individual states of the rotational bands of primary fission fragments, so that the third condition of adiabaticity can also be thought to be satisfied for fission.

6. PARTIAL FISSION WIDTHS IN THE ADIABATIC APPROXIMATION

In describing the angular distributions of fragments emitted in the spontaneous fission of oriented nuclei, use is presently made of the A. Bohr formula [8]

$$\frac{dP^J_{JK_i}(\Omega)}{d\Omega} = \frac{2J+1}{8\pi} \times \left[|D^J_{JK_i}(\omega)|^2 + |D^J_{J,-K_i}(\omega)|^2\right]|_{\beta=\theta}, \quad (28)$$

where $D^J_{MK_i}(\omega)$ is a generalized spherical Wigner function depending on the Euler angles $\{\alpha, \beta, \text{and } \gamma\} \equiv \omega$, which characterize the orientation of the parent-nucleus axes with respect to the axes of the laboratory frame; Ω is the solid angle characterizing the direction of the radius vector $\mathbf{R}$ in the laboratory frame (the angles θ and φ appear in the definition of this solid angle); and M and K_i are the projections of the spin J of the parent axisymmetric nucleus onto, respectively, the Z axis in the laboratory frame and the symmetry axis of the parent nucleus. This formula was obtained on the basis of the qualitative physical assumption that fission fragments escape from the parent nucleus only along or against its symmetry axis. According to this assumption, the angular distribution of fission fragments in the intrinsic coordinate frame of the parent nucleus as a function of the angles Ω' characterizing the direction of the radius vector $\mathbf{R}$ in this frame is of a strictly delta-function character. From the quantum-mechanical uncertainty relation for the relative orbital angular momentum l of fission fragments and the quantities $\xi' = \cos\theta'$ and φ' appearing in the definition of the solid angle Ω', it follows, however, that the delta function $\delta(\xi' \pm 1)$, which specifies the fixed angular values of $\theta' = 0$ and π, can arise only in the case where l is completely undetermined, which corresponds to the set of values $l \leq \infty$. Since this result cannot in principle reflect a real experimental situation, it is clear that formula (28) is only of an approximate character. Our further investigation is aimed at obtaining the conditions under which formula (28) can be deduced and at deriving deviations from this formula.

In the strong-coupling approximation [9], the wave function describing the transition state of the parent nucleus and possessing correct transformation properties under time inversion can be represented as

$$\psi^{JM}_{tK_i} = \sqrt{\frac{2J+1}{16\pi^2}}\left[1 + \delta_{K_i,0}\left(\frac{1}{\sqrt{2}} - 1\right)\right] \times \left\{D^J_{MK_i}(\omega)\chi_{tK_i}(q(\omega)) + \pi(-1)^{J+K_i}D^J_{M-K_i}(\omega)\chi_{\overline{tK_i}}(q(\omega))\right\}, \quad (29)$$

where $\chi_{tK_i}(q(\omega))$ is its intrinsic wave function depending on the set of coordinates $q(\omega)$ of the nucleus in its intrinsic coordinate frame, and $\chi_{\overline{tK_i}}(q(\omega))$ is the function obtained from the preceding one by time inversion.

The fission-fragment wave functions $\psi^{J_1M_1}_{\sigma_1K_1}(\omega_1)$ and $\psi^{J_2M_2}_{\sigma_2K_2}(\omega_2)$ appearing in the definition of the channel function (25) will also be represented in the form (29), where one must replace K_i by K_1 and K_2, M by M_1 and M_2, J by J_1 and J_2, π by π_1 and π_2, t by σ_1 and σ_2, and the set of intrinsic coordinates $q(\omega)$ by the sets $q_1(\omega_1)$ and $q_2(\omega_2)$. It follows that the channel function U^{JM}_{cjl} (25), together with the radial function for the relative motion of the fragments, depends on the $(3A-3)$ coordinates $\mathbf{R}, \omega_1, \omega_2, q_1(\omega_1)$, and $q_2(\omega_2)$. At the same time, the function in (29) also depends on the $(3A-3)$ coordinates ω and $q(\omega)$. If, among the $(3A-6)$ intrinsic coordinates $q(\omega)$ of the parent nucleus, we single out the $(3A-9)$ coordinates $q_1(\omega)$, $q_2(\omega)$, and $\mathbf{R}$ corresponding to the fission fragments, there will remain, among the coordinates $q(\omega)$, three coordinates that can be represented as the set of three Euler angles ω' characterizing the relative orientation of the intrinsic fragment axes described by the intrinsic coordinates $q_1(\omega)$ and $q_2(\omega)$. Since the orientation of the intrinsic axes of the set of coordinates $q_1(\omega)$ and $q_2(\omega)$ is close to the orientation of the intrinsic axes of the parent nucleus, the wave function $\varphi(\omega')$ depending on the Euler angles ω' can be approximately considered as a δ function of the angles ω'.

Among the intrinsic coordinates $q_1(\omega_1)$ and $q_2(\omega_2)$ of fission fragments, one can also single out coordinates that are associated with the deformation parameters $\beta_{\lambda 1}$ and $\beta_{\lambda 2}$ $(\lambda = 2, 4, ...)$ of these fragments. At the same time, the effective deformation parameters $\beta^0_{\lambda 1}$ and $\beta^0_{\lambda 2}$ characterizing deviations of the nuclei of would-be fission fragments from a spherical shape can also be singled out for the set of coordinates $q_1(\omega)$ and $q_2(\omega)$ corresponding to the intrinsic coordinates of the fission fragments in the parent nucleus.

In the channel function (25), we now go over to the intrinsic coordinate frame of the parent nucleus by means of the Wigner transformation [9]

$$D^{J_1}_{M_1K_1}(\omega_1) = \sum_{K'_1} D^{J_1}_{M_1K'_1}(\omega)D^{J_1}_{K'_1K_1}(\omega'_1), \quad (30)$$

$$Y_{lm_l}(\Omega) = \sum_{k_l} D^l_{m_lk_l}(\omega)Y_{lk_l}(\Omega'),$$

where ω'_1 are Euler angles that characterize the orientation of the intrinsic axes of the A_1 fragment with respect to the intrinsic axes of the parent nucleus.

In this case, the channel function (25) becomes a function of four angular sets $\omega, \omega'_1, \omega'_2$, and Ω'.

We further introduce the orthonormalized generalized channel function $\bar{U}^{JM}_{cjl}$, adding the function $\varphi(\omega')$ to the channel function (25) and considering the Euler angles ω, ω' and ω'_1, ω'_2 as independent variables. Substituting the function $\bar{U}^{JM}_{cjl}$ for the channel function U^{JM}_{cjl} (25) in formula (27), we can introduce the concept of the amplitude of the generalized partial-fission width, $\sqrt{\bar{\Gamma}^{J}_{tK_icjl}(\omega'_1, \omega'_2)}$. Upon integration in (27) with respect to the complete set of coordinates of the parent nucleus, including the Euler angles ω and ω', the above amplitude of the generalized partial width will depend on the Euler angles ω'_1 and ω'_2 as on parameters. This dependence can be written explicitly, if we consider that the definition of the amplitude $\sqrt{\bar{\Gamma}_{tK_icjl}(\omega'_1, \omega'_2)}$ involves an integral with respect to the intrinsic coordinates q_1 and q_2 of the fission fragments that has the form

$$D(\omega, \omega_1, \omega_2, \omega', \mathbf{R}') \tag{31}$$
$$= \langle \chi_{\sigma_1 K_1}(q_1(\omega_1))\chi_{\sigma_2 K_2}(q_2(\omega_2)) \times |V_{A_1A_2}|\chi_{tK_i}(q(\omega))\rangle ,$$

where the set of intrinsic variables $q(\omega)$ of the parent nucleus includes, as was mentioned above, the coordinates $\mathbf{R}'$ and ω' along with the coordinates $q_1(\omega)$ and $q_2(\omega)$. This integral takes the maximal absolute value if the intrinsic axes of fission fragments coincide with the intrinsic axes of the parent nucleus and decreases fast as the deviations of the Euler angles ω_1 and ω_2 from the angles ω increase. The integral in (31) can then be approximately represented as

$$D(\omega, \omega_1, \omega_2, \omega', \mathbf{R}') \tag{32}$$
$$= \delta^{1/2}_{\Delta}(\omega'_1)\delta^{1/2}_{\Delta}(\omega'_2)D(\omega, \omega, \omega, \omega', \mathbf{R}'),$$

where $\delta_{\Delta}(\omega'_1)$ is a δ function smeared over a rather narrow interval Δ in the vicinity of $\omega'_1 = 0$.

Owing to a strong semiclassical character of the fission process, the main contribution to the integral in (31) comes from the region of values of the radius R that are close to the points $\mathbf{R}_{sc}$ of scission of the parent nucleus into two fragments. From this and from formula (31), it follows that the deformation parameters $\beta_{\lambda 1}$ and $\beta_{\lambda 2}$ of the fission fragments in the region of their formation must be close to the deformation parameters $\beta^0_{\lambda 1}$ and $\beta^0_{\lambda 2}$ of the nuclei of these fragments in the parent nucleus near the point of its scission into fragments; all this corresponds to the ideas developed in [23]. As a matter of fact, these conclusions are in line with the conjecture that the effects of bending and torsion [24] play an insignificant role in the scission of the parent nucleus into fission fragments.

The use of formula (32) in determining the generalized partial-fission width and the asymptotic behavior of the wave function for the transition state in the form (5) leads to the conclusion that, at small values of Δ, the generalized channel function $\bar{U}^{JM}_{cjl}$ can be replaced by the modified channel function $\tilde{U}^{JM}_{cjl}$ defined by formula (25) where $\omega_1 = \omega_2 = \omega$.

We note that the condition $\omega_1 = \omega_2 = \omega$ means that there exists a strong correlation between the Wigner D functions describing the rotational states of a light and the complementary heavy fission fragment. If use is made of the adiabatic approximation, this correlation leads to the coherent interference between the wave functions for the relative motion of the fragments for different values of the fragment spins J_1 and J_2.

Using formula (30) at $\omega'_1 = \omega'_2 = 0$ and the multiplication theorem for D functions [9], we obtain the modified channel function in the form

$$\tilde{U}^{JM}_{cjl} = \frac{1}{16\pi^2}\sqrt{(2J+1)(2j+1)} \tag{33}$$
$$\times \sum_{Kk_l} D^{J}_{MK}(\omega)Y_{lk_l}(\Omega')(-1)^{j-l}$$
$$\times \{(-1)^{K_2} C^{J_1-K_1}_{Jj-K(K-K_1)}$$
$$\times C^{J_2-K_2}_{jl(K_1-K)k_l}\chi_{\sigma_1K_1}(q_1)\chi_{\sigma_2K_2}(q_2)$$
$$+ (-1)^{J_1+K_1+K_2} C^{J_1K_1}_{Jj-K(K+K_1)}$$
$$\times C^{J_2-K_2}_{jl(-K-K_1)k_l}\chi_{\overline{\sigma_1K_1}}(q_1)\chi_{\sigma_2K_2}(q_2)$$
$$+ (-1)^{J_2} C^{J_1-K_1}_{Jj-K(K-K_1)}$$
$$\times C^{J_2K_2}_{jl(K_1-K)k_l}\chi_{\sigma_1K_1}(q_1)\chi_{\overline{\sigma_2K_2}}(q_2)$$
$$+ (-1)^{J_1-J_2+K_1} C^{J_1K_1}_{Jj-K(K+K_1)}$$
$$\times C^{J_2K_2}_{jl(-K-K_1)k_l}\chi_{\overline{\sigma_1K_1}}(q_1)\chi_{\overline{\sigma_2K_2}}(q_2)\},$$

By way of example, we have presented here the case where $\pi = \pi_1 = \pi_2 = (+1)$, $K_1 \neq 0$, and $K_2 \neq 0$.

Let us now consider the structure of the partial-fission-width amplitudes $\sqrt{\Gamma^{J}_{tK_icjl}}$, which are determined, apart from the constant a arising because of the need for preserving the correct number of integration variables, by formula (27) if the channel functions U^{JM}_{cjl} (25) are replaced by the modified channel functions $\tilde{U}^{JM}_{cjl}$ (33). Let us investigate the properties of the function $A_{tK_i\sigma_1K_1\sigma_2K_2}(\Omega')$ which appears in the definition of the partial-fission-width amplitude (27) and which has the form

$$A_{tK_i\sigma_1K_1\sigma_2K_2}(\Omega') = \sqrt{2\pi} \tag{34}$$

$$\times \left\langle \frac{1}{R}\tilde{f}_c(R)\chi_{\sigma_1 K_1}(q_1)\chi_{\sigma_2 K_2}(q_2)\middle| V_{A_1A_2} \middle|\chi_{tK_i}(q)\right\rangle,$$

where integration is performed with respect to all the intrinsic variables $q(\omega)$ of the parent nucleus, with the exception of the angles Ω'. We now make use of the idea that the Bohr formula (28) is approximately valid—that is, fission fragments are emitted from the parent nucleus predominantly in the direction that is parallel or antiparallel to the symmetry axis of this nucleus.

Using the completeness and orthonormality of the basis of spherical harmonics, we can introduce, in the intrinsic coordinate frame of the parent nucleus, the δ functions normalized to unity over the entire space ($-1 \le \xi' \le 1$ and $0 \le \varphi' \le 2\pi$) of the solid angle Ω', whose element $d\Omega'$ is given by $d\Omega' = d\xi' d\varphi'$, where $\xi' = \cos\theta'$. As a result, we have

$$\frac{1}{2\pi}\delta(\xi' \mp 1) = \sum_{lm} Y_{l_m}(\xi', \varphi')Y^*_{l_m}(\pm 1, \varphi'_0). \quad (35)$$

Since $Y^*_{l_m}(\xi', \varphi') = Y_{l0}(\pm 1)\delta_{m,0}$ at $\xi' = \pm 1$ and since this spherical harmonic is independent of the azimuthal angle φ', the function in (35) can be recast into the form

$$\frac{1}{2\pi}\delta(\xi' \mp 1) = \sum_l Y_{l0}(\xi')Y_{l0}(\pm 1) = \sum_l P_l(\xi')\frac{(2l+1)}{4\pi}(\pm 1)^l. \quad (36)$$

We note that, in the sums over l in formulas (35) and (36), the quantity l takes values in the region $0 \le l \le \infty$—this reflects the quantum-mechanical uncertainty relation between the values of orbital angular momentum l and the angle θ'.

Adopting the assumption that the Bohr formula (28) is valid approximately, taking into account the l independence of the radial function $\tilde{f}_l(R)$, and using the parity-conservation law, we represent the function in (34) in the form

$$A_{tK_i\sigma_1 K_1\sigma_2 K_2}(\Omega') = F_{l_m}(\theta')B_{tK_i\sigma_1 K_1\sigma_2 K_2}, \quad (37)$$

where the function $F_{l_m}(\theta')$ is expressed in terms of the amplitudes of smeared δ functions of the form (36) as

$$F_{l_m}(\theta') = \left[\tilde{\delta}^{1/2}(\xi' - 1) + \pi\pi_1\pi_2\,\tilde{\delta}^{1/2}(\xi' + 1)\right]\frac{1}{\sqrt{4\pi}} = b(l_m)\left\{\sum_{l=0}^{l_m} Y_{l0}(\xi')Y_{l0}(1)\left[1 + \pi\pi_1\pi_2(-1)^l\right]\right\}. \quad (38)$$

Here, the constant $b(l_m)$ is found from the normalization condition

$$\int F^2_{l_m}(\theta')d\Omega' = \int\left[\tilde{\delta}(\xi' - 1) + \tilde{\delta}(\xi' + 1)\right]\frac{d\Omega}{4\pi} = 1. \quad (39)$$

The result is

$$b(l_m) = \left\{\sum_{l=0}^{l_m}\frac{(2l+1)}{2\pi}[1 + \pi\pi_1\pi_2(-1)^l]\right\}^{-1/2}. \quad (40)$$

The representation in (37) preserves azimuthal symmetry for the directions of fission-fragment emission since the spherical harmonics $Y_{l0}(\xi', \varphi')$ do not depend on the azimuthal angle φ'. Formulas (37) and (38) involve the maximal value l_m of the relative orbital angular momentum l of fission fragments. The greater this value, the closer the function $\tilde{\delta}(\xi' - 1)$ to an exact δ function—that is, the smaller the angle θ' between the directions of the fission-fragment emission and the symmetry axis of the parent nucleus. In other words, rather high values of l_m are required for the Bohr formula (28) to be fairly accurate. At the same time, the values of l must not be overly high in order that one could neglect the effect of the centrifugal potential $V^{cf}_{cl}(R)$ on the radial functions $f_{cl}(R)$ and on the phase shifts $\bar{\delta}_{cl}$ for potential scattering (see above). This means that deviations from the Bohr formula (28) for the angular distributions of fission fragments cannot be very small; therefore, one can hope to discover them experimentally.

Considering that integration in (27) with respect to ω with the aid of formulas (33) and (29) leads to the coincidence of the quantity K appearing in the sum in formula (33) with the quantities $\pm K_i$ and taking into account the relation $\int Y^*_{lk_l}(\Omega')Y_{l0}(\Omega')d\Omega' = \delta_{k_l,0}$, we can see that the partial-fission-width amplitude (27) receives contribution from three types of channels c labeled with the index r, where the values of $r = 1, 2$, and 3 correspond to the $K_1 + K_2 = K_i$ channel, the $K_1 - K_2 = K_i$ channel for $K_1 > K_2$, and the $K_i = K_2 - K_1$ channel for $K_2 > K_1$. With the aid of formula (37), the partial-fission-width amplitude $\sqrt{\Gamma^{Jr}_{tK_i\sigma_1 K_1 J_1\sigma_2 K_2 J_2 jl}}$ (27) for these channels can be represented as

$$\sqrt{\Gamma^{Jr}_{tK_i\sigma_1 K_1 J_1\sigma_2 K_2 J_2 jl}} = a\Theta(l - l_m)\sqrt{\frac{2j+1}{8\pi^2}}\sqrt{\frac{2l+1}{4\pi}}b(l_m) \quad (41)$$

$$\times 2[1+(-1)^l\pi\pi_1\pi_2]M^{(r)}_{\sigma t K_i\sigma_1 K_1 J_1\sigma_2 K_2 J_2},$$

$$M^{(1)}_{tK_i\sigma_1K_1J_1\sigma_2K_2J_2} = (-1)^{j+l+K_2}C^{J_1-K_1}_{Jj-K_i(K_i-K_1)}C^{J_2-K_2}_{jl(K_1-K_i)0}B_{tK_i\sigma_1K_1\sigma_2K_2}; \quad (42)$$

$$M^{(2)}_{tK_i\sigma_1K_1J_1\sigma_2K_2J_2} \quad (43)$$
$$= (-1)^{J_2}C^{J_1K_1}_{JjK_i(K_1-K_i)}C^{J_2-K_2}_{jl(K_i-K_1)0}B_{\overline{tK_i}\,\overline{\sigma_1K_1}\sigma_2K_2},$$

$$M^{(3)}_{tK_i\sigma_1K_1J_1\sigma_2K_2J_2} \quad (44)$$
$$= (-1)^{J_2}C^{J_1-K_1}_{JjK_i(-K_i-K_1)}C^{J_2K_2}_{jl(K_1+K_i)0}B_{\overline{tK_i}K_1\sigma_1\overline{K_2\sigma_2}}.$$

As can be seen from formulas (41)–(44), which determine the dependence of the partial-fission widths on the channel indices J_1, J_2, j, and l, this dependence is of a dynamical character, stems predominantly from the Clebsch–Gordan coefficients, and differs significantly from the analogous dependence of these widths that is obtained by using various statistical assumptions [12].

7. ANGULAR DISTRIBUTIONS OF FRAGMENTS ORIGINATING FROM THE FISSION OF ORIENTED NUCLEI

Let us consider the asymptotic expression for the parent-nucleus wave function ψ^{JM}_σ (5) for $R\to\infty$. We have

$$\psi^{JM}_\sigma = \sum_{A_1Z_1t\sigma_1K_1J_1\sigma_2K_2J_2rjl}\tilde U^{JM}_{\sigma_1K_1J_1\sigma_2K_2J_2jl} \quad (45)$$
$$\times\frac{e^{ik_cR}}{R}e^{i\bar\delta_{\sigma_1K_1\sigma_2K_2}}\alpha^J_{\sigma t}\sqrt{\frac{\Gamma^{Jr}_{tK_i\sigma_1K_1J_1\sigma_2K_2J_2jl}}{\hbar\upsilon_c}}.$$

Substituting expression (33) for the channel function $\tilde U^{JM}_{\sigma_1K_1J_1\sigma_2K_2J_2jl}$ into (45) and using the representation in (41) and formulas of the type

$$\sum_{J_1}C^{J_1K_1}_{JjK_iK_1-K_i}C^{J_1K_1}_{JjKK_1-K} = \delta_{K,K_i}, \quad (46)$$

we recast the asymptotic expression (45) into the form

$$\psi^{JM}_\sigma = \sum_{A_1Z_1t\sigma_1K_1\sigma_2K_2rj}\tilde a\alpha^J_{\sigma t} \quad (47)$$
$$\times\sqrt{\frac{2J+1}{16\pi^2}}[D^J_{M,\,-K_i}(\omega)\chi_{\sigma_1K_1}(q_1)\chi_{\sigma_2K_2}(q_2)$$
$$+(-1)^{J+K_i}D^J_{M-K_i}(\omega)\chi_{\overline{\sigma_1K_1}}(q_1)$$
$$\times\chi_{\overline{\sigma_2K_2}}(q_2)](2j+1)$$
$$\times F_{l_m}(\theta')B^{(r)}_{tK_i\sigma_1K_1\sigma_2K_2}\frac{e^{i\bar k_cR}}{R}e^{i\bar\delta_{\sigma_1K_1\sigma_2K_2}}\sqrt{\frac{1}{\hbar\upsilon_c}},$$

where $\Theta(x)$ is the sign function and

where

$$\tilde a = a\frac{1}{\sqrt{2}}\frac{1}{\sqrt{8\pi^2}}. \quad (48)$$

Using now the wave function (47) to determine the multiparticle density j^{JM}_σ (8) of the fission-fragment flux and integrating this density with respect to the coordinates ω, q_1, and q_2 with allowance for the orthonormality of the functions $\chi_{\sigma_1K_1}$ and $\chi_{\sigma_2K_2}$, we obtain the following expression for the single-particle density $j^{JM}_\sigma(\mathbf{R})$ of the fragment flux in the direction of the radius $\mathbf{R}$ in the laboratory frame:

$$j^{JM}_\sigma(\mathbf{R}) = \frac{1}{R^2}\sum_{A_1Z_1t\sigma_1K_1\sigma_2K_2rj}\tilde a^2\left|\alpha^J_{\sigma t}\right|^2 \quad (49)$$
$$\times\int d\omega\frac{(2J+1)}{16\pi^2}\left[|D^J_{MK_i}(\omega)|^2+|D^J_{M,\,-K_i}(\omega)|^2\right]$$
$$\times\left(\sum_j(2j+1)\right)^2F^2_{l_m}(\theta')\left|B^{(r)}_{tK_i\sigma_1K_1\sigma_2K_2}\right|^2\frac{1}{\hbar}.$$

In the channel $\sigma_1k_1\sigma_2k_2r$, the total number of light and heavy fission fragments that is recorded per unit time by detectors ensuring a 4π coverage will then be equal to the integral of the corresponding term of the sum in formula (46) with respect to Ω'; that is,

$$N^{JM}_{\sigma A_1Z_1\sigma_1K_1\sigma_2K_2r} \quad (50)$$
$$= \sum_t\left|\alpha^J_{\sigma t}\right|^2\cdot|\tilde a|^2\left(\sum_j(2j+1)\right)^2$$
$$\times\left|B^{(r)}_{tK_i\sigma_1K_1\sigma_2K_2}\right|^2\frac{1}{\hbar} = \frac{1}{\hbar}\Gamma^J_{\sigma A_1Z_1\sigma_1K_1\sigma_2K_2r},$$

where $\Gamma^J_{\sigma A_1Z_1\sigma_1K_1\sigma_2K_2r}$ is the fission width of the parent nucleus in the channel $A_1Z_1\sigma_1K_1\sigma_2K_2r$. In the form normalized to unity, the angular distribution of fragments originating from the fission of an oriented parent nucleus ($M=J$) through the channel $A_1Z_1\sigma_1K_1\sigma_2K_2r$ is then given by the universal formula

$$\frac{dP^J_{\sigma K_iA_1Z_1\sigma_1K_1\sigma_2K_2r}(\Omega)}{d\Omega} = \left(\frac{2J+1}{16\pi^2}\right) \quad (51)$$
$$\times\int d\omega\left[\left|D^J_{JK_i}(\omega)\right|^2+\left|D^J_{J,\,-K_i}(\omega)\right|^2\right]F^2_{lm}(\theta'),$$

which does not depend on the channel indices $A_1Z_1\sigma_1K_1\sigma_2K_2r$ or on the structure of the transition

states t. This result is caused by the use of the adiabatic approximation, which leads to a coherent mixing of the wave functions for the relative motion of fragments for channels characterized by different values of J_1, J_2, and j at fixed indices $t\sigma_1 K_1 \sigma_2 K_2 r$. It is the reason why, in studying even–even and odd (the latter are associated with parity-nonconservation effects) correlations in the fission experiments [13, 25], one observes coherent effects universal for all fission fragments.

For $l_m \to \infty$, the function $F^2_{l_m}(\theta') \cdot 2\pi$ reduces to the true delta function $\delta(\xi' - 1)$, which is equivalent to a delta function of the form $\delta(\xi - \xi_\beta)$, where $\xi = \cos\theta$ and $\xi_\beta = \cos\beta$, since, in the case where fission fragments fly out in the direction coincident with the symmetry axis of the parent nucleus, the angle θ characterizing the direction in which the fragments fly out in the laboratory frame coincides with the Euler angle β between the Z axis of the laboratory frame and the Z' axis of the intrinsic coordinate frame of the parent nucleus. Upon taking into account the fact that the expression $\left[\left|D^J_{JK_i}(\omega)\right|^2 + \left|D^J_{J,\,-K_i}(\omega)\right|^2\right]$ remains invariant under the substitution of $(\pi - \beta)$ for β in performing integration with respect to ω, formula (51) for the angular distribution then reduces to the Bohr formula (28).

In conclusion, we will assess the dependence of the angle between the direction of fission-fragment emission and the symmetry axis of the parent nucleus on the maximum value l_m of the orbital angular momentum of the relative motion of fragments. For this purpose, we will investigate the l_m dependence of the FWHM $\Delta\theta'$ (in radians) of the distribution $F^2_{l_m}(\theta')$ in the vicinity of the point $\theta' = 0$. In the case of $\pi\pi_1\pi_2 = +1$ and even l and in the case of $\pi\pi_1\pi_2 = -1$ and odd l, the quantity $\Delta\theta'$ is independent of the parity of l and is approximately equal to $\Delta\theta' = 1.5/l_m$, provided that $l_m > 10$. In the case of $l_m \approx 30$, the angle $\Delta\theta'$ therefore takes a value of $\Delta\theta' \approx 0.05$, which, in units of angular degree, corresponds to $\Delta\theta' = 3^\circ$.

The value of l_m can be estimated on the basis of data from experiments that studied correlations between the direction of the emission of prompt photons from fission fragments and the directions along which the fission fragments in question move [26]. In those experiments, the mean values of the fission-fragment spins J_1 and J_2 are $\langle J_{1,2}\rangle = 6$–$8$ (in $\hbar$ units), whence, for l_m values satisfying the condition $l_m \gg J$, one can obtain the estimate $l_m \approx I_m$, where I_m is the maximum value of the total spin I of fission fragments; this maximum spin value can be estimated as $I_m = (J_1)_m + (J_2)_m$. If $(J_1)_m$ and $(J_2)_m$ are estimated at 10 to 15—this corresponds to the doubled value of the mean spins J_1 and J_2 of the fission fragments—l_m proves to be close to 20–30. As was shown above, this value of l_m leads to $\Delta\theta' \approx (3$–$5)^\circ$. It should be noted that values in the range $l_m \approx (20$–$30)$ can be obtained on the basis of the above estimate $l_m \approx k_c(\mathbf{R}_{scl})d$ for $E^{\rm kin}_c(\mathbf{R}_{scl}) > 100$ MeV at $d = 2$ fm. In all probability, so large a value of $E^{\rm kin}_c(\mathbf{R}_{scl})$ requires changing the estimate of the neck diameter d toward considerably greater values. In order to estimate the neck diameter correctly, it is necessary to take additionally into account a strong nonsphericity of the Coulomb and nuclear potentials describing the interaction of fission fragments.

8. CONCLUSION

Our analysis of the angular distributions of fragments originating from the protonic, alpha, and cluster decays of oriented nuclei has demonstrated that the adiabatic approximation is inapplicable to their description. At the same time, the use of this approximation has proved to be an appropriate means for studying the fission widths of oriented nuclei and angular distributions of fission fragments originating from them. The methods developed in this study for analyzing fission widths and fission-fragment angular distributions may greatly contribute to obtaining deeper insights into various fission processes and correlations both between fission fragments and between these fragments and their decay products, as well as to exploring various forms of ternary nuclear fission.

ACKNOWLEDGMENTS

I am grateful to V.E. Bunakov, G.A. Petrov, W.I. Furman, and A.L. Barabanov for stimulating discussions and valuable advice.

This work was supported by INTAS (grant no. 99-00229) and the program "Universities of Russia" (grant no. UR-01.01.011).

REFERENCES

1. P. O. Fröman, K. Dan. Vidensk. Selsk. Mat. Fys. Medd. **1(3)** (1957).
2. J. K. Poggenburg, H. J. Mang, and J. O. Rasmussen, Phys. Rev. **181**, 1697 (1969).
3. S. G. Kadmenskiĭ, V. E. Kalechits, and A. A. Martynov, Yad. Fiz. **14**, 343 (1971) [Sov. J. Nucl. Phys. **14**, 193 (1972)].
4. T. Berggren and P. Olanders, Nucl. Phys. A **473**, 189 (1987).
5. P. S. Delion, A. Insolia, and R. J. Liotta, Phys. Rev. C **49**, 3024 (1994).
6. A. M. Lane and R. G. Thomas, Rev. Mod. Phys. **30**, 257 (1958).

7. S. G. Kadmensky and V. I. Furman, *Alpha Decay and Related Nuclear Reactions* (Énergoatomizdat, Moscow, 1985).
8. A. Bohr, in *Proceedings of the United Nations International Conference on Peaceful Uses of Atomic Energy* (United Nations, New York, 1956), Vol. 2, p. 151.
9. A. Bohr and B. Mottelson, *Nuclear Structure* (Benjamin, New York, 1969, 1975), Vols. 1, 2.
10. V. M. Strutinskiĭ, Zh. Éksp. Teor. Fiz. **37**, 861 (1959) [Sov. Phys. JETP **10**, 613 (1960)].
11. L. Nowickiy, M. Berlanger, B. Borderil, *et al.*, Phys. Rev. C **26**, 1114 (1982).
12. A. L. Barabanov and D. P. Grechukhin, Yad. Fiz. **47**, 648 (1988) [Sov. J. Nucl. Phys. **47**, 411 (1988)].
13. A. L. Barabanov and W. I. Furman, Z. Phys. A **357**, 411 (1997).
14. V. I. Furman, in *Proceedings of FJ/OM Spring Session, Geel, Belgium, 1999,* p. 248.
15. S. G. Kadmensky and A. A. Sanzogni, Phys. Rev. C **62**, 054601 (2000).
16. S. G. Kadmensky, Yad. Fiz. **65**, 863 (2002) [Phys. At. Nucl. **65**, 831 (2002)].
17. V. P. Bugrov, S. G. Kadmenskiĭ, V. I. Furman, and V. G. Khlebostroev, Yad. Fiz. **41**, 1123 (1985) [Sov. J. Nucl. Phys. **41**, 717 (1985)].
18. V. P. Bugrov and S. G. Kadmenskiĭ, Yad. Fiz. **49**, 1562 (1989) [Sov. J. Nucl. Phys. **49**, 967 (1989)].
19. S. G. Kadmensky, Yad. Fiz. **63**, 613 (2000) [Phys. At. Nucl. **63**, 551 (2000)].
20. K. Wildermuth and Y. C. Tang, *A Unified Theory of the Nucleus* (Vieweg, Braunschweig, 1977).
21. S. G. Kadmensky, Yad. Fiz. **64**, 478 (2001) [Phys. At. Nucl. **64**, 423 (2001)].
22. S. G. Kadmenskiĭ, V. I. Furman, and Yu. M. Chuvil'skiĭ, Izv. Akad. Nauk SSSR, Ser. Fiz. **50**, 1786 (1986).
23. V. A. Rubchenya and S. G. Yavshits, Yad. Fiz. **40**, 649 (1984) [Sov. J. Nucl. Phys. **40**, 416 (1984)].
24. J. R. Nix and W. J. Swiatecki, Nucl. Phys. **71**, 1 (1965).
25. G. V. Danilyan, Pis'ma Zh. Éksp. Teor. Fiz. **24**, 380 (1976) [JETP Lett. **24**, 344 (1976)].
26. Yu. N. Kopach *et al.*, Phys. Rev. Lett. **82**, 303 (1999).

Translated by A. Isaakyan

Physics of Atomic Nuclei, Vol. 65, No. 8, 2002, pp. 1403–1410. From Yadernaya Fizika, Vol. 65, No. 8, 2002, pp. 1438–1445.

NUCLEI
Theory

Novel Features of the Fragment Mass Variance in Fission of Hot Nuclei*

W. Wagner[1)], I. I. Gontchar, A. E. Gettinger, L. A. Litnevsky, H.-G. Ortlepp[1)], and D. V. Kamanin[1),2)]

Omsk State Railway University, Russia

Received March 12, 2001; in final form, August 8, 2001

Abstract—On the basis of data obtained by the incomplete fusion reactions ^{7}Li(43A MeV) + ^{232}Th and ^{14}N(34A MeV) + ^{197}Au, the energy dependence of the variance (σ_M^2) of the fragment mass in fission of highly heated nuclei has been investigated for total excitation energies $E^*_{\rm tot}$ ranging from 50 up to 350 MeV. The dependence $\sigma_M^2(E^*_{\rm tot})$ shows some unexpected features when $E^*_{\rm tot}$ exceeds a value of about 70 MeV. After this value, the steady increase of σ_M^2 expected from its temperature dependence changes to some kind of plateau between 100 and 200 MeV. Further on, at $E^*_{\rm tot}$ in excess of about 250 MeV, the variance is found to increase again sharply. In order to analyze this behavior quantitatively, a dynamical stochastic model has been developed. The model employs the one-body dissipation mechanism and describes the decay of highly excited and rotating nuclei by fission and light-particle evaporation. It satisfactorily explains the measured prior-to-scission neutron multiplicities and the experimental mass variances up to $E^*_{\rm tot} \cong 250$ MeV, but the stochastic treatment does not reveal any increase in σ_M^2 at higher excitation energies in contradiction with the data. © *2002 MAIK "Nauka/Interperiodica".*

1. INTRODUCTION

The fission fragment mass distribution was repeatedly measured for total excitation energies ($E^*_{\rm tot}$) smaller than 100 MeV (see, e.g., [1] for a review). Several measurements performed at higher $E^*_{\rm tot}$ were published in [2–4].

It is well known that, at $E^*_{\rm tot}$ larger than 50 MeV, the fission fragment mass distribution has a symmetrical (Gaussian-like) shape. The mean value of this distribution does not contain any information about the dynamics of fission, since it depends only upon the mass loss due to particle evaporation both from the fissioning compound system and from flying-away fragments. The variance of mass distribution (σ_M^2) reflects the dynamics of the mass-asymmetry degree of freedom, since it is being formed up to the scission point.

It has been shown in [1] that, for fixed values of $E^*_{\rm tot}$ as well as of the angular momentum (L), the function $\sigma_M^2(Z^2/A)$ has a broad and flat minimum located in the region $31 \le Z^2/A \le 37$. In that work, it has also been found that σ_M^2 increases with L for fixed Z^2/A and $E^*_{\rm tot}$ of the compound nucleus. Concerning the function $\sigma_M^2(E^*_{\rm tot})$, the linear dependence of σ_M^2 on the temperature (T) at the saddle point has been established for $E^*_{\rm tot} \le 100$ MeV (cf. Fig. 4 of [1]).

The last observation supports the expectation that σ_M^2 is governed by a Brownian collective motion. For a Brownian oscillator, the equilibrium variance of its coordinate is defined by the temperature and the stiffness. In fission, the stiffness (Q_M) is supposed to refer to the mass-asymmetry degree of freedom. The exact definition of Q_M is given in [1]. The observation just discussed is, therefore, in agreement with the simple formula

$$\sigma_M^2 = \frac{T}{Q_M}. \qquad (1)$$

In the present work, we made an effort to explore the behavior of $\sigma_M^2(E^*_{\rm tot})$ at energies $E^*_{\rm tot}$ up to 350 MeV. The main difficulties one meets in such kind of investigation are connected with the facts that

(i) the fission yield resulting from complete fusion becomes rather small and

(ii) the angular momentum brought to the compound nucleus increases with increasing incident energy.

The σ_M^2 data used in this work were extracted for fission after incomplete fusion reaction, i.e., after incomplete transfer of the linear momentum of the projectile. This enabled us to increase both the statistics

*This article was submitted by the authors in English.

[1)]Forschungszentrum Rossendorf, Institute of Nuclear and Hadron Physics, Dresden, Germany.

[2)]Joint Institute for Nuclear Research, Dubna, Moscow oblast, 141980 Russia.

of fission events under investigation and $E^*_{\rm tot}$ without substantial increase in the angular momentum.

2. EXPERIMENTAL DATA

The fission fragment data analyzed in the present work have been measured at the 4π fragment spectrometer FOBOS [5] using the incomplete fusion reactions ^{7}Li(43A MeV) + ^{232}Th and ^{14}N(34A MeV) + ^{197}Au [6, 7]. Details of these measurements and the procedures applied for data processing, as well as other experimental results, were published earlier in [5, 8–12]. The total excitation energy ($E^*_{\rm tot}$) of the intermediate compound-like system was estimated by means of the massive transfer approach. This method allows us to select systems with different average $E^*_{\rm tot}$ out of the variety of nuclei produced in the incomplete fusion reaction.

The recently published analysis [13] of the fission delay time was based on the ^{7}Li(43A MeV) + ^{232}Th measurement [6] alone. In that work, the energy interval $E^*_{\rm tot} = 57$–205 MeV is considered, and the first conclusions have been drawn with respect to the influence of the cooling down of the heated nuclear system on the mass variance in binary fission. The present work aims to give a dynamical description of the mass variance in fission of hot nuclei taking into consideration the interplay with the evaporation of light particles.

3. THE MODEL

A detailed description of our dynamical stochastic model developed for modeling the fission accompanied with the emission of light particles (neutrons, protons, deuterons, α particles, and also giant dipole γ quanta) was published recently in [14]. A short sketch of the model is given in the following. The model is realized in a computer code that is the successor of the code DESCEND [15]. It is based on the stochastic differential equations of Langevin type

$$p_i^{(n+1)} = p_i^{(n)} - \left[\frac{1}{2}\left\{\partial_{q_i}\left(m^{-1}\right)_{jk}\right\}^{(n)} p_j^{(n)} p_k^{(n)} + \gamma_{ij}^{(n)}\left(m^{-1}\right)_{jk}^{(n)} p_k^{(n)} - K_i^{(n)}\right]\tau + g_{ij}^{(n)} w_j^{(n)}\sqrt{\tau}, \quad (2)$$

$$q_i^{(n+1)} = q_i^{(n)} + (m^{-1})_{ij}^{(n)} p_j^{(n)}\tau,$$

where q_i ($i = 1, 2$) are the collective coordinates $q_1 = c$, $q_2 = \alpha$ in a (c, h, α) parametrization of the shape of the fissioning nucleus (cf. [16]), m_{ij} and γ_{ij} are the inertia and friction tensors, $p_i^{(n)}$ are the collective momenta after n time steps τ, $K_i^{(n)}$ denote the regular forces, and $w_j^{(n)}$ denote random numbers which are distributed normally with variance 2.

Since a fully three-dimensional calculation in the phase space of (c, h, α) is extremely computer-time and computer-memory consuming, the simulations of the fission fragment mass distribution were made in the (c, α) subspace along the bottom of the fission valley which was determined before in the (c, h, $\alpha = 0$) subspace. Such a method, unfortunately, restricts the calculated mass distribution, representing only fission events of most probable total kinetic energies (TKE).

Among previous works only that of [17] mentioned a three-dimensional calculation of the fragment mass distribution, but no comparison with experimental data was presented. Dynamical Langevin calculations of the mass distribution of fission have recently been published in [18], but neither presaddle dynamics nor particle emission was included, which makes the results obtained questionable. Hence, our model can be considered as the first attempt at an intrinsically consistent systematic dynamical description of the width of the fragment mass distribution of fission that includes particle evaporation.[3)] One important ingredient for such calculations is the multidimensional potential (deformation) surface energy ($V(q)$) of the fissioning nucleus. We define $V(q)$ as the minimum energy that the system can possess at fixed deformation q. The energy $V(q)$ enters the calculation in two different ways:

(i) It defines the intrinsic excitation energy ($E^*(q)$) and, consequently, the temperature (T) via the energy conservation law.

(ii) It defines the regular (driving) forces.

In this work, $V(q)$ is calculated by means of the liquid-drop model of [19]. This model was used earlier in the works reviewed in [20] and with slightly corrected coefficients also in [21].

It is well known that the regular forces acting in a thermodynamical system must be calculated from a thermodynamical potential (which we henceforth call the "driving potential") but not from the bare potential energy $V(q)$. In the present work (as well as in [15]), the regular forces are calculated via the entropy (S) by

$$K_i = T\left(\frac{\partial S}{\partial q_i}\right)_{E^*_{\rm tot}}. \quad (3)$$

[3)] *Note added in proof*. In their recent article, Karpov *et al.*, Phys. Rev. C **63**, 054610 (2001), presented three-dimensional Langevin calculations of the mass–energy distribution of fission fragments. In calculating the driving forces, they employed, however, a bare potential energy (not a thermodynamic potential) despite the use of a deformation-dependent level-density parameter.

The entropy calculated in the framework of the Fermi gas model reads

$$S(q,p) = 2\sqrt{a(q)\left[E^*_{\rm tot} - V(q) - E_{\rm kin}(q,p)\right]}, \quad (4)$$

where $E_{\rm kin}$ is the kinetic energy of collective motion. The single-particle level density parameter $a(q)$ will be discussed below. The temperature of the fissioning nucleus given,

$$T(q,p) = \sqrt{\frac{E^*_{\rm tot} - V(q) - E_{\rm kin}(q,p)}{a(q)}}, \quad (5)$$

defines the magnitudes (g_{ij}) of the fluctuation forces via the Einstein relations

$$\sum g_{ik}g_{kj} = T\gamma_{ij}. \quad (6)$$

It is worthwhile to note that only the bare potential $V(q)$ must be used in Eqs. (4) and (5), and not any kind of "generalized" potential like, e.g., the free energy.

The particle emission is simulated discretely, as was first proposed in [22]. In this approach, it is supposed that the small probability (dP) of emitting a particle is proportional to the time step (τ) of the simulation:

$$dP = \frac{\Gamma_{\rm tot}\tau}{\hbar}. \quad (7)$$

Here, $\Gamma_{\rm tot}$ denotes the total statistical emission width of a particle. Equation (7) is a direct consequence of the radioactive decay law, or, in other words, it results from the fact that the decay rate is constant and the time step of simulations is small enough.

According to the classical equipartition theorem, the average energy of the collective subsystem must be of the order of T. Consequently, the fissioning nucleus can spend a very long time moving near the ground state provided its excitation energy, which initially was very high, became, due to particle evaporation, only slightly larger than the fission barrier. The trajectories corresponding to the so-called long-lifetime fission events cannot be treated dynamically. Therefore, an additional contrivance is needed for switching over to the statistical regime.

The prescription for the switching over applied in this work was already used in [22]. We start each trajectory dynamically from the ground state with zero collective momenta. The switching over to the statistical branch of the model is carried out provided three conditions are fulfilled:

(i) The trajectory is still running in the vicinity of the ground state; i.e., the saddle point has not yet been passed.

(ii) The difference between the values of the entropy at the ground state and at the saddle point ($B_S = S_{\rm gs} - S_{\rm sd}$; gs—ground state, sd—saddle point) is larger than some certain value (we chose $B_S \geq 2$).

(iii) The trajectory was running in the dynamical branch of the model at least for $\tau_d = 50$ zs (1 zs = 10^{-21} s).

All three conditions are of the same strength.

In the statistical branch, we calculate the probability for the system to disintegrate by fission or to emit particles by means of the usual hit-and-miss Monte Carlo procedure. The statistical fission rate is calculated by

$$R_f = \frac{\omega_{\rm K}}{2\pi} \times \left[\frac{T_{\rm sd}\det\{m_{\rm sd}\}\left|\det\left\{S''_{\rm gs}\right\}\right|}{T_{\rm gs}\det\{m_{\rm gs}\}\det\left\{S''_{\rm sd}\right\}}\right]^{1/2} \exp\left(-B_S\right), \quad (8)$$

where $\det\{m\}$ denotes the determinant of the inertia tensor and $\det\{S''\}$ is the determinant of the second derivatives of the entropy. According to the equipartition theorem for two degrees of freedom, the $S_{\rm gs}$ and $S_{\rm sd}$ are calculated for $E_{\rm kin} = T$. In Eq. (8), $\omega_{\rm K}$ is the so-called Kramers frequency that is the only positive root of the equation

$$\det\left\{\omega^2_{\rm K}m + \omega_{\rm K}\gamma + S''T\right\} = 0. \quad (9)$$

All deformation-dependent quantities in (9) are calculated at the saddle point, and the entropy is taken again at $E_{\rm kin} = \langle E_{\rm kin}\rangle = T$.

The single-particle level-density parameter (a) is also an important ingredient of any statistical calculation. It was proved (cf. [23]) that a is deformation-dependent and reads

$$a(q) = a_v A + a_s A^{2/3} B_s(q), \quad (10)$$

where the dimensionless surface-energy coefficient (B_s) is shape-dependent and equals unity for a sphere. Among the variety of sets of coefficients a_v and a_s, those of [23] ($a_v = 0.073$ MeV^{-1}, $a_s = 0.095$ MeV^{-1}) were selected for use in the present work. The arguments in favor of this set are given in [24].

The inertia parameters are calculated using Werner–Wheeler approximation [25] to incompressible and approximately irrotational flow. The friction parameters are calculated in the framework of the one-body dissipation model of [26].

Provided a nucleus happened to fission, after being in the statistical branch the corresponding trajectory returns to the dynamical branch of the model. The initial collective coordinates and momenta are then chosen to be the equilibrium ones at the ridge line, where such collective momenta driving the nucleus

Comparison of the calculated fission fragment mass variances (σ_M^2 (calc.)) and prior-to-scission neutron multiplicities ($n_{\rm pre}$ (calc.)) with experimental values from [1]

Reaction	Z^2/A	σ_M^2 (exp.), (amu)^2	σ_M^2 (calc.), (amu)^2	$n_{\rm pre}$ (syst.)	$n_{\rm pre}$ (calc.)	N_f, 10^3
^{18}O(159 MeV) + ^{169}Tm → ^{187}Ir	31.7	219	213	3.7	4.0	1.1
^{4}He(80 MeV) + ^{197}Au → ^{201}Tl	32.6	159	159	3.0	2.0	0.4
^{16}O(128 MeV) + ^{183}W → ^{199}Pb	33.8	211	180	3.3	3.4	1.2
^{12}C (97 MeV) + ^{206}Pb → ^{218}Ra	35.5	203	234	2.3	2.8	1.2
^{16}O(128 MeV) + ^{197}Au → ^{213}Fr	35.5	256	258	3.7	3.6	1.3
^{16}O(128 MeV) + ^{206}Pb → ^{222}Th	36.5	296	282	3.2	2.9	1.2

Note: The calculations were performed with spin distributions according to the recipe of [15] and with level-density parameters of [23]. The values of $n_{\rm pre}$ (syst.) from [1] were obtained on the basis of some systematics proposed in [27]. The number of available fission events (N_f) is presented in the last column.

back to the ground-state region are rejected. This procedure allows one to account for the motion of the nucleus towards the scission line. Since during the descent phase additional light particles can be emitted, the final mass asymmetry of the fission fragments is formed at this stage. Note that in [18] only the descent stage of fission has been considered but without taking into account particle emission.

The calculation of each fission trajectory is terminated when the scission condition was reached. For this condition, we require the radius of the neck between the two future fragments to be equal to zero. Note that the scission condition is mostly important for the TKE distribution of the fission fragments, while the fragment mass distribution is less sensitive to the condition.

4. COMPARISON OF MODEL CALCULATIONS WITH EXPERIMENTAL DATA

4.1. Fission after Complete Fusion

The reliability of our model calculations for low energy was proved in [14] by comparison with the fusion–fission data obtained in [1]. Among numerous reactions investigated, we selected six given in the table. The values of the Coulomb parameter (Z^2/A) of the fissioning nuclei, the measured as well as calculated fission fragment mass variances, and the corresponding neutron multiplicities are also presented in the table.

Agreement of the calculated variances with the data of [1] has been obtained within an uncertainty of about 10%. Furthermore, the calculated variances show the same dependence on Z^2/A as the measured ones. Agreement of the calculated prior-to-scission neutron multiplicities ($n_{\rm pre}$) with those given in [1] is also observed except for the reaction ^{4}He(80 MeV) + ^{197}Au. It must, however, be mentioned that the neutron multiplicities given in [1] are not experimental ones but are taken from the systematics proposed in [27].

Note that the values of Z^2/A of the compound nuclei formed in the reactions of the table cover the region for those nuclei which are expected to be produced by the incomplete fusion reactions ^{7}Li(43A MeV) + ^{232}Th and ^{14}N(34A MeV) + ^{197}Au considered in the following.

4.2. Fission from ^{7}Li(43A MeV) + ^{232}Th

Since in the incomplete fusion reaction no large angular momentum of the fissioning nuclei is expected, all calculations have been performed for $L = 0$. On the other hand, the variance of the fragment mass distribution does not show substantial dependence upon angular momentum up to $L \approx 25\hbar$.

The main uncertainty for any comparison between measured data and model calculations is related to the definition of the fissioning nucleus. We, therefore, performed calculations for both nuclei ^{235}Np and ^{236}Th, which represent the most and the least fissile nuclides, respectively, formed in the incomplete fusion reaction considered.

The calculated fission fragment mass variances are compared with the experimental values obtained

for the reaction ^{7}Li(43A MeV) + ^{232}Th [13] in Fig. 1a. As is expected from the data of the table, the values of σ_M^2 calculated for ^{235}Np ($Z^2/A = 36.8$) are substantially larger than those for ^{236}Th ($Z^2/A = 34.3$). The satisfactory agreement in the latter case allows us to conclude that, obviously, ^{236}Th represents the most probable fissioning nucleus in these reactions.

The saturation-like behavior of $\sigma_M^2(E^*_{\rm tot})$ observed at $E^*_{\rm tot} \approx 100$–$180$ MeV [13] can be explained in the following way. With increasing $E^*_{\rm tot}$ (or T), the average time for neutron emission (τ_n) decreases. This decrease is approximately described by the expression

$$\tau_n \sim \frac{\exp(B_n/T)}{T^2}, \qquad (11)$$

where B_n is the neutron binding energy. Note that this expression supersedes the estimation given in [13]. Retarded by the dissipation, the Brownian collective motion of the system is slow enough to let the system cool down by particle emission. Since the system loses a substantial fraction of its initial intrinsic excitation energy, the magnitude of mass-asymmetry mode fluctuations becomes smaller, resulting in a narrower fragment mass distribution than actually expected from Eq. (1). It has already been shown in [28] that, as a general feature, the scission of the nucleus into the two fragments occurs at approximately 70 MeV, irrespective of its initial excitation energy. Our experimental as well as theoretical results (Fig. 1a) are qualitatively in accordance with this finding; i.e., σ_M^2 does not increase anymore with increasing $E^*_{\rm tot}$.

We proved the reliability of our calculations by comparing the obtained average fragment masses ($\langle M\rangle$) with the experimental ones (Fig. 1b). The measured $\langle M\rangle$ are below the calculated values in both cases because postscission particle emission is not included in the calculations. It is interesting that the values of $\langle M\rangle$ calculated for fission of ^{236}Th and ^{235}Np are very close to each other. This is, however, not the case for the prior-to-scission neutron multiplicities (Fig. 1c). The excess of $\langle n_{\rm pre}\rangle$ observed for fission of ^{236}Th reflects the isospin dependence of the neutron binding energy.

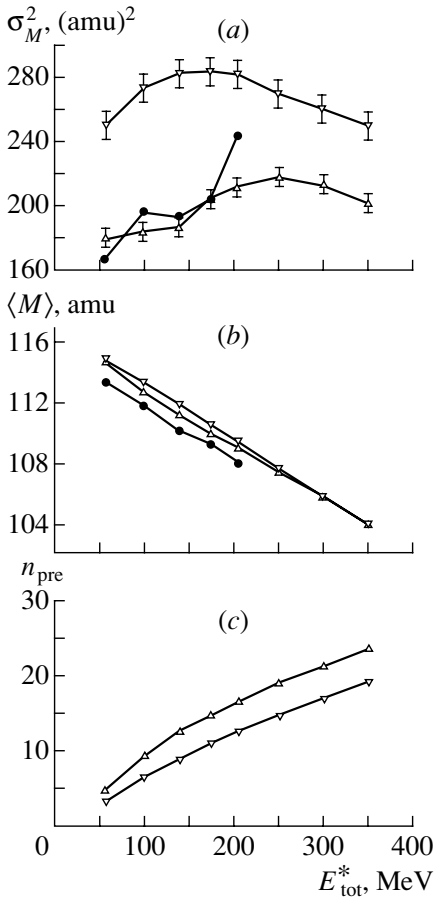

Fig. 1. The fragment mass variances (σ_M^2 in units of (amu)^2) (a), the average fragment masses ($\langle M\rangle$ in units of amu) (b), and prior-to-scission neutron multiplicities ($n_{\rm pre}$) (c) are shown versus the excitation energy ($E^*_{\rm tot}$). Experimental data (full circles) are presented for the incomplete fusion reaction ^{7}Li(43A MeV) + ^{232}Th. Their uncertainties are those of [13] and are not presented here so as to not clutter up the figure. The calculations have been performed for $4n$ + ^{232}Th → ^{236}Th (up triangles) and $3p$ + ^{232}Th → ^{235}Np (down triangles). The errors of the calculated values are given by the statistics of the simulations and do not exceed the size of the symbols used in the panels (b) and (c).

4.3. Fission from ^{14}N (34A MeV) + ^{197}Au

The situation in the case of the reaction ^{14}N(34A MeV) + ^{197}Au is more complicated (Fig. 2a). In the region of excitation energies of $E^*_{\rm tot} \approx 100$–$180$ MeV, the plateau-like behavior of the fragment mass variance is observed as for the reaction ^{7}Li(43A MeV) + ^{232}Th (cf. Fig. 1a). At larger values of $E^*_{\rm tot}$, however, the variance starts to rise steeply (from ≈ 250 (amu)^2 at $E^*_{\rm tot} \approx 180$ MeV up to ≈ 370 amu^2 at $E^*_{\rm tot} \approx 270$ MeV). A hint for such behavior seems to have already been found in [4], but it is difficult to make any definite conclusion from the data of this work because of the rather large experimental errors. Evidence of this trend can, however, also be seen in the measured data represented in Fig. 1a at $E^*_{\rm tot} \approx 200$ MeV.

From a rather simple analysis [29] of the shape of the fragment mass distribution with increasing $E^*_{\rm tot}$, it has been suggested that a different reaction mecha-

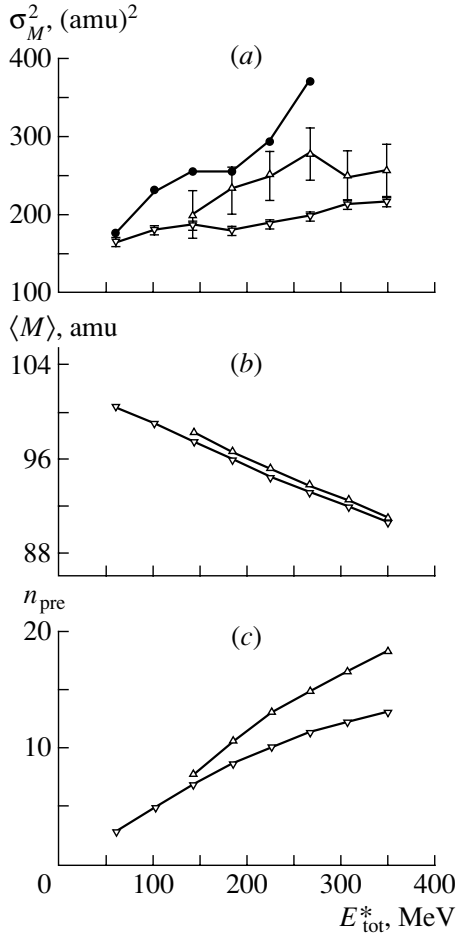

Fig. 2. The same data as presented in Fig. 1, but for the incomplete fusion reaction ^{14}N(34A MeV) + ^{197}Au. The calculations have been performed for $7n$ + ^{197}Au → ^{204}Au (up triangles) and $7p$ + ^{197}Au → ^{204}Rn (down triangles).

nism than ordinary fission becomes possible at higher excitation energies. Since such mechanism should be characterized by a broader fragment mass distribution extending to very asymmetric mass splittings, this process is supposed to be faster than ordinary fission. Therefore, it was conditionally named "binary fragmentation" [29]. The separation of the fragments originating from these superimposing disintegration processes by means of conventional multidimensional analysis procedures, however, turned out to be difficult.

Recently, a new method for heavy-ion induced reaction data analysis has been developed, which is based on the consideration of the excitation energy sharing between the binary fragments [30]. By applying this method to binary-decay data obtained for the reactions ^{14}N(53A MeV) + ^{197}Au [31], ^{14}N(53A MeV) + ^{232}Th [12], ^{40}Ar(36A MeV) + ^{248}Cm [12, 32], and ^{40}Ar(36A MeV) + $^{\text{nat}}$Ag [12, 32], it could be clearly demonstrated for the first time that several reaction mechanisms contribute to the final fragment mass distributions [30, 33, 34]. For the case of binary fragmentation, it was indeed found that a nonequilibrium excitation energy sharing occurs [34, 35].

Concerning the fragment mass variance from the reaction ^{14}N(34A MeV) + ^{197}Au (Fig. 2a), the steep rise of σ_M^2 observed at high E^*_{tot} is, therefore, likely to result from another disintegration process. Since our dynamical stochastic model is confined to the description of ordinary fission, we shall ignore it in the following considerations referring to a forthcoming paper [35].

The calculations performed for σ_M^2 from ^{14}N(34A MeV) + ^{197}Au (see Fig. 2a) also concern two extreme cases. Namely, if all the protons of the projectile are transferred to the composite system, we have to consider fission of a hot ^{204}Rn nucleus ($Z^2/A = 36.3$), and contrary to that, if all neutrons of the projectile are transferred, the fissioning nucleus is ^{204}Au ($Z^2/A = 30.6$). With reference to the findings of [1], one can expect that neither of them provides the lowest limit of σ_M^2 because the dependence of the mass variance on Z^2/A shows a broad minimum in the region of $31 \leq Z^2/A \leq 37$. However, as shown in Fig. 2a, our calculations underestimate the measured data.

The first extreme assumption (with all the protons transferred) completely disagrees with the experimental data and can be excluded. It is interesting that this case is excluded for the reaction ^{14}N(34A MeV) + ^{197}Au because the calculated values of σ_M^2 are definitely below the measured data, whereas they are definitely above the data for the reaction ^{7}Li(43A MeV) + ^{232}Th (cf. Fig. 1a).

Somewhat better agreement between calculations and measurement can be observed for the fissioning nucleus assumed to be ^{204}Au. The large error bars at the calculated values are in this case caused by the very small fission probability of ^{204}Au (typically $\approx 0.5\%$) resulting in moderate statistics of the simulations carried out. For the same reason, calculations at energies below 140 MeV could not have been performed. Since a variety of composite systems can be produced by the incomplete fusion reaction considered, the resulting σ_M^2 is, of course, formed by their initial partitions.

Recalling binary fragmentation, the influence of such a process should generally lead to an enlargement of the average fragment mass variance finally observed, and so even below that value of E^*_{tot}

where it eventually becomes dominating. Evidence of such influence in the energy region where σ_M^2 shows a plateau-like behavior has already been found in [29]. Furthermore, it was shown in [30] that very asymmetric binary disintegrations also occur after semiperipheral collisions, which do not proceed via an equilibrated compound-like system but are known as PLF–TLF formation (PLF—projectile-like fragments, TLF—targetlike fragments). Hence, some contribution to the fragment mass variance from binary disintegration processes other than ordinary fission might possibly explain that the calculated values are mostly below the measured ones. This effect should also be stronger for the reaction ^{14}N(34A MeV) + ^{197}Au than for ^{7}Li(43A MeV) + ^{232}Th, where fissile Th-like nuclei are produced.

Since processes other than ordinary fission are out of the scope of our model, a more detailed investigation of the behavior of σ_M^2 at $E_{\rm tot}^* > 200$ MeV needs a proper separation of all contributing reaction types. Such an attempt was made by means of a nonconventional analysis [30] in [35].

The average fission fragment masses and the prior-to-scission neutron multiplicities calculated for the reaction ^{14}N(34A MeV) + ^{197}Au are given for completeness in Figs. 2*b* and 2*c*, respectively.

5. SUMMARY

The fragment mass variances measured for fission of hot compound systems created in the incomplete fusion reactions ^{7}Li(43A MeV) + ^{232}Th and ^{14}N(34A MeV) + ^{197}Au can be rather well described up to excitation energies of about 200 MeV by a recently developed dynamical stochastic model of fission and light-particle emission. The plateau-like behavior of the fragment mass variance observed at excitation energies larger than about 100 MeV is connected with the decrease in the average neutron emission time. The relatively slow Brownian collective motion of the compound nucleus governed by large one-body friction enables the system to considerably cool down by light-particle emission before fission.

The model does not predict any rapid increase of the fragment mass variance observed at energies in excess of 200 MeV. This fact might indicate that, starting from an initial excitation energy of about 200 MeV, ordinary fission stops being a dominating decay process, and the binary disintegration becomes governed by nonequilibrium reaction mechanisms.

ACKNOWLEDGMENTS

The authors of this paper are cordially grateful to V.V. Pashkevich, A.Ya. Rusanov, and M. Morjean for valuable discussions, remarks, and advice; to L.V. Guryan for his help in performing the calculations; and to W. Neubert for attracting their attention to an earlier work.

This work was supported by the BMBF, Germany, under contract 06 DR 671. The research was partly enabled by the grants 211d and 1683s from the International Soros Science Educational Program and the Government of the Russian Federation.

REFERENCES

1. A. Ya. Rusanov, M. G. Itkis, and V. N. Okolovich, Yad. Fiz. **60**, 773 (1997) [Phys. At. Nucl. **60**, 683 (1997)].
2. C. Lebrun *et al.*, Nucl. Phys. A **321**, 207 (1979).
3. B. Borderie *et al.*, Z. Phys. A **299**, 263 (1981).
4. L. N. Andronenko *et al.*, Z. Phys. A **318**, 97 (1984).
5. H.-G. Ortlepp *et al.*, Nucl. Instrum. Methods Phys. Res. A **403**, 65 (1998).
6. A. A. Aleksandrov *et al.*, Report FZR-35 (Forschungszentrum Rossendorf, 1994), p. 55.
7. A. A. Aleksandrov *et al.*, Report FZR-78 (Forschungszentrum Rossendorf, 1995), p. 77.
8. A. A. Aleksandrov *et al.*, Nucl. Phys. A **583**, 465 (1994).
9. H.-G. Ortlepp *et al.*, in *Proceedings of the XV Nuclear Physics Divisional Conference of the European Physical Society on Low-Energy Nuclear Dynamics, St. Petersburg, Russia, 1995,* Ed. by Yu. Oganessian, W. von Oertzen, and R. Kalpakchieva (World Sci., Singapore, 1995), p. 231.
10. W. Wagner *et al.*, in *Proceedings of the 2nd International Symposium on Heavy-Ion Physics and its Applications, Lanzhou, China, 1995,* Ed. by Y. X. Luo, G. M. Jin, and J. Y. Liu (World Sci., Singapore, 1996), p. 217.
11. W. Wagner *et al.*, in *Advances in Nuclear Dynamics 2,* Ed. by W. Bauer and G. D. Westfall (Plenum, New York, 1996), p. 341.
12. C.-M. Herbach, H.-G. Ortlepp, and W. Wagner, in *Proceedings of the VI International School-Seminar on Heavy-Ion Physics, Dubna, Russia, 1997,* Ed. by Yu. Ts. Oganessian and R. Kalpakchieva (World Sci., Singapore, 1998), p. 232.
13. H.-G. Ortlepp *et al.*, Nucl. Phys. A **642**, 407 (1997).
14. I. I. Gontchar *et al.*, Yad. Fiz. **63**, 1778 (2000) [Phys. At. Nucl. **63**, 1688 (2000)].
15. I. Gontchar, L. A. Litnevsky, and P. Fröbrich, Comput. Phys. Commun. **107**, 223 (1997).
16. M. Brack *et al.*, Rev. Mod. Phys. **44**, 320 (1972).
17. Y. Abe *et al.*, Phys. Rep. **275**, 49 (1996).
18. D. V. Vanin, G. I. Kosenko, and G. D. Adeev, Phys. Rev. C **59**, 2114 (1999).
19. W. D. Myers and W. J. Swiatecki, Nucl. Phys. **81**, 1 (1966); Ark. Fys. **36**, 343 (1967).

20. P. Fröbrich and I. Gontchar, Phys. Rep. **292**, 132 (1998).
21. G.-R. Tillack *et al.*, Phys. Lett. B **296**, 296 (1992).
22. N. D. Mavlitov, P. Fröbrich, and I. Gontchar, Z. Phys. A **342**, 195 (1992).
23. A. V. Ignatyuk *et al.*, Yad. Fiz. **21**, 1185 (1975) [Sov. J. Nucl. Phys. **21**, 10 (1975)].
24. E. M. Rastopchin *et al.*, Yad. Fiz. **49**, 24 (1989) [Sov. J. Nucl. Phys. **49**, 15 (1989)].
25. K. T. R. Davies, A. J. Sierk, and J. R. Nix, Phys. Rev. C **13**, 2385 (1976).
26. J. P. Blocki, H. Feldmeier, and W. J. Swiatecki, Nucl. Phys. A **459**, 145 (1986).
27. E. M. Kozulin, A. Ya. Rusanov, and G. N. Smirenkin, Yad. Fiz. **56** (2), 37 (1993) [Phys. At. Nucl. **56**, 166 (1993)].
28. D. Hilscher and H. Rossner, Ann. Phys. (Paris) **17**, 471 (1992).
29. W. Wagner and H.-G. Ortlepp, *Heavy-Ion Physics,* Scientific Report 1995/96, E7-97-206, JINR (Joint Institute for Nuclear Research, Dubna, 1997), p. 243.
30. D. V. Kamanin, PhD Thesis (Technische Universität Dresden, Forschungszentrum Rossendorf, 1999).
31. A. A. Aleksandrov *et al.*, Report FZR-130 (Forschungszentrum Rossendorf, 1996), p. 95.
32. A. A. Aleksandrov *et al.*, Report FZR-215 (Forschungszentrum Rossendorf, 1998), p. 57.
33. D. V. Kamanin *et al.*, Report FZR-271 (Forschungszentrum Rossendorf, 1999), p. 83.
34. D. V. Kamanin, W. Wagner, and H. Freiesleben, Report FZR-271 (Forschungszentrum Rossendorf, 1999), p. 84.
35. D. V. Kamanin *et al.*, submitted to Nucl. Phys. A.

Physics of Atomic Nuclei, Vol. 65, No. 8, 2002, pp. 1411–1416. Translated from Yadernaya Fizika, Vol. 65, No. 8, 2002, pp. 1446–1451.

NUCLEI
Theory

Spin Dependence of the Shape of Even–Even Nuclei within the Davydov–Chaban Model

I. E. Kashuba and O. I. Davidovskaya*

Institute of Nuclear Research, National Academy of Sciences of Ukraine, pr. Nauki 47, 03680 Kiev, Ukraine

Received March 28, 2001; in final form, July 27, 2001

Abstract—Within a model of a nonaxial even–even nucleus soft in β vibrations, the shape parameters of the ^{154}Gd, ^{156,158,160}Dy, ^{164,168}Er, ^{168}Yb, ^{176}Hf, and ^{180}W nuclei are calculated in the quadrupole approximation as functions of the excited-state spin. © *2002 MAIK "Nauka/Interperiodica".*

1. INTRODUCTION

Microscopic models of nuclear systems are still unable to predict satisfactorily the values of some physical variables characterizing the nucleus and nuclear interactions. This is one of the reasons why much attention is given to creating and developing phenomenological models that make it possible to describe quite simply and clearly a broad variety of nuclear properties. A comparison of quantities calculated on the basis of such models with those measured experimentally enable one to determine model parameters of the nucleus, feasible modes of the motion, and their interplay for specific nuclei and nuclear reactions.

A model of a nonaxial deformed even–even nucleus soft with respect to β vibrations of the surface (the Davydov–Chaban model [2], below referred to as the DChM) underlies one of such approaches based on the use of the A. Bohr Hamiltonian [1]. Just like other models of this class, it implies that there is a relation between the sequence of the spin values of excited nuclear states and the dependence of their energy spectrum on the shape parameters of the nucleus involved; all this enables one to determine the type of collective mode (a rotational, a vibrational, or a mixed one).

A systematic analysis of the energy spectrum and of the electromagnetic structure of nuclei on the basis of available experimental data (see, for example, [3, 4]) revealed general regularities both in the classification of the nuclei according to their excitation mode and in the behavior of their model parameters versus the nucleonic composition of nuclei and the quantum numbers of their states. This made it possible to determine, on the basis of the identification of nuclear states, the disposition of their energy bands in accordance with the $SU(3)$ symmetry group.

A feature peculiar to even–even nuclei is that levels that are observed in their excitation spectra and which belong to the ground-state and the β-rotational band do not satisfy the rule of $I(I+1)$ intervals for a spin I. The deviation from this rule becomes more pronounced with increasing nonaxiality parameter γ. Within the vibrational–rotational model of Greiner [5], this effect is considered as a consequence of the centrifugal tension of a nucleus, while, within the DChM involving a quadrupole deformation, it is taken into account by the parameter μ_β of nuclear softness with respect to longitudinal β vibrations of the surface. The inclusion of nuclear-surface γ vibrations [6] generates additional energy bands featuring their own sets of quantum numbers for both positive- and negative-parity states.

The structure of nucleus excitations can be described in various ways. Within models employing the Bohr Hamiltonian (for example, in the DChM), excited states are considered as eigenfunctions of this Hamiltonian, while, within the interacting-boson model [7], the excited states are treated as ground-state excitations. However, many relations obtained within different approaches agree well with one another and are quite appropriate for revealing general regularities in the phenomenology of the nuclear structure [8, 9]. In particular, a variation of the Hamiltonian parameters in the interacting-boson model leads to a change (a smooth or a sharp one) in the equilibrium shape of the nucleus [10]; that is, the shape parameters may depend not only on the nuclear-deformation parameters, but also on the spin variable I of an excited state. Nuclear features extracted from available data on reduced $E2$-transition probabilities $B(E2; I \to I-1)$ indicate that nuclear softness may increase with increasing spin of the state [11]. Our results obtained within the DChM also confirm that the calculated energies of excited nuclear states agree worse with experimental data

*e-mail: odavi@kinr.kiev.ua

1063-7788/02/6508-1411$22.00

as the spin increases. This suggests that it is necessary either to introduce additional compensation terms in the DChM Hamiltonian or to assume that the model shape parameters of the nuclei for which this is observed depend on the spin of their state. This assumption seems more appropriate since the model remains associated with the Bohr Hamiltonian. The explicit form of these dependences can be found from an analysis of relevant experimental energy spectra of nuclear excitations, and this is precisely the objective of the present study.

2. FUNDAMENTALS OF THE MODEL OF A SOFT NUCLEUS

Any collective nuclear model based on the Bohr Hamiltonian [1] must include various pure modes of motion and their mixtures. The choice of the DChM for analyzing the energy spectra of excited even–even nuclei seems quite reasonable since this model implies the presence of various rotational–vibrational states in the form of bands whose disposition on the energy scale correlates with a specific nuclear shape and with its dynamics. For the model Hamiltonian, use is made of the expression

$$\hat{H} = \hat{T}_\beta + \frac{\hbar^2}{4B\beta^2}\hat{T}_{\rm rot} + V(\beta). \qquad (1)$$

In the four-dimensional space spanned by the Euler angles $\hat{\theta} = \{\theta_1, \theta_2, \theta_3\}$ and the total deformation β, individual terms characterize, respectively, the kinetic energy of longitudinal β vibrations, rotation, and the potential energy of the deformed nucleus at a fixed value of the variable $\gamma = \gamma_{\rm eff}$, which is an effective parameter of its nonaxiality. Specifically, we have (see [2, 3])

$$\hat{T}_\beta = -\frac{\hbar^2}{2B\beta^3}\frac{\partial}{\partial\beta}\left(\beta^3\frac{\partial}{\partial\beta}\right), \qquad (2)$$

$$\hat{T}_{\rm rot} = \frac{1}{2}\sum_{\lambda=1}^{3}\sin^{-2}\left(\gamma - \frac{2\pi}{3}\lambda\right)\hat{I}_\lambda^2, \qquad (3)$$

$$V(\beta) = \frac{1}{2}C_\beta(\beta - \beta_0)^2, \qquad (4)$$

where β_0 is the parameter of the longitudinal deformation of the nucleus in the ground state; B and C_β are, respectively, the mass parameter and the elasticity of the nucleus with respect to longitudinal vibrations; and $\hat{I}_\lambda$ are the projections (in units of $\hbar$) of the total angular momentum of the nucleus onto the axes of its intrinsic coordinate frame.

If we take into account the effect of nuclear tension due to its rotation and associate the softness of the nucleus with respect to longitudinal spinless vibrations with the energy $\hbar\omega_0$(DChM), we arrive at the Schrödinger equation with the operator in (1) for the wave function

$$\Psi_{IM\tau}(\beta, \hat{\theta}) = F_{I\tau}(\beta)\,\Phi_{IM\tau}(\hat{\theta}), \qquad (5)$$

provided that β vibrations are independent of the Euler angles $\hat{\theta}$. Each of the factors in (5) satisfies the relevant equation; that is,

$$[\,\hat{T}_{\rm rot} - \varepsilon_{I\tau}\,]\,\Phi_{IM\tau}(\hat{\theta}) = 0, \qquad (6a)$$

$$\left[\hat{T}_\beta + V(\beta) + \frac{\hbar^2}{4B\beta^2}\varepsilon_{I\tau} - E_{I\tau}\right]F_{I\tau}(\beta) = 0, \qquad (6b)$$

where $E_{I\tau}$ and $\varepsilon_{I\tau}$ are, respectively, the energies of nuclear states with allowance for β vibrations of the nuclear surface and the dimensionless eigenvalues of the operator in (3).

Solutions to Eqs. (6) depend on the parameters $\gamma_{\rm eff}$ and μ_β and on the energy factor $\hbar\omega_0$, which are determined numerically by fitting the chosen basic set of calculated excited states to experimental data on energy levels [12]. The choice of the quantum-number set (τ is the number of states for the spin value of I, while n_β is the ordinal number of the β band) for characterizing nuclear states or the inclusion of additional numbers—for example, n_γ (the number of the γ band)—leads to different values of the model parameters for each specific set of basic states. This effect is also confirmed by previous studies aimed at determining $\gamma_{\rm eff}$ by using various ratios of energy levels—in particular, (a) $E(2_2^+)/E(2_1^+)$ and (b) $E(4_1^+)/E(2_1^+)$ yield $\gamma_{\rm eff}$(a) $<$ $\gamma_{\rm eff}$(b) [12].

In order to explore this situation further, we have calculated, on the basis of the DChM, energy spectra of the even–even nuclei ^{154}Gd, ^{156,158,160}Dy, ^{164,168}Er, ^{168}Yb, ^{176}Hf, and ^{180}W for the ground-state rotational band ($n_\beta = 0$, $n_\gamma = 0$, $\tau = 1$), the β rotational band ($n_\beta = 1$, $n_\gamma = 0$, $\tau = 1$), and the first anomalous γ band ($n_\beta = n_\gamma = 0$). While, in previous studies (see, for example, [3]), the spin independence of the parameters μ_β, $\gamma_{\rm eff}$, and $\hbar\omega_0$ was assumed, the existence of such a spin dependence induced by pairing in the nuclear system [13] or by phase transitions for its states [14] is admitted here.

According to the fundamentals of the DChM (see [2, p. 116]), the value of the β deformation depends on the quantum numbers τ and I—that is, $\beta = \beta_{I\tau}$—while the parameter μ_β is functionally related, by definition, to B, C_β, and β_0 by the equation

$$\mu_\beta = \beta_0^{-1}\,[\,\hbar^2/(BC_\beta)\,]^{\,1/4}, \qquad (7a)$$

which can be rewritten in terms of the eigenvalues of the operator in (3) as

$$\mu_\beta = \left\{2\left(\beta_{I\tau}/\beta_0\right)^3\left[\left(\beta_{I\tau}/\beta_0\right)-1\right]\varepsilon_{I\tau}^{-1}\right\}^{1/4}. \quad (7b)$$

As to the behavior of the nonaxiality parameter γ_{eff} in the DChM, we can state [6] that, similarly to β vibrations, γ vibrations lead to a transverse softness of the nucleus with the corresponding consequences in the spin dependence of the parameter γ_{eff}.

3. THEORETICAL ANALYSIS OF THE ENERGY SPECTRUM OF AN EVEN–EVEN NUCLEUS ON THE BASIS OF THE DChM

In the absence of γ vibrations, a state of an even–even nucleus with allowance for rotational–vibrational coupling within the DChM has the excitation energy [3]

$$\Delta E^{\text{th}}_{I\tau n_\beta} = \hbar\omega_0\left\{\left(\nu_{I\tau n_\beta}+\frac{1}{2}\right)\sqrt{4-\frac{3}{p_{I\tau}}} \right. \quad (8)$$
$$\left. +\frac{\varepsilon_{I\tau}}{4}\left(\frac{\mu_\beta}{p_{I\tau}}\right)^2\left[1+\frac{\varepsilon_{I\tau}}{2}\left(\frac{\mu_\beta}{p_{I\tau}}\right)^4\right]-\nu_0-\frac{1}{2}\right\},$$

where $p_{I\tau}$ controls the increase in the equilibrium deformation β_0 of the ground state of the nucleus upon its transition to the state $|I,\tau\rangle$ and is independent of the quantum number n_β and $\nu_{I\tau n_\beta}$ and ν_0 are parametric zeros of the parabolic-cylinder functions for the excited and the ground state, respectively. These zeros are found as solutions to the equation

$$D_\nu\left[-\sqrt{2}\mu_\beta^{-1}p_{I\tau}\left(4-3p_{I\tau}^{-1}\right)^{1/4}\right]=0 \quad (9)$$

in ν for the equilibrium value of the longitudinal deformation $\beta_{I\tau}$.

Numerical values of the parameters μ_β, γ_{eff}, and $\hbar\omega_0$ were determined by minimizing the mean-square deviation of experimental data (expt) on the energy levels from those calculated according to (8) (calc),

$$\min\chi^2 \quad (10)$$
$$=\min\left\{\frac{1}{N}\sum_{i=1}^{N}\left[\left(E_i^{\text{expt}}-\Delta E_i^{\text{theor}}\right)\Big/E_i^{\text{expt}}\right]^2\right\},$$

where N is the number of nuclear levels for which the model energies $\Delta E_i^{\text{theor}}$ of the levels are fitted to the experimental values E_i^{expt}. The parameters μ_β and γ_{eff} were varied independently, while the factor $\hbar\omega_0$, which controls the energy scale (see [2, p. 136]), was found by minimizing the functional in (10).

In [3], the levels of the ground-state rotational band ($n_\beta=0$, $\tau=1$, $I=2,4,6,\ldots$) and of the anomalous γ band ($n_\beta=0$, $I=2,3,4,\ldots$, $\tau=1,2$) were chosen as basic ones in determining the nuclear-shape parameters within the DChM. The parameters μ_β and γ_{eff} obtained in this way describe the positions of the energy levels much better than the results obtained within the model of a hard nonaxial nucleus (Davydov–Filippov model, also known as DFM) [2], where the absence of nucleus softness is partly compensated by a larger nonaxiality parameter γ_{eff} than in the DChM, since an increase in μ_β leads to an increase in the difference $\Delta\gamma\equiv\gamma^{\text{DFM}}-\gamma^{\text{DChM}}>0$. For example, we have $\mu_\beta=0.199$, $\gamma^{\text{DChM}}=11.7^\circ$ [3], and $\gamma^{\text{DFM}}=14.8^\circ$ [12] for the ^{160}Dy nucleus and $\mu_\beta=0.378$, $\gamma^{\text{DChM}}=13.7^\circ$ [3], and $\gamma^{\text{DFM}}=23.6^\circ$ [12] for ^{156}Dy. Hence, the parameters γ_{eff} and μ_β can be treated, to some extent, as correlated ones. This fact is illustrated by the above example of the calculation within models assuming the spin independence of their parameters.

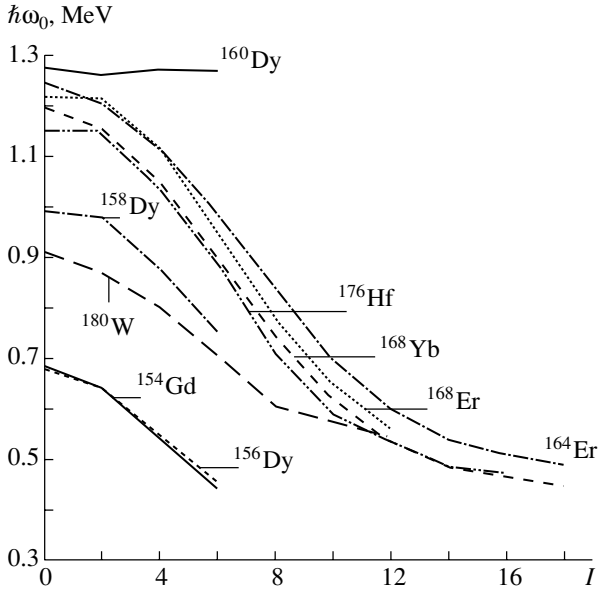

Energy factor $\hbar\omega_0$ as a function of the spin I of an excited state of an even–even nucleus within the model of a nonaxial rotator soft with respect to β vibrations.

The DChM calculation including only states characterized by a fixed value of the spin I (see Table 1, column 2) yields different parameter values in each specific case (see columns 3–5), which, in the linear approximation, can be described by the functions $\mu_\beta(A)$ and $\gamma_{\text{eff}}(A)$ (column 6), where $A\equiv I(I+1)$. At $I=0$, these dependences agree well with the results presented in [3].

As to the factors $\hbar\omega_0(I)$ for excited states that are not presented in Table 1, column 2, they can be calculated by fitting the experimental energies of the levels of the ground-state rotational band at the

Table 1. Results obtained by fitting the DChM parameters γ_{eff}, μ_β, and $\hbar\omega_0$ of even–even nuclei to the energies of levels for states characterized by the same value of the spin I and their approximation as functions of the variable $A \equiv I(I+1)$

Nucleus	I^π	γ_{eff}, grad	μ_β	$\hbar\omega_0$, MeV	Approximation of the functions $\gamma_{\text{eff}}(A)$, $\mu_\beta(A)$
1	2	3	4	5	6
^{154}Gd	$2+$	12.38	0.423	0.6373	$\gamma_{\text{eff}} = 12.6 - 0.059A$ $\mu_\beta = 0.380 + 0.0064A$
	4^+	11.25	0.503	0.5339	
	6^+	10.18	0.662	0.4392	
^{156}Dy	$2+$	13.09	0.407	0.6350	$\gamma_{\text{eff}} = 13.3 - 0.047A$ $\mu_\beta = 0.364 + 0.0069A$
	4^+	12.37	0.498	0.5410	
	6^+	11.38	0.655	0.4521	
^{158}Dy	$2+$	12.29	0.300	0.9747	$\gamma_{\text{eff}} = 12.5 - 0.0186A$ $\mu_\beta = 0.288 + 0.00233A$
	4^+	12.24	0.337	0.8737	
	6^+	11.65	0.384	0.7501	
^{160}Dy	$2+$	11.44	0.243	1.2615	$\gamma_{\text{eff}} = 11.4 - 0.0031A$ $\mu_\beta = 0.242 + 0.0000345A$
	4^+	11.32	0.242	1.2702	
	6^+	11.31	0.244	1.2665	
^{164}Er	$2+$	12.38	0.253	1.2048	$\gamma_{\text{eff}} = 12.42 - 0.0073A$ $\mu_\beta = 0.241 + 0.00145A$
	4^+	12.28	0.264	1.1168	
	6^+	12.12	0.287	0.9844	
^{168}Er	$2+$	11.99	0.238	1.2145	$\gamma_{\text{eff}} = 12.0 + 0.0229A$ $\mu_\beta = 0.226 + 0.0021A$
	4^+	12.71	0.270	1.1146	
	6^+	12.85	0.313	0.9412	
^{168}Yb	$2+$	11.34	0.256	1.1533	$\gamma_{\text{eff}} = 11.4 + 0.0093A$ $\mu_\beta = 0.245 + 0.0021A$
	4^+	11.85	0.292	1.0470	
	6^+	11.72	0.332	0.8947	
^{176}Hf	$2+$	9.60	0.260	1.1469	$\gamma_{\text{eff}} = 9.99 - 0.0148A$ $\mu_\beta = 0.247 + 0.0024A$
	4^+	9.99	0.300	1.0331	
	6^+	9.54	0.341	0.8853	
	8^+	8.80	0.423	0.7056	
^{180}W	$2+$	13.81	0.338	0.8659	$\gamma_{\text{eff}} = 13.7 - 0.0056A$ $\mu_\beta = 0.315 + 0.0025A$
	4^+	13.52	0.359	0.7981	
	6^+	13.37	0.409	0.7041	
	8^+	13.39	0.507	0.6022	

parameters $\mu_\beta(A)$ and $\gamma_{\text{eff}}(A)$ set to the values in Table 1 (column 6). The results of this analysis for the function $\hbar\omega_0(I)$ are shown in the figure by broken lines for each of the nuclei considered; they can be approximated by the function

$$\hbar\omega_0(I) = \exp\left\{\sum_{m=0}^{M} C_m I^m\right\}, \qquad (11)$$

where the coefficients C_m are determined by fitting the energy levels of the ground-state rotational band. By

Table 2. Experimental values of the excitation energies of the ^{164}Er nucleus along with theoretical values calculated on the basis of the DChM in various approximations

I	n_β, τ	Parameters			Energy level, MeV		
		$\gamma_{\text{eff}}(I)$, grad	$\mu_\beta(I)$	$\hbar\omega_0(I)$, MeV	experiment [15]	theory, DChM	
						table 1	[3]
1	2	3	4	5	6	7	8
2	0, 1	12.38	0.253	1.203	0.09139	0.0913	0.091
4	0, 1	12.28	0.264	1.108	0.29946	0.297	0.299
6	0, 1	12.12	0.287	0.978	0.6144	0.610	0.617
2	0, 2	12.38	0.253	1.203	0.8603	0.859	0.858
3	0, 1	12.35	0.257	1.161	0.9463	0.938	0.946
8	0, 1	11.90	0.328	0.838	1.0246	1.033	1.032
4	0, 2	12.28	0.264	1.108	1.0583	1.047	1.068
5	0, 1	12.22	0.274	1.046	1.1975	1.178	1.211
0	1, 1	12.43	0.248	1.242	1.2459	1.242	
2	1, 1	12.38	0.253	1.203	1.3145	1.310	
6	0, 2	12.12	0.287	0.978	1.3588	1.350	1.401
4	1, 1	12.28	0.264	1.108	1.4696	1.450	
10	0, 1	11.63	0.394	0.709	1.5180	1.553	1.533
7	0, 1	12.02	0.305	0.908	1.5451	1.531	1.587
6	1, 1	12.12	0.287	0.978	1.7066	1.693	
8	0, 2	11.90	0.328	0.838	1.7446	1.771	1.861
12	0, 1	11.30	0.497	0.604	2.0827	2.110	2.110
14	0, 1	10.90	0.650	0.529	2.7025	2.665	2.760
16	0, 1	10.45	0.867	0.490	3.4112	3.261	3.478
18	0, 1	9.93	1.166	0.495	4.1212	3.845	

way of example, we indicate that, for the ^{164}Er nucleus, we used the following values of the coefficients in (11): $C_0 = 0.21672$, $C_1 = -2.0962 \times 10^{-3}$, $C_2 = -7.06921 \times 10^{-3}$, $C_3 = 7.50317 \times 10^{-5}$, and $C_4 = 9.24518 \times 10^{-6}$.

For the ^{164}Er nucleus taken as an example, the values of the parameters $\mu_\beta(I)$ and $\gamma_{\text{eff}}(I)$ and of the energy factor $\hbar\omega_0(I)$ calculated according to (11) are quoted in Table 2 along with the energies of the levels, both the experimental ones from [15] and their theoretical counterparts calculated with the parameters from Table 1 and the parameters from [3].

4. DISCUSSION

Table 2 shows that the results of the model calculations of the excited-state energies of the ^{164}Er nucleus agree well with experimental data. It is of importance that the description of many energy levels is based on employing the spin-dependent parameters $\gamma_{\text{eff}}(I)$ and $\mu_\beta(I)$ and the factor $\hbar\omega_0$. It can be seen from the figure that, for the nuclei investigated here (with the exception of the ^{160}Dy nucleus), the factor $\hbar\omega_0$ decreases with increasing spin, which anticorrelates with the behavior of the parameter $\mu_\beta(I)$.

The description of the spectrum of several energy bands reveals their common nature. Moreover, it has been found that, upon the inclusion of the spin dependence of the nuclear-shape parameter, the DChM enables us to describe the states of the ground-state rotational band even in that region of spin values ($I > I_{\text{crit}}$) where backbending occurs. The standard version of the DChM can only specify the value I_{crit}

[16] at which the agreement with experimental data becomes sharply poorer.

Our results on the spin dependence of the parameters γ and μ agree well with the predictions obtained on the basis of the cranking model [14] in studying the properties of the deformed nucleus ^{164}Er in the Hartree–Fock–Bogolyubov approximation. Even if, in the cranking model, these dependences differ from those that we have obtained, the very fact of the spin dependence is present, which is the most important point. It can be seen from the figure that the spin dependences $\hbar\omega_0(I)$ are similar for all the nuclei considered here and that, within our approach, this factor is related to the energy of spinless β vibrations rather than equal to it.

REFERENCES

1. A. Bohr, K. Dan. Vidensk. Selsk. Mat. Fys. Medd. **26** (14) (1952).
2. A. S. Davydov, *Excited States of Atomic Nuclei* (Atomizdat, Moscow, 1967).
3. I. E. Kashuba and É. Yu. Kotishevskaya, Izv. Akad. Nauk SSSR, Ser. Fiz. **39**, 617 (1975).
4. W. K. Koo and L. J. Tassie, Nucl. Phys. A **315**, 21 (1979).
5. J. M. Eisenberg and W. Greiner, *Nuclear Theory,* Vol. 1: *Nuclear Models* (North-Holland, Amsterdam, 1970; Atomizdat, Moscow, 1975).
6. I. E. Kashuba and Yu. V. Porodzinskiĭ, Ukr. Fiz. Zh. **44**, 677 (1999).
7. R. V. Jolos and Yu. V. Pal'chikov, Yad. Fiz. **63**, 633 (2000) [Phys. At. Nucl. **63**, 570 (2000)].
8. M. I. El Zaiki, H. O. Nafie, and K. E. Abd El Mageed, Indian J. Pure Appl. Phys. **30**, 113 (1992).
9. H. M. Mittal, S. Sharma, and J. B. Gupta, Phys. Scr. **43**, 558 (1991).
10. S. Kuyucak, V.-S. Lac, and I. Morrison, Phys. Lett. B **263**, 146 (1991).
11. I. Hamamoto, Nucl. Phys. A **520**, 297 (1990).
12. Y. P. Varshni and S. Bose, Nucl. Phys. A **144**, 645 (1970).
13. D. Karadzhov, I. N. Mikhaĭlov, E. Nadzhakov, and I. Piperova, Yad. Fiz. **24**, 888 (1976) [Sov. J. Nucl. Phys. **24**, 464 (1976)].
14. K. Tanabe and K. Sugawara-Tanabe, Nucl. Phys. A **390**, 385 (1982).
15. E. N. Shurshikov, Nucl. Data Sheets **47**, 433 (1986).
16. I. E. Kashuba, É. Yu. Kotishevskaya, and V. I. Ovcharenko, Ukr. Fiz. Zh. **19**, 805 (1974).

Translated by O. Chernavskaya

Physics of Atomic Nuclei, Vol. 65, No. 8, 2002, pp. 1417–1420. From Yadernaya Fizika, Vol. 65, No. 8, 2002, pp. 1452–1455.

NUCLEI
Theory

Effective Theory of *NN* Interactions in a Separable Representation*

B. V. Krippa and B. L. G. Bakker

Department of Physics and Astronomy, Free University, Amsterdam, the Netherlands

Received November 28, 2001

Abstract—We consider the effective field theory of the *NN* system in a separable representation. The pionic part of the effective potential is included nonperturbatively and approximated by a separable potential. The use of a separable representation allows for the explicit solution of the Lippmann–Schwinger equation and a consistent renormalization procedure. The phase shifts in the $^1S_0$ channel are calculated to subleading order. © *2002 MAIK "Nauka/Interperiodica".*

1. INTRODUCTION

Throughout the last few years, the effective field theory (EFT) has extensively been used for the study of nucleon—nucleon (*NN*) interactions. The activity in this field was inspired by the Weinberg proposal [1] that the EFT approach could be useful in low-energy nuclear physics. Since Weinberg's original paper, many aspects of this problem have been discussed [2].

Contrary to more phenomenological models of hadron interactions, EFT, which is based on the separation of light and heavy hadronic scales, allows for systematic expansion of the scattering amplitude order by order and the possibility of estimating a priori the anticipated errors at each order of the expansion using power-counting rules. Moreover, the EFT method offers a consistent way to avoid the otherwise uncontrollable uncertainties related to off-shell ambiguities. These ambiguities can, at least in principle, be eliminated in the EFT approach by having the freedom to work in different low-energy representations of the underlying QCD. The typical expansion parameter of EFT is the ratio p/Λ, where p and Λ are the generic low- and high-energy scales of the problem. However, while applied to the two-nucleon systems, EFT encounters a serious difficulty due to the existence of the extremely large S-wave scattering length (compared to the pion Compton wavelength). Thus, it turns out that the EFT description of the *NN* forces must be nonperturbative to incorporate this large scale. In the original work [1], Weinberg proposed applying counting rules to irreducible diagrams in order to construct the effective potential to be iterated in the Lippmann–Schwinger (LS) equation. It differs from the standard approach of chiral perturbation theory, where counting rules are applied to the whole scattering amplitude. In the case of the *NN* interactions, the effective potential consists of pointlike interactions and standard meson-exchange contributions. The leading order (LO) effective potential in the Weinberg approach is given by pointlike interactions without derivatives, and the one-pion-exchange term is assumed to be of order $O(p^0)$. One notes that on the level of the scattering amplitudes, the possibility of a consistent chiral counting is lost. Immediately one can see a complication. The corresponding effective potential is highly singular. The origin of this singularity is the local nature of the *NN* coupling. In order to obtain finite physical observables, one needs to carry out the procedure of regularization and renormalization. The issue of renormalization is much more involved in the case of the *NN* interaction as compared to the standard perturbative situation, where the renormalization can be carried out for a set of individual Feynman diagrams using the standard textbook methods. For the problem at hand, nonperturbative renormalization is required so that at every order the divergences of the whole nonperturbative amplitude must be subtracted.

A somewhat different way of constructing the EFT of the *NN* forces was proposed some time ago by Kaplan, Savage, and Wise (KSW) [3]. The idea was to sum up a certain subclass of LO diagrams, given by the lowest order contact interactions. In the KSW approach, the LO amplitude is assumed to be of order $O(p^{-1})$. The rest, including the higher order contact interactions and graphs with pions, can then be treated perturbatively. This approach is systematic, chirally symmetric, and is formulated in such a way that chiral counting rules can be applied directly to the *NN* scattering amplitude. The leading nonperturbative amplitude can be calculated in analytic form, allowing for the renormalization to be carried out in an explicit and transparent way. The renormalization

*This article was submitted by the authors in English.

of the perturbative corrections can be performed using the standard methods of dealing with divergencies of Feynman diagrams. However, the perturbative "pionic part" of this approach seems to show a rather slow convergence in some particular channels [4], making practical use of this approach somewhat problematic.

In the Weinberg approach, pion effects are treated to all orders. At very low energies, when pion degrees of freedom can safely be integrated out, the scattering amplitude can be derived analytically and so no problem with the renormalization arises. In the more general case of a potential consisting of the contact terms and a long-range one-pion-exchange (OPEP) contribution, the analytic solution of the three-dimensional LS equation is no longer possible and the problem must be treated numerically. However, it is not at all clear how to carry out the renormalization in such a nonperturbative case. One notes that it is not enough to regularize the integral part of the LS equation by imposing a simple cutoff or using form factors. In this case, one is still left with bare couplings and the physical amplitude may strongly depend on the value of the cutoff parameter. It contradicts the renormalization group requirements, according to which [5] the physical *NN* amplitude must be cutoff-independent (at least up to the order one is dealing with). To remove the unwanted cut-off dependence, one needs to switch to renormalized effective couplings. However, this is difficult to implement in the situation where the analytical solution is not known.

In this paper, we propose an approximate method of how to carry out the renormalization if an exact solution of the LS equation is not possible. Namely, we propose using the approximate analytical solution, which can be obtained if we represent the pionic part of the effective Lagrangian by a sum of separable terms. In this case, the integral equation can be transformed into a matrix equation and an analytical solution becomes possible. Then the renormalization can be carried out by subtracting the loop integrals at some fixed kinematical point $p^2 = -\mu^2$ and by replacing the bare constants with running ones, depending on the point of subtraction.

2. MODEL

We start from the standard nonrelativistic effective Lagrangian

$$\mathcal{L} = N^\dagger i\partial_t N - N^\dagger \frac{\nabla^2}{2m} N - \frac{1}{2} C (N^\dagger N)^2 \quad (1)$$
$$- \frac{1}{2} C_2 (N^\dagger \nabla^2 N)(N^\dagger N) + \mathcal{L}_\pi + \text{h.c.} + \ldots$$

Here, $\mathcal{L}_\pi$ is the pionic part of the effective chiral Lagrangian, m is the mass of a nucleon, and the nucleon field is denoted by N. This Lagrangian leads to the following effective potential for the ${}^1S_0$ *NN* scattering [1]:

$$V(p,p') = C' + C_2(p^2 + p'^2) + V_\pi(p,p'), \quad (2)$$

where

$$C' = C + \frac{g_A^2}{2f_\pi^2}; \quad V_\pi(p,p') = -\frac{\alpha_\pi}{q^2 + m_\pi^2}; \quad (3)$$
$$\alpha_\pi = \frac{g_A^2 m_\pi^2}{2f_\pi^2},$$

$\mathbf{q} = \mathbf{p} - \mathbf{p}'$, $g_A = 1.25$, and $f_\pi = 132$ MeV are the axial and pion decay constants, respectively. As mentioned above, the consistent numerical realization of the renormalization program in the nonperturbative situation is a very difficult task [6]; therefore, we adopt the strategy of an approximate analytic solution of the LS equation allowing for the explicit realization of the renormalization procedure. To achieve this goal, we represent the OPEP contribution by a sum of separable terms. As we shall henceforth limit our discussion to S waves only, the matrix elements are functions of the magnitudes of the momenta only. We write

$$V_\pi(p,p') = \sum_{j=1}^{n} \alpha_j \eta_j(p) \eta_j(p'). \quad (4)$$

One notes that, in principle, $V_\pi(p,p')$ can be parametrized with arbitrary accuracy, but in this short letter we would rather like to emphasize the issues related to renormalization in the effective description of the *NN* interaction. So, in practice, we retain only one term in a separable expansion. This turns out to be enough to illustrate the main features of our approach. Of course, this is quite a crude description of the OPEP, which approximates the exact pionic part of the effective Lagrangian with an average error of about 10–12% in the momentum region $0.4 < p < 1.4$ fm^{-1}. We postpone detailed analysis of the *NN* observables in the different partial waves and spin–isospin channels to a future publication.

After the separable approximation is substituted, the effective potential can be represented in the following matrix form:

$$V^{\text{eff}}(p,p') = \sum_{ij} g_i(p) M_{ij} g_j(p'), \quad (5)$$

where

$$g(p) = \begin{pmatrix} 1 \\ p^2 \\ \eta_1(p) \end{pmatrix} \quad \text{and} \quad M = \begin{pmatrix} C' & C_2 & 0 \\ C_2 & 0 & 0 \\ 0 & 0 & \alpha_1 \end{pmatrix}. \quad (6)$$

The solution of the LS equation can be represented as

$$T(p,p';E) = g_i(p)\tau_{ij}(E)g_j(p'). \qquad (7)$$

We denote by τ the 3×3 matrix containing the loop integrals $I_{ij}(E)$, given by

$$\tau(E) = [1 - M\,I(E)]^{-1}\,M, \qquad (8)$$

where

$$I_{ij}(E) = \int_0^\infty \frac{dqq^2}{2\pi^2}\frac{g_i(q)g_j(q)}{E+i\epsilon - E(q)}. \qquad (9)$$

Here, we define $E(q) = q^2/m$. The matrix $\tau(E)$ contains convergent and divergent integrals; therefore regularization and renormalization must be carried out. We use a subtraction scheme similar to the one suggested in [7]. Namely, all loop integrals are subtracted at some kinematical point $p^2 = -\mu^2$. The renormalized T matrix is

$$T^{\rm Reg}(p,p';E) = g_i(p)\;\tau_{ij}^{\rm Reg}(E)g_j(p'). \qquad (10)$$

In the following, we will omit the superscript "Reg," implying that we always work with the renormalized amplitude. One notes that the choice of the subtraction point is, in principle, arbitrary and the physical amplitude, being an observable, cannot depend on it. According to the standard rules of quantum field theory, the dependence of the regularized amplitude on the subtraction point is compensated if the fixed bare coupling constants are replaced by the running μ-dependent renormalized ones. The concrete form of this dependence is fixed by the Renormalization Group (RG) equation. The whole procedure is analogous to that commonly used in the standard chiral perturbation theory, when the perturbative expansion is applicable. Requiring that $dT/d\mu = 0$ and using the expression for the T matrix, one obtains the following RG equations for the LO coupling C:

$$\frac{\partial C(\mu)}{\partial\mu} = \left(C + \frac{g_A^2}{2f_\pi^2}\right)^2\frac{m}{4\pi} \qquad (11)$$
$$- 2\alpha_\pi\eta_1^2(\mu)\left(C + \frac{g_A^2}{2f_\pi^2}\right)\frac{m}{4\pi}.$$

Neglecting the term with the form factors $\eta_i(p)$, we arrive at the variant of the RG equations first derived by Kaplan *et al.* [3], where pions were included perturbatively. In the region where the second term becomes nonnegligible, the pionic effect must be treated in a nonperturbative manner.

Numerical results for the phase shifts $\delta(^1S_0)$ in degrees obtained within the separable approximation to the OPEP compared to the results from the Nijmegen phase-shift analysis ($T_{\rm lab}$ is given in MeV and p in fm^{-1})

$T_{\rm lab}$	p	$\delta_{\rm sep\ pot}$	$\delta_{\rm Nijm}$
20	0.48	46.9	53.6
50	0.77	43.6	40.1
70	0.91	40.1	34.3
90	1.02	34.7	29.1
110	1.13	26.8	24.6
130	1.24	17.6	20.6
150	1.32	10.0	16.9
170	1.41	2.6	13.6

3. NUMERICAL RESULTS

We used an exponential form for the separable form factors to parametrize the one-pion exchange potential

$$\eta_1(p) = \exp(-\beta p). \qquad (12)$$

The cutoff parameter β and strength parameter α are taken to be 0.78 fm and 1.73 fm^2, respectively. It provides a rather crude fit of the pionic part of the effective potential in the relevant energy region. However, as already mentioned, the purpose of this paper is rather to formulate a consistent renormalization procedure in the nonperturbative situation when an exact solution is not possible. A detailed comparison to the experimental phase shifts in different channels using a better fit with several separable terms will be reported elsewhere. The values of the effective constants used to calculate the phase shifts are $C(m_\pi) = -3.2$ fm^2 and $C_2(m_\pi) = 2.5$ fm^4. Their numerical values were fixed so as to reproduce phase shifts at low energies ($p < 10$ MeV/c). These values are to be compared with the chiral counting rules, according to which the effective couplings $C_{2n}(\mu) \sim 4\pi/(M\Lambda^n\mu^{n+1})$, where Λ is the scale where chiral perturbation theory breaks down and $n = 0, 1, 2\ldots$. Assuming $\Lambda \sim 300$–400 MeV, one finds that the values of the effective constants are indeed consistent with the counting rules, although somewhat lower than those obtained in [3]. One notes that it is hard to compare the effective constants obtained in different regularization schemes, since the coupling is known to be a scheme-dependent quantity.

Nonperturbative corrections due to a separable potential with a form factor $\eta_1(p)$ become noticeable at $p \sim 100$ MeV/c. This agrees with the estimates obtained in [8]. Of course, the precise region where

pions become nonperturbative may somehow depend on concrete form factors used, but the general tendency of the pion effects becoming too strong to be treated perturbatively at $p > 0.5$ fm^{-1} seems quite robust, making the whole problem much more complicated.

As already mentioned in this paper, we focus on the $^1S_0$ channel and calculate observables up to next-to-leading order. The main goal was to develop a reasonable calculation scheme with consistent renormalization procedure so that we retain only one term in the separable expansion of the OPEP contribution. Of course, this gives only a crude parametrization of the long-range part of the effective Lagrangian so that our comparison of the theoretical results with the experimental phase shifts has a somewhat illustrative character for demonstrating the feasibility of the method proposed. The results obtained are shown in the table.

The deviation from the Nijmegen phase shifts [9] is about 12–15% on average in the kinematical region $0.4 < p < 1.35$ fm^{-1}. At lower momenta, the pionic effects can either be integrated out or safely treated perturbatively. At larger momenta, the next-next-to-leading order corrections, such as two-pion-exchange or $O(p^4)$ contact terms, become more and more important and must be taken into account. The errors of the theoretical analysis are comparable with those introduced by the separable representation of the effective potential, so no significant additional uncertainties are introduced by the loop integration. Therefore, one could hope that taking into account a few more terms in the separable expansion of the effective potential will bring the theoretical results into better agreement with the experimental phase shifts. Work in this direction is in progress.

In summary, we have analyzed the problem of renormalization in the effective theory of *NN* interaction when the perturbative chiral expansion is not valid. In Weinberg's approach, where pions are treated nonperturbatively, the scattering amplitude can be found only numerically, making the procedure of consistent renormalization difficult to implement. On the other hand, in the approach proposed by KSW, pions are treated perturbatively, so that renormalization can be carried out in the standard way. The latter approach, however, shows rather slow convergence in some channels. The procedure we propose is based on an approximate but nonperturbative treatment of pionic effects based on a separable expansion of the long-range part of the effective potential and allowing for the renormalization to be carried out in an analytic form. Our method gives a reasonable description of the $^1S_0$ *NN* phase shifts in the laboratory-energy region up to $T_{\rm lab} \sim 140$ MeV.

REFERENCES

1. S. Weinberg, Nucl. Phys. B **363**, 3 (1991).
2. D. B. Kaplan, M. Savage, and M. B. Wise, Nucl. Phys. B **478**, 629 (1996); Phys. Lett. B **424**, 390 (1998); U. van Kolck, nucl-th/9808007; J. V. Steele and R. J. Furnstahl, Nucl. Phys. A **637**, 46 (1998); T.-S. Park, K. Kubodera, D.-P. Min, and M. Rho, Phys. Rev. C **58**, R637 (1998); G. P. Lepage, nucl-th/9706029; T. Mehen and I. W. Stewart, nucl-th/9806038; E. Epelbaoum, W. Gloëckle, and Ulf-G. Meissner, Nucl. Phys. A **637**, 107 (1998); nucl-th/9910064; S. Beane, T. D. Cohen, and D. Phillips, Nucl. Phys. A **632**, 445 (1997).
3. D. B. Kaplan, M. Savage, and M. B. Wise, Nucl. Phys. B **534**, 329 (1998).
4. S. Fleming, T. Mehen, and I. W. Stewart, nucl-th/9911001.
5. M. C. Birse, J. A. McGovern, and Keith G. Richardson, Phys. Lett. B **464**, 169 (1999).
6. D. R. Phillips, I. R. Afnan, and A. G. Henry-Edwards, nucl-th/9910063.
7. J. Gegelia, Phys. Lett. B **429**, 227 (1998).
8. T. D. Cohen and J. M. Hansen, Phys. Rev. C **59**, 13 (1999).
9. V. G. J. Stoks, R. A. M. Klomp, M. C. M. Rentmeester, and J. J. de Swart, Phys. Rev. C **48**, 792 (1993).

Physics of Atomic Nuclei, Vol. 65, No. 8, 2002, pp. 1421–1430. Translated from Yadernaya Fizika, Vol. 65, No. 8, 2002, pp. 1456–1465.

NUCLEI
Theory

Nonlocal Interactions of Nucleons and Anomalous Off-Shell Behavior of Two-Nucleon Amplitudes

R. Kh. Gainutdinov and A. A. Mutygullina

Kazan State University, ul. Kremlevskaya 18, Kazan, 420008 Tatarstan, Russia

Received February 14, 2001; in final form, September 4, 2001

Abstract—The problem of ultraviolet divergences that arise in describing low-energy nucleon dynamics is analyzed. By considering some examples of exactly solvable models, it is shown that, upon renormalization, the interaction that governs nucleon dynamics appears to be nonlocal in time. The effect of this nonlocality on the character of the dynamics of a nucleon system is investigated. It is shown that the time nonlocality of nucleon–nucleon interactions leads to an anomalous off-shell behavior of two-nucleon amplitudes and this anomalous behavior can significantly affect the dynamics of multinucleon systems. © *2002 MAIK "Nauka/Interperiodica".*

1. INTRODUCTION

Investigations aimed at assessing the extent to which quarks and gluons bound in hadrons can affect low-energy nucleon dynamics are of great importance for obtaining deeper insights into the nature of strong interactions. These fundamental degrees of freedom manifest themselves, for example, as symmetries in low-energy nucleon–nucleon interaction (NN) that are compatible with QCD symmetries. In the most natural way, the symmetries in question are taken into account within an effective field theory [1], which is extensively used at present in describing low-energy nucleon dynamics. Quark and gluon degrees of freedom also manifest themselves in that the interaction of nucleons must be nonlocal in time because of the presence of these intrinsic degrees of freedom. Accordingly, the effective potentials of NN interaction must be energy-dependent. The possibility of using such potentials in describing hadron–hadron interactions at low and intermediate energies was extensively discussed in the literature [2]. It may seem that this time nonlocality of the effective operator of NN interaction is not compatible with an effective field theory, which is a local theory. However, this is not so. Indeed, an effective field theory leads to effective NN-interaction operators whose ultraviolet behavior is "bad"; that is, matrix elements as functions of momenta decrease at infinity insufficiently fast for the Schrödinger and Lippmann–Schwinger equations to be meaningful. For this reason, it is necessary to regularize these equations and to renormalize the potentials. Ultraviolet divergences stem from locality of the theory; that is, they are due to the disregard of the fact that NN interaction cannot be local because of the presence of intrinsic quark and gluon degrees of freedom.

As a matter of fact, we run here into the same problem as in quantum field theory: locality of the theory leads to ultraviolet divergences, but the introduction of a nonlocal form factor in the Hamiltonian or in the interaction Lagrangian violates the covariance of the theory. The reason behind this is quite obvious. The Schrödinger equation is local in time, and the Hamiltonian describes an instantaneous interaction; in relativistic theory, a process that is local in time must be local in space as well. For the introduction of a nonlocality in a theory to be self-consistent, it is necessary to extend quantum dynamics to the case of the evolution of quantum systems whose dynamics is governed by an interaction that is nonlocal in time. For the first time, this problem was solved in [3], where it was shown that the simultaneous use of basic principles of the canonical and the Feynman formulation of quantum theory opens the possibility for generalizing quantum dynamics in this way. The generalized dynamical equation derived in [3] by using only generally accepted principles of quantum theory makes it possible to describe the evolution of quantum systems not only for the case where the fundamental interaction is instantaneous (it then reduces to the Schrödinger equation) but also in the case where the interaction is nonlocal in time. It was shown in [3] that generalized quantum dynamics developed in this way opens new possibilities for solving the problem of ultraviolet divergences in quantum field theory. An exactly solvable model was constructed in [4, 5] for investigating the character of the dynamics of quantum systems controlled by an interaction that is nonlocal in time and was used, by way of example [3], to show that there is a one-to-one correspondence

1063-7788/02/6508-1421$22.00

between the ultraviolet behavior of the model form factors and the nonlocality of the interaction. If the high-momentum behavior of the form factors satisfies the usual requirements of the Hamiltonian formalism, the interaction in the system is inevitably local, but, if this is not so (that is, the behavior of the form factors leads to ultraviolet divergences in Hamiltonian dynamics), the interaction in the system can only be nonlocal. In the latter case, the form of the nonlocal interaction operator is unambiguously determined by the asymptotic high-momentum behavior of the form factors, the dynamics of the system not being Hamiltonian here.

In connection with the fact that effective field theories lead to models where the effective potentials of NN interaction exhibit a "bad" ultraviolet behavior (see above), interest in studying such models—in particular, in their regularization and renormalization—has been quickened in recent years. For example, the problem of a dimensional regularization of the Lippmann–Schwinger equation was studied in [6] by considering the example of a model where NN interaction is described by a separable potential featuring a form factor that leads to a logarithmic singularity. In that study, the application of the regularization and renormalization procedure to the coupling constant made it possible to obtain the T matrix that coincides with the T matrix of the nonlocal model proposed in [4, 5] for the corresponding form factor. Thus, it was found that, upon the renormalization, the effective NN interaction, which governs the dynamics of the system being considered, becomes nonlocal in time, the evolution of the system being described by a dynamical equation that is not equivalent to the Schrödinger equation, but which is an equation of the type associated with generalized quantum dynamics. It should be emphasized that, in the case being discussed, generalized quantum dynamics permits treating the evolution of the system as rigorously as this is done in the case where the ultraviolet behavior of the form factors is such that the dynamics of the system is Hamiltonian. A construction of the model in question by applying the renormalization method only makes it possible to determine the two-nucleon T matrix, but it gives no way to derive an equation that would describe nucleon dynamics. The latter in turn prevents the use of these results in describing the dynamics of multinucleon systems. At the same time, the theory of renormalizations can provide the possibility of constructing, on the basis of an effective field theory, an effective NN-interaction operator that is nonlocal in time and which is compatible with its symmetries. This operator can then be employed to describe nucleon dynamics in terms of the dynamical equation of generalized quantum dynamics. This may open new possibilities for developing the theory of NN interactions that is based on the effective field theory. Needless to say, realistic models to which the effective field theory must lead will be more involved than the model considered in [4, 5]. As we have already mentioned, this exactly solvable model reflects, however, a crucial feature of the NN interaction—namely, the bad ultraviolet behavior of matrix elements as functions of momenta, which takes place if the interaction is nonlocal in time. In the present study, we address the problem of assessing the extent to which the nonlocality of the NN interaction in time can affect the character of nucleon dynamics. We will show that this nonlocality of the NN interaction leads to an anomalous off-shell behavior of two-nucleon amplitudes, which has a pronounced effect on the dynamics of multinucleon systems.

2. GENERALIZED QUANTUM DYNAMICS

It is well known that, in the canonical formulation of quantum theory, states and observables of a quantum system are represented by, respectively, vectors and operators in Hilbert space. This fact, together with the way in which these vectors and operators are related to observables, is reflected in postulates that define quantum statics. In the canonical formulation, these postulates are used in combination with the dynamical postulate according to which the evolution of the system is described by the Schrödinger equation. In [3], it was shown that, in describing quantum dynamics, one can dispense with this postulate, which, by virtue of the locality of the Schrödinger equation, admits only an instantaneous interaction for a fundamental interaction in the system; instead, one can use, along with the postulates of quantum statics, the basic postulate of Feynman's formulation—that is, the statement that the amplitude of the probability of any event is the sum of the amplitudes of alternative probabilities through which this event may be realized. From the postulates of the canonical formulation, it follows that the evolution of the system can be described in terms of the evolution operator $U(t_2, t_1)$, which must be unitary,

$$U^+(t_2,t_1)U(t_2,t_1) = U(t_2,t_1)U^+(t_2,t_1) = \mathbf{1}, \quad (1)$$

and which must satisfy the composition law

$$U(t_2,t_1)U(t_1,t_0) = U(t_2,t_0), \quad U(t_0,t_0) = \mathbf{1}. \quad (2)$$

At the same time, the basic postulate of Feynman's formulation implies that, in the interaction representation, the evolution operator can be written as

$$\langle\psi_2|U(t,t_0)|\psi_1\rangle = \langle\psi_2|\psi_1\rangle \quad (3)$$
$$+ \int_{t_0}^{t} dt_2 \int_{t_0}^{t_2} dt_1 \langle\psi_2|\tilde{S}(t_2,t_1)|\psi_1\rangle,$$

where $\langle\psi_2|\tilde{S}(t_2,t_1)|\psi_1\rangle$ is the amplitude of the probability that, if, for $t\to-\infty$, the state of the system was $|\psi_1\rangle$, the interaction in the system will begin at the instant t_1 and terminate at the instant t_2, with the result that, for $t\to\infty$, the system will be found in the state $|\psi_2\rangle$. The first term on the right-hand side of (3) corresponds to an evolutionary path along which the system undergoes no interaction at any instant of time. In order to illustrate this statement, we note that, according to the basic postulate of Feynman's formulation, the amplitude of the probability of the event described by the matrix element $\langle\psi_2|U(t,t_0)|\psi_1\rangle$ can be represented as the sum of the contributions of all alternative possibilities of the realization of the relevant evolutionary process. For such alternatives, we can consider processes where the instants of the commencement and of the termination of the interaction processes are strictly specified, with the amplitudes $\langle\psi_2|\tilde{S}(t_2,t_1)|\psi_1\rangle$ determining the contributions to the amplitude $\langle\psi_2|U(t,t_0)|\psi_1\rangle$ from these alternatives. For closed systems, the operator $\tilde{S}(t_2,t_1)$ (more precisely, this is an operator-valued distribution of the the variables t_1 and t_2 [3]) can be represented in the form $\tilde{S}(t_2,t_1)=\exp(iH_0t_2)\tilde{T}(t_2-t_1)\exp(-iH_0t_1)$, where H_0 is the free Hamiltonian.

It was shown in [3] that, for the evolution operator specified by Eq. (3) to satisfy the unitarity condition and the composition law, the operator $\tilde{S}(t_2,t_1)$ must satisfy the equation

$$(t_2-t_1)\tilde{S}(t_2,t_1) \tag{4}$$
$$=\int_{t_1}^{t_2}dt_4\int_{t_1}^{t_4}dt_3(t_4-t_3)\tilde{S}(t_2,t_4)\tilde{S}(t_3,t_1).$$

Equation (4) makes it possible to determine the amplitudes $\langle\psi_2|\tilde{S}(t_2,t_1)|\psi_1\rangle$ for any instants t_1 and t_2, provided that the amplitudes $\langle\psi_2|\tilde{S}(t_2',t_1')|\psi_1\rangle$ are known for infinitely short interaction times $\tau=t_2'-t_1'$. It is natural to assume that, in the limit of an infinitely short interaction time, $t_2\to t_1$, the main contribution to the evolution operator comes from processes that can be associated with the fundamental interaction in the system being considered. If this contribution is denoted by $H_{\rm int}(t_2,t_1)$, the operator $\tilde{S}(t_2,t_1)$ can be represented as

$$\tilde{S}(t_2,t_1)=H_{\rm int}(t_2,t_1)+\tilde{S}_1(t_2,t_1), \tag{5}$$

where $\tilde{S}_1(t_2,t_1)$ is that part of the operator $\tilde{S}(t_2,t_1)$ whose contribution to the evolution operator is negligible, in the limit $t_2\to t_1$, in relation to $H_{\rm int}(t_2,t_1)$. We will assume that the operator $H_{\rm int}(t_2,t_1)$ contains the entire body of dynamical information that is necessary for constructing the evolution operator. From the mathematical point of view, this requirement means that the operator $H_{\rm int}(t_2,t_1)$ must have a form such that Eq. (4) has a unique solution whose behavior near the point $t_2=t_1$ is given by

$$\tilde{S}(t_2,t_1)\underset{t_2\to t_1}{\longrightarrow}H_{\rm int}(t_2,t_1)+o(\tau^{\varepsilon}), \tag{6}$$

where $\tau=t_2-t_1$ and where ε depends on the form of the operator $H_{\rm int}(t_2,t_1)$.

The operator $H_{\rm int}(t_2,t_1)$ plays the role that the interaction Hamiltonian in conventional quantum theory does; that is, it generates dynamics in the system. This operator may be considered as a generalization of the interaction Hamiltonian; therefore, it is referred to as the generalized interaction operator. Given the form of the generalized interaction operator, one can obtain the operator $\tilde{S}(t_2,t_1)$ on the basis of Eq. (4). With the aid of the representation in (3), it is then possible to construct the evolution operator $U(t_2,t_1)$ for any t_1 and t_2. Thus, Eq. (4) can be considered as the equation of motion for states of a quantum system; in generalized quantum dynamics, it is used as a basic dynamical equation.

Equation (4) is equivalent to the differential equation

$$\frac{dT(z)}{dz}=-\sum_n\frac{T(z)|n\rangle\langle n|T(z)}{(z-E_n)^2} \tag{7}$$

for the operator $T(z)$ whose matrix elements are defined as

$$\langle n_2|T(z)|n_1\rangle \tag{8}$$
$$=i\int_0^{\infty}d\tau\exp(iz\tau)\langle n_2|\tilde{T}(\tau)|n_1\rangle,$$

where $|n\rangle$ are eigenvectors of the free Hamiltonian, $H_0|n\rangle=E_n|n\rangle$, which form a complete system of vectors in the space of free states, and n represents the set of discrete and continuous parameters fully characterizing the state $|n\rangle$. According to (6) and (8), the boundary condition for Eq. (7) has the form

$$\langle n_2|T(z)|n_1\rangle\underset{|z|\to\infty}{\longrightarrow}\langle n_2|B(z)|n_1\rangle+o(|z|^{-\beta}), \tag{9}$$

where $\beta=1+\varepsilon$ and

$$B(z)=i\int_0^{\infty}d\tau\exp(iz\tau)H_{\rm int}^{(s)}(\tau) \tag{10}$$

with $H_{\rm int}^{(s)}(\tau)=\exp(-iH_0t_2)H_{\rm int}(t_2,t_1)\exp(iH_0t_1)$. The operator $B(z)$, which was called the effective interaction operator, must be so close to the sought solution to Eq. (7) in the limit $|z|\to\infty$ that this differential equation has a unique solution with the asymptotic behavior specified by Eq. (9).

The dynamics described by Eq. (4) is equivalent to Hamiltonian dynamics if the generalized interaction operator has the form [3]

$$H_{\rm int}(t_2,t_1) = -2i\delta(t_2-t_1)H_I(t_1), \qquad (11)$$

where $H_I(t_1)$ is the interaction Hamiltonian in the interaction representation. In this case, Eq. (4) reduces to the Schrödinger equation. The presence of the delta function $\delta(\tau)$ in (11) indicates that the fundamental interaction is instantaneous in this case. Thus, the Schrödinger equation is obtained from the generalized Eq. (4) of motion in the case where the interaction that generates the dynamics in the system being considered is instantaneous. At the same time, Eq. (4) admits a generalization to the case where the operator $H_{\rm int}(t_2,t_1)$ does not have a delta-function singularity at the point $t_2 = t_1$. In that case, the fundamental interaction generating the dynamics of a quantum system is nonlocal in time: the evolution operator is specified by the generalized interaction operator $H_{\rm int}(t_2,t_1)$ treated as a function of the interaction time $\tau = t_2 - t_1$. Below, we will demonstrate this by considering some examples of exactly solvable models.

3. MODEL FEATURING A NONLOCAL INTERACTION IN TIME AND NUCLEON DYNAMICS

Let us consider the problem of describing the dynamics of two nucleons in the c.m. frame that have a specific relative momentum $\mathbf{p}$ and the reduced mass $\mu = M/2$, where M is the nucleon mass. Suppose that, in the Schrödinger representation, the generalized interaction operator has the form

$$\langle \mathbf{p}_2|H^{(s)}_{\rm int}(\tau)|\mathbf{p}_1\rangle = \psi(\mathbf{p}_2)\psi^*(\mathbf{p}_1)f(\tau), \qquad (12)$$

where $f(\tau)$ is a function of the interaction time τ. We are interested in the high-momentum asymptotic behavior of the form factors $\psi(\mathbf{p})$. Suppose, for example, that $\psi(\mathbf{p})$ has the form

$$\psi(\mathbf{p}) = |\mathbf{p}|^{-\alpha} + g(\mathbf{p}), \qquad (13)$$

and that, in the limit $|\mathbf{p}| \to \infty$, the function $g(\mathbf{p})$ has the asymptotic behavior $g(\mathbf{p}) = o(|\mathbf{p}|^{-\delta})$, where $\delta > \alpha$ and $\delta > 3/2$. The solution $\langle \mathbf{p}_2|T(z)|\mathbf{p}_1\rangle$ will have the separable form

$$\langle \mathbf{p}_2|T(z)|\mathbf{p}_1\rangle = \psi(\mathbf{p}_2)\psi^*(\mathbf{p}_1)t(z).$$

From (7), we then obtain the equation

$$\frac{dt(z)}{dz} = -t^2(z)\int d^3k \frac{|\psi(\mathbf{k})|^2}{(z-E_k)^2} \qquad (14)$$

with the boundary condition

$$t(z) \underset{z\to-\infty}{\longrightarrow} f_1(z) + o(|z|^{-\beta}), \qquad (15)$$

where $f_1(z) = i\int_0^\infty f(\tau)\exp(iz\tau)d\tau$ and where the parameter β is dependent on the form of the generalized interaction operator and is defined in such a way that the differential equation in question has a unique solution.

Equation (14) has a unique solution upon imposing a boundary condition that specifies the value of the function $t(z)$ at some point $a \in (-\infty, 0)$. For example, the solution to Eq. (14) with the boundary condition $t(a) = g_a$, where g_a is a constant, has the form

$$t(z) = g_a \qquad (16)$$
$$\times \left(1 + (z-a)g_a\int d^3k \frac{|\psi(\mathbf{k})|^2}{(z-E_k)(a-E_k)}\right)^{-1}.$$

If $\alpha > 1/2$, in which case the form factors $\psi(\mathbf{p})$ satisfy the usual requirements of quantum mechanics, the function $t(z)$ tends to a constant for $|z| \to \infty$,

$$t(z) \underset{|z|\to\infty}{\longrightarrow} \lambda; \qquad (17)$$

that is, $f_1(z) = \lambda$. From the definition of $f_1(z)$, it follows that this implies that, in the vicinity of the point $\tau = 0$, the function $f(\tau)$ must involve a delta-function singularity, $f(\tau) = -2i\delta(\tau) + f'(\tau)$. From this, it follows in turn that the generalized interaction operator must have the form

$$\langle \mathbf{p}_2|H^{(s)}_{\rm int}(\tau)|\mathbf{p}_1\rangle = -2i\lambda\delta(\tau)\psi(\mathbf{p}_2)\psi^*(\mathbf{p}_1); \qquad (18)$$

therefore, the dynamics generated by this operator is local and is equivalent to the dynamics described by the Schrödinger equation with the separable potential $\langle \mathbf{p}_2|V|\mathbf{p}_1\rangle = \lambda\psi(\mathbf{p}_2)\psi^*(\mathbf{p}_1)$. Solving Eq. (14) with the boundary condition (17), one does indeed easily obtain the well-known expression for the T matrix in the model with the above separable potential:

$$\langle \mathbf{p}_2|T(z)|\mathbf{p}_1\rangle \qquad (19)$$
$$= \lambda\psi(\mathbf{p}_2)\psi^*(\mathbf{p}_1)\left(1 - \lambda\int d^3k\frac{|\psi(\mathbf{k})|^2}{z-E_k}\right)^{-1}.$$

Standard quantum mechanics gives no way to generalize this model to the case where the behavior of the form factors $\psi(\mathbf{p})$ is "bad" in the limit $|\mathbf{p}| \to \infty$ [$\alpha \le 1/2$ in (13)]. Indeed, the integral on the right-hand side of (19) diverges for such form factors. We will now demonstrate how generalized quantum dynamics makes it possible to extend the model to the case of $-1/2 < \alpha \le 1/2$. We specify the class of functions $f_1(z)$ and, accordingly, the values of β in such a way that, for them, Eq. (14) has a unique solution that exhibits the analytic behavior specified by Eq. (15). In the case of $\alpha \le 1/2$, the function $t(z)$ tends to zero for $|z| \to \infty$; that is,

$$\begin{cases} t(z) \underset{|z|\to\infty}{\longrightarrow} b_1(\alpha)(-z)^{\alpha-\frac{1}{2}} + b_2(\alpha)(-z)^{2\alpha-1} + o(|z|^{2\alpha-1}), \quad -1/2 < \alpha < 1/2; \\ t(z) \underset{|z|\to\infty}{\longrightarrow} b_1(\frac{1}{2})\ln^{-1}(-z) + b_2(\frac{1}{2})\ln^{-2}(-z) + o(\ln^{-2}(-z)), \quad \alpha = 1/2, \end{cases} \tag{20}$$

where

$$\begin{cases} b_1(\alpha) = -\dfrac{1}{2}\cos(\alpha\pi)\pi^{-2}(2\mu)^{\alpha-\frac{3}{2}}; \\ b_2(\alpha) = b_1(\alpha)|a|^{\frac{1}{2}-\alpha} - b_1^2(\alpha)(M(a) + g_a^{-1}), \quad -1/2 < \alpha < 1/2; \\ b_1(\dfrac{1}{2}) = -(4\pi\mu)^{-1}, \quad b_2(\dfrac{1}{2}) = b_1(\dfrac{1}{2})\ln(-a) - b_1^2(\dfrac{1}{2})(M(a) + g_a^{-1}), \end{cases} \tag{21}$$

$$M(a) = \int \frac{|\psi(\mathbf{k})|^2 - |\mathbf{k}|^{-2\alpha}}{a - E_k} d^3k. \tag{22}$$

It should be emphasized that, in conventional quantum mechanics, the vanishing of the T matrix at infinity implies the vanishing of the potential. From the point of view of standard theory, this case is therefore trivial: there is no scattering in the system. On the other hand, we have shown above that, in the case of $\alpha \le 1/2$ in (13), Eq. (14) has a nontrivial solution that tends to zero for $|z| \to \infty$, the dynamics here being governed by the character of the vanishing of the T for $|z| \to \infty$ rather than by its value at infinity. It can easily be proven that all integral curves of the differential Eq. (14) have the same asymptotic behavior specified by Eq. (20) with the same first term, differing only by the values of the parameter $b_2(\alpha)$. In order to obtain a unique solution to Eq. (14), we therefore have to determine the first two terms in the asymptotic expansion of $t(z)$ for $|z| \to \infty$, whence it follows that the function $f_1(z)$ must have the form

$$\begin{cases} f_1(z) = b_1(\alpha)(-z)^{\alpha-\frac{1}{2}} + b_2(\alpha)(-z)^{2\alpha-1}, \quad -1/2 < \alpha < 1/2; \\ f_1(z) = b_1(\dfrac{1}{2})\ln^{-1}(-z) + b_2(\dfrac{1}{2})\ln^{-2}(-z), \quad \alpha = 1/2, \end{cases}$$

where $b_1(\alpha)$ is given by (21) and where only the parameter $b_2(\alpha)$ is arbitrary. If, however, there is a bound state in the system, like that in the ${}^3S_1$ channel of the NN system, this parameter is determined by the energy E_c of this bound state. Indeed, the fact that the T matrix then has a pole at $z = E_c$—that is, $[t(E_c)]^{-1} = 0$—can be used as the boundary condition for Eq. (14), in which case Eq. (16) yields

$$[t(z)]^{-1} = (z - E_c)\int d^3k \frac{|\psi(\mathbf{k})|^2}{(z - E_c)(E_c - E_k)}. \tag{23}$$

In this case, the parameter $b_2(\alpha)$ will accordingly have the value

$$\begin{cases} b_2(\alpha) = b_1(\alpha)(-E_c)^{\frac{1}{2}-\alpha} - b_1^2(\alpha)M(E_c), \quad -1/2 < \alpha < 1/2; \\ b_2(\dfrac{1}{2}) = b_1(\dfrac{1}{2})\ln(-E_c) - b_1^2(\dfrac{1}{2})M(E_c). \end{cases}$$

Considering that $f(\tau) = \dfrac{i}{2\pi}\int_{-\infty}^{\infty}\exp(-iz\tau)f_1(z)dz$, we obtain the generalized interaction operator in the form

$$\begin{cases} \langle \mathbf{p}_2|H_{\rm int}^{(s)}(\tau)|\mathbf{p}_1\rangle = \psi(\mathbf{p}_2)\psi^*(\mathbf{p}_1)\left(a_1\tau^{-\alpha-\frac{1}{2}} + a_2\tau^{-2\alpha}\right), \quad -1/2 < \alpha < 1/2; \\ \langle \mathbf{p}_2|H_{\rm int}^{(s)}(\tau)|\mathbf{p}_1\rangle = \psi(\mathbf{p}_2)\psi^*(\mathbf{p}_1)\dfrac{i}{2\pi}\int\limits_{-\infty}^{\infty}\exp(-iz\tau)\left(\dfrac{b_1(\frac{1}{2})}{\ln(-z)} + \dfrac{b_2(\frac{1}{2})}{\ln^2(-z)}\right)dz, \quad \alpha = 1/2, \end{cases} \tag{24}$$

where $a_1 = -ib_1(\alpha)\Gamma^{-1}(1/2 - \alpha)\exp[i(-\dfrac{\alpha}{2} + \dfrac{1}{4})\pi]$ and $a_2 = b_2(\alpha)\Gamma^{-1}(1 - 2\alpha)\exp(-i\alpha\pi)$. By using Eq. (16), it can easily be proven that the relevant solution for the T matrix has the form

$$\langle \mathbf{p}_2|T(z)|\mathbf{p}_1\rangle = N(z)\psi(\mathbf{p}_2)\psi^*(\mathbf{p}_1), \tag{25}$$

where

$$\begin{cases} N(z) = b_1^2(\alpha)\left(-b_2(\alpha) + b_1(\alpha)(-z)^{\frac{1}{2}-\alpha} + M(z)b_1^2(\alpha)\right)^{-1}, & -1/2 < \alpha < 1/2; \\ N(z) = b_1^2(\frac{1}{2})\left(-b_2(\frac{1}{2}) + b_1(\frac{1}{2})\ln(-z) + M(z)b_1^2(\frac{1}{2})\right)^{-1}, & \alpha = 1/2. \end{cases}$$

Considering that the T matrix is related to the evolution operator by the equation [3]

$$U(t,t_0) = \mathbf{1} + \frac{i}{2\pi} \times \int\limits_{-\infty}^{\infty} dx \frac{\exp[-i(z-H_0)t]}{(z-H_0)} T(z) \frac{\exp[i(z-H_0)t_0]}{(z-H_0)}, \quad (26)$$

where $z = x + iy$ and $y > 0$, we can find for the evolution operator that

$$\langle \mathbf{p}_2|U(t,t_0)|\mathbf{p}_1\rangle = \langle \mathbf{p}_2|\mathbf{p}_1\rangle + \frac{i}{2\pi} \times \int\limits_{-\infty}^{\infty} dx \frac{\exp[-i(z-E_{p_2})t]\exp[i(z-E_{p_1})t_0]}{(z-E_{p_2})(z-E_{p_1})} \times N(z)\psi(\mathbf{p}_2)\psi^*(\mathbf{p}_1). \quad (27)$$

By using (27), we can then construct a vector representing the state of the system at any instant of time t. It can be shown that the evolution operator (27) is unitary if the parameter $b_2(\alpha)$ is real-valued and that it satisfies the composition law.

It should also be noted that there is a one-to-one relationship between the behavior of the form factors $\psi(\mathbf{p})$ for $|\mathbf{p}| \to \infty$ and the character of dynamics: if the form factors satisfy the usual requirements of quantum mechanics [for $\alpha > 1/2$ in the asymptotic expression (13)], the generalized interaction operator must have the form (18). In this case, the fundamental interaction is instantaneous. At $\alpha \le 1/2$, in which case the high-momentum behavior of the form factors in Hamiltonian dynamics leads to ultraviolet divergences, the only possible form of $H_{\rm int}^{(s)}(\tau)$ is that which is given by (24); that is, the fundamental interaction that generates dynamics in the quantum system being considered is nonlocal in time.

We have shown that generalized quantum dynamics makes it possible to describe, in a natural way, the evolution of quantum systems where the interaction leads to ultraviolet divergences in Hamiltonian dynamics. It was indicated above that, in effective field theories, one has to deal with precisely such interactions, with the result that it becomes necessary to invoke various regularization and renormalization procedures. In [6], this problem was investigated for the example where the NN interaction is described by the separable potential $\langle \mathbf{p}_2|V|\mathbf{p}_1\rangle = \lambda\psi(\mathbf{p}_2)\psi^*(\mathbf{p}_1)$ with form factor $\psi(\mathbf{p}) = (d^2 + \mathbf{p}^2)^{-\frac{1}{4}}$. The parameter α, which determines the asymptotic behavior of the form factor, is $1/2$, and the relevant solution to the Lippmann–Schwinger equation, $t(z) = \left(\lambda^{-1} - J(z)\right)^{-1}$, where $J(z) = \int d^3k \frac{|\psi(\mathbf{k})|^2}{z - E_k}$, has an ultraviolet logarithmic singularity. A dimensional regularization was used in [6] to render the Lippmann–Schwinger equation meaningful. In momentum space of dimension $\mathcal{D} = 3 - \varepsilon$, the solution to this equation has the form

$$[t_\varepsilon(z)]^{-1} = \lambda_\varepsilon^{-1} - J_\varepsilon(z), \quad (28)$$

where $J_\varepsilon(z) = \int d^{3-\varepsilon}k \frac{|\psi(\mathbf{k})|^2}{z - E_k}$. Prior to making ε tend to zero, it is necessary to renormalize the coupling constant. For the ${}^3S_1$ channel of the NN system, the value of the coupling constant λ_ε must be chosen in such a way as to ensure the existence of a bound state at $E_c = -2.2246$ MeV in this channel, in which case the T matrix must have a pole at $z = E_c$. Thus, the following condition must be satisfied:

$$\lambda_\varepsilon^{-1} = J_\varepsilon(E_c). \quad (29)$$

The substitution of (29) into (28) then yields

$$[t_\varepsilon(z)]^{-1} = J_\varepsilon(E_c) - J_\varepsilon(z) = (z - E_c)\int d^{3-\varepsilon}k \frac{|\psi(\mathbf{k})|^2}{(z - E_k)(E_c - E_k)}.$$

It can easily be proven that, upon going over to the limit $\varepsilon \to 0$ in this expression, we arrive at formula (23), which was previously obtained for the T matrix; that is, the above renormalization procedure leads to the dynamics described by the interaction that is specified by Eq. (24) and which is nonlocal in time. Let us now consider this situation from the point of view of Hamiltonian dynamics. In the limit $\varepsilon \to 0$, the renormalized coupling constant λ_ε and, hence, the renormalized Hamiltonian tend to zero, while the T matrix (25) does not satisfy the Lippmann–Schwinger equation; therefore, the dynamics in question is not described by the Schrödinger equation. Thus, we see that, although each of the set of dynamics that correspond to the dimensionality $\mathcal{D} = 3 - \varepsilon$ for $\varepsilon > 0$ is a Hamiltonian dynamics, we have a non-Hamiltonian dynamics in

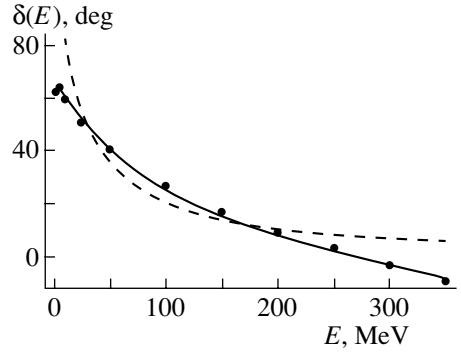

Fig. 1. Phase shift $\delta(E)$ for proton–neutron scattering as a function of the laboratory energy for the ${}^1S_0$ channel. Experimental data from [8] are shown by points. The results of the calculation with the generalized interaction operator (24) are represented by the solid curve. Also given for the sake of comparison are the results of the calculation with the Yamaguchi potential (dashed curve).

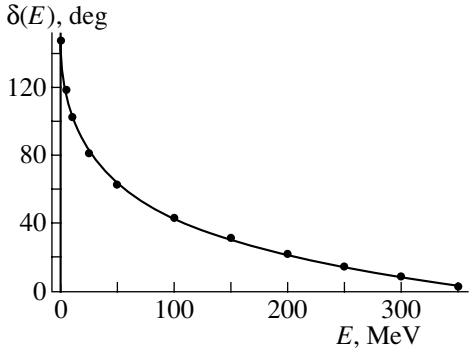

Fig. 2. Phase shift $\delta(E)$ for proton–neutron scattering as a function of the laboratory energy for the ${}^3S_1$ channel. Experimental data from [8] are shown by points. The results of the calculation with the generalized interaction operator (24) are represented by the solid curve.

the limiting case $\mathcal{D} = 3$. This situation is typical of any theory where a renormalization procedure is required to remove ultraviolet divergences. At the same time, the T matrix satisfies Eq. (7), which is one of the possible forms of the master dynamical Eq. (4) of generalized quantum dynamics. But Eq. (4) leads to the Lippmann–Schwinger equation only in the particular case where $H_{\rm int}(t_2, t_1)$ has the form (11)—that is, in the case of an instantaneous interaction. The dynamics of a renormalized theory is nonlocal in time; that is, it belongs to the class of dynamics that can be described only on the basis of generalized quantum dynamics. For the renormalized model considered here, the generalized interaction operator is given by (24). This operator can then be used in a dynamical equation to describe the dynamics of systems featuring an arbitrary number of nucleons.

4. ANOMALOUS OFF-SHELL BEHAVIOR OF TWO-NUCLEON AMPLITUDES

Thus, we have shown that the regularization of the Schrödinger and Lippmann–Schwinger equations, which is necessary in using effective interaction operators constructed within effective field theories, results in that the interaction generating nucleon dynamics appears to be nonlocal in time. The evolution of systems governed by such interactions is described in a natural way, by generalized quantum dynamics and by models constructed on its basis [4, 5]. In [5], the NN interaction was described on the basis of the model where the generalized interaction operator has the form (24) with form factor $\psi(\mathbf{p}) = g_{\rm Y}(\mathbf{p}) - \phi(\mathbf{p})$, where $g_{\rm Y}(\mathbf{p})$ is the Yamaguchi form factor [7], which, in the S channel, is given by $g_{\rm Y}(p) = \dfrac{\lambda}{b^2 + p^2}$, and $\phi(p) = (d^2 + p^2)^{-\alpha/2}$ with $-\dfrac{1}{2} < \alpha < \dfrac{1}{2}$; that is, $\phi(p)$ is the form factor whose ultraviolet behavior corresponds to an interaction that is nonlocal in time. The parameters of the model were determined from the best fit to the experimental values [8] of the phase shift for nucleon–nucleon scattering at low energies. For the ${}^1S_0$ and the ${}^3S_1$ channel, the quality of our fits to the experimental values of the phase shifts for nucleon–nucleon scattering is illustrated in Figs. 1–3. The parameters of the model are quoted in the table. For the sake of comparison, the energy dependence of the phase shift for nucleon–nucleon scattering is also displayed in Fig. 1. From this figure, it can be seen that, in the Yamaguchi model, the main flaw, which consists in its inability to reproduce the reversal of the sign of the phase shift in the ${}^1S_0$ channel, can be removed by generalizing this model to the case where the interaction is nonlocal in time.

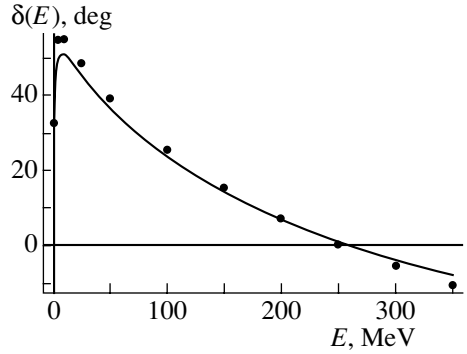

Fig. 3. Phase shift $\delta(E)$ for proton–proton scattering as a function of the laboratory energy in the ${}^1S_0$ channel. Experimental data from [8] are shown by points. The results of the calculation with the generalized interaction operator (24) are represented by the solid curve.

Parameters of the generalized interaction operator (24), $\rho = 1$ MeV^{-1}

Channel	α	λ	$b \cdot \rho$	$d \cdot \rho$	$b_2 \cdot \rho^{1-2\alpha}$
$^3S_1(np)$	0.499	133.5×10^2	433.8	766.2	1.696×10^{-7}
$^1S_0(np)$	0.499	131.8	356.3	3.651×10^6	1.694×10^{-7}
$^1S_0(pp)$	0.499	320.0	371.7	6.763×10^5	1.695×10^{-7}

Needless to say, the NN-interaction potential constructed in this study is nothing but a model-dependent quantity. A realistic effective NN-interaction operator that takes into account QCD symmetries must be derived within an effective field theory by using a renormalization procedure. However, our exactly solvable model can be employed the study the effect of the nonlocality of NN interaction on the character of nucleon dynamics. Among data from two-nucleon physics, information about the off-shell behavior of two-nucleon amplitudes is of great importance, since it substantially affects the dynamics of three-nucleon and multinucleon systems [9]. Let us consider the effect of nonlocality of the NN interaction on this behavior of two-nucleon amplitudes. First of all, we consider the behavior of $f(z) = \langle \mathbf{p}_2|T(z)|\mathbf{p}_1\rangle$ as a function of z at fixed $\mathbf{p}_1$ and $\mathbf{p}_2$. It is well known that, for $|z| \to \infty$, the solutions $\langle \mathbf{p}_2|T(z)|\mathbf{p}_1\rangle$ to the Lippmann–Schwinger equation tend to $\langle \mathbf{p}_2|V|\mathbf{p}_1\rangle$, where V is the potential.

Thus, we see that, in the case where the NN interaction is described by some potential—that is, this interaction is local in time—the two-nucleon amplitude $\langle \mathbf{p}_2|T(z)|\mathbf{p}_1\rangle$ tends to a nonzero constant for $|z| \to \infty$. At the same time, $\langle \mathbf{p}_2|T(z)|\mathbf{p}_1\rangle$ taken at fixed $\mathbf{p}_1$ and $\mathbf{p}_2$ always tends to zero for $|z| \to \infty$ in the case of an interaction that is nonlocal in time. Indeed, we have already indicated that, in the nonlocal case, $H^{(s)}_{\rm int}(\tau)$ does not have a delta-function singularity at the point $\tau = 0$, whence one can immediately conclude that $B(z)$, which is defined by the relation (10), tends to zero for $|z| \to \infty$. According to (9), it immediately follows that, in this limit, $\langle \mathbf{p}_2|T(z)|\mathbf{p}_1\rangle$ also tends to zero. For our nonlocal model, as well as for the Yamaguchi model, Fig. 4 illustrates the behavior of the function $f(z)$ in the $^3S_1(np)$ channel. It is obvious that this anomalous behavior of two-nucleon amplitudes, which is due to the nonlocality of the NN interaction in time, can significantly affect the dynamics of multinucleon systems.

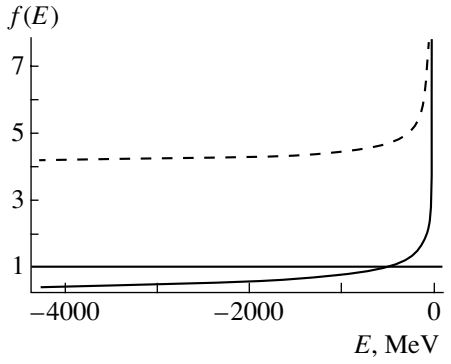

Fig. 4. Behavior of the two-nucleon amplitude $f(z) = \langle \mathbf{p}_2|T(z)|\mathbf{p}_1\rangle$ at the fixed momenta $|\mathbf{p}_2| = |\mathbf{p}_1| =$ 500 MeV in the $^3S_1(np)$ channel. The solid curve represents the results of the calculations based on the model involving the generalized interaction operator (24), whose parameters are quoted in the table. Also given for the sake of comparison are the results obtained on the basis of the Yamaguchi model (dashed curve).

As was shown above, the generalized interaction operator can be nonlocal in time only if its matrix elements $\langle \mathbf{p}_2|H^{(s)}_{\rm int}(\tau)|\mathbf{p}_1\rangle$ as functions of momenta have an ultraviolet behavior that leads to divergences in Hamiltonian dynamics. Accordingly, the T-matrix elements $\langle \mathbf{p}_2|T(z)|\mathbf{p}_1\rangle$ as functions of $\mathbf{p}_1$ and $\mathbf{p}_2$ will not decrease at infinity as fast as is required in Hamiltonian dynamics. This brings about the question of how this circumstance can affect the character of nucleon dynamics. The importance of the off-shell behavior of the two-nucleon T matrix is associated with the fact that it appears in the Faddeev equation for the three-nucleon T matrix. It can straightforwardly be shown, however, that, if $\langle \mathbf{p}_2|T(z)|\mathbf{p}_1\rangle$ does not decrease sufficiently fast in the high-momentum limit, then the Schmidt norm for the kernel of the Faddeev equation does not exist at any value of z. Thus, we see that, in the case of an interaction that is nonlocal in time, the off-shell behavior of two-nucleon amplitudes is anomalous, which results in that the Faddeev equation is not well defined. That effective field theories lead to a Faddeev equation whose kernel decreases at infinity insufficiently fast for this equation to be well-defined is one of the most serious problems in such theories [6]. It is important that generalized quantum dynamics admits a generalization to the case where the Faddeev equation, as well as Lippmann–Schwinger equation, is not well defined. One must then directly use the dynamical Eq. (4) or (7).

In our above analysis, we have considered the case where the interaction is nonlocal in time and is described by the interaction operator in the form (24). At the same time, it was shown in [5] that the generalized interaction operator may have the form

$$H_{\rm int}(t_2,t_1) = H_{\rm non}(t_2,t_1) - 2i\delta(t_2-t_1)H_I(t_1), \quad (30)$$

where the first term on the right-hand side, $H_{\rm non}(t_2,t_1)$, describes the nonlocal part of the interaction, while the second term describes its instantaneous part. This form of the interaction operator seems natural in the case of NN interactions. Indeed, it is well known that, at long and intermediate distances, the NN interaction is well approximated by realistic NN potentials based on the concept of meson exchange. This part of the NN interaction is described by the second term on the right-hand side of (30). At the same time, there is every reason to believe that a nonlocal interaction operator offers a natural way to treat the short-range part of the interaction, where quark and gluon degrees of freedom are expected to manifest themselves. From the above analysis, it follows that the asymptotic high-momentum behavior of the matrix elements $\langle \mathbf{p}_2|H_{\rm int}(t_2,t_1)|\mathbf{p}_1\rangle$ of the interaction operator (30) is controlled by the nonlocal term $H_{\rm non}(t_2,t_1)$. Even if this term makes a negligible contribution to two-nucleon phase shifts at low energies, it changes qualitatively the off-shell behavior of two-nucleon amplitudes and, hence, affects substantially three-nucleon data. This highlights the importance of taking into account nonlocality effects in describing the short-range part of the NN interaction. The use of nonlocal interaction operators for the short-range part of the NN interaction, along with realistic NN employed at present, may lead to a better description of three-nucleon and multinucleon data. We hope that it will be possible to construct such operators—that is, those nonlocal interaction operators that would describe the short-range part of the NN interaction—on the basis of effective field theories.

5. CONCLUSION

By considering the example of an exactly solvable model, we have shown that, upon the application of regularization and renormalization procedures, the dynamics of a nucleon system governed by an interaction that involves ultraviolet divergences is not Hamiltonian—it is described by the dynamical Eq. (4) featuring a generalized interaction operator that is nonlocal in time. Here, we are dealing with dynamics that can be consistently described only within generalized quantum dynamics. Thus, generalized quantum dynamics opens new possibilities for solving problems associated with the fact that effective field theories lead to effective nucleon–nucleon interaction operators involving ultraviolet divergences. It can be expected that nucleon dynamics to which effective field theories must lead will be described by some generalized interaction operator that is nonlocal in time. If, within an effective field theory, one will be able to construct such an operator, which will then respect QCD symmetries, it will be possible to use Eq. (4) to describe nucleon dynamics. For the example of the aforementioned model, we have shown that such an operator can be constructed. We have investigated the effect of the nonlocality of NN interaction in time on the character of nucleon dynamics. Our analysis has revealed that these effects lead to an anomalous off-shell behavior of two-nucleon amplitudes: the two-nucleon amplitudes $\langle \mathbf{p}_2|T(z)|\mathbf{p}_1\rangle$ at fixed momenta vanish for $|z|\to\infty$ and, treated as functions of $\mathbf{p}_1$ and $\mathbf{p}_2$, decrease insufficiently fast at infinity for the Faddeev equation to be well defined. This may substantially affect the dynamics of multinucleon systems. As we have shown, the nonlocal interaction operator constructed here can be used for the nonlocal part of the NN-interaction operator. At the same time, realistic NN potentials can be taken for its instantaneous part describing the NN interaction at intermediate and long distances. The introduction of such nonlocal corrections to realistic NN potentials may significantly improve the description of three-nucleon and multinucleon data, which is one of the challenging problems in nucleon physics.

ACKNOWLEDGMENTS

We are grateful to W. Scheid for stimulating discussions and for the hospitality extended to us at the Justus-Leibig-Universität, in Giessen.

This work was supported by the Academy of Sciences of Tatarstan [grant no. 14-98/2000(F)].

REFERENCES

1. S. Weinberg, Phys. Lett. B **251**, 288 (1990); Nucl. Phys. B **363**, 3 (1991); C. Ordonez and U. van Kolck, Phys. Lett. B **291**, 459 (1992); C. Ordonez, L. Ray, and U. van Kolck, Phys. Rev. Lett. **72**, 1982 (1994); Phys. Rev. C **53**, 2086 (1996); U. van Kolck, Phys. Rev. C **49**, 2932 (1994).
2. Yu. S. Kalashnikova, N. M. Narodetskiĭ, and V. P. Yurov, Yad. Fiz. **49**, 632 (1989) [Sov. J. Nucl. Phys. **49**, 392 (1989)]; A. G. Baryshnikov, L. D. Blokhintsev, I. M. Narodetskiĭ, and D. A. Savin, Yad. Fiz. **48**, 1273 (1988) [Sov. J. Nucl. Phys. **48**, 809 (1988)]; A. N. Safronov, Yad. Fiz. **57**, 208 (1994) [Phys. At. Nucl. **57**, 194 (1994)]; Yu. A. Kuperin, K. A. Makarov, and S. P. Merkur'ev, Teor. Mat. Fiz. **75**, 431 (1988); **76**, 242 (1989); A. Abdurakhmanov and A. L. Zubarev,

Z. Phys. A **322**, 523 (1985); M. Orlowski, Helv. Phys. Acta **56**, 1053 (1983); B. O. Kerbikov, Yad. Fiz. **41**, 725 (1985) [Sov. J. Nucl. Phys. **41**, 461 (1985)]; Teor. Mat. Fiz. **65**, 379 (1985); Yu. A. Simonov, Phys. Lett. B **107B**, 1 (1981).
3. R. Kh. Gainutdinov, J. Phys. A **32**, 5657 (1999).
4. R. Kh. Gaĭnutdinov and A. A. Moutygoullina, Yad. Fiz. **60**, 938 (1997) [Phys. At. Nucl. **60**, 841 (1997)].
5. R. Kh. Gaĭnutdinov and A. A. Moutygoullina, Yad. Fiz. **62**, 2061 (1999) [Phys. At. Nucl. **62**, 1905 (1999)].
6. D. R. Phillips, I. R. Afnan, and A. G. Henry-Edwards, Phys. Rev. C **61**, 044002 (2000).
7. Y. Yamaguchi, Phys. Rev. **95**, 1628 (1954).
8. V. G. J. Stoks, R. A. M. Klomp, M. C. M. Rentmeester, and J. J. de Swart, Phys. Rev. C **48**, 792 (1993).
9. R. Machleidt, F. Sammarruca, and Y. Song, Phys. Rev. C **53**, 1483 (1996).

Translated by A. Isaakyan

Physics of Atomic Nuclei, Vol. 65, No. 8, 2002, pp. 1431–1443. Translated from Yadernaya Fizika, Vol. 65, No. 8, 2002, pp. 1466–1478.

NUCLEI
Theory

Nuclear Masses and Properties of Nuclei in the Vicinity of the Remote Magic Nucleus ^{100}Sn

V. I. Isakov and K. I. Erokhina[1)]

Petersburg Nuclear Physics Institute, Russian Academy of Sciences, Gatchina, 188350 Russia

Received April 28, 2001

Abstract—Results are presented that were obtained by calculating various properties of nuclei occurring in the vicinity of the doubly magic neutron-deficient nuclide ^{100}Sn, which are being intensively studied at present. The calculated features include the masses of 25 nuclei and the properties of excited states of the magic nuclide and of nuclei belonging to the *magic core plus two quasiparticles* type. The problems of effective quadrupole charges and of the renormalization of the weak axial constant in nuclei lying in the vicinity of ^{100}Sn are considered. © *2002 MAIK "Nauka/Interperiodica".*

1. INTRODUCTION

Theoretical investigations were previously performed for nuclei that lie in the vicinity of the doubly magic nuclide ^{208}Pb [1, 2] and for nuclei that occupy remote positions in the new magic regions around ^{132}Sn and ^{78}Ni, but which are nevertheless stable with respect to nucleonic-decay modes (see [3–8]). At the same time, a theoretical analysis was performed in [9] for nuclides of ultimately high neutron deficit in the region of the hypothetical doubly magic nucleus ^{164}Pb, which lies beyond the region of nucleonic stability, but which has, only owing to the Coulomb barrier, a lifetime of about 10^{-12} s with respect to proton emission, a value that is rather large on the nuclear scales. For nuclei close to ^{132}Sn and, partly, for nuclides from the region around ^{78}Ni, experimental information about the nuclear masses, as well as about the properties of their excited states and about their decay characteristics, has already been obtained; on the contrary, nuclei close to ^{164}Pb can hardly become the subject of such investigations in the near future because it is difficult to obtain them in experiments and because their lifetimes are short. At the same time, a different region of magic neutron-deficient nuclei with $N \sim Z$—that which occurs in the vicinity of the doubly magic nuclide ^{100}Sn, which is more stable than ^{164}Pb—is being intensively studied in present-day experiments. Since currently available experimental information about nuclei from this region is scanty, one can adopt an alternative way to assess their properties, that of theoretical calculations; a version of such calculations is proposed in this article. Since basic formulas of the computational scheme used here were presented previously, we will quote here predominantly our numerical results, supplementing them, when necessary, with brief explanations.

2. DETERMINATION OF THE "MASS RELIEF" FOR THE SET OF NUCLIDES IN THE VICINITY OF THE ^{100}Sn NUCLEUS

In order to determine the masses of nuclei from the region around the doubly magic nuclide ^{100}Sn, we employed two methods, that which is based on the multiparticle shell model and that which based on self-consistent calculations.

The calculations within the shell model rely (see [6, 9]) on the concept of a mean field that generates a single-particle spectrum and the concept of an effective interaction between valence nucleons. Since there are no detailed experimental data on the spectrum of single-particle states in odd nuclei neighboring ^{100}Sn (available extrapolations from the region of nuclei less remote from the drip line can be found in [10], while fragmentary data for nuclei having a somewhat greater number of neutrons are quoted in [11]), the choice of an appropriate phenomenological mean-field potential that can faithfully reproduce relevant experimental data in other magic regions is an important ingredient of the calculations. For this, we took the potential

$$U(r,\hat{\sigma}) = \frac{U_0}{1+\exp[(r-R)/a]} + U_{ls}r_0^2\frac{1}{r}\frac{d}{dr}\left[\frac{1}{1+\exp[(r-R)/a]}\right]\hat{\mathbf{l}}\cdot\hat{\mathbf{s}}, \quad (1)$$

[1)] Ioffe Institute for Physics and Technology, Russian Academy of Sciences, Politekhnicheskaya ul. 26, St. Petersburg, 194021 Russia.

1063-7788/02/6508-1431$22.00

where

$$U_0 = V_0\left(1 + \frac{1}{2}\beta\frac{N-Z}{A}\tau_3\right),$$

$$U_{ls} = V_{ls}\left(1 + \frac{1}{2}\beta_{ls}\frac{N-Z}{A}\tau_3\right),$$

$R = r_0A^{1/3}$, and $\tau_3 = 1$ for protons and $\tau_3 = -1$ for neutrons (for protons, we added the potential of a uniformly charged sphere of radius $R_c = r_{0c}A^{1/3}$).

The parameters appearing in (1) were evaluated in [8] by fitting the single-particle energies for nuclei in the vicinity of known magic nuclei; the results proved to be the following: $V_0 = -51.8$ MeV, $V_{ls}r_0^2 = 35.9$ MeV fm^2, $\beta = 1.33$, $\beta_{ls} \sim -0.6$, $r_0 = 1.27$ fm, and $r_{0c} = 1.25$ fm. The values obtained for the diffuseness parameter a showed a wider scatter, changing, for various nuclei, between 0.55 and 0.66 fm.

Our effective interaction has the form

$$\vartheta = (V + V_\sigma\boldsymbol{\sigma}_1\cdot\boldsymbol{\sigma}_2 + V_TS_{12} + V_\tau\boldsymbol{\tau}_1\cdot\boldsymbol{\tau}_2 + V_{\sigma\tau}(\boldsymbol{\sigma}_1\cdot\boldsymbol{\sigma}_2)(\boldsymbol{\tau}_1\cdot\boldsymbol{\tau}_2) + V_{\tau T}S_{12}\boldsymbol{\tau}_1\cdot\boldsymbol{\tau}_2)\exp\left(-\frac{r^2}{r_{00}^2}\right) \quad (2)$$

(in the case of two protons, we added the pair Coulomb potential). The parameters appearing in (2) were also determined in previous studies and were successfully used to describe a wide set of experimental data around the doubly magic nuclei ^{78}Ni, ^{132}Sn, and ^{208}Pb [1–6]. Their values are the following (all V terms are in MeV units): $V = -9.95$, $V_\sigma = 2.88$, $V_T = -1.47$, $V_\tau = 5.90$, $V_{\sigma\tau} = 4.91$, $V_{\tau T} = 1.51$, and $r_{00} = 1.8$ fm.

Another important idea of shell-model calculations consists in the use of the ground state of a doubly magic nucleus for a vacuum; with respect to this vacuum, all nuclei close to the magic nuclide in question are few-quasiparticle systems. In the representation of Hartree–Fock eigenfunctions, the Hamiltonian of such a nucleus can then be written as

$$H = E_0 + \sum_\alpha \varepsilon_\alpha N(a_\alpha^+a_\alpha) + \frac{1}{4}\sum_{\alpha,\beta,\gamma,\delta} {}_a\langle\alpha\beta|\vartheta|\gamma\delta\rangle_a N(a_\alpha^+a_\beta^+a_\delta a_\gamma), \quad (3)$$

where the single-particle orbitals $|\alpha\rangle$ were determined from a self-consistent procedure of the Hartree–Fock type for the core nucleus, E_0 is the vacuum energy (sign-reversed binding energy of the ground state of the magic nucleus), and $N(\ldots)$ is an operator product normally ordered with respect to the chosen vacuum. In the shell-model calculations, use was made of a Hamiltonian in the form (3) with interaction (2) and with the substitution of the orbitals associated with the mean field (1) for self-consistent orbitals. In implementing this procedure, all energies are defined apart from an unknown quantity E_0, which does not appear, however, in the decay energies, which are of prime interest to us. For the cases of two-, three-, and four-quasiparticle nuclei, formulas for calculating the quantity $\Delta B = B(Z,N) - B(\text{core})$ can be found in [6, 9]. The calculations were performed in the matrix representation.

Since the nuclei that are investigated here are characterized by a large neutron deficit, far extrapolations of phenomenological parameters that, in the shell-model approach, define the mean field and the residual interaction may prove to be hazardous. In order to determine the masses in the vicinity of ^{100}Sn, we have therefore performed, in addition, fully self-consistent calculations, relying on the combination of the Hartree–Fock and Bardeen–Cooper–Schrieffer methods (HF + BCS method) and using an interaction of the Skyrme III type; we have also added a contact pairing in order to take into account pairing correlations. In this approach, the total ground-state energy E of the nucleus being considered can be represented in the form (see [12–15])

$$E = 4\pi\int_0^\infty H(r)r^2dr - \frac{\Delta_p^2}{G_p} - \frac{\Delta_n^2}{G_n}. \quad (4)$$

Pair correlations in the modified Hartree–Fock energy density $H(r)$ were taken into account by introducing the orbital-occupation numbers v^2 in single-particle matter densities, in kinetic-energy densities, and in spin densities. After that, the Hartree–Fock problem with the densities modified in this way was solved in the coordinate representation, while a simultaneous solution to the equations of the HF + BCS method was constructed by applying an iterative procedure. In performing the self-consistent calculations, we took into account all terms in the energy functional that contribute to the spin–orbit splitting, including terms depending on the spin density. As to the exchange Coulomb interaction, it was treated in the Slater approximation. The details of the computational scheme used can be found in [9]. In the calculations, we employed the values of $G_p = 23/A$ MeV and $G_n = 21/A$ MeV.

The calculations were performed for 25 nuclides, including the ^{100}Sn nucleus and its nearest neighbors. For the ground states of the nuclei, the results of the calculation of the differences of the binding energies, ΔB, are quoted in Table 1, along with the relevant systematics (given for the sake of comparison) from [16–18] for the binding energies. The results of the shell-model calculations in Table 1

Table 1. Mass relief for nuclei in the vicinity of ^{100}Sn: Values of $\Delta B = B(Z,N) - B(^{100}\mathrm{Sn})$ (in MeV) for the ground states of the nuclei from [16–18] and values computed in the present study (for details, see main body of the text)

Nucleus	ΔB(syst.)			J^π	ΔB(theor.)		
	[16]	[17]	[18]		sh.m.	av.sh.m. (σ_{n-1})	HF + BCS
$^{96}_{48}$Cd$_{48}$	−31.48(0.66)	−31.40(1.36)	−31.31	0^+	-35.79	−35.44(1.65)	−34.14
$^{97}_{48}$Cd$_{49}$	−18.91(0.59)	−18.59(1.35)	−17.83	$9/2^+$	-20.59	−20.26(1.21)	−19.88
$^{98}_{48}$Cd$_{50}$	−3.98(0.48)	−3.57(1.37)	−3.14	0^+	-4.67	−4.60(0.86)	−4.36
$^{99}_{48}$Cd$_{51}$	6.48(0.48)	7.16(1.36)	7.48	$5/2^+$	5.84	6.00(0.95)	4.82
$^{100}_{48}$Cd$_{52}$	19.08(0.44)	19.75(1.38)	19.83	0^+	18.17	18.22(1.16)	16.18
$^{97}_{49}$In$_{48}$	–	−32.65(1.35)	−32.34	$9/2^+$	-34.35	−34.14(1.36)	−33.47
$^{98}_{49}$In$_{49}$	−18.42(0.66)	−18.55(1.44)	−18.26	0^+	-18.29	−18.14(0.81)	−18.79
$^{99}_{49}$In$_{50}$	−3.24(0.66)	−3.20(1.40)	−2.70	$9/2^+$	-3.13	−3.08(0.45)	−2.79
$^{100}_{49}$In$_{51}$	8.05(0.57)	8.46(1.43)	8.62	6^+	8.48	8.50(0.57)	6.75
$^{101}_{49}$In$_{52}$	20.40(0.52)	21.03(1.37)	21.09	$9/2^+$	21.09	20.98(0.87)	18.50
$^{98}_{50}$Sn$_{48}$	–	−31.89(1.42)	−31.18	0^+	-32.41	−32.06(1.08)	−31.67
$^{99}_{50}$Sn$_{49}$	–	−17.47(1.41)	−16.82	$9/2^+$	-17.15	−16.99(0.54)	−16.47
$^{100}_{50}$Sn$_{50}$	0.0(0.43)	0.0(1.08)	0.0	0^+	0.0	0.0	0.0
$^{101}_{50}$Sn$_{51}$	10.77(0.66)	11.66(1.49)	11.44	$5/2^+$	11.78	11.56(0.43)	10.05
$^{102}_{50}$Sn$_{52}$	24.03(0.59)	25.04(1.47)	24.65	0^+	25.20	24.87(0.83)	22.18
$^{99}_{51}$Sb$_{48}$	–	−35.57(1.51)	–	$5/2^+$	-36.15	−36.01(1.23)	−36.12
$^{100}_{51}$Sb$_{49}$	–	−20.22(1.51)	–	6^+	-19.75	−19.65(0.67)	−20.65
$^{101}_{51}$Sb$_{50}$	–	−2.77(1.44)	–	$5/2^+$	-2.43	−2.32(0.21)	−3.71
$^{102}_{51}$Sb$_{51}$	–	10.58(1.53)	10.15	1^+	11.13	11.09(0.37)	6.89
$^{103}_{51}$Sb$_{52}$	22.34(0.66)	24.24(1.51)	23.48	$5/2^+$	24.00	23.82(0.62)	19.65
$^{100}_{52}$Te$_{48}$	–	−37.59(1.64)	–	0^+	-38.38	−38.18(1.32)	−38.87
$^{101}_{52}$Te$_{49}$	–	−22.23(1.61)	–	$9/2^+$	-21.68	−21.51(0.79)	−22.80
$^{102}_{52}$Te$_{50}$	–	−4.00(1.52)	–	0^+	-3.63	−3.43(0.38)	−5.39
$^{103}_{52}$Te$_{51}$	–	9.62(1.51)	–	$5/2^+$	9.48	9.51(0.20)	5.95
$^{104}_{52}$Te$_{52}$	–	25.08(1.66)	24.24	0^+	23.77	23.60(0.77)	19.23

Note: Values of J^π correspond to the theoretical predictions for the ground states of the nuclei.

for the binding-energy differences ΔB(sh.m.) were obtained with the mean-field-potential and effective-interaction parameters set to the values indicated above and with $a_p = a_n = 0.60$ fm. As to the values ΔB(av.sh.m.) "averaged" over the parameters of the shell model, they are the binding-energy differences averaged over various combinations of the diffuseness parameters ($a = 0.55$, 0.60, 0.66 fm) for protons and neutron independently, as well as over some other mean-field potentials that we used previously. Of course, the calculations by the HF + BCS method—their results are given in the last column of Table 1—also yield the ^{100}Sn binding energy, 824.16 MeV, which is to be compared with the data of the systematics from [16], 824.88(±0.43) MeV, and with the experimental result from [19], 825.78(±0.95) MeV. At the same time, the calculations performed within relativistic mean-field theory [20] lead to an exaggerated value of about 833 MeV for this binding energy. As to the energies of nucleon separation from ^{100}Sn, our results are qualitatively consistent with those presented in [20], although they show a

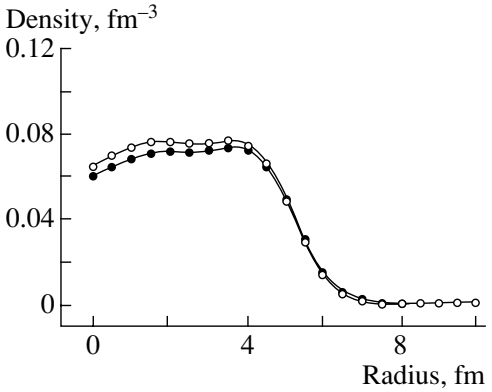

Fig. 1. Proton (closed circles) and neutron (open circles) densities in the neutron-deficient nucleus ^{100}Sn ($\langle r_n \rangle = 4.388$ fm, $\langle r_p \rangle = 4.464$ fm, $\langle r_m \rangle = 4.426$ fm).

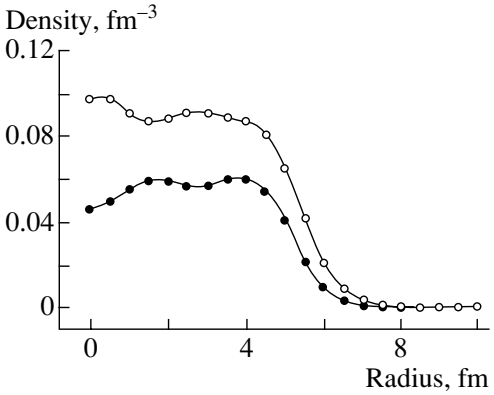

Fig. 2. Proton (closed circles) and neutron (open circles) densities in the neutron-rich nucleus ^{132}Sn ($\langle r_n \rangle = 4.905$ fm, $\langle r_p \rangle = 4.724$ fm, $\langle r_m \rangle = 4.837$ fm).

somewhat weaker binding of protons and neutrons in the core nucleus than that in [20]. Figure 1 displays the distributions of the proton and neutron densities in the ^{100}Sn nucleus. It can be seen that the densities become lower toward the center of the nucleus and that the root-mean-square radius of the proton distribution is somewhat greater than that of the neutron distribution. This result ($\Delta r_{p,n} = 0.076$ fm) is nearly coincident with that obtained in [21], where the calculations were performed within the theory of finite Fermi systems, and is somewhat less than that in [20]. For the sake of comparison, similar results for the doubly magic neutron-rich isotope ^{132}Sn are presented in Fig. 2. The spectrum of single-particle states in the vicinity of ^{100}Sn is given in Table 2 according to our shell-model calculation and according to the calculations from some other studies. The energy gaps between the filled and the free neutron and proton shells are rather wide, with the result that there are no pairing correlations in the core nucleus either in the approximation of constant pairing or in the approximation where the interaction of the form (2) is used in the pairing channel.

3. PROPERTIES OF $A = 100$ ISOBARIC NUCLEI

Here, we will consider the results of the calculations for the spectra of the ^{100}In and ^{100}Sn nuclei, whose properties are likely to be investigated earlier than the properties of other $A = 100$, $Z \sim 50$ isobars.

The ^{100}In nucleus was considered within the theoretical scheme that is based on the particle–hole random-phase approximation (RPA) in the charged channel and which was used previously in [1, 4] to study the ^{208}Bi, ^{208}Tl, ^{132}Sb, and ^{132}In nuclei, the interaction used here, that which is specified by Eq. (2), being coincident with the interaction in the quoted studies. As was noted above, there are presently no experimental data about the energies of single-particle states in the vicinity of ^{100}Sn—available information comes only from extrapolations of the corresponding energies from the region of more stable nuclei featuring greater numbers of neutrons. In view of this and in view of some uncertainty in the mean-field parameters, the calculations were performed with single-particle energies that correspond to a potential belonging to the type in (1) and having various values of the diffuseness parameter a. The computed spectrum of the levels in ^{100}In is given in Table 3, which shows that low-lying levels of this nuclide are weakly mixed two-quasiparticle states corresponding to the isospin value of $T = 1$. It can be seen that the 6^+ state is the lowest one, in contrast to the prediction of [22], where this was the 7^+ state and where a shell-model calculation was performed for various versions of the interaction, but with a rather small single-particle basis. At the same time, our prediction for the quantum numbers of the ^{100}In ground state agrees with the result obtained in [23] within the fermion–boson–fermion model, where the 1^+ level has, however, an overly low energy of about 1 MeV.

Addressing the core nucleus ^{100}Sn, we note from the outset that there is presently no information about the spectrum of its excited states. Before relevant experiments are performed, information about its properties can only be deduced from theoretical calculations—in particular, from those presented below. With the aim of achieving the highest predictive power, these calculations were performed within the theoretical scheme that is based on the particle–hole RPA formalism in the neutral channel without pairing and which was successfully used earlier (see relevant equations in [5]) to describe the properties

Table 2. Energies of single-particle levels (in MeV) in the vicinity of ^{100}Sn: Results of our calculation with the phenomenological potential (sh.m.) at $a_p = a_n = 0.60$ fm, along with the data from the systematics reported in [10] and the results of the calculation from [21]

nlj	Protons			Neutrons		
	syst. [10]	sh.m.	theor. [21]	syst. [10]	sh.m.	theor. [21]
$1h11/2$	–	4.79	5.63	−8.6	−8.66	−8.23
$2d3/2$	–	5.18	4.84	−9.2	−8.89	−8.83
$3s1/2$	–	4.50	4.68	−9.3	−9.40	−8.99
$1g7/2$	3.90	3.29	4.65	−10.93	−11.09	−9.20
$2d5/2$	3.00	2.43	2.90	−11.13	−11.78	−11.10
$1g9/2$	−2.92	−3.13	−2.85	−17.93	−17.15	−16.96
$2p1/2$	−3.53	−3.89	−3.82	−18.38	−19.03	−18.16
$2p3/2$	−6.38	−5.50	−5.21	–	−20.59	−19.68
$1f5/2$	−8.71	−6.36	−5.69	–	−21.28	−19.91
$1f7/2$	–	−10.58	–	–	−25.17	–

Table 3. Energies E of the levels in the ^{100}In nucleus of isospin $T = 1$ at various values of the diffuseness parameter $a_p = a_n = a$ (in fm), the corresponding computed values of $\Delta B = B(^{100}\text{In; g.s.}) - B(^{100}\text{Sn; g.s.})$ being 8.13, 8.48, and 8.90 MeV

Level	Leading configuration	E, MeV		
		$a = 0.55$	$a = 0.60$	$a = 0.66$
$1^+(*)$	$\nu 1g7/2\overline{\pi 1g9/2} + \ldots$	2.240	2.657	3.310
$2^+(*)$	$0.93\nu 2d5/2\overline{\pi 1g9/2} + 0.36\nu 1g7/2\overline{\pi 1g9/2} + \ldots$	0.590	0.677	0.714
$2^+(**)$	$-0.36\nu 2d5/2\overline{\pi 1g9/2} + 0.93\nu 1g7/2\overline{\pi 1g9/2} + \ldots$	1.168	1.492	1.903
$3^+(*)$	$\nu 2d5/2\overline{\pi 1g9/2} + \ldots$	0.223	0.219	0.218
$3^+(**)$	$\nu 1g7/2\overline{\pi 1g9/2} + \ldots$	0.665	1.076	1.518
$4^+(*)$	$\nu 2d5/2\overline{\pi 1g9/2}$	0.097	0.100	0.101
$4^+(**)$	$\nu 1g7/2\overline{\pi 1g9/2} + \ldots$	0.566	0.971	1.411
$5^+(*)$	$\nu 2d5/2\overline{\pi 1g9/2} + \ldots$	0.080	0.078	0.077
$5^+(**)$	$\nu 1g7/2\overline{\pi 1g9/2} + \ldots$	0.426	0.839	1.285
$6^+(*)$	$\nu 2d5/2\overline{\pi 1g9/2} + \ldots$	g.s.	g.s.	g.s.
$6^+(**)$	$\nu 1g7/2\overline{\pi 1g9/2} + \ldots$	0.463	0.874	1.317
$7^+(*)$	$0.99\nu 2d5/2\overline{\pi 1g9/2} - 0.13\nu 1g7/2\overline{\pi 1g9/2} + \ldots$	0.212	0.232	0.235
$7^+(**)$	$0.13\nu 2d5/2\overline{\pi 1g9/2} + 0.99\nu 1g7/2\overline{\pi 1g9/2} + \ldots$	0.385	0.777	1.222
$8^+(**)$	$\nu 1g7/2\overline{\pi 1g9/2} + \ldots$	0.795	1.211	1.660
1^-	$0.89\nu 2d5/2\overline{\pi 2p3/2} + 0.32\nu 1h11/2\overline{\pi 1g9/2} + \ldots$	2.663	2.957	3.575
2^-	$0.98\nu 2d5/2\overline{\pi 2p1/2} + 0.19\nu 2d5/2\overline{\pi 2p3/2} + \ldots$	0.855	1.151	1.519
3^-	$0.98\nu 2d5/2\overline{\pi 2p1/2} - 0.14\nu 2d5/2\overline{\pi 2p3/2} + \ldots$	0.836	1.132	1.500
4^-	$\nu 1g7/2\overline{\pi 2p1/2} + \ldots$	0.885	1.598	2.411
5^-	$0.83\nu 1h11/2\pi 1g9/2 - 0.49\nu 1g7/2\overline{\pi 2p3/2} + \ldots$	2.632	3.186	3.479

of ^{208}Pb and ^{132}Sn also on the basis of the effective interaction (2). As before, the basis employed included one shell above the Fermi energy and one shell below it for both neutrons and protons in the core nucleus. The results of the calculations for the spectrum of levels in ^{100}Sn are quoted in Table 4. It can be seen that the 3^- level at an energy of about 3 MeV is the lowest excitation, the explicit form

Table 4. Energies E of the levels in the core nucleus ^{100}Sn at various values of the diffuseness parameter $a_p = a_n = a$ (in fm) (for each excitation, the probability fraction of the $T = 0$ or the $T = 1$ component is indicated in the table)

Level	Leading configuration, T	E, MeV		
		$a = 0.55$	$a = 0.60$	$a = 0.66$
1^+	$1g7/2\overline{1g9/2}, 99.9\%\ T = 0$	7.317	7.339	7.314
$1^+(*)$	$1g7/2\overline{1g9/2}, 99.9\%\ T = 1$	8.203	8.222	8.196
2^+	$2d5/2\overline{1g9/2}, 99.98\%\ T = 0$	4.217	3.788	3.278
$2^+(*)$	$2d5/2\overline{1g9/2} + 1g7/2\overline{1g9/2},\ 99.9\%\ T = 1$	6.456	6.191	5.729
2^+	$1g7/2\overline{1g9/2}, 99.7\%\ T = 0$	6.543	6.487	6.462
$2^+(**)$	$1g7/2\overline{1g9/2} + 2d5/2\overline{1g9/2} + \ldots,\ 99.7\%\ T = 1$	7.134	7.067	7.004
3^+	$2d5/2\overline{1g9/2}, 99.6\%\ T = 0$	5.543	5.119	4.611
$3^+(*)$	$2d5/2\overline{1g9/2}, 99.6\%\ T = 1$	6.146	5.724	5.234
3^+	$1g7/2\overline{1g9/2}, 98.3\%\ T = 0$	6.308	6.329	6.305
$3^+(**)$	$1g7/2\overline{1g9/2}, 98.3\%\ T = 1$	6.657	6.666	6.627
4^+	$2d5/2\overline{1g9/2} + 3s1/2\overline{1g9/2},\ 99.9\% T = 0$	5.043	4.638	4.138
$4^+(*)$	$2d5/2\overline{1g9/2}, 99.97\%\ T = 1$	6.025	5.610	5.114
4^+	$1g7/2\overline{1g9/2} + 2d5/2\overline{1g9/2},\ 98.9\%\ T = 0$	6.072	6.067	6.022
$4^+(**)$	$1g7/2\overline{1g9/2}, 98.9\%\ T = 1$	6.562	6.567	6.332
5^+	$2d5/2\overline{1g9/2}, 98.8\%\ T = 0$	5.748	5.332	4.815
$5^+(*)$	$2d5/2\overline{1g9/2}, 98.8\%\ T = 1$	6.013	5.591	5.111
5^+	$1g7/2\overline{1g9/2}, 97.6\%\ T = 0$	6.066	6.082	6.059
$5^+(**)$	$1g7/2\overline{1g9/2}, 97.6\%\ T = 1$	6.431	6.441	6.406
6^+	$2d5/2\overline{1g9/2} + 1g7/2\overline{1g9/2} + \ldots, 99.5\%\ T = 0$	5.247	4.909	4.435
$6^+(*)$	$2d5/2\overline{1g9/2}, 99.9\%\ T = 1$	5.862	5.512	5.020
6^+	$1g7/2\overline{1g9/2} + 2d5/2\overline{1g9/2} + \ldots, 99.2\%\ T = 0$	5.936	5.803	5.739
$6^+(**)$	$1g7/2\overline{1g9/2}, 99.4\%\ T = 1$	6.463	6.474	6.439
7^+	$2d5/2\overline{1g9/2} + \ldots, 90.9\%\ T = 0$	5.902	5.602	5.067
$7^+(*)$	$2d5/2\overline{1g9/2} + 1g7/2\overline{1g9/2} + \ldots,\ 91.3\%\ T = 1$	6.048	5.744	5.285
7^+	$1g7/2\overline{1g9/2} + 2d5/2\overline{1g9/2} + \ldots,\ 98.6\%\ T = 0$	6.144	5.939	5.916
$7^+(**)$	$1g7/2\overline{1g9/2},\ 98.4\%\ T = 1$	6.376	6.377	6.344
8^+	$1g7/2\overline{1g9/2} + 1h11/2\overline{1f5/2} + \cdots,\ 99.9\%\ T = 0$	4.704	4.721	4.691
$8^+(**)$	$1g7/2\overline{1g9/2} + \ldots,\ 99.95\%\ T = 1$	6.774	6.793	6.767
1^-	Mixed config., $96.7\%\ T = 0$	6.336	6.198	6.027
1^-	Mixed config., $98.9\%\ T = 0$	7.565	7.240	6.861
1^-	Mixed config., $74.8\%\ T = 0$	8.831	8.489	7.964
1^-	$2d5/2\overline{2p3/2} + 1h11/2\overline{1g9/2} + \ldots,\ 69\%\ T = 1$	8.949	8.685	8.478
2^-	Mixed config., $73.1\%\ T = 0$	6.415	6.262	6.091
2^-	Mixed config., $95\%\ T = 0$	6.950	6.904	6.827
2^-	Mixed config., $60\%\ T = 1$	7.671	7.531	7.368

Table 4. (Contd.)

Level	Leading configuration, T	E, MeV		
		$a = 0.55$	$a = 0.60$	$a = 0.66$
2^-	Mixed config., T mixing	8.055	7.898	7.714
3^-	Mixed config., 99.2% $T = 0$	3.141	3.076	2.949
3^-	Mixed config., 82% $T = 0$	6.168	6.139	6.062
3^-	Mixed config., T mixing	6.925	7.049	7.058
3^-	Mixed config., T mixing	7.421	7.323	7.353
3^-	Mixed config., T mixing	7.811	7.831	7.671
4^-	Mixed config., 62% $T = 0$	6.820	7.105	7.337
4^-	Mixed config., 78% $T = 0$	7.565	7.557	7.565
4^-	Mixed config., T mixing	7.903	8.117	7.903
4^-	Mixed config., T mixing	8.262	8.190	8.018
4^-	$2d5/2\overline{1f5/2} + \ldots, T$ mixing	8.382	8.567	8.458
5^-	Mixed config., 97% $T = 0$	6.673	6.659	6.522
5^-	Mixed config., 68% $T = 0$	7.990	7.962	7.633
5^-	Mixed config., 72% $T = 0$	8.591	8.421	8.391
5^-	Mixed config., T mixing	8.705	8.684	8.766

Note: Asterisks label levels appearing to be isobaric analogs of the states of ^{100}In that are presented in Table 3.

of the amplitude of this excited state suggesting a strong configuration mixing; the results obtained by projecting this amplitude onto the $T = 0$ and $T = 1$ components indicate that the $T = 0$ components (which are symmetric in coordinate–spin space and antisymmetric in isospin space) contribute about 99% to this level in probability. The 2^+ level at an energy in the interval between 3 and 4 MeV, the specific value of this energy being dependent on the version of the mean field, is the next excited level, which is close to that mentioned immediately above; the 2^+ level is also predominantly an isoscalar one, but it is a two-quasiparticle level featuring nearly identical fractions of proton and neutron particle–hole components. The diagram of ^{100}Sn levels that was obtained in the present study resembles, to some extent, the spectra of the ^{208}Pb and ^{132}Sn nuclei and differs from the predictions of [22], where the 2^+ or the 8^+ is the lowest excited state and where the 3^- level occurs considerably higher. The last circumstance stems from the use of a rather narrow basis in [22], where only the $2p1/2$ state was taken into account among negative-parity levels below $N = 50$.

Within the RPA method, we have also calculated the probabilities of electromagnetic transitions between the levels of ^{100}Sn. Here, we would like to note that, since the diagrams determining the phonon structure in the core nucleus are identical to those that determine the probability of phonon decay, the quantities $B(E\lambda; \lambda \to \text{g.s.})$ must be calculated with the bare effective charges ($e_p = 1$, $e_n = 0$). This leads to $B(E3; 3_1^- \to \text{g.s.}) = 28$ W.u. and $B(E2; 2_1^+ \to \text{g.s.}) = 2.6$ W.u. However, the basis that we have used (one shell above the Fermi energy and one shell of opposite parity below it) may prove to be insufficient for describing the probabilities of positive-parity $E2$ transitions. In view of this, there arises the need for introducing the effective charges e_p and e_n corresponding to a nuclear medium. In the case of $E\lambda$ transitions between isoscalar levels of $Z = N$ nuclei, the dependence of $B(E\lambda)$ on the effective charges is reflected by the factor $(e_p + e_n)^2$, which has a value of about $(2.5)^2$ for $E2$ transitions; we have used the experimental values of the quadrupole charges in the vicinity of ^{208}Pb. The resulting value of $B(E2; 2_1^+ \to \text{g.s.}) \sim 16$ W.u. is an upper bound on the probability of this $E2$ transition; it corresponds to the coherent contribution of the $E2$ matrix elements of the non-spin-flip proton and neutron $2d5/2 \to 1g9/2$ transitions. As to transitions between excited one-phonon (two-quasiparticle) states, they must be calculated with

renormalized (effective) charges because, for the core nucleus, the RPA method does not take into account admixtures of, say, *two particles plus hole* type to single-particle states entering into the phonon basis. Here, the analytic dependence of $B(E\lambda)$ on the effective charges for transitions between isoscalar levels also has the form indicated above. The calculations yield $B(E2; 4_1^+ \to 2_1^+) = 0.22$ W.u., $B(E2; 6_1^+ \to 4_1^+) = 0.17$ W.u., $B(E2; 8_1^+ \to 6_1^+) = 0.043$ W.u., and $B(E2; 5_1^- \to 3_1^-) = 0.046$ W.u. (these numerical results correspond to that version in Table 4 in which the diffuseness parameter is set to $a = 0.60$ fm). The above values of $B(E2)$ were obtained with the bare charges, but they can easily be rescaled to different charge values.

Among the levels given in Table 4, we would like to highlight $T = 1$ states, which are isobaric analogs of the ^{100}In levels indicated in Table 3. That the levels in question are analogous is manifested both in the similarity of the state amplitudes, which differ only by a rotation in isotopic space, and in the similarity of the disposition of all these levels on the energy scale. By way of example, we indicate that, upon taking into account the computed data on the binding energies—these data are partly presented (for $a = 0.60$ fm) in Table 1—the quantity obtained by averaging the difference of the total energies of the isobaric analogous states in the ^{100}Sn and ^{100}In nuclei over all values of the parameter a and over all individual $(J^\pi, T = 1)$ states presented in Tables 3 and 4 amounts to 14.019 ± 0.067 MeV. That the dependence of the aforementioned (Coulomb) difference on the diffuseness parameter is very weak (in contrast to what is observed for the energies of individual levels) stems from the fact that, at $a_p = a_n$, the mean nuclear potential conserves isospin (a smooth Coulomb field apart). At the same time, the Coulomb energy taken in the approximation of a uniformly charged sphere of radius $R_c = r_{0c}A^{1/3}$ is the sum of the direct and the exchange (according to Slater) term:

$$E_{\mathrm{Coul}} = \frac{3}{5}\frac{e^2}{r_{0c}}\frac{Z^2}{A^{1/3}} - 3\left(\frac{3}{16\pi}\right)^{2/3}\frac{e^2}{r_{0c}}\frac{Z^{4/3}}{A^{1/3}}. \quad (5)$$

At the value of $r_{0c} = 1.25$ fm, which we used in the potential (1), this yields the difference $\Delta E_{\mathrm{Coul}}(Z, Z-1) = 14.18$ MeV, which is in good agreement with the Coulomb shift value obtained on the basis of RPA calculations.

4. BETA DECAY OF THE ^{100}Sn GROUND STATE

Since the weak axial current is not conserved, we have $g_A = -1.24g_V$ even for a free nucleon. In a nucleus, g_A can suffer an additional renormalization caused by the admixture of nonnucleonic degrees of freedom (see, for example, [24–26]); however, an experimental determination of this renormalization requires theoretically calculating a matrix element of the Gamow–Teller type with a reliable inclusion of nucleonic degrees of freedom, the use of sum rules [27] in this calculation being highly desirable. Such a calculation is possible in principle for the β^+ decay of $Z > N$ nuclei, in which case a resonance of the Gamow–Teller type may be excited in the daughter nucleus. Here, however, the "window" accessible in an experiment for the excitation energies of the daughter nucleus may not cover all the components of the aforementioned resonance. Relevant experiments were performed only for light nuclei. The result was $|g_A/g_V| \sim 1.0$ [28]. Investigation of the β^- decay of nuclei is a means for studying the Gamow–Teller resonance in $N > Z$ nuclei. In this case, however, the accessible energy "window" in the daughter nucleus is even considerably smaller, as a rule. In actual practice, relevant experiments are therefore performed for a direct charge-exchange (p, n) reaction at zero angle and at an appropriate energy by using the similarity of the amplitude of this reaction and the amplitude for a β decay of the Gamow–Teller type. The results of such experiments and their treatment yielded $|g_A/g_V| \sim 0.8$–0.9 [29–31]. At the same time, the treatment in [32] led to a value of $|g_A/g_V| \sim 1.0$. A third means to find the value of g_A is to determine it from experimental and computational data for nuclei close to filled shells or well-separated subshells, where the calculations are the most reliable and where the experimental probabilities of Gamow–Teller transitions are rather high. Actually, use was made in the experiments and the computations of the situation in nuclei around the ^{146}Gd nucleus, which has the $Z = 64$ (sub)shell, where the spin-flip β^+ $\pi 1h11/2 \to \nu 1h9/2$ transitions manifest themselves by virtue of the neutron deficit. Here, experimental results and their theoretical treatment [33, 34] yielded $|g_A/g_V| \sim 0.7$–0.9. Finally, we note that investigations into β^+ transitions between light odd mirror nuclei, along with data on "isoscalar" magnetic moments of the aforementioned nuclides, led to the value of $|g_A/g_V| \sim 1.12$ [35]. In this connection, we will consider the situation in nuclei around ^{100}Sn for the most interesting example.

According to data presented in [36], the half-life of the 0^+ ground state of the ^{100}Sn nucleus with respect to the weak transition through the β^+-channel is $0.94(^{+0.54}_{-0.27})$ s. The final state of this transition is that of the daughter nucleus ^{100}In at 2760 keV, its quantum numbers (spin–parity) being presumably 1^+. Our calculations by the RPA

method in the charged particle–hole channel predict the spin–parity of $J^\pi = 6^+$ for the ground state of ^{100}In and the presence of a 1^+ level in the energy range between 2.2 and 3.3 MeV, its specific position being dependent on the choice of mean-field version (see Table 3). It is of importance that, according to the calculations, there are no 1^+ levels other than that indicated above in the energy interval extending up to several MeV units. At the same time, conceivable $0^+ \to 0^+$ beta transitions of the Fermi type from the ground ($T = 0$) state of the ^{100}Sn nucleus to levels of ^{100}In, where $T \geq 1$, are forbidden by isospin selection rules. In view of the aforesaid, the allowed $0^+ \to 1^+$ Gamow–Teller transition to the level at 2760 keV is the only real possibility for the deexcitation of the ^{100}Sn ground state. As can be seen from Table 3, the leading configuration in the amplitude of the states forming this level has a structure of the $\nu 1g7/2(\pi 1g9/2)^{-1}$ type, so that the relevant beta-decay process proceeds through a single-particle spin-flip transformation of the $\pi 1g9/2 \to \nu 1g7/2$ type, in which case the Gamow–Teller matrix element is great. It is of importance that the initial proton orbital $\pi 1g9/2$ is completely filled and that the final neutron state $\nu 1g7/2$ is absolutely free. As a result, the reduced Gamow–Teller transition probability $B(\mathrm{GT}; 0^+ \to 1^+)$ corresponding to the above single-particle transformation takes the value of $160/9 \equiv 17.(7)$ for the example of the multiparticle shell model without mixing. Allowances for weak configuration mixing and, predominantly, for ground-state correlations (that is, for the distinctions between the shell model involving mixing and the RPA method) reduce slightly the above value, so that, for the mean-field version corresponding to the diffuseness-parameter value of $a = 0.60$ fm, in which case the energy of the relevant 1^+ level is 2.657 MeV, the reduced probability in question is $B(\mathrm{GT}; 0^+ \to 1^+) = 14.8$, changing only slightly upon going over to different versions and to other reasonable effective forces. We emphasize here that the difference "sum rule" [27] is satisfied exactly in the theoretical method used. It is worth noting that qualitatively similar conclusions on the distribution of $B(\mathrm{GT})$ in the decay of ^{100}Sn follow from the calculations presented in [37]. So large a value of $B(\mathrm{GT})$, which is reliably determined from theoretical calculations, is unique and can be used for an adequate determination of the quantity $|g_A/g_V|$ in nuclear matter.

Recalling the known formulas for the probability of the allowed Gamow–Teller decay through the β^+ channel and taking into account K capture, we arrive at the expression [38, 39]

$$(g_A/g_V)^2 = \frac{6163}{T_{1/2}(\mathrm{GT})\left[\frac{\pi}{2}\Phi_0 E_\nu^2 + f_0(Q_{\beta^+}, Z)\right] B(\mathrm{GT})}, \quad (6)$$

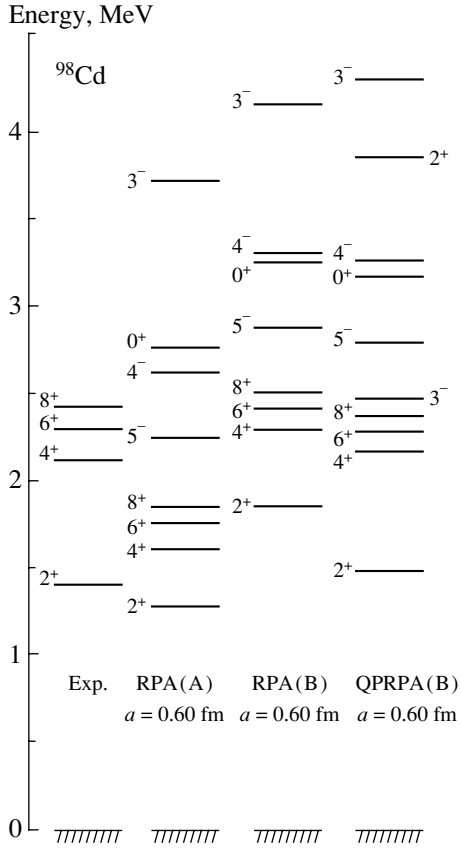

Fig. 3. Experimental and computed spectrum of levels in the ^{98}Cd nucleus. In the calculation by the quasiparticle RPA (QPRPA) method, there arise two extra (2^+ and 3^-) states that are close in properties to the corresponding particle–hole excitations of the core.

where f_0 is the integrated Fermi function for the allowed β^+ decay of the (Z, N) nucleus, $Q_{\beta^+} = B(Z-1, N+1) - B(Z, N) + m_p - m_n - E_{\mathrm{exc}}(Z-1, N+1) - m_e$ is the corresponding decay energy, $E_\nu = Q_{\beta^+} + 2m_e - |\varepsilon_{1s}|$ is the neutrino energy in K capture, ε_{1s} is the $1s$-electron energy, and Φ_0 is the density of K electrons at the origin. By using the values of Φ_0 and f_0 from [39] and the results of our averaged shell-model calculation of the binding-energy difference ΔB, we obtain $|g_A/g_V| = 0.77\left(^{+0.34}_{-0.21}\right)\left(^{+0.14}_{-0.16}\right)$, where the figures in the first parentheses reflect the uncertainties in ΔB, while the figures in the second parentheses correspond to the uncertainties in determining $T_{1/2}$. At the same time, the result obtained on the basis of data from the systematics of the binding energies B [16] is $|g_A/g_V| = 1.00\left(^{+0.40}_{-0.27}\right)\left(^{+0.18}_{-0.20}\right)$. Experimental data presented in [19] correspond to $Q_{\beta^+} = 3.102 \pm 1.0$ MeV, where the main contribution

to the root-mean-square error comes from the statistical uncertainty in determining the mass of ^{100}Sn; as a result, we obtain $|g_A/g_V| = 1.28\,(^{+1.08}_{-0.56})\,(^{+0.24}_{-0.26})$. All of the above values are consistent with one another; however, the errors are overly large to determine the ratio g_A/g_V to the required degree of precision. They stem primarily from the uncertainty in the nuclear masses, which manifests itself in the very sharp ($f_0 \sim Q_\beta^5$) dependence of the quantity being determined on the masses of the nuclides involved. Therefore, improvements in the accuracy of experimental data, predominantly those on nuclear masses, would provide a clue to solving the problem.

To conclude this section, we note that, according to our calculations, the fraction of K capture in the decay of ^{100}Sn is 7–14%, which is to be compared with the experimental result presented in [36], where it is less than 17%. So small a fraction of K capture is associated with a high transition energy.

5. TWO-QUASIPARTICLE EVEN–EVEN NUCLIDES IN THE VICINITY OF ^{100}Sn

Experimental information about the properties of ^{98}Cd and ^{102}Sn, which are characterized by the highest stability among nuclei belonging to the type indicated above and lying in the vicinity of ^{100}Sn, is presently available [40, 41]. We have investigated theoretically both these nuclei on the basis of the RPA method in the particle–particle channel without pairing, employing an effective interaction and the mean field whose parameters are quoted above. The results concerning ^{102}Sn were presented in an earlier article of our group (see [42]). In the case of ^{98}Cd, positive-parity low-lying levels form a multiplet of states where the leading components of state vectors correspond to the $(\pi 1g9/2)^{-2}$ configuration. These levels were reproduced both in our calculation (see Fig. 3) and in the calculations reported in [43], which were based on the idea of the ^{100}Sn nucleus as a doubly magic nucleus and which were performed with the shell-model basis including the $\pi 1g9/2$ and $\pi 2p1/2$ single-particle states. In other studies (see, for example, [44]), the spectra of even–even neutron-deficient nuclei with $N = 50$ were considered within the multiparticle shell model by using a wider basis and an interaction expressed in terms of the G matrix, but the ^{100}Sn nucleus was also taken there for the core.

In the case of ^{98}Cd, the problem of effective quadrupole charges is of greatest interest. As follows from [40], the corresponding charge determined on the basis of data on the $8_1^+ \to 6_1^+$ transition in ^{98}Cd [the half-life with respect to this transition is $T_{1/2}(8_1^+) = 0.48(\pm 0.16)$ μs, which corresponds to $B(E2; 8_1^+ \to 6_1^+) \approx 12.0|e|^2$ fm^4] by using our estimates concerning the structure of the states involved proved to be $0.85(^{+0.20}_{-0.10})|e|$. Our calculations lead to a close effective-quadrupole-charge value of $0.88(^{+0.20}_{-0.12})|e|$, which is also less than unity. Here, we would like to mention the results obtained in [42], where the neutronic two-quasiparticle nuclei ^{130}Sn and ^{134}Sn were studied both theoretically and experimentally and where it was shown that, for loosely bound particle states (in ^{134}Sn), the electric quadrupole charge for neutrons is about $0.7|e|$, which is much less than its value for deeper hole orbitals in ^{130}Sn ($\sim 0.9|e|$). This fact has the following natural explanation: as the binding energy of a neutron decreases when we approach the neutron drip line, its effective charge tends to the bare value, which is equal to zero for a free neutron. A similar effect must also occur in neutron-deficient nuclei in the vicinity of ^{100}Sn, but for protons, whose effective charges for loosely bound states must decrease in this region, in relation to, for example, their value in the region of the neutron-rich nucleus ^{132}Sn, where $e_p \sim 1.85|e|$ [45], and in relation to the value of $e_p \sim 1.6|e|$ in the region of the stable nucleus ^{208}Pb. However, the effective quadrupole charge for protons cannot become less than the bare value, which is equal to unity.

Leaving aside the question of a fairly large uncertainty in experimental data, we will try to give a possible explanation of the above effect. For this, we will analyze the structure of the $(\pi 1g9/2)^n$ multiplet in the even–even nuclei ^{92}Mo, ^{94}Ru, ^{96}Pd, and ^{98}Cd ($n = 2$, 4, 6, and 8, respectively); information about the energies and lifetimes of the 8_1^+ levels being considered can also be found in [40]. Relevant data are quoted in Table 5, along with the results of our analysis. It can be seen that, in the experiments, the dependence of $B(E2; 8_1^+ \to 6_1^+)$ on the number n of valence protons occupying the $\pi 1g9/2$ subshell is very strong, whereas the dependence of the energies of the levels in question on n is very weak. Both dependences can be qualitatively explained within the diagonal approximation of the multiparticle shell model if we assume that the structure of all states is described in terms of the $|(\pi 1g9/2)^n J, s = 2\rangle$ configuration. Within this model, we performed calculations on the basis of the technique of fractional-parentage expansions [46] by using either the interaction given above (version A) or the interaction (version B) that also has the form (2), but whose parameters are set to $V = -16.65$, $V_\sigma = 2.33$, $V_T = -3.00$, $V_\tau = 3.35$, $V_{\tau\sigma} = 4.33$, $V_{\tau T} = 3.00$ (all these values are given in MeV units), and $r_{00} = 1.75$ fm. The latter version was used in [47] to describe the spectra of odd–odd nuclei

Table 5. Energies of low-lying levels (in MeV), reduced transition probabilities $B(E2; 8_1^+ \to 6_1^+)$ (in $|e|^2$ fm^4), and quadrupole moments $Q_{8_1^+}$ (in $|e|$ fm^2 units) in $N = 50$ isotones according to the calculations performed with two sets of the interaction parameters (A and B; see main body of the text) at $e_p = 1$ and $e_n = 0$

J^π	E_{expt}	$E_{\mathrm{sh.m.}}$(A)	$E_{\mathrm{sh.m.}}$(B)	E_{QPRPA}(A)	$E_{\mathrm{QPRPA}}(B)$
^{92}Mo: $B_{\mathrm{expt}} = 31.0$, $B_{\mathrm{sh.m.}} = 16.0$, $B_{\mathrm{QPRPA}}(\mathrm{A}) = 3.74$, $B_{\mathrm{QPRPA}}(\mathrm{B}) = 2.57$, $Q_{\mathrm{QPRPA}}(\mathrm{B}) = -9.88$					
8^+	2.760	0.969	1.257	1.728	2.629
6^+	2.612	0.926	1.208	1.686	2.567
4^+	2.282	0.855	1.109	1.562	2.380
2^+	1.509	0.661	0.816	1.114	1.508
^{94}Ru: $B_{\mathrm{expt}} = 0.091$, $B_{\mathrm{sh.m.}} = 1.8$, $B_{\mathrm{QPRPA}}(\mathrm{A}) = 0.20$, $B_{\mathrm{QPRPA}}(\mathrm{B}) = 0.064$, $Q_{\mathrm{QPRPA}}(\mathrm{B}) = -1.52$					
8^+	2.645	0.968	1.257	1.598	2.471
6^+	2.499	0.929	1.213	1.550	2.406
4^+	2.187	0.851	1.105	1.405	2.206
2^+	1.431	0.662	0.818	0.903	1.308
^{96}Pd: $B_{\mathrm{expt}} = 9.10$, $B_{\mathrm{sh.m.}} = 1.8$, $B_{\mathrm{QPRPA}}(\mathrm{A}) = 1.12$, $B_{\mathrm{QPRPA}}(\mathrm{B}) = 1.34$, $Q_{\mathrm{QPRPA}}(\mathrm{B}) = 7.23$					
8^+	2.530	0.945	1.225	1.578	2.407
6^+	2.424	0.909	1.183	1.537	2.338
4^+	2.099	0.833	1.079	1.392	2.145
2^+	1.415	0.665	0.807	0.885	1.314
^{98}Cd: $B_{\mathrm{expt}} = 12.2$, $B_{\mathrm{sh.m.}} = 16.0$, $B_{\mathrm{QPRPA}}(\mathrm{A}) = 6.68$, $B_{\mathrm{QPRPA}}(\mathrm{B}) = 6.85$, $Q_{\mathrm{QPRPA}}(\mathrm{B}) = 16.3$					
8^+	2.431	0.946	1.226	1.674	2.426
6^+	2.283	0.904	1.178	1.626	2.355
4^+	2.083	0.838	1.084	1.504	2.190
2^+	1.395	0.653	0.805	1.091	1.534

Note: For the quantities being considered, the results of the calculations are independent (in the case of the shell-model and RPA calculations) or are virtually independent (in the case of the QPRPA calculations) of e_n; therefore, they can easily be rescaled to other values of the quadrupole charge e_p.

in the vicinity of ^{132}Sn. For particles of the same type, this version coincides with that of the effective forces employed in [7, 48] to describe the excited states of $N = 82$ even–even nuclei that are close to and those that are far off filled proton shells. It should be emphasized that the strong dependence of the probabilities of $E\lambda$ transitions on the number of valence particles in the subshell being considered (strong suppression) is characteristic [49] of transitions between states involving identical numbers of quasiparticles in systems with fully developed pairing; the last circumstance is reflected in the appearance of the factor $(uu' - vv')$ in front of the transition matrix element $\langle j||m(E\lambda)||j'\rangle$. Therefore, we have also performed our calculations within the RPA method with pairing (QPRPA) [7, 50] using a unified interaction in the form (2) in the particle–particle, the particle–hole, and the pairing channel. The results of these calculations are also illustrated in Table 5 and in Fig. 3. It can be seen that, for the ^{92}Mo, ^{96}Pd, and ^{98}Cd nuclei, the experimental results can be reproduced upon the introduction of the effective proton charge, whose value is greater than unity, this charge being $e_p = 1.35|e|$ in the case of the ^{98}Cd nucleus, which is of greatest interest. These results fit in the systematics of the dependence of e_p on the binding energy of valence protons. As to ^{94}Ru, the factor $(uu' - vv')$ is close to zero here and the results of the calculations greatly depend on the single-particle scheme and on the interaction used.

Addressing the spectra of levels in Fig. 3, we can see that the RPA and the QPRPA method yield close results for the ^{98}Cd nucleus. At the same time, the

latter is more general, since, in ^{98}Cd, it has also enabled us to reproduce extra 2^+ and 3^- levels, which are predominantly of the particle–hole nature and which are close in properties to the corresponding excitations in the core nucleus. It should be noted, however, that the application of the QPRPA method without taking into account the blocking effect in ^{98}Cd, which differs from a magic nucleus by only two nucleons, may prove to be quite hazardous; this would be justified if the proton subsystem of ^{100}Sn exhibited (in contrast to the predictions based on the single-particle scheme used here) some properties of superfluidity characterized by weak pairing. If, nonetheless, the experimental data on the quantity $B(E2; 8_1^+ \to 6_1^+)$ in ^{98}Cd are confirmed, they may suggest that the $Z = 50$ proton shell in the ^{100}Sn nucleus is rather weak. This will possibly lead to a modification of the core-nucleus spectrum, where the 2_1^+ state may become the lowest excitation, occupying a lower position on the energy scale than that which is dictated by the data in Table 4. In this case, the $T = 0$ 8_1^+ and 6_1^+ levels with $T = 0$, which originally occur at an energy of about 4.5 MeV (see Table 4) and for which $B(E2; 8_1^+ \to 6_1^+) = 1.2(e_p + e_n)^2\ |e|^2\ \text{fm}^4$, would also descend. It can be seen that, if the lowest 8_1^+ and 6_1^+ states in ^{98}Cd are interpreted as core excitations, the experimental data on the lifetime of the 8^+ level at 2.431 MeV can also be explained on the basis of standard ideas of the effective charges. Both possibilities are realized in the case where the ^{100}Sn nucleus is not magic. However, investigation of this scenario is beyond the scope of the present study.

ACKOWLEDGMENTS

We are grateful to Prof. J. Blomqvist for discussions on the problems considered in this study.

This work was supported by the Russian Foundation for Basic Research (project no. 00-15-96610 in support of scientific schools).

REFERENCES

1. V. I. Isakov, S. A. Artamonov, and L. A. Sliv, Izv. Akad. Nauk SSSR, Ser. Fiz. **41**, 2074 (1977).
2. S. A. Artamonov, V. I. Isakov, S. G. Kadmenskiĭ, *et al.*, Yad. Fiz. **36**, 829 (1982) [Sov. J. Nucl. Phys. **36**, 486 (1982)].
3. K. I. Erokhina and V. I. Isakov, Izv. Akad. Nauk, Ser. Fiz. **56** (11), 78 (1992).
4. K. I. Erokhina and V. I. Isakov, Yad. Fiz. **57**, 212 (1994) [Phys. At. Nucl. **57**, 198 (1994)].
5. K. I. Erokhina and V. I. Isakov, Yad. Fiz. **59**, 621 (1996) [Phys. At. Nucl. **59**, 589 (1996)].
6. V. I. Isakov, K. A. Mezilev, Yu. N. Novikov, *et al.*, Yad. Fiz. **63**, 1828 (2000) [Phys. At. Nucl. **63**, 1740 (2000)].
7. K. I. Erokhina, V. I. Isakov, B. Fogelberg, and H. Mach, Preprint No. 2136, PNPI (Petersburg Nuclear Physics Institute, Gatchina, 1996).
8. V. I. Isakov, K. I. Erokhina, H. Mach, *et al.*, Preprint No. 2375, PNPI (Petersburg Nuclear Physics Institute, Gatchina, 2000).
9. V. I. Isakov, K. I. Erokhina, B. Fogelberg, *et al.*, Part. Nucl. Lett. **102** (5), 44 (2000).
10. H. Grawe, R. Shubart, K. H. Maier, *et al.*, Phys. Scr. T **56**, 71 (1995).
11. C. Fahlander *et al.*, in *Proceedings of the PINGST-2000 Workshop, Lund, 2000,* p. 34.
12. D. Vautherin and D. M. Brink, Phys. Rev. C **5**, 626 (1972).
13. M. Beiner, H. Flocard, Nguen Van Giai, and P. Quentin, Nucl. Phys. A **238**, 29 (1975).
14. M. Waroquier, J. Sau, K. Heyde, *et al.*, Phys. Rev. C **19**, 1983 (1979).
15. K. Heyde, *The Nuclear Shell Model* (Springer-Verlag, Berlin, 1990).
16. G. Audi and A. H. Wapstra, Nucl. Phys. A **595**, 409 (1995).
17. E. Comay, I. Kelson, and A. Zidon, At. Data Nucl. Data Tables **39**, 235 (1988).
18. J. Janecke and P. I. Masson, At. Data Nucl. Data Tables **39**, 265 (1988).
19. M. Chartier, G. Auger, W. Mittig, *et al.*, Phys. Rev. Lett. **77**, 2400 (1996).
20. J. Schaffner, J. A. Maruhn, H. Stöcker, and W. Greiner, Z. Phys. A **350**, 91 (1994).
21. I. N. Borzov, S. A. Fayans, *et al.*, Z. Phys. A **355**, 117 (1996).
22. I. P. Johnstone and L. D. Skouras, J. Phys. G **21**, L63 (1995).
23. Zs. Dombradi, A. Algora, S. Brant, and V. Paar, Phys. Scr. **56**, 236 (1995).
24. M. Rho, Nucl. Phys. A **231**, 493 (1974).
25. H. Sagawa, Prog. Theor. Phys. Suppl. **74–75**, 342 (1983).
26. V. I. Isakov and Yu. I. Kharitonov, Izv. Akad. Nauk SSSR, Ser. Fiz. **50**, 1803 (1986).
27. C. Gaarde, J. Rapaport, *et al.*, Nucl. Phys. A **369**, 258 (1981).
28. J. C. Hardy and I. S. Towner, J. Phys. (Paris) **45**, C4-417 (1984).
29. C. Gaarde, Nucl. Phys. A **396**, 127 (1983).
30. F. Osterfeld, Phys. Rev. C **26**, 762 (1982).
31. F. Osterfeld and A. Schulte, Phys. Lett. B **138B**, 23 (1984).
32. J. Bang, S. A. Fayans, F. A. Gareev, *et al.*, Nucl. Phys. A **440**, 445 (1985).
33. G. D. Alkhazov, A. A. Bykov, V. D. Vitman, *et al.*, Pis'ma Zh. Éksp. Teor. Fiz. **38**, 144 (1983) [JETP Lett. **38**, 171 (1983)].
34. G. D. Alkhazov, S. A. Artamonov, V. I. Isakov, *et al.*, Phys. Lett. B **198**, 37 (1987).
35. D. H. Wilkinson, Phys. Rev. C **7**, 930 (1973).
36. P. Kienle, Hyperfine Interact. **103**, 49 (1996).
37. A. Brown, Phys. Rev. C **50**, R2270 (1994).

38. A. Bohr and B. R. Mottelson, *Nuclear Structure,* Vol. 1: *Single-Particle Motion* (Benjamin, New York, 1969; Mir, Moscow, 1971).
39. B. S. Dzhelepov, L. N. Zyryanova, and Yu. P. Suslov, *Beta Processes* (Nauka, Leningrad, 1972).
40. M. Górska, M. Lipoglavšek, H. Grawe, *et al.*, Phys. Rev. Lett. **79**, 2415 (1997).
41. M. Lipoglavšek, M. Górska, J. Nybert, *et al.*, Z. Phys. A **356**, 239 (1996).
42. K. I. Erokhina, V. I. Isakov, B. Fogelberg, and H. Mach, Preprint No. 2225, PNPI (Petersburg Nuclear Physics Institute, Gatchina, 1998).
43. J. Blomqvist and L. Rydström, Phys. Scr. **31**, 31 (1985).
44. J. Sinatkas *et al.*, J. Phys. G **18**, 1377 (1992).
45. J. P. Omtvedt, H. Mach, B. Fogelberg, *et al.*, Phys. Rev. Lett. **75**, 3090 (1995).
46. B. F. Bayman and A. Lande, Nucl. Phys. **77**, 1 (1966).
47. A.-J. Aas, V. I. Isakov, *et al.*, submitted to Nucl. Phys. A.
48. K. Heyde and M. Waroquier, Nucl. Phys. A **167**, 545 (1971).
49. V. G. Soloviev, *Theory of Complex Nuclei* (Nauka, Moscow, 1971; Pergamon, Oxford, 1976).
50. M. Baranger, Phys. Rev. **120**, 957 (1960).

Translated by A. Isaakyan

Physics of Atomic Nuclei, Vol. 65, No. 8, 2002, pp. 1444–1455. Translated from Yadernaya Fizika, Vol. 65, No. 8, 2002, pp. 1479–1490.

NUCLEI
Theory

Diffractive Scattering in the Ericson Model for the S Matrix

A. V. Shebeko[1)] and E. V. Zemlyanaya

Joint Institute for Nuclear Research, Dubna, Moscow oblast, 141980 Russia

Received November 22, 2000; in final form, May 10, 2001

Abstract—The elastic scattering of spinless charged particles on nuclei is considered within the strong-absorption model proposed by Ericson for the S matrix in the angular-momentum representation. Our analytic method for summing partial-wave amplitudes, which is based on a generalization of the Abel–Plana formula, makes it possible to take into account the contributions from the possible singularities of the S matrix in the right-hand half-plane of the complex-valued variable l. The uniform asymptotic behavior obtained in the present study for the scattering amplitude offers a fresh view on the origin of the diffraction patterns in the angular distributions of elastically scattered heavy particles. Special attention is given to Coulomb–nuclear interference (in particular, to refraction phenomena) in the case of scattering into the classically allowed region (illuminated region) and the classically forbidden region (shadow region). In contrast to other analytic results, our solutions to the diffraction problem within the Ericson model do not give grounds whatsoever to draw profound analogies either with Fresnel diffraction in optics or with the phenomenon of rainbow scattering in classical mechanics. © *2002 MAIK "Nauka/Interperiodica"*.

1. INTRODUCTION

The existing descriptions of hadron–nucleus and nucleus–nucleus collisions at intermediate energies (for example, the scattering of heavy ions of energies ranging between a few MeV units to about ten MeV per nucleon) always take into account, in one way or another, nuclear absorption and refraction. These features of nuclear interaction may be reflected either in the properties of the real and imaginary parts of the optical potentials used or in models of the scattering matrix that satisfy some analytic requirements [1]. One of such models, that which was formulated by Ericson [2] for the S matrix that describes the elastic scattering of strongly absorbed particles, played an important role in the development of nuclear-diffraction theory.

Along with other studies that explored these realms [3–6], the applications of this theory (see, for example, [7]) formed a basis for obtaining qualitative insights into diffraction patterns found in the scattering of extremely light nuclei and heavy ions at collision energies above the Coulomb barrier. Above all, we mean applications to analyzing the effect of Coulomb–nuclear interference on the formation of the angular distributions of scattered particles and to drawing analogies between various modes of nuclear diffraction, on one hand, and the phenomena of Fresnel and Fraunhofer diffraction in optics and of rainbow scattering in classical mechanics, on the other hand. A comprehensive review of these issues can be found in [8] (see also references therein).

Owing to a simple dependence of partial elements of the model S matrix in the angular-momentum representation on physical parameters, it is possible to obtain closed analytic expressions for the scattering amplitude (see, for example, [1]). In practice, one has to invoke various approximations, retaining only the "leading" terms in these expressions, where the interplay of basic physical ingredients is reflected only partly. It is obvious that such a partition into leading and nonleading contributions is a delicate point in solving the diffraction problem, which involves several characteristic quantities. These quantities specify the relation between the radius R of nuclear-interaction (strong-absorption) region and the de Broglie wavelength λ in the input scattering channel and the relation between R and the thickness of the surface layer of this region, where there occurs a smooth transition from the transmission of incident partial waves without distortions to their complete absorption. In the case of charged-particle scattering, it is of paramount importance to single out correctly Coulomb repulsion effects, whose relative role is controlled by the Sommerfeld parameter.

In our opinion, available analytic results for diffractive scattering in the Ericson model are not free from drawbacks. Here, we mean, above all, not the

[1)] Kharkov Institute for Physics and Technology, Akademicheskaya ul. 1, Kharkov, Ukraine.

1063-7788/02/6508-1444$22.00

methods for deducing these results but misleading conclusions drawn from formulas whose applicability range is rather limited.

The objective of this article is to present new calculations of the elastic-scattering amplitude within this popular model and, then, to propose a possible interpretation of specific diffraction patterns in nuclear scattering (for example, owing to the refraction of incident waves). The analyses performed in [9, 10] for alpha-particle and pion scattering on nuclei in the energy region around 1 GeV furnished additional motivation to this study. The relevant expressions for the scattering amplitudes disregard some exponentially small contributions that cannot be ignored for not overly small values of the scattering angle. A detailed discussion of these contributions can be found in [11, 12].

Our further consideration will rely on previous theoretical elaborations [13] and on experience gained in deriving uniform asymptotic expansions [14] for typical diffraction integrals (Section 2). Section 3 is devoted to constructing an alternative description of oscillations of the Fresnel (or rainbow) type in the angular dependence of the ratio of the cross section for elastic scattering to the Rutherford cross section, $\sigma(\theta)/\sigma_{\mathrm{R}}(\theta)$, for scattering angles in the illuminated region ($\theta < \theta_{\mathrm{C}}$, where θ_{C} is the Coulomb angle corresponding to the motion of a charged particle in the Coulomb field of a force center along the grazing trajectory for which the distance of closest approach to this center is equal to R. In the same section, we formulate conditions under which there appears a dip in regular Fraunhofer-type oscillations of the elastic-scattering cross section $\sigma(\theta)$ for angles $\theta > \theta_{\mathrm{C}}$ (shadow region). Within the method of complex angular momenta, this phenomenon was explained many years ago in [15].

2. CALCULATION OF THE AMPLITUDE FOR THE SCATTERING OF STRONGLY ABSORBED PARTICLES

2.1. Ericson Model and Related Quantities

In the model proposed in [2], the S-matrix elements appearing in the expansion

$$f(\theta) = \frac{1}{2ik}\sum_{l=0}^{\infty}(2l+1)(S_l \exp[2i\sigma_l] - 1) \times \exp\left[-(l+1/2)\,\gamma\right] P_l(\cos\theta) \quad (1)$$

of the amplitude for the elastic scattering of spinless charged particles (here, σ_l is the Coulomb phase shift and k is the wave number) are approximated by the Fermi-like distribution

$$S_l \equiv \eta_l \exp[2i\delta_l] = \left[1 + \exp\frac{\bar{l}_0 - l}{\Delta}\right]^{-1}, \quad (2)$$

$$\bar{l}_0 = l_0 + il_I,$$

where $\bar{l}_0$ and Δ are model parameters. From this relation, we find the absorption coefficient

$$\eta_l \equiv |S_l| = \frac{1-\eta_{\mathrm{F}}(l)}{[1 + 4\Delta D_{\mathrm{F}}(l)\sin^2(l_I/(2\Delta))]^{1/2}} \quad (3)$$

and the "nuclear" phase shift

$$\delta_l \equiv \frac{1}{2}\arg S_l \quad (4)$$
$$= -\frac{1}{2}\arctan\left[\frac{\eta_{\mathrm{F}}(l)}{1 - 2\eta_{\mathrm{F}}(l)\sin^2\dfrac{l_I}{2\Delta}}\sin l_I/(\Delta)\right],$$

where we have used the notation[2)] $\eta_{\mathrm{F}}(l) = [1 + \exp((l-l_0)/\Delta)]^{-1}$ for the Fermi distribution and

$$D_{\mathrm{F}}(l) \equiv \frac{d\eta_{\mathrm{F}}(l)}{dl} = -\frac{1-\eta_{\mathrm{F}}(l)}{\Delta}\eta_{\mathrm{F}}(l) \quad (5)$$

for the corresponding absorptive shape function (compare with [16]).

Here, it is reasonable to introduce a nuclear (quantum) deflection function

$$\Theta_N(l) \equiv 2\frac{d\delta(l)}{dl} \quad (6)$$
$$= \frac{1-\eta_{\mathrm{F}}(l)}{\Delta}\frac{\eta_{\mathrm{F}}(l)}{1 + 4\Delta D_{\mathrm{F}}(l)\sin^2 l_I/(2\Delta)}\sin\frac{l_I}{\Delta}.$$

The quantities S_l satisfy the unitarity condition

$$|S_l| \le 1 \quad (l = 0, 1, 2, \ldots), \quad (7)$$

so that

$$\cos\frac{l_I}{\Delta} \ge 0. \quad (8)$$

We recall that the grazing angular momentum l_0 is determined by the semiclassical relation

$$l_0 + 1/2 \equiv L = kR\sqrt{1 - B/E} = kR\sqrt{1 - \frac{2n}{kR}}, \quad (9)$$

where $B = Z_1 Z_2 e^2/R$ is the height of the Coulomb barrier at the nuclear-interaction boundary, E is the collision energy, and $k = \lambda^{-1}$ is the corresponding wave number. The Sommerfeld parameter $n = Z_1 Z_2 e^2/\mu k$ (Coulomb parameter) depends on the charges Z_1 and Z_2 of colliding particles and on their reduced mass μ.

[2)] It is implied that, for the function g_l specified at nonnegative integral values of l, an analytic continuation $g(l)$ to the complex plane of l is implemented by substituting any complex values of l in formulas of the type (2)–(4).

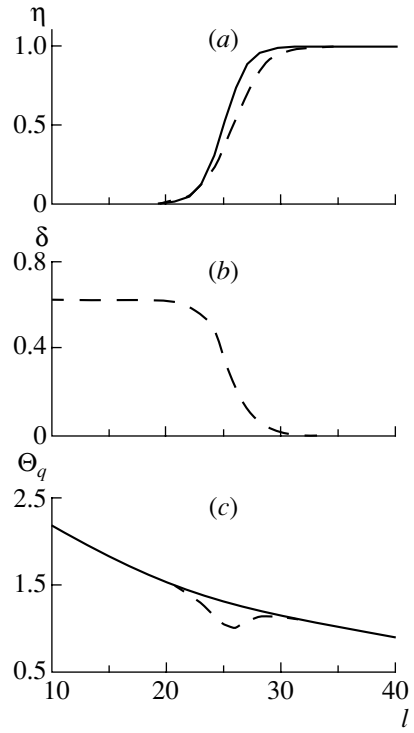

Fig. 1. Absorption coefficient $\eta(l)$, phase-shift function $\delta(l)$, and total quantum deflection function $\Theta_q(l) \equiv \Theta_N(l) + \theta_C(l)$ in the Ericson model for two parameter sets: (i) $l_0 = 25$, $n = 20$, $\Delta = 1.00$, and $l_I = 0$ (solid curve in Fig. 1*a*) and (ii) $l_0 = 25.45$, $n = 20$, $\Delta = 1.20$, and $l_I = -1.50$ (dashed curves). The solid curve in Fig. 1*c* represents the l dependence of the Coulomb deflection function $\theta_C(l) = 2\arctan[n/(l + 1/2)]$.

By definition, the Coulomb scattering angle θ_C is given by

$$\theta_C = 2\arctan\frac{n}{L}, \tag{10}$$

so that $n = L\tan(\theta_C/2)$.

As can be seen from Fig. 1, the coefficient $\eta(l)$ (which is sometimes referred to as a profile function) increases monotonically from small values to unity. This growth occurs over a characteristic interval Δ of l values in the vicinity of l_0. Strong absorption can be defined as the situation where

$$\Delta \ll l_0. \tag{11}$$

Together with the other strong inequality

$$l_0 \sim kR \gg 1, \tag{12}$$

which is the short-wavelength condition, this idea, which was put forth a priori and which was then corroborated by numerical calculations, proved to be very seminal for developing various analytic methods.

We can see that, in the three-parameter strong-absorption model under consideration, the necessary element of description of potential scattering—namely, the refraction of incident waves in nuclear matter—is introduced by replacing the grazing angular momentum l_0 in this model without refraction (at $\delta_l \equiv 0$) by the complex value $\bar{l}_0 = l_0 + il_I$. Not only does this replacement cause the emergence of an additional phase shift δ_l, but it also modifies the factor η_l. This seems reasonable from the physical point of view since scattering on the real and imaginary parts of the nuclear potential must be reflected simultaneously in the absorptive and refractive properties of the S matrix. Similarly, there is no precise separation of nuclear and Coulomb effects whatsoever (in particular, the corresponding contributions to the total phase shift are not additive). In this context, the nuclear phase shift δ_l characterizes the deflection of this phase shift (see Fig. 1) from the phase shift σ_l for Coulomb (Rutherford) scattering:

$$\exp[2i\sigma_l] = \frac{\Gamma(l + 1 + in)}{\Gamma(l + 1 - in)}. \tag{13}$$

It is obvious that, under condition (11), the behavior of δ_l for peripheral values of $l \geq l_0 \gg 1$ [in fact, only in the relatively narrow transition region $l_0 - \Delta \leq l \leq l_0 + \Delta$, because, for high values of l, the centrifugal barrier suppresses the phase shift ($\delta_l \to 0$)] becomes especially important.

In this connection, we emphasize that the l dependences of the absorption coefficient and of the phase shift in Fig. 1 are typical of other strong-absorption models (compare with, for example, [3]) and are corroborated by calculations based on the optical model (see, for example, [17]) that include a larger number of parameters. Hence, the Ericson model involving three parameters ensures a plausible and economical description of the S-matrix properties that satisfies the necessary physical requirements.

We also note that, in the Glauber–Sitenko approach, the profile function $S_F(b)$ has a similar behavior versus the impact parameter $b = (l + 1/2)/k$ (compare with a smooth variation in $|S_F(b)|$ from zero to unity with increasing b in Fig. 5 of [18]). Indeed, we have $S_F(b) = \exp[-\gamma t(b)]$, where the quantity γ having $\mathrm{Re}\,\gamma > 0$ depends on the properties of the amplitude for projectile interaction with a target nucleon and $t(b) > 0$ is determined by the Glauber integral of the nuclear density. For a standard density of the Woods–Saxon type in the peripheral region $b > R$, where R is the nuclear radius, one can see that $t(b)$ decreases exponentially; that is, $t(b) \to 0$ as b tends to infinity.

Since the nuclear phase shift does not take very large values for peripheral collisions, the unitarity of

the S matrix constrains [see the inequality in (8)] the possible values of the parameter l_I:

$$\frac{|l_I|}{\Delta} \leq \frac{\pi}{2}. \tag{14}$$

Indeed, it follows from (4) that

$$\delta(l_0) = -\frac{1}{4}\frac{l_I}{\Delta}. \tag{15}$$

In the case of motion along a grazing trajectory, the angle of nuclear deflection is given by

$$\theta_N \equiv \Theta_N(l_0) = \frac{1}{2\Delta}\tan\frac{l_I}{2\Delta} = -\frac{1}{2\Delta}\tan[2\delta(l_0)]. \tag{16}$$

For this angle to be negative, it is therefore necessary that l_I be negative. This yields a positive nuclear phase shift corresponding to a grazing trajectory.

Along with the ratios l_0/Δ and $|l_I|/\Delta$, there are also two important quantities $l_0\theta$ and $\Delta\theta$. The first of these characterizes oscillations of the cross sections for diffractive scattering, while the second determines the slope of the envelopes of the diffraction maxima toward the interior of the illuminated region ($\theta < \theta_C$) and of the shadow region ($\theta > \theta_C$).

The values of the diffuseness parameter (as a rule, empirical ones) depend on the type of colliding particles and on collision energies (by way of example, we indicate that, for pion–nucleus scattering at intermediate energies, the authors of [10] established the dependence $\Delta \simeq ka$, where the parameter a characterizes the smearing of the nuclear density at the boundary of the strong-interaction region). In any case, we assume that

$$\Delta \simeq 1. \tag{17}$$

Prior to presenting the results of our calculations within the Ericson model, we note that the cutoff factor $\exp[-\gamma(l+1/2)]$ with $\gamma > 0$ was introduced in [13] in order to ensure the convergence of series (1) in the presence of long-range Coulomb interaction. Of course, it is necessary to specify the meaning of this convergence. This subtle question of scattering theory was the subject of thorough investigations in the 1970s (see, for example, [19], where it was shown that such expansions must be considered as distributions). Without going into details, we note that the parameter γ must be made to tend to zero only at the end of the calculations.

2.2. Summation of Partial-Wave Amplitudes: Typical Diffraction Integrals

In the region of scattering angles that are not very close to zero or π, where, under the condition

$$L\theta \gg 1, \tag{18}$$

the Legendre polynomials can be replaced by their asymptotic expressions,

$$P_l(\cos\theta) \sim \sqrt{\frac{2}{\pi(l+1/2)\sin\theta}}\cos\left[(l+1/2)\,\theta - \frac{\pi}{4}\right], \tag{19}$$

it can be shown with the aid of formula (6) from [13] (compare with [14]) that

$$f(\theta) = \frac{1}{ik}\frac{1}{\sqrt{2\pi\sin\theta}}\left\{\bar{I}_+(\theta)e^{-i\pi/4}\right. \tag{20}$$
$$+ \bar{I}_-(\theta)e^{i\pi/4} + \bar{C}_+(\theta)\exp\left[i\bar{L}\theta - i\frac{\pi}{4}\right]$$
$$\left. + \bar{C}_-(\theta)\exp\left[-i\bar{L}\theta + i\frac{\pi}{4}\right]\right\},$$

$$\bar{I}_\pm(\theta) = \int_{\bar{L}}^{\infty}\sqrt{t}\exp\phi_\pm(t)dt, \tag{21}$$

$$\phi_\pm(t) = 2i\sigma\,(t-1/2) \pm i\theta t,$$

$$\bar{C}_\pm(\theta) = \int_0^{\infty}\left\{\sqrt{\bar{L}+t}\exp\left[2i\sigma\left(\bar{L}-1/2+t\right)\right.\right. \tag{22}$$
$$\left.\pm\, i\theta t\right] - \sqrt{\bar{L}-t}\exp\left[2i\sigma\left(\bar{L}-1/2-t\right)\mp i\theta t\right]\Big\}$$
$$\times\frac{dt}{\exp(t/\Delta)+1},$$

where $\sigma \equiv \sigma_l$ is the Coulomb phase shift and $\bar{L} = \bar{l}_0 + 1/2 = L + il_I$. Among important elements in our derivation of expression (20), we would like to indicate the relation

$$\int_0^{\infty}\frac{\exp(-vs)}{1+\exp((\bar{L}-s)/\Delta)}ds = \pi\Delta\frac{\exp(-\bar{L}v)}{\sin(\pi\Delta v)} \tag{23}$$
$$+ \frac{\Delta\exp(-\bar{L}/\Delta)}{\Delta v - 1}$$
$$\times F(1, 1-\Delta v; 2-\Delta v; -\exp(-\bar{L}/\Delta))\ (\mathrm{Re}v > 0)$$

and the recipe [14] that makes it possible to establish close links with the analysis of diffractive scattering in a strong-absorption model for the case of a sharp edge,

$$S_l = \Theta(l-l_0) = \begin{cases} 0 & (l < l_0) \\ 1 & (l \geq l_0), \end{cases} \tag{24}$$

where integrals of the type in (23) arise upon substituting l_0 for complex-valued $\bar{L}$ in formulas (21) and (22).

We note that formula (23) follows from the integral representation of the Gauss hypergeometric function $F(a, b; c; z)$ {see [20], p. 124, formula (15)} and one of

the Kummer relations {see [20], p. 116, formula (2)} for the analytic continuation of the hypergeometric series on the right-hand side of (23) (see also [21], where a similar relation was used in calculating elastic and inelastic nuclear form factors).

The representation in (20) is accurate to terms of two types: those of order $\exp(-L/\Delta)$ and those of order $\exp[-(\pi\Delta - |l_I|)(2\pi - \theta)]$. The latter type characterizes the contribution of the line of poles $l_k = \bar{l}_0 + i(2k-1)\pi\Delta$ $(k = 0, \pm1, \pm2, ...)$. Owing to the unitarity of the Ericson model, the distance $\pi\Delta - |l_I|$ of the pole l_1 from the real axis in the l plane cannot be less than $(\pi/2)\Delta$. It should be emphasized that, even if the strong inequalities

$$\exp\left(-\frac{L}{\Delta}\right) \ll 1 \tag{25}$$

and

$$\exp\left[-\frac{\pi}{2}\Delta(2\pi - \theta)\right] \ll 1 \tag{26}$$

are satisfied, the disregard of these exponentially small contributions is not always justified against the background of retained contributions of order $\exp[-\pi\Delta(\theta \pm \theta_C)]$, which are given below (compare with the thorough investigation of this issue in [11, 12]).

By analogy with the Coulomb angle θ_C, we now introduce the complex critical angle $\bar{\theta}_C$ as

$$n\cot\frac{\bar{\theta}_C}{2} = \bar{L} \quad \text{or} \quad \cot\frac{\bar{\theta}_C}{2} = \cot\frac{\theta_C}{2} + i\frac{l_I}{n}. \tag{27}$$

For this angle, we have

$$\bar{\theta}_C = -i\ln\frac{\cot(\bar{\theta}_C/2) + i}{\cot(\bar{\theta}_C/2) - i}$$
$$= \theta_C - 2i\frac{l_I}{n}\sin^2(1/2)\theta_C + O(n^{-2}).$$

To terms of order of n^{-2} and for $L \gg n$, this yields

$$\bar{\theta}_C = \theta_C + i\frac{|l_I|}{L}\sin\theta_C. \tag{28}$$

By using the Stirling asymptotic expression for the gamma function, we find for complex values of t $(|t| \gg 1)$ that

$$\phi_\pm(t) = t\ln\frac{t+in}{t-in} + in\ln(t^2+n^2) \tag{29}$$
$$\pm i\theta t - 2in + \frac{i}{4}\frac{n}{t^2+n^2} + O(|t|^{-3}).$$

Experience gained in solving the nuclear-diffraction problems makes it possible to write, to a good approximation, the relation (see [13])

$$\bar{C}_\pm(\theta) = i\sqrt{\bar{L}}\exp\left[2i\sigma\left(\bar{L} - 1/2\right)\right] \tag{30}$$
$$\times\left\{\frac{\pi\Delta}{\sinh[\pi\Delta(\bar{\theta}_C \pm \theta)]} - \frac{1}{\bar{\theta}_C \pm \theta}\right\}.$$

By means of integration by parts, we can derive the expansions

$$\bar{I}_\pm(\theta) = i\sqrt{\bar{L}}\exp\left[2i\sigma\left(\bar{L} - 1/2\right)\right]\frac{\exp(\pm i\bar{L}\theta)}{\bar{\theta}_C \pm \theta} \tag{31}$$
$$\times\left\{1 + 2i\frac{\sin^2(\bar{\theta}_C/2)}{n(\bar{\theta}_C \pm \theta)^2} + ...\right\}.$$

Under the condition

$$\frac{\sin^2(\theta_C/2)}{n|\bar{\theta}_C - \theta|^2} \ll 1, \tag{32}$$

we can retain only the first term in (31), so that we have

$$\bar{I}_\pm(\theta) = i\sqrt{\bar{L}}\frac{\exp\phi_\pm(\bar{L})}{\bar{\theta}_C \pm \theta}. \tag{33}$$

However, the inequality in (32) can be violated at angles θ close to θ_C, in which case expression (33) becomes invalid for $\bar{I}_-(\theta)$. This is associated with the fact that, at such scattering angles, the integral $\bar{I}(\theta)$ can receive contributions not only from the vicinity of the end point $t_0 = \bar{L}$ but also from the vicinity of the stationary point $t_s = L_s$, which is specified by the relation $\phi'_-(L_s) = 0$; that is,

$$L_s = n\cot\frac{\theta}{2} + O\left(\frac{1}{n}\right). \tag{34}$$

In order to obtain the asymptotic expression for $\bar{I}_-(\theta)$ uniform with respect to $\theta \to \theta_C$, we can use (as was done in [14]) the method developed in [22]. As a result, we have

$$\bar{I}_-(\theta) = i\sqrt{\frac{2\pi L_s}{\phi''_-(L_s)}}\bar{G}_1(\theta)\exp[\phi_-(L_s)] \tag{35}$$
$$+ i\sqrt{\bar{L}}\frac{\exp[\phi_-(L)]}{\bar{\theta}_C - \theta},$$

$$\bar{G}_1(\theta) = \bar{G}(\theta) - \frac{\exp(-\tau^2)}{2\sqrt{\pi}\tau}, \tag{36}$$

$$\bar{G}(\theta) = 1/2\left[1 - \frac{2}{\sqrt{\pi}}\mathrm{Erf}(\tau)\right], \tag{37}$$

and

$$\tau = [\phi_-(L_s) - \phi_-(\bar{L})]^{1/2}. \tag{38}$$

Simple calculations involving (29) yield

$$\phi''_-(L_s) = -\frac{2i}{n}\sin^2\frac{\theta}{2}. \tag{39}$$

To terms of order n^{-1}, we then obtain

$$\tau^2 = i\bar{L}(\theta - \bar{\theta}_C) + 2in\ln\frac{\sin(\bar{\theta}_C/2)}{\sin(\theta/2)}, \quad (40)$$

where it is assumed that, for $|L_s - \bar{L}| \ll 1$, we must set $\tau \simeq [-\phi''_-(L_s)/2]^{1/2}(\bar{L} - L_s)$ and take the principal value of the square root.

Combining all the above results, we find that the scattering amplitude within the Ericson model can be represented as

$$f(\theta) = f_R^{as}(\theta)\left[\bar{G}(\theta) - \frac{\exp(-\tau^2)}{2\sqrt{\pi}\tau}\right] + \bar{f}^{(+)}(\theta) + \bar{f}^{(-)}(\theta), \quad (41)$$

where

$$\bar{f}^{(\pm)}(\theta) = \frac{\pi\Delta}{k}\left[\frac{\bar{L}}{2\pi\sin\theta}\right]^{1/2}\frac{\exp[\phi_\pm(\bar{L}) \mp i\pi/4]}{\sinh[\pi\Delta(\bar{\theta}_C \pm \theta)]}, \quad (42)$$

$\bar{f}^{(+)}(\bar{f}^{(-)})$ being the "far-side" ("near-side") branch of the amplitude in terms of the geometric theory of diffraction [23], and

$$f_R^{as}(\theta) = (2ik)^{-1}e^{-2in}n^{1+2in}\left(\sin\frac{\theta}{2}\right)^{-2-2in} \quad (43)$$

is the asymptotic form of the Rutherford scattering amplitude for $n \gg 1$.

For the characteristic cross-section ratio $\sigma(\theta)/\sigma_R(\theta) = |f(\theta)|^2/|f_R(\theta)|^2$, we thus obtain

$$\frac{\sigma(\theta)}{\sigma_R(\theta)} = \left|\bar{G}(\theta) - \frac{\exp(-\tau^2)}{2\sqrt{\pi}\tau} + \frac{\bar{f}^{(+)}(\theta) + \bar{f}^{(-)}(\theta)}{f_R^{as}(\theta)}\right|^2, \quad (44)$$

considering that $|f_R(\theta)| = |f_R^{as}(\theta)|$, where $f_R(\theta)$ is the exact amplitude for Rutherford scattering.

3. REFRACTION PHENOMENA IN VARIOUS MODES OF NUCLEAR DIFFRACTION

Figures 2 and 3 illustrate the angular dependence of the elastic-scattering cross section under consideration and the accuracy of asymptotic expressions that were obtained with and without allowance for the nuclear phase shift on the basis of the Ericson model. In order to facilitate a comparison with known results, we reproduce here the calculations (see Fig. 1 in [14]) according to the asymptotic formula

$$\frac{\sigma_{sco}(\theta)}{\sigma_R(\theta)} = \left|G(\theta) + \mathrm{sgn}(\theta_C - \theta)\times\frac{\exp(-ix - i\pi/4)}{2(\pi x)^{1/2}} + \frac{f^{(+)}(\theta) + f^{(-)}(\theta)}{f_R^{as}(\theta)}\right|^2, \quad (45)$$

where σ_{sco} is the cross section computed on the basis of the absorption model with of a sharp cutoff,

$$G(\theta) = \frac{1}{2}[1 + 2\pi^{-1/2}\mathrm{sgn}(\theta_C - \theta)\mathrm{Erf}(\sqrt{ix})], \quad (46)$$

$$x = n\left\{(\theta - \theta_C)\cot(\theta_C/2) + 2\ln\frac{\sin\frac{\theta_C}{2}}{\sin(\theta/2)}\right\}, \quad (47)$$

$$f^{(\pm)}(\theta) = (2k)^{-1}(L/(2\pi\sin\theta))^{1/2} \times e^{2i\sigma(l_0 - 1/2)}\frac{\exp(\pm il_0\theta \mp i\pi/4)}{\sin[(\theta_C \pm \theta)/2]}. \quad (48)$$

This approximate solution to the diffraction problem involving a sharp cutoff can be obtained from formula (41) by replacing $\bar{L}$ by L ($\bar{\theta}_C$ by θ_C)[3] and the factors $\pi\Delta/\sinh[\pi\Delta(\bar{\theta}_C \pm \theta)]$ by $[2\sin((\theta_C \pm \theta))]^{-1}$.

The dashed curve in Fig. 2 was calculated by the formula

$$\frac{\sigma_{sco}(\theta)}{\sigma_R(\theta)} = |G(\theta)|^2 = 1/2\left\{[1/2 + \mathrm{sgn}(\theta_C - \theta)C(x)]^2 + [1/2 + \mathrm{sgn}(\theta_C - \theta)S(x)]^2\right\}, \quad (49)$$

where

$$C(x) = \frac{1}{\sqrt{2\pi}}\int_0^x\frac{\cos t}{\sqrt{t}}dt, \quad S(x) = \frac{1}{\sqrt{2\pi}}\int_0^x\frac{\sin t}{\sqrt{t}}dt$$

are the Fresnel integrals. The angular dependence of the factor $|G(\theta)|^2$ gives (upon appropriately redefining physical parameters) the Fresnel law for the angular distribution of the intensity of light scattered by the edge of an infinite half-plane.

This analogy between nuclear diffraction and Fresnel diffraction in optics was first drawn by Frahn and Venter (see, for example, [24]) and is often used in interpreting data on the elastic scattering of heavy ions. As was previously indicated in [8, 14] (compare with the critical comments in [25]), the argument of these authors is not, however, compelling, because they assumed that the approximate expression (49) is accurate in the illuminated region ($\theta < \theta_C$). But in fact, a thorough investigation revealed [14] that formula (49) is valid apart from quickly oscillating terms of order $n^{-1/2}$ only in the penumbra region ($\theta \simeq \theta_C$), which shrinks to θ_C in accordance with (32)

[3] We neglect the difference between $\theta_0 = 2\arctan(n/l_0)$ and $\theta_C = 2\arctan(n/L)$.

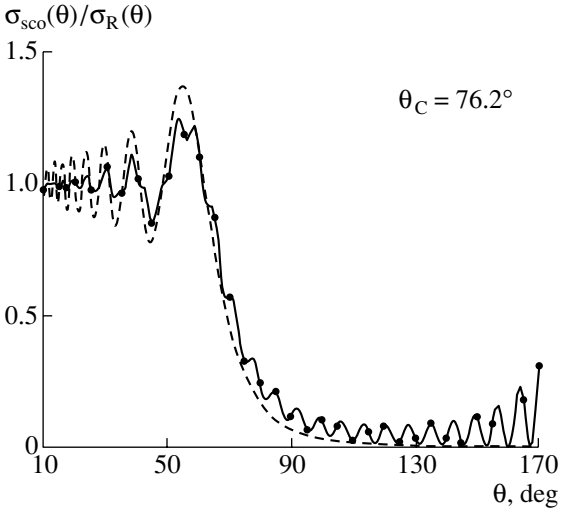

Fig. 2. Ratio of the elastic-scattering cross section in the strong-absorption model with a sharp cutoff ($l_0 = 25$, $n = 20$) to the Rutherford cross section. The solid and the dashed curve were calculated by formulas (45) and (49), respectively. Points represent the results of a numerical summation of the partial-wave amplitudes.

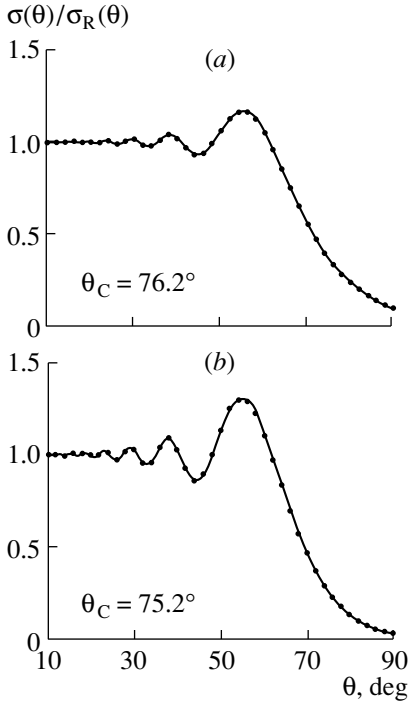

Fig. 3. Comparison of the results of the calculations by formula (44) (solid curves) with the results of numerical calculations (points) for two parameter sets indicated in the caption under Fig. 1.

(with θ_C instead of $\bar{\theta}_C$), following the $n^{-1/2}$ law—that is, in the region where there are no oscillations of the Fresnel type.

We note that very good agreement between the analytic and numerical results in Figs. 2 and 3 is not exceptional. It is not destroyed by variations of the physical parameters within reasonable limits. This creates reliable basis for subsequent qualitative conclusions.

3.1. Coulomb–Nuclear Interference for $\theta < \theta_C$

Pursuing further the analysis of diffraction patterns generated by the amplitude in (41), we consider scattering angles not very close to θ_C such that

$$|\tau| \gg 1. \tag{50}$$

We then have [26, p. 152]

$$\mathrm{Erf}(\tau) \sim \frac{\sqrt{\pi}}{2}\left[\mathrm{sgn}(\mathrm{Re}\tau) - \frac{\exp(-\tau^2)}{\sqrt{\pi}\tau}\right], \tag{51}$$

so that the amplitude can be represented as

$$f(\theta) = \Theta(-\mathrm{Re}\tau) f_R^{as}(\theta) + \bar{f}^{(+)}(\theta) + \bar{f}^{(-)}(\theta). \tag{52}$$

Moreover, it can be shown that, for angles θ satisfying the inequality

$$|\theta - \theta_C| \gg \frac{\sin(\theta_C/2)}{\sqrt{n}}, \tag{53}$$

the following relation holds to a good approximation:

$$\mathrm{Re}\tau = \sqrt{\frac{x}{2}}\,\mathrm{sgn}(\theta - \theta_C). \tag{54}$$

Here, we imply the principal value of the square root of the positive-definite quantity x. The nonnegativity of x, $x = x(\theta) \geq 0$, for $0 \leq \theta \leq \pi$ follows from

$$\frac{dx}{d\theta} = n\left(\cot\frac{1}{2}\theta_C - \cot\frac{1}{2}\theta\right)$$

and

$$\frac{d^2x}{d\theta^2} = \frac{1}{2}\frac{n}{\sin^2(\theta/2)}.$$

We then have $\Theta(-\mathrm{Re}\tau) = \Theta(\theta_C - \theta)$, and the amplitude in (52) takes the form

$$f(\theta) = \Theta(\theta_C - \theta) f_R^{as}(\theta) + \bar{f}^{(+)}(\theta) + \bar{f}^{(-)}(\theta). \tag{55}$$

In the illuminated region, we therefore have

$$f(\theta) = f_R^{as}(\theta) + \bar{f}^{(+)}(\theta) + \bar{f}^{(-)}(\theta), \tag{56}$$

and the ratio we are interested in has the form

$$\frac{\sigma(\theta)}{\sigma_R(\theta)} = \left|1 + \frac{\bar{f}^{(+)}(\theta) + \bar{f}^{(-)}(\theta)}{f_R^{as}(\theta)}\right|^2; \tag{57}$$

that is, its deviation from unity is determined by the interference between the amplitude of purely

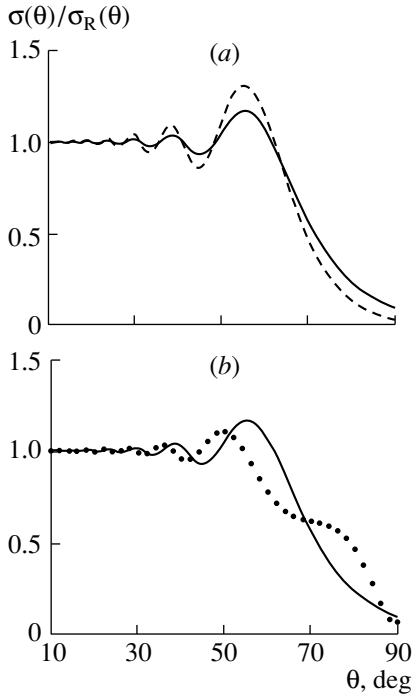

Fig. 4. Our asymptotic results obtained on the basis of the Ericson model: (solid curve) results of the calculations by formula (44) for the parameter set (i) from the caption under Fig. 1, (dashed curve) results of the calculations by formula (44) for the parameter set (ii) from the caption under Fig. 1, and (dotted curve) results of the calculations by formula (58) for set (i). The values of the angle θ_C for the first and the second set are 76.2° and 75.2°, respectively.

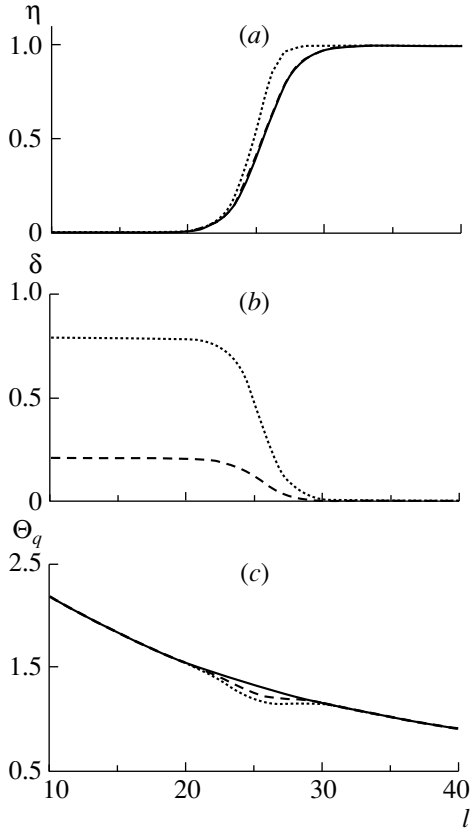

Fig. 5. As in Fig. 1, but for the parameter sets employing the identical values of $l_0 = 25.45$, $n = 20$, and $\Delta = 1.20$ and different values of the parameter l_I (which characterizes the strength of nuclear refraction): (solid curves) $l_I = 0$, (dashed curves) $l_I = -0.5$, and (dotted curves) $l_I = -(\pi/2)\Delta$. The last set corresponds to the situation of rainbow-type scattering.

Coulomb scattering and the branches $\bar{f}^{(\pm)}(\theta)$ of the Fraunhofer type. Owing to the attenuation factors $\pi\Delta/\sinh[\pi\Delta(\bar{\theta}_C \pm \theta)]$, these branches behave differently within the illuminated region. In particular, one can set

$$\frac{\sigma(\theta)}{\sigma_R(\theta)} = \left|1 + \frac{\bar{f}^{(-)}(\theta)}{f_R^{as}(\theta)}\right|^2 \tag{58}$$

for θ rather far from θ_C. In order to isolate nuclear-refraction effects more explicitly, we transform (42) by expanding the Coulomb phase shift in the function $\phi_\pm$ [see formula (21)] as

$$2i\sigma(\bar{L} - 1/2) \simeq 2i\sigma(L - 1/2) \tag{59}$$
$$+ 2\sigma'(L - 1/2)|l_I| = 2i\sigma(L - 1/2) + |l_I|\theta_C,$$

whence it follows that

$$\bar{f}^{(\pm)}(\theta) = M_\pm(\theta)e^{|l_I|(\theta_C \pm \theta)} f_0^{(\pm)}(\theta), \tag{60}$$
$$M_\pm(\theta) = \frac{\sinh[\pi\Delta(\theta_C \pm \theta)]}{\sinh[\pi\Delta(\bar{\theta}_C \pm \theta)]},$$

where $f_0^{(\pm)}(\theta)$ stands for the Fraunhofer branches in the case where the nuclear phase shift is switched off; that is,

$$f_0^{(\pm)}(\theta) = \bar{f}^{(\pm)}(\theta)|_{l_I=0}. \tag{61}$$

Further, setting

$$\sinh[\pi\Delta(\theta + \theta_C)] \simeq 1/2\exp[\pi\Delta(\theta + \theta_C)],$$

we obtain

$$M_+(\theta) = \exp[\pi\Delta(\theta_C - \bar{\theta}_C)] \tag{62}$$
$$= \exp\left[-i\frac{\pi\Delta}{L}|l_I|\sin\theta_C\right].$$

As we move away from θ_C, in which case

$$\exp[-\pi\Delta|\theta - \theta_C|] \ll 1, \tag{63}$$

we then arrive at

$$M_-(\theta) = \exp\left[-i\frac{\pi\Delta}{L}\mathrm{sgn}(\theta_C - \theta)|l_I|\sin\theta_C\right]. \tag{64}$$

By using these relations, we obtain the following expression for the Fraunhofer component of the ampli-

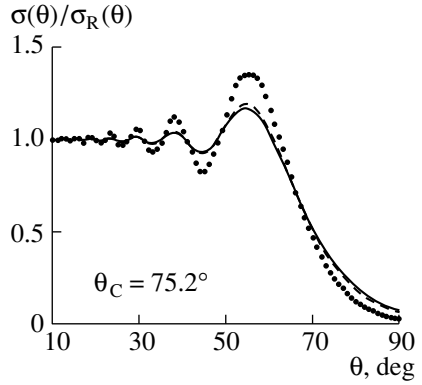

Fig. 6. Enhancement of the swing of oscillations of the elastic-scattering cross section due to nuclear refraction. Curves correspond to various values of the parameter l_I in the Ericson model: (solid curve) $l_I = 0$, (dashed curve) $l_I = -0.5$, and (dotted curve) $l_I = -(\pi/2)\Delta$.

tude in the illuminated region:

$$f_{\rm Fr} \equiv \bar{f}^{(+)}(\theta) + \bar{f}^{(-)}(\theta) = \frac{\Delta}{k}\left[\frac{2\pi L}{\sin\theta}\right]^{1/2} \times e^{2i\sigma(L-1/2)} \exp\left[-i\frac{\pi\Delta}{L}|l_I|\sin\theta_{\rm C}\right] \times \left\{e^{-(\pi\Delta-|l_I|)(\theta_{\rm C}+\theta)} \exp\left[iL\theta - i\frac{\pi}{4}\right] + e^{-(\pi\Delta-|l_I|)(\theta_{\rm C}-\theta)} \exp\left[-iL\theta + i\frac{\pi}{4}\right]\right\}. \quad (65)$$

It follows that the inclusion of the refraction of waves in nuclear matter enhances the "asymmetry" between the positive and the negative branch: the amplitude $\bar{f}^{(+)}(\theta)$ ($\bar{f}^{(-)}(\theta)$) increases (decreases) in relation to $f_0^{(+)}(\theta)$ ($f_0^{(-)}(\theta)$). This results in the enhancement of the swing of oscillations of $\sigma/\sigma_{\rm R}$ at scattering-angle values in the region $\theta < \theta_{\rm C}$. It is obvious that this effect is especially pronounced in the region of the first, highest, maximum in these oscillations (see Fig. 4*a*).

Such an enhancement effect is associated by some authors with the phenomenon of rainbow scattering in classical mechanics (see, for example, [25] and references therein). Recall that rainbow scattering corresponds to the situation where $\Theta'_q(l_r) = \Theta'_N(l_r) + \Theta'_{\rm C}(l_r) = 0$; in this case, the classical deflection function $\Theta_{\rm cl}(b)$ has an extremum at the impact parameter value $b_r = (l_r + 1/2)/k$, whence it follows that the scattering cross section is $\sigma_{\rm cl}(\theta_r) = \infty$, where the rainbow-scattering angle is given by $\theta_r \equiv \Theta_{\rm cl}(b_r)$ at $\theta_r \neq 0, \pi$. In other words, the classical cross section $\sigma_{\rm cl}(\theta)$ becomes very large near θ_r. In the Ericson model, the equation

$$\Theta'_N(l) + \Theta'_{\rm C}(l) = 0 \quad (66)$$

is equivalent to the equation

$$-\frac{1}{2\Delta}\Theta_N(l)\eta^2(l)[1 - e^{-2(l-l_0)/\Delta}] = \frac{n}{(l+1/2)^2 + n^2}. \quad (67)$$

Solutions to this equation, if they exist,[4)] are the values $l_r > l_0$; that is, $l_r = l_0 + \epsilon$ ($\epsilon > 0$). It can be shown that, in a typical situation where there are two solutions (it is shown by the dotted curve in Fig. 5*c*), the shift ϵ_1 of the value $l_r^{(1)}$ closest to l_0 is

$$\epsilon_1 = -\frac{\Delta^2}{n}\frac{\sin^2(\theta_{\rm C}/2)}{\theta_N\eta^2(l_0)}, \quad (68)$$

$$\eta^2(l_0) = \left[2\left(1 + \cos\frac{l_I}{\Delta}\right)\right]^{-1}. \quad (69)$$

To a high precision, the corresponding rainbow-scattering angle is given by

$$\theta_r^{(1)} \equiv \Theta_q(l_0 + \epsilon_1) \simeq \theta_{\rm C} + \theta_N. \quad (70)$$

For the limiting value of $|l_I| = (\pi/2)\Delta$, we have $\theta_N = -1/(2\Delta)$, so that the angle $\theta_r^{(1)}$ corresponds to scattering into the interior of the region if the diffuseness parameter is $\Delta \simeq 1$.

Without explicitly presenting the second solution $l_r^{(2)}$, we note that, although it corresponds to more peripheral collisions, $l_r^{(2)} > l_r^{(1)}$, we have $\theta_r^{(2)} \simeq \theta_{\rm C}(l_r^{(2)}) > \theta_r^{(1)}$ because of the nonmonotonicity of the function $\Theta_q(l)$. All these properties inherent in the Ericson model are shown in Fig. 5.

It should be emphasized that the above trends in the diffraction patterns manifest themselves not only in the cases where the quantum deflection function $\Theta_q(l)$ has one or a few extrema but also in the case where it has no extrema (compare the dashed and the dotted curves in Fig. 6). Similar qualitative variations in the angular dependence of the cross sections for diffractive scattering due to nuclear refraction are observed both near the classical scattering angle θ_r and far from them. Our uniform asymptotic expression, which is valid over a broad angular interval, differs from those that are obtained by using different asymptotic methods for calculating typical diffraction integrals (see [27] and references therein). The corresponding analytic expressions yield angular dependences of the Airy type, which, in our opinion, have nothing to do with nuclear-diffraction problems.

To complete this discussion of the effect of nuclear refraction in the illuminated region, we demonstrate

[4)] It can easily be seen that, at preset values of n and l_0 ($n < l_0$), Eq. (67) has no solution in the interval of interest $0 \leq l < \infty$ in the case of sufficiently weak refraction, $|l_I| \ll \Delta$.

the interference of the negative branch $\bar{f}^{(-)}(\theta)$ (scattering by the "near" side of the strong-interaction region) and the Rutherford scattering amplitude (Coulomb repulsion). As can be seen from Fig. 4*b*, this interference cannot reproduce the behavior of σ/σ_R at all $\theta < \theta_C$. We draw attention to this point because, in some approaches (see [7, 28]) where the negative branch is calculated by the method of complex angular momenta that takes into account the contribution of the S-matrix pole that lies in the first quadrant of the l plane and which is the closest to the real axis, it is usually assumed that the approximate relation (58) is well justified.

3.2. Dip Phenomenon in the Elastic-Scattering Cross Section in the Shadow Region ($\theta > \theta_C$)

At $\theta > \theta_C$, it follows from (55) that

$$f(\theta) = f_{Fr}(\theta) = \bar{f}^{(+)}(\theta) + \bar{f}^{(-)}(\theta), \quad (71)$$

$$\bar{f}^{(\pm)}(\theta) = \frac{\Delta}{ik}\left[\frac{2\pi L}{\sin\theta}\right]^{1/2} e^{2i\sigma(L-1/2)} F_{\pm}(\theta) \quad (72)$$

$$\times \exp\left[\pm i\left(L\theta + \frac{\pi}{4} - \frac{\pi\Delta}{L}|l_I|\sin\theta_C\right)\right],$$

$$F_{\pm}(\theta) = \exp[-(\pi\Delta \mp |l_I|)(\theta \pm \theta_C)], \quad (73)$$

whence we obtain

$$\sigma(\theta) = |f_{Fr}(\theta)|^2 = \frac{8\pi L}{k^2}\Delta^2 \frac{F_+(\theta)F_-(\theta)}{\sin\theta} \quad (74)$$

$$\times \left\{\cos^2\left[L\theta + \frac{\pi}{4} - \frac{\pi\Delta}{L}|l_I|\sin\theta_C\right] + \sinh^2\xi(\theta)\right\},$$

$$\xi(\theta) = -1/2\ln\frac{F_+(\theta)}{F_-(\theta)} = \pi\Delta\theta_C - |l_I|\theta. \quad (75)$$

From formula (74), it follows that, if the function $\xi(\theta)$ also has a zero in the vicinity of the angle $\theta = \theta_{dip}$, at which the cosine on the right-hand side of (74) vanishes, the cross section becomes very small near this angle (dip effect). One can see that, in the Ericson model, this angle is given by

$$\theta_{dip} = \frac{\pi\Delta}{|l_I|}\theta_C. \quad (76)$$

Owing to the constraint in (14), the minimal value of this angle is $\theta_{dip}^{min} = 2\theta_C$ at a preset value of θ_C.

It goes without saying that, at not very small values of the Coulomb angle θ_C such that

$$\exp(2\pi\Delta\theta_C) \gg 1, \quad (77)$$

the purely Fraunhofer pattern of oscillations does not have time to develop, with the result that, in the shadow region, the cross section decreases exponentially as $\exp(-2\pi\Delta\theta)$ without oscillations (so-called Coulomb damping), and the possibility of such a phenomenon disappears together with these oscillations.

Within strong-absorption models involving smooth cutoff, the dip angles in the diffractive-scattering cross section were considered in [15]. Later in [7] (compare with [14]), the condition of the dip in the cross section within the Ericson model was formulated in studying the elastic scattering of heavy ions. The authors of [7] explain the appearance of the corresponding angle in the classically forbidden region by a Coulomb–nuclear interference of the rainbow type at large scattering angles. In our opinion, this interpretation can be misleading. Most probably, we deal here with a specific refractive phenomenon that can manifest itself in the shadow region even in the case of a weak refraction of waves owing to Coulomb repulsion and nuclear attraction.

As was emphasized in [15], the presence of the dip angle can be used in estimating the nuclear phase shift for grazing trajectories.

4. CONCLUSION

Relying on the Ericson model for the S matrix in the angular-momentum representation, we have investigated the concerted effect of Coulomb repulsion and nuclear interaction (Coulomb–nuclear interference) on the formation of typical diffraction patterns in the elastic scattering of particles strongly interacting with nuclei (these may be, for example, pions, antiprotons, alpha particles, and heavy ions). Not only does this model reflect the most important condition of nuclear diffraction—almost complete absorption of a large set of incident waves having angular momenta that span the region from zero to values close to the grazing angular momentum—but it also takes into account refraction of waves in a nuclear medium, a phenomenon that is accompanied by a fast change in the nuclear phase shift in the region of grazing trajectories.

In the present study, emphasis has been placed not on describing experimental data by fitting three model parameters (grazing angular momentum, width of the transition region near this value of the angular momentum, and parameter whose nonzero value is responsible for the emergence of an imaginary part in the nuclear S matrix)—fitting of this type can always be performed with the aid of computers without elaborating relevant theories further—but on deriving accurate analytic expressions for the elastic-scattering amplitude over wide angular intervals, the conditions specifying the applicability ranges of these expressions being dependent on the above three parameters and on the Sommerfeld parameter n. As we have seen, our approach, which is based on a generalization of the Abel–Plana summation formula (its

derivation can be found in [13]; see also [20, p. 38]), makes it possible to reduce this problem for not overly large scattering angles to considering two integrals along the real axis in the complex plane of the variable l. These integrals can be evaluated in a compact form by combining the procedure of integration by parts with the method of steepest descent.

Thus, it is sufficient to know the behavior of the S matrix near the real axis, the analytic properties of partial-wave amplitudes near its poles playing only a secondary role in this approach because of a strong suppression of the contribution from the entire line of these poles in the right-hand half-plane of the complex variable l. Herein lies the main distinction of this approach from the method of complex angular momenta that is based on the Watson–Sommerfeld transformation [29] and where it is necessary to sum residues at all poles of this line for scattering into the illuminated region ($\theta < \theta_C$), the scattering amplitude in the shadow region ($\theta > \theta_C$) being determined by the residues at the two poles closest to the real axis.

As was shown in Subsection 2.2, the required amplitude can be represented as the sum of the Rutherford scattering amplitude multiplied by a damping factor and two diffraction branches $f^{(\pm)}(\theta)$ of the Fraunhofer type. At large values of the Sommerfeld parameter n, this damping factor reduces (apart from additive corrections of order n^{-1}) to the Fermi step $\Theta(\theta_C - \theta)$ everywhere, with the exception of a narrow interval of width about $n^{-1/2}$ in the vicinity of the Coulomb angle (penumbra region). In the extreme case where $n \to \infty$ and $\theta_C = \text{const}$—that is, in the C limit, according to the terminology adopted in [24]—this region shrinks to θ_C, so that the analogy with the Gibbs phenomenon in approximating discontinuous functions by continuous ones suggests itself. Thereby, we single out the effect of a sharp boundary in the diffractive scattering of charged particles.

In the illuminated region, the contribution of Rutherford scattering interferes with the oscillating diffraction contributions $f^{(\pm)}(\theta)$, whose relative importance is controlled by the exponentials $\exp[-\pi\Delta(\theta_C \pm \theta)]$, so that the characteristic deviations from unity (purely Rutherford scattering) are observed in the angular dependence of the cross-section ratio $\sigma(\theta)/\sigma_R(\theta)$. As was shown in Section 3, there is only an apparent similarity between this angular dependence and the Fresnel law of diffraction in optics. In the Ericson model, Fraunhofer oscillations superimposed on a comparatively smooth dependence $f_R(\theta)$ lead to a typical pattern of nuclear diffraction for angles in the region $\theta < \theta_C$.

In the shadow (classically forbidden) region, where $\theta > \theta_C$, the contribution of Rutherford scattering dies out fast, but Coulomb effects are still present in the negative $[f^{(-)}(\theta)]$ and the positive $[f^{(+)}(\theta)]$ branch, which interfere with each other. Their competition is determined by the interplay of the suppression factors $F_-(\theta)$ and $F_+(\theta)$ [see formula (73)], which decrease exponentially toward the interior of this region. Indeed, the ratio $F_+(\theta)/F_-(\theta) = \exp[-2\pi\Delta\theta_C + 2|l_I|\theta]$ ceases to depend on the scattering angle upon switching nuclear refraction off ($l_I = 0$), so that Coulomb repulsion enhances the contribution of diffractive scattering off the near side of the nuclear surface over the entire region $\theta > \theta_C$. If the strong inequality in (77) is satisfied, this contribution becomes dominant, with the result that Fraunhofer oscillations cease to be visible against the background of the exponential decay of the cross section $\sigma(\theta)$. The refraction of waves that is due to nuclear attraction compensates for this Coulomb damping to such an extent that, even under the condition in (77), the contributions $f^{(\pm)}(\theta)$ can be commensurate; as a result, the cross section will oscillate with the period L/π from $\theta \simeq 2\theta_C$. Yet, it should be borne in mind that, for such scattering angles, other exponentially small terms associated with nondiffractive scattering can contribute to the amplitude within the shadow region (see [11, 12]). In the Ericson model, this issue deserves a dedicated consideration.

It has been demonstrated how the phenomenon of a dip in the dependence $\sigma(\theta)$ in the shadow region—the emergence of one or a few neighboring minima that are much deeper than those in the regular pattern of cross-section oscillations without nuclear refraction—can be explained within the Ericson model.

Our analytic results are valid over a broad angular interval. The uniformity of the asymptotic expressions that we have obtained ensures reliable solutions to the diffraction problem in the case where model parameters are needed to be varied within broad ranges. Combined with the adiabatic approximation, these expressions can be used in describing diffraction phenomena in the inelastic scattering of nuclei.

ACKNOWLEDGMENTS

A.V. Shebeko is grateful to V.K. Lukyanov for the kind hospitality extended to him at the Laboratory of Theoretical Physics at the Joint Institute for Nuclear Research (Dubna), where this work was begun.

The work of E.V. Zemlyanaya was supported by the Russian Foundation for Basic Research (project no. 0001-006-17).

REFERENCES

1. W. E. Frahn, *Diffractive Processes in Nuclear Physics* (Clarendon Press, Oxford, 1985).
2. T. E. O. Ericson, in *Preludes in Theoretical Physics,* Ed. by A. de Shalit, H. Feshbach, and L. van Hove (North-Holland, Amsterdam, 1966), p. 321.
3. E. E. McIntyre, K. H. Wang, and L. C. Becker, Phys. Rev. **117**, 1337 (1960).
4. W. E. Frahn and R. H. Venter, Ann. Phys. (N. Y.) **24**, 243 (1963).
5. E. V. Inopin, Zh. Éksp. Teor. Fiz. **48**, 1090 (1965) [Sov. Phys. JETP **21**, 1090 (1965)].
6. A. V. Shebeko, Yad. Fiz. **5**, 766 (1966) [Sov. J. Nucl. Phys. **5**, 543 (1967)].
7. N. Rowley and C. Marty, Nucl. Phys. A **266**, 494 (1976).
8. E. V. Inopin and A. V. Shebeko, *Diffractive Interactions of Hadrons with Nuclei* (Naukova Dumka, Kiev, 1987), p. 154.
9. D. C. Choudhury and T. Guo, Phys. Rev. C **39**, 1883 (1989).
10. D. C. Choudhury and M. A. Scura, Phys. Rev. C **50**, 979 (1994).
11. A. V. Shebeko, in *Proceedings of the 8th International Conference on Nuclear Reaction Mechanisms, Varenna, 1997,* Ed. by E. Gadioli, p. 483.
12. V. V. Kotlyar and A. V. Shebeko, Izv. Akad. Nauk, Ser. Fiz. **63**, 188 (1999).
13. E. V. Inopin and A. V. Shebeko, Yad. Fiz. **11**, 140 (1970) [Sov. J. Nucl. Phys. **11**, 78 (1970)].
14. V. V. Kotlyar and A. V. Shebeko, Yad. Fiz. **34**, 370 (1981) [Sov. J. Nucl. Phys. **34**, 210 (1981)].
15. B. I. Tishchenko and A. V. Shebeko, Zh. Éksp. Teor. Fiz. **50**, 1674 (1966) [Sov. Phys. JETP **23**, 1113 (1966)].
16. W. E. Frahn and D. N. Gross, Ann. Phys. (N. Y.) **101**, 520 (1976).
17. R. Robertson *et al.*, Phys. Rev. C **4**, 2176 (1971).
18. S. Wallace, Nucl. Phys. A **374**, 203c (1982).
19. J. R. Taylor, Nuovo Cimento B **23**, 313 (1974).
20. *Higher Transcendental Functions (Bateman Manuscript Project),* Ed. by A. Erdelyi (McGraw-Hill, New York, 1953; Nauka, Moscow, 1965), Vol. 1.
21. A. V. Shebeko, Yad. Fiz. **25**, 477 (1977) [Sov. J. Nucl. Phys. **25**, 397 (1977)].
22. N. Bleinstein, Commun. Pure Appl. Math. **19**, 353 (1966).
23. V. Levy and M. Keller, Commun. Pure Appl. Math. **12**, 159 (1959).
24. W. E. Frahn, Nucl. Phys. **75**, 577 (1966).
25. S. H. Fricke *et al.*, Nucl. Phys. A **500**, 399 (1989).
26. *Higher Transcendental Functions (Bateman Manuscript Project),* Ed. by A. Erdelyi (McGraw-Hill, New York, 1953; Nauka, Moscow, 1966), Vol. 2.
27. W. E. Frahn, in *Heavy-Ion High-Spin States and Nuclear Structure* (IAEA, Vienna, 1975), Vol. 1, p. 157.
28. R. C. Fuller and P. J. Moffa, Phys. Rev. C **14**, 1721 (1976).
29. A. Sommerfeld, in *Partial Differential Equations in Physics* (Academic, New York, 1949).

Translated by A. Isaakyan

Physics of Atomic Nuclei, Vol. 65, No. 8, 2002, pp. 1456–1458. From Yadernaya Fizika, Vol. 65, No. 8, 2002, pp. 1491–1493.

NUCLEI
Theory

Doorway States for One-Nucleon Transfer Reactions as a Test for Current Approaches to Nuclei*

B. L. Birbrair and **V. I. Ryazanov**

Petersburg Nuclear Physics Institute, Russian Academy of Sciences, Gatchina, 188350 Russia

Received September 25, 2001

Abstract—It is shown that the naturalness concept of the effective field theory is not confirmed.

Devoted to the memory of Sergey Fayans

1. INTRODUCTION

The doorway states for one-nucleon transfer reactions are eigenstates of a nucleon in the static field of a nucleus which is the convolution of the free-space nucleon–nucleon forces with the nucleon density distributions in the nucleus [1]. They are model-independent quantities because (i) the free-space NN forces are independent of nuclear medium effects and (ii) the nucleon density distributions are deduced from the electron–nucleus [2] and proton–nucleus [3] elastic scattering data. The corresponding eigenvalue problem is that of a nucleon in a central field which can be solved with any desired accuracy. For these reasons, the doorway states can be used as a very trustworthy test for current nuclear models.

Let us discuss some results of [1] from this point of view.

1. The nuclear relativity within the Walecka [4] model is confirmed to be an actually existing phenomenon.

2. The dominant contribution to the isovector part of the static field arises from the many-particle NN forces because the ρ-meson (vector–isovector) and δ meson (scalar–isovector) fields arising from the two-particle forces nearly cancel each other. At the same time, the isovector nuclear potential is exclusively of the ρ meson origin within the quantum hadrodynamics [5, 6]. The reason for this wrong QHD result is the neglect of the δ-meson field in spite of the fact that both ρ- and δ-meson exchanges are taken into account in the two-particle NN forces [7–9].

3. The contributions from the two, three, and four-particle forces to the isoscalar part of the static field are found to be $U_2 \approx -80$ MeV, $U_3 \approx +96$ MeV, $U_4 \approx -104$ MeV. This is in conflict with such leading principles of the effective field theory as naive dimensional analysis (NDA) and naturalness [10, 11]. Indeed, the values of the forces which are estimated according to the above principles are [12]

$$V_2 \approx 30 \text{ MeV}, \quad V_3 \approx \frac{V_2^2}{m} \approx 1 \text{ MeV}, \quad V_4 \approx \frac{V_2^3}{m^2} \approx 0.03 \text{ MeV} \tag{1}$$

(m is the mass of nucleon), and therefore the expected relation between U_2, U_3, and U_4 is $|U_2| : |U_3| : |U_4| \approx 1 : 10^{-3/2} : 10^{-3}$. In fact, it is $1 : 1.2 : 1.3$, thus suggesting that there is something wrong with the naturalness. Discussion of this point is continued in the next section.

2. NONLINEARITY AS A SOURCE OF MANY-PARTICLE FORCES

As discussed in [1], the isoscalar part of the static field may contain contributions from higher (five-particle, six-particle, etc.) many-particle forces. They could be taken into account by increasing the number of terms in the power series expansion

$$U_m(r) = \sum_{n=2}^{\infty} a_n \rho^n(r) \tag{2}$$

for the static field [1] ($\rho(r)$ is the nucleon density distribution), thus introducing an indeterminate number of additional adjustable parameters. Instead, we use the fact that ultimately the underlying reason for many-particle forces is the nonlinearity of strong interaction. We introduce an auxiliary scalar–isoscalar field ϕ with the Lagrangian density

$$L = \frac{1}{2}\partial_\mu \phi \partial^\mu \phi - U(\phi) - g\bar{\psi}\psi\phi, \tag{3}$$

*This article was submitted by the authors in English.

**e-mail: birbrair@thd.pnpi.spb.ru

$$U(\phi) = \frac{1}{2}\Lambda^2\phi^2 + \frac{1}{3}\lambda_3\phi^3 + \frac{1}{4}\lambda_4\phi^4, \qquad (4)$$

thus obeying the following equation:

$$\Lambda^2\phi + \lambda_3\phi^2 + \lambda_4\phi^3 = -g\rho_s + \Delta\phi, \qquad (5)$$

where $\rho_s(r) = \langle A_0|\bar{\psi}(r)\psi(r)|A_0\rangle$ is the nuclear scalar density ($\langle A_0|$ is the ground state of nucleus A). As discussed in [1], the many-particle forces of all ranks are taken into account in this way.

The field ϕ contains the "two-particle" component ϕ_2 obeying the equation

$$\Lambda^2\phi_2 = -g\rho_s + \Delta\phi_2. \qquad (6)$$

This component must be eliminated because the two-particle contribution to the static field is determined by the free-space two-particle forces [8, 9]. So, the many-particle contribution to the scalar–isoscalar field is

$$W(r) = g(\phi(r) - \phi_2(r)). \qquad (7)$$

Let us analyze this expression disregarding for a moment the Laplace terms of (5) and (6) which are responsible for the finite range of the forces, although these terms are included in the actual calculations. But as demonstrated in [13], they are of little importance, thus not affecting the results of the below analysis. As demonstrated in [1], the radial dependence of $W(r)$ has the form which is schematically shown in the figure. As seen from the figure, it is negative at $r < r_1$, positive at $r > r_1$ with a maximum W_m in this region, and vanishing at $r = r_1$. Without the Laplace terms,

$$W(r) = -\frac{g\lambda_4}{\Lambda^2}\phi^2(r)\left(\frac{\lambda_3}{\lambda_4} + \phi(r)\right). \qquad (8)$$

So,

$$\phi(r_1) = -\frac{\lambda_3}{\lambda_4}. \qquad (9)$$

But as follows from (6) and (7),

$$\phi(r_1) = -\frac{g}{\Lambda^2}\rho_s(r_1), \qquad (10)$$

and therefore

$$\frac{\lambda_3}{\lambda_4} = \frac{g\rho_1}{\Lambda^2}, \qquad (11)$$

where $\rho_1 = \rho_s(r_1)$. Let us introduce the dimensionless quantities $y(r)$ and $y_2(r)$,

$$\phi(r) = -\frac{g}{\Lambda^2}\rho_1 y(r), \quad \phi_2(r) = -\frac{g}{\Lambda^2}\rho_1 y_2(r). \qquad (12)$$

In these units,

$$W(r) = -\frac{g^4\rho_1^3}{\Lambda^8}y^2(r)(1 - y(r))\lambda_4. \qquad (13)$$

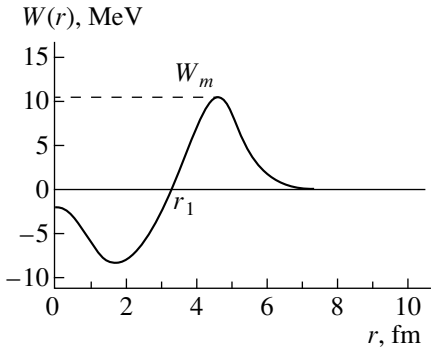

Many-particle contribution to the static field.

The maximum W_m occurs at $y = 2/3$, so

$$\lambda_4 = -\frac{27\Lambda^8 W_m}{4g^4\rho_1^3}, \qquad \lambda_3 = -\frac{27\Lambda^6 W_m}{4g^3\rho_1^2}. \qquad (14)$$

The parameter λ_4 is negative since $W_m > 0$ (see figure). The parameter λ_3 is negative too, provided the coupling constant g is positive. Actually, the sign of g is insignificant since the physical field is $g\phi$, thus being expressed through g^2.

The potential energy of the scalar field is also of the form (4) within the relativistic mean-field approach (RMF) [14, 15], the parameters λ_3 and λ_4 being negative too. In this way, the sign of the RMF parameters is confirmed. It should be mentioned that the values of the RMF parameters are determined from the experimental data which include the important correlation effects (binding energies, density distributions, low-energy spectra, etc.), and therefore they are model-dependent (the model-independent treatment of the correlations does not exist). In contrast, our parameters are determined from the doorway state energies, thus being model-independent.

In terms of the y and y_2 quantities, the contribution to the scalar–isoscalar field from the many-particle forces is

$$W(r) = -\frac{9xW_m}{4}(y(r) - y_2(r)) + \frac{1}{2}\beta\left(\rho_s^-(r)\right)^2, \qquad (15)$$

$$x = \frac{4g^2\rho_1}{9\Lambda^2 W_m}, \quad \rho_s^-(r) = \rho_{sn}(r) - \rho_{sp}(r), \qquad (16)$$

where ρ_{sn} and ρ_{sp} are neutron and proton scalar densities, respectively. The second term on the right-hand side of (15) arises from the symmetry energy. The quantities $y(r)$ and $y_2(r)$ obey the equations

$$y(r) + \frac{3}{x}y^2(r)(1 - y(r)) = \frac{\rho_s(r)}{\rho_1} + \frac{1}{\Lambda^2}\Delta y(r), \qquad (17)$$

$$y_2(r) = \frac{\rho_s(r)}{\rho_1} + \frac{1}{\Lambda^2}\Delta y_2(r). \qquad (18)$$

The details of calculations will be described in a forthcoming publication. The resulting values of the parameters are found to be

$$\rho_1 = 0.146 \text{ fm}^{-3}, \quad W_m = 11.393 \text{ MeV}, \qquad (19)$$
$$x = 16.004, \quad \Lambda = 986.64 \text{ MeV}, \quad \beta = 5.583 \text{ fm}^5.$$

The NDA prescription [10, 11] for the scalar field potential energy is [16]

$$U(\phi) = f_\pi^2\Lambda^2 \sum_{n=2}^{\infty} \frac{\kappa_n}{n!}\left(\frac{\phi}{f_\pi}\right)^n, \qquad (20)$$

where $f_\pi = 93$ MeV. According to the concept of naturalness, all the coefficients κ_n must be of the order of unity. Comparison between (20) and (4) together with (14) and (16) gives

$$\kappa_2 = 1, \quad \kappa_3 = \frac{2f_\pi}{\Lambda^2}\lambda_3 = -4\Lambda\frac{f_\pi}{x\rho_1}\left(\frac{\rho_1}{xW_m}\right)^{1/2}, \qquad (21)$$
$$\kappa_4 = \frac{6f_\pi^2}{\Lambda^2}\lambda_4 = -8\Lambda^2\frac{f_\pi^2}{x^2\rho_1 W_m}.$$

As follows from the values (19) of the parameters $\kappa_3 = -1.6$ and $\kappa_4 = -20.5$, the concept of naturalness thus not being confirmed.

As demonstrated by the calculations for the few-nucleon systems, the effect of many-particle forces is relatively small [12]. This result is confirmed, but the underlying physical reason is different from that provided by the effective field theory. According to the latter, the strength of the forces decreases with increasing rank of the interaction [see Eq. (1)]. As follows from above, this scenario does not hold: the actual reason is the cancellation of the contributions from many-particle forces of different ranks (the physics is believed to be the same for complex nuclei and few-nucleon systems).

REFERENCES

1. B. L. Birbrair and V. I. Ryazanov, Yad. Fiz. **63**, 1842 (2000) [Phys. At. Nucl. **63**, 1753 (2000)].
2. H. de Vries *et al.*, At. Data Nucl. Data Tables **36**, 495 (1987).
3. G. D. Alkhazov *et al.*, Nucl. Phys. A **381**, 430 (1982).
4. J. D. Walecka, Ann. Phys. (N. Y.) **83**, 491 (1974).
5. B. D. Serot and J. D. Walecka, Int. J. Mod. Phys. **6**, 515 (1977).
6. R. J. Furnstahl and B. D. Serot, nucl-th/9911019.
7. K. Erkelenz, Phys. Rep. **13**, 191 (1974).
8. R. Machleidt, K. Holinde, and Ch. Elster, Phys. Rep. **149**, 1 (1987).
9. L. Jäde and H. V. von Geramb, Phys. Rev. C **57**, 496 (1998).
10. A. Manohar and H. Georgi, Nucl. Phys. B **234**, 189 (1984).
11. H. Georgi, Phys. Lett. B **298**, 187 (1993).
12. J. L. Friar, nucl-th/0005076.
13. B. L. Birbrair and V. I. Ryazanov, Yad. Fiz. **64**, 471 (2001) [Phys. At. Nucl. **64**, 416 (2001)].
14. P. G. Reinhard *et al.*, Z. Phys. A **323**, 13 (1986).
15. G. A. Lalazissis, J. König, and P. Ring, Phys. Rev. C **55**, 540 (1997).
16. R. J. Furnstahl, B. D. Serot, and H. B. Tang, Nucl. Phys. A **618**, 446 (1997).

Physics of Atomic Nuclei, Vol. 65, No. 8, 2002, pp. 1459–1473. Translated from Yadernaya Fizika, Vol. 65, No. 8, 2002, pp. 1494–1509.

NUCLEI
Theory

Comparative Analysis of the Mechanisms of Fast-Light-Particle Formation in Nucleus–Nucleus Collisions at Low and Intermediate Energies

A. S. Denikin and V. I. Zagrebaev

Joint Institute for Nuclear Research, Dubna, Moscow oblast, 141980 Russia

Received February 5, 2001; in final form, May 25, 2001

Abstract—The dynamics and the mechanisms of preequilibrium-light-particle formation in nucleus–nucleus collisions at low and intermediate energies are studied on the basis of a classical four-body model. The angular and energy distributions of light particles from such processes are calculated. It is found that, at energies below 50 MeV per nucleon, the hardest section of the energy spectrum is formed owing to the acceleration of light particles from the target by the mean field of the projectile nucleus. Good agreement with available experimental data is obtained. © *2002 MAIK "Nauka/Interperiodica".*

1. INTRODUCTION

The formation of preequilibrium light particles (n, p, d, t, α) in nucleus–nucleus collisions is determined by the evolution that the nuclear system involved in the reaction being considered undergoes at the initial reaction stage. It is well known that the cross section for light-particle yield from heavy-ion collisions constitutes a significant part of the total reaction cross section even at low energies of about 10 MeV per nucleon; that is, the formation of light particles is peculiar to all nuclear reactions featuring heavy ions. This implies that investigation of the mechanism of formation of such particles may furnish direct information both about the dynamics of the initial stage of the reaction and about the potential and dissipative forces of nucleus–nucleus interaction. Basic regularities in the behavior of the angular and energy distributions of light particles—in particular, the presence of high-energy components in them—cannot be described within the usual statistical model of excited-nucleus decay [1–16]. A large number of theoretical approaches considering various mechanisms of fast-light-particle formation have been proposed in recent years. These include the moving-source model [3], the hot-spot model [17], the model of disintegration and incomplete fusion [18–21], the model of dissipative disintegration accompanied by the massive-transfer process [22, 23], and the fermion-jet model and models close to it in spirit [24–29]. A detailed survey of experimental and theoretical studies devoted to this problem can be found in [30].

In view of a considerable improvement of the technical characteristics of measuring equipment, it became possible to measure precisely the angular and energy spectra of light particles. The most recent experiments discovered preequilibrium light particles whose velocities are more than twice as great as the velocity of beam particles [11–14]. This sparked anew the interest of researchers in the problem and reinforced motivations behind the hypothesis that nucleon–nucleon collisions play a dominant role in the formation of ultrafast light particles.

In the present study, the role of nucleon–nucleon collisions and of mean nuclear fields in the formation of the spectra of preequilibrium light particles is investigated in detail on the basis of the four-dimensional classical model of nucleus–nucleus collisions. Among other things, it is shown that the effect of mean nuclear fields is crucial at beam energies in the region $E_0 < 50$ MeV per nucleon. The ensuing exposition is organized as follows. In Section 2, we give an account of the model that underlies the present analysis of the methods used here to calculate the differential cross sections for light particles formed in nucleus–nucleus collisions and the multiplicities of these particles. In Section 3, we consider various mechanisms of preequilibrium-light-particle formation that are realized in the model developed here. In Section 4, the results of our calculations for the above cross sections are compared with experimental data. In Section 5, we investigate the dependence of our results on physical model parameters, such as potentials of fragment interaction and forces of nuclear friction. In the last section, we formulate basic conclusions that can be drawn from our study.

1063-7788/02/6508-1459$22.00

2. FOUR-BODY MODEL OF NUCLEUS–NUCLEUS COLLISIONS

In studying the mechanisms of light-particle formation in nucleus–nucleus collisions, we rely here on a semiclassical four-body model that makes it possible to establish explicitly the role of mean nuclear fields and the role of nucleon–nucleon collisions. Within this model, the projectile (P) and the target (T) nucleus are taken in the form of two-particle subsystems; that is, $P = (A + a)$ and $T = (B + b)$, where A and B stand for heavy nuclear cores, while a and b represent light fragments (n, p, d, t, α).

Introducing six pair interaction potentials $V(r_{ij})$ (where the subscripts i and j correspond to particles A, B, a, and b and where $r_{ij} = |\mathbf{r}_i - \mathbf{r}_j|$ is the distance between particles i and j), we specify the Hamiltonian for the system being considered as

$$H = \sum_i \frac{\mathbf{p}_i^2}{2m_i} + \sum_{ij, i\neq j} V(r_{ij}). \qquad (1)$$

The potentials taken to represent the heavy-core interaction with light particles are chosen here in the Woods–Saxon form with the parameters corresponding to optical potentials constructed on the basis of an analysis of elastic-scattering data [31]. The interaction between cores A and B is chosen in the form of the Coulomb potential energy and the nuclear interaction simulated by either the proximity potential from [32] or the Woods–Saxon potential. Coupling to reaction channels that are not taken explicitly into account within the four-body model was described in terms of dissipative forces introduced with the aid of the corresponding dissipative function D. In order to solve numerically the set of equations of motion

$$\frac{d\mathbf{r}_i}{dt} = \frac{\partial H}{\partial \mathbf{p}_i}; \quad \frac{d\mathbf{p}_i}{dt} = -\frac{\partial H}{\partial \mathbf{r}_i} - \frac{\partial D}{\partial \boldsymbol{\nu}_i}, \qquad (2)$$

where $\mathbf{p}_i$ and $\boldsymbol{\nu}_i$ are the vectors of, respectively, the momentum and the velocity of particle i, it is necessary to preset boundary conditions for the vectors $\mathbf{r}_i$ and $\mathbf{p}_i$. The internal spatial configuration of the projectile nucleus is completely determined by the vector $\mathbf{r}_{Aa}$ of the relative distance between the projectile fragments, the energy E_{Aa} of their relative motion (that is, the projectile binding energy), and the vector $\mathbf{l}_{Aa}$ of the orbital angular momentum associated with the relative motion of these particles. The components of the vector $\mathbf{r}_{Aa}(t = 0)$ are chosen via their generation at random on the basis of some spatial-distribution function. Our calculations revealed that the form of the radial dependence of this distribution affects only slightly the final result. This is explained by the specificity of the classical model, where, as the time of approach of the nuclei involved increases, any initial distribution tends to a purely classical distribution, in which case the particle resides for a longer time in the vicinity of the external turning point. At the same time, a decrease in the time of approach entails an increase in the computational error. In the case being considered, the relative position of particles A and a was chosen to be equiprobable in the energetically allowed region of space. In order to determine the relative momentum $\mathbf{p}_{Aa}$ unambiguously, it is necessary to fix, in addition to the relative energy E_{Aa}, the distance $|\mathbf{r}_{Aa}|$ between the fragments, and the orbital angular momentum $|\mathbf{l}_{Aa}|$, one of the components of the vector $\mathbf{l}_{Aa}$ as well (this is also done via a generation at random). Applying the same procedure to the target nucleus and specifying the relative motion of the centers of mass of the target and the projectile nucleus in accordance with a given reaction, we fully define boundary conditions that are necessary for solving the set of Eqs. (2).

The function D in Eqs. (2) is an ordinary Rayleigh dissipative function that describes the dissipation of energy and of the angular momentum of the relative motion of the nuclei involved. In the case where fragments a and b are much lighter than cores A and B, it is assumed that the friction forces act only between the cores. In terms of spherical coordinates, the Rayleigh function then has the diagonal form

$$D = \frac{1}{2} f(r) \left(\gamma_r \dot{r}^2 + \gamma_\theta r^2 \dot{\theta}^2 + \gamma_\varphi r^2 \sin^2\theta \dot{\varphi}^2 \right), \quad \gamma_t = \gamma_\theta = \gamma_\varphi, \qquad (3)$$

where γ_r and γ_t are, respectively, the radial and the tangential coefficient of friction; $f(r)$ is the radial form factor for dissipative forces; and $\mathbf{r} = \mathbf{r}_A - \mathbf{r}_B \equiv \{r, \theta, \varphi\}$ is the vector of the relative motion of particles A and B. In choosing the coefficients γ_r and γ_t and the form factor $f(r)$, we followed [33].

Thus, we have a set of 24 coupled classical differential equations of motion [set of Eqs. (2)]; we construct here its numerical solutions directly in the laboratory frame using Cartesian coordinates. By performing a numerical integration of Eqs. (2) with respect to time for different initial conditions, we arrive at various output channels. It can easily be shown that, within the four-body model used, there are 15 output reaction channels. These are scattering channels, channels involving the breakup of the projectile or the target (or both), particle-transfer channels, and

channels of complete and incomplete fusion:

$$P+T\equiv(Aa)+(Bb)\to\begin{cases}(Aa)+(Bb),\\ A+a+B+b,\\ \ldots\\ (Ab)+(Ba),\\ (Aab)+B,\\ \ldots\\ (ABb)+a,\\ (AaBb).\end{cases}\qquad(4)$$

Here, parentheses enclose bound states of two or more fragments.

In describing the relative motion of particles $(a+B)$ and $(b+\mathrm{A})$, the differential cross sections for various channels can be estimated more correctly in terms of the probability of their absorption. We define this probability P_{ij}^{abs} as

$$P_{ij}^{\mathrm{abs}}=1-\exp\left(-\frac{s_{ij}}{\lambda_{ij}}\right)\qquad(5)$$
$$\equiv 1-\exp\left(-\int\limits_{\mathrm{tr}}\frac{2W_{ij}(r')dr'}{\hbar\nu_{ij}(r')}\right),$$

where s_{ij} is the distance that particle i travels in nucleus j, λ_{ij} is the corresponding mean range, $W_{ij}(r)$ is the imaginary part of the optical potential (it describes absorption in the case of the elastic scattering of particle i by nucleus j), and ν_{ij} is their relative velocity. Integration in (5) is performed along the actual trajectory of the fragments.

In classical dynamics, the relative energy of two particles in a bound state can take any admissible value—in particular, collapse onto the potential-well bottom is possible. In studying the formation of bound states of two or more particles in output channels, it is therefore necessary to check additionally their relative energy in order to eliminate unphysical events where the energy of the fragments is below the experimental energy of their bound state.

For any reaction channel in (4), the differential cross section is calculated by the formula

$$\frac{d^2\sigma_\mu}{dEd\Omega}(E,\theta)\qquad(6)$$
$$=\int\limits_0^\infty 2\pi\rho d\rho\left[\frac{\Delta N_\mu(\rho,E,\theta)}{N_{\mathrm{tot}}(\rho)}\frac{1-P_\mu(\rho)}{2\pi\sin\theta\Delta\theta\Delta E}\right],$$

where $\Delta N_\mu(\rho,E,\theta)$ is the number of events in which the system goes over into the channel μ at a given value of the impact parameter ρ, $N_{\mathrm{tot}}(\rho)$ is the total number of simulated events for a given value of ρ, and $P_\mu(\rho)$ is the probability of absorption in this channel. The bracketed factor in the integrand on the right-hand side of (6) is the partial differential multiplicity for the event type being considered. Upon individually integrating this factor with respect to the impact parameter, we would obtain the differential multiplicity, which is a quantity often measured in experiments instead of the corresponding cross section.

The main contribution to the soft section of the energy spectrum of light particles comes from the evaporation of particles from excited reaction products. As a rule, the multiplicity of evaporated light particles considerably exceeds the multiplicity of preequilibrium particles in this energy range. In the proposed model, evaporation processes are taken into account in the following way. The introduction of phenomenological forces of friction in the equations of motion (2) leads to a dissipation of part of the kinetic energy, whereby it is converted into the excitation energy of heavy fragments. Since the problem of how the excitation energy is shared among colliding nuclei has not yet been solved conclusively, we describe here the evaporation section of the spectrum, assuming that the total excitation energy is shared among colliding nuclei according to the simplest mechanism of equality of their temperatures, in which case the excitation energy is shared in proportion to the masses of the colliding nuclei. In the source rest frame, evaporated particles have a Maxwell distribution with respect to energy and an isotropic angular distribution. In the laboratory frame, the energy distribution of light fragments evaporated from the ith source has the form

$$f_i(\rho,E,\theta,\varphi)=\frac{1}{2(\pi T_i(\rho))^{3/2}}\sqrt{E-V_{\mathrm{C}}}\qquad(7)$$
$$\times\exp\Big(-(E-V_{\mathrm{C}}+\varepsilon_i(\rho)$$
$$-2\sqrt{(E-V_{\mathrm{C}})\varepsilon_i(\rho)}\cos\theta')/T_i(\rho)\Big).$$

Here, E is the laboratory energy of the light particle; V_{C} is the height of the Coulomb barrier for this particle in escaping from a heavy fragment; $\varepsilon_i(\rho)=m\nu_i^2(\rho)/2$, where m is the mass of the emitted light particle and ν_i is the laboratory velocity of the ith emitted fragment; $T_i(\rho)=\sqrt{E_i^*(\rho)/a_i}$ is its temperature, where $E^*(\rho)$ is the fragment excitation energy; a_i is the level-density parameter in the corresponding nucleus; and $\cos\theta'=\sin\theta\sin\theta_i(\cos\varphi\cos\varphi_i+\sin\varphi\sin\varphi_i)+\cos\theta\cos\theta_i$, with $(\theta_i,\ \varphi_i)$ and $(\theta,\ \varphi)$ being the spherical angles of emission of, respectively, the ith hot fragment and the evaporated particle in the laboratory fragment. The quantities ε_i and T_i, as well as the angles θ_i and φ_i, are functions of the impact parameter ρ and are calculated by performing averaging over the total number of events at given ρ

that have resulted in the formation of the ith fragment. The averaging of the function $f_i(\rho, E, \theta, \varphi, \theta_i, \varphi_i)$ over the azimuthal angle φ_i can be performed analytically, whereupon the dependence on the light-particle emission angle φ also disappears. In general, averaging over the polar angle θ_i of the heavy fragment can be performed only numerically.

Within the model used here, three types of evaporated fragments can be formed. These are a projectile-like fragment (PLF), a targetlike fragment (TLF), and a compound nucleus (CN). In general, we therefore obtain three evaporation components of the energy spectrum of light particles. Within the model proposed here, the double-differential cross section for the formation of evaporated light particles is calculated by the formula

$$\frac{d^2\sigma^{\mathrm{EV}}}{dEd\Omega}(E,\theta) = \int_0^{\rho_{\max}} 2\pi\rho d\rho [P_{\mathrm{CN}}(\rho)C_{\mathrm{CN}}f_{\mathrm{CN}} \quad (8)$$
$$+ (1 - P_{\mathrm{CN}}(\rho))(C_{\mathrm{PLF}}f_{\mathrm{PLF}} + C_{\mathrm{TLF}}f_{\mathrm{TLF}})],$$

where $P_{\mathrm{CN}}(\rho)$ is the probability of the formation of a compound nucleus in a collision occurring at an impact parameter ρ and C_i are constant normalization factors. These factors were introduced in order to normalize correctly the evaporation spectrum to experimental data; as a matter of fact, they are proportional to the measured value of the multiplicity of evaporated particles. The experimental normalization of the evaporation section of the spectrum of light particles makes it possible to single out their relative contribution to the total cross section, whereupon we can focus on preequilibrium light particles, which are the subject of our main interest.

3. MECHANISMS OF PREEQUILIBRIUM-LIGHT-PARTICLE FORMATION

Within the proposed model, there are eight reaction channels contributing to the total cross for the formation of preequilibrium light particles. These are

$$(Aa) + (Bb) \to \begin{cases} A + B + a + b \\ (Bb) + A + a \\ (Aa) + B + b \end{cases} \text{complete and incomplete breakup,}$$
$$\begin{cases} (Ab) + B + a \\ (Ba) + A + b \end{cases} \text{break–transfer process,} \quad (9)$$
$$\begin{cases} (AB) + a + b \\ (ABa) + b \\ (ABb) + a \end{cases} \text{incomplete fusion.}$$

Our calculations revealed that, even at beam energies of about 30 MeV per nucleon, the main contribution to the cross section for light-particle formation comes from the breakup and breakup–transfer channels. Channels featuring a bound state of the heavy cores (ABx) contribute significantly only at low energies ($E_0 \leq 20$ MeV per nucleon).

From the scheme given by (9), it can be seen that the set of preequilibrium light particles can be broken down into two subsets including particles emitted from the projectile (particle a) and particles emitted from the target (particle b). Thus, three evaporation components of the energy spectrum of light particles are supplemented with two components of preequilibrium light particles. In just the same way as in the case of the evaporation spectra of light particles, it is necessary to introduce constant normalization factors for the preequilibrium target and the preequilibrium projectile component, since, in the four-body model used here, the multiplicity is always less than or equal to two. The values of these factors were chosen in such a way that the calculated cross sections at the tails of the energy distributions would coincide in amplitude with experimental cross sections, since, in this region of the spectrum, only preequilibrium particles contribute.

As a first example, we applied the proposed model to studying the properties of neutrons emitted in $^{20}\mathrm{Ne} + {}^{165}\mathrm{Ho} \to n + X$ reactions at a beam energy of $E_0 = 20$ MeV per nucleon. In this case, the target and the projectile nucleus are both represented as a bound state of a core and a neutron: $^{20}\mathrm{Ne} = {}^{19}\mathrm{Ne} + n$ and $^{165}\mathrm{Ho} = {}^{164}\mathrm{Ho} + n$. The binding energies of these systems were chosen on the basis of experimental data. Figure 1 shows the results of our calculations for the (a) angular and (b) energy distributions of neutrons for the above reactions. Curve *1* corresponds to equilibrium neutrons evaporated from PLF, TLF, and CN fragments of the reactions. Curves *2* and *3* represent the contributions of preequilibrium neu-

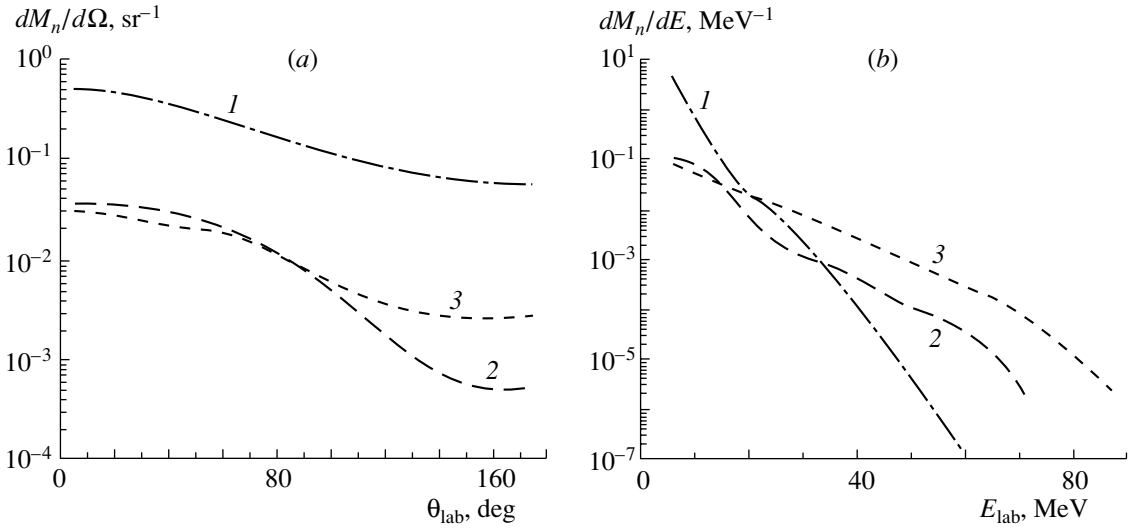

Fig. 1. Differential multiplicity of neutrons produced in ^{20}Ne(20A MeV) + ^{165}Ho $\to n + X$ reactions versus (*a*) the neutron emission angles and (*b*) the neutron energy. Curves *1* represent the total contribution of evaporated neutrons, while curves *2* and *3* depict the contributions of preequilibrium neutrons emitted the projectile and the target, respectively.

trons emitted from the projectile (particle a) and from the target (particle b), respectively.

In plotting the angular distribution displayed in Fig. 1*a*, integration of the differential multiplicity $d^2M_n/(dEd\Omega)$ with respect to energy was performed with the energy spectrum cut off in the low-energy section ($E_n > 5$ MeV). It can be seen that the evaporation component is dominant over the entire angular range, both preequilibrium components being forward directed to a considerable extent.

As can be seen from Fig. 1*b*, it is the preequilibrium components (curves *2* and *3*) that make a dominant contribution to the energy distribution at high neutron energies (at their velocities higher than the velocity of beam particles). That the hardest part of the spectrum corresponds to neutrons emitted from the target nucleus (and not from the projectile nucleus, as has usually been assumed so far) is a remarkable fact, which could not be anticipated from the outset. There is a simple explanation of this phenomenon, which is quite unusual at first glance.

Under the assumption that the core masses are much greater than the neutron mass, we will now calculate the maximum possible values that kinematics allows for the energy of neutrons emitted from the projectile and from the target. In doing this, we disregard the neutron–neutron interaction and the distortion of the trajectories of the heavy fragments A and B. The velocity of the projectile neutron in the laboratory frame (see Fig. 2*a*) is equal to the sum of the beam-particle velocity $\boldsymbol{\nu}_0$ ($E_0 = m_n\nu_0^2/2$) and the velocity of the internal motion of the neutron in the mean field $\boldsymbol{\nu}_n$ of the projectile nucleus (in the case of a square well, we have $m\nu_n^2/2 - U_0 = -E_{\rm sep}$). Thus, the projectile nucleon emitted from a nucleus–nucleus collision has the energy

$$E_n = \left(\frac{m}{2}(\boldsymbol{\nu}_0 + \boldsymbol{\nu}_n)^2 - U_0\right)\Big|_{\nu_n = v_{\rm F},\, \theta_n = 0^\circ} = \frac{m}{2}\left(\nu_0^2 + 2\nu_0\nu_{\rm F}\right) - E_{\rm sep}, \qquad (10)$$

where m is the neutron mass, U_0 is the depth of the mean field V_{Aa}, $E_{\rm sep}$ is the neutron-separation energy, and $\nu_{\rm F}$ is the Fermi velocity of projectile nucleons. If, for example, $\nu_0 \sim \nu_{\rm F}$ and $E_0 \gg E_{\rm sep}$, the maximum energy of the emitted nucleon is $E_n^{\rm max} \sim 3E_0$. This mechanism of fast-light-particle formation was comprehensively investigated in [25, 29].

The mechanism responsible for the formation of high-energy neutrons from the target is more complicated. The main role in this process is played by the potential of the interaction between the projectile nucleus A and the target neutron b. Let us first consider a simplified model where the interaction V_{Ab} is replaced by the interaction of neutron b with an infinitely heavy moving wall. Suppose that b moves at a velocity ν_n toward the core A, which, in turn, has a velocity ν_0 directed oppositely. In their c.m. frame, the neutron velocity is $(\nu_0 + \nu_n)$; after an elastic collision, the neutron acquires the velocity $-(\nu_0 + \nu_n)$, which corresponds to the velocity $\nu_{\rm out} = (2\nu_0 + \nu_n)$ in the laboratory frame. Under the condition that the internal-motion velocity of the target neutron, ν_n, is equal to the Fermi velocity $\nu_{\rm F}$, its asymptotic energy is

$$E_n|_{\nu_n = \nu_{\rm F}, \theta_n = 0^\circ} = \frac{m}{2}\left(2\nu_0 + \nu_{\rm F}\right)^2 - U_0 \qquad (11)$$

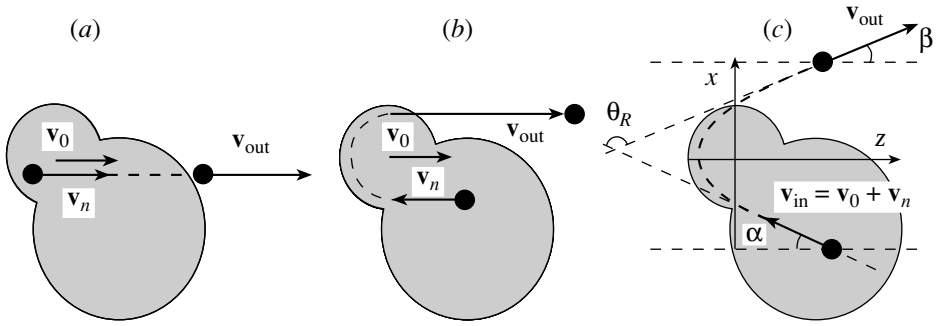

Fig. 2. Schematic representation of preequilibrium-nucleon formation in a nucleus–nucleus collision: (*a*) emission of a nucleon from the projectile, (*b*) acceleration of a nucleon under the conditions of orbiting in the projectile field (this is equivalent to scattering on a moving reflecting wall), and (*c*) general case of nucleon emission from the target in projectile rest frame (for the notation, see main body of the text).

$$= 2m\left(\nu_0^2 + \nu_0\nu_{\text{F}}\right) - E_{\text{sep}},$$

where U_0 is the depth of the mean field V_{Bb} and E_{sep} is the energy of target-neutron separation. At $\nu_0 \sim \nu_{\text{F}}$ and $E_0 \gg E_{\text{sep}}$, the maximum energy is thus $E_n^{\max} \sim 8E_0$, which is 2.5 times as great as the corresponding limit for neutrons emitted from the projectile.

The elastic scattering of neutrons at an angle of $\theta_{\text{c.m.}} = -180°$ in the attractive mean field of the projectile nucleus is kinematically equivalent to their reflection from a repulsive wall (see Fig. 2*b*). The scattering of neutrons at such large angles ($\theta_{\text{c.m.}} \leq -180°$), which is actually an orbiting process, is possible only at comparatively low neutron energies. At c.m. energies of $E_0 \geq AE_{\text{F}} \approx 40A$ MeV, neutrons can be deflected by the mean field ($U_0 \approx 50$ MeV) by not more than at a limiting negative angle θ_R that is referred to as the rainbow-scattering angle. By virtue of this, the maximum energy of neutrons emitted from the target depends strongly on the projectile energy, on the interaction potential V_{Ab}, on the neutron binding energy in the target, and on the friction forces. Disregarding the effect of neutrons on the motion of heavy fragments, assuming that the neutron acquires the maximum energy upon scattering by the projectile at the angle θ_R in the neutron–projectile c.m. frame (see Fig. 2*c*), and setting the initial neutron velocity in the target to the relevant Fermi velocity, we can estimate the asymptotic neutron energy (at $\nu_n = \nu_{\text{F}}$) as

$$E_n = m\Big(\nu_0^2 + \nu_0\nu_{\text{F}}\cos\alpha + \nu_0\cos\beta\sqrt{\nu_0^2 + \nu_{\text{F}}^2 + 2\nu_0\nu_{\text{F}}\cos\alpha}\Big) - E_{\text{sep}}, \quad (12)$$

where α is the angle at which the neutron is incident on the target in the reference frame comoving with the target and β is the emission angle in the same reference frame (see Fig. 2*c*). The two angles are related to each other through the nuclear-rainbow-scattering angle, for which there is the empirical relation [34]

$$\theta_R = \left(V_{\text{C}} - 0.56U_0\sqrt{R_V/a_V}\right)/E_{\text{c.m.}}, \quad (13)$$

where V_{C} is the height of the Coulomb barrier (it is equal to zero for a neutron), while U_0, R_V, and a_V are, respectively, the depth, the range, and the diffuseness of the interaction potential V_{Ab}. It turned out that the empirical formula (13), with the coefficient 0.56, agrees poorly with the exact classical calculation of the angle θ_R for the scattering of light particles (such as a proton or a neutron) on nuclei; therefore, we use here the coefficient 0.7. It can be seen that, at $\alpha = \beta = 0$ (that is, at $\theta_R = -180°$), formula (12) reduces to (11).

The maximum energies of preequilibrium neutrons originating from (solid curves) ^{20}Ne + ^{165}Ho and (dashed curves) ^{165}Ho + ^{165}Ho interactions are displayed in Fig. 3 versus the beam energy E_0. Curves *1* correspond to the results obtained by calculating, on the basis of (10), the maximum energy of neutrons emitted from the projectile; curves *2* represent the energies of neutrons emitted from the target, their values being calculated by formula (12). From Fig. 3, it can be seen that, at energies below 100 MeV per nucleon, the fastest neutrons are emitted from the target and that, upon going over to the heavier projectile, the maximum energy of the emitted neutron becomes higher. This is because the range of the potential V_{Ab} increases, which entails an increase in the absolute value of the rainbow-scattering angle θ_R [see (13)].

Thus, an experimental investigation of reactions where projectiles different in mass are incident on the same target may be one of the tests of validity of conclusions that we have drawn. For nucleons emitted from the target and the projectile to be unambiguously identified, it is necessary that the spectrum of the projectile nucleons change insignificantly upon going from one system to another. In this case, the

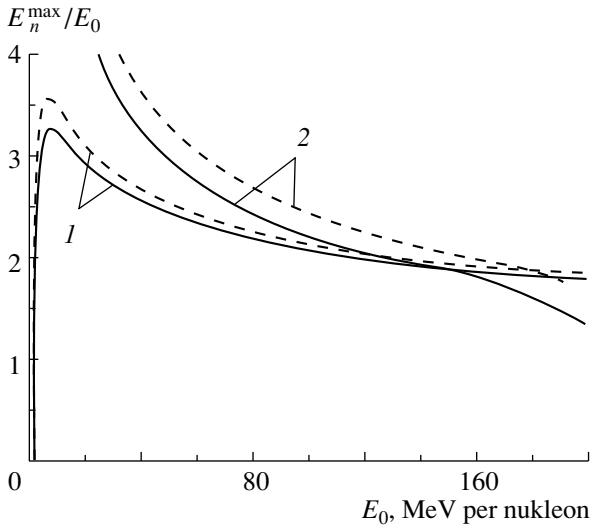

Fig. 3. The maximum energy $E_n^{\max}$ of preequlibrium neutrons as a function of the incident-beam energy E_0 for (solid curves) $^{20}\mathrm{Ne} + {}^{165}\mathrm{Ho} \to n + X$ and (dashed curves) $^{165}\mathrm{Ho} + {}^{165}\mathrm{Ho} \to n + X$ according to the calculations based on formulas (10) and (12). Curves *1* correspond to the maximum energy of neutrons emitted from the projectile, while curves *2* represent the energies of neutrons emitted from the target.

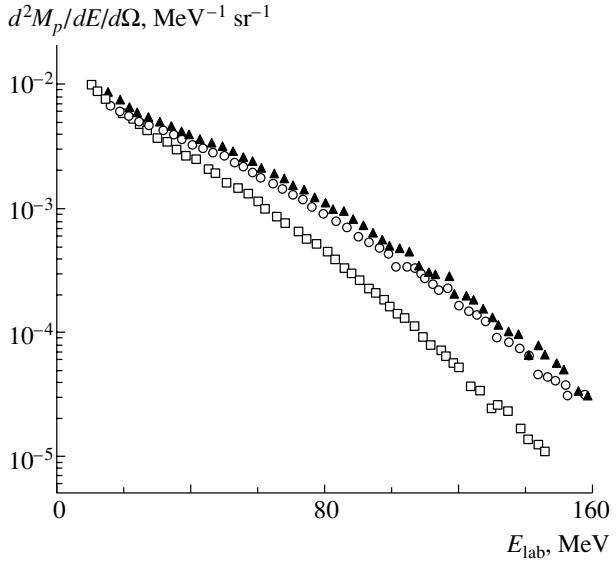

Fig. 4. Measured differential multiplicities of protons emitted at an angle of $\theta_{\mathrm{lab}} = 51^\circ$ in (open boxes) $^{40}\mathrm{Ar} + {}^{51}\mathrm{V} \to p + X$, (open circles) $^{132}\mathrm{Xe} + {}^{51}\mathrm{V} \to p + X$, and (closed triangles) $^{132}\mathrm{Xe} + {}^{197}\mathrm{Au} \to p + X$ interactions at a beam energy of 44 MeV per nucleon [16].

distinction between the distributions of preequilibrium nucleons will be determined completely by the yield of precisely target nucleons. In order to ensure the invariability of the spectra of preequilibrium nucleons emitted from the projectile, it is necessary to select projectile nuclei with similar features (such as the angular momentum of valence nucleons and the energies of their separation).

Figure 4 shows the measured differential multiplicities of protons originating at an angle of $\theta_{\mathrm{lab}} = 51^\circ$ from $^{40}\mathrm{Ar} + {}^{51}\mathrm{V} \to p + X$, $^{132}\mathrm{Xe} + {}^{51}\mathrm{V} \to p + X$, and $^{132}\mathrm{Xe} + {}^{197}\mathrm{Au} \to p + X$ interactions at a beam energy of 44 MeV per nucleon [16]. It can be seen that, upon going over from the projectile nucleus of ^{40}Ar to the heavier species of ^{132}Xe, the slope of the proton spectrum decreases, which corresponds to an increase in the yield of fast light particles. On the contrary, the replacement of the target nucleus causes virtually no changes in the energy distribution of protons. The change in the character of the spectra in response to going over from one projectile-nucleus species to another can hardly be explained by different properties of the projectile species, because the internal structure of the projectile (the height of the Coulomb barrier, the binding energy, shell effects, etc.) does not have a significant effect on the properties of preequilibrium protons at the high beam energies considered here. Moreover, the mechanism of light-particle emission from the projectile nucleus is independent of its mass—only the multiplicity of light particles (that is, the absolute normalization of their spectrum) depends on it. The effect of dissipative forces, which directly depend on the target-nucleus mass, leads to a moderation of protons emitted from the projectile nucleus. It follows that the use of a heavier target nucleus would lead to a decrease in the yield of fast protons (because of the intensification of dissipative processes) if they were formed only via stripping from the target. However, a comparison of the data presented in Fig. 4 for $^{132}\mathrm{Xe}\,(44A\ \mathrm{MeV}) + {}^{51}\mathrm{V}, {}^{197}\mathrm{Au}$ interactions does not reveal any significant change in the proton spectra. Nonetheless, the above mechanism of the acceleration of target nucleons in the mean field of the projectile is very sensitive to the geometric dimensions of the the projectile (that is, to its mass). Thus, we can conclude that the main contribution to the high-energy section of the spectra displayed in Fig. 4 comes precisely from protons emitted from the target and accelerated by the mean field of the projectile. The conclusion that the energy spectrum of protons depends weakly on the choice of target nucleus also follows from the data presented by Jasak *et al.* [10], who studied the target-mass dependence of the yields of various products (including protons) from the reactions induced by $^{40}\mathrm{Ar} + {}^{197}\mathrm{Au}$ and $^{40}\mathrm{Ar} + {}^{40}\mathrm{Ca}$ collisions at an energy of $E_0 = 42$ MeV per nucleon.

Within our model, we will now consider the effect of nucleon–nucleon collisions on the formation of fast light particles. Suppose that, in the laboratory

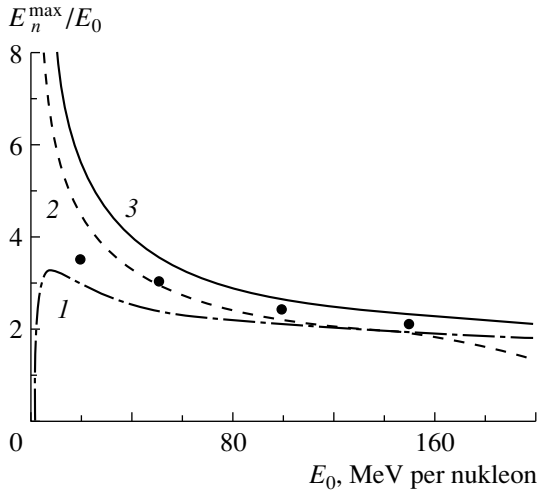

Fig. 5. Maximum energy of preequilibrium neutrons originating from $^{20}\mathrm{Ne} + {}^{165}\mathrm{Ho} \to n + X$ reactions as a function of the beam energy. Curves *1* and *2* represent the data analogous to those depicted by the corresponding curves in Fig. 3. Curve *3* corresponds to the maximum energy acquired by the neutron upon an elastic nucleon–nucleon collision in the mean field of the relevant dinuclear system [according to the calculation by formula (14) not allowing for the Pauli exclusion principle]. The points represent the results obtained with allowance for the Pauli exclusion principle (for details, see main body of the text).

frame, a target nucleon has a velocity $\boldsymbol{\nu}_j$ prior to a collision event; the velocity of a projectile nucleon is equal to the sum of the beam-particle velocity $\boldsymbol{\nu}_0$ and the nucleon velocity $\boldsymbol{\nu}_i$ within the projectile. One of the nucleons can acquire the maximum velocity if, upon the collision event, it carries away the entire amount of the relative-motion energy. In this case the maximum energy of the emitted nucleon is ($i = a, b$)

$$E_i^{\max} = \frac{m}{2}\left(\nu_b^2 + (\nu_0 + \nu_a)^2\right) - \frac{m\nu_i^2}{2} - E_i^{\mathrm{sep}}. \quad (14)$$

From (14), it follows that, if $\nu_0 \sim \nu_i \sim \nu_{\mathrm{F}}$, then $E_i^{\max} \sim 4E_0$. For $^{20}\mathrm{Ne} + {}^{165}\mathrm{Ho} \to n + X$ reactions, Fig. 5 displays the maximum neutron energy as a function of the beam energy according to the calculations based on formulas (curve *1*) (10), (*2*) (12), and (*3*) (14). It can be seen that, over the entire energy range, nucleon–nucleon collisions in this reaction can in principle lead to the formation of yet more energetic light particles in relation to the first two mechanisms considered above.

In actual experiments, the boundaries depicted by the curves in Fig. 5 will be smeared because of the high-energy component of the momentum distributions in the projectile and the target nucleus ($\nu_n > \nu_{\mathrm{F}}$); in the case corresponding to curve *3*, there is also the contribution to this smearing from the Pauli exclusion principle, which forbids nucleons that suffered a collision to occur in states already occupied by other intranuclear nucleons, with the result that the probability of the acceleration of nucleons to the maximum possible degree is considerably suppressed.

Let us introduce a nucleon–nucleon interaction featuring a repulsive core at short distances. Solving the set of Eqs. (2) for initial conditions chosen at random, we can determine numerically the maximum energy acquired by a nucleon upon a nucleon–nucleon collision in the mean field of the relevant dinuclear system. Testing, in the output channels, the binding energy of the recoil nucleon, we can also take into account the Pauli exclusion principle in our calculations. The results of our calculations for $^{20}\mathrm{Ne} + {}^{165}\mathrm{Ho} \to n + X$ reactions versus E_0 are shown in Fig. 5 by points. It can be seen that, at low initial energies ($E_0 \sim 20$ MeV per nucleon), the Pauli exclusion principle has a crucial effect on the formation of fast preequilibrium neutrons in nucleon–nucleon collisions. In this case, the energy of the emitted particles does not exceed $3.5\mathrm{E}_0$. At higher values of the beam energy E_0, the discrepancy between the predictions of formula (14) and the results of the calculation decreases gradually. It should be noted that the maximum energy of neutrons was calculated with allowance for dissipative forces acting between the heavy cores and exerting, as will be shown below, a pronounced effect on the spectra of preequilibrium light particles. The dissipative forces moderate the projectile nucleus; that is, they reduce the velocity ν_0. This leads to an additional decrease in the quantity $E_n^{\max}$ in nucleon–nucleon collisions. With increasing initial energy E_0, the effect of dissipative forces becomes less pronounced, since the valence nucleon does not have time to "experince" the moderating influence of the projectile mean field. Thus, we can conclude that, up to beam energies of $E_0 \sim AE_{\mathrm{F}}$, the role of nucleon–nucleon collisions is less significant than the role of the mean fields. At higher beam energies, the maximum energy acquired by nucleons as the result of nucleon–nucleon collisions becomes greater than the energy of target nucleons accelerated by the projectile mean field.

4. COMPARISON WITH EXPERIMENTAL DATA

In order to verify the qualitative conclusions drawn in the preceding section, we have analyzed the differential cross sections for the yield of neutrons and protons from a few nuclear reactions and performed a comparison with available experimental data.

The double-differential cross sections measured in [15] for the yield of neutrons from $^{36}\mathrm{Ar}(35A\ \mathrm{MeV}) + {}^{107}\mathrm{Ag} \to n + X$ reactions are displayed in Fig. 6*a*, along with the results of the relevant calculations.

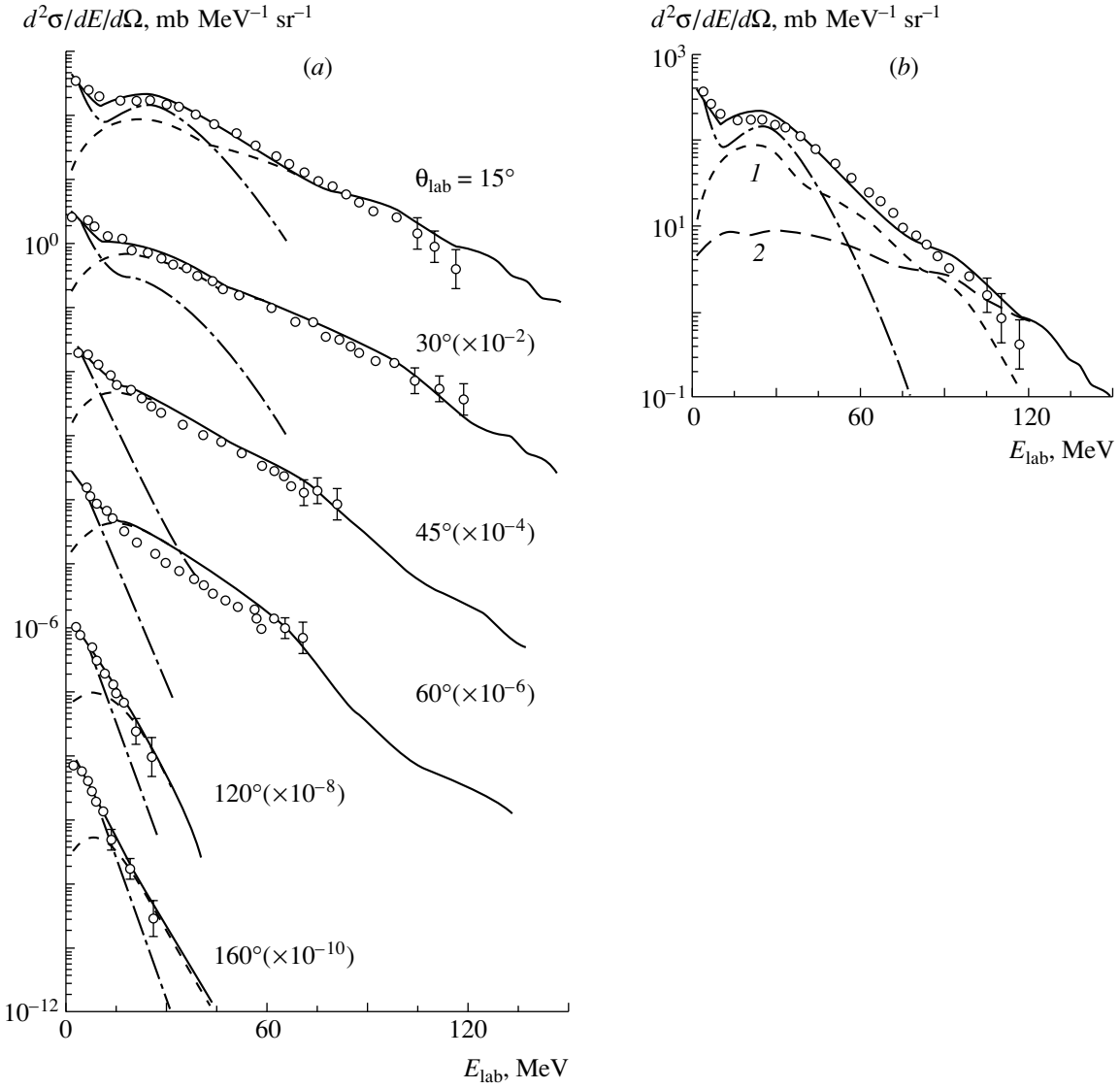

Fig. 6. (*a*) Measured and calculated differential cross sections for neutron formation in ^{36}Ar(35A MeV) + ^{107}Ag → $n + X$ reactions: (points) experimental data from [15], (dash-dotted curves) contribution of evaporated neutrons, (dashed curves) total contribution of preequilibrium neutrons emitted from the projectile and the target, and (solid curves) sum of the evaporation and the preequilibrium component; (*b*) theoretical results for the single angle of $\theta_{lab} = 15°$ that are basically the same as in Fig. 6*a*, except that the contribution to the differential cross section from neutrons emitted (curve *1*) by the projectile and (curve *2*) by the target are shown individually instead of their total contribution.

The dash-dotted, the dashed, and the solid curve represent, respectively, the evaporation component, the preequilibrium component, and their sum. The equilibrium part of the spectrum receives contributions from neutrons evaporated by a targetlike fragment (this is the isotropic low-energy component completely saturating the evaporation spectrum at large angles) and from neutrons evaporated by a projectilelike fragment, the maximum in the distribution corresponding to forward angles and energies close to the beam energy.

Figure 6*b* gives a more detailed pattern for the contribution of preequilibrium neutrons emitted from (curve *1*) the projectile and (curve *2*) the target at an angle of $\theta_{lab} = 15°$. The solid and the dash-dotted curve are identical to their counterparts in Fig. 6*a*. It can be seen that the hardest section of the spectrum is associated with neutrons emitted from the target nucleus. For intermediate values of the emission angle ($\theta_{lab} < 90°$), this trend is conserved; only in the region of large angles are the contributions of the two preequilibrium components approximately equal.

Figure 7*a* displays experimental data from [16] on the differential multiplicity of protons emitted in ^{132}Xe(44A MeV) + ^{197}Au → $p + X$ reactions. In that figure, the solid curves represent the calculated

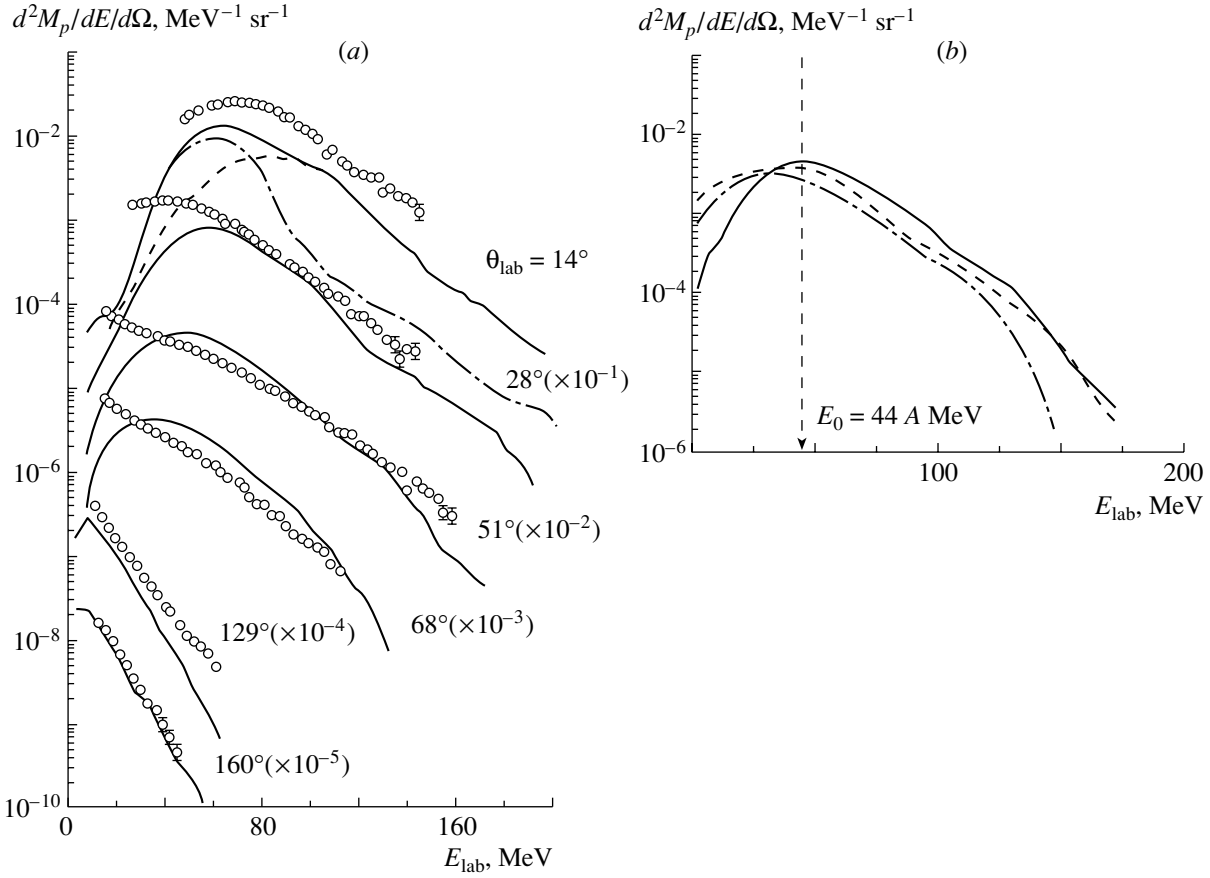

Fig. 7. *a* Comparison of (points) the measured [16] and (solid curves) the calculated differential multiplicity of preequilibrium protons formed in ^{132}Xe (44A MeV) + ^{197}Au $\rightarrow p + X$ reactions. The dashed and the dash-dotted curve represent the contributions of preequilibrium protons emitted at an angle of $\theta_{lab} = 14°$ from the target and the projectile, respectively. The contribution of evaporated protons is not shown. (*b*) Calculated differential multiplicities of protons emitted at an angle of $\theta_{lab} = 51°$ in (solid curve) ^{132}Xe + ^{197}Au $\rightarrow p + X$, (dashed curve) ^{132}Xe + ^{51}V $\rightarrow p + X$, and (dash-dotted curve) ^{40}Ar + ^{51}V $\rightarrow p + X$ reactions at the beam energy of 44 MeV per nucleon.

energy distribution of preequilibrium protons; shown additionally for the emission angle of $\theta_{lab} = 14°$ are the contributions of protons escaping from (dashed curve) the target and (dash-dotted curve) the projectile. The contribution of evaporated protons is not presented. The theoretical results for the proton spectrum at $\theta_{lab} = 14°$ noticeably underestimate the experimental cross section in magnitude, but they reproduce quite well the behavior of experimental data. On the contrary, the theoretical curves in the region of backward angles ($\theta_{lab} = 129°, 160°$) lie somewhat above the experimental data on the differential multiplicity of preequilibrium protons. This is because the evaporation component must be dominant in this region. We can see that, despite the use of quite a simple semiclassical model, the agreement with experimental data is by and large satisfactory.

Figure 7*b* shows the computed energy distributions of preequilibrium protons emitted at an angle of $\theta_{lab} = 51°$ in (solid curve) ^{132}Xe + ^{197}Au $\rightarrow p + X$, (dashed curve) ^{132}Xe + ^{51}V $\rightarrow p + X$, and (dash-dotted curve) ^{40}Ar + ^{51}V $\rightarrow p + X$ reactions at a beam energy of 44 MeV per nucleon. It can be seen that, in the region of high energies, the spectrum of product protons is harder for the heavier projectile of ^{132}Xe than for the lighter projectile of ^{40}Ar owing to particles emitted from the target nucleus. No such effect arises upon replacing the target nucleus by a heavier one. Comparing the curves in Fig. 7*b* with the experimental data in Fig. 4, we can see that the agreement between the results of the theoretical calculations and the experimental data is quite satisfactory.

In Fig. 8*a*, the double-differential cross section measured in [4] for proton formation in ^{16}O(20A MeV) + ^{197}Au $\rightarrow p + X$ reactions is contrasted against the results of the theoretical calculations based on the model employed here. The solid curves correspond to the total contribution of preequilibrium protons emitted from the target and the projectile. The dash-dotted curves represent

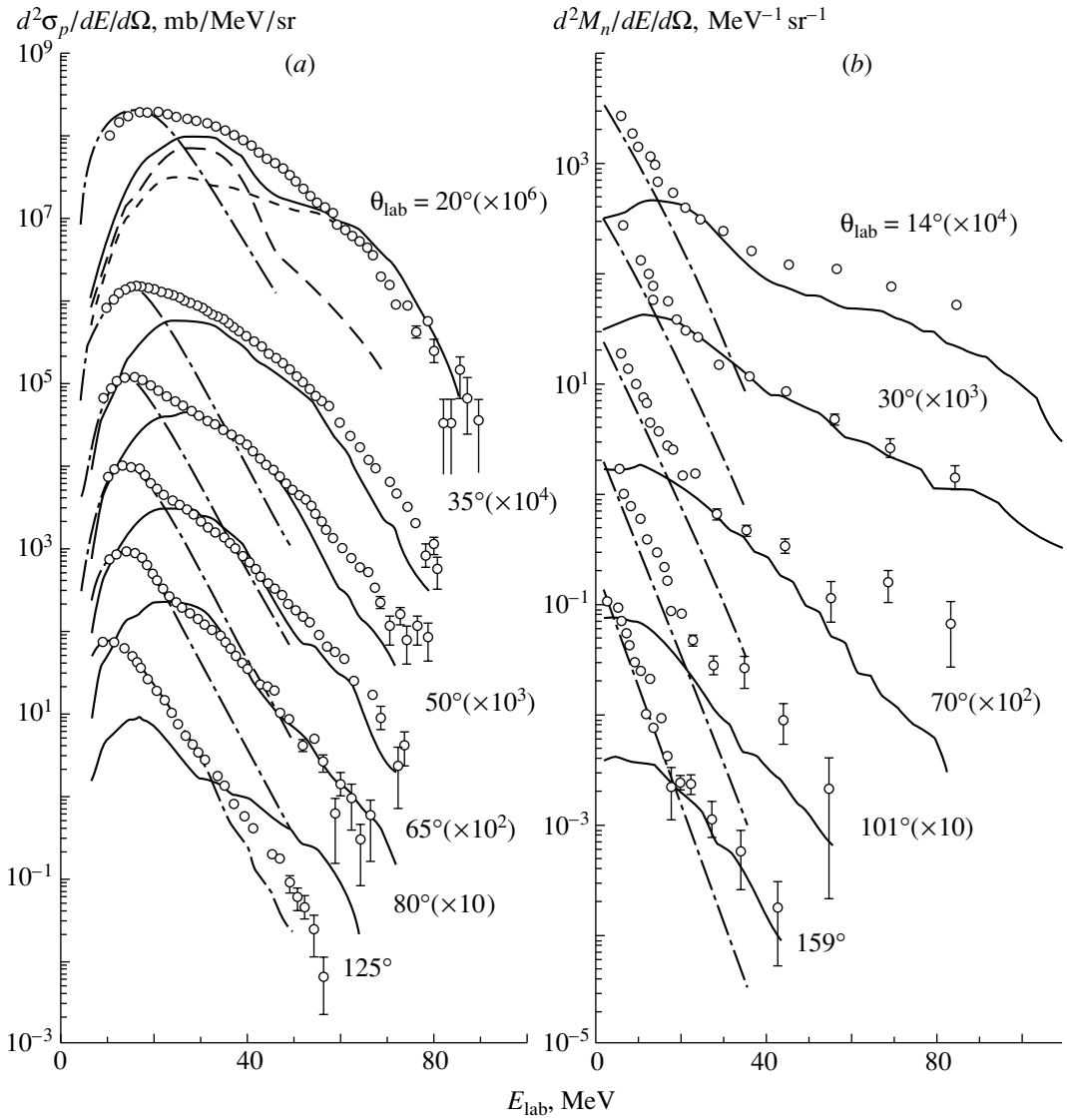

Fig. 8. (*a*) Measured and calculated double-differential cross sections for proton production in $^{16}O(20A\ MeV) + {}^{197}Au \to p + X$ reactions and (*b*) measured and calculated differential multiplicity of neutrons from $^{20}Ne(30A\ MeV) + {}^{165}Ho \to n + ER$ ($\theta_{ER} = 5.6°$) reactions: (solid curves in Figs. 8*a* and 8*b*) computed distributions of preequilibrium protons and neutrons, respectively; (dash-dotted curves) contribution to the distributions from evaporated light particles; and (points) experimental data. In Fig. 8*a*, the contributions of preequilibrium protons emitted from the projectile and from the target at an angle of $\theta_{lab} = 20°$ are shown individually by long and short dashes, respectively.

the contribution of evaporated protons. For protons emitted at an angle of $\theta_{lab} = 20°$, more detailed dependences are shown individually for protons escaping from (long dashes) the projectile and (short dashes) the target. The cross sections calculated for the reactions in question agree well with experimental data at small and intermediate values of the emission angle. As in the preceding case, however, the cross section is overestimated at large values of the proton emission angle.

In [8], the differential multiplicity was measured for neutron formation in coincidence with the evaporation residue in the reaction $^{20}Ne(30A\ MeV) + {}^{165}Ho \to n + ER(\theta_{ER} = 5.6°)$. Within the model used here, we can calculate the differential multiplicity of neutrons in coincidence with the evaporation residue, taking, however, no account of its emission angle θ_{ER}. This limitation is due to the fact that we can only roughly estimate the contribution of evaporation processes to the cross section for the formation light fragments; in doing this, we underestimate the multiplicities of preequilibrium particles, so that we cannot calculate precisely the emission angle for the evaporation residue. In Fig. 8*b*, the multiplicities

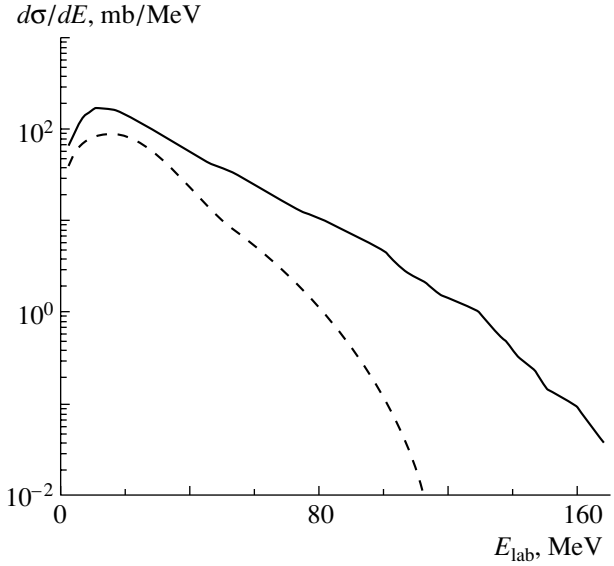

Fig. 9. Differential cross section for preequilibrium neutrons originating from ^{36}Ar(35A MeV) + ^{107}Ag → n + X reactions for impact-parameter values from the intervals (dashed curve) $\rho \in [0, 4]$ fm and (solid curve) $\rho \in [4, 9]$ fm.

calculated in the present study are contrasted against the experimental data from [8]. In that figure, the dash-dotted curve represents the total contribution of evaporated neutrons, while the solid curve corresponds to the total distribution of preequilibrium neutrons. At some values of the emission angle, there is a sizable discrepancy between the results of theoretical calculations and experimental data in the region of high energies. In all probability, this is due to imperfections of the model in dealing with correlation experiments, which require a precise treatment of the statistical decay of an excited nucleus.

By and large, we can state that, despite the simplicity of the proposed model, there is good agreement, in the energy range being considered, between the calculated cross sections for the yield of light particles from nucleus–nucleus collisions and relevant experimental data.

5. DYNAMICS OF LIGHT-PARTICLE FORMATION AND ROLE OF DISSIPATIVE FORCES

In treating the dynamics of nucleus–nucleus collisions on the basis of the semiclassical approach involving two-particle interactions, there remains an ambiguity in choosing the parameters of these interactions. In assessing the parameters of the potentials that simulate the interaction between a light particle and a heavy fragment, we relied here on experimental data obtained by exploring elastic scattering and on the results of their treatment within the optical model [31]. It is well known, however, that the optical model leads to a discrete and a continuous ambiguity in the potential parameters. In the present calculations, these parameters were therefore varied within 10–20% in order to determine the stability of the results of these calculations and conclusions drawn from them. In particular, the potentials V_{Aa} and V_{Bb} (that is, the interaction of a valence nucleon with a nuclear core) chosen in the Woods–Saxon form had the parameters of $U_0 = 50$–60 MeV, $r_0 = 1.15$–1.25 fm, and $a_V = 0.45$–0.6 fm. Variations of these parameters in the above ranges do not have a strong effect on the angular and energy distributions of preequilibrium light particles.

The potentials V_{Ab} and V_{Ba} play a much more significant role. As was shown above, the former is responsible for the acceleration of the target valence nucleon and, as a consequence, for the formation of the spectrum of preequilibrium light particles emitted from the target. The latter determines the angular distribution of light particles emitted by the projectile. The parameters of the potential V_{Ab} specify the rainbow-scattering angle in (13), which sets a kinematical limit on the energy of the emitted light particle b. In the calculations, the parameters of these potentials for various nuclei were taken in the following ranges: $U_0 = 45$–55 MeV, $r_0 = 1.15$–1.25 fm, and $a_V = 0.45$–0.65 fm.

In addition to the real parts of the potentials V_{Ab} and V_{Ba}, we also introduced imaginary parts (see Section 2). It turned out that these imaginary parts, which determine the absolute values of the cross sections, have virtually no effect on other observables, such as the slope of the spectrum and the position of the maximum. In the case being considered, the imaginary parts of the potentials V_{Ab} and V_{Ba} were chosen in the Woods–Saxon form with parameters $W_0 \leq 20$ MeV, $r_0 = 1.2$–1.35 fm, and $a_W = 0.5$–0.8 fm.

The potential V_{AB} simulating the nucleus–nucleus interaction plays a significant role in the formation of light particles at low beam energies of $E_0 < 20$ MeV per nucleon, but it becomes less important as the beam energy increases. The potential V_{AB} determines the trajectories of the projectile, which is responsible for the acceleration of target nucleons. That the projectile moves along trajectories not coinciding with a straight line smears the region of forward angles in the spectrum of the fastest light particles. Such particles are produced in peripheral collisions characterized by impact-parameter values close to that of tangential collision. Figure 9 shows the differential distribution of the cross section with respect to energy for preequilibrium neutrons originating from ^{36}Ar(35A MeV) + ^{107}Ag interactions

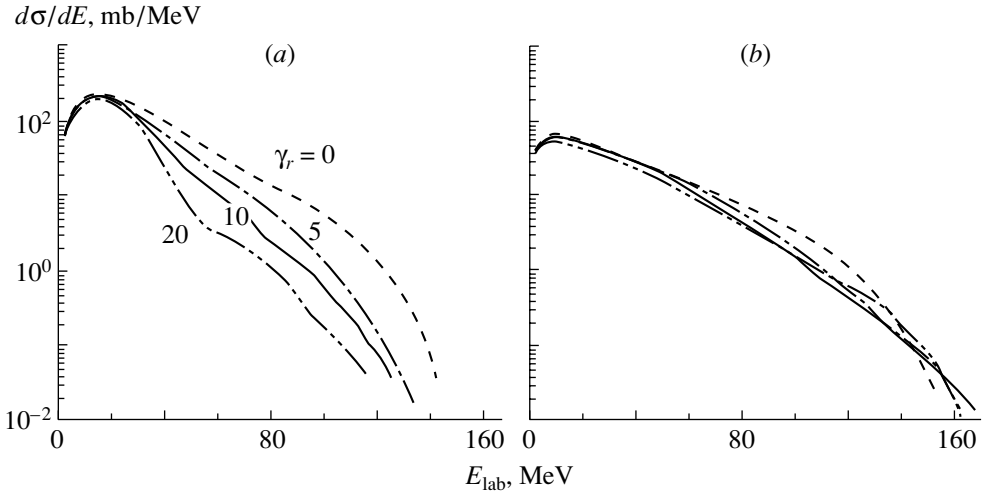

Fig. 10. Differential cross sections calculated for preequilibrium neutrons emitted by (a) the projectile and (b) the target in $^{36}\mathrm{Ar}(35A\ \mathrm{MeV}) + {}^{107}\mathrm{Ag} \to n + X$ reactions. Different curves correspond to different values of the radial coefficient of friction γ_r. The values of this coefficient in 10^{-22} MeV s fm^{-2} units are indicated on each curve in Fig. 10a.

at impact-parameter values from various ranges. The dashed curve represents the results for impact parameters satisfying the condition $\rho < 4$ fm, while the solid curve corresponds to ρ values between 4 and 9 fm. In the case of a tangential collision, the impact parameter is about 8.5 fm. From Fig. 9, it can be seen that the main contribution to the cross section comes from events where the impact parameter is large (solid curve). Therefore, the cross section for the yield of the most energetic light particles from nuclear reactions is governed primarily by the dynamics of peripheral collisions, which in turn depends on the nuclear component of the interaction potential V_{AB}.

As was demonstrated above, the relative velocity of the light particle from the target and the heavy projectile core determines the maximum angle [see Eq. (13)] at which the light particle can be scattered and, hence, the maximum energy of this particle. At beam energies E_0 of about the Fermi energy, the relative velocities are so great that the angle at which the light particle is scattered is small, and so is therefore its energy. On the other hand, it is well known from experiments that, in the hard section of the spectrum, the energy of light particles can be as large as about $4E_0$ to $6E_0$. The inclusion of nuclear friction in the model being considered is a mechanism that could ensure the reduction of the relative velocity in the scattering of the light fragment b on the projectile core A. As was indicated above, we introduce only the forces of friction between the cores of the projectile and the target. The form factor of dissipative forces is not known precisely; therefore, use was made here of a phenomenological form factor of the Fermi type both for the radial and for the tangential component. In [33], it was indicated that, at the same values of the coefficient of friction, a form factor of this type leads to identical friction between two light and two heavy nuclei at equal distances between their surfaces. This means that, in this case, the coefficients of friction must depend on the masses of colliding nuclei; therefore, one cannot expect that there exist universal values of these coefficients for any nuclear system.

For preequilibrium neutrons originating from $^{36}\mathrm{Ar}(35A\ \mathrm{MeV}) + {}^{107}\mathrm{Ag} \to n + X$ reactions, we have calculated the formation cross sections at various values of the radial coefficient of friction. In Fig. 10, the results of these calculations are presented individually for neutrons emitted by (a) the projectile and (b) the target. From Fig. 10a, it can be seen that nuclear friction exerts the strongest effect on the cross section for the yield of projectile neutrons. The dissipation of energy leads to a decrease in the relative velocity ν_0 of the nuclei and, hence, to a reduction of the maximum energy of neutrons emitted by the projectile [see Eq. (10)]. For particles emitted from the target, an increase in the coefficients of friction leads, however, to an increase in their maximum energy (by 10 to 15 MeV in the case being considered) owing to a decrease in the energy of the relative motion of the target neutron and the projectile and, consequently, owing to the growth of the angle of rainbow neutron scattering in the field of the projectile [see Eqs. (12), (13)]. That the form of the energy spectrum of neutrons escaping from the target shows a relatively weak dependence on dissipative nuclear forces is explained predominantly by the peripheral character of processes leading to neutron emission. Needless to say, an indefinite increase in the coefficient of friction would not lead to a steady growth of the maximum energy of neutrons escaping from the target—in other

Parameters of dissipative forces

Reaction	γ_r, 10^{-22} MeV s fm^{-2}	γ_t, 10^{-22} MeV s fm^{-2}	R_{fr}, fm	A_{fr}, fm
^{132}Xe (44A MeV) + ^{197}Au	45	0.4	13.1	0.7
^{20}Ne (30A MeV) + ^{165}Ho	15	0.1	9.4	0.7
^{36}Ar (35A MeV) + ^{107}Ag	10	0.1	9.3	0.7
^{16}O (20A MeV) + ^{197}Au	6	0.05	9.2	0.7

words, there is a maximum in the γ_r dependence of $E_n^{\max}$.

Fixing the initial configurations of the projectile and the target nucleus, the collision energy E_0, and the impact parameter ρ, we can single out, from the entire set of events, the following two subsets: one comprising events where the light particle is emitted from the projectile and the other comprising events where the light particle is emitted from the target. The initial parameters can be chosen in such a way that the process of light-particle formation in each of these subsets would be affected predominantly by any mechanism of those that were described in Section 3. By varying the parameters of nuclear friction for each of these event types, one can investigate their effect on collision dynamics and on the properties of the emitted light particle—that is, on its energy and emission angle. Such an analysis was performed in this study for preequilibrium neutrons originating from ^{36}Ar(35A MeV) + ^{107}Ag interaction. As was anticipated, the asymptotic energy of target neutrons accelerated by the mean field of the projectile nucleus grows as the coefficient γ_r is increased up (15–20) $\times$ 10^{-22} MeV s fm^{-2}. A further increase in γ_r leads to a fast reduction of the neutron energy. The neutron emission angle in the laboratory frame decreases with increasing radial coefficient of friction. Thus, we can state that small friction as if focuses preequilibrium light particles from the target in the beam direction and leads to the growth of their energy.

With increasing γ_r, the energy of a neutron emitted by the projectile nucleus decreases monotonically, while its emission angle grows in absolute value, remaining negative. This means that, when the velocity of the relative motion of the nuclei involved is reduced because of the effect of dissipative forces, the projectile neutron is subjected, for a longer time, to the effect of the attracting target field, which, as the coefficient γ_r is increased, distorts its trajectory ever more strongly and which, in the case of strong nuclear friction, can even lead to neutron capture by the target. Therefore, the effect of the growth of dissipative forces on light particles emitted from the projectile is opposite to the effect of the analogous growth on target light particles.

We also note that the introduction of a small friction does not affect the total cross section (that is, the total multiplicity) for the production of preequilibrium light particles, changing only the character of the differential cross section as a function of energy and emission angle; that is, this leads to a redistribution of emitted light particles in terms of the coordinates E_n and θ_n. And only in the case of large dissipative forces does the multiplicity of preequilibrium light particles decrease significantly.

We can see that the properties of the angular and the energy distributions of light particles are sensitive to the form of dissipative nuclear forces; therefore, valuable information about the magnitude of the coefficients of nuclear friction and about other parameters of the dissipative function—in particular, about their dependence on the masses of colliding nuclei and on energy—can be extracted from an analysis of a vast body of experimental data on the yields of fast preequilibrium particles. By way of example, the friction-parameter values used in calculating the cross sections for the formation of light particles in Section 4 are given in the table. In each case, we have chosen a radial form factor of the Fermi type; its radius R_{fr} and its diffuseness parameter a_{fr} are also quoted in the table.

6. CONCLUSION

In order to study intermediate-energy ($E_0 <$ 100 MeV per nucleon) heavy-ion collisions leading to the production of fast light particles, we have proposed a classical four-body model. Within this model, projectile and target nuclei are represented as two-particle subsystems, each consisting of a heavy core and a light fragment (for example, a proton, a neutron, an alpha particle, etc.).

The proposed approach has been used to study in detail the dynamics and the mechanisms of formation of preequilibrium light particles originating from ^{20}Ne(20, 30A MeV) + ^{165}Ho $\to n +$ ER, ^{16}O(20A MeV) + ^{197}Au $\to p + X$,

^{36}Ar(35A MeV) + ^{107}Ag $\rightarrow n + X$, ^{40}Ar(44A MeV) + ^{51}V $\rightarrow p + X$, and ^{132}Xe(44A MeV) + ^{51}V, ^{197}Au $\rightarrow p + X$ reactions treated by way of example. Our theoretical estimates agree well with experimental data.

The role of two-body interactions in the process of light-particle formation has been investigated in detail, and the main mechanisms of this process have been determined. It has been shown that the high-energy component in the spectrum of neutrons and protons from these reactions corresponds to preequilibrium particles emitted both by the projectile and by the target nucleus. It has has been found that the yield of ultrafast preequilibrium light particles from the target nucleus exceeds the yield of light particles from the projectile nucleus, almost completely saturating the hardest section of their energy spectrum. The process of target-nucleon acceleration by the projectile mean field plays a dominant role here. Nucleon–nucleon collisions are insignificant in this respect at energies below 50 MeV per nucleon. With increasing projectile energy, the effect of the mean fields weakens, whereas nucleon–nucleon collisions become a dominant process in the formation of the hard section of light-particle spectra.

It has been revealed that nuclear-friction forces strongly affect the character of the angular and energy distributions of preequilibrium light particles. At high energies, the introduction of dissipative forces leads, among other things, to a moderation of the projectile, with the result that the mean fields exert a more pronounced effect on the nucleons of colliding nuclei. The forces of friction reduce the yield of fast particles from the projectile nucleus, but they increase the maximum energy of light particles emitted by the target nucleus. More detailed information about the character and the magnitude of dissipative nuclear forces would be deduced from a comprehensive analysis of extensive experimental data on the cross sections for light-particle formation within this approach.

The proposed new mechanism of preequilibrium-light-particle formation (acceleration of target nucleons in the projectile mean field) is indirectly confirmed by experimental data. In order to obtain more compelling pieces of evidence in favor of the existence of this mechanism, one could, for example, study the spectra of neutrons or protons emitted in collisions of two different projectile species with the same target nucleus. In doing this, it is necessary to select the combinations of projectiles and targets in such a way that one could separate light particles emitted by the projectile nucleus from those emitted by the target nucleus. For this, it is required that the spectrum of light particles originating from the projectile change insignificantly upon going over from one projectile species to another. In this case, the change in the observed distribution of preequilibrium light particles will be completely determined by the change in the distribution of light particles emitted by the target.

REFERENCES

1. R. M. Eisberg and G. Igo, Phys. Rev. **93**, 1039 (1954).
2. R. M. Eisberg, Phys. Rev. **94**, 739 (1954).
3. T. C. Awes *et al.*, Phys. Rev. C **24**, 89 (1981).
4. T. C. Awes *et al.*, Phys. Rev. C **25**, 2361 (1982).
5. T. C. Awes *et al.*, Phys. Lett. B **103B**, 417 (1981).
6. J. Kasagi, Phys. Lett. B **104B**, 434 (1981).
7. B. Ludewigt *et al.*, Phys. Lett. B **108B**, 15 (1982).
8. D. Hilscher *et al.*, Nucl. Phys. A **471**, 77c (1987).
9. E. Holub *et al.*, Phys. Rev. C **33**, 143 (1986).
10. B. V. Jacak *et al.*, Phys. Rev. C **35**, 1751 (1987).
11. G. Lanzano *et al.*, Phys. Rev. C **58**, 281 (1998).
12. Yu. E. Penionzhkevich *et al.*, Preprint No. E7-98-282, OIYaF (Joint Inst. of Nuclear Research, Dubna, 1998).
13. D. Prindle *et al.*, Phys. Rev. C **57**, 1305 (1998).
14. P. Sapienza *et al.*, Nucl. Phys. A **630**, 215c (1998).
15. D. Sackett *et al.*, Phys. Rev. C **44**, 384 (1991).
16. R. Alba *et al.*, Phys. Lett. B **322**, 38 (1994).
17. S. I. A. Garpman, D. Sperber, and M. Zielinska-Pfabe, Phys. Lett. B **90B**, 53 (1980).
18. T. Udagawa and T. Tamura, Phys. Rev. Lett. **45**, 1311 (1980).
19. V. E. Bunakov, V. I. Zagrebaev, and A. A. Kolozhvari, Izv. Akad. Nauk SSSR, Ser. Fiz. **44**, 2331 (1980).
20. V. I. Zagrebaev and A. Yu. Kozhin, Izv. Akad. Nauk SSSR, Ser. Fiz. **52**, 104 (1988).
21. V. E. Bunakov and V. I. Zagrebaev, Z. Phys. A **333**, 57 (1989).
22. V. I. Zagrebaev, Ann. Phys. (N.Y.) **197**, 33 (1990).
23. V. I. Zagrebaev, in *Proceedings of the First International School in Nuclear Physics, Kiev, 1990*, p. 471.
24. S. Leray *et al.*, Z. Phys. A **320**, 383 (1985).
25. J. P. Bondorf *et al.*, Nucl. Phys. A **333**, 285 (1980).
26. K. Mohring, W. J. Swiatecki, and M. Zielinska-Pfabe, Nucl. Phys. A **440**, 89 (1985).
27. F. Sebil and B. Remaud, Z. Phys. A **310**, 99 (1983).
28. J. Randrup and R. Vanderbosch, Nucl. Phys. A **474**, 219 (1987).
29. V. Zagrebaev, in *Proceedings of the XV Nuclear Physics Divisional Conference LEND-95, St. Petersburg, 1995* (World Sci., Singapore, 1995), p. 457.
30. V. Zagrebaev and Yu. Penionzhkevich, Prog. Part. Nucl. Phys. **35**, 575 (1995).
31. C. M. Perey and F. G. Perey, At. Data Nucl. Data Tables **13**, 293 (1974).
32. J. Blocki, J. Randrup, W. J. Swiatecki, and C. F. Tsang, Ann. Phys. (N.Y.) **105**, 427 (1977).
33. D. H. E. Gross and H. Kalinowski, Phys. Rep. **45**, 175 (1978).
34. J. Knoll and R. Schaeffer, Ann. Phys. (N.Y.) **97**, 307 (1976).

Translated by A. Isaakyan

Physics of Atomic Nuclei, Vol. 65, No. 8, 2002, pp. 1474–1478. Translated from Yadernaya Fizika, Vol. 65, No. 8, 2002, pp. 1510–1514.

ELEMENTARY PARTICLES AND FIELDS
Experiment

Heavy-Nucleus Multifragmentation Induced by Coherent Bremsstrahlung Photons with Endpoint Energy $E_\gamma^{\max} = 4.1$ GeV

G. L. Bayatyan, G. S. Vartanyan, N. K Grigoryan, S. G. Knyazyan, V. P. Likhachev[1)], A. T. Margaryan[*], G. G. Marikyan, and T. A. Rostomyan

Erevan Physics Institute, ul. brat'ev Alikhanian 2, Erevan, 375036 Armenia

Received October 5, 2000; in final form, October 30, 2001

Abstract—New experimental data are presented that were obtained by studying the multifragmentation of ^{197}Au, ^{209}Bi, ^{238}U, and ^{243}Am nuclei in a coherent bremsstrahlung-photon beam with an endpoint energy of 4.1 GeV from the Erevan Synchrotron. For the first time, four or more fragments are observed. For all the nuclei studied here, the respective production cross sections are about $(1–3) \times 10^{-3}$ of the total inelastic photon–nucleus cross section. The fragment yields are isotropic. © *2002 MAIK "Nauka/Interperiodica".*

Experimental results obtained by studying heavy-nucleus fragmentation caused by bremsstrahlung photons whose endpoint energy is 1.85 GeV were presented in [1]. The emerging fragments were recorded with a multiwire proportional low-pressure chamber. Within a solid angle of 0.3π sr, the measured fraction of three or more fragments for a ^{243}Am target was about 10^{-3} of the events involving the production of fragments; for ^{208}Pb, ^{209}Bi, ^{235}U, ^{238}U, and ^{239}Pu, this fraction was about 10^{-4}. The experiment was performed in order to study the mechanism of the breakup of a highly excited nucleus. In addition to evaporation and fission occurring at low excitation energies (of about 1 MeV/A), there is a new deexcitation mechanism that has been widely discussed in the past few years. This is multifragmentation involving the breakup of a nucleus into three or more fragments of mass numbers $A \geq 10$ and energies about a few tens of MeV. Multifragmentation may proceed through a process where a liquid–gas phase transition in highly excited nuclear matter [2] of excitation energy 3–6 MeV/A is followed by cooling [3, 4].

Within the statistical-multifragmentation model, the probability of the production of three or more fragments depends only on the excitation energy of the nucleus involved [4]. The nuclei that we study receive approximately the same amount of excitation energy in the bremsstrahlung beam [5], but it was found in [1] that, for ^{208}Pb, ^{209}Bi, ^{235}U, ^{238}U, and ^{239}Pu nuclei, the probabilities of the production of three or more fragments are different, and so are the yields of binary fission. This behavior conforms to the predictions of the cascade model of ternary fission [6]. This model assumes that the initial nucleus undergoes binary fission followed by the fission of daughter nuclei.

The experiment reported in [1] established an upper limit of 10^{-4} of the total inelastic-interaction cross section on the cross section for the production of four or more fragments. A similar pattern was also observed in [7], where the multifragmentation process

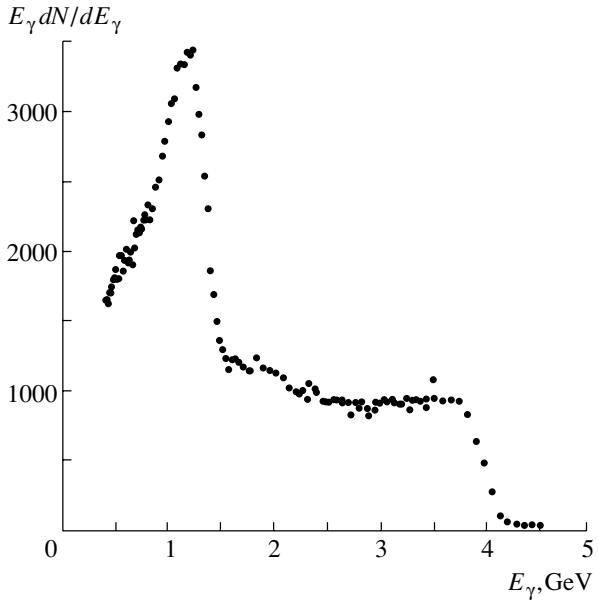

Fig. 1. Coherent bremsstrahlung spectrum for $E_\gamma^{\max} = 4.1$ GeV and $E_\gamma^{\text{peak}} = 1.25$ GeV.

[1)]Universidade de São Paulo, CP 66318, BR-05389-970 São Paulo, SP, Brazil.
[*]e-mail: mat@jerewan1.yerphi.am

1063-7788/02/6508-1474$22.00

was studied in the annihilation of 1.2-GeV antiprotons in heavy nuclei (U, Au, Ho). In that case, the processes of fission and evaporation were dominant in nuclear-fragment production, just as in the case of the interaction of bremsstrahlung photons whose endpoint energy is 1.85 GeV with heavy nuclei.

Here, we present new results on multiparticle fragment production in a beam of coherent bremsstrahlung photons with an endpoint energy of 4.1 GeV. These data were obtained in the experiment performed simultaneously with an experiment that studied deuteron photodisintegration [8]. The peak energy of coherent-bremsstrahlung photons was in the range between 0.9 and 1.8 GeV. Figure 1 shows a typical spectrum of coherent-bremsstrahlung photons with a peak energy of 1.25 GeV. The product fragments were recorded by a detector formed by four identical proportional low-pressure chambers ensuring an overall coverage of 0.3π sr. The beam of coherent-bremsstrahlung photons was incident on a target mounted in the detector. The beam diameter on the target position was about 10 mm, and the geometry and the size of the detector were given in [1].

The multiwire proportional low-pressure chambers (LPC) [9] were filled with a hexane vapor at a pressure of about 20 torr.

In the chosen operation mode of the detector within the range 600–800 V, fission fragments were recorded with an efficiency of about 100%. As voltage increased above 700 V, fragments lighter than those from the fission were also recorded efficiently. Fragments having mass numbers in the region $A \geq 20$ and energies of about a few tens of MeV were recorded with a probability close to 100%, since their ionization losses were close to the ionization losses of the fission fragments. However, this detector is insensitive to relativistic particles. In the chosen operation mode of the detector (780 V), the probability of recording α particles was not greater than 1% for the ^{243}Am target having natural α radioactivity. Thus, this detector permits one to study the multiparticle production of fragments with mass numbers of $A \geq 20$ and energies of about a few tens of MeV in intense photon beams.

Thickness of the targets used (T_t) and their substrates (T_s)

Nucleus	T_t, mg/cm^2	T_s, mg/cm^2
^{197}Au	1.16	1.8
^{209}Bi	1.30	3.4
^{238}U	1.00	94.5
^{243}Am	0.01	27.0

The signal wires of each detector plane were combined into separate independent channels. Information from all the planes was gated by a 2.5-ms synchronized accelerator pulse, the beam-spill time and the ejection frequency being 1.5 ms and 50 Hz, respectively. An additional gating pulse of the same duration with a delay of 7.5 ms was used to initiate signals associated with information about events of detector actuation in the time lapse between two beam bunches. The gated pulses were then transferred to the majority coincidence schemes with a time resolution of about 20 ns to determine the multiplicities of coincidences from one to four. This corresponds to recording two to five or more nuclear fragments, because the geometry of the detector allows one to record only forward-emitted fragments in the angular

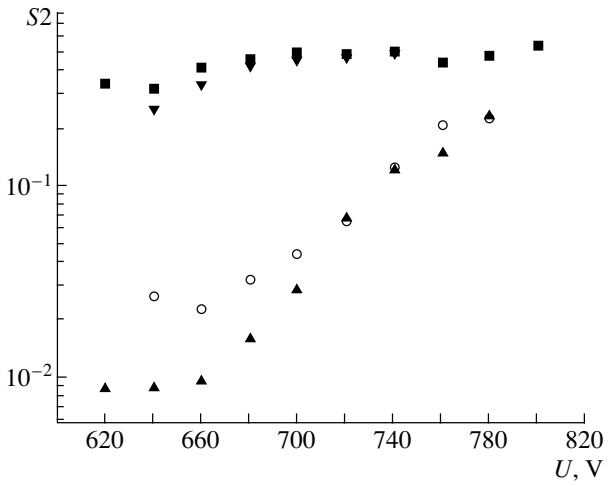

Fig. 2. Production yields of two or more fragments (in relative units) versus the detector voltage (U) for (■) ^{238}U, (○) ^{209}Bi, (▲) ^{197}Au, and (▼) ^{243}Am targets.

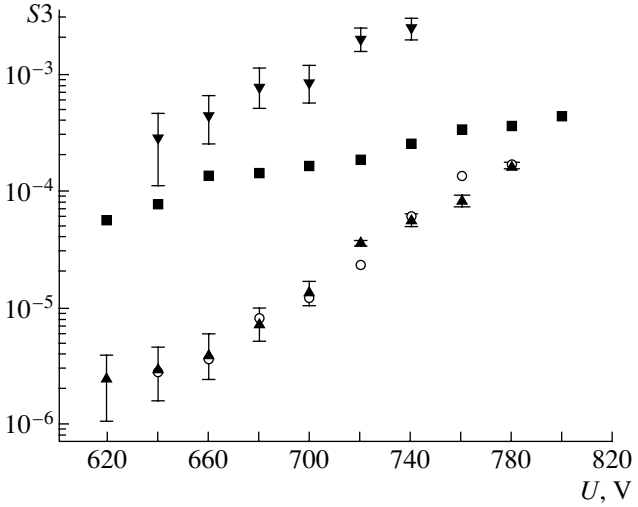

Fig. 3. As in Fig. 2, but for the case of the yields of three or more fragments.

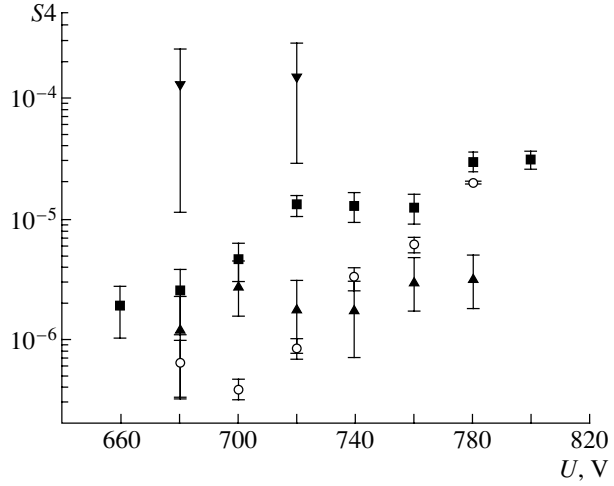

Fig. 4. As in Fig. 2, but for the case of the yields of four or more fragments.

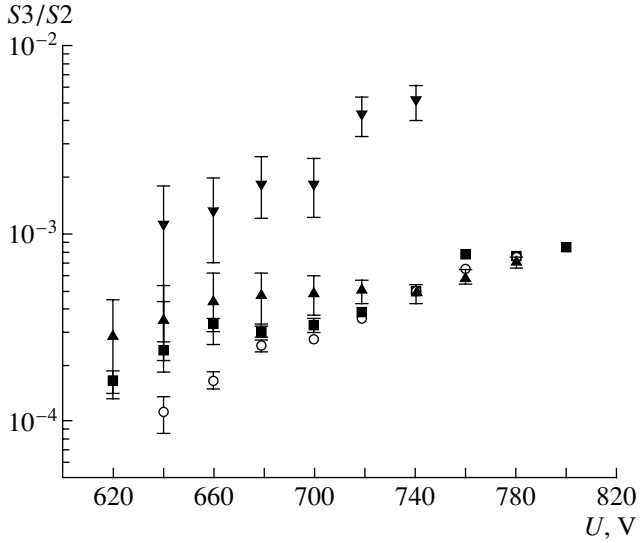

Fig. 5. Ratio of the yield from the fragmentation into three or more fragments to that from the fragmentation into two or more fragments as a function of the detector voltage. The notation is identical to that used in Fig. 2.

range of 10°–48° with respect to the photon-beam direction. Thus, the detection of one fragment by the detector operated at up to 700 V is due primarily to target-nucleus fission into two fragments, since, at the momentum transfer to the target nucleus in the range 0–3.5 GeV/c, the opening angle for binary-fission fragments varies between 140° and 180° in the laboratory frame. Similarly, the detection of two fragments by the detector is due to ternary fission, etc. With increasing voltage supplied to the detector, the efficiency of light-fragment detection becomes higher.

Another low-pressure chamber involving a ^{238}U target 1.01 mg/cm^2 thick was used as a monitor. The chamber was operated in the mode that allowed one to record only heavy fission fragments. Since the fissility of a ^{238}U nucleus in a photon beam whose energy is not less than 40 MeV is close to 100% [10–12], the monitor counts corresponded to the number of inelastic photon interactions with ^{238}U.

The efficiencies of the monitor of the fragment detector were tested continuously throughout the experimental run by an additional plane in the detectors.

We used ^{209}Bi, ^{238}U, and ^{243}Am targets deposited onto an aluminum substrate and a ^{197}Au target deposited onto a Mylar substrate. The thicknesses of the targets and the substrates are given in the table.

In order to determine the contribution from the substrates of the ^{238}U and ^{243}Am targets, the measurements were also performed for the inverted arrangement of the target–substrate pair, in which case fission fragments from the targets being studied were absorbed in the substrates, so that only fragments originating from the fission of the substrate material were recorded; the direct measurements record both fragments produced in the target and in the substrate because of a small target thickness. The substrates of the ^{209}Bi and ^{197}Au targets were thin; therefore, fragments produced in those targets could penetrate through them in the measurements for the inverted positions of the target and substrate. For these targets, the substrate contribution was taken to be equal to the detector background level without targets, which was also measured at regular time intervals throughout the experiment.

The procedure for data processing was described in [1]. Figures 2–4 show the production yields for two or more fragments ($S2$), three or more fragments ($S3$), and four or more fragments ($S4$); these yields are given in relative units; that is, they are normalized to the yield from ^{238}U fission in the monitor. The indicated uncertainties are purely statistical.

At low voltages, in which case only heavy fragments are recorded, the ratio of the yields of two or more fragments for ^{197}Au, ^{209}Bi, and ^{238}U nuclei (Fig. 2) corresponds to the known cross sections for the fission of these nuclei. The ratio determined for ^{238}U and ^{243}Am nuclei shows that, in the coherent bremsstrahlung beam used, the yields $S2$ are identical for them. As can be seen from Fig. 2, $S2$ increases for ^{197}Au and ^{209}Bi nuclei as the detector voltage increases, which improves the efficiency of light-fragment detection. Obviously, this increase is caused by evaporation processes associated both with the primary nucleus and with daughter nuclei produced in primary-nucleus fission, because the primary-nucleus excitation energy is shared among

the daughter nuclei in the course of fission. A slight increase in $S2$ for ^{238}U and ^{243}Am nuclei is due to their high fissility (about 100%).

Figure 5 shows the ratio of the production yield of three or more fragments to that of two or more fragments ($S3/S2$) as a function of the detector voltage. These ratios are about $(2–5) \times 10^{-4}$ for ^{197}Au, ^{209}Bi, and ^{238}U and about 10^{-3} for ^{243}Am if only heavy fission fragments are recorded; these results agree with those obtained in the bremsstrahlung beam with an endpoint energy of 1.85 GeV. According to the calculation from [13], fission into three or four fragments of equal masses is more favorable energetically for ^{243}Am nuclei than fission into two fragments; this can result in a larger cross section for the direct production of three or more fragments [14]. As voltage is increased up to 760–780 V, in which case light fragments are also recorded, the ratio of the production yields of three or more fragments to that of two or more fragments is identical for all the nuclei studied here, with the exception of ^{243}Am, and is about 7×10^{-4}. For ^{238}U, this ratio is about 4×10^{-4} in the bremsstrahlung beam with an endpoint energy of 1.85 GeV.

In this experiment, in contrast to the previous one, we also recorded the production of four or more fragments (the results are presented in Fig. 4). In principle, four or more fragments can be produced through a sequential (cascade) fission of daughter fragments [6] or through the mechanism of fission and evaporation. Within the sequential-fission model, the ratio presented in Fig. 5 is equal to the probability of the fission of daughter nuclei. For the nuclei studied here, the fission fragments are characterized by $Z^2/A = 15–20$; their fission probabilities are about $(2–4) \times 10^{-3}$ at the excitation energies being considered [15]. With allowance for the detector acceptance, the expected yield of four or more fragments that is due to the cascade-fission mechanism is $\leq 10^{-7}$ for nuclei with a fissility of about 100% and is $\leq 10^{-8}$ for ^{197}Au and ^{209}Bi. However, the experimental result is about 10^{-5} for ^{238}U at the detector voltage of ≥ 740 V (Fig. 4) and is about 3×10^{-6} for ^{197}Au and ^{209}Bi. The geometric probability of recording four or more fragments is about 3×10^{-3}; therefore, the probability of such production is about 3×10^{-3} of the total interaction cross section for ^{238}U and is about 10^{-3} for ^{197}Au and ^{209}Bi. For the probability of the production of four or more fragments on heavy nuclei with close mass numbers, such values are expected within the statistical multifragmentation model, according to which the probability of multifragmentation depends only on the excitation energy of nuclei [4]. The distinction between the mass numbers of the nuclei studied here is $\leq 20\%$; therefore, they receive approximately equal excitation energies [5] and participate in the multifragmentation process with approximately identical probabilities. The probability of the production of four or more fragments and the probability of the fission of daughter nuclei are on the same order of magnitude; hence, the observed increase in $S3$ (Fig. 3) and $S3/S2$ (Fig. 5) with increasing fragment-detector voltage is due both to cascade fission and to multifragmentation.

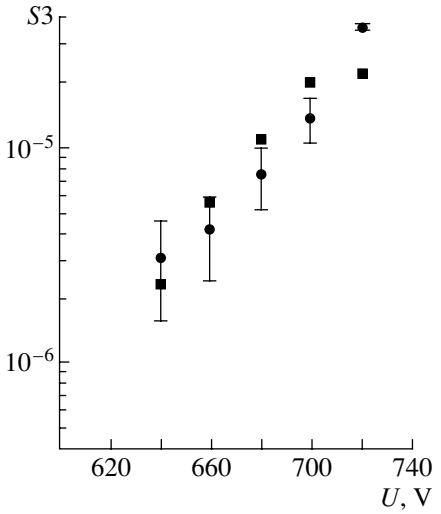

Fig. 6. Yields of three or more fragments for an Au target as a function of the detector voltage for (•) $\Delta\theta = 10°–48°$ and (■) $\Delta\theta = 132°–170°$.

For ^{197}Au and ^{243}Am nuclei, we have also performed measurements with the detector rotated through 180°, in which case it records fragments produced in the angular range of 132°–170°. Figure 6 shows the yields of three or more fragments within the angular ranges 10°–48° and 132°–170°. It is evident from the figure that the yields of fragments within these two ranges are identical. The fragmentation yields of two or more fragments and of four or more fragments behave similarly. The distribution of fragments is isotropic within the errors; this is indicative of the production of an excited intermediate compound nucleus and its subsequent decay.

ACKNOWLEDGMENTS

We are grateful to the directorate of the Yerevan Physics Institute for their support of our study and interest in it, to the staff of the accelerator of this institution, and to Professor G.A. Vartapetyan for repeated discussions on our results.

REFERENCES

1. E. A. Arakelyan, G. L. Bayatyan, G. S. Vartanyan, *et al.*, Yad. Fiz. **58**, 263 (1995) [Phys. At. Nucl. **58**, 219 (1995)].
2. A. Mekjian, Phys. Rev. Lett. **38**, 640 (1977).
3. J. P. Bondorf, R. Donangelo, H. Schulz, *et al.*, Phys. Lett. B **162B**, 30 (1985).
4. D. H. E. Gross, Zhang Xiao-ze, and Xu Shu-yan, Phys. Rev. Lett. **56**, 1544 (1986).
5. V. S. Barashenkov, F. G. Gereghi, A. S. Iljinov, *et al.*, Nucl. Phys. A **231**, 4 (1974).
6. Yu. A. Muzychka, Yu. Ts. Oganesyan, B. I. Pustyl'nik, and G. N. Flerov, Yad. Fiz. **6**, 306 (1967) [Sov. J. Nucl. Phys. **6**, 222 (1967)].
7. U. Jahnke, W. Bohne, T. von Egidy, *et al.*, Phys. Rev. Lett. **83**, 4959 (1999).
8. F. Adamian, A. Aganiants, Yu. Borzunov, *et al.*, Eur. Phys. J. A **8**, 42 (2000).
9. E. A. Arakelyan, G. L. Bayatyan, N. K. Grigoryan, *et al.*, Prib. Tekh. Éksp., No. 3, 88 (1989).
10. H. Ries, U. Kneissl, G. Mank, *et al.*, Phys. Lett. B **139B**, 254 (1984).
11. J. Ahrens, J. Arends, P. Bourgeois, *et al.*, Phys. Lett. B **146B**, 303 (1984).
12. E. A. Arakelyan, A. R. Bagdasaryan, G. L. Bayatyan, *et al.*, Yad. Fiz. **52**, 1387 (1990) [Sov. J. Nucl. Phys. **52**, 878 (1990)].
13. W. J. Swiatecki, Phys. Rev. **101**, 651, 993 (1956).
14. H. Diehl and W. Greiner, Phys. Lett. B **45**, 35 (1973).
15. V. G. Nedorezov and Yu. N. Ranyuk, *Photofission of Nuclei above the Giant Resonance* (Naukova Dumka, Kiev, 1989).

Translated by E. Kozlovskiĭ

Physics of Atomic Nuclei, Vol. 65, No. 8, 2002, pp. 1479–1486. From Yadernaya Fizika, Vol. 65, No. 8, 2002, pp. 1515–1522.

ELEMENTARY PARTICLES AND FIELDS
Experiment

Study of Multiparticle Azimuthal Correlations in Central CNE, MgMg, CCu, and OPb Interactions at Energy of 3.7 GeV per Nucleon*

L. V. Chkhaidze, T. D. Djobava, and L. L. Kharkhelauri

High Energy Physics Institute, Tbilisi State University, 9 University Street, GE-380086 Tbilisi, Georgia

Received December 25, 2000; in final form, September 10, 2001

Abstract—Azimuthal correlations between protons and between pions have been investigated in central CNe, MgMg, CCu, and OPb collisions at an energy of 3.7 GeV/nucleon. Negative (back-to-back) correlations have been observed for protons in CNe, CCu, and for π^- mesons in CNe and MgMg collisions. For π^- mesons, positive (side-by-side) azimuthal correlations have been observed for heavy systems of CCu and OPb. The Quark–Gluon String Model satisfactorily describes the experimental results both for protons and π^- mesons. © *2002 MAIK "Nauka/Interperiodica"*.

1. INTRODUCTION

Relativistic nucleus–nucleus collisions are very well suited for investigation of excited nuclear matter properties, which are the subject of intense studies, both experimentally and theoretically. Theoretical models predict the formation of exotic states of nuclear matter, for example, the phase transition to a quark–gluon plasma [1, 2]. One of the main goals of relativistic heavy-ion-collision experiments is to study nuclear matter under extreme conditions of high densities and temperatures. The most impressive results of high-energy heavy-ion research so far are new collective phenomena that have been discovered in these reactions. The study of multiparticle correlations offers unique information about space–time evolution of the collective system. During recent years, an intensive analysis of experimental data has been carried out using collective variables, which depend on the momentum of all secondary particles, to reveal nontrivial effects in nucleus–nucleus collisions.

The experimental discovery of such transitions is impossible without an understanding of the mechanism of collisions and a study of the characteristics of multiparticle production in nucleus–nucleus interactions. Multiparticle correlations were investigated for the first time at BEVALAC more than ten years ago [3].

In this article, we present the results of an analysis of multiparticle correlations in central CNe, MgMg, CCu, and OPb collisions at an energy of 3.7 GeV/nucleon. Azimuthal correlations between protons and pions and the dependence of these correlations on the projectile (A_P) and target (A_T) nucleus have been investigated.

2. EXPERIMENT

Data were obtained using a 4π SKM-200–GIBS spectrometer (JINR, Dubna, Russia) [4, 5]. The SKM-200-GIBS setup consists of a 2-m streamer chamber with a fiducial volume of $2 \times 1 \times 0.6$ m, placed in a magnetic field of ~0.8 T (~0.9 T for MgMg), and a triggering system. The streamer chamber was exposed to beams of C, O, and Mg nuclei accelerated in the synchrophasotron up to an energy of 3.7 GeV per incident nucleon. Solid targets in the form of thin discs with thicknesses of 0.2–0.5 g/cm^2 (the thickness of Mg was 1.5 g/cm^2; neon-gas filling of the chamber also served as a nuclear target) were mounted inside the chamber at a distance of 70 cm from the entrance window and at a height of 8 cm above the middle electrode. Photographs of the events were taken using an optical system with three lenses. The experimental setup and the logic of the triggering system are presented in Fig. 1. The triggering system allowed selection of inelastic and central collisions.

The "inelastic" trigger, consisting of two sets of scintillation counters mounted upstream (S_1–S_4) and downstream (S_5, S_6) the chamber, selected all inelastic interactions of incident nuclei on a target.

The "central" triggering system consisted of the same upstream part as in the inelastic system and of scintillation veto counters (S_{ch}, S_{neu}), to reject a projectile and its charged and neutral spectator fragments, in the downstream part. All counters were made from plastic scintillators and worked with PM-30 photomultipliers. The S_1 counter with a scintillator

*This article was submitted by the authors in English.

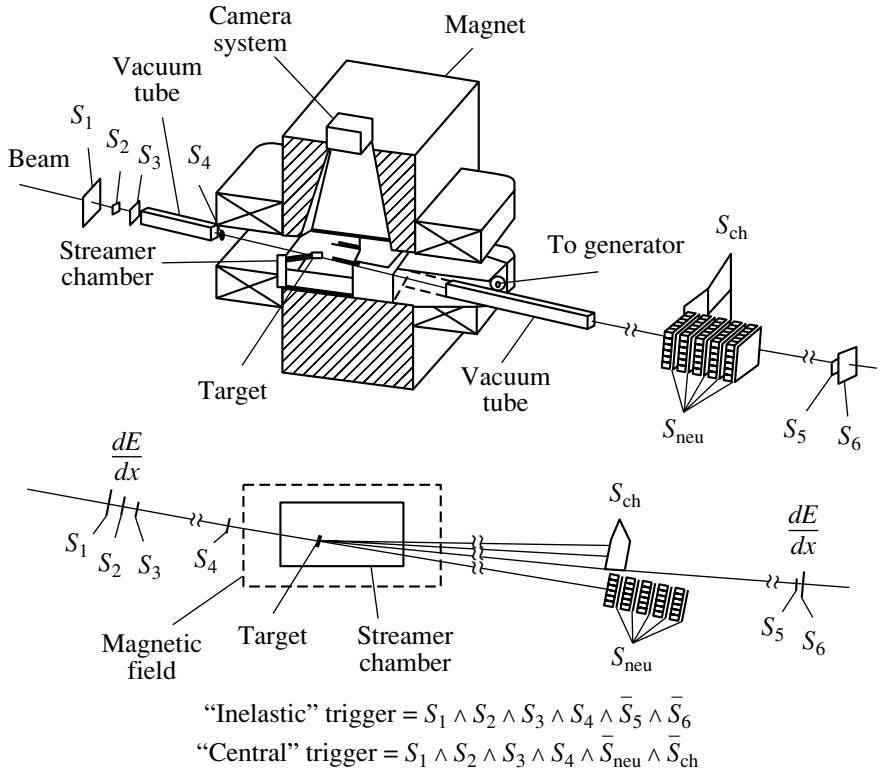

Fig. 1. Experimental setup. The trigger and trigger distances are not to scale.

of $20 \times 20 \times 0.5$ cm worked in the amplitude regime and identified the beam nuclei by their charge. The nuclei from the beam, heading to the target, were selected using the profile counters S_2, S_3 with plastic of 0.15-mm diameter and 3-mm thickness and a "thin" counter S_4 (15 mm and 0.1 mm, correspondingly). The S_{ch} counters (two counters with plastic $40 \times 40 \times 0.5$ cm in size) were placed at a distance of 4 m downstream from the target and registered secondary charged particles emitted from the target within a cone of half-angle $\theta_{ch} = 2.4^\circ$ or 2.9°. The S_{neu} counters registered the neutrons emitted from the target in the same solid angle $\theta_{neu} = 2.4^\circ$ or 2.9°. The S_{neu} telescope consisted of counters $40 \times 40 \times 2$ cm in size, layered by 10-cm-thick iron blocks. The central trigger selected events defined as those with no charged projectile spectator fragments and spectator neutrons ($p/Z > 3$ GeV/c) emitted at angles of $\theta_{ch} = \theta_{neu} = 2.4^\circ$ or 2.9° (~ 4 msr). The trigger efficiency was 99 and 80% for charged and neutral projectile fragments, respectively. The trigger mode for each exposure is defined as Tr(θ_{ch}, θ_{neu}) (θ_{ch} and θ_{neu} are expressed in degrees and rounded to the closest integer value). Thus, nucleus–nucleus interactions obtained with this setup correspond to the following Tr(θ_{ch}, θ_{neu}) triggers: CNe—Tr(2, 0), MgMg—Tr(2, 2), CCu—Tr(2, 0) and Tr(3, 3), and OPb—Tr(2, 0).

Biases and correction procedures were discussed in detail in [4, 5]. The ratio $\sigma_{cent}/\sigma_{inel}$ (which characterizes the centrality of selected events) is $(9 \pm 1)\%$ for CNe and $(21 \pm 3)\%$ for CCu; the fraction of central MgMg events is $\approx 4 \times 10^{-4}$ among all inelastic interactions. Average momentum measurement errors $\langle \Delta p/p \rangle = 8$–$10\%$ for protons and 5% for pions; the corresponding errors of the production angles are $\Delta\theta = (1$–$2)^\circ$ and 0.5° (for π^- mesons in MgMg interactions, $\langle \Delta p/p \rangle = 1.5\%$, $\Delta\theta = 0.3^\circ$).

3. QUARK–GLUON STRING MODEL

Several theoretical models of nucleus–nucleus collisions at high energy were proposed in [6, 7]. These models allow one to test various assumptions concerning the mechanism of particle production at extreme conditions achieved only in nucleus–nucleus collisions. The Quark–Gluon String Model (QGSM) has been used for the comparison with our experimental results. The QGSM is presented in detail in papers [8, 9]. The QGSM is based on the Regge and string phenomenology of particle production in inelastic binary hadron collisions. For the description of the evolution of the hadron and quark–gluon phases, a coupled system of Boltzmannlike kinetic equations is used. Nuclear collisions are treated as a mixture of independent interactions of the projectile

and target nucleons, stable hadrons, and short-lived resonances. The QGSM includes low-mass vector mesons and baryons with 3/2 spin, mostly $\Delta(3/2, 3/2)$ via resonant reactions. Pion absorption by NN quasideuteron pairs is also taken into account. The coordinates of nucleons are generated according to a realistic nuclear density. The sphere of the nucleus is filled with the nucleons under the condition that the distance between them is greater than 0.8 fm. The nucleon momenta are distributed in a range of $0 \leq p \leq p_{\mathrm{F}}$. The maximum nucleon Fermi momentum is

$$p_{\mathrm{F}} = (3\pi^2)^{1/3} h \rho^{1/3}(r), \qquad (1)$$

where $h = 0.197$ fm GeV/c, $\rho(r)$ is nuclear density.

The procedure of event generation consists of three steps: the definition of configurations of colliding nucleons, production of quark–gluon strings, and fragmentation of strings (breakup) into observed hadrons. The model includes also the formation time of hadrons. The QGSM has been extrapolated to the range of intermediate energy ($\sqrt{s} \leq 4$ GeV) to use it as a basic process during the generation of hadron–hadron collisions. Masses of "strings" produced at $\sqrt{s} = 3.6$ GeV were small (usually not greater than 2 GeV), and they fragmented mainly ($\approx 90\%$) through two-particle decays. For the main NN and πN interactions, the following topological quark diagrams [7] were used: binary, "undeveloped" cylindrical, diffractive, and planar. The binary process makes the main contribution, which is proportional to $1/p_{\mathrm{lab}}$. It corresponds to quark rearrangement without direct particle emission in the string decay. This reaction predominantly results in the production of resonances (for instance, $p + p \to N + \Delta^{++}$), which are the main source of pions. Comparable contributions to the inelastic cross section, which decreases however with decreasing p_{lab}, come from diagrams corresponding to the undeveloped cylindrical diagrams and from the diffractive processes. Transverse momenta of pions produced in quark–gluon string fragmentation processes are the product of two factors: string motion on the whole as a result of transverse motion of constituent quarks and $q\bar{q}$ production in string breakup. The transverse motion of quarks inside hadrons was described by the Gaussian distribution with a variance of $\sigma^2 \approx 0.3$ $(\mathrm{GeV}/c)^2$. Transverse momenta k_T of the produced $q\bar{q}$ in the c.m.s. of the string follow the dependence

$$W(k_T) = 3B/\pi(1 + Bk_T^2)^4, \qquad (2)$$

where $B = 0.34\,(\mathrm{GeV}/c)^{-2}$.

The cross section of hadron interactions were taken from experiments. Isotopic invariance and predictions of the additive quark model [10] (for meson–meson cross sections, etc.) were used to avoid data deficiency. The resonance cross sections were assumed to be identical to the stable particle cross sections with the same quark content. For the resonances, tabulated widths were used.

The QGSM simplifies the nuclear effects. In particular, coupling of nucleons inside the nucleus is neglected, and the decay of excited recoil nuclear fragments and coalescence of nucleons are not included.

We have generated CNe, CCu, OPb, and MgMg interactions using the COLLI Monte Carlo generator [11], which is based on the QGSM and then traced through the detector and trigger filter. In the COLLI generator, there are two possibilities to generate events: (i) at unfixed impact parameter $\tilde{b}$ and (ii) at fixed b. From the impact parameter distributions, we obtained a mean value of $\langle b \rangle = 2.2$, 1.3, 2.7, and 3.7 fm for CNe, MgMg, CCu, and OPb collisions. For the obtained values of $\langle b \rangle$, we generated a total sample of events 6270, 9320, 2430, and 6200, respectively.

The QGSM overestimates the production of low-momentum protons with $p < 0.2$ GeV/c, which are mainly the target fragments and were excluded from the analysis. From the analysis of the generated events, protons with deep angles greater than 60° were excluded because in the experiment, the registration efficiency of such vertical tracks is low.

4. AZIMUTHAL CORRELATIONS BETWEEN PROTONS AND BETWEEN PIONS

In [12, 13], a procedure for studying the correlation between groups of particles has been developed. The azimuthal correlation function was defined by the relative opening angle between the transverse momentum vector sums of particles emitted forward and backward with respect to the rest frame of the target nucleus (a rapidity of $y_0 = 0.2$).

We applied this method to our data, but the analysis was carried out in the central rapidity region instead of the target rapidity range of [12, 13]. The analysis was performed event by event; in each event we denote the vectors

$$\mathbf{Q}_B = \sum_{y_i < \langle y \rangle} \mathbf{P}_{Ti} \qquad (3)$$

and

$$\mathbf{Q}_F \sum_{y_i \geq \langle y \rangle} \mathbf{P}_{Ti}, \qquad (4)$$

where $\langle y \rangle$ is the average rapidity in each event.

Then, the correlation function $C(\Delta\varphi)$ was constructed as follows:

$$C(\Delta\varphi) = dN/d\Delta\varphi, \qquad (5)$$

Table 1. The number of π^+ and π^- mesons and their average kinematical characteristics in CNe and CCu collisions after the identification of protons and π^+ mesons

$A_P A_T$	Particle	N_π	$\langle n_\pi \rangle$	$\langle p_T \rangle$, GeV/c	$\langle p \rangle$, GeV/c
CNe	π^+	3089	4.26 ± 0.06	0.234 ± 0.003	0.600 ± 0.009
	π^-	3120	4.31 ± 0.07	0.226 ± 0.005	0.612 ± 0.009
CCu	π^+	3713	5.74 ± 0.09	0.222 ± 0.003	0.522 ± 0.008
	π^-	3635	5.68 ± 0.10	0.213 ± 0.005	0.508 ± 0.009

Table 2. The number of experimental events (N_{event}) and participating protons (N_p), the asymmetry coefficient (ξ), the strength of the correlation (ζ), and the mean rapidity ($\langle y \rangle$) of protons

$A_P A_T$	N_{event}	N_p	ξ	ζ	$\langle y \rangle$
CNe	723	9201	-0.23 ± 0.05	0.63 ± 0.09	1.07 ± 0.07
CCu	663	12715	-0.35 ± 0.05	0.48 ± 0.06	0.73 ± 0.05

where $\Delta\varphi$ is the angle between the vectors $\mathbf{Q}_B$ and $\mathbf{Q}_F$:

$$\Delta\varphi = \arccos(\mathbf{Q}_B \cdot \mathbf{Q}_F)/(|\mathbf{Q}_B||\mathbf{Q}_F|). \qquad (6)$$

Essentially, $C(\Delta\varphi)$ measures whether the particles in the backward and forward hemispheres are preferentially emitted back-to-back ($\Delta\varphi = 180^\circ$) or side-by-side ($\Delta\varphi = 0^\circ$) [12]. The protons from CNe and CCu collisions were analyzed using this method.

For the analysis, it is necessary to perform an identification of π^+ mesons, the admixture of which amongst the charged positive particles is about 25–27%. The statistical method was used for identification of π^+ mesons. The main assumption is based on the similarity of spectra of π^- and π^+ mesons (n_π, p_T, p_L). A two-dimensional distribution of (p_T, p_L) variables was used for identification of π^+ mesons. The whole plane is divided into seven zones. For example, for CNe collisions,

1) $p_L > 2.5$ GeV/c or $p_T > 0.9$ GeV/c;

2) $0 \le p_L \le 1.4$ GeV/c and $p_T \le 0.7$ GeV/c (PMAX);

3) $0 \le p_L \le 1.4$ GeV/c and $p_T > 0.7$ GeV/c;

4) $1.4 < p_L < 2.5$ GeV/c;

5) $-0.2 \le p_L \le 0$ GeV/c and $p_T \le 0.3$ GeV/c;

6) $-0.2 \le p_L \le 0$ GeV/c and $p_T > 0.3$ GeV/c;

7) $p_L < -0.2$ GeV/c.

Zone 2 of maximal overlap—PMAX—in its turn, is divided into $7 \times 7 = 49$ cells. The probability of hitting each zone and, respectively, the cell by π^- mesons and charged positive particles are defined, and the relative probability of hitting π^- mesons is calculated as a result. The admixture of π^+ mesons in zone 1 is negligible. The procedure of dividing the (p_T, p_L) plane into cells allows one to simplify the mathematical algorithm and improves the accuracy of identification. It was assumed that π^+ and π^- mesons hit a given cell with equal probability (equal probability densities for π^+ and π^- were assumed).

The identification, in fact, is equal to summing the hitting probabilities into each cell and, when the sum reaches the critical value, the particle is considered as a π^+ meson. The rest of the particles are assumed to be protons. For each proton and π^+ meson, the sign is recorded on Data Summar Tape (DST), which indicates to which zone of the (p_T, p_L) plane the given particle belongs and what the probability is. Particles with $p_T > 0.9$ GeV/c or $p_L > 2.5$ GeV/c are unambiguous protons with a probability equal to 1.

After identification of π^+ mesons in the event, the difference of π^+ and π^- mesons Δn is determined. If $|\Delta n| > 2$, in the PMAX region, the identification $\pi^+ \leftrightarrow$ proton is interchanged and for that reason particles with smaller probability are chosen. If the condition of approachment of multiplicities is not fulfilled, then in this case, information of the event such a sign is recorded into the "head," which allows one to exclude the given event from further analysis.

After identification is performed, the admixture of π^+ mesons amongst the protons does not exceed 5–7%. The mean values of multiplicity, momentum, and transverse momentum for π^+ and π^- mesons are presented in Table 1. One can see that the average kinematical characteristics of π^+ and π^- mesons coincide satisfactorily within the errors.

The numbers of events for CNe and CCu collisions and the mean rapidities of the analyzed protons $\langle y \rangle$ are listed in Table 2. Figure 2 shows the experimental correlation function $C(\Delta\varphi)$ for protons from central

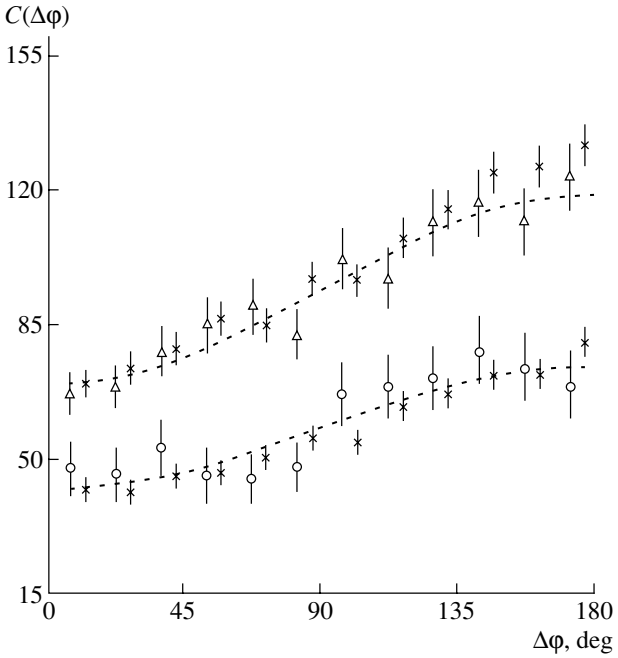

Fig. 2. The correlation function $C(\Delta\varphi)$ for protons from (○) CNe and (△) CCu collisions; (×) represent the QGSM data. Dashed curves are the results of the approximation of the data (see text).

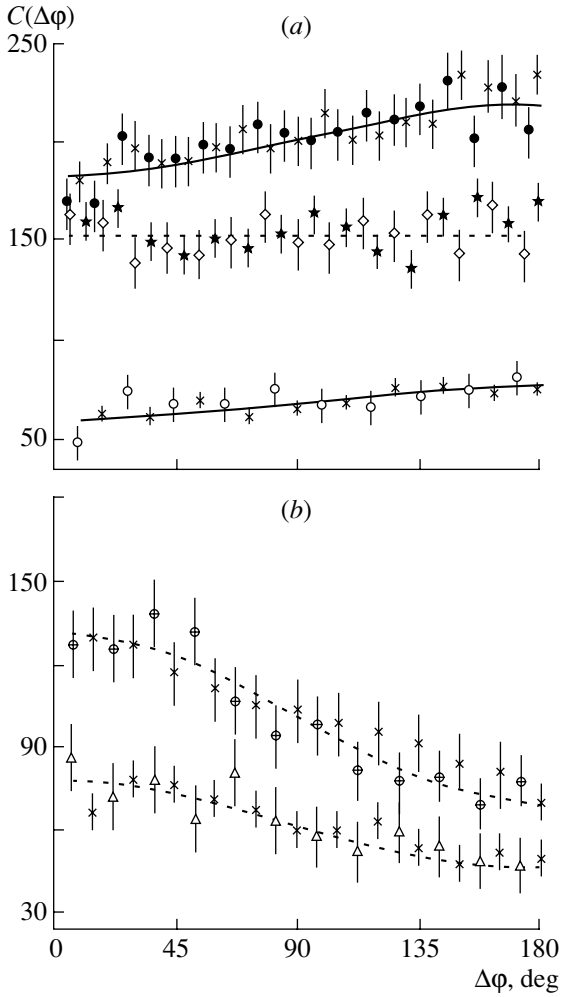

Fig. 3. The correlation function $C(\Delta\varphi)$ for π^- mesons (a) from (○) CNe, (●) MgMg ($n_- > 7$), (◇) MgMg ($n_- \leq 7$) collisions and (b) from (△) CCu, (⊕) OPb collisions; (×, ⋆) are the QGSM data. Solid and dashed curves are the results of the approximation of the data (see text).

CNe and CCu collisions. One can observe from Fig. 2 a clear correlation for protons (correlation increases with $\Delta\varphi$ and reaches maximum at $\Delta\varphi = 180°$). To quantify these experimental results, the data were fitted by

$$C(\Delta\varphi) = 1 + \xi\cos(\Delta\varphi). \qquad (7)$$

The results of the fitting are listed in Table 2. The strength of the correlation is defined as

$$\zeta = C(0°)/C(180°) = (1+\xi)/(1-\xi). \qquad (8)$$

As can be seen from Table 2, the asymmetry coefficient $\xi < 0$ and, thus, the strength of correlation $\zeta < 1$ for protons in both CNe and CCu interactions, meaning the negative correlations of back-to-back preferential emission of protons. Absolute values of ξ increase, and of ζ decrease, when the target mass increases.

A similar negative (back-to-back) correlation was observed by Plastic Ball collaboration at BEVALAC between the slow ($40 < E < 240$ MeV) and fast ($E > 240$ MeV) fragments for symmetric (^{40}Ca $+^{40}$ Ca, ^{93}Nb $+^{93}$ Nb) and asymmetric (^{20}Ne $+^{93}$ Pb) pairs of nuclei in an energy interval of 0.4 to 1-GeV/nucleon [14, 15] and also between protons in pAu collisions at an energy of 4.9 GeV/nucleon [12, 13]. The investigation of large-angle two-particle correlations [16] was carried out at Dubna for collisions of ^{4}He and ^{12}C with different nuclear targets (^{27}Al, ^{64}Cu, and ^{93}Pb) at an energy of 3.6 GeV/nucleon. For protons and deuterons, negative (back-to-back) correlation was observed for all targets. In CC inelastic interactions at a momentum of 4.2 GeV/c per nucleon in the 2-m Propan Bubble Chamber of JINR [17], back-to-back azimuthal correlations between the groups of the particles (protons) emitted in the forward and backward hemispheres in the c.m.s. of the collisions (see Fig. 5a in [17]) were obtained. Protons showed a typical back-to-back (negative) correlation in the p-, O-, and S-induced reactions on different nuclei (Au, Ag, Al, C) at the CERN-SPS (WA80 collaboration) at an energy of 60 and 200 GeV/nucleon [12, 13]. Azimuthal correlations in a target rapidity range of $0.1 \leq y_0 \leq 0.3$ were obtained, and within these limits, no significant change of the correlation functions was observed. We studied the strength of the correlation

Table 3. Values of the asymmetry coefficient (ξ) for protons in CNe and CCu collisions for different intervals of emission angle (θ) and rapidity (y_0)

θ, deg	y_0	CNe	CCu
Central region	0.5–2.5	-0.23 ± 0.05	-0.35 ± 0.05
10–180	0.2	–	-0.22 ± 0.05
	0.3	-0.11 ± 0.03	-0.27 ± 0.05
20–180	0.2	–	-0.13 ± 0.05
	0.3	–	-0.19 ± 0.05
30–180	0.2	–	-0.07 ± 0.01
	0.3	–	-0.09 ± 0.02

Table 4. The number of experimental events (N_{event}) and π^- mesons (N_{π^-}), the asymmetry coefficient (ξ), the strength of the correlation (ζ), and the mean rapidity ($\langle y \rangle$) of π^- mesons ("*" denotes that π^+ mesons are also included)

$A_P A_T$	N_{event}	N_{π^-}	ξ	ζ	$\langle y \rangle$
CNe	723	6209*	-0.08 ± 0.02	0.85 ± 0.08	1.17 ± 0.06
MgMg	6239	50775	-0.09 ± 0.02	0.84 ± 0.09	1.23 ± 0.07
CCu	1866	12390	0.12 ± 0.03	1.29 ± 0.27	0.93 ± 0.06
OPb	732	7023	0.23 ± 0.05	1.61 ± 0.35	0.73 ± 0.07

functions in central CNe and CCu collisions for different rapidities (y_0) and emission-angle (θ) intervals in the laboratory system (see Table 3). One can see from the Table 3 that the absolute values of the asymmetry coefficient decrease from the central rapidity region to the target fragmentation range.

The back-to-back (negative) emission of protons can be understood as resulting from (local) total momentum conservation [13]. This behavior is in a good agreement with the collective nuclear matter flow concept [16].

In view of the strong coupling between the nucleons and pions, it is interesting to know the origin of correlations between pions. The π^- mesons in our experiment were identified nearly unambiguously, and the admixture of e^-, $\bar{p}$, and K^- mesons is almost negligible [4]. We also studied correlations between π^- mesons. For CNe interactions, π^+ mesons were also included into the analysis in order to increase the multiplicity in each event. Correlation functions for π^- mesons in CNe, MgMg, CCu, and OPb interactions are presented in Fig. 3. One can observe from Fig. 3*a* clear back-to-back ($\xi < 0$, $\zeta < 1$, i.e., negative) correlations for pions for a light system of CNe (similar to for the protons in CNe collisions). Study of interactions of the symmetric pair of nuclei MgMg (6239 collisions, 50775 π^- mesons) gives the possibility of a better manifestation of nuclear effects than for the asymmetric pairs of nuclei. For MgMg collisions, back-to-back pion correlations were obtained only for the events with a multiplicity of $n_- > 7$ and no correlations for $n_- \leq 7$ (Fig. 3*a*).

For heavy asymmetric pairs of CCu and OPb nuclei, the side-by-side ($\xi > 0$ and $\zeta > 1$, i.e., positive) correlations of pions can be seen from Fig. 3*b*. Similar side-by-side correlations of pions have been observed in pAu collisions at BEVALAC (4.9 GeV/nucleon) and CERN-SPS (60 and 200 GeV/nucleon) energies [12, 13]. These results agree with that of [18, 19]. Large-angle two-particle correlations carried out at energy of 3.6 GeV/nucleon at JINR [18] for ^{4}He and ^{12}C beams showed negative (back-to-back) pion correlations for the light target (Al) and positive (side-by-side) correlations for the heavy target (Pb) (no correlation for the medium target Cu).

One can see from Tables 2 and 4 that the absolute values of the asymmetry coefficient ($|\xi|$) increase and the strength of correlations (ζ) decreases, while the target mass increases for both proton and pion back-to-back (negative) correlations, in contrast to the results of [13], where back-to-back asymmetry of protons tends to vanish with an increase of the target mass in proton-induced reactions at 200 GeV/c (see Fig. 4 in [13]). For side-by-side (positive) correlations of pions in CCu and OPb collisions, ξ and ζ increase with the target mass due to the increasing amount of matter in their path.

The reason for the observed difference behavior between protons and pions comes from the pion ab-

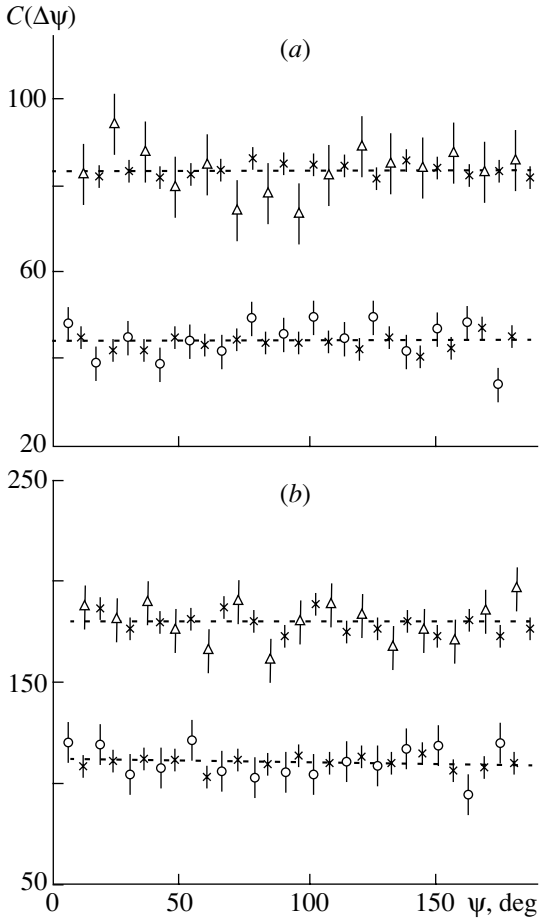

Fig. 4. The correlation function $C(\Delta\psi)$ in CCu collisions for (a) protons and (b) π^- mesons: (○) for particles emitted in the backward hemisphere, (△) for particles emitted in the forward hemisphere; (×) are the QGSM data. Curves are the results of the approximation of the data by first-order polynomials.

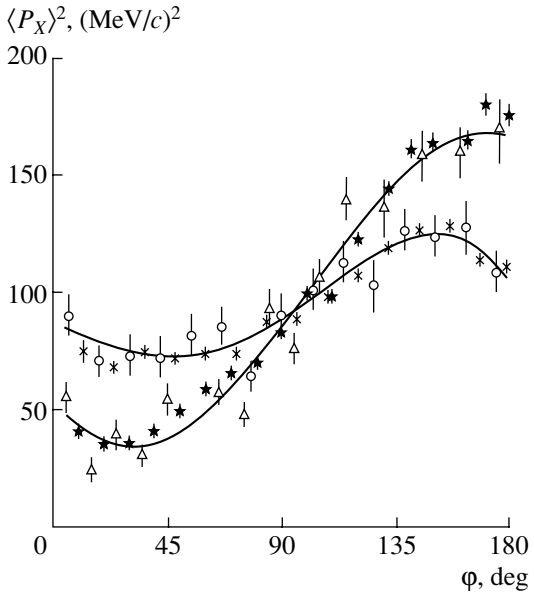

Fig. 5. The dependence of $\langle P_X\rangle^2$ on φ (as described in the text) for protons in (○) CNe and (△) CCu collisions; (×, ⋆) are the QGSM data. Solid curves are the results of the approximation of the data by fourth-order polynomials.

sorption in the excited target matter ($\pi + N \to \Delta$ and $\Delta + N \to N + N$) [12, 13]. While the back-to-back emission of protons can be understood as resulting from transverse momentum conservation, the pion correlations show, in the data, an opposite behavior. The side-by-side correlation of pions can naturally be explained based on the picture that pions, which are created in collision at an impact parameter $b \neq 0$ fm, either suffer rescattering or even complete absorption in the target spectator matter. Both processes will result in a relative depletion of pions in the geometrical direction of the target spectator matter and, hence, will cause an azimuthal side-by-side (positive) correlation as observed in the experimental data. This picture is further supported by calculations within the framework of the RQMD model [20], which includes pion absorption by excited nuclear matter based on experimentally measured cross sections.

The QGSM yields significant azimuthal correlations that follow trends similar to the experimental data (Figs. 2, 3).

To be convinced that the azimuthal correlations in Figs. 2, 3 (for both experimental and QGSM data) between protons and between pions are due to correlations between these particles and cannot be the result of detector biases or finite-multiplicity effects, we obtained data for the dependence of $C(\Delta\psi)$ on ψ for secondaries, where ψ is the angle between the transverse momentum of each particle emitted in the backward (forward) hemisphere and $\mathbf{Q}_B$ ($\mathbf{Q}_F$) vector, respectively. One can see from Fig. 4 that there is no correlation for CCu interactions, both for protons (Fig. 4a) and for pions (Fig. 4b). Similar results were obtained for CNe collisions, too.

As obtained in our previous articles [21–23], the dependence of the mean transverse momentum in the reaction plane $\langle P_X\rangle$ on the normalized rapidity y/y_p in the laboratory system showed the typical S-shape behavior in CNe and CCu collisions for protons and pions. For CNe collisions, $\langle P_X\rangle$ for pions is directed in the same direction as for protons, i.e., flows of protons and pions are correlated, while for CCu interactions, the $\langle P_X\rangle$ of π^- mesons is directed oppositely to that of the protons (antiflow) (see Fig. 1 in [22]). In MgMg central collisions [24], for π^- mesons with a multiplicity of $n_- > 7$, the dependence of $\langle P_X(Y)\rangle$ on Y exhibits an S-shape behavior similar to the form of the $\langle P_X\rangle$ spectra for protons and pions in central CNe collisions.

In order to extend these investigations, we obtained the relation between $\langle P_X \rangle^2$ and the angle φ, where φ is the opening angle between $\mathbf{Q}_B$ and $\mathbf{Q}_F$ vectors. One can see from Fig. 5 that for protons in CNe and CCu collisions, the distributions show an S-shape behavior and slopes of distributions increase with target mass. One can see from Fig. 5 that at $\varphi = 90°$ the values of $\langle P_X \rangle$ not depend on A_T.

5. CONCLUSION

Azimuthal correlations between protons and between pions in central CNe, MgMg, CCu, and OPb collisions have been studied. The results can be summarized as follows:

(i) For protons, back-to-back (negative) correlations have been observed in CNe and CCu interactions. The asymmetry coefficient $\xi(\xi < 0)$ increases, and the strength of correlation $\zeta(\zeta < 1)$ decreases with an increase of the target mass.

(ii) Back-to-back pion correlations have been obtained for light symmetric pairs of nuclei (CNe and MgMg), where the parameters ξ and ζ have the same behavior as protons.

(iii) For heavy pairs of nuclei (CCu and OPb), side-by-side (positive) pion correlations have been observed. The asymmetry coefficient $(\xi > 0)$ and the strength of correlations $(\zeta > 1)$ increase with an increase of the projectile (A_P) and target (A_T) mass.

(iv) The dependence of the square of the mean transverse momentum in the reaction plane, $\langle P_X \rangle^2$, on φ (the angle between the vector sums of the forward and backward emitted particles) shows an S-shaped behavior. Slopes of distributions increase with the target mass.

(v) The QGSM satisfactorily describes azimuthal correlations of protons and π^- mesons for all pairs of nuclei.

ACKNOWLEDGMENTS

We would like to thank M. Anikina, A. Golokhvastov, S. Khorozov, and J. Lukstins for fruitful collaboration during the obtaining of the data. We are very grateful to Z. Menteshashvili for reading the manuscript.

REFERENCES

1. M. Jacob and J. Tran Thanh Van, Phys. Rep. **88**, 325 (1982).
2. H. Stöcker *et al.*, Phys. Lett. B **81B**, 303 (1979).
3. H. A. Gustafsson *et al.*, Phys. Lett. B **142B**, 141 (1984).
4. M. Anikina *et al.*, Preprint No. E1-84-785, JINR (Joint Inst. for Nuclear Research, Dubna, 1984).
5. M. Anikina *et al.*, Phys. Rev. C **33**, 895 (1986).
6. S. Nagamiya and M. Gyalassy, Adv. Nucl. Phys. **13**, 201 (1984).
7. B. A. Li, W. Bauer, and G. Bertsch, Phys. Rev. C **44**, 450 (1991).
8. N. S. Amelin *et al.*, Yad. Fiz. **52**, 272 (1990) [Sov. J. Nucl. Phys. **52**, 172 (1990)].
9. N. Amelin *et al.*,Phys. Rev. C **44**, 1541 (1991).
10. V. V. Anisovich *et al.*, Nucl. Phys. B **133**, 477 (1978).
11. N. S. Amelin, Preprint No. P2-86-837, JINR (Joint Inst. for Nuclear Research, Dubna, 1986).
12. H. R. Schmidt *et al.*, Nucl. Phys. A **544**, 449 (1992).
13. T. C. Awes *et al.*, Phys. Lett. B **381**, 29 (1996).
14. H. A. Gustafsson *et al.*, Z. Phys. A **321**, 389 (1985).
15. P. Beckmann *et al.*, Mod. Phys. Lett. A **2**, 169 (1987).
16. B. P. Adyasevich *et al.*, Nucl. Phys. B (Proc. Suppl.) **16**, 419 (1990); Yad. Fiz. **57**, 268 (1994) [Phys. At. Nucl. **57**, 253 (1994)].
17. A. Kh. Vinitsky *et al.*, Yad. Fiz. **54**, 1636 (1991) [Sov. J. Nucl. Phys. **54**, 1002 (1991)].
18. B. P. Adyasevich *et al.*, Yad. Fiz. **57**, 2057 (1994) [Phys. At. Nucl. **57**, 1981 (1994)].
19. H. Sorge *et al.*, Z. Phys. C **47**, 629 (1990).
20. Th. Lister *et al.*, Preprint No. 94-1, GSI (University of Munster, 1994).
21. L. Chkhaidze *et al.*, Phys. Lett. B **411**, 26 (1997).
22. L. Chkhaidze *et al.*, Phys. Lett. B **479**, 21 (2000).
23. L. Chkhaidze *et al.*, nucl-ex/0008001, submitted to Eur. Phys. J.
24. L. Chkhaidze *et al.*, Eur. Phys. J. A **1**, 2996 (1998).

Physics of Atomic Nuclei, Vol. 65, No. 8, 2002, pp. 1487–1490. Translated from Yadernaya Fizika, Vol. 65, No. 8, 2002, pp. 1523–1527.

ELEMENTARY PARTICLES AND FIELDS
Theory

Diffractive Photoproduction of Charm at the HERA *ep* Collider

A. V. Berezhnoy[1)], V. V. Kiselev[2)], I. A. Korzhavina[1)], and A. K. Likhoded[2)]

Received March 14, 2001; in final form, July 3, 2001

Abstract—For various kinematical domains, the cross section for the diffractive photoproduction of D^* mesons at the HERA *ep* collider is calculated within a model based on perturbation theory. The results obtained by using different models of the Pomeron are compared. © *2002 MAIK "Nauka/Interperiodica".*

From experimental data obtained at the HERA *ep* collider [1, 2], it can be seen that the charm-production model proposed in [3] (hereafter, it is referred to as the BKL model) describes fairly well the inclusive photoproduction and the deep-inelastic production of $D^{*\pm}(2010)$ mesons,[3)] as well as the inclusive photoproduction of D_s mesons over a wide range of kinematical variables.

The problem of describing diffractive charm photoproduction on the basis of the BKL model is now of topical interest in view of the appearance of preliminary ZEUS data on the diffractive photoproduction of D^* mesons [4].

Let us outline the basic features of the BKL model. In this model, the production of D^* mesons proceeds as follows: a c quark and a $\bar{d}$ antiquark, which are then to become valence quarks in the product meson, are first produced perturbatively and after that undergo hadronization through a soft process, forming the meson in question. If these c and $\bar{d}$ are in the singlet state, the hadronization process is described by the expectation value

$$\langle O_{(1)}\rangle = \frac{1}{12M_{D^*}}\left(-g^{\mu\nu}+\frac{p^\mu_{D^*}p^\nu_{D^*}}{M^2_{D^*}}\right) \times \langle D^*(p_{D^*})|(\bar{c}\gamma_\mu d)(\bar{d}\gamma_\nu c)|D^*(p_{D^*})\rangle, \quad (1)$$

where p_{D^*} and M_{D^*} are the D^*-meson momentum and mass, respectively. In the nonrelativistic potential model, this expectation value is equal to the square of the wave function at the origin: $\langle O_{(1)}\rangle|_{\mathrm{NR}} = |\Psi(0)|^2$. The hadronization process in the octet state is described by the expectation value of a similar operator:

$$\langle O_{(8)}\rangle = \frac{1}{8M_{D^*}}\left(-g^{\mu\nu}+\frac{p^\mu_{D^*}p^\nu_{D^*}}{M^2_{D^*}}\right) \times \langle D^*(p_{D^*})|(\bar{c}\gamma_\mu \lambda^a d)(\bar{d}\gamma_\nu \lambda^b c)|D^*(p_{D^*})\rangle\frac{\delta^{ab}}{8}. \quad (2)$$

It should be noted that the BKL model is based on the parton concept of the hadron structure. In the parton model, the valence-quark structure functions in the infinite-momentum frame are given by

$$f^v_c(x,p_T) = f_c(x,p_T) - f_{\bar{c}}(x,p_T), \quad (3)$$
$$f^v_{\bar{d}}(x,p_T) = f_{\bar{d}}(x,p_T) - f_d(x,p_T),$$

where p_T is the parton transverse momentum in the hadron and x is the hadron-momentum fraction carried away by the parton. The mean hadron-momentum fractions carried away by the valence quarks are given by

$$\langle x^v_c\rangle = \int d^2p_T dx\; x\cdot f^v_c(x,p_T) \approx \frac{m_c}{M_{D^*}}, \quad (4)$$
$$\langle x^v_{\bar{d}}\rangle = \int d^2p_T dx\; x\cdot f^v_{\bar{d}}(x,p_T) \approx \frac{\bar{\Lambda}}{M_{D^*}},$$

where $\langle x^v_c\rangle + \langle x^v_{\bar{d}}\rangle \approx 1$ and $\bar{\Lambda}$ is the binding energy of the quarks in the meson. In the BKL model, we neglect the dispersion of the velocities of the valence quarks and set them equal to each other: $v_c = v_{\bar{d}}$; we also take the effective light-quark mass m_d, which plays the role of an infrared cutoff, equal to $\bar{\Lambda}$. As a result, we arrive at

$$\langle x^v_c\rangle = x^v_c = \frac{m_c}{M_{D^*}}, \quad (5)$$
$$\langle x^v_{\bar{d}}\rangle = x^v_{\bar{d}} = \frac{m_d}{M_{D^*}}.$$

The above means that the BKL provides an extension of the parton model to the case of final hadrons in the valence-quark approximation.

This distinguishes the BKL model from the perturbative computations [5–7] based on the fragmentation model of hadronization, where a single c quark produced perturbatively undergoes subsequently hadronization at large distances, transferring,

[1)]Institute of Nuclear Physics, Moscow State University, Vorob'evy gory, Moscow, 119899 Russia.
[2)]Institute for High Energy Physics, Protvino, Moscow oblast, 142284 Russia.
[3)]In what follows, the $D^{*\pm}(2010)$ mesons are denoted by D^*.

to the meson, the fraction z of its transverse momentum k_T with the probability determined by the fragmentation function $D_{c\to D^*}(z,\mu)$ according to the formula

$$\frac{d^2\sigma_{D^*}}{dz dp_T^{D^*}} = \left.\frac{d\hat{\sigma}_{c\bar{c}}(k_T,\mu)}{dk_T}\right|_{k_T=\frac{p_T}{z}} \frac{D_{c\to D^*}(z,\mu)}{z}, \quad (6)$$

where $D_{c\to D^*}(z,\mu)$ is the fragmentation function normalized to the probability $w(c\to D^*)$ measured in [8] that the c quark produced in e^+e^- annihilation transforms into a D^* meson [$w(c\to D^*) = 0.22 \pm 0.014 \pm 0.014$] and the cross section $d\hat{\sigma}_{c\bar{c}}/dk_T$ for the production of a $c\bar{c}$ pair is estimated perturbatively within the parton model at the scale μ.

It is evident that the hadronization of a c quark due to its interaction with the quark sea in the initial hadron (recombination) cannot be taken into consideration in the fragmentation approach; therefore, it must be included within some additional model. In the BKL approach, both the fragmentation and the recombination mechanism are considered in a natural way through a unified set of gauge-invariant diagrams. Fully in accord with the factorization theorem, the fragmentation mechanism is dominant at high transverse momenta of the D^* meson. At low transverse momenta, the main contribution to meson production comes from the recombination process in which the c quark involved merges with a light quark from the sea in the initial hadron. It should be noted that the recombination contribution to the cross section is the highest twist correction to the transverse-momentum distribution; hence, it decreases with increasing the transverse momentum much faster than the fragmentation contribution.

According to experience gained in many studies on the fragmentation model, the results of the calculations do not greatly depend on the form of the fragmentation function. The majority of the studies employed the Peterson fragmentation function [9]

$$D(z) = N\frac{1}{z\left(1-\frac{1}{z}-\frac{\epsilon}{1-z}\right)^2}, \quad (7)$$

where N is a normalization factor and ϵ is a free phenomenological parameter depending on the scale μ. However, the basic result does not change significantly if, instead, use is made of the Kartvelishvili–Likhoded–Petrov fragmentation function [10]

$$D(z) = Nz^{-\alpha_c}(1-z)^{\gamma-\alpha_d}, \quad (8)$$

where $\alpha_c = -3$, $\alpha_d = 1/2$, and $\gamma = 3/2$.

In the BKL model, the cross section for D^*-meson production at high transverse momenta ($p_T^{D^*} > 20$ GeV) can be obtained with the aid of the fragmentation formula (6) by using, for the fragmentation function, the perturbatively motivated expression [11]

$$D_{c\to D^*}(z) = \frac{8\alpha_s^2\langle O^{\rm eff}\rangle}{27m_d^3}\frac{rz(1-z)^2}{(1-(1-r)z)^6} \times [2-2(3-2r)z+3(3-2r+4r^2)z^2 - 2(1-r)(4-r+2r^2)z^3 + (1-r)^2(3-2r+2r^2)z^4], \quad (9)$$

where $r = m_d/(m_d+m_c)$ and

$$\langle O^{\rm eff}\rangle = \langle O_{(1)}\rangle + \frac{1}{8}\langle O_{(8)}\rangle. \quad (10)$$

That meson production in e^+e^- annihilation is due exclusively to the fragmentation mechanism makes it possible to express $\langle O^{\rm eff}\rangle$ in terms of $w(c\to D^*)$ and the quark masses by using the equation

$$w(c\to D^*) = \int_0^1 D_{c\to D^*}(z)dz = \frac{\alpha_s^2(\mu)\langle O_{(1)}(\mu)\rangle}{m_d^3} I(r), \quad (11)$$

where the function $I(r)$ was defined in [3].

The function $w(c\to D^*)$ is known from experimental data; given m_d, m_c, and μ, we can therefore find $\langle O^{\rm eff}\rangle$. If, for example, we have

$$\mu = m_{D^*}, \quad m_d = 0.3\ \text{GeV}, \quad m_c = 1.5\ \text{GeV}, \quad w(c\to D^*) = 0.22, \quad (12)$$

then

$$\langle O^{\rm eff}(m_{D^*})\rangle = 0.25\ \text{GeV}^3.$$

Within this approach, the best description of the data on the photoproduction and deep-inelastic production of charm at the HERA collider is achieved at $\langle O_{(8)}\rangle/\langle O_{(1)}\rangle = 1.3$.

In contrast to the fragmentation model, which is applicable only at high transverse momenta (according to our estimates at $p_T^{D^*} > 20$ GeV), the BKL model works well at low transverse momenta as well. At the above values of the parameters of the BKL model, we have also computed the cross section for diffractive D^*-meson photoproduction, choosing the parametrization of the Pomeron flux factor in the proton in the simplest form [12]

$$f_{\mathbb{P}/p}(x_{\mathbb{P}},t) = \frac{1}{2}\frac{1}{2.3}\frac{1}{x_{\mathbb{P}}} \quad (13)$$

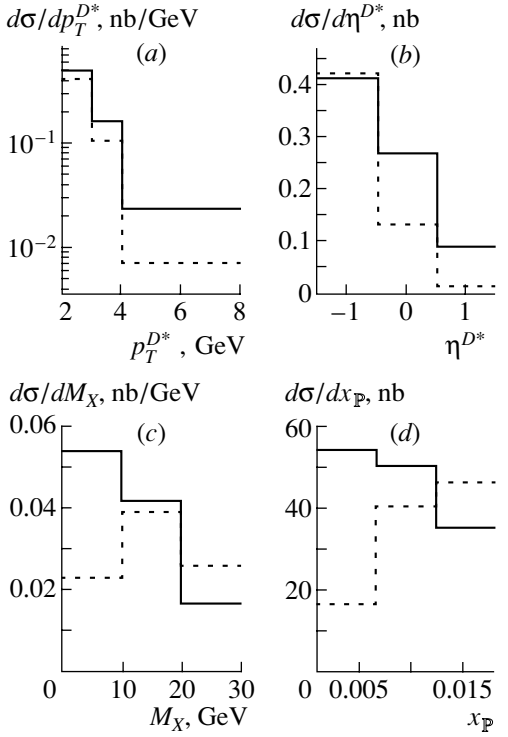

Fig. 1. Predictions of the BKL model for the differential cross sections describing the diffractive photoproduction of D^* mesons in the kinematical domain specified by the inequalities $130 < W < 280$ GeV, $Q^2 < 1$ GeV^2, $p_T^{D^*} > 2$ GeV, $|\eta^{D^*}| < 1.5$, and $0.001 < x_{\mathbb{P}} < 0.018$ [shown are the results obtained with (solid-line histograms) a hard and (dashed-line histograms) a soft Pomeron]: (a) $p_T^{D^*}$ distribution of the cross section, (b) η^{D^*} distribution of the cross section, (c) M_X distribution of the cross section, and (d) $x_{\mathbb{P}}$ distribution of the cross section.

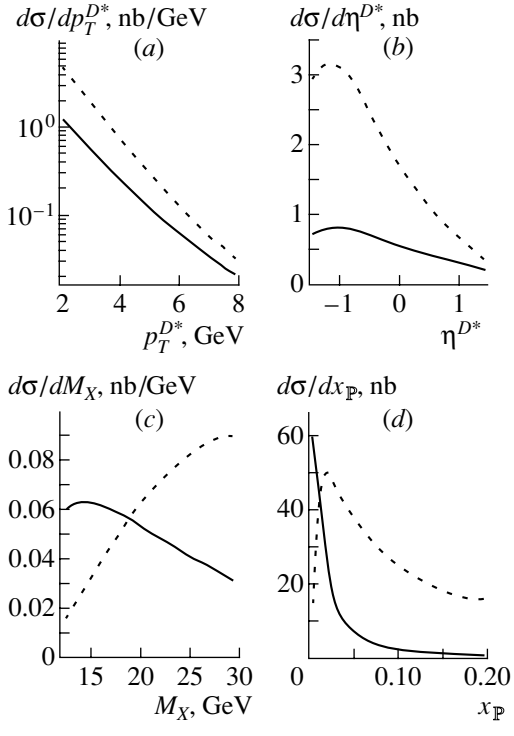

Fig. 2. Predictions of the BKL model for the differential cross sections describing the diffractive photoproduction of D^* mesons in the kinematical domain specified by the inequalities $130 < W < 280$ GeV, $Q^2 < 1$ GeV^2, $p_T^{D^*} > 2$ GeV, $|\eta^{D^*}| < 1.5$, and $0.001 < x_{\mathbb{P}} < 0.2$ [shown are the results obtained with (solid-line histograms) a hard and (dashed-line histograms) a soft Pomeron]: (a) $p_T^{D^*}$ distribution of the cross section, (b) η^{D^*} distribution of the cross section, (c) M_X distribution of the cross section, and (d) $x_{\mathbb{P}}$ distribution of the cross section.

$$\times \left[6.38e^{-8|t|} + 0.424e^{-3|t|}\right],$$

where t is the square of the momentum transfer at the proton vertex and $x_{\mathbb{P}}$ is the proton-momentum fraction carried away by the Pomeron.

Assuming that the Pomeron involves only gluons, we used two forms of the gluon distribution $G(\beta)$ in the Pomeron,

$$\beta G(\beta) = \begin{cases} 6\beta(1-\beta), \text{ hard Pomeron;} \\ 6(1-\beta)^5, \text{ soft Pomeron,} \end{cases} \qquad (14)$$

where β is the Pomeron momentum fraction carried away by a gluon.

We also assumed that the photon and gluon momenta are parallel to the beam axis; this means that, in calculating the amplitude for the photon interaction with the gluon from the Pomeron in the vertex, we neglected the photon, gluon, and Pomeron transverse momenta.

The parameters appearing in (12), which are involved in the calculation of the photon–gluon interaction in the BKL model, were set to values identical to those in [3], where the cross section for D^*-meson photoproduction was evaluated beyond the diffraction approach.

The differential cross sections calculated on the basis of the BKL model are shown in Fig. 1 versus (a) the transverse momentum, (b) the pseudorapidity, (c) the invariant mass M_X of the diffraction system, and (d) $x_{\mathbb{P}}$. These calculations were performed for the cases of a hard and a soft Pomeron for the kinematical domain investigated by the ZEUS collaboration [4] and specified by the inequalities $130 < W < 280$ GeV, $Q^2 < 1$ GeV^2, $p_T^{D^*} > 2$ GeV, $|\eta^{D^*}| < 1.5$, and $0.001 < x_{\mathbb{P}} < 0.018$, where W is the invariant mass of the photon–proton system, Q^2 is the photon virtuality, and η^{D^*} is the pseudorapidity of the D^* meson. The pseudorapidity η^{D^*} is expressed in terms of

the angle θ between the initial-proton momentum and the $D^{*\pm}$-meson momentum as $\eta^{D^*} = -\ln(\tan\theta/2)$.

The transverse-momentum distribution shows that a soft Pomeron yields a faster decrease in the cross section with increasing transverse momentum.

As can be seen from the pseudorapidity distributions, the cross section for the production of a D^* meson with momentum parallel to the primary-proton momentum in the model of a hard Pomeron is substantially larger than that in the model of a soft Pomeron. In the case of backward production, the predictions of the two models are close to each other.

The model of a hard Pomeron leads to an invariant-mass distribution having a maximum at small values of M_X, the cross section becoming smaller with increasing M_X. The distribution in the case of a soft Pomeron peaks at M_X of about 15 GeV.

In the case of a hard Pomeron, the cross section decreases monotonically with increasing $x_{\mathbb{P}}$ over the entire range of $x_{\mathbb{P}}$ under investigation. Conversely, this cross section increases with this variable in the case of a soft Pomeron.

The values of the total cross section that were evaluated within the BKL model for the different Pomerons are

$$\sigma^{\mathrm{BKL}} = \begin{cases} 0.77 \pm 0.02 \ \text{nb, hard Pomeron;} \\ 0.56 \pm 0.03 \ \text{nb, soft Pomeron.} \end{cases}$$

Since the ZEUS collaboration is going to continue studying the diffractive production of D^* mesons, we predict total and differential cross sections over the range $0.001 < x_{\mathbb{P}} < 0.2$ (Fig. 2):

$$\sigma^{\mathrm{BKL}} = \begin{cases} 1.64 \pm 0.02 \ \text{nb, hard Pomeron;} \\ 5.45 \pm 0.02 \ \text{nb, soft Pomeron.} \end{cases}$$

We also predict the total cross sections over the range $0.001 < x_{\mathbb{P}} < 0.1$:

$$\sigma^{\mathrm{BKL}} = \begin{cases} 1.51 \pm 0.03 \ \text{nb, hard Pomeron;} \\ 3.56 \pm 0.03 \ \text{nb, soft Pomeron.} \end{cases}$$

Over the above intervals of $x_{\mathbb{P}}$ values, the difference between the cases of a soft and a hard Pomeron is much more pronounced than the analogous difference over the range $0.001 < x_{\mathbb{P}} < 0.018$, the cross section in the case of a soft Pomeron being much larger than the cross section in the case of a hard Pomeron.

ACKNOWLEDGMENTS

This work was supported in part by the Russian Foundation for Basic Research (project nos. 00-15-96645 and 99-02-16558).

REFERENCES

1. ZEUS Collab. (J. Breitweg *et al.*), Eur. Phys. J. C **6**, 67 (1999).
2. ZEUS Collab. (J. Breitweg *et al.*), Phys. Lett. B **481**, 213 (2000).
3. A. V. Berezhnoy, V. V. Kiselev, and A. K. Likhoded, Phys. Rev. D **62**, 074013 (2000).
4. I. A. Korzhavina (for ZEUS Collab.), Yad. Fiz. **65**, 274 (2002) [Phys. At. Nucl. **65**, 249 (2002)]; hep-ex/0103003.
5. S. Frixione, M. L. Mangano, P. Nason, and G. Ridolfi, Phys. Lett. B **348**, 633 (1995); S. Frixione, P. Nason, and G. Ridolfi, Nucl. Phys. B **454**, 3 (1995).
6. B. A. Kniehl, G. Kramer, and M. Spira, Z. Phys. C **76**, 689 (1997); J. Binnewies, B. A. Kniehl, and G. Kramer, Z. Phys. C **76**, 677 (1997); Phys. Rev. D **58**, 014014 (1998).
7. M. Cacciari and M. Greco, Z. Phys. C **69**, 459 (1996); M. Cacciari, M. Greco, S. Rolli, and A. Tanzini, Phys. Rev. D **55**, 2736 (1997); M. Cacciari and M. Greco, Phys. Rev. D **55**, 7134 (1997).
8. OPAL Collab. (K. Akerstaff *et al.*), Eur. Phys. J. C **1**, 439 (1998).
9. C. Peterson *et al.*, Phys. Rev. D **27**, 105 (1983).
10. V. G. Kartvelishvili, A. K. Likhoded, and V. A. Petrov, Phys. Lett. B **78B**, 615 (1978).
11. C.-M. Chang and Y.-Q. Chen, Phys. Rev. D **46**, 3845 (1992); **50**, 6013 (1994); E. Braaten, K. Cheung, and T. C. Yuan, Phys. Rev. D **48**, 4230 (1993); V. V. Kiselev, A. K. Likhoded, and M. V. Shevlyagin, Z. Phys. C **63**, 77 (1994); T. C. Yuan, Phys. Rev. D **50**, 5664 (1994); K. Cheung and T. C. Yuan, Phys. Rev. D **53**, 3591 (1996).
12. P. Bruni and G. Ingelman, Phys. Lett. B **331**, 317 (1994); in *Proceedings of the EPS International High Energy Physics Conference, Marseille, France, 1993,* Ed. by J. Carr and M. Perrottet (Frontières, Paris, 1993); P. Bruni, G. Ingelman, and A. Solano, in *Proceedings of the Workshop on Physics at HERA,* Ed. by W. Buchmüller and G. Ingelman (DESY, Hamburg, 1991), Vol. 1, p. 363.

Translated by R. Rogalyov

Physics of Atomic Nuclei, Vol. 65, No. 8, 2002, pp. 1491–1500. Translated from Yadernaya Fizika, Vol. 65, No. 8, 2002, pp. 1528–1538.

ELEMENTARY PARTICLES AND FIELDS
Theory

Investigation of the Reaction $pp \to p\pi^+\pi^+\pi^-n$ in the Double-Pion-Exchange Model: Can Pion Exchange Simulate an Exotic State?

A. F. Nilov and V. E. Tarasov*

Institute of Theoretical and Experimental Physics, Bol'shaya Cheremushkinskaya ul. 25, Moscow, 117259 Russia

Received January 29, 2001; in final form, September 29, 2001

Abstract—The reaction $pp \to p\pi^+\pi^+\pi^-n$ at the incident proton momentum of $P_{\rm lab} = 70$ GeV/c, where candidates for an exotic baryon were found, is analyzed in the model involving a double exchange of a Reggeized π meson. The model is tested by using available data on the above reaction at $P_{\rm lab} = 6.92$ and 19 GeV/c. The model provides a satisfactory description of the energy dependence of the reaction cross section. At the same time, it fails to explain the experimentally observed fact that, at $P_{\rm lab} = 70$ GeV/c, the mass spectrum of the $\Delta^{++}\pi^+$ system has peaks at 1.42 and 1.64 GeV/c^2 in the Feynman variable interval $0.5 < x_{\rm F}(p\pi^+\pi^+) < 0.8$. On the basis of the model in question, upper limits on the cross sections for the production of candidates for the exotic baryon E_{55} were estimated at $\sigma_{1.42} \approx 2.3$ μb and $\sigma_{1.64} \approx 1.0$ μb.

1. INTRODUCTION

The most interesting problems in modern elementary-particle physics include searches for exotic hadrons—that is, particles whose quark is not that involving two quarks for mesons or that involving three quarks for baryons. At the moment, the existence of exotic baryons has not yet been proven conclusively, but there are a great many candidates. The E_{55} baryon, which has been sought in a number of experiments (for an overview, see [1]) is one of the candidates in open exotic states. However, the results of these experiments have insufficient statistical significance and often contradict one another. The state in question was sought in the effective-mass spectra of the $p\pi^+\pi^+$ and $n\pi^-\pi^-$ systems in the reactions

$$\pi^+p \to p\pi^+\pi^+\pi^-, \quad pp \to p\pi^+\pi^+\pi^-\pi^-p,$$
$$\pi^-p \to n\pi^+\pi^+\pi^-\pi^-,$$
$$\pi^-d \to n\pi^-\pi^-\pi^+p_s, \quad \pi^+d \to p\pi^+\pi^+\pi^-n_s,$$
$$K^-d \to n\pi^-\pi^-\pi^+\bar{K}^0p_s,$$
$$\pi^+p \to \pi^-(MM)^{+++}, \quad np \to n\pi^+\pi^+\pi^-\pi^-p,$$
$$np \to n\pi^+\pi^+\pi^-\pi^-p\pi^0$$

and in the reaction

$$pp \to p\pi^+\pi^+\pi^-n, \qquad (1)$$

which is considered below.

The E_{55} baryon decays predominantly through the $\Delta\pi$ channel. It is worth noting that the state characterized by the isospin projection 5/2 involves two identical π mesons, in which case the mass spectrum of the $N\pi\pi$ system can develop a maximum owing to the kinematical domain where the effective masses of the systems formed by a nucleon with each of two pions fall within the region of the Δ isobar. It is in terms of precisely this effect that the structure observed in the mass spectrum at $M(p\pi^+\pi^+) \approx 1520$ MeV/c^2 was explained in [2].

The distributions suggesting the possible production of the five-quark E_{55} baryon in the reaction

$$p{\rm Be} \to p\pi^+\pi^+ + X \qquad (2)$$

at the proton-beam momentum of $P_{\rm lab} = 70$ GeV/c were presented in [1]. The main contribution to process (2) (with allowance for the trigger used) comes from the reaction

$$pp \to p\pi^+\pi^+\pi^-n(+m\pi^0) \quad (m = 0, 1, 2, \ldots). \qquad (3)$$

Other reactions were suppressed by the experimental trigger that required the presence of three "fast" and not more than one "slow" charged particle. The possible mechanisms of the production of the E_{55} baryon in reaction (1) can be represented by the Feynman diagrams in Fig. 1.

It was shown in [3–14] that πp and pp interactions that produce less than five particles in the final state are satisfactorily described by the model involving

*e-mail: tarasov@vxitep.itep.ru

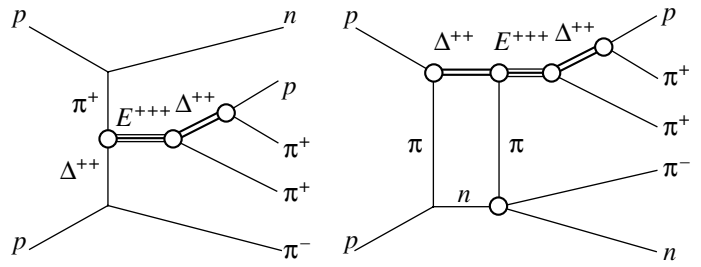

Fig. 1. Mechanisms that can be responsible for the production of the E_{55} baryon in reaction (1).

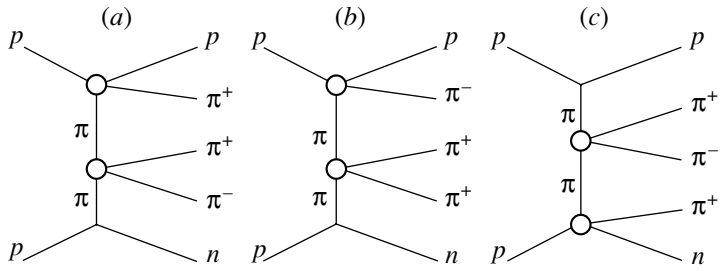

Fig. 2. Three-vertex diagrams involving double pion exchange and contributing to reaction (1).

the t-channel exchange of one Reggeized pion up to rather high energies. It is natural to assume that reaction (1) at $P_{\text{lab}} = 70$ GeV/c also receives a dominant contribution from pion-exchange diagrams. Analysis of such diagrams must answer whether they can produce a maximum in the mass spectrum of the $\Delta\pi$ system near the threshold (Deck effect) and whether a maximum can appear owing to the production of $\rho(770)$ and $f(1270)$ mesons in the $\pi\pi$ system with a large cross section.

In this study, we explore reaction (1) in the model of the Reggeized one-pion exchange.

2. FORMULATION OF THE MODEL

The model of Reggeized one-pion exchange was formulated for the reaction $pp \to pn\pi^+$ [3]. Later, this model and its modifications were used to describe the features of the processes $pn \to pp\pi^-$, $\pi^-p \to \pi^+\pi^-n$, $\pi^-p \to \pi^-\pi^+\pi^-p$, $pp \to pp\pi^+\pi^-$, and $\pi^+p \to \pi^+\pi^-\pi^+p$ [4–10]. An analysis of multiparticle pion production in NN collisions and a qualitative analysis of the inclusive spectra of secondaries from πN and NN collisions were also performed within this conceptual framework. The inclusive spectra in pp collisions and some other relevant quantities were computed in [11]. The calculations in [3–11] employed two-vertex diagrams. Only in [12] was use made of three-vertex diagrams involving double pion exchange. As is illustrated in Fig. 2, such exchanges contribute to reaction (1).

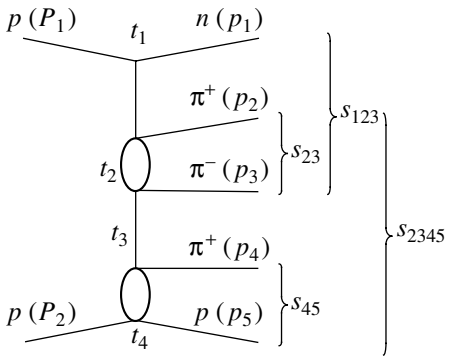

Fig. 3. Diagram illustrating kinematical variables in the matrix element.

Owing to the presence of identical π^+ mesons, the diagram in Fig. 2*a* actually represents two diagrams rather than one and so does the diagram in Fig. 2*c*. Allowance for the symmetry of the colliding particles yields five more diagrams. Therefore, we obtain ten diagrams involving the exchange of two pions. A general Feynman diagram of double pion exchange is shown in Fig. 3, which also indicates physical variables used in the calculations. With allowance for factorization, the matrix element for this diagram can be represented in the form

$$M = \frac{G\sqrt{2}}{t_1 - \mu^2}\bar{u}(p_1)\gamma_5 u(P_1) \tag{4}$$
$$\times T_{\pi_1^+\pi^-}(s_{23}, t_1, t_2, t_3)F_1(t_1, s_{123}, s_{23}, t_2, \ldots)$$
$$\times T_{p\pi_2^+}(s_{45}, t_3, t_4)F_2(s_{2345}, s_{23}, s_{45}, t_3, \ldots)\frac{1}{t_3 - \mu^2},$$

where P_1 and P_2 are the colliding-proton 4-momenta; p_1, p_2–p_4, and p_5 are the 4-momenta of the produced neutron, pions, and proton, respectively; and

$$S = (P_1 + P_2)^2, \quad t_1 = (P_1 - p_1)^2, \tag{5}$$
$$t_2 = (P_1 - p_1 - p_2)^2, \quad t_3 = (P_2 - p_4 - p_5)^2,$$
$$t_4 = (P_2 - p_5)^2, \quad s_{23} = (p_2 + p_3)^2,$$
$$s_{123} = (p_1 + p_2 + p_3)^2, \quad s_{45} = (p_4 + p_5)^2,$$
$$s_{2345} = (P_1 + P_2 - p_1)^2 = (p_2 + p_3 + p_4 + p_5)^2.$$

In (4), G is the coupling constant in the πNN vertex ($G^2/4\pi = 14.6$); $T_{\pi\pi}$ and $T_{\pi p}$ are the $\pi\pi$ and πp scattering amplitudes, respectively; F_1 and F_2 are the form factors that take into account the Reggeization of the pion propagators and off-shell effects in the vertex πNN and the amplitudes $T_{\pi\pi}$ and $T_{\pi p}$; μ is the pion mass; and $\bar{u}(p_1)$ and $u(P_1)$ are the nucleon wave functions (4-spinors).

The $\pi\pi$ and πN scattering amplitudes were set to their on-shell values, apart from the contribution of the vacuum pole P to them. The contributions of the vacuum pole to these amplitudes involve an additional dependence on the masses of virtual π mesons, which is not contained in the form factors F_1 and F_2; that is,

$$T^P_{\pi\pi}(s_{23}, t_1, t_2, t_3) \tag{6}$$
$$= \exp[R_p^2(t_1 + t_3 - 2\mu^2)]T^P_{\pi\pi}(s_{23}, \mu^2, t_2, \mu^2),$$

$$T^P_{\pi N}(s_{45}, t_3, t_4) \tag{7}$$
$$= \exp[R_p^2(t_3 - \mu^2)]T^P_{\pi N}(s_{45}, \mu^2, t_4).$$

In presenting the on-shell $\pi\pi$ and πN scattering amplitudes at high masses [$M(\pi\pi) > 1.4$ GeV/c^2, $M(\pi N) > 2$ GeV/c^2], we employed the Regge parametrization involving the P, P' and ρ poles (see [14]); in the low-mass region, we relied on the results of the partial-wave analysis.

In the linear approximation for the pion trajectory [$\alpha_\pi(t) = \alpha'_\pi(t - \mu^2)$], the form factors were taken in the form

$$F_1 = \exp[(R_1^2 + \alpha'_\pi \ln(s_{123}\kappa^2/s_0 s_{23}))(t_1 - \mu^2)], \tag{8}$$
$$\kappa^2 = \begin{cases} p_{T2}^2 + \mu^2 - C(t_1 - \mu^2) & (p_{L3} < p_{L2}) \\ p_{T3}^2 + \mu^2 - C(t_1 - \mu^2) & (p_{L2} < p_{L3}); \end{cases}$$

$$F_2 = \exp[(R_2^2 + \alpha'_\pi \ln(s_{2345}\kappa_1^2\kappa_2^2/s_0 s_{23} s_{45})) \tag{9}$$
$$\times (t_3 - \mu^2)],$$
$$\kappa_1^2 = \begin{cases} p_{T2}^2 + \mu^2 - C(t_3 - \mu^2) & (p_{L2} < p_{L3}) \\ p_{T3}^2 + \mu^2 - C(t_3 - \mu^2) & (p_{L3} < p_{L2}), \end{cases}$$

$$\kappa_2^2 = p_{T4}^2 + \mu^2 - C(t_3 - \mu^2)$$

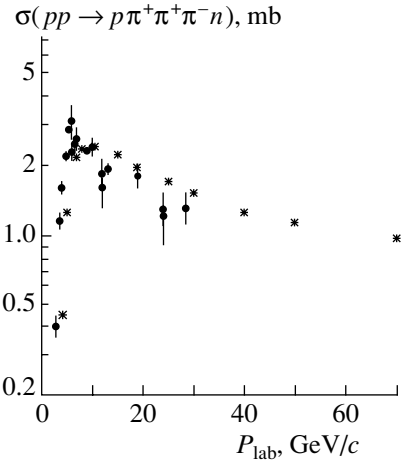

Fig. 4. Cross section for reaction (1) versus the incident-proton momentum: (•) experimental data from [15] and (∗) results of the calculations based on the model presented in the main body of the text.

($s_0 = 1$ GeV/c^2). By p_T and p_L, we have denoted, respectively, the transverse and the longitudinal component of the pion momenta in the c.m. frame of reaction (1), with the z axis being directed along the beam momentum P_1. The condition $p_{L3} < p_{L2}$ in expressions (8) and (9) separates the configuration where the pion of momentum p_2 is faster than the pion of momentum p_3 from the configuration where the inverse relation holds ($p_{L2} < p_{L3}$). The form factors F_1 and F_2 have different forms in these configurations [14].[1)]

3. MODEL PARAMETERS

From the above expressions, it follows that, within the model of Reggeized one-pion exchange, it is necessary to know the parameters R_1^2, R_2^2, α'_π, R_p^2, and C in order to describe reaction (1) proceeding via double pion exchange. In contrast to three- and four-particle reactions considered in [4–10], the block of $\pi\pi$ scattering in reaction (1) involves two virtual incoming pions. Therefore, we can assume that the quantities R_1^2 and R_2^2 defined in the quoted articles are inappropriate for describing the process being studied and must be treated as free parameters of the model. In addition, processes proceeding via pion exchange are known to receive a significant contribution from rescattering. In [13], the slope of the pion trajectory was determined in the pole version [$\alpha'_\pi = 1.11 \pm$

[1)] Expressions (8) and (9) for the form factors F_1 and F_2 were obtained in [14] from an analysis of the regions of two- and three-Reggeon kinematics in exclusive reactions involving the production of, respectively, one pion and two pions.

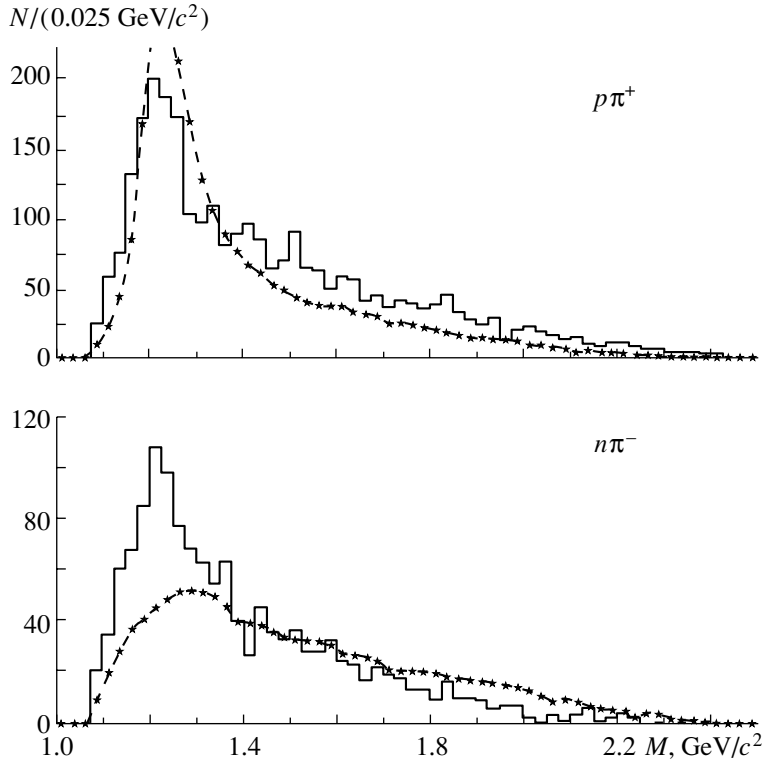

Fig. 5. Effective-mass spectra of the $p\pi^+$ and $n\pi^-$ systems at a primary momentum of 6.92 GeV/c: (histograms) experimental data from [16] and (curves) results of the calculations based on the model used.

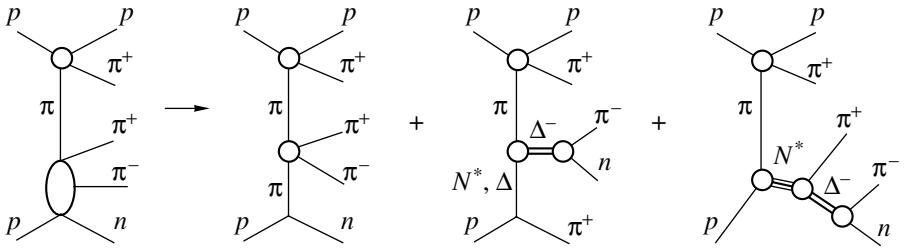

Fig. 6. Diagrams illustrating the mechanisms of the production of a Δ^- isobar in reaction (1) owing to pion–baryon exchange and of the s-channel production of an N^* isobar of mass in the range 1.66–1.69 GeV/c^2.

$0.14\,(\mathrm{GeV}/c)^{-2}$] and with allowance for branch points ($\alpha'_\pi = 0.4 \pm 0.1\,(\mathrm{GeV}/c)^{-2}$).

Taking into consideration the aforesaid, we chose the value of $\alpha'_\pi = 0.5\ (\mathrm{GeV}/c)^{-2}$ for our calculations. The values of $R_p^2 = 1.3\ (\mathrm{GeV}/c)^{-2}$ and $C = 0.08\,(\mathrm{GeV}/c)^{-2}$ were taken from [14]. Since there is no argument on whether one of the parameters R_1^2 or R_2^2 stands out, we changed their values presented in [14] by the same factor in such a way as to describe the absolute value of the cross section for reaction (1). This was achieved at $R_1^2 = 0.4\ (\mathrm{GeV}/c)^{-2}$ and $R_2^2 = 0.16\,(\mathrm{GeV}/c)^{-2}$.

4. COMPARISON WITH EXPERIMENTAL DATA

Figure 4 displays the cross section for reaction (1) versus the incident-proton momentum. Experimental data on the cross section were taken from [15]. Our model calculations were performed with the parameter values given in the preceding section. From Fig. 4, we can see that the model whose parameters are set to values that we found above satisfactorily describes the energy dependence of the cross section for reaction (1) in the primary-momentum range 7–30 GeV/c.

Unfortunately, data on reaction (1) are scanty. We have compared our model predictions for the absolute cross section with the most complete set of experi-

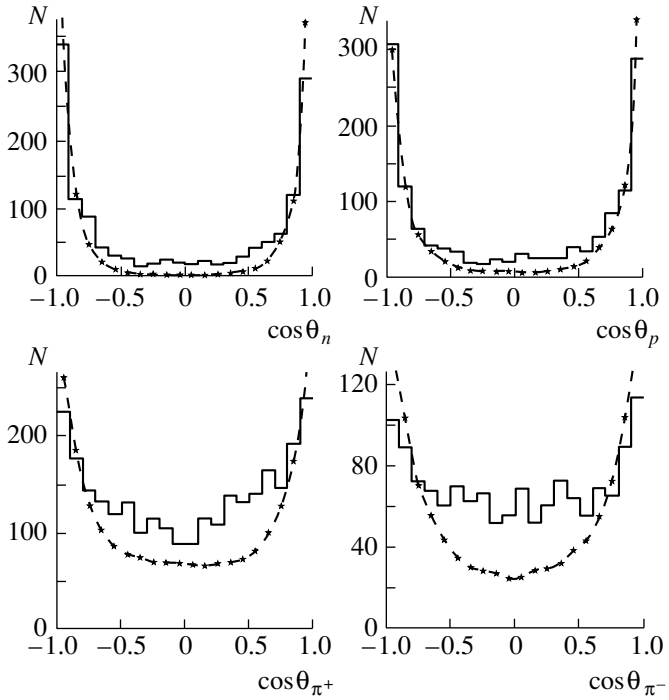

Fig. 7. Distributions with respect to the cosine of the secondary-particle emission angle in the c.m. frame of reaction (1) at a primary momentum of 6.92 GeV/c [16]. The curves represent the results of the model calculations.

mental data obtained at the incident-proton momenta of 6.92 [16] and 19 GeV/c [17].

Figure 5 presents the experimental and the calculated effective-mass spectra of the $p\pi^+$ and $n\pi^-$ systems. It can be seen from this figure that the model describes satisfactorily the mass spectrum of the $p\pi^+$ system, but that it fails to reproduce the mass spectrum of the $n\pi^-$ system in the mass region of the Δ^- isobar. We recall that, in the process being considered, a Δ^- isobar cannot be produced through the pion-exchange mechanism.[2)] It is produced owing to pion–baryon exchange and the s-channel production of the N^* isobar of mass in the range 1.66–1.69 GeV/c^2. The relevant processes are represented by the diagrams in Fig. 6.

Figure 7 displays the distributions with respect to the cosine of the secondary-particle emission angle in the c.m. frame of reaction (1) at a primary momentum of 6.92 GeV/c. It can be seen from the figure that the model qualitatively reproduces the data. However, the calculated distributions are sharper than the experimental ones.

Figure 8 presents the calculated distributions with respect to the proton Feynman variable $x_F(p)$ for various intervals of the neutron variable $x_F(n)$ in the c.m. frame of reaction (1) at an incident-proton momentum of 19 GeV/c. A comparison with the data shows that the contribution of pion exchange is small in the region $0 < x_F(n) < 0.4$. The model reproduces the data in the interval $0.4 < x_F(n) < 0.8$. In the interval $0.8 < x_F(n) < 1$, the position of the maximum in the calculated distribution with respect to $x_F(p)$ agrees with that in the experimental one, but the model overestimates the number of fast neutrons approximately by a factor of 2. Therefore, we can conclude that, at $P_{lab} = 19$ GeV/c, a significant contribution to reaction (1) comes from the processes that are different from pion exchange and which were indicated above.

Concluding this section, we emphasize that the model considered here provides a qualitatively correct description of many features of reaction (1). The application of the model can be of use in pinpointing kinematical regions where mechanisms other than those involving pion exchange are significant in the reaction being considered.

5. INVESTIGATION OF REACTION (1) AT $P_{lab} = 70$ GeV/c

Having tested the model, we now address the main goal of our study—that of clarifying the question of

[2)] It was indicated by G.A. Leksin that, in the model being considered, the Δ^- isobar could have been produced if we had additionally taken into account π^-n final-state interaction (FSI). In this study, however, we did not include FSI effects remaining within the model allowing only for pole diagrams.

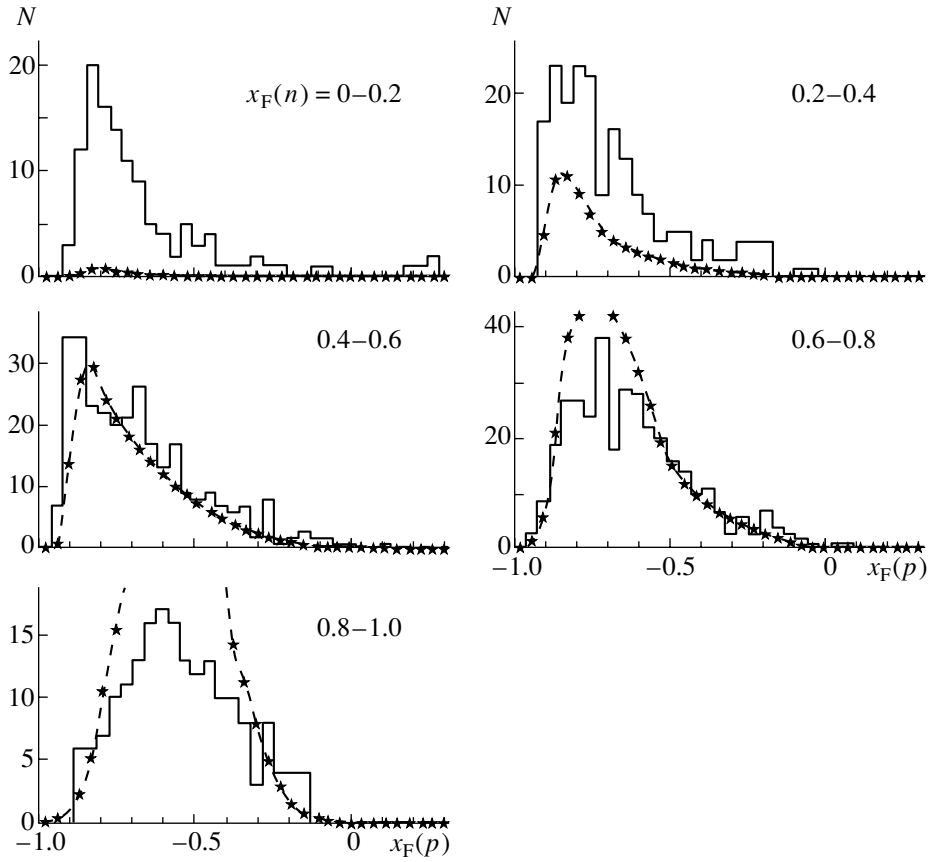

Fig. 8. Distributions with respect to the proton Feynman variable $x_F(p)$ for various selections in the neutron variable $x_F(n)$ in the c.m. frame of reaction (1) at a primary momentum of 19 GeV/c [17]. The curves represent the results of the model calculations.

whether the proposed model approach can reproduce the results obtained in [1] for effective-mass distribution of the $p\pi^+\pi^+$ system. We begin by making a few introductory comments. We have calculated the contributions of various diagrams to the cross section for reaction (1) at a momentum of 70 GeV/c and found that the main contribution to the cross section (about 87%) comes from the diagram in Fig. 2*a*. The contributions of the diagrams in Figs. 2*b* and 2*c* proved to be about 11.5 and 1.5%, respectively. The interference fraction (we took into account only the permutations of identical π^+ mesons) was about 6% of the total cross section for reaction (1). For the total reaction cross section with and without allowance for the interference, we obtained 0.95 (Fig. 4) and 0.90 mb, respectively.

The facility at which the experimental data subjected to the present analysis were obtained imposes a number of geometric and kinematical restrictions, which must be taken into account in order to compare correctly the experimental and the calculated distributions. For example, the calculations must take into account the following conditions of the "on-line" and the "off-line" trigger for the detection of the $p\pi^+\pi^+$ system:

(i) There are only three positively charged particles and no negative particles within the angle 20 mrad around the beam direction.

(ii) The proton momentum exceeds 8 GeV/c (condition of a reliable identification).

(iii) The momentum of a π^+ meson exceeds 3 GeV/c (slower particles are deflected by the magnetic field).

Under these conditions, the calculated integrated efficiency of the facility with respect to the cross section was about 2.5%.

It turned out that, according to condition (ii), the spectrometer did not detect events described by the diagrams featuring a proton in the lower vertex (target fragmentation), because, in this case, the proton momentum in the model varies within the interval 0–4.5 GeV/c, its distribution having a maximum close to zero. For the remaining diagrams, the momentum spectrum of pions in the model peaks near zero, has a shape close to that of a hyperbola, and extends to approximately 50–55 GeV/c; 40 to 50% of their

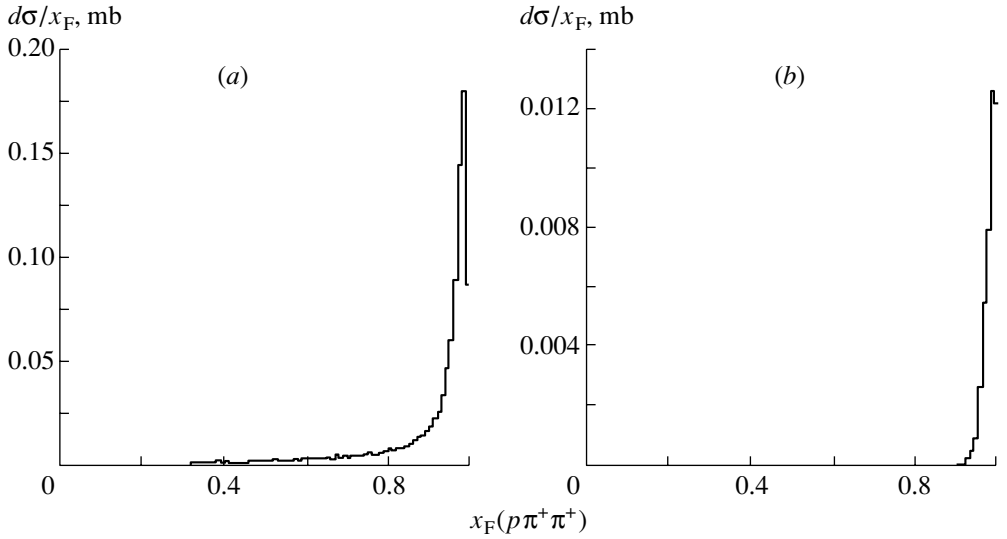

Fig. 9. Distributions with respect to the Feynman variable of $p\pi^+\pi^+$ system, $x_F(p\pi^+\pi^+)$, according to the calculation within the model based on five diagrams with allowance for the interference: (*a*) results of the calculation for 4π geometry and (*b*) results of the calculation that takes into account the conditions of detection and event processing [conditions (i)–(iii) in the main body of the text].

tracks have momenta below 3.5 GeV/c and are not detected by the facility according to condition (iii). For the remaining five diagrams, the momentum distribution of protons also has the shape of a hyperbola; it begins approximately from 14 GeV/c, grows to a maximum at about 66–67 GeV/c, and then abruptly tends to zero. Owing to the addition of the positive longitudinal components of the π^+ momenta to the longitudinal momentum of the proton, the resulting distribution with respect to the variable x_F of the $p\pi^+\pi^+$ system is sharper and is concentrated more closely to the edge $x_F = 1$. Figure 9*a* displays the $x_F(p\pi^+\pi^+)$ distribution calculated within the model on the basis of five diagrams (with allowance for interference) for 4π geometry. Upon taking into account the event-detection and event-processing conditions [conditions (i), (ii), and (iii)], the distribution changes significantly. As can be seen from Fig. 9*b*, all this results in that the spectrum $x_F(p\pi^+\pi^+)$ is entirely concentrated in the narrow interval $0.9 < x_F(p\pi^+\pi^+) < 1$.

Table 1 presents results of our model calculations for the cross section describing the production of the $p\pi^+\pi^+$ system in the mass interval 1.3–3.2 GeV/c^2 for various intervals of the variable $x_F(p\pi^+\pi^+)$, the mass of the $p\pi^+$ system being selected in the region of the Δ isobar (1.17–1.27 GeV/c^2). For the same kinematical regions, Table 2 gives the experimental numbers of respective events (no absolute normalization of the cross sections is imposed).

A comparison of the data in the two tables shows that the experimental dependence of the cross section on the variable $x_F(p\pi^+\pi^+)$ differs significantly from the model dependence. The model cross section calculated with allowance for the trigger decreases fast with decreasing x_F and virtually vanishes in the interval 0.5–0.8. Owing to the multiperipheral character of the model, the calculated cross section is exponentially suppressed by the form factors (8) and (9) in this region. At the same time, the experimental dependence of the cross section on $x_F(p\pi^+\pi^+)$ is rather weak. A significant part of the experimental cross section is concentrated in the interval 0.5–0.8; this suggests the existence of other particle-production mechanisms.

We recall that the experimental mass spectrum of the $\Delta^{++}\pi^+$ system [1] featured an excess of events above the polynomial background curve. Figure 10 displays this mass spectrum for the interval $0.5 < x_F(p\pi^+\pi^+) < 0.8$ of the Feynman variable of the $p\pi^+\pi^+$ system. The smooth solid curve in Fig. 10 corresponds to a description of the spectrum by the background and two resonances, while the dashed curve represents the background. The parameters of the enhancements are $M_1 = 1.42 \pm 0.14$ GeV/c^2, $\Gamma_1 = 0.064 \pm 0.02$ GeV/c^2, $M_2 = 1.64 \pm 0.02$ GeV/c^2, and $\Gamma_2 = 0.025 \pm 0.016$ GeV/c^2. The excess of the number of events over the background curve is above eight standard deviations in the band 1.38–1.46 GeV/c^2 and above four standard deviations in the band 1.60–1.66 GeV/c^2. This result was interpreted as an observation of candidates for five-quark states.

Table 1. Results of the model calculations for the cross sections (mb) describing the production of the $p\pi^+\pi^+$ system in reaction (1) at $P_{\text{lab}} = 70$ GeV/c within various kinematical regions

Interval of $x_F(p\pi^+\pi^+)$	$\Delta(p\pi_f^+)$		$\Delta(p\pi_s^+)$		$\Delta(p\pi_f^+) + \Delta(p\pi_s^+)$	
	4π geometry	trigger + selections	4π geometry	trigger + selections	4π geometry	trigger + selections
0.5–0.7	9.8×10^{-4}	8.8×10^{-24}	2.6×10^{-3}	1.6×10^{-26}	3.58×10^{-3}	8.8×10^{-24}
0.7–0.8	6.1×10^{-4}	1.5×10^{-9}	2.2×10^{-3}	1.7×10^{-9}	2.81×10^{-3}	3.2×10^{-9}
0.8–0.85	3.4×10^{-4}	3.5×10^{-7}	1.9×10^{-3}	4.1×10^{-7}	2.24×10^{-3}	7.6×10^{-7}
0.85–0.9	5.3×10^{-4}	2.0×10^{-5}	3.1×10^{-3}	2.8×10^{-5}	3.63×10^{-3}	4.8×10^{-5}
0.9–0.95	1.3×10^{-3}	3.4×10^{-4}	5.9×10^{-3}	4.4×10^{-4}	7.2×10^{-3}	7.8×10^{-4}
0.95–1.0	7.45×10^{-3}	6.3×10^{-3}	2.14×10^{-2}	8.3×10^{-3}	2.89×10^{-2}	1.46×10^{-2}

Note: $\Delta(p\pi_i^+)$ columns present the cross sections for the case where the mass is selected in the region of the Δ isobar, $1.17 < M(p\pi_i^+) < 1.27$ GeV/c^2; $\Delta(p\pi_f^+) + \Delta(p\pi_s^+)$ column contains the sum of the results for the $\Delta(p\pi_f^+)$ and $\Delta(p\pi_s^+)$ bands.

Of course, a kinematical maximum in the effective-mass spectrum of the $\Delta^{++}\pi^+$ system can arise owing to the presence of two identical π^+ mesons and the choice of narrow bands in the effective-mass spectra of $p\pi_f^+$- and $p\pi_s^+$ systems. In order to explore this kinematical region, we have constructed the experimental distribution (see Fig. 11) with respect to the effective mass $M(\Delta^{++}\pi^+)$ for events where both $M(p\pi_f^+)$ and $M(p\pi_s^+)$ fall within the band of the Δ isobar (1.17–1.27 GeV/c^2). The mean mass of the $p\pi^+\pi^+$ system proved to be $M = 1.508 \pm 0.011$ ГэВ/c^2 in this case. This value, which is associated with the effect of the overlap of Δ bands, agrees with the mean mass for the excess of events in the mass spectrum of the $\Delta^{++}\pi^+$ system in the range $0.95 < x_F(p\pi^+\pi^+) < 1$ (see Fig. 12*a*). In Fig. 12*a*, the histogram represents the experimental data, along with statistical errors, while the dashed curve corresponds to the polynomial background. In the low-mass region in Fig. 12*a*, there is a significant excess of the number of events above the background curve. In order to describe the experimental spectrum, we added a Breit–Wigner distribution. The solid curve in Fig. 12*a* represents the results of a fit to the data by using a superposition of the background and a Breit–Wigner curve. The widths of the mass spectrum $M(\Delta^{++}\pi^+)$ in Fig. 11

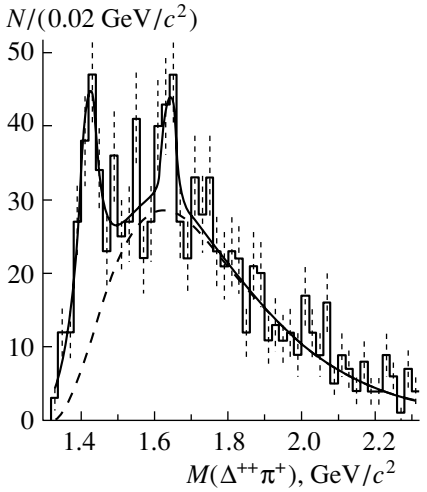

Fig. 10. Mass spectrum of the $\Delta^{++}\pi^+$ system for the interval $0.5 < x_F(p\pi^+\pi^+) < 0.8$ in the c.m. frame of reaction (3) at a primary momentum of 70 GeV/c: (histogram) experimental data from [1], (solid curve) description of the data by two resonances and a polynomial background, and (dashed curve) background contribution.

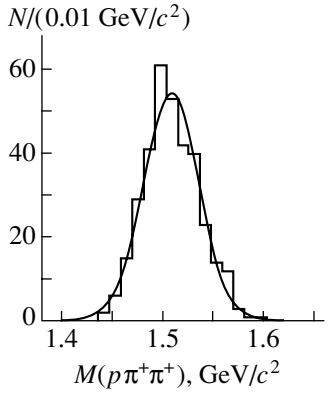

Fig. 11. Effective-mass distribution of the $p\pi^+\pi^+$ system for the simultaneous selection of the effective masses of $p\pi_f^+$ and $p\pi_s^+$ systems in the Δ-isobar band 1.17–1.27 GeV/c^2 {reaction (3) at a primary momentum of 70 GeV/c [1]}. The solid curve represents a Gaussian fit to the experimental spectrum.

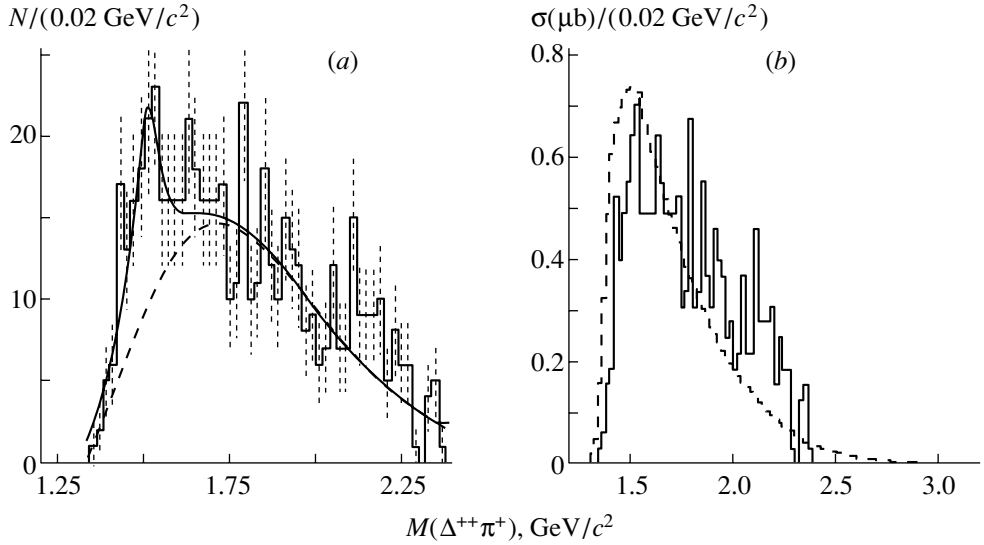

Fig. 12. Mass spectrum of the $\Delta^{++}\pi^+$ system for the interval $0.95 < x_\mathrm{F}(p\pi^+\pi^+) < 1$. The histograms represent experimental data on reaction (3) at a primary momentum of 70 GeV/c [1]. The solid curve in Fig. 12*a* illustrates an approximation of the data by a polynomial background and a Breit–Wigner resonance, the background contribution being shown individually in this panel by the dashed curve. The dashed curve in Fig. 12*b* represents the results of our model calculations.

and of the excess of events (over the background) in Fig. 12*a* are also commensurate with each other. For example, the width in the case of the overlap of the Δ bands in Fig. 11 is $\Gamma = 0.078 \pm 0.064$ GeV/c^2; that for the excess of events in Fig. 12*a* is $\Gamma = 0.067 \pm 0.039$ GeV/c^2. There is a similar correspondence for the number of events: 80 events occur in the overlap of the Δ bands, and 78 events correspond to the excess in the mass spectrum of $\Delta^{++}\pi^+$ in the range $0.95 < s_\mathrm{F}(p\pi^+\pi^+) < 1$. The model gives a similar distribution for the case of the overlap of the Δ bands: $M \approx 1.510$ GeV/c^2 and $\Gamma \approx 0.110$ GeV/c^2.

We have compared the model prediction with the experimental data in the Feynman variable interval $0.95 < x_\mathrm{F} < 1$ for the $p\pi^+\pi^+$ system, where pion exchange must be dominant. Figure 12*b* displays the experimental mass spectrum $M(\Delta^{++}\pi^+)$ (identical to that in Fig. 12*a*) and the model distribution (dashed curve) normalized to the area below the experimental histogram. It can be seen from the figure that, by and large, the model distribution is concentrated in the low-mass region and completely covers the experimental spectrum in the mass region $M(\Delta^{++}\pi^+) < 1.8$ GeV/c^2. Therefore, it is meaningless to consider the excess of events in the mass region around 1.5 GeV/c^2. We deem that this is a nice illustration of usefulness of model calculations, although their agreement with experimental data is not sufficiently good. There are two reasons to be emphasized: the statistical significance of the experimental data is insufficient, and the model involves no mechanisms that could produce N^* isobars decaying through three-particle channels, for example, into $\Delta\pi$ and $N\rho$ systems.

Table 2. Number of events of reaction (3) at $P_\mathrm{lab} = 70$ GeV/c that were observed experimentally for various selections

Interval of $x_\mathrm{F}(p\pi^+\pi^+)$	$\Delta(p\pi_f^+)$	$\Delta(p\pi_s^+)$	$\Delta(p\pi_f^+) + \Delta(p\pi_s^+)$
0.5–0.7	193	380	573
0.7–0.8	180	329	509
0.8–0.85	139	187	326
0.85–0.9	171	239	410
0.9–0.95	199	349	538
0.95–1.0	277	362	639

Assuming that, in the range $0.95 < x_\mathrm{F}(p\pi^+\pi^+) < 1$, our model describes the absolute values of the reaction cross section, we used this cross section as a normalization to estimate the contributions of other physical mechanisms in the reaction being studied. By estimating the absolute normalization of an individual event in this way, we have obtained an upper limit on the production cross section for the experimentally observed structures (Fig. 10): $\sigma_{1.42} \approx 2.3\ \mu$b and $\sigma_{1.64} \approx 1.0\ \mu$b. These values may be overestimated, and we consider them as upper limits. Indeed, in considering the data on reaction (1) at 19 GeV/c (Section 4), we have already emphasized the possible

existence of reaction mechanisms other than those represented by the diagrams in Fig. 2. Therefore, our normalization of the model to the total cross sections for reaction (1) (see Fig. 4) means that the contribution to the cross section from the diagrams in Fig. 2 may be overestimated: these diagrams correspond to the peripheral part of the process—that is, to a smaller cross section.

6. CONCLUSION

For the first time, we have applied the model of Reggeized one-pion exchange to describing reaction (1). Here, we formulate the results of our study.

The model describes satisfactorily the energy dependence of the cross section for reaction (1) at incident-proton momenta in the range $7 < P_{\text{lab}} < 30$ GeV/c and qualitatively reproduces many features of the reaction at $P_{\text{lab}} = 6.92$ and 19 GeV/c.

The model can be used as a background to study other physical mechanisms in reaction (1).

In the interval $0.95 < x_{\text{F}}(p\pi^+\pi^+) < 1$, the model reproduces qualitatively the behavior of the spectrum of the $\Delta^{++}\pi^+$ system that originates from reaction (3) at a primary momentum of 70 GeV/c, yielding a peak in the cross section near the mass value of about 1.5 GeV/c^2 (Fig. 12*b*). Thus, there are no grounds to interpret this peak as that which is associated with a candidate for an exotic baryon.

Despite the intense production of the Δ^{++} isobar and of $\rho(770)$ and $f_0(1270)$ mesons owing to pion exchange, the model fails to explain the narrow structures in the mass spectrum of the $\Delta^{++}\pi^+$ system (Fig. 10), which were observed experimentally at a primary momentum of 70 GeV/c in the Feynman variable range $0.5 < x_{\text{F}}(p\pi^+\pi^+) < 0.8$. This might have been expected since the model involves no mechanisms that could lead to the resonance production of the $p\pi^+\pi^+$ system. Moreover, the model makes a very small contribution to the cross section in this region (for the specific experiment with its specific geometric and triggering conditions and specific physical selections) and does not describe the background contribution, which is relatively large in the experiment being discussed (see the dashed curve in Fig. 10). All this is a consequence of a multiperipheral character of the model.

The model provides a reasonable description of the data in the range $0.95 < x_{\text{F}}(p\pi^+\pi^+) < 1$ at a primary momentum of 70 GeV/c; in this region, we can estimate the absolute normalization of the cross section for experimental events. In this way, the model has been used to estimate upper limits on the cross sections for the production of candidates for exotic E_{55} baryons (excesses of events over the background curve in Fig. 10). They proved to be $\sigma_{1.42} \approx 2.3$ μb and $\sigma_{1.64} \approx 1.0$ μb.

Of course, the discovery of an exotic baryon would be an important milestone in the understanding of elementary-particle physics.

ACKNOWLEDGMENTS

We are grateful to A.B. Kaidalov, V.Z. Kolganov, G.A. Leksin, G.S. Lomkatsi, and V.T. Smolyankin for stimulating discussions.

REFERENCES

1. A. F. Nilov, Preprint No. 63-95, ITEP (Institute of Theoretical and Experimental Physics, Moscow, 1995).
2. M. Yu. Bogolyubski *et al.*, Preprint No. 86-219, IHEP (Institute for High Energy Physics, Protvino, 1986).
3. K. G. Boreskov, A. B. Kaĭdalov, V. I. Lisin, *et al.*, Yad. Fiz. **15**, 361 (1972) [Sov. J. Nucl. Phys. **15**, 203 (1972)].
4. K. G. Boreskov, A. P. Gasparyan, A. B. Kaĭdalov, *et al.*, Yad. Fiz. **15**, 557 (1972) [Sov. J. Nucl. Phys. **15**, 309 (1972)].
5. K. G. Boreskov, A. B. Kaĭdalov, and L. A. Ponomarev, Yad. Fiz. **17**, 1285 (1973) [Sov. J. Nucl. Phys. **17**, 669 (1973)].
6. A. F. Nilov, T. A. Garanina, G. S. Lomkatsi, and L. A. Ponomarev, Yad. Fiz. **22**, 583 (1975) [Sov. J. Nucl. Phys. **22**, 302 (1975)].
7. A. N. Kamalov and L. A. Ponomarev, Yad. Fiz. **23**, 1072 (1976) [Sov. J. Nucl. Phys. **23**, 566 (1976)].
8. K. G. Boreskov, A. B. Kaidalov, and L. A. Ponomarev, in *Elementary Particles: Proceedings of the First ITEP School in Physics* (Atomizdat, Moscow, 1973), Vol. 2, p. 94.
9. L. A. Ponomarev, Yad. Fiz. **22**, 807 (1975) [Sov. J. Nucl. Phys. **22**, 418 (1975)].
10. K. G. Boreskov, V. V. Glagolev, V. N. Emel'yanenko, *et al.*, Preprint No. R1-8164, OIYaI (Joint Inst. for Nuclear Research, Dubna, 1974).
11. K. G. Boreskov, A. A. Grigoryan, and A. B. Kaĭdalov, Yad. Fiz. **24**, 789 (1976) [Sov. J. Nucl. Phys. **24**, 411 (1976)].
12. A. F. Nilov, Preprint No. 173-87, ITEP (Institute of Theoretical and Experimental Physics, Moscow, 1987).
13. V. M. Guzhavin, M. S. Dubovikov, A. V. Lebedev, and A. F. Nilov, Yad. Fiz. **19**, 401 (1974) [Sov. J. Nucl. Phys. **19**, 199 (1974)].
14. L. A. Ponomarev, Fiz. Élem. Chastits At. Yadra **7**, 186 (1976) [Sov. J. Part. Nucl. **7**, 70 (1976)].
15. V. Flaminio *et al.*, CERN–HERA 8401 (1984).
16. G. Yekutieli, S. Toaff, A. Shapira, *et al.*, Nucl. Phys. B **18**, 301 (1970).
17. R. Boggild, E. Dahl-Jensen, I. Dahl-Jensen, *et al.*, Nucl. Phys. B **91**, 365 (1975).

Translated by M. Kobrinsky

Physics of Atomic Nuclei, Vol. 65, No. 8, 2002, pp. 1501–1512. From Yadernaya Fizika, Vol. 65, No. 8, 2002, pp. 1539–1550.

ELEMENTARY PARTICLES AND FIELDS
Theory

Conserved Currents of the Three-Reggeon Interaction*

D. R. Karakhanyan[1)] and R. Kirschner[2)]

Received November 30, 2000; in final form, July 25, 2001

Abstract—We consider an extension of Lipatov's conjecture about the deep relation between amplitudes in the high-energy limit of QCD (gluodynamics) and *XXX* Heisenberg chains with noncompact spins to the case of presence fermions (quarks). © *2002 MAIK "Nauka/Interperiodica"*.

1. INTRODUCTION

In Regge theory the high-energy asymptotic behavior of the hadron–hadron scattering amplitudes are determined by singularities of partial waves in the complex angular momentum plane. It was observed [1] that the regularity of quantum mechanics, which relates high-energy scattering amplitudes to the singularities of the partial waves in the complex angular momentum plane, is valid for quantum field theory as well. Namely, in Regge kinematics

$$s \gg -t \sim M^2, \tag{1}$$

where M is a characteristic hadronic mass scale, s and t are famous Mandelstam variables, $s = (p_1 + p_2)^2$ is the energy of the scattered particles in the center-of-mass system, and $t = p - p_1'$ is the momentum transferred, the hadron-hadronic scattering amplitude $A(s,t)$

$$A(s,t) = is \int\limits_{\epsilon - i\infty}^{\epsilon + i\infty} \frac{dJ}{2\pi i} \left(\frac{s}{M^2}\right)^J f(J,t) \tag{2}$$

is governed by singularities of the partial waves $f(J,t)$, by Regge poles and Regge cuts. Among the Regge singularities, there is one with vacuum quantum numbers, the so-called Pomeron, which provides the dominant contribution to the scattering amplitude. The bootstrap conjecture has been proposed, according to which all particle-like excitations correspond to some Regge singularity and are related to each other via unitarity of the S matrix and sum rules.

However, the program of building the axiomatic quantum field theory from assumptions of only unitarity and analyticity of the S matrix failed, because Regge theory itself does not allow one to calculate the positions of these singularities. Now, QCD as a theory of strong interaction is called to describe the Regge behavior of the scattering amplitudes [2]. V.N. Gribov proposed the conjecture that Reggeons form new collective excitations and QCD in the high-energy limit can be replaced by an effective Reggeon theory [3]. This has been confirmed in a series of works, initiated by Lipatov [4]. It was shown that, in the leading logarithmic approximation (LLA), which is the natural approximation in the Regge limit of QCD, $A(s,t)$ can be expressed as a sum of Feynman diagrams describing the multiple exchange of Reggeized gluons in the t channel. The perturbative expressions for corresponding Feynman diagrams including large logarithmic factors $\alpha^n \log^m s$ ($m = n, n-1, \ldots$) have to be resummed to all orders in α_s (α is the strong coupling constant), because bare gluons and quarks are not a good approximation in the Regge limit. The leading contribution ($m = n$) comes from ladder diagrams, corresponding to the exchange of n Reggeons in t channel. Being built from an infinite number of perturbative gluons, the Reggeons carry the quantum numbers of the gluon and become a new collective excitation in the Regge limit (1). It is well known that the LLA results in an asymptotic behavior that violates the Froissart bound. Unitarity is restored by taking into account subleading contributions as well. In the generalized LLA (GLLA) some minimal set of nonleading terms is included to restore unitarity [5]. The interaction of the Reggeons is determined by LLA.

In LLA, the dominant contribution to the partonic scattering amplitude comes from the soft gluons and this leads to the gluon Reggeization property. It can be shown that infrared divergences are canceled for colorless external states due to gauge invariance.

Of course the distribution of partons inside the hadron is described by the nonperturbative wave function of the hadron. The nonperturbative effects can be taken into account in the approach

*This article was submitted by the authors in English.

[1)]Erevan Physics Institute, Armenia.

[2)]Naturwissenschaftlich-Theoretisches Zentrum und Institut für Theoretische Physik, Universität Leipzig, Germany.

of constructing the high-energy effective action [6]. However, the perturbative investigation of high-energy QCD makes sense as a first approximation to begin with. In particular, the results obtained in the BFKL (Balitskii, Fadin, Kuraev, Lipatov) Pomeron approximation are in a good agreement with experimental data of semihard processes and especially of deep-inelastic scattering at small x. Then, some information about nonperturbative corrections can be extracted from analyzing the behavior of the perturbative series in the infrared region [7].

2. HIGH-ENERGY QCD AS AN INTEGRABLE MODEL

As mentioned above, the high-energy asymptotic behavior of the scattering amplitude in LLA is determined by the contribution of diagrams describing two-Reggeon exchange in the t channel. It is a result of summing up an infinite number ladder diagrams [4] and corresponds to the exchange of the Pomeron. Contributions of diagrams with three (Odderon) and more Reggeized gluons can be considered as higher corrections. Pomeron contribution corresponds to elastic scattering. Diagrams with Odderon exchange describe processes with the exchange of negative-charge parity.

The dominating contribution in LLA comes from the multi-Regge kinematics:

$$\begin{gathered} s = (p_A + p_B)^2 \approx 2p_A \cdot p_B, \qquad (3)\\ s_i = (k_i + k_{i+1})^2 \approx 2k_i \cdot k_{i-1},\\ i = 1, \ldots, n+1, \quad k_0 = p_A,\\ k_i = q_{i+1} - q_i, \quad k_{n+1} = p_B,\\ s \gg s_i \gg |\, q_i \,|^2,\\ s_1 s_2 \cdots s_{n+1} = s\prod_{i=1}^{n}(-k_{\perp i}^2),\\ k_1 \cdot p_A \ll k_2 \cdot p_A \ll \ldots \ll k_n \cdot p_A,\\ k_1 \cdot p_B \gg k_2 \cdot p_B \gg \ldots \gg k_n \cdot p_B, \end{gathered}$$

where p_A and p_B are momenta of initial particles, while k_i, $i = 1, \ldots, n$, are momenta of final ones, and $k_\perp$ is defined by the Sudakov decomposition

$$k^\mu = \frac{k \cdot p_A}{p_A \cdot p_B} p_B^\mu + \frac{k \cdot p_B}{p_A \cdot p_B} p_A^\mu + k_\perp^\mu.$$

Owing to this decomposition, the scattering amplitudes in the Regge limit exhibit the remarkable separation of the longitudinal and transverse directions with respect to the plane spanned by the momenta of the initial particles.

In the GLLA, the interaction between Reggeons is elastic and pairwise. We shall restrict ourselves to the case where the number of Reggeons in the t channel N is conserved. For a given N the Reggeon Green's function $f_{\{i_k\}}$, describing the elastic scattering of N Reggeons, satisfies the Bethe–Salpeter-like equation [5]

$$\omega f_{\{i_k\}} = f^{(0)}_{\{i_k\}} + \sum_{i<j} \mathcal{H}^{(i,j)}_{\{i_k\},\{j_k\}} f_{\{j_k\}}, \qquad (4)$$

where $f^{(0)}_{\{i_k\}}$ correspons to the free propagation of N Reggeons in the t channel.

The set $\{i_k\} = (i_1 \ldots i_r)$ labels the Reggeons, $i = G$ stands for gluon, and $i = F$ or $i = \bar{F}$ stands for Reggeized quarks of corresponding helicity. The partial wave f carries also an index α_i, labeling the gauge group representation of the corresponding Reggeons, and depends on their transverse momenta $k_{\perp i}$ or their impact parameters x_i.

The r-Reggeon contribution to the partial wave is obtained by contracting the r-Reggeon Green's function with the parton distribution functions of the scattered particles. The angular momentum is

$$J = 1 + \omega - \frac{r_f}{2}, \qquad (5)$$

where r_f is the number of exchanged fermions. The pairwise interaction of the Reggeons is described by the Hamiltonian

$$\begin{gathered} \mathcal{H}^{(i,j)} f_{i_1 \ldots i \ldots i_r} = \frac{g^2}{(2\pi)^3} \qquad (6)\\ \times \int dk_i' dk_j' \delta(k_i + k_j - k_i' - k_j')\\ \times [(T_i \otimes T_j)_{\mathcal{H}} \mathcal{H}_{i,j} f_{i_1 \ldots i \ldots j \ldots i_r}\\ + (T_i \otimes T_j)_{\mathcal{G}} \mathcal{G}_{ij} f_{i_1 \ldots i \ldots j \ldots i_r}]; \end{gathered}$$

T_i^a, $a = 1, \ldots, n$, is $SU(n)$ generators in representation of i Reggeon. The first term in the square brackets corresponds to the interaction via an s-channel gluon:

$$\begin{gathered} (T_i \otimes T_j)_{\mathcal{H}_{\{\alpha_k, \alpha_k'\}}} \qquad (7)\\ = \prod_{k \neq i,j}^{r} \delta_{\alpha_k, \alpha_k'} (T^a)_{\alpha_i \alpha_i'} (T^a)_{\alpha_j \alpha_j'}; \end{gathered}$$

therefore, the gauge group matrix is obtained from the generators by summing over the gluon color states a. The second one corresponds to the interaction via an s-channel fermion, and the gauge group matrix is obtained by summing over the fermion color state α (say, if $i = G$ and $j = F$):

$$\begin{gathered} (T_i \otimes T_j)_{\mathcal{G}_{\{\alpha_k, \alpha_k'\}}} \qquad (8)\\ = \prod_{k \neq i,j}^{r} \delta_{\alpha_k, \alpha_k'} (T^{\alpha_i'})_{\alpha_i \alpha} (T^{\alpha_j})_{\alpha \alpha_j'}. \end{gathered}$$

The explicit expressions for $\mathcal{H}$ and $\mathcal{G}$ are given below. The overall group state in the t channel has to be the gauge singlet.

While the longitudinal part of the scattering amplitude is extracted as a kinematical factor, the transverse dynamical part can be described by simple Feynman rules, corresponding to the multi-Reggeon effective action [6]. These graphical rules allow the simple derivation of the interaction kernels in Eq. (6). As operators in impact space, these kernels take the following form

$$\begin{gathered}\mathcal{H}_{GG} = H_G + H_G^*, \qquad (9)\\ \mathcal{H}^{\omega}_{F\bar{F}} = H^{\omega}_F + \mathcal{P}_{12}H^{*(\omega)}_F\mathcal{P}_{12},\\ \mathcal{H}_{FF} = H_G + H^*_F,\\ \mathcal{H}_{FG} = H_G + \mathcal{P}_{12}H^*_F\mathcal{P}_{12},\\ \mathcal{G}_{FG} = (x^*_{12}\partial^*_2)^{-1},\end{gathered}$$

where

$$\begin{gathered}H_G = -2\psi(1) + \partial_1^{-1}\log x_{12}\partial_1 \qquad (10)\\ + \partial_2^{-1}\log x_{12}\partial_2 + \log\partial_1\partial_2,\\ H^{\omega}_F = -2\psi(1) + \partial_1^{-1+\omega/2}\log x_{12}\partial_1^{1-\omega/2}\\ + \partial_2^{-\omega/2}\log x_{12}\partial_2^{\omega/2} + \log\partial_1\partial_2,\end{gathered}$$

and $\psi(1) = -\gamma$ is the Euler number, derivatives are defined over impact space parameters x_1 and x_2, "$*$" stands for complex conjugation, and $\mathcal{P}_{12}$ represents the operator permuting the Reggeons 1 and 2.

Lipatov [8] solved equations for wave functions of compound states of n Reggeized gluons using the quantum inverse-scattering method. The eigenvalue problem related to the operators (10) arises because the position of the singularities in ω of the t-channel partial wave $f_{\{i_k\}}$ is determined by their eigenvalues.

Lipatov proposed to diagonalize the problem of N-Reggeon exchange by establishing the correspondence between the operators (10) and the *XXX* Heisenberg model. He noticed that the operator H_G has two equivalent representations:

$$\begin{gathered}H_G = \partial_1^{-1}\log x_{12}\partial_1 + \partial_2^{-1}\log x_{12}\partial_2 \qquad (11)\\ + \log\partial_1\partial_2 - 2\psi(1) = x_{12}\log\partial_1\partial_2 x_{12}^{-1}\\ + 2\log x_{12} - 2\psi(1),\end{gathered}$$

and therefore the transposed operator can be represented in two different ways as follows:

$$\begin{gathered}(H_G)^T = \partial_1\log x_{12}\partial_1^{-1} + \partial_2\log x_{12}\partial_2^{-1} \qquad (12)\\ + \log\partial_1\partial_2 - 2\psi(1) = \partial_1\partial_2 H_G(\partial_1\partial_2)^{-1}.\end{gathered}$$

On the other hand, we have

$$\begin{gathered}(H_G)^T = x_{12}^{-1}\log\partial_1\partial_2 x_{12} \qquad (13)\\ + 2\log x_{12} - 2\psi(1) = x_{12}^{-2}H_G x_{12}^2.\end{gathered}$$

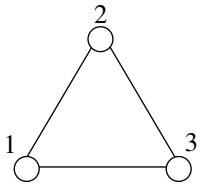

Fig. 1.

Then, we can deduce

$$[H_G; \mathcal{C}^{00}] = 0, \quad \mathcal{C}^{00} = x_{12}^2\partial_1\partial_2. \qquad (14)$$

This equation expresses the fact of conformal invariance of H_G. Indeed, this operator coincides with Casimir operator of $SL(2)$ of zero conformal weights $\mathcal{C}^{00}$. Then it is reasonable to denote H_G as H^{00}.

The Hamiltonian

$$\begin{gathered}H_{123} = H^{00}_{12} + H^{00}_{23} + H^{00}_{31} \qquad (15)\\ = \partial_1^{-1}\log x_{31}x_{12}\partial_1 + \partial_2^{-1}\log x_{12}x_{23}\partial_2\\ + \partial_3^{-1}\log x_{23}x_{31}\partial_3 + 2\log\partial_1\partial_2\partial_3 - 6\psi(1)\\ = x_{12}\log\partial_1\partial_2 x_{12}^{-1} + x_{23}\log\partial_2\partial_3 x_{23}^{-1}\\ + x_{31}\log\partial_1\partial_3 x_{31}^{-1} + 2\log x_{12}x_{23}x_{31} - 6\psi(1)\end{gathered}$$

corresponds to the exchange of three Reggeized gluons (Fig. 1).

The transposition gives

$$\begin{gathered}(H_{123})^T = \partial_1\partial_2\partial_3 H_{123}(\partial_1\partial_2\partial_3)^{-1} \qquad (16)\\ = (x_{12}x_{23}x_{31})^{-1}H_{123}x_{12}x_{23}x_{31};\end{gathered}$$

i.e., it commutes with the operator A_3:

$$[H_G; A_3] = 0, \quad A_3 = x_{12}x_{23}x_{31}\partial_1\partial_2\partial_3. \qquad (17)$$

Notice that operator A_3 is the commutator of partial Casimir operators of the chain links:

$$A_3 = [\mathcal{C}^{00}_{12}, \mathcal{C}^{00}_{31}] = [\mathcal{C}^{00}_{23}, \mathcal{C}^{00}_{12}] = [\mathcal{C}^{00}_{31}, \mathcal{C}^{00}_{23}]. \qquad (18)$$

Therefore, Eq. (17) is a consequence of (18) and the Jacobi identity. It is easy to check that the N-Reggeon Hamiltonian

$$H_N = \sum_{i=1}^{N} H_{i,i+1}, \quad H_{N,N+1} \equiv H_{N,1}, \qquad (19)$$

commutes with

$$A_N = \left(\prod_{i=1}^{N-1} x_{i\,i+1}\right)\left(\prod_{j=1}^{N}\partial_j\right). \qquad (20)$$

It can be checked also that H_N commutes with $\mathcal{C}_N$,

$$\mathcal{C}_N = \sum_{1\le i<j\le N} x_{ij}^2\partial_i\partial_j. \qquad (21)$$

The eigenvalue problem:

$$\tilde{A}\Psi_\Delta(x_1,x_2,x_3)=\tilde{a}\Psi_\Delta(x_1,x_2,x_3), \quad (22)$$
$$\tilde{\mathcal{C}}\Psi_\Delta(x_1,x_2,x_3)=\Delta(1-\Delta)\Psi_\Delta(x_1,x_2,x_3);$$

here, Δ stands for the total conformal weight of Reggeon state under consideration. The set of equations above can be considered instead of the original eigenvalue problem:

$$\tilde{H}_{123}\Psi_\Delta(x_1,x_2,x_3)=\tilde{E}_{123}\Psi_\Delta(x_1,x_2,x_3), \quad (23)$$

which looks to be much more complicated.

The eigenproblem $\mathcal{C}_N\Psi_N=D_N\Psi_N$ expresses the conformal invariance of the N-Reggeon system and suggests the connection with the isotropic $sl(2)$ Heisenberg model with N sites and cyclic boundary conditions, because $\mathcal{C}_N$ can be identified with the Casimir operator of this symmetry algebra.

Lipatov has related to each site of the Heisenberg chain the following Lax operator

$$L_i=\begin{pmatrix}\lambda+S_i^0 & S_i^-\\ -S_i^+ & \lambda-S_i^0\end{pmatrix}, \quad (24)$$

where the $sl(2)$ spin operators S_i^a

$$[S_i^0;S_j^\pm]=\pm\delta_{ij}S_i^\pm, \quad [S_i^+;S_j^-]=-2\delta_{ij}S_i^0 \quad (25)$$

are represented as differential operators

$$S_i^+=x_i^2\partial_i+2\Delta_i x_i, \quad (26)$$
$$S_i^0=x_i\partial_i+\Delta_i, \quad S_i^-=\partial_i,$$

and λ is the spectral parameter. The Lax operator (21) satisfies the Yang–Baxter equation. Therefore, the trace of the monodromy matrix

$$T(\lambda)=\prod_{i=1}^{N}L_i(\lambda) \quad (27)$$

is the generating function for the set of N mutually commuting differential operators Q_k:

$$Q_k=\sum_{i_1<i_2<\ldots<i_k}x_{i_1i_2}x_{i_2i_3}\ldots x_{i_ki_1}\partial_{i_1}\partial_{i_2}\ldots\partial_{i_k}. \quad (28)$$

Now, it is plausible enough that all operators Q_k commute with the Hamiltonian and the latter can be represented as a function of Q_k. Explicit calculations for low-N cases and additional mathematical arguments [9] confirm this. Moreover, the relation between the high-energy QCD kernels and the *XXX* Heisenberg spin chains turns out to be much deeper. Namely, this connection can be extended to the case where fermions are incorporated. The ideas of conformal symmetry in Regge asymptotic behavior [10] have been developed in application to the fermion exchange in [11].

3. REVIEW OF INTEGRABLE CHAINS

Let us review the main facts of the theory of integrable systems concerning the *XXX* Heisenberg magnet. In our review, we shall follow Sklyanin's work [12]. The phenomenon of the integrability of quantum systems can be understood by means of their relation to linear ones via separation of variables. Namely, a quantum system is integrable if its nonlinear equations of motion can be represented as the zero-curvature conditions of some integrable linear system [13]. Physically this means that the interaction of such systems reduces to elastic scattering and the only result of it consists in the exchange of quantum numbers (momenta, etc.) of the scattered particles. Accordingly, the S matrix of the theory is factorized into the product of blocks, corresponding to $2\to2$ scattering and also $1\to1$ in the presence of a boundary [14].

A set of (annihilation) operators $Z_a(\lambda)$ satisfying the Zamolodchikov algebra

$$Z_a(\lambda)Z_b(\mu)=S_{ab,cd}(\lambda-\mu)Z_d(\mu)Z_c(\lambda), \quad (29)$$

where S is an $n^2\times n^2$ matrix, has been proposed for an algebraic description of the factorizable scattering. The consistency condition of this system, which follows from the associativity property of the triple product $Z_{a_1}(\lambda_1)Z_{a_2}(\lambda_2)Z_{a_3}(\lambda_3)$, is the Yang–Baxter equation for the S matrix:

$$S_{a_ja_k}(\lambda_j-\lambda_k)S_{a_ja_l}(\lambda_j-\lambda_l)S_{a_ka_l}(\lambda_k-\lambda_l) \quad (30)$$
$$=S_{a_ka_l}(\lambda_k-\lambda_l)S_{a_ja_l}(\lambda_j-\lambda_l)S_{a_ja_k}(\lambda_j-\lambda_k).$$

Extending this algebra by adding n conjugated (creation) operators $Z_a^\dagger(\mu)$, one gets the Zamolodchikov–Faddeev algebra

$$Z_a(\lambda)Z_b^\dagger(\mu)=\delta_{ab}\delta(\lambda-\mu) \quad (31)$$
$$+Z_c^\dagger(\mu)\hat{S}_{ac,bd}(\lambda-\mu)Z_d(\lambda),$$

or, in matrix notation,

$$A(\lambda)\otimes A(\mu)\equiv A_1(\lambda)A_2(\mu) \quad (32)$$
$$=S_{12}(\lambda-\mu)A_2(\mu)A_1(\lambda),$$
$$A_1^\dagger(\lambda)A_2^\dagger(\mu)=A_2^\dagger(\mu)A_1^\dagger(\lambda)S_{21}^\dagger(\mu-\lambda),$$
$$A_1(\lambda)\otimes A_1^\dagger(\mu)=I_1\delta(\lambda-\mu)$$
$$+A_2^\dagger(\mu)\hat{S}_{12}(\mu-\lambda)A_2(\lambda),$$

where $A(\lambda)$ and $A^\dagger(\mu)$ are the column $(Z_1(\lambda),\ldots,Z_n(\lambda))^t$ and the row $(Z_1^\dagger(\mu),\ldots,Z_n^\dagger(\mu))$, correspondingly; subscripts refer to the corresponding isotopic spaces $\mathbb{C}^n\otimes\mathbb{C}^n\equiv V_1V_2$ and $S_{21}=\mathcal{P}S_{12}\mathcal{P}$, $\hat{S}_{12}=\mathcal{P}S_{12}$; and $\mathcal{P}$ is the permutation operator in $\mathbb{C}^n\otimes\mathbb{C}^n$. The complete scattering matrix $S(\{\lambda_k\})$ of the M particles is then factorized into the ordered product

of $M(M-1)/2$ two-particle S matrices (29). For example, the S matrix of the jth particle on the other $M-1$ particles is given by $t(\lambda_j;\{\lambda_m\})$, i.e., the particular value of the transfer matrix for $\lambda=\lambda_j$:

$$t(\lambda;\{\lambda_m\}) = \mathrm{tr}_a T(\lambda;\{\lambda_m\}) \equiv \mathrm{tr}_a \prod_k S_{ak}(\lambda-\lambda_k). \tag{33}$$

The trace in this expression is taken over the auxiliary space V_a, while the transfer matrix acts in the quantum space $\otimes_{k=1}^{M} V_k$. In the framework of the quantum inverse-scattering method (QISM) [12, 15], instead of the original nonlinear problem, the auxiliary linear one is considered:

$$\frac{d}{dx}T(\lambda,x) = L(\lambda,x)T(\lambda,x) \tag{34}$$

or

$$T(n+1,\lambda) = L_{n+1}(\lambda)T(n,\lambda)$$

in the discrete case. This is the Lax operator of the QISM [16]. The solution of (34),

$$T(\lambda,x) = P\exp\left(\int^{x} L(\lambda,y)dy\right) \tag{35}$$

or

$$T(n,\lambda) = L_n(\lambda)L_{n-1}(\lambda)\ldots L_1(\lambda)$$

in the discrete case, defines the monodromy matrix $T(\lambda)$. Its entries are the new variables (the quantum scattering data), whose commutation relations are defined by

$$\sum_{j_1,j_2=1}^{n} R_{i_1i_2,j_1j_2}(\lambda-\mu)T_{j_1k_1}(\lambda)T_{j_2k_2}(\mu) = \sum_{j_1,j_2=1}^{n} T_{i_2j_2}(\mu)T_{i_1j_1}(\lambda)R_{j_1j_2,k_1k_2}(\lambda-\mu). \tag{36}$$

We see that integrable systems are specified by the R matrix, which acts on $\mathbb{C}^n\otimes\mathbb{C}^n$ and satisfies the Yang–Baxter equation

$$\sum_{j_1,j_2,j_3=1}^{n} R_{i_1i_2,j_1j_2}(\lambda)R_{j_1i_3,k_1j_3}(\lambda+\mu) \times R_{j_2j_3,k_2k_3}(\mu) = \sum_{j_1,j_2,j_3=1}^{n} R_{i_2i_3,j_2j_3}(\mu) \times R_{i_1j_3,j_1k_3}(\lambda+\mu)R_{j_1j_2,k_1k_2}(\lambda). \tag{37}$$

In general, the R matrix depends on the spectral parameter λ and other parameters. Although there is no complete mathematical theory of the Yang–Baxter equation, a variety of solutions are known as well as different fields of their application. They are classified by the Lie algebra, its irreducible representations, and the spectral parameter dependence: rational, trigonometric, and elliptic ones [17]. Given a solution $R(\lambda)$, one can define the quadratic algebra $\mathcal{T}_R$ of $n\times n$ matrix elements T_{ij}, which is generated by Eq. (36). The associative algebra $\mathcal{T}_R$ realizes the representation space of a quantum integrable system. The commutative integrals of motion are $t(\lambda) = \mathrm{tr}T(\lambda)$, which follows from (36), taking the trace of $T_1T_2 = R_{12}^{-1}T_2T_1R_{12}$. The algebra $\mathcal{T}_R$ possesses the comultiplication property: If $T_1(\lambda)$ and $T_2(\lambda)$ are two representations of $\mathcal{T}_R$ in the quantum spaces V_1 and V_2, then the matrix

$$T_{ik}(\lambda) = T_{1,ij}(\lambda)T_{2,jk}(\lambda) \tag{38}$$

is a representation of $\mathcal{T}_R$ in the tensor product $V_1\otimes V_2$. This property allows one to represent $T(\lambda)$ as a product of elementary representations, the so-called Lax operators $L_i(\lambda)$. The Lax operator makes a shift by one step along the chain:

$$L_n(\lambda)\psi_n = \psi_{n+1}.$$

Hence, the full product $T(\lambda) = \prod_{n=1}^{N} L_{N+1-n}(\lambda)$ defines the full monodromy along the closed chain. It follows from $sl(2)$ symmetry of the R matrix that an arbitrary constant $d\times d$ matrix K provides the simplest representation of the algebra $\mathcal{T}_R$. This algebra has a central element, the quantum determinant of $T(\lambda)$:

$$\begin{aligned}\Delta(\lambda) \equiv \det_q T(\lambda) &= D(\lambda+\eta/2) \times A(\lambda-\eta/2) - B(\lambda-\eta/2)C(\lambda+\eta/2)\\ &= A(\lambda-\eta/2)D(\lambda+\eta/2) - C(\lambda-\eta/2) \times B(\lambda+\eta/2) = A(\lambda+\eta/2)D(\lambda-\eta/2)\\ &- B(\lambda+\eta/2)C(\lambda-\eta/2) = D(\lambda+\eta/2) \times A(\lambda-\eta/2) - C(\lambda+\eta/2)B(\lambda-\eta/2).\end{aligned} \tag{39}$$

Here, η is some model parameter and we used the representation of the monodromy matrix as a block matrix

$$T(\lambda) = \begin{pmatrix} A(\lambda) & B(\lambda) \\ C(\lambda) & D(\lambda)\end{pmatrix}$$

in order to define the quantum determinant which has the following remarkable properties:

$$\det_q T_1(\lambda)T_2(\lambda) = \det_q T_1(\lambda)\det_q T_2(\lambda) \tag{40}$$

and

$$\det_q K = \det K. \tag{41}$$

The next representation is given by the Lax operator, mentioned above, which takes an especially

simple form for the XXX spin chain:

$$L(\lambda) = \lambda + \eta \sum_{\alpha=1}^{3} S_\alpha \sigma_\alpha \qquad (42)$$
$$= \begin{pmatrix} \lambda + \eta S^0 & \eta S^- \\ -\eta S^+ & \lambda - \eta S^0 \end{pmatrix},$$

where operators S_α belonging to some irreducible representation of $sl(2)$ have commutation relation (26). Note that the R matrix itself can be chosen as a Lax operator if the auxiliary space is two-dimensional. We have

$$\det_q L(\lambda) = \lambda^2 - \eta^2(\mathcal{C} + 1/4), \qquad (43)$$
$$\mathcal{C} = (S^0)^2 - \frac{1}{2}(S^+S^- + S^-S^+).$$

Since the $L(\lambda)$ operator, being the elementary representation of $\mathcal{T}_R$, satisfies the Yang–Baxter relation and the R matrix depends only on the difference of the spectral parameters, the shift $L(\lambda) \to L(\lambda - \omega)$ defines an automorphysm in $\mathcal{T}_R$:

$$R(\lambda - \omega_1 + S_1^\alpha \sigma_\alpha)(\lambda - \omega_2 + S_2^\beta \sigma_\beta) \qquad (44)$$
$$= (\lambda - \omega_2 + S_2^\beta \sigma_\beta)(\lambda - \omega_1 + S_1^\alpha \sigma_\alpha) R.$$

Separating the terms linear in λ in this equation, one deduces that the R matrix is $sl(2)$-invariant,

$$[R; S_1^\alpha + S_2^\alpha] = 0, \qquad (45)$$

and depends only on difference $\omega_{12} = \omega_1 - \omega_2$. The $sl(2)$ invariance implies that the R matrix has to have the form

$$R = \sum \rho_j(\omega_{12}) P_j, \qquad (46)$$

where P_j are the projectors corresponding to the decomposition of the tensor product of two initial representations into the sum of irreducible representations labeled by spin j.

Furthermore, after separating the λ dependence in Eq. (44), the terms which contain no λ are combined into an equation which gives the recurrence relation for $\rho_j(\omega_{12})$:

$$\rho_{j+1}(\omega_{12}) = \frac{\omega_{12} + \eta(j+1)}{\omega_{12} - \eta(j+1)} \rho_j(\omega_{12}), \qquad (47)$$

which determines R up to a scalar factor.

Particular solutions of the Yang–Baxter equation have properties that are important for different applications, but which are not necessarily valid for a given solution. These are the property of regularity,

$$R(0) = \rho(0)^{1/2} \mathcal{P}_{12};$$

the property of P symmetry,

$$\mathcal{P} R_{12}(\lambda) \mathcal{P} \equiv R_{21}(\lambda) = R_{12}(\lambda);$$

the property of T symmetry,

$$R_{12}^{t_1 t_2}(\lambda) = R_{12}(\lambda);$$

the property of unitarity,

$$R_{12}(\lambda) = R_{21}(-\lambda) = \rho(\lambda) I;$$

the property of crossing symmetry,

$$R_{12}(\lambda) = V_{(1)} R_{12}^{t_2}(-\lambda - \eta) V_{(1)}^{-1};$$

and the semiclassical property,

$$R(\lambda, \eta) = I + \eta r(\lambda) + \mathcal{O}(\eta^2).$$

Here, the superscript t_i denotes matrix transposition in space V_i, $r(\lambda)$ is the classical R matrix, $\rho(\lambda)$ is an even scalar function, η is the crossing parameter, and V determines the crossing matrix $M \equiv V^t V = M^t$. The quasiclassical property gives rise to the direct connection of the quantum model to the corresponding classical one. Many R matrices have only the combined PT symmetry: $R_{12}^t(\lambda) = R_{21}(\lambda)$. The regularity is used to extract from $t(\lambda)$ the local integrals of motion.

Thus, the general solution to (44) is given by

$$T(\lambda, \boldsymbol{\omega}) \qquad (48)$$
$$= K L_N(\lambda - \omega_N) \dots L_2(\lambda - \omega_2) L_1(\lambda - \omega_1)$$
$$= \begin{pmatrix} A(\lambda) & B(\lambda) \\ C(\lambda) & D(\lambda) \end{pmatrix}.$$

It can be easily checked step by step using (44) because any permutation of the multipliers gives the equivalent result in the algebra $\mathcal{T}_R$. Notice that the L operator is nothing else than an R matrix, acting in auxiliary and quantum spaces $\mathbb{C}^2 \otimes V_i$: $L_i(\lambda) \equiv R_{ai}(\lambda)$.

The corresponding quantum determinant is

$$\Delta(\lambda) = \det_q T(\lambda) \qquad (49)$$
$$= \det K \prod_{i=1}^{N} ((\lambda - \omega_i)^2 - \eta^2(\mathcal{C}_i + 1/4)).$$

Now, it follows from

$$R_{12}(\lambda - \mu) T^{(1)}(\lambda, \boldsymbol{\omega}) T^{(2)}(\mu, \boldsymbol{\omega}) \qquad (50)$$
$$= T^{(2)}(\mu, \boldsymbol{\omega}) T^{(1)}(\lambda, \boldsymbol{\omega}) R_{12}(\lambda - \mu)$$

that

$$[t(\lambda, \boldsymbol{\omega}); t(\mu, \boldsymbol{\omega})] = 0, \qquad (51)$$

where $t(\lambda, \boldsymbol{\omega}) = \mathrm{tr} T(\lambda, \boldsymbol{\omega})$, The trace is taken over the auxiliary space.

Among the integrals of motion (51), we look for local ones, i.e., quantities $H^{(k)}$, $k = 1, 2, 3, \ldots$, which can be expressed as the sum of local operators,

$$H^{(k)} = \sum_{i=1}^{N} H^{(k)}_{i,\, i-1 \ldots i-k+1}. \qquad (52)$$

The periodicity of the spin chain, $N + 1 \equiv 1$, is supposed. The local densities $H^{(k)}_{i,\, i-1 \ldots i-k+1}$ should involve only k adjacent spins $S_i, S_{i+1}, \ldots, S_{i-k+1}$. An important case when such local integrals exist is that of the homogeneous spin chain, corresponding to equal spins $\Delta_i = \Delta$ and zero shifts $\boldsymbol{\omega} = 0$. It has the important property of translational invariance. The corresponding R matrix is regular. The similarity transformation has the form

$$US^{\alpha}_i U^{-1} = S^{\alpha}_{i+1}, \quad US_N U^{-1} = \mathcal{K}_1 S_1 \mathcal{K}_1^{-1}, \quad (53)$$

where $\mathcal{K}$ permutes with the boundary matrix K and with the Lax operator L_1: $KL_1(\lambda) = \mathcal{K}^{-1} L(\lambda) K\mathcal{K}$. This transformation generalizes the ordinary translation for the periodic chain ($K = 1$) to the twisted periodic boundary condition, specified by the matrix K and $U^N \neq 1$ in contrast to the case $K = 1$, when operator U takes the especially simple form $U = \mathcal{P}_{12}\mathcal{P}_{23} \ldots \mathcal{P}_{N-1N}$. The unitarity of U allows one to represent it in exponential form

$$U = e^{iP}, \qquad (54)$$

where operator P has the physical meaning of the total momentum of the chain. The Hamiltonian of the model then acquires the form

$$H = \frac{d}{d\lambda} t(\lambda)|_{\lambda=0} = \sum_{i=1}^{N} \frac{d}{d\lambda} \mathcal{P}_{i\, i+1} R_{i\, i+1}(\lambda)|_{\lambda=0}. \quad (55)$$

Faddeev and Korchemsky have shown [9] that the N-Reggeon Hamiltonian which is a direct extension of (15), corresponding to the homogeneous chain, can be obtained in this manner. Unfortunately, the R matrix, corresponding to the inhomogeneous chain (see below), possesses no regularity property and the corresponding Hamiltonian cannot be related to the derivative of the transfer-matrix in a simple way.

The analysis of the integrable systems is modified upon considering the open chains, i.e., when boundary conditions different from the periodic ones are imposed. This case is related to the factorizable scattering of particles with internal degrees of freedom on a half-line [18]. The algebraic description via ZF algebra [19] includes then the new object—boundary operator B:

$$Z_a(\lambda) B = K_{ab}(\lambda) Z_b(-\lambda) B, \qquad (56)$$

where K_{ab} is some nondegenerate "constant" matrix. Then, the two-particles' factorizability gives rise to the reflection equation [compare (29)]:

$$S_{12}(\lambda - \mu) K_1(\lambda) S_{21}(\lambda + \mu) K_2(\mu) \qquad (57)$$
$$= K_2(\mu) S_{12}(\lambda + \mu) K_1(\lambda) S_{21}(\lambda - \mu)$$

in addition to the Yang–Baxter equation (30). The reflection matrix has the same properties as the R matrix, i.e., regularity: $K(0) = I$, unitarity: $K(\lambda) \times K(-\lambda) = I$, T symmetry: $K^t(\lambda) = K(\lambda)$; the crossing symmetry is more elaborated and it involves the S matrix as well [19].

Then the boundary operator B can be constructed by

$$B = \exp\left(\int \phi(\lambda) d\lambda \right) \qquad (58)$$

from the combination

$$\phi(\lambda) = Z_a(-\lambda) K_{ab}(\lambda) Z_b(-\lambda), \qquad (59)$$

which is a "local" field $\phi(\lambda)$: $[\phi(\lambda); \phi(\mu)] = 0$. Due to the $sl(2)$ symmetry of the S matrix, the corresponding K matrix can be transformed, $K \to K' = GKG^{-1}$ with arbitrary G, and the general solution of the reflection equation (57) for the rational case, which we are interested in, is

$$K(\lambda) = \xi I + \lambda E, \qquad E^2 = I. \qquad (60)$$

The reflection equation has an important covariance property: if $T(\lambda)$ is defined as an ordered operator along the chain product of the R matrices and if $K(\lambda)$ defined above satisfies relations (37) and (57), then $K'(\lambda) = T(\lambda) K(\lambda) T(-\lambda)^{-1}$ is also a solution to (79) (see below), provided that the entries of $K(\lambda)$ and $T(\lambda)$ commute, $[K_{ab}(\lambda), T_{cd}(\lambda)] = 0$. The proof follows easily by the substitution of $K'(\lambda)$ into (79) and by using the fundamental Yang–Baxter relation in the different form

$$T^{-1}_{(2)}(-\mu) R_{12}(\lambda + \mu) T_{(1)}(\lambda)$$
$$= T^{-1}_{(1)}(\lambda) R_{12}(\lambda + \mu) T_{(2)}(-\mu).$$

If the matrix $T(\lambda)$ is constructed as an ordered product of N independent Lax operators, then $K'(\lambda)$ can be interpreted as the monodromy matrix of the N-site lattice model with a boundary interaction described by the operator-valued reflection matrix $K(\lambda)$. It is called Sklyanin's monodromy matrix. The corresponding transfer matrix is defined as the trace

$$t(\lambda) = \mathrm{tr} \bar{K}(\lambda) T(\lambda) K(\lambda) T^{-1}(-\lambda),$$

where the matrix $\bar{K}(\lambda)$ is any solution of (57) corresponding to the other boundary, which is commutative [12]

$$[t(\lambda), t(\mu)] = 0.$$

In the context of the Heisenberg chain Eq. (57) takes the form:

$$R_{12}(\lambda-\mu)K^-_{(1)}(\lambda)R^{t_1t_2}_{12}(\lambda+\mu)K^-_{(2)}(\mu) \quad (61)$$
$$= K^-_{(2)}(\mu)R_{12}(\lambda+\mu)K^-_{(1)}(\lambda)R^{t_1t_2}_{12}(\lambda-\mu),$$

$$R_{12}(-\lambda+\mu)(K^+_{(1)})^{t_1}(\lambda)M^{-1}_{(1)} \quad (62)$$
$$\times R^{t_1t_2}_{12}(-\lambda-\mu-2\eta)M_{(1)}(K^+_{(2)})^{t_2}(\mu)$$
$$= (K^+_{(2)})^{t_2}(\mu)M_{(1)}R_{12}(-\lambda-\mu-2\eta)$$
$$\times M^{-1}_{(1)}(K^+_{(1)})^{t_1}(\lambda)R^{t_1t_2}_{12}(-\lambda+\mu),$$

where M is crossing matrix defined above. In practice, if $K^-(\lambda)$ is a solution of (61), then $K^+(\lambda) = (K^-(-\lambda-\eta))^tM$ is a solution of (62). Equation (57) has an important covariance property: if $T(\lambda,\boldsymbol{\omega})$ and $K_\pm(\lambda)$ satisfy the relations (37) and (61), (62), then Sklyanin's monodromy matrix

$$U(\lambda,\boldsymbol{\omega}) = T(\lambda,\boldsymbol{\omega})K^-(\lambda)\tilde{T}(\lambda,\boldsymbol{\omega}), \quad (63)$$

where $\tilde{T}(\lambda,\boldsymbol{\omega}) = R_{Na}(\lambda-\omega_N)\dots R_{2a}(\lambda-\omega_2)\times R_{1a}(\lambda-\omega_1)$ [cf. with (48)], satisfies the relation

$$R_{12}(\lambda-\mu)U_{(1)}(\lambda,\boldsymbol{\omega})R^{t_1t_2}_{12}(\lambda+\mu)U_{(2)}(\mu,\boldsymbol{\omega}) \quad (64)$$
$$= U_{(2)}(\mu,\boldsymbol{\omega})R_{12}(\lambda+\mu)U_{(1)}(\lambda,\boldsymbol{\omega})R^{t_1t_2}_{12}(\lambda-\mu).$$

Indeed, we note that unitarity and crossing symmetry together imply the relation

$$M_{(1)}R^{t_2}_{12}(-\lambda-\eta)M^{-1}_{(1)}R^{t_2}_{12}(\lambda-\eta) = \rho(\lambda). \quad (65)$$

Futhermore, we see that unitarity implies $T(\lambda,\boldsymbol{\omega})\times\tilde{T}(-\lambda,\boldsymbol{\omega}) = \prod\rho(\lambda-\omega_i)$. Therefore, up to a scalar factor, $\tilde{T}(-\lambda,\boldsymbol{\omega})$ is the inverse of $T(\lambda,\boldsymbol{\omega})$.

The commutativity of the transfer matrix $t(\lambda,\boldsymbol{\omega})$ implies integrability of the open quantum spin chain with the Hamiltonian [12]:

$$H = \sum_{i=1}^{N-1} H_{ii+1} + 1/2(K^{(1)}_-)^t \quad (66)$$
$$+ \frac{\mathrm{tr}_0K^{(0)}_+(0)H_{N0}}{\mathrm{tr}K_+(0)},$$

whose two-site terms are given by

$$H_{ii+1} = \frac{d}{d\lambda}\mathcal{P}_{ii+1}R_{ii+1}(\lambda)|_{\lambda=0} \quad (67)$$

in the standard fashion.

4. CLOSED XXX HEISENBERG CHAIN

There are two ways of including fermions. The first corresponds to considering closed Heisenberg chains with different spins, i.e., chains containing the operators $\mathcal{G}_{FG}$ and H_F together with H_G. This case arises in amplitudes with the exchange of two adjoint fermions and one gluon. The same Hamiltonian also describes the exchange of three fermions in the fundamental representation of $SU(3)$, unless all three helicities are the same. In the first case, the Regge singularity is placed near $j=0$ and, in the second, is placed near $j=-1/2$. The second way of including fermions will be considered in the next section.

We consider the conformally covariant operator obtained from H^ω_F by substituting $\omega=0$,

$$H^{0\frac12} = \partial_1^{-1}\log x_{12}\partial_1 + \log x_{12} \quad (68)$$
$$+ \log\partial_1\partial_2 - 2\psi(1) == x_{12}\log\partial_1x_{12}^{-1}$$
$$+ \log\partial_2 + 2\log x_{12} - 2\psi(1)$$

with $\Delta_1=0$, $\Delta_2=1/2$ and the conjugated operator

$$H^{\frac120} = \partial_2^{-1}\log x_{12}\partial_2 + \log x_{12} \quad (69)$$
$$+ \log\partial_1\partial_2 - 2\psi(1) = x_{12}\log\partial_2x_{12}^{-1}$$
$$+ \log\partial_1 + 2\log x_{12} - 2\psi(1)$$

with $\Delta_1=1/2$, $\Delta_2=0$. We also have $\tilde{H}_F$, which should be denoted by

$$H^{\frac12\frac12} = 2\log x_{12} + \log\partial_1\partial_2 = x_{12}^{-1}H^{00}x_{12} \quad (70)$$

with the weights $\Delta_1=\Delta_2=1/2$. We have used the identity

$$(x_{12}\partial_2)^{-1} = \partial_2^{-1}\log x_{12}\partial_2 - \log x_{12}.$$

The operator $H^{\frac12\frac12}$ is selfconjugated:

$$(H^{\frac12\frac12})^T = H^{\frac12\frac12}, \quad (71)$$

and for $H^{0\frac12}$ we have

$$(H^{0\frac12})^T = \partial_1\log x_{12}\partial_1^{-1} + \log x_{12} \quad (72)$$
$$+ \log\partial_1\partial_2 - 2\psi(1) = \partial_1H^{0\frac12}\partial_1^{-1}$$
$$= x_{12}^{-1}\log\partial_1x_{12} + \log\partial_2 + 2\log x_{12}$$
$$- 2\psi(1) = \mathcal{P}_{12}x_{12}^{-1}H^{0\frac12}x_{12}\mathcal{P}_{12}.$$

Therefore,

$$[H^{0\frac12};\mathcal{P}_{12}x_{12}\partial_1] = 0. \quad (73)$$

Taking into account that

$$(\mathcal{P}_{12}x_{12}\partial_1)^2 = \mathcal{P}_{12}x_{12}\partial_1\mathcal{P}_{12}x_{12}\partial_1 \quad (74)$$
$$= x_{21}\partial_2x_{12}\partial_1 = -\mathcal{C}^{0\frac12}$$

and comparing with the general expression

$$\mathcal{C}^{\Delta_1\Delta_2} = (S_1+S_2)^2 = x_{12}^2\partial_1\partial_2 \quad (75)$$
$$+ 2x_{12}(\Delta_1\partial_2 - \Delta_2\partial_1) + (\Delta_1+\Delta_2)(1-\Delta_1-\Delta_2),$$

we can conclude that, indeed, under conformal transformations the operator $H^{0\frac12}$ transforms covariantly

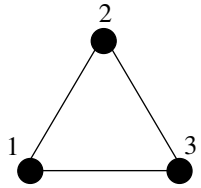

Fig. 2.

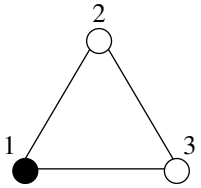

Fig. 3.

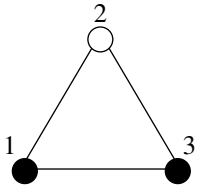

Fig. 4.

with weights $0, \frac{1}{2}$. Consider first the homogeneous closed chain, which consists of three fermions (see Fig. 2). The corresponding Hamiltonian is given by

$$H_{123}^{\frac{1}{2}\frac{1}{2}\frac{1}{2}} = H_{32}^{\frac{1}{2}\frac{1}{2}} + H_{21}^{\frac{1}{2}\frac{1}{2}} + H_{13}^{\frac{1}{2}\frac{1}{2}} \tag{76}$$
$$= 2\log x_{12}x_{23}x_{31} + 2\log \partial_1\partial_2\partial_3.$$

Conjugation arguments, as described above, give nothing for $H^{\frac{1}{2}\frac{1}{2}}$, while the commutators of particular Casimir operators provide us with two conserved currents:

$$D^{(3)}_{\frac{1}{2}\frac{1}{2}\frac{1}{2}} = x_{12}x_{23}x_{31}\partial_1\partial_2\partial_3 \tag{77}$$
$$+ \frac{1}{2}(x_{23}(x_{31}-x_{12})\partial_2\partial_3$$
$$+ x_{12}(x_{23}-x_{31})\partial_1\partial_2 + x_{31}(x_{12}-x_{23})\partial_3\partial_1)$$
$$- \frac{1}{2}(x_{12}\partial_3 + x_{23}\partial_1 + x_{31}\partial_2)$$

is a third order differential operator and

$$D^{(2)}_{\frac{1}{2}\frac{1}{2}\frac{1}{2}} = (x_{12}^2\partial_1\partial_2 + x_{23}^2\partial_2\partial_3 + x_{31}^2\partial_3\partial_1) \tag{78}$$
$$+(x_{31}-x_{12})\partial_1 + (x_{12}-x_{23})\partial_2 + (x_{23}-x_{31})\partial_3$$

is a second-order one. The latter reflects the conformal symmetry of the system. The relations

$$\left[H_{123}^{\frac{1}{2}\frac{1}{2}\frac{1}{2}}, D^{(2)}_{\frac{1}{2}\frac{1}{2}\frac{1}{2}}\right] = 0 \tag{79}$$

and

$$\left[H_{123}^{\frac{1}{2}\frac{1}{2}\frac{1}{2}}, D^{(3)}_{\frac{1}{2}\frac{1}{2}\frac{1}{2}}\right] = 0 \tag{80}$$

can be checked by direct calculations. These conserved currents can be also obtained in a more regular way. They appear as coefficients in front of λ^1 and λ^0 in the monodromy matrix expansion $t(\lambda)$, where

$$t(\lambda) = \mathrm{tr}(L_1^{1/2}(\lambda)L_2^{1/2}(\lambda)L_3^{1/2}(\lambda)) \tag{81}$$
$$= D^{(3)}_{\frac{1}{2}\frac{1}{2}\frac{1}{2}} + \lambda D^{(2)}_{\frac{1}{2}\frac{1}{2}\frac{1}{2}} + \lambda^3 + 1/4,$$

and the Lax operators $L_i^{\Delta}(\lambda)$ are defined in (24).

Let us consider now the inhomogeneous closed chain, which consisits of one fermion and two gluons (see Fig. 3). The corresponding Hamiltonian is

$$\tilde{H}_{123}^{\frac{1}{2}00} = H_{32}^{00} + H_{21}^{0\frac{1}{2}} + H_{13}^{\frac{1}{2}0} \tag{82}$$
$$= 2\log x_{12}x_{23}x_{31} + 2\log \partial_1\partial_2\partial_3$$
$$+ \partial_3^{-1}(x_{23}^{-1} - x_{31}^{-1}) + \partial_2^{-1}(x_{12}^{-1} - x_{23}^{-1}).$$

Transposition arguments do not work here. However, for closed chains with three sites there is always a third-order differential operator, commuting with operator of total spin of chain $\mathcal{C}$. Indeed, the result for the commutator

$$[\mathcal{C}_{12}^{\Delta_1\Delta_2}; \mathcal{C}^{\Delta_3\Delta_1}] = [x_{12}^2\partial_1\partial_2 \tag{83}$$
$$+ 2x_{12}(\Delta_1\partial_2 - \Delta_2\partial_1); x_{31}^2\partial_3\partial_1$$
$$+ 2x_{31}(\Delta_3\partial_1 - \Delta_1\partial_3)] = x_{12}x_{23}x_{31}\partial_1\partial_2\partial_3$$
$$+ \Delta_3 x_{12}(x_{23}-x_{31})\partial_1\partial_2 + \Delta_2 x_{31}(x_{12}-x_{23})\partial_3\partial_1$$
$$+ \Delta_1 x_{23}(x_{31}-x_{12})\partial_2\partial_3 - 2(\Delta_2\Delta_3 x_{23}\partial_1$$
$$+ \Delta_3\Delta_1 x_{31}\partial_2 + \Delta_1\Delta_2 x_{12}\partial_3) \equiv D^{(3)}_{\Delta_1\Delta_2\Delta_3}$$

is symmetric under cyclic permutation of indices (123). Therefore its commutator with $D^{(2)}_{\Delta_1\Delta_2\Delta_3} \equiv \mathcal{C}_{12}^{\Delta_1\Delta_2} + \mathcal{C}_{23}^{\Delta_2\Delta_3} + \mathcal{C}_{31}^{\Delta_3\Delta_1}$ vanishes due to the Jacoby identity. However, the Hamiltonian $\tilde{H}_{123}^{\frac{1}{2}00}$, while commuting with $D^{(2)}_{\frac{1}{2}00}$, does not commute with $D^{(3)}_{\frac{1}{2}00}$:

$$[\tilde{H}_{123}, D^{(3)}] \tag{84}$$
$$= \Big[(2\log x_{12}x_{23}x_{31} + 2\log \partial_1\partial_2\partial_3$$
$$+ \partial_3^{-1}(x_{23}^{-1} - x_{31}^{-1}) + \partial_2^{-1}(x_{12}^{-1} - x_{23}^{-1})),$$
$$\Big(x_{12}x_{23}x_{31}\partial_1\partial_2\partial_3 + \frac{1}{2}(x_{12}^2 - x_{31}^2)\partial_2\partial_3\Big)\Big]$$
$$= \frac{1}{2}\partial_3^{-1}x_{12}^2x_{31}^{-2}\partial_2 - \frac{1}{2}\partial_2^{-1}x_{31}^2x_{12}^{-2}\partial_3.$$

The operators $D^{(2)}, D^{(3)}$ also appear as coefficients in front of λ^1 and λ^0 in the monodromy matrix

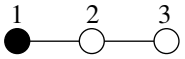

Fig. 5.

expansion $t(\lambda)$, where

$$t(\lambda) = \mathrm{tr}(L_1^{1/2}(\lambda)L_2^0(\lambda)L_3^0(\lambda)) \quad (85)$$
$$= D^{(3)} + \lambda D^{(2)} + \lambda^2(2\lambda - 1).$$

The next inhomogeneous chain (see Fig. 4) is the one with one gluon and two fermions.

The corresponding Hamiltonian commutes with the Casimir operator,

$$[(x_{12}\partial_1 x_{12}\partial_2 + x_{23}\partial_3 x_{23}\partial_2 \quad (86)$$
$$+ x_{31}\partial_1\partial_3 x_{31}); (2\log x_{12}x_{23}x_{31}$$
$$+ 2\log\partial_1\partial_2\partial_3 + \partial_2^{-1}(x_{12}^{-1} - x_{23}^{-1})] = 0,$$

and does not commute with the next current,

$$\left[\left(x_{23}\partial_3 x_{31}\partial_1 x_{12}\partial_2 - \frac{1}{2}x_{31}\partial_1\partial_3 x_{31}\right); \quad (87)\right.$$
$$(2\log x_{12}x_{23}x_{31} + 2\log\partial_1\partial_2\partial_3$$
$$\left. + \partial_2^{-1}(x_{12}^{-1} - x_{23}^{-1})\right]$$
$$= \frac{1}{2}\partial_2^{-1}x_{31}(x_{23}^{-2}\partial_1 - x_{12}^{-2}\partial_3)x_{31}.$$

The same happens for the longer closed chains. The Hamiltonians for those chains commute only with the first current, the Casimir operator. This means that, in order to describe the integrable model, the corresponding Hamiltonian should be modified. Indeed, the inhomogeneous chains (Figs. 3, 4) have to be considered as the chains with impurity. Probably, the expression for $H^{0\frac{1}{2}}$ has to be changed slightly.

5. XXX HEISENBERG CHAIN WITH OPEN BOUNDARY

The second way of including fermions is to build an open chain with the fermions (now in the fundamental gauge group representation) at the ends. This open chain corresponds to the Regge exchange with meson quantum numbers in the t channel.

Let us consider the Hamiltonian corresponding to the chain depicted in Fig. 5:

$$H_{123}^{\frac{1}{2}00} = H_{32}^{00} + H_{21}^{0\frac{1}{2}} \quad (88)$$
$$= \log x_{12} + \partial_2^{-1}\log x_{32}x_{21}\partial_2 + \log\partial_1\partial_2^2\partial_3$$
$$+ \partial_3^{-1}\log x_{32}\partial_3 = \log\partial_1 + x_{32}\log\partial_2\partial_3 x_{32}^{-1}$$
$$+ x_{21}\log\partial_2 x_{21}^{-1} + 2\log .x_{21}x_{32}.$$

The transposed Hamiltonian has the form

$$(H_{123}^{\frac{1}{2}00})^T = \partial_2\partial_3 H_{123}\partial_2\partial_3 \quad (89)$$
$$= \mathcal{P}_{123}(x_{32}x_{21})^{-1}H_{123}x_{32}x_{21}\mathcal{P}_{123}.$$

Then, H commutes with

$$A_{123}^{\frac{1}{2}00} = \mathcal{P}_{123}x_{32}x_{21}\partial_2\partial_3\mathcal{P}_{123}. \quad (90)$$

The permutation operator $\mathcal{P}_{123}$ maps the sites $1, 2, 3$ of the chain into the sites $3, 2, 1$, correspondingly.

In a similar way, the conserved operator of the highest order in the derivatives can be obtained for the open chain with $N-2$ gluonic operators and fermions of opposite spin at the ends:

$$H_{12\ldots N}^{\frac{1}{2}0\ldots0} = \partial_2^{-1}\log x_{21}\partial_2 \quad (91)$$
$$+ \log x_{21} + \log\partial_2\partial_1 + \sum_{i=2}^{N-1} H_{ii+1}^{00}$$

commutes with the charge operator

$$A_{12\ldots N} = \mathcal{P}_{12\ldots N}x_{NN-1}\ldots x_{21}\partial_N\partial_{N-1}\ldots\partial_2. \quad (92)$$

For simplicity, we set the reflection matrices $K^{\pm}$ equal to unity. From Eq. (56), one can see that this implies the transfer matrix to be an even function of the spectral parameter. In our case, we obtain up to insignificant numerical terms

$$t(\lambda) = (4\lambda^2 - 1)\Big(D_{\frac{1}{2}00}^{(4)} - \omega_2 D_{\frac{1}{2}00}^{(3)} \quad (93)$$
$$- (\lambda^2 - \omega_2^2)D_{\frac{1}{2}00}^{(2)} + (\lambda^2 - \omega_2^2)^2\Big),$$

where $D_{\frac{1}{2}00}^{(3)}$ and $D_{\frac{1}{2}00}^{(2)}$ are the same as in (38) for the closed chain and

$$D_{\frac{1}{2}00}^{(4)} = x_{12}^2x_{23}^2\partial_1\partial_2 + x_{12}x_{23}(x_{12} - x_{23})\partial_1$$
$$+ x_{12}x_{23}^2\partial_2 + x_{23}(x_{12} - x_{23})\partial_2\partial_3.$$

It coincides with the square of the operator (75), obtained above using transposed operator.

Setting here $\omega_3^2 = \omega_2^2 = \omega_1^2 + 3/4$, one notices that second-order operator $D^{(2)}$ coincides with $\mathcal{C}^{0\,1/2}$. Now, the operator $D^{(2)}$ commutes with the Hamiltonian. Thus, for the open chain (Fig. 5), described by the Hamiltonian H_{123}, as in Eq. (67), the eigenproblem here can be replaced by the one with the same Casimir operator and with the fourth-order differential operator $D^{(4)}$ instead of $D^{(3)} = \tilde{A}$ as for the closed chain.

So, we see that for the open chains we are able to find a sufficient amount of conserved currents to solve the eigenproblem for QCD Reggeon interactions. Moreover, for the open chain Fig. 6 with one fermion

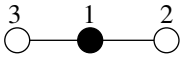

Fig. 6.

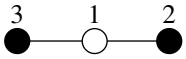

Fig. 7.

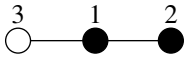

Fig. 8.

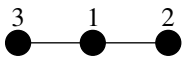

Fig. 9.

inside again, everything is all right. The Hamiltonian and transfer matrix are given by

$$H_{312}^{0\frac{1}{2}0} = H_{31}^{0\frac{1}{2}} + H_{12}^{\frac{1}{2}0} = 2\log x_{12}x_{31} \qquad (94)$$
$$+ 2\log\partial_1^2\partial_2\partial_3 + \partial_2^{-1}\log x_{12} - \partial_3^{-1}\log x_{31},$$

$$t(\lambda) = 4\lambda(\lambda+1)x_{31}\partial_1 x_{12}^2\partial_1 x_{31}\partial_2\partial_3 \qquad (95)$$
$$+ 4\lambda^2(\lambda+1)^2(x_{23}\partial_2\partial_3$$
$$+ x_{31}\partial_1 x_{31}\partial_3 + x_{12}\partial_1 x_{12}\partial_2).$$

The case of the open chain with two fermions and one gluon can be considered as well. For the chain depicted in Fig. 7, we have two conserved currents:

$$[x_{12}x_{23}\partial_1\partial_2\partial_3 x_{12}x_{23}\partial_2; (2\log x_{12}x_{23} \qquad (96)$$
$$+ \log\partial_1\partial_2^2\partial_3 + \partial_2^{-1}(x_{12}^{-1} - x_{23}^{-1}))] = 0,$$

$$[(x_{12}\partial_1 x_{12}\partial_2 + x_{23}\partial_3 x_{23}\partial_2 + x_{31}\partial_1\partial_3 x_{31}); \qquad (97)$$
$$(2\log x_{12}x_{23} + \log\partial_1\partial_2^2\partial_3 + \partial_2^{-1}(x_{12}^{-1} - x_{23}^{-1}))] = 0.$$

Another chain with two fermions and one gluon is shown in Fig. 8. One has the following relations for this chain:

$$[x_{12}\partial_2 x_{23}\partial_3 x_{23}\partial_2 x_{12}\partial_1; (2\log x_{12}x_{23} \qquad (98)$$
$$+ \log\partial_1\partial_2^2\partial_3 - \partial_1^{-1}x_{12}^{-1})] = 0,$$

$$[(x_{12}\partial_2 x_{12}\partial_1 + x_{23}\partial_2\partial_3 x_{23} + x_{31}\partial_3 x_{31}\partial_1); \qquad (99)$$
$$(2\log x_{12}x_{23} + \log\partial_1\partial_2^2\partial_3 - \partial_1^{-1}x_{12}^{-1})] = 0.$$

For completeness we consider also the open chain with three fermions, shown in Fig. 9:

$$[(\partial_1 x_{12}\partial_2 x_{23}\partial_3 x_{23}\partial_2 x_{12} \qquad (100)$$
$$+ x_{12}\partial_2 x_{23}\partial_3 x_{23}\partial_2 x_{12}\partial_1);$$
$$(2\log x_{12}x_{23} + \log\partial_1\partial_2^2\partial_3)] = 0,$$

$$[(x_{12}\partial_1\partial_2 x_{12} + x_{23}\partial_3\partial_2 x_{23} + x_{31}\partial_1\partial_3 x_{31}); \qquad (101)$$
$$(2\log x_{12}x_{23} + \log\partial_1\partial_2^2\partial_3)] = 0.$$

Thus, all possible open chains with three sites corresponding to gluonic or fermionic Reggeons are integrable. The conserved currents can be derived from the transfer matrix with boundaries represented by unity reflection matrices. The Hamiltonians are constructed from the QCD kernels given above and commute with these two conserved currents given by the second- and fourth-order differential operators, respectively. We believe that integrability is an important intrinsic property of high-energy limit of QCD and holds for the longer open chains too.

6. CONCLUSIONS

The examples considered above, except for the difficulties with the inhomogeneous closed chains, are good evidence of the validity of Lipatov's conjecture about the deep connection between the kernels of high-energy gluodynamics scattering amplitudes and the exactly solvable two-dimensional models in the case, when fermions are present as well. In the pure gluonic case this connection context has already been used for the solution of the Odderon problem [20]. The case of open chain differs from the closed-chain case by the higher order of nontrivial conserved charge; the fourth order appears instead of the third.

Recently, it has been shown that the considered integrable structures appear also in hard (exclusive and deep-inelastic) scattering [21], corresponding to a different limiting region of high-energy scattering amplitudes in QCD.

ACKNOWLEDGMENTS

This work was supported by BMBF (Germany).

REFERENCES

1. V. de Alfaro and T. Regge, *Potential Scattering* (North-Holland, Amsterdam, 1965); P. D. B. Collins, *An Introduction to Regge Theory and High-Energy Physics* (Cambridge Univ. Press, Cambridge, 1977).
2. F. Low, Phys. Rev. D **12**, 163 (1975); V. N. Gribov, E. M. Levin, and M. G. Ryskin, Phys. Rep. **100**, 1 (1983).
3. V. N. Gribov, Zh. Éksp. Teor. Fiz. **53**, 654 (1968) [Sov. Phys. JETP **26**, 414 (1968)]; Nucl. Phys. B **106B** 189 (1976).

4. L. N. Lipatov, Yad. Fiz. **23**, 642 (1976) [Sov. J. Nucl. Phys. **23**, 338 (1976)]; E. A. Kuraev, L. N. Lipatov, and V. S. Fadin, Phys. Lett. B **60B**, 50 (1975); Zh. Éksp. Teor. Fiz. **71**, 840 (1976) [Sov. Phys. JETP **44**, 443 (1976)]; Zh. Éksp. Teor. Fiz. **72**, 377 (1977) [Sov. Phys. JETP **45**, 199 (1977)]; Ya. Ya. Balitskii and L. N. Lipatov, Yad. Fiz. **28**, 1597 (1978) [Sov. J. Nucl. Phys. **28**, 822 (1978)].
5. J. Bartels, Nucl. Phys. B **175**, 365 (1980); J. Kwiecinski and M. Praszalowicz, Phys. Lett. B **94B**, 413 (1980); L. N. Lipatov, in *Perturbative QCD,* Ed. by A. H. Mueller (World Sci., Singapore, 1989).
6. R. Kirschner, L. N. Lipatov, and L. Szymanowski, Phys. Rev. D **51**, 838 (1995); Nucl. Phys. B **425**, 519 (1994); R. Kirschner and L. Szymanowski, Phys. Lett. B **419**, 348 (1998); Phys. Rev. D **58**, 14004 (1998).
7. G. P. Korchemsky and G. Sterman, Nucl. Phys. B **437**, 415 (1995).
8. L. N. Lipatov, Padova Preprint DFPD/93/TH/70; hep-th/9311037; Pis'ma Zh. Éksp. Teor. Fiz. **59**, 571 (1994) [JETP Lett. **59**, 596 (1994)].
9. L. D. Faddeev and G. P. Korchemsky, Phys. Lett. B **342**, 311 (1994).
10. L. N. Lipatov, Phys. Lett. B **251**, 284 (1990).
11. R. Kirschner, Z. Phys. C **65**, 505 (1995); **67**, 459 (1995).
12. E. K. Sklyanin, J. Phys. A **21**, 2375 (1988); *Nankai Lectures in Mathematical Physics, Introduction to Quantum Group and Integrable Massive Models of Quantum Field Theory* (World Sci., Singapore, 1992), p. 63.
13. A. B. Zamolodchikov, Zh. Éksp. Teor. Fiz. **79**, 641 (1980) [Sov. Phys. JETP **52**, 325 (1980)]; A. B. Zamolodchikov and Al. B. Zamolodchikov, Ann. Phys. (N.Y.) **120**, 253 (1979).
14. V. E. Korepin, N. M. Bogoliubov, and A. G. Izergin, *Quantum Inverse Scattering Method and Correlation Functions* (Cambridge Univ. Press, Cambridge, 1993).
15. L. D. Faddeev, *Integrable Models in (1+1)-Dimensional Quantum Field Theory: Proceedings of Les Houches XXXIX,* Ed. by J.-B. Zuber and R. Stora (North-Holland, Amsterdam, 1984), p. 561.
16. L. D. Faddeev and L. A. Takhtadjan, *Hamiltonian Methods in the Theory of Solitons* (Springer-Verlag, Berlin, 1987).
17. P. P. Kulish and E. K. Sklyanin, Lect. Notes Phys. **151**, 61 (1982); M. Jimbo, *Yang–Baxter Equation in Integrable Systems* (World Sci., Singapore, 1990), p. 715; R. J. Baxter, *Exactly Solved Models in Statistical Mechanics* (Academic, New York, 1992).
18. I. V. Cherednik, Theor. Math. Phys. **61**, 977 (1984).
19. S. Ghoshal and A. B. Zamolodchikov, Int. J. Mod. Phys. A **9**, 3841 (1994).
20. R. A. Janik and J. Wosiek, Cracow Preprint TPJU 2/98; hep-th/9802100; M. Praszalowicz and A. Rostworowski, Cracow Preprint TPJU 8/98; hep-ph/9805245.
21. V. M. Braun, S. E. Derkachov, and A. N. Manashov, hep-ph/9805225; Phys. Rev. Lett. **81**, 2020 (1998).

Physics of Atomic Nuclei, Vol. 65, No. 8, 2002, pp. 1513–1527. From Yadernaya Fizika, Vol. 65, No. 8, 2002, pp. 1551–1565.

ELEMENTARY PARTICLES AND FIELDS
Theory

Photon–Reggeon-Interaction Vertices in the NLA*

V. S. Fadin[1)], D. Yu. Ivanov[2),3)]***, and M. I. Kotsky[4)]******

Budker Institute of Nuclear Physics, Siberian Division, Russian Academy of Sciences, pr. akademika Lavrent'eva II, Novosibirsk, 630090 Russia

Received June 19, 2001

Abstract—We calculate the effective vertices for the quark–antiquark and the quark–antiquark–gluon production in the virtual-photon–Reggeized gluon interaction. The last vertex is considered at the Born level; for the first one the one-loop corrections are obtained. These vertices have a number of applications; in particular, they are necessary for calculation of the virtual photon impact factor in the next-to-leading logarithmic approximation. © *2002 MAIK "Nauka/Interperiodica".*

1. INTRODUCTION

Investigation of processes with Pomeron exchange remains one of the important problems of high-energy physics. Special attention is attracted by so-called semihard processes, where large values of typical momentum transfers Q^2 give a possibility of using perturbative QCD for their theoretical description. The most common basis for such description is given by the BFKL approach [1]. It became widely known after the discovery at HERA of the sharp rise of the proton structure function upon a decrease in the Bjorken variable x (see, for example, [2]). Recently, the total cross section of the interaction of two highly virtual photons was measured at LEP. This process, being a one-scale process, seems to be even more natural for the application of the BFKL approach than the two-scale process of the deep-inelastic scattering at small x, since here the evolution in x described by the BFKL equation does not interfere with the evolution in Q^2 described by the DGLAP equation.

For a consistent comparison with the experimental data, the theoretical predictions must be obtained in the next-to-leading approximation (NLA), where, together with the leading terms $(\alpha_s \ln(s))^n$, the terms $\alpha_s(\alpha_s \ln(s))^n$ are also resummed. The radiative corrections to the kernel of the BFKL equation were calculated several years ago [3–8], and the explicit form of the kernel of the equation in the NLA is known now [9, 10] for the case of forward scattering. But the problem of calculation in the NLA of the so-called impact factors, which describe the coupling of the Pomeron to the scattering particles, remains unsolved.

Let us recall (see, for example, [11] for details) that, in the BFKL approach, the relevant to the irreducible representation $\mathcal{R}$ of the color group in the t-channel part $(\mathcal{A}_\mathcal{R})^{A'B'}_{AB}$ of the scattering amplitude for the process $AB \to A'B'$ at large c.m.s. energy $\sqrt{s} \to \infty$ and fixed momentum transfer $q \approx q_\perp$ ($\perp$ means transverse to the initial particle momenta plane) is expressed in terms of the Mellin transform of the Green's function of the two interacting Reggeized gluons $G^{(\mathcal{R})}_\omega$ and of the impact factors of the colliding particles $\Phi^{(\mathcal{R},\nu)}_{A'A}$ and $\Phi^{(\mathcal{R},\nu)}_{B'B}$:

$$\mathrm{Im}_s\left(\mathcal{A}_\mathcal{R}\right)^{A'B'}_{AB} = \frac{s}{(2\pi)^{D-2}} \times \int \frac{d^{D-2}q_1}{\mathbf{q}_1^2(\mathbf{q}_1-\mathbf{q})^2} \int \frac{d^{D-2}q_2}{\mathbf{q}_2^2(\mathbf{q}_2-\mathbf{q})^2} \times \sum_\nu \Phi^{(\mathcal{R},\nu)}_{A'A}(\mathbf{q}_1,\mathbf{q},s_0) \times \int\limits_{\delta-i\infty}^{\delta+i\infty} \frac{d\omega}{2\pi i}\left[\left(\frac{s}{s_0}\right)^\omega G^{(\mathcal{R})}_\omega(\mathbf{q}_1,\mathbf{q}_2,\mathbf{q})\right] \times \Phi^{(\mathcal{R},\nu)}_{B'B}(-\mathbf{q}_2,-\mathbf{q},s_0), \tag{1.1}$$

where Im_s means the s-channel imaginary part, the vector sign is used for denotation of the transverse

*This article was submitted by the authors in English.

[1)]Novosibirsk State University, ul. Pirogova 2, Novosibirsk, 630090 Russia.
[2)]Institute of Mathematics, Siberian Division, Russian Academy of Sciences, Universitetskiĭ pr. 4, Novosibirsk, 630090 Russia.
[3)]Regensburg University, Germany.
[4)]Istituto Nazionale di Fisica Nucleare, Gruppo collegato di Cosenza, Arcavacata di Rende, Italy
** e-mail: fadin@inp.nsk.su
*** e-mail: d-ivanov@math.nsc.ru
**** e-mail: M.I.Kotsky@inp.nsk.su

components, ν enumerates the states in the representation $\mathcal{R}$, $D = 4 + 2\epsilon$ is the spacetime dimension different from 4 to regularize both infrared and ultraviolet divergences, and the parameter s_0 is artificial and is introduced for convenience. While the Green's function obeys the generalized BFKL equation [11]

$$\omega G_\omega^{(\mathcal{R})}(\mathbf{q}_1,\mathbf{q}_2,\mathbf{q}) = \mathbf{q}_1^2(\mathbf{q}_1-\mathbf{q})^2\delta^{(D-2)}(\mathbf{q}_1-\mathbf{q}_2) + \int \frac{d^{D-2}k}{\mathbf{k}^2(\mathbf{k}-\mathbf{q})^2}\mathcal{K}^{(\mathcal{R})}(\mathbf{q}_1,\mathbf{k},\mathbf{q})G_\omega^{(\mathcal{R})}(\mathbf{k},\mathbf{q}_2,\mathbf{q}) \tag{1.2}$$

with the NLA kernel $\mathcal{K}^{(\mathcal{R})}$ and is completely defined by this equation, the impact factors should be calculated separately. The definition of the NLA impact factors is given in [11]; in the case of definite colors of c and c' of the Reggeized gluons, the impact factor has the form [12]

$$\begin{aligned}\Phi_{AA'}^{cc'}(\mathbf{q}_1,\mathbf{q},s_0) &= \left(\frac{s_0}{\mathbf{q}_1^2}\right)^{\omega(-\mathbf{q}_1^2)/2}\left(\frac{s_0}{(\mathbf{q}_1-\mathbf{q})^2}\right)^{\omega(-(\mathbf{q}_1-\mathbf{q})^2)/2} \\ &\times \sum_{\{f\}}\int\frac{d\kappa}{2\pi}\theta(s_\Lambda-\kappa)d\rho_f\Gamma^c_{\{f\}A}\left(\Gamma^{c'}_{\{f\}A'}\right)^* \\ &- \frac{1}{2}\int\frac{d^{D-2}k}{\mathbf{k}^2(\mathbf{k}-\mathbf{q})^2}\Phi_{AA'}^{c_1c_1'(\mathrm{Born})}(\mathbf{k},\mathbf{q},s_0) \\ &\times \left(\mathcal{K}_r^{\mathrm{Born}}\right)_{c_1c}^{c_1'c'}(\mathbf{k},\mathbf{q}_1,\mathbf{q})\ln\frac{s_\Lambda^2}{s_0(\mathbf{k}-\mathbf{q}_1)^2},\end{aligned} \tag{1.3}$$

where $\omega(t)$ is the Reggeized gluon trajectory and the intermediate parameter s_Λ should go to infinity. The integration in the first term of the above equality is carried out over the phase space $d\rho_f$ and over the squared invariant mass κ of the system $\{f\}$ produced in the fragmentation region of the particle A, $\Gamma^c_{\{f\}A}$ are the particle–Reggeon effective vertices for this production, and the sum is taken over all systems $\{f\}$ that can be produced in the NLA. The second term in Eq. (1.3) is the counterterm for the LLA part of the first one, so that the logarithmic dependence of both terms on the intermediate parameter $s_\Lambda \to \infty$ disappears in their sum; $\mathcal{K}_r^{\mathrm{Born}}$ is the part of the leading-order BFKL kernel related to the real gluon production (see [12] for more details). It was shown in [13] that definition (1.3) guarantees infrared finiteness of the colorless-particle impact factors.

It is clear from the above that, for a complete NLA description in the BFKL approach, one needs to know the impact factors; analogously, as in the DGLAP approach one should know not only the parton distributions, but also the coefficient functions.

This paper is an extended version of the short note [14], which can be considered as the first step in the calculation of the virtual-photon impact factor in the NLA. We calculate here the virtual photon–Reggeon effective vertices which enter the definition (1.3) in the case when the particle A is the virtual photon. In the NLA, the states that can be produced in the Reggeon–virtual-photon collision are the quark–antiquark and the quark–antiquark–gluon ones. In the next section, we present the effective vertices for production of these states in the Born approximation. This approximation is sufficient to find, in the NLA, the contribution to the virtual-photon impact factor from the quark–antiquark–gluon state. In the case of the quark–antiquark state, we need to know the effective production vertex with one-loop accuracy. Sections 3–5 are devoted to the calculation of the one-loop corrections. In Sections 3 and 4, we consider the two-gluon- and the one-gluon-exchange diagrams, respectively; in Section 5 the total one-loop correction is presented. The results obtained are discussed in Section 6. Some details of the calculation are given in the Appendix.

In the following, the photon–Reggeon effective vertices presented in this paper will be used for the calculation of the photon impact factor. But they could have many other applications, for example, in the diffractive production of quark jets and so on.

2. THE BORN INTERACTION VERTICES

In this section, we present the vertices for the $q\bar{q}$ and the $q\bar{q}g$ production in the Reggeon–virtual-photon collision in the Born approximation for the case of completely massless QCD. These vertices can be obtained from the high-energy amplitudes with the octet color state and the negative signature in the t channel for collision of the virtual photon with any particle if the corresponding system is produced in the virtual-photon fragmentation region. For simplicity, we always consider collision of the virtual–photon with the momentum p_A and the quark with the momentum p_B. We use everywhere below the Feynman gauge for the gluon field; the Sudakov decomposition of momenta

$$p = \beta p_1 + \alpha p_2 + p_\perp, \quad \alpha = \frac{p^2+\mathbf{p}^2}{s\beta}, \quad p_1^2 = p_2^2 = 0, \tag{2.1}$$
$$s = 2p_1p_2 \to \infty, \quad \mathbf{p}^2 \equiv -p_\perp^2,$$

with the lightcone basis in the longitudinal space defined by

$$p_A = p_1 - \frac{Q^2}{s}p_2, \quad p_A^2 = -Q^2, \tag{2.2}$$
$$p_B = p_2, \quad p_B^2 = 0\,;$$

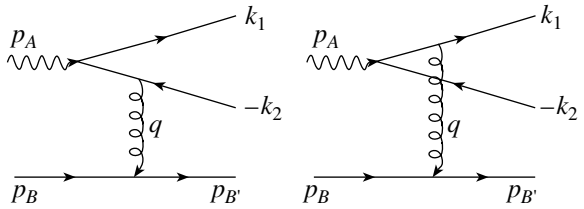

Fig. 1. The lowest order Feynman diagrams for the process $\gamma^* Q \to (q\bar{q})Q$.

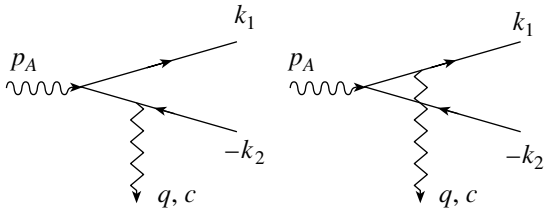

Fig. 2. Schematic representation of the vertex $\Gamma^{c(0)}_{\gamma^* q\bar{q}}$.

and the usual trick of retaining only the first term in the decomposition of the metric tensor

$$g^{\mu\nu} = \frac{2p_2^\mu p_1^\nu}{s} + \frac{2p_1^\mu p_2^\nu}{s} + g_\perp^{\mu\nu} \to \frac{2p_2^\mu p_1^\nu}{s} \qquad (2.3)$$

in the numerator of the gluon propagator connecting vertices μ and ν with momenta predominantly along p_1 and p_2, respectively. The virtual-photon polarization vector e is taken in the gauge $ep_2 = 0$, so that

$$e = e_\perp + \frac{2ep_1}{s}p_2. \qquad (2.4)$$

Then the polarization vector $\tilde{e}$ in the usual gauge $\tilde{e}p_A = 0$ is

$$\tilde{e} = e + \frac{ep_1}{Q^2}p_A, \qquad (2.5)$$

so that, in the case of the longitudinal polarization, when $\tilde{e}_L^2 = 1$, we have $e_L p_1 = Q$.

Let us start with the calculation of the quark–antiquark production vertex. The diagrams of the production process contributing to the Regge asymptotic behavior are shown in Fig. 1.

As was already mentioned, the quark–antiquark pair is produced in the photon fragmentation region, so that the invariant mass $\sqrt{\kappa}$ of the pair is of the order of typical transverse momenta and does not grow with s. The Regge form of the production amplitude $\mathcal{A}^{(0)}_{Q\gamma^*\to Qq\bar{q}}$ is

$$\mathcal{A}^{(0)}_{Q\gamma^*\to Qq\bar{q}} = \Gamma^{c(0)}_{\gamma^* q\bar{q}} \frac{2s}{t} \Gamma^{c(0)}_{QQ}, \qquad (2.6)$$

where $t = q^2$ and $\Gamma^{c(0)}_{\gamma^* q\bar{q}}$ and $\Gamma^{c(0)}_{QQ}$ are corresponding particle–Reggeon effective vertices in the Born approximation. Let us note that the amplitude of Fig. 1 has automatically only the octet color state and the negative signature in the t channel, so that it is not necessary here to perform any projection. The notation for all momenta is shown in Fig. 1. The quark–Reggeon vertex is known up to NLA accuracy, and its Born part is

$$\Gamma^{c(0)}_{QQ} = g t^c_{B'B} \bar{u}_{B'} \frac{\not{p}_1}{s} u_B, \qquad (2.7)$$

where g is the coupling constant, t^c are the color group generators in the fundamental representation, and u is a quark spinor wave function. Then, comparing Eqs. (2.6) and (2.7) with the explicit form of the amplitude given by the diagrams of Fig. 1, one can easily obtain for $\Gamma^{c(0)}_{\gamma^* q\bar{q}}$ the diagrammatic representation of Fig. 2 (see [13]), where the zigzag lines represent the Reggeon with the momentum

$$q = -\frac{\kappa + Q^2 + \mathbf{q}^2}{s}p_2 + q_\perp,$$
$$t = q^2 = q_\perp^2 = -\mathbf{q}^2, \qquad (2.8)$$

and the color index c. The lowest order effective vertices for interaction of the Reggeon with quarks and gluons are defined in Fig. 3 (see [13]).

The vertex $\Gamma^{c(0)}_{\gamma^* q\bar{q}}$ can be obtained from the diagrams of Fig. 2 by the usual Feynman rules as the amplitude of the quark–antiquark production in collision of the virtual photon with the Reggeon. This procedure gives us the result

$$\Gamma^{c(0)}_{\gamma^* q\bar{q}} = -eq_f g t^c_{i_1 i_2} \bar{u}_1 \left(\frac{\hat{\Gamma}_1}{t_1} - \frac{\hat{\Gamma}_2}{t_2} \right) \frac{\not{p}_2}{s} v_2 \qquad (2.9)$$
$$= -eq_f g t^c_{i_1 i_2} \left(\left[\bar{u}_1 \frac{\hat{\Gamma}_1}{t_1} \frac{\not{p}_2}{s} v_2 \right] - [1 \leftrightarrow 2] \right),$$

where eq_f is the electric charge of the produced quark; i_1 and i_2 are the color indices of the quark and antiquark, respectively; v is the spinor wave function of the produced antiquark; and

$$\hat{\Gamma}_1 = \frac{1}{x_1}\left(2x_2(ek_1) - \not{e}_\perp \not{k}_{1\perp}\right), \qquad (2.10)$$
$$\hat{\Gamma}_2 = \frac{1}{x_2}\left(2x_1(ek_2) - \not{k}_{2\perp} \not{e}_\perp\right),$$
$$t_i = (p_A - k_i)^2 = -\frac{\mathbf{k}_i^2 + x_1 x_2 Q^2}{x_i},$$

with the variables x_i defined by the Sudakov decompositions of the produced quark and antiquark momenta

$$k_i = x_i p_1 + \frac{\mathbf{k}_i^2}{s x_i} p_2 + k_{i\perp}, \quad k_i^2 = 0, \quad i = 1, 2. \qquad (2.11)$$

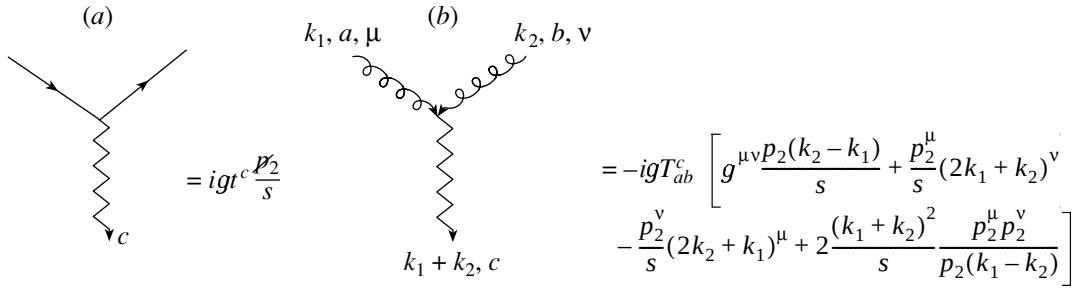

Fig. 3. The quark–quark–Reggeon and the gluon–gluon–Reggeon effective vertices. T^c is the color group generator in the adjoint representation.

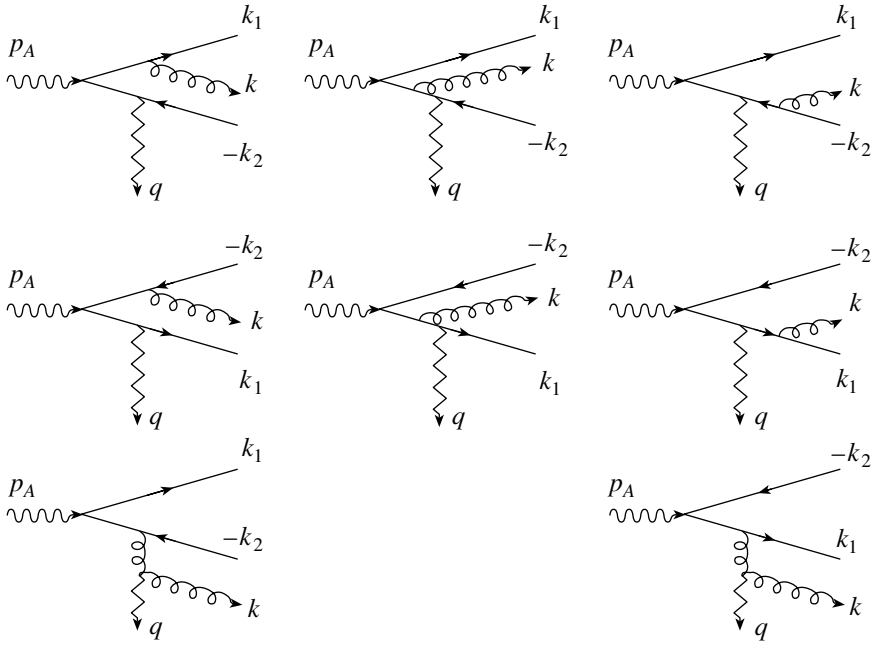

Fig. 4. Schematic representation of the vertex $\Gamma^{c(0)}_{\gamma^* q\bar{q}g}$.

The substitution $1 \leftrightarrow 2$ in Eq. (2.9) means replacement quark $\leftrightarrow$ antiquark, i.e., $x_1 \leftrightarrow x_2$, $\mathbf{k}_1 \leftrightarrow \mathbf{k}_2$ together with replacement of the polarizations. The validity of the second equality in (2.9) can be easily verified using the charge conjugation matrix. We will need later the Born effective vertex $\Gamma^{c(0)}_{\gamma^* q\bar{q}}$ also in the helicity representation for the case of the spacetime dimension D equal 4. To obtain it, we use the polarization matrix

$$\hat{\rho} \equiv (v_2 \bar{u}_1) = \frac{1}{\sqrt{x_1 x_2}} \frac{1}{4} \tag{2.12}$$
$$\times \left[\left(x_2 k_1 + x_1 k_2 - \kappa \frac{p_2}{s} \right)^\mu - 2i\xi e^{\mu\nu\sigma\rho} k_{2\nu} k_{1\sigma} \frac{p_2\rho}{s} \right] \times \gamma_\mu (1 - \xi\gamma_5),$$

where

$$e^{0123} = 1, \quad \gamma_5 = i\gamma^0\gamma^1\gamma^2\gamma^3, \tag{2.13}$$

and $\xi = \pm 1$ is a double helicity of the produced quark. The polarization matrix satisfies the evident relations

$$\not k_2 \hat{\rho} = \hat{\rho} \not k_1 = (1 - \xi\gamma_5)\hat{\rho} = \hat{\rho}(1 + \xi\gamma_5) = 0. \tag{2.14}$$

For the virtual photon polarization vector, we also use the helicity representation

$$e^\mu(\lambda) = \frac{1}{\sqrt{-2t}} \left[(\delta_{\lambda,1} + \delta_{\lambda,-1}) \times \left(q_\perp^\mu + 2i\lambda e^{\mu\nu\sigma\rho} q_\nu p_{1\sigma} \frac{p_2\rho}{s} \right) + \delta_{\lambda,0} \sqrt{-2tQ^2} \frac{2p_2^\mu}{s} \right], \quad \lambda = 0, \pm 1. \tag{2.15}$$

Using Eqs. (2.9)–(2.15), we get

$$\Gamma^{c(0)}_{\gamma^* q\bar{q}} = -\frac{2eq_f g t^c_{i_1 i_2}}{\sqrt{-2tx_1x_2}} \left(\left[\frac{x_2}{t_1} \left\{ \delta_{\lambda,0} \sqrt{2} q Q x_1 x_2 \right. \right. \right. \tag{2.16}$$

$$- (\mathbf{k}_1\cdot\mathbf{q} + i\lambda P)\,(x_2\delta_{\lambda,-\xi} - x_1\delta_{\lambda,\xi})\Big\}\Big]$$
$$- [1\leftrightarrow 2]\Big) = \frac{2eq_f g t^c_{i_1 i_2}}{\sqrt{-2t x_1 x_2}}\Big[\delta_{\lambda,0}\sqrt{2}qQx_1x_2$$
$$\times\left(\frac{x_1}{t_2} - \frac{x_2}{t_1}\right) + (x_2\delta_{\lambda,-\xi} - x_1\delta_{\lambda,\xi})$$
$$\times\left(\frac{x_2}{t_1}(\mathbf{k}_1\cdot\mathbf{q} + i\lambda P) + \frac{x_1}{t_2}(\mathbf{k}_2\cdot\mathbf{q} - i\lambda P)\right)\Big],$$

where $q = |\mathbf{q}|$,

$$P = 2e^{\mu\nu\sigma\rho}k_{1\mu}k_{2\nu}p_{1\sigma}\frac{p_{2\rho}}{s}, \qquad (2.17)$$

with the property $P^2 = \mathbf{k}_1^2\cdot\mathbf{k}_2^2 - (\mathbf{k}_1\cdot\mathbf{k}_2)^2$, and the replacement $(1\leftrightarrow 2)$ is $x_1\leftrightarrow x_2, \mathbf{k}_1\leftrightarrow\mathbf{k}_2, \xi\leftrightarrow -\xi$.

Next, we perform the calculation of the quark–antiquark–gluon production effective vertex $\Gamma^{c(0)}_{\gamma^*q\bar{q}g}$. It can be obtained through the usual Feynman rules with the elementary Reggeon vertices defined in Fig. 3 as the amplitude of the quark–antiquark–gluon production in the virtual-photon–Reggeon collision represented by the diagrams of Fig. 4, where the denotations of momenta are presented. The color indices of the Reggeon and the emitted gluon are c and b, respectively. The Reggeon momentum is given by Eq. (2.8), where κ now is the quark–antiquark–gluon squared invariant mass. The vertex $\Gamma^{c(0)}_{\gamma^*q\bar{q}g}$ obtained in this way is invariant with respect to the gauge transformations of the emitted-gluon polarization vector e_g and can be simplified by appropriate choice of the gauge. We use the axial gauge

$$e_g p_2 = 0, \quad e_g = -\frac{2(e_{g\perp}k_\perp)}{s\beta}p_2 + e_{g\perp}, \qquad (2.18)$$

where β is defined by $k = \beta p_1 + \mathbf{k}^2/(s\beta)p_2 + k_\perp$. In this gauge, the last nonlocal term in the expression for the gluon–Reggeon interaction vertex of Fig. 3*b* disappears and we obtain

$$\Gamma^{c(0)}_{\gamma^*q\bar{q}g}(eq_f g^2)^{-1} = \langle 1|t^b t^c|2\rangle \qquad (2.19)$$
$$\times\Bigg[\bar{u}_1\Bigg\{\frac{1}{(p_A-k_1)^2(k_2+q)^2}$$
$$\times\ \not e(\not p_A - \not k_1)\ \not e^*_g(\not k_2+\not q)\frac{\not p_2}{s}$$
$$+\frac{1}{(k+k_1)^2(p_A-k_2)^2}$$
$$\times\ \not e^*_g(\not k+\not k_1)\frac{\not p_2}{s}(\not p_A - \not k_2)\ \not e$$
$$-\frac{1}{(k+k_1)^2(k_2+q)^2}$$
$$\times\ \not e^*_g(\not k+\not k_1)\ \not e\times(\not k_2+\not q)\frac{\not p_2}{s}$$
$$+\left(\frac{\gamma_\mu(\not p_A-\not k_2)\not e}{(p_A-k_2)^2} - \frac{\not e(\not p_A-\not k_1)\gamma_\mu}{(p_A-k_1)^2}\right)$$
$$\times\ \frac{1}{(k+q)^2}\left(\beta e^{*\mu}_g - \frac{p_2^\mu}{s}(2qe^*_g)\right)\Bigg\}v_2\Bigg]$$
$$+\langle 1|t^c t^b|2\rangle\,[1\leftrightarrow 2]$$
$$= \langle 1|t^b t^c|2\rangle\Bigg[\bar{u}_1\Bigg\{\frac{1}{(p_A-k_1)^2(k_2+q)^2}$$
$$\times\ \not e(\not p_A - \not k_1)\ \not e^*_g(\not k_2+\not q)\frac{\not p_2}{s}$$
$$+\frac{1}{(k+k_1)^2(p_A-k_2)^2}$$
$$\times\ \not e^*_g(\not k+\not k_1)\frac{\not p_2}{s}(\not p_A - \not k_2)\ \not e\ \not e$$
$$-\frac{1}{(k+k_1)^2(k_2+q)^2}$$
$$\times\ \not e^*_g(\not k+\not k_1)\ \not e(\not k_2+\not q)\frac{\not p_2}{s}$$
$$+\left(\frac{\gamma_\mu(\not p_A-\not k_2)\ \not e}{(p_A-k_2)^2} - \frac{\not e(\not p_A-\not k_1)\gamma_\mu}{(p_A-k_1)^2}\right)$$
$$\times\ \frac{1}{(k+q)^2}\left(\beta e^{*\mu}_g - \frac{p_2^\mu}{s}(2qe^*_g)\right)\Bigg\}v_2\Bigg]$$
$$+\langle 1|t^c t^b|2\rangle\Bigg[\bar{u}_1\Bigg\{\frac{1}{(p_A-k_2)^2(k_1+q)^2}$$
$$\times\frac{\not p_2}{s}(\not k_1+\not q)\ \not e^*_g(\not p_A - \not k_2)\ \not e$$
$$+\frac{1}{(k+k_2)^2(p_A-k_1)^2}$$
$$\times\ \not e(\not p_A-\not k_1)\frac{\not p_2}{s}(\not k+\not k_2)\ \not e^*_g$$
$$-\frac{1}{(k+k_2)^2(k_1+q)^2}$$
$$\times\frac{\not p_2}{s}(\not k_1+\not q)\ \not e(\not k+\not k_2)\ \not e^*_g$$
$$+\left(\frac{\not e(\not p_A-\not k_1)\gamma_\mu}{(p_A-k_1)^2} - \frac{\gamma_\mu(\not p_A-\not k_2)\ \not e}{(p_A-k_2)^2}\right)$$
$$\times\ \frac{1}{(k+q)^2}\left(\beta e^{*\mu}_g - \frac{p_2^\mu}{s}(2qe^*_g)\right)\Bigg\}v_2\Bigg].$$

3. THE ONE-LOOP CORRECTION: THE TWO-GLUON EXCHANGE DIAGRAMS

In this section, we consider the contribution of the two-gluon-exchange diagrams to $\Gamma^c_{\gamma^*q\bar{q}}$. There are six diagrams of such kind for the process we consider; they are shown in Fig. 5.

Now, we have to perform the projection on the negative signature and the octet color state in the t channel. This is done by the following replacement

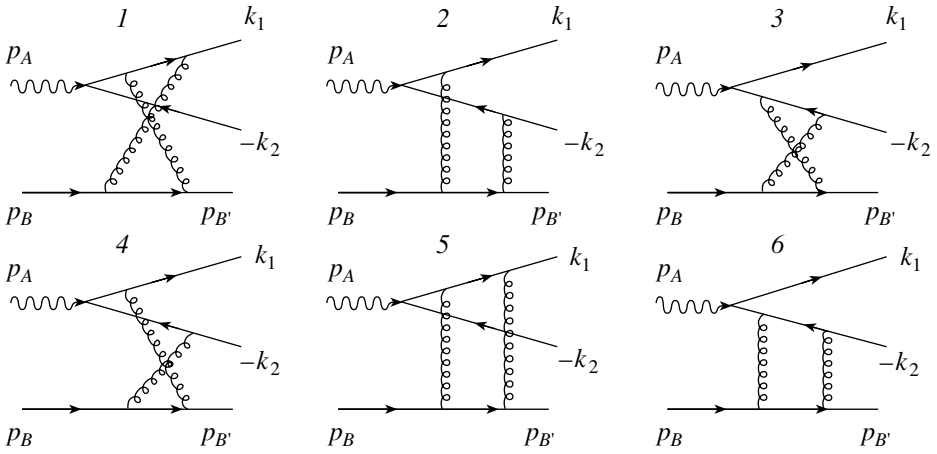

Fig. 5. The two-gluon-exchange Feynman diagrams for the process $\gamma^*Q \to (q\bar{q})Q$.

of the color factor of the lowest line of diagrams from Fig. 5:

$$(t^b t^a)_{B'B} \to \frac{1}{2}\left(t^b t^a - t^a t^b\right)_{B'B} = \frac{1}{2} T^c_{ab} t^c_{B'B}. \quad (3.1)$$

Then, we obtain

$$\mathcal{A}^{(2g)(8,-)(1)}_{Q\gamma^*\to Qq\bar{q}} = \frac{1}{4} N t^c_{i_1 i_2} t^c_{B'B} \{[(D_1 + D_2) - (1 \leftrightarrow 2)] - [s \leftrightarrow -s]\}, \quad (3.2)$$

where N is the number of colors, D_1 is the amplitude represented by the diagram of Fig. 5(*1*) with omitted color generators on any vertex, and $2D_2$ is such amplitude for the diagram of Fig. 5(*2*).

The calculation of D_1 is quite straightforward. Note here that, since our final goal is the virtual-photon impact factor in physical spacetime and since the integration over the quark–antiquark states in Eq. (1.3) is not singular, we need to retain in the vertex $\Gamma^c_{\gamma^* q\bar{q}}$ and, consequently, in the amplitude $\mathcal{A}^{(2g)(8,-)(1)}_{Q\gamma^*\to Qq\bar{q}}$ only the terms which do not vanish at $\epsilon \to 0$. Therefore all one-loop results are presented in this paper with such accuracy. In a convenient form for us, we have

$$(D_1 - D_1(1 \leftrightarrow 2)) - (s \leftrightarrow -s) \quad (3.3)$$
$$= (-1)\frac{4}{N} g\bar{u}_{B'} \frac{\not{p}_1}{s} u_B e q_f g \bar{u}_1 \left(\frac{\hat{\Gamma}_1}{t_1} - \frac{\hat{\Gamma}_2}{t_2}\right)$$
$$\times \frac{\not{p}_2}{s} v_2 \frac{s}{t} \omega^{(1)}(t) \left(\ln\left(\frac{s}{-t}\right) + \ln\left(\frac{-s}{-t}\right)\right)$$
$$+ 4g\bar{u}_{B'} \frac{\not{p}_1}{s} u_B \frac{2s}{t} e q_f g^3 \frac{\Gamma(2-\epsilon)}{(4\pi)^{2+\epsilon}} \frac{1}{2\epsilon}$$
$$\times \left\{\left[\bar{u}_1 \frac{\hat{\Gamma}_1}{t_1} \frac{\not{p}_2}{s} v_2 \left(2(-t)^\epsilon \times \left(\frac{1}{\epsilon} + 1 + 2(1+\epsilon)\ln x_2 + \epsilon - 5\epsilon\psi'(1)\right) + \int_0^1 \frac{dy}{(-(1-y)t - yt_1)^{1-\epsilon}} \times 2(1+\epsilon)\left(t - 2(t-t_1)y^\epsilon\right)\right)\right] - [1 \leftrightarrow 2]\right\},$$

where the first term is responsible for the Reggeization of the amplitude $\mathcal{A}^{(8,-)}_{Q\gamma^*\to Qq\bar{q}}$ with $\omega^{(1)}$ being the one-loop Reggeized gluon trajectory,

$$\omega^{(1)}(t) = -g^2 N \frac{\Gamma(1-\epsilon)}{(4\pi)^{2+\epsilon}} \left(\mathbf{q}^2\right)^\epsilon \frac{\Gamma^2(\epsilon)}{\Gamma(2\epsilon)}, \quad (3.4)$$

and $\Gamma(z)$ and $\psi(z)$ are the Euler Γ function and its logarithmic derivative, respectively. The calculation of D_2 is more complicated, and we present some details of it in the Appendix. Here, we write only the result

$$(D_2 - D_2(1 \leftrightarrow 2)) - (s \leftrightarrow -s) = 4g\bar{u}_{B'} \frac{\not{p}_1}{s} u_B \frac{2s}{t} e q_f g^3 \frac{\Gamma(2-\epsilon)}{(4\pi)^{2+\epsilon}} \frac{1}{2\epsilon}$$
$$\times \left\{\left[\bar{u}_1 \int_0^1 \int_0^1 \frac{dy_1 dy_2}{\left[(1-y_2)\left(-(1-y_1)t - y_1 t_2\right) + y_2\left(-(1-y_1)t_1 + y_1 Q^2\right)\right]^{2-\epsilon}} \times \left(y_1^{\epsilon-1}(1-y_1) y_2^{-\epsilon}\left(x_1^\epsilon x_2^{-\epsilon} - 2\epsilon^2\psi'(1)\right) 2t\hat{\Gamma}_1 + (1-y_1) 4t(ek_1)\right.\right. \quad (3.5)$$

$$+\left(y_1^{\epsilon}y_2^{-\epsilon}x_1^{\epsilon}x_2^{-\epsilon}-1\right)4x_2t(ep_1))\frac{\not p_2}{s}v_2\Bigg]-[1\leftrightarrow 2]\Bigg\}.$$

Note that the imaginary parts of D_2 (in the $(p_{B'}+k_2)^2$ channel) and $D_2(1\leftrightarrow 2)$ (in the $(p_{B'}+k_1)^2$ channel) which would destroy the Reggeization cancel in the amplitude $\mathcal{A}^{(8,-)}_{Q\gamma^*\to Qq\bar q}$. Although in the NLA BFKL approach there is no requirement of the Reggeization of full amplitudes (the Reggeization of their real parts is sufficient), we see that nevertheless the Reggeization also holds without omitting any imaginary part for the process $Q\gamma^*\to Qq\bar q$.

The amplitude $\mathcal{A}_{Q\gamma^*\to Qq\bar q}$ with the octet color state and the negative signature in the t channel has the following Reggeized form:

$$\begin{aligned}\mathcal{A}^{(8,-)}_{Q\gamma^*\to Qq\bar q}&=\Gamma^c_{\gamma^*q\bar q}\frac{s}{t}\\ &\times\left[\left(\frac{s}{-t}\right)^{\omega(t)}+\left(\frac{-s}{-t}\right)^{\omega(t)}\right]\Gamma^c_{QQ}\\ &\approx\Gamma^{c(0)}_{\gamma^*q\bar q}\frac{2s}{t}\Gamma^{c(0)}_{QQ}+\Gamma^{c(0)}_{\gamma^*q\bar q}\frac{s}{t}\omega^{(1)}(t)\\ &\times\left[\ln\left(\frac{s}{-t}\right)+\ln\left(\frac{-s}{-t}\right)\right]\Gamma^{c(0)}_{QQ}\\ &+\Gamma^{c(0)}_{\gamma^*q\bar q}\frac{2s}{t}\Gamma^{c(1)}_{QQ}+\Gamma^{c(1)}_{\gamma^*q\bar q}\frac{2s}{t}\Gamma^{c(0)}_{QQ}.\end{aligned}\tag{3.6}$$

Let us now split the one-loop contributions to this amplitude and both of the effective vertices according to the three sets of one-loop diagrams for $\mathcal{A}_{Q\gamma^*\to Qq\bar q}$: the two-gluon exchange diagrams, the t-channel gluon self-energy diagrams, and the one-gluon-exchange diagrams

$$\begin{aligned}&\mathcal{A}^{(2g)(8,-)(1)}_{Q\gamma^*\to Qq\bar q}+\mathcal{A}^{(se)(8,-)(1)}_{Q\gamma^*\to Qq\bar q}+\mathcal{A}^{(1g)(8,-)(1)}_{Q\gamma^*\to Qq\bar q}\\ &=\left\{\Gamma^{(2g)c(1)}_{\gamma^*q\bar q}\frac{2s}{t}\Gamma^{c(0)}_{QQ}+\Gamma^{c(0)}_{\gamma^*q\bar q}\frac{2s}{t}\Gamma^{(2g)c(1)}_{QQ}\right.\\ &\left.+\Gamma^{c(0)}_{\gamma^*q\bar q}\frac{s}{t}\omega^{(1)}(t)\left[\ln\left(\frac{s}{-t}\right)+\ln\left(\frac{-s}{-t}\right)\right]\Gamma^{c(0)}_{QQ}\right\}\\ &+\left\{\Gamma^{(se)c(1)}_{\gamma^*q\bar q}\frac{2s}{t}\Gamma^{c(0)}_{QQ}+\Gamma^{c(0)}_{\gamma^*q\bar q}\frac{2s}{t}\Gamma^{(se)c(1)}_{QQ}\right\}\\ &+\left\{\Gamma^{(1g)c(1)}_{\gamma^*q\bar q}\frac{2s}{t}\Gamma^{c(0)}_{QQ}+\Gamma^{c(0)}_{\gamma^*q\bar q}\frac{2s}{t}\Gamma^{(1g)c(1)}_{QQ}\right\},\end{aligned}\tag{3.7}$$

where the self-energy diagrams and one-gluon exchange diagrams have automatically only the octet color state and negative signature in the t channel, so that

$$\mathcal{A}^{(se)(8,-)(1)}_{Q\gamma^*\to Qq\bar q}\equiv\mathcal{A}^{(se)(1)}_{Q\gamma^*\to Qq\bar q},\tag{3.8}$$

$$\mathcal{A}^{(1g)(8,-)(1)}_{Q\gamma^*\to Qq\bar q}\equiv\mathcal{A}^{(1g)(1)}_{Q\gamma^*\to Qq\bar q}.$$

We recall that, in our case of completely massless quantum field theory, the contribution from the renormalization of the external lines is absent in the dimensional regularization. Now, from the representations of Eqs. (3.7) and (3.8), it is easy to see that $\Gamma^{(1g)c(1)}_{\gamma^*q\bar q}$ is given by the radiative corrections to the amplitude of the quark–antiquark production in collision of the virtual photon with the gluon having momentum q, color index c, and polarization vector $-p_2^{\mu}/s$, whereas $\Gamma^{(1g)c(1)}_{QQ}$ is defined by the radiative corrections to the vertex of interaction of this gluon with the quark Q. In both cases, the gluon self-energy is not included in these corrections; it is divided into equal parts between $\Gamma^{(se)c(1)}_{\gamma^*q\bar q}$ and $\Gamma^{(se)c(1)}_{QQ}$. For the two-gluon-exchange contributions, we have the relation

$$\begin{aligned}&\Gamma^{(2g)c(1)}_{\gamma^*q\bar q}\frac{2s}{t}\Gamma^{c(0)}_{QQ}+\Gamma^{c(0)}_{\gamma^*q\bar q}\frac{2s}{t}\Gamma^{(2g)c(1)}_{QQ}\\ &=\mathcal{A}^{(2g)(8,-)(1)}_{Q\gamma^*\to Qq\bar q}-\Gamma^{c(0)}_{\gamma^*q\bar q}\frac{s}{t}\omega^{(1)}(t)\\ &\times\left[\ln\left(\frac{s}{-t}\right)+\ln\left(\frac{-s}{-t}\right)\right]\Gamma^{c(0)}_{QQ},\end{aligned}\tag{3.9}$$

which shows that we need to know the correction $\Gamma^{(2g)c(1)}_{QQ}$. This correction can be obtained from the two-gluon contribution to the Qq elastic-scattering amplitude with the color octet and the negative signature in the t channel in the Regge kinematical region. From Eq. (3.9) with the replacements

$$\begin{aligned}\Gamma^{(2g)c(0,1)}_{\gamma^*q\bar q}&\to\Gamma^{(2g)c(0,1)}_{qq},\\ \mathcal{A}^{(2g)(8,-)(1)}_{Q\gamma^*\to Qq\bar q}&\to\mathcal{A}^{(2g)(8,-)(1)}_{Qq\to Qq},\end{aligned}\tag{3.10}$$

denoting

$$\Gamma^{(2g)c(1)}_{qq}=\delta^{(2g)}(t)\Gamma^{c(0)}_{qq},\ \ \Gamma^{(2g)c(1)}_{QQ}=\delta^{(2g)}(t)\Gamma^{c(0)}_{QQ},\tag{3.11}$$

we get

$$\begin{aligned}\delta^{(2g)}(t)=\frac{t}{4s\Gamma^{c(0)}_{qq}\Gamma^{c(0)}_{QQ}}&\left\{\mathcal{A}^{(2g)(8,-)(1)}_{Qq\to Qq}\right.\\ &\left.-\Gamma^{c(0)}_{qq}\Gamma^{c(0)}_{QQ}\frac{s}{t}\omega^{(1)}(t)\left[\ln\left(\frac{s}{-t}\right)+\ln\left(\frac{-s}{-t}\right)\right]\right\}.\end{aligned}\tag{3.12}$$

The value $\mathcal{A}^{(2g)(8,-)(1)}_{Qq\to Qq}$ is given by the contribution of two diagrams of Fig. 6 through the same procedure (3.1) for the lowest line of these diagrams to project

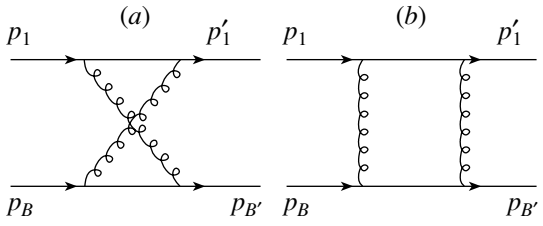

Fig. 6. The two-gluon exchange Feynman diagrams for the process $qQ \to qQ$.

on the negative signature and the color octet in the t channel. In this way, one gets

$$\mathcal{A}_{Qq\to Qq}^{(2g)(8,-)(1)} = \frac{1}{4}N\langle 1'|t^c|1\rangle\langle B'|t^c|B\rangle\left(D_3 - D_3(s\leftrightarrow -s)\right), \tag{3.13}$$

where D_3 is the amplitude represented by the diagram of Fig. 6a with omitted color factors. The calculation of this diagram is quite simple, and we do not present any details here. The result for $\delta^{(2g)}$ can be obtained in an exact form without ϵ expansion,

$$\delta^{(2g)}(t) = \frac{1}{2}\omega^{(1)}(t) \times\left[\frac{1}{\epsilon} + \psi(1) + \psi(1-\epsilon) - 2\psi(1+\epsilon)\right] \tag{3.14}$$
$$\approx -g^2N\frac{\Gamma(2-\epsilon)}{(4\pi)^{2+\epsilon}}\frac{1}{\epsilon}(-t)^\epsilon\left(\frac{1}{\epsilon} + 1 + \epsilon - 4\epsilon\psi'(1)\right),$$

where the last approximate equality shows the result expanded in ϵ, which is sufficient for our purposes. Now, using Eqs. (2.7), (2.9), (3.2)–(3.5), (3.9), (3.11), and (3.14), we obtain

$$\Gamma_{\gamma^*q\bar q}^{(2g)c(1)}\left(eq_f g^3 N t^c_{i_1i_2}\frac{\Gamma(2-\epsilon)}{(4\pi)^{2+\epsilon}}\frac{1}{2\epsilon}\right)^{-1} \tag{3.15}$$
$$= \left[\bar u_1\left(2(-t)^\epsilon\left(2(1+\epsilon)\ln x_2 - \epsilon\psi'(1)\right)\frac{\hat\Gamma_1}{t_1} + \int_0^1\frac{dy}{(-(1-y)t - yt_1)^{1-\epsilon}}\right.\right.$$
$$\times 2(1+\epsilon)\left(t - 2y^\epsilon(t-t_1)\right)\frac{\hat\Gamma_1}{t_1} + \int_0^1\int_0^1\frac{dy_1dy_2}{(-y_1y_2\kappa - t - y_2(t_1-t) - y_1(t_2-t))^{2-\epsilon}}$$
$$\times\left\{y_1^{\epsilon-1}(1-y_1)y_2^{-\epsilon}\left(x_1^\epsilon x_2^{-\epsilon} - 2\epsilon^2\psi'(1)\right)2t\hat\Gamma_1 + (1-y_1)4t(ek_1)\right.$$
$$\left.\left.\left. + \left(y_1^\epsilon y_2^{-\epsilon}x_1^\epsilon x_2^{-\epsilon} - 1\right)4x_2t(ep_1)\right\}\right)\frac{\not p_2}{s}v_2\right] - [1\leftrightarrow 2].$$

The last equality gives the integral representation for the one-loop two-gluon-exchange part of the Reggeon–virtual-photon effective vertex for the quark–antiquark production. Although all the integrals in (3.15) can be expressed in terms of elementary functions and dilogarithms with the necessary accuracy in ϵ expansion, it seems more convenient to leave the result in such an unintegrated form in order to have the possibility of using usual Feynman parametrization and to change orders of integrations over all Feynman parameters at a subsequent calculation of the impact factor. Performing the integrations in Eq. (3.15), one loses this possibility and has to do a step back to an unintegrated result to restore it. Let us finally note that the method of extraction of $\Gamma_{\gamma^*q\bar q}^{(2g)c(1)}$ from the corresponding part of the amplitude we used here is absolutely equivalent to the one proposed in [13] and gives the same result that has been checked by direct comparison.

4. THE ONE-LOOP CORRECTION: THE ONE-GLUON EXCHANGE DIAGRAMS

In this section, we consider the contribution of the one-gluon-exchange diagrams to the vertex $\Gamma^c_{\gamma^*q\bar q}$. It is presented by the diagrams of Fig. 7 with the gluon polarization vector equal to $-p_2^\mu/s$, as was already explained in the previous section. Calculating the color factors of the diagrams, one can easily obtain the representation

$$\Gamma_{\gamma^*q\bar q}^{(1g)c(1)} = Nt^c_{i_1i_2}\left\{\left[-\frac{2C_F}{N}(R_1+R_2)\right.\right. \tag{4.1}$$
$$\left.\left. + \frac{N-2C_F}{N}(R_3+R_4) + R_5 + \tilde R_6\right] - [1\leftrightarrow 2]\right\},$$

with the usual notation

$$C_F = \frac{N^2-1}{2N} \tag{4.2}$$

and the notation $2R_1, ..., 2R_4, -2R_5$, and $4\tilde R_6$ for the amplitudes represented by the diagrams of

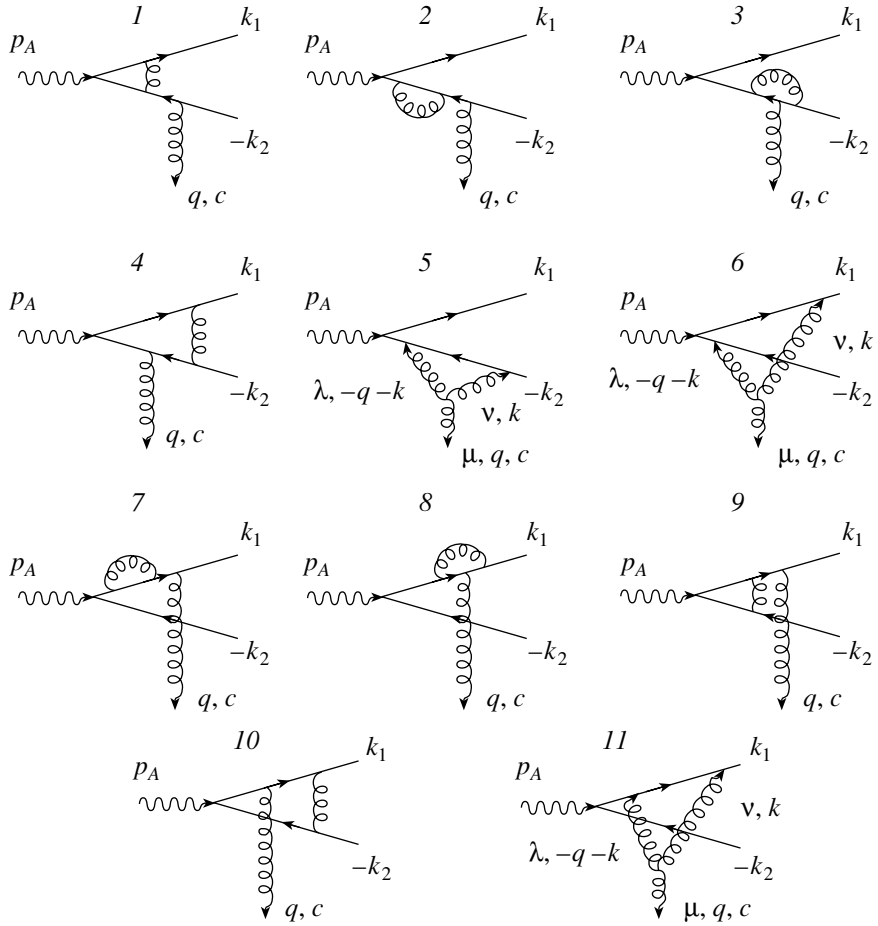

Fig. 7. The diagrams corresponding to the correction $\Gamma^{(1g)c(1)}_{\gamma^* q\bar{q}}$.

Figs. 7(*1*),...,(*4*), (*5*), and (*6*), respectively, with omitted color generators on any vertex and the external virtual gluon polarization vector equal to p_2^μ/s. While the definition of $R_1, ..., R_4$ is absolutely clear, R_5 and $\tilde{R}_6$ are not well defined by the above prescription because of the presence of three-gluon vertices in the corresponding diagrams, Figs. 7(*5*) and 7(*6*). To complete their definition, we have indicated explicitly the momenta and vector indices for the three-gluon vertex for which the following expression should be used after the omission of color generators:

$$\gamma_{\lambda\nu\mu}(-k-q,k) = ig\left[-g_{\lambda\nu}(2k+q)_\mu + g_{\lambda\mu}(k+2q)_\nu + g_{\nu\mu}(k-q)_\lambda\right]. \tag{4.3}$$

The calculation of R_1, R_2, R_3, and R_5 is simple, and we present here only the list of the results in integral form without any details:

$$R_1 = -eq_f g^3 \frac{\Gamma(2-\epsilon)}{(4\pi)^{2+\epsilon}} \frac{1}{2\epsilon} \bar{u}_1 \times \int_0^1 \frac{dy}{((1-y)Q^2 - yt_1)^{1-\epsilon}} \times \left\{(1+2\epsilon)\frac{Q^2}{t_1}\hat{\Gamma}_1 + 2\epsilon(ep_1) + y\left[(1-2\epsilon)\left(\frac{Q^2}{t_1}+1\right)\hat{\Gamma}_1 + 2(2-\epsilon)(ek_1)\right]\right\}\frac{\not{p}_2}{s} v_2, \tag{4.4}$$

$$R_2 = -eq_f g^3 \frac{\Gamma(2-\epsilon)}{(4\pi)^{2+\epsilon}} \frac{1}{2\epsilon} \bar{u}_1 \frac{\hat{\Gamma}_1}{(-t_1)^{1-\epsilon}} \frac{\not{p}_2}{s} v_2,$$

$$R_3 = eq_f g^3 \frac{\Gamma(2-\epsilon)}{(4\pi)^{2+\epsilon}} \frac{1}{2\epsilon} \bar{u}_1 \times \int_0^1 \frac{dy}{(-(1-y)t - yt_1)^{1-\epsilon}} \left\{(1+2\epsilon)\frac{t}{t_1}\hat{\Gamma}_1 + y\left[(1-2\epsilon)\left(\frac{t}{t_1}-1\right)\right.\right. \tag{4.5}$$

$$\times \hat{\Gamma}_1 + (2-\epsilon)x_2\left(\hat{\Gamma}_1+\hat{\Gamma}_2-2(e_\perp q_\perp)\right)\Big]\Big\}\frac{\not{p}_2}{s}v_2,$$

$$R_5 = eq_f g^3 \frac{\Gamma(2-\epsilon)}{(4\pi)^{2+\epsilon}}\frac{1}{2\epsilon}\bar{u}_1 \tag{4.7}$$

$$\times\int\limits_0^1 \frac{dy}{\left(-(1-y)t-yt_1\right)^{1-\epsilon}}$$

$$\times\Big\{-(1-2\epsilon)\frac{t}{t_1}\hat{\Gamma}_1-(2+\epsilon)\hat{\Gamma}_1+(1+2\epsilon)x_2$$

$$\times\left(\hat{\Gamma}_1+\hat{\Gamma}_2-2(e_\perp q_\perp)\right)+y\Big[\Big(\frac{t}{t_1}$$

$$-1\Big)\hat{\Gamma}_1-(1+\epsilon)x_2\left(\hat{\Gamma}_1+\hat{\Gamma}_2-2(e_\perp q_\perp)\right)\Big]\Big\}\frac{\not{p}_2}{s}v_2.$$

The calculation of R_4 and $\tilde{R}_6$ is, actually, also quite straightforward, although it is very tedious. To simplify the representation of the results, we split the corresponding diagrams into two parts: infrared divergent part and convergent part. For the first part, we present results in the spinor representation and, for the other part, in the helicity representation with the use of the definitions of Eqs. (2.12) and (2.15). In addition, instead of the result for $\tilde{R}_6$, we present the result for R_6,

$$\tilde{R}_6 = \frac{1}{2}\left(R_6 - R_6(1\leftrightarrow 2)\right), \tag{4.8}$$

which can evidently be used in (4.1) instead of $\tilde{R}_6$. The results for the singular parts are

$$R_4^{(s)} = eq_f g^3\frac{\Gamma(2-\epsilon)}{(4\pi)^{2+\epsilon}}\bar{u}_1$$

$$\times\int\limits_0^1\int\limits_0^1\int\limits_0^1 \frac{dzdy_1dy_2\theta\left(1-y_1-y_2\right)z^{1+\epsilon}\kappa}{\left[zy_1y_2\left(-\kappa-i\delta\right)+(1-z)\left(y_1Q^2-y_2t-(1-y_1-y_2)t_1\right)\right]^{2-\epsilon}} \tag{4.9}$$

$$\times\Big[(1-y_1-y_2)\left((1-z(1-y_2))\,x_2\left(\hat{\Gamma}_1+\hat{\Gamma}_2-2(e_\perp q_\perp)\right)-\hat{\Gamma}_1\right)$$

$$-\,2y_1(1-zy_1)(ek_1)\Big]\frac{\not{p}_2}{s}v_2,$$

$$R_6^{(s)} = eq_f g^3\frac{\Gamma(2-\epsilon)}{(4\pi)^{2+\epsilon}}\frac{1}{2\epsilon}\int\limits_0^1\int\limits_0^1 \frac{dy_1dy_2(1-y_1)}{\left(-y_1y_2\kappa-t-y_2(t_1-t)-y_1(t_2-t)\right)^{2-\epsilon}} \tag{4.10}$$

$$\times\bar{u}_1\left\{2(t_2-t)\left(\hat{\Gamma}_1+2y_1(ek_1)\right)-x_1((1-y_1)t_1-y_1Q^2)\left(\hat{\Gamma}_1+\hat{\Gamma}_2-2(e_\perp q_\perp)\right)\right\}\frac{\not{p}_2}{s}v_2.$$

The results for the regular parts are

$$R_4^{(r)} = \frac{eq_f g^3}{(4\pi)^2}\frac{2}{\sqrt{2x_1x_2\mathbf{q}^2}} \tag{4.11}$$

$$\times\int\limits_0^1\int\limits_0^1\int\limits_0^1 \frac{dzdy_1dy_2\theta\left(1-y_1-y_2\right)z}{\left[zy_1y_2\left(-\kappa-i\delta\right)+(1-z)\left(y_1Q^2-y_2t-(1-y_1-y_2)t_1\right)\right]^2}$$

$$\times\left\{\left[(1-z)\left(y_1Q^2-y_2t-(1-y_1-y_2)t_1\right)-zy_1y_2\kappa\right]\right.$$

$$\times\left[((1-y_2)(\mathbf{k}_1\cdot\mathbf{q}+i\lambda P)-y_2x_1\mathbf{q}^2)zx_2\delta_{\lambda,-\xi}-\left((1-zy_1)\left(x_1\mathbf{q}^2+\mathbf{k}_1\cdot\mathbf{q}+i\lambda P\right)\right.\right.$$

$$\left.+\,(1-z)x_2\mathbf{q}^2\right)x_1\delta_{\lambda,\xi}\Big]+y_1x_2\kappa\Big[\,(1-z(1-y_2))\,x_1(\sqrt{2}qQx_1\delta_{\lambda,0}$$

$$-\,(\mathbf{k}_1\cdot\mathbf{q}+i\lambda P)(\delta_{\lambda,\xi}+\delta_{\lambda,-\xi}))-zy_2x_1\mathbf{q}^2\delta_{\lambda,-\xi}\Big]+(1-z)\left[(1-y_1-y_2)\left(\left(x_2\mathbf{q}^4\right.\right.\right.$$

$$\left.\left.+\,((\mathbf{k}_1-\mathbf{k}_2)\cdot\mathbf{q})(\mathbf{k}_2\cdot\mathbf{q}-i\lambda P)\right)x_1\delta_{\lambda,\xi}+x_2\mathbf{k}_1^2\cdot\mathbf{q}^2(\delta_{\lambda,-\xi}-\delta_{\lambda,\xi})\right)+y_2x_1\mathbf{q}^2\left(x_2\mathbf{q}^2\delta_{\lambda,-\xi}\right.$$

$$\left.-\,(\mathbf{k}_2\cdot\mathbf{q}-i\lambda P)\delta_{\lambda,\xi})\,\right]+(1-z)\left(y_1x_1+(1-y_2)x_2\right)$$

$$\times\left[(x_1(\mathbf{k}_2\cdot\mathbf{q}-i\xi P)-zy_1(\mathbf{k}_1\cdot\mathbf{q}-i\xi P-x_1t_1))\sqrt{2}qQ\delta_{\lambda,0}+z(1-y_1-y_2)\right.$$

$$\times\left(\left(\mathbf{k}_1^2\cdot\mathbf{q}^2-x_1t_1(\mathbf{k}_1\cdot\mathbf{q}+i\lambda P)\right)(\delta_{\lambda,-\xi}-\delta_{\lambda,\xi})+2(\mathbf{k}_1\cdot\mathbf{k}_2-x_1x_2Q^2)\right.$$

$$\left.\left.\times\,(\mathbf{k}_1\cdot\mathbf{q}+i\lambda P)\delta_{\lambda,-\xi}-(\mathbf{k}_1\cdot\mathbf{q}-i\xi P-x_1t_1)\sqrt{2}qQx_2\delta_{\lambda,0})+zy_2\mathbf{q}^2\right.\right.$$

$$\times \left((\mathbf{k}_1\cdot\mathbf{q}+i\lambda P-x_1t_1)(\delta_{\lambda,-\xi}-\delta_{\lambda,\xi})-2(\mathbf{k}_1\cdot\mathbf{k}_2-x_1x_2Q^2)\delta_{\lambda,\xi}\right]\Big\}$$

and

$$R_6^{(r)}=\frac{eq_fg^3}{(4\pi)^2\sqrt{2x_1x_2\mathbf{q}^2}}\int\limits_0^1\int\limits_0^1\frac{dy_1dy_2}{\left(-y_1y_2\kappa-t-y_2(t_1-t)-y_1(t_2-t)\right)^2} \tag{4.12}$$

$$\times\Bigg(y_1\delta_{\lambda,0}\sqrt{2}qQx_1\left\{\left(x_1x_2Q^2-\mathbf{k}_1\cdot\mathbf{k}_2-i\xi P\right)(1-3x_2)+2x_2(t_2-t)\right\}+(1-y_1)$$

$$\times\Big\{\left[2\left(-y_1y_2\kappa-t-y_2(t_1-t)-y_1(t_2-t)\right)+y_1(t_2-t-\kappa)\right]x_1x_2$$

$$\times\Big((\delta_{\lambda,-\xi}+\delta_{\lambda,\xi})(\mathbf{k}_1\cdot\mathbf{q}+i\lambda P)-\delta_{\lambda,0}\sqrt{2}qQx_1\Big)$$

$$+\left[2x_1t_1+2x_2t_2-2t-y_2x_2(t_2-t-\kappa)\right]$$

$$\times\Big(\delta_{\lambda,0}\sqrt{2}qQx_1x_2-\delta_{\lambda,-\xi}x_2(\mathbf{k}_1\cdot\mathbf{q}+i\lambda P)-\delta_{\lambda,\xi}x_1(\mathbf{k}_2\cdot\mathbf{q}-i\lambda P)\Big)$$

$$-\Big[t\left(2x_1\delta_{\lambda,\xi}+3x_2\delta_{\lambda,-\xi}\right)+y_1x_1\Big(t\delta_{\lambda,-\xi}-\delta_{\lambda,0}\sqrt{2}qQx_1\Big)\Big]$$

$$\times\left(x_1x_2Q^2-\mathbf{k}_1\cdot\mathbf{k}_2-i\xi P\right)+\Big[3\left(x_2^2t_2\delta_{\lambda,-\xi}-x_1^2t_1\delta_{\lambda,\xi}\right)+y_1x_1x_2\left(t_2\delta_{\lambda,-\xi}-t_1\delta_{\lambda,\xi}\right)$$

$$-\,y_1x_1Q^2\delta_{\lambda,\xi}\Big](\mathbf{k}_1\cdot\mathbf{q}+i\lambda P)+x_1t\left[3x_2^2Q^2\delta_{\lambda,-\xi}\right.$$

$$\left.-\,3\mathbf{k}_1^2\delta_{\lambda,\xi}+y_1x_1Q^2\left(\delta_{\lambda,-\xi}x_2+\delta_{\lambda,\xi}x_1\right)+2y_2x_2\kappa\delta_{\lambda,\xi}\right]\Big\}\Bigg).$$

The result for the correction $\Gamma^{(1g)c(1)}_{\gamma^*q\bar{q}}$ is obtained now by Eq. (4.1) with the replacement

$$\tilde{R}_6\to R_6, \tag{4.13}$$

where R_1, R_2, R_3, and R_5 are presented by Eqs. (4.4), (4.5), (4.6), and (4.7), respectively, and R_4 and R_6 are given by Eqs. (4.9)–(4.12) and by the relation

$$R_{4,6}=R^{(s)}_{4,6}+R^{(r)}_{4,6}. \tag{4.14}$$

5. THE TOTAL ONE-LOOP CORRECTION

There is one more one-loop contribution to the vertex $\Gamma^c_{\gamma^*q\bar{q}}$ related to the t-channel gluon self-energy. It is given by the half of the amplitude schematically represented in Fig. 8 with the gluon polarization vector equal to $-p_2^\mu/s$, as was already explained in Section 3. To find the correction $\Gamma^{(\mathrm{se})c(1)}_{\gamma^*q\bar{q}}$, one should only know the one-loop gluon vacuum polarization and the Born Reggeon–virtual-photon vertex. We obtain

$$\Gamma^{(\mathrm{se})c(1)}_{\gamma^*q\bar{q}}\left(eq_fg^3Nt^c_{i_1i_2}\frac{\Gamma(2-\epsilon)}{(4\pi)^{2+\epsilon}}\frac{1}{2\epsilon}\right)^{-1} \tag{5.1}$$

$$=\Bigg[\bar{u}_1\,(-t)^\epsilon\left\{\frac{5}{3}-\frac{2}{3}\frac{n_f}{N}\right.$$

$$\left.+\,\epsilon\left(\frac{4}{9}\frac{n_f}{N}-\frac{16}{9}\right)\right\}\frac{\hat{\Gamma}_1}{t_1}\frac{\not{p}_2}{s}v_2\Bigg]-[1\leftrightarrow 2]\,,$$

where n_f is the number of quark flavors.

We present the total one-loop correction to the vertex of the quark–antiquark production in the virtual-photon–Reggeized-gluon collision in the form

$$\Gamma^{c(1)}_{\gamma^*q\bar{q}}=\Gamma^{(\mathrm{sing})c(1)}_{\gamma^*q\bar{q}}+\Gamma^{(\mathrm{reg})c(1)}_{\gamma^*q\bar{q}}, \tag{5.2}$$

with

$$\Gamma^{(reg)c(1)}_{\gamma^*q\bar{q}} \tag{5.3}$$

$$=Nt^c_{i_1i_2}\left\{\left[\frac{N-2C_F}{N}R_4^{(r)}+R_6^{(r)}\right]-[1\leftrightarrow 2]\right\},$$

where $R_4^{(r)}$ and $R_6^{(r)}$ are given by Eqs. (4.11) and (4.12), respectively, and

$$\Gamma^{(\mathrm{sing})c(1)}_{\gamma^*q\bar{q}}=\Gamma^{(2g)c(1)}_{\gamma^*q\bar{q}}+\Gamma^{(\mathrm{se})c(1)}_{\gamma^*q\bar{q}} \tag{5.4}$$

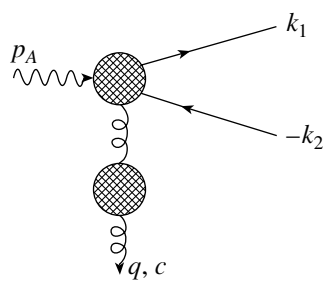

Fig. 8. Schematic representation of the correction $\Gamma^{(\mathrm{se})c(1)}_{\gamma^*q\bar{q}}$.

$$+ Nt^c_{i_1i_2}\left\{\left[-\frac{2C_F}{N}\,(R_1+R_2)+\frac{N-2C_F}{N}\right.\right.$$
$$\left.\left.\times\left(R_3+R_4^{(s)}\right)+R_5+R_6^{(s)}\right]-[1\leftrightarrow 2]\right\},$$

where $\Gamma^{(2g)c(1)}_{\gamma^*q\bar q}, \Gamma^{(se)c(1)}_{\gamma^*q\bar q}$, $R_1-R_3, R_5, R_4^{(s)}$, and $R_6^{(s)}$ are defined in Eqs. (3.15), (5.1), (4.4)–(4.6), (4.7), (4.9), and (4.10), respectively. Using the last set of relations, one can easily obtain

$$\Gamma^{(\mathrm{sing})c(1)}_{\gamma^*q\bar q}\left(eq_fg^3Nt^c_{i_1i_2}\frac{\Gamma(2-\epsilon)}{(4\pi)^{2+\epsilon}}\frac{1}{2\epsilon}\right)^{-1} \tag{5.5}$$
$$=\left[\bar u_1\left((-t)^\epsilon\left\{\frac{5}{3}-\frac{2}{3}\frac{n_f}{N}+4(1+\epsilon)\ln x_2\ +2\epsilon\left(\frac{2}{9}\frac{n_f}{N}-\frac{8}{9}-\psi'(1)\right)\right\}\frac{\hat\Gamma_1}{t_1}\right.\right.$$
$$+\frac{2C_F}{N}\frac{\hat\Gamma_1}{(-t_1)^{1-\epsilon}}+\frac{2C_F}{N}\int\limits_0^1\frac{dy}{((1-y)Q^2-yt_1)^{1-\epsilon}}$$
$$\times\left\{(1+2\epsilon)\frac{Q^2}{t_1}\hat\Gamma_1+2\epsilon(ep_1)+y\left[(1-2\epsilon)\left(\frac{Q^2}{t_1}+1\right)\hat\Gamma_1+2(2-\epsilon)\,(ek_1)\right]\right\}$$
$$+\frac{1}{N}\int\limits_0^1\frac{dy}{(-(1-y)t-yt_1)^{1-\epsilon}}\left\{2\left((1+3\epsilon)N-(1+2\epsilon)C_F\right)\frac{t}{t_1}\hat\Gamma_1\right.$$
$$-(2+\epsilon)N\hat\Gamma_1+(1+2\epsilon)Nx_2\left(\hat\Gamma_1+\hat\Gamma_2-2(e_\perp q_\perp)\right)-y^\epsilon 4(1+\epsilon)N\left(\frac{t}{t_1}-1\right)\hat\Gamma_1$$
$$+y\left[2\left((1-\epsilon)N-(1-2\epsilon)C_F\right)\left(\frac{t}{t_1}-1\right)\hat\Gamma_1+\left((1-2\epsilon)N\right.\right.$$
$$\left.\left.\left.-\ 2(2-\epsilon)C_F\right)x_2\left(\hat\Gamma_1+\hat\Gamma_2-2(e_\perp q_\perp)\right)\right]\right\}+\frac{N-2C_F}{N}$$
$$\times\int\limits_0^1\int\limits_0^1\int\limits_0^1\frac{dzdy_1dy_2\theta\,(1-y_1-y_2)\,z^{1+\epsilon}2\epsilon\kappa}{\left[zy_1y_2\,(-\kappa-i\delta)+(1-z)\,(y_1Q^2-y_2t-(1-y_1-y_2)t_1)\right]^{2-\epsilon}}$$
$$\times\left[(1-y_1-y_2)\left((1-z(1-y_2))\,x_2\left(\hat\Gamma_1+\hat\Gamma_2-2(e_\perp q_\perp)\right)-\hat\Gamma_1\right)\right.$$
$$\left.-\ 2y_1(1-zy_1)\,(ek_1)\right]+\int\limits_0^1\int\limits_0^1\frac{dy_1dy_2}{(-y_1y_2\kappa-t-y_2(t_1-t)-y_1(t_2-t))^{2-\epsilon}}$$
$$\times\left\{y_1^{\epsilon-1}(1-y_1)y_2^{-\epsilon}\left(x_1^\epsilon x_2^{-\epsilon}-2\epsilon^2\psi'(1)\right)2t\hat\Gamma_1+\left(y_1^\epsilon y_2^{-\epsilon}x_1^\epsilon x_2^{-\epsilon}-1\right)4x_2t(ep_1)\right.$$
$$+(1-y_1)\left[2(t_2-t)\hat\Gamma_1-x_1t_1\left(\hat\Gamma_1+\hat\Gamma_2-2(e_\perp q_\perp)\right)+4t(ek_1)\right]$$
$$\left.+\ y_1(1-y_1)\left[4(t_2-t)(ek_1)+x_1(t_1+Q^2)\left(\hat\Gamma_1+\hat\Gamma_2-2(e_\perp q_\perp)\right)\right]\right\}\frac{\not p_2}{s}v_2\Bigg]-[1\leftrightarrow 2]\,.$$

Relations (5.2), (5.3), and (5.5), together with Eqs. (4.11) and (4.12), present the one-loop correction to the $\gamma^*R\to q\bar q$ vertex.

6. DISCUSSION

In this paper, we have calculated the effective vertices for the Reggeon–virtual-photon interaction. Starting from already known expressions (2.9) and (2.10) for the $q\bar q$-production vertex in the Born approximation, we have represented this vertex in the helicity basis (2.16) and then have obtained in the same approximation the vertex (2.19) for the $q\bar qg$ production. Most of the paper is devoted to the calculation of the one-loop corrections for the $q\bar q$-production vertex, which are presented in Eqs. (5.2), (5.5), (5.3), (4.11), and (4.12). In order to simplify the

presentation, the last three results are given in the helicity basis, that caused the representation in this basis also of the Born $q\bar{q}$-production vertex (2.16).

The obtained results can be used for theoretical analysis of a number of processes related to the quark–antiquark production in the photon fragmentation region. In particular, they are necessary for calculation of the virtual-photon impact factor at the next-to-leading order [see Eq. (1.3)]. We have used the integral representation for a part of the one-loop corrections to the $q\bar{q}$-production vertex since it is convenient for further calculation of the virtual-photon impact factor in the next-to-leading order.

Note that everywhere in the paper g is the unrenormalized coupling constant, so that the one-loop correction contains the ultraviolet singularities in ϵ. In order to remove them one should only express g in terms of the renormalized coupling constant $g(\mu)$. After the renormalization, there still remain the infrared singularities, which must cancel in physical quantities (in the virtual-photon impact factor they cancel [13] with corresponding terms in the contributions from the additional gluon emission and from the counterterm [see Eq. (1.3)].

Recently, an independent calculation of the $\gamma^* \to q\bar{q}$ vertex was reported in [15]. The results of [15] are presented in the form where all integrations are performed. At the moment, we can only say that these results are very long and complicated. Some time is definitely needed to make a comparison between our and their results.

ACKNOWLEDGMENTS

This work is partly supported by the INTAS (grant nos. 00-0036 and 00-00679) and by the Russian Foundation for Basic Research (project nos. 99-02-16822, 99-02-17211, 00-15-96691, and 01-02-16042). Two of us (M.K. and D.I.) thank the Dipartimento di Fisica della Università della Calabria for the warm hospitality while part of this work was done. D.I. was supported by Alexander von Humboldt Stiftung.

APPENDIX

In this section, we explain very briefly important steps for calculation of the most complicated diagram D_2 [Fig. 5(*2*)] to make our results checkable step by step. According to its definition, we obtain from the corresponding diagram

$$D_2 = \frac{-ieq_f g^4}{2(2\pi)^D} \int \frac{d^D k \bar{u}_1 \gamma^\mu (\not{k}+\not{p}_A-\not{k}_2)\ \not{e}\,(\not{k}-\not{k}_2)\,\gamma^\lambda v_2 \bar{u}_{B'} \gamma^\rho (\not{k}+\not{p}_{B'})\,\gamma^\nu u_B g_{\mu\nu} g_{\lambda\rho}}{[(k+p_{B'})^2+i\delta]\,[(k+p_A-k_2)^2+i\delta]\,[(k-k_2)^2+i\delta]\,[k^2+i\delta]\,[(k+q)^2+i\delta]}. \quad \text{(A.1)}$$

It was explained in detail in [13] that the negative t-channel signature combination of the two pentagon diagrams of Fig. 5, or, what is the same, the $s \leftrightarrow -s$ antisymmetric part of the D_2, gets the contribution only from the integration region where

$$\mathbf{q}^2 \sim \mathbf{k}^2 \sim |kp_1| \ll |kp_2| \sim s, \quad \text{(A.2)}$$

and therefore we can replace from the beginning

$$\frac{1}{(k+p_{B'})^2+i\delta} \to \mathrm{P}\frac{1}{2kp_2} \quad \text{(A.3)}$$

and understand this singularity in a sense of the principal value everywhere below. In order to simplify also the numerator of D_2, we use the familiar replacement (2.3) for the t-channel gluon propagators. These simplifications lead to the following representation for D_2:

$$D_2 = -2ieq_f g^4 s \bar{u}_{B'} \frac{\not{p}_1}{s} u_B \int \frac{d^D k}{(2\pi)^D} \quad \text{(A.4)}$$
$$\times \frac{1}{[(k+p_A-k_2)^2+i\delta]\,[(k-k_2)^2+i\delta]\,[k^2+i\delta]\,[(k+q)^2+i\delta]}$$
$$\times \bar{u}_1 \left\{ \not{e}\,(\not{k}-\not{k}_2) + (\not{k}+\not{q})\not{e} + \frac{s}{2kp_2}\,(x_1 \not{e}\,(\not{k}-\not{k}_2) - x_2\,(\not{k}+\not{q})\ \not{e}) \right\} \frac{\not{p}_2}{s} v_2.$$

Since the structure of D_2 is like the box diagram with two massive external lines in opposite corners, it is convenient to perform the Feynman parametrization joining first the pairs of propagators which meet at each of the vertices with massless external lines, and then to join two denominators obtained in this way

using the third Feynman parameter. Doing so, we naturally get the result of momentum integration in the form where the dependence on the third Feynman parameter factorizes and the integration over this parameter can be performed straightforwardly. So, we use in Eq. (A.4) the representation

$$\frac{1}{[(k+p_A-k_2)^2+i\delta]\,[(k-k_2)^2+i\delta]\,[k^2+i\delta]\,[(k+q)^2+i\delta]} \tag{A.5}$$
$$= 6\int\limits_0^1 \frac{d^3y y_3(1-y_3)}{[k^2+2k\,((1-y_3)(q+y_1k_1)-y_3y_2k_2)+(1-y_3)\,((1-y_1)t+y_1t_2)+i\delta]^4}.$$

For the term with $1/(2kp_2)$ in Eq. (A.4), we use the relation

$$\frac{1}{a^4b} = 4\int\limits_0^\infty \frac{du}{(a+bu)^5}, \tag{A.6}$$

which leads, together with Eq. (A.5), to the expression

$$D_2 = -12ieq_fg^4s\bar u_{B'}\frac{\not p_1}{s}u_B\bar u_1\int\limits_0^1 d^3y y_3(1-y_3)\int\frac{d^Dk}{(2\pi)^D}\left\{\frac{\not e\,(\not k-\not k_2)+(\not k+\not q)\not e}{[(k+p)^2-y_3(1-y_3)b^2+i\delta]^4}\right. \tag{A.7}$$
$$\left. +\,4\int\limits_0^\infty du\frac{s\,(x_1\not e\,(\not k-\not k_2)-x_2\,(\not k+\not q)\not e)}{[(k+p+up_2)^2-y_3(1-y_3)b^2-su\,((1-y_3)y_1x_1-y_2y_3x_2)+i\delta]^5}\right\}\frac{\not p_2}{s}v_2,$$

where the notation

$$p=(1-y_3)(q+y_1k_1)-y_2y_3k_2, \tag{A.8}$$
$$b^2=(1-y_2)\,(-(1-y_1)t-y_1t_2)+y_2\left(-(1-y_1)t_1+y_1Q^2\right)$$

has been introduced.

Now the k integration and then the integration over u are immediately performed. The result is

$$D_2 = g\bar u_{B'}\frac{\not p_1}{s}u_B\frac{2s}{t}eq_fg^3\frac{\Gamma(2-\epsilon)}{(4\pi)^{2+\epsilon}}t\bar u_1 \tag{A.9}$$
$$\times\int\limits_0^1\frac{d^2y}{(b^2)^{2-\epsilon}}\mathrm{P}\int\limits_0^1\frac{dy_3}{[y_3(1-y_3)]^{1-\epsilon}}$$
$$\times\{(\not q-\not p)\not e-\not e\,(\not k_2+\not p)$$
$$+\,\frac{x_2\,(\not q-\not p)\not e+x_1\not e\,(\not k_2+\not p)}{x_1\,((1-y_3)y_1-zy_3y_2)}\Big\}\frac{\not p_2}{s}v_2,$$

with

$$z=x_2/x_1. \tag{A.10}$$

After some simplifying algebra with the use of the fact that D_2 enters into our result for the vertex only in the antisymmetric combination under the replacement $1\leftrightarrow 2$ [see Eq. (3.2)] we come to the representation

$$D_2 = 2g\bar u_{B'}\frac{\not p_1}{s}u_B\frac{2s}{t}eq_fg^3\frac{\Gamma(2-\epsilon)}{(4\pi)^{2+\epsilon}} \tag{A.11}$$
$$\times\,\bar u_1t\frac{\not p_2}{s}\int\limits_0^1\int\limits_0^1\frac{dy_1dy_2}{[(1-y_2)\,(-(1-y_1)t-y_1t_2)+y_2\,(-(1-y_1)t_1+y_1Q^2)]^{2-\epsilon}}$$
$$\times\left[\frac{1-y_1}{x_1}\,(2x_2(k_{1\perp}e_\perp)-\not e_\perp\not k_{1\perp})\,\mathrm{P}\int\limits_0^1\frac{dy_3y_3^{\epsilon-1}(1-y_3)^\epsilon}{((1-y_3)y_1-zy_3y_2)}\right.$$
$$\left.+\,x_2(ep_1)\,\mathrm{P}\int\limits_0^1\frac{dy_3y_3^{\epsilon-1}(1-y_3)^{\epsilon-1}}{((1-y_3)y_1-zy_3y_2)}+\frac{2}{\epsilon}\,((ek_1)\,(1-y_1)-x_2(ep_1))\right]v_2,$$

and, finally, the relations

$$\mathrm{P}\int_0^1 \frac{dy_3 y_3^{\epsilon-1}(1-y_3)^{\epsilon}}{((1-y_3)y_1 - z y_3 y_2)} \qquad (A.12)$$
$$= \frac{1}{\epsilon}\left(1 - 2\epsilon^2\psi'(1)\right) z^{-\epsilon} y_1^{\epsilon-1} y_2^{-\epsilon}$$

and

$$\mathrm{P}\int_0^1 \frac{dy_3 y_3^{\epsilon-1}(1-y_3)^{\epsilon-1}}{((1-y_3)y_1 - z y_3 y_2)} \qquad (A.13)$$
$$= \frac{1}{\epsilon}\left(1 - 2\epsilon^2\psi'(1)\right) z^{-\epsilon}\left(y_1^{\epsilon-1} y_2^{-\epsilon} - z^{2\epsilon-1} y_2^{\epsilon-1} y_1^{-\epsilon}\right),$$

which are valid with sufficient accuracy for us in the ϵ expansion, lead to the result (3.5).

REFERENCES

1. V. S. Fadin, E. A. Kuraev, and L. N. Lipatov, Phys. Lett. B **60B**, 50 (1975); E. A. Kuraev, L. N. Lipatov, and V. S. Fadin, Zh. Éksp. Teor. Fiz. **71**, 840 (1976) [Sov. Phys. JETP **44**, 443 (1976)]; Zh. Éksp. Teor. Fiz. **72**, 377 (1977) [Sov. Phys. JETP **45**, 199 (1977)]; Ya. Ya. Balitskii and L.N. Lipatov, Yad. Fiz. **28**, 1597 (1978) [Sov. J. Nucl. Phys. **28**, 822 (1978)].
2. A. M. Cooper-Sarkar, R. C. E. Devenish, and A. De Roeck, Int. J. Mod. Phys. A **13**, 3385 (1998) and references therein.
3. L. N. Lipatov and V. S. Fadin, Yad. Fiz. **50**, 1141 (1989) [Sov. J. Nucl. Phys. **50**, 712 (1989)].
4. V. S. Fadin, R. Fiore, and M. I. Kotsky, Phys. Lett. B **359**, 181 (1995).
5. V. S. Fadin, R. Fiore, and M. I. Kotsky, Phys. Lett. B **387**, 593 (1996).
6. V. S. Fadin and L. N. Lipatov, Nucl. Phys. B **406**, 259 (1993).
7. V. S. Fadin, R. Fiore, and A. Quartarolo, Phys. Rev. D **50**, 5893 (1994); V. S. Fadin, R. Fiore, and M. I. Kotsky, Phys. Lett. B **389**, 737 (1996); V. S. Fadin and L. N. Lipatov, Nucl. Phys. B **477**, 767 (1996); V. S. Fadin, M. I. Kotsky, and L. N. Lipatov, Phys. Lett. B **415**, 97 (1997); V. S. Fadin, R. Fiore, A. Flachi, and M. I. Kotsky, Phys. Lett. B **422**, 287 (1998).
8. S. Catani, M. Ciafaloni, and F. Hautman, Phys. Lett. B **242**, 97 (1990); Nucl. Phys. B **366**, 135 (1991); G. Camici and M. Ciafaloni, Phys. Lett. B **386**, 341 (1996); Nucl. Phys. B **496**, 305 (1997).
9. V. S. Fadin and L. N. Lipatov, Phys. Lett. B **429**, 127 (1998).
10. G. Camici and M. Ciafaloni, Phys. Lett. B **430**, 349 (1998).
11. V. S. Fadin and R. Fiore, Phys. Lett. B **440**, 359 (1998).
12. V. S. Fadin, R. Fiore, M. I. Kotsky, and A. Papa, Phys. Rev. D **61**, 094006 (2000); **61**, 094005 (2000).
13. V. S. Fadin and A. D. Martin, Phys. Rev. D **60**, 114008 (1999).
14. V. Fadin, D. Ivanov, and M. Kotsky, in *New Trends in High-Energy Physics,* Ed. by L. L. Jenkovszky (Kiev, 2000), p. 190; hep-ph/0007119.
15. J. Bartels, S. Gieseke, and C. F. Qiao, Phys. Rev. D **63**, 056014 (2001); hep-ph/0009102.

Physics of Atomic Nuclei, Vol. 65, No. 8, 2002, pp. 1528–1536. From Yadernaya Fizika, Vol. 65, No. 8, 2002, pp. 1566–1574.

ELEMENTARY PARTICLES AND FIELDS
Theory

Analysis of the $\phi \to \gamma\pi\eta$ and $\phi \to \gamma\pi^0\pi^0$ Decays*

N. N. Achasov ** **and V. V. Gubin*****

Sobolev Institute for Mathematics, Siberian Division, Russian Academy of Sciences, Novosibirsk, Russia

Received February 23, 2001; in final form, June 7, 2001

Abstract—We study interference patterns in the $\phi \to (\gamma a_0 + \pi^0\rho) \to \gamma\pi\eta$ and $\phi \to (\gamma f_0 + \pi^0\rho) \to \gamma\pi^0\pi^0$ reactions. Taking into account the interference, we fit the experimental data and show that the background reaction does not distort the $\pi^0\eta$ spectrum in the decay $\phi \to \gamma\pi\eta$ everywhere over the energy region and does not distort the $\pi^0\pi^0$ spectrum in the decay $\phi \to \gamma\pi^0\pi^0$ in the wide region of the $\pi^0\pi^0$-system invariant mass, $m_{\pi\pi} > 670$ MeV, or when the photon energy is less than 300 MeV. We discuss the details of the scalar meson production in the radiative decays and note that there are reasonable arguments in favor of the one-loop mechanism $\phi \to K^+K^- \to \gamma a_0$ and $\phi \to K^+K^- \to \gamma f_0$. We also discuss distinctions between the four-quark, molecular, and two-quark models and argue that the Novosibirsk data give evidence in favor of the four-quark nature of the scalar $a_0(980)$ and $f_0(980)$ mesons. © *2002 MAIK "Nauka/Interperiodica"*.

1. INTRODUCTION

As was shown in a number of papers (see [1–6] and references therein), the study of the radiative decays $\phi \to \gamma a_0 \to \gamma\pi\eta$ and $\phi \to \gamma f_0 \to \gamma\pi\pi$ can shed light on the problem of the scalar $a_0(980)$ and $f_0(980)$ mesons. These decays have been studied not only theoretically but also experimentally. At the present time, there have already been published the data obtained in Novosibirsk with the detectors SND [7–10] and CMD-2 [11], which give the following branching ratios: $\mathrm{BR}(\phi \to \gamma\pi\eta) = (0.88 \pm 0.14 \pm 0.09) \times 10^{-4}$ [9], $\mathrm{BR}(\phi \to \gamma\pi^0\pi^0) = (1.221 \pm 0.098 \pm 0.061) \times 10^{-4}$ [10] and $\mathrm{BR}(\phi \to \gamma\pi\eta) = (0.9 \pm 0.24 \pm 0.1) \times 10^{-4}$, $\mathrm{BR}(\phi \to \gamma\pi^0\pi^0) = (0.92 \pm 0.08 \pm 0.06) \times 10^{-4}$ [11].

These data give evidence in favor of the four-quark ($q^2\bar{q}^2$) [1, 12–16] nature of the scalar $a_0(980)$ and $f_0(980)$ mesons. Note that the isovector $a_0(980)$ meson is produced in the radiative ϕ meson decay as intensively as the well-studied η' meson involving essentially strange quarks $s\bar{s}$ ($\approx 66\%$) responsible for the decay.

As was shown in the papers [1, 3, 17], the background situation for studying the radiative decays $\phi \to \gamma a_0 \to \gamma\pi^0\eta$ and $\phi \to \gamma f_0 \to \gamma\pi^0\pi^0$ is very good. For example, in the case of the decay $\phi \to \gamma a_0 \to \gamma\pi^0\eta$, the process $\phi \to \pi^0\rho \to \gamma\pi^0\eta$ is the dominant background. The estimation for the soft, by strong interaction standard, photon energy, $\omega < 100$ MeV, gives $\mathrm{BR}(\phi \to \pi^0\rho^0 \to \gamma\pi^0\eta, \omega < 100\ \mathrm{MeV}) \approx 1.5 \times 10^{-6}$. The influence of the background process is negligible, provided $\mathrm{BR}(\phi \to \gamma a_0 \to \gamma\pi^0\eta, \omega < 100\ \mathrm{MeV}) \geq 10^{-5}$. In this paper, in Section 2, we calculate the expression for the $\phi \to \gamma\pi^0\eta$-decay amplitude taking into account the interference between the $\phi \to \gamma a_0 \to \gamma\pi^0\eta$ and $\phi \to \pi^0\rho^0 \to \gamma\pi^0\eta$ processes. We show that, for the obtained experimental data, the influence of the background processes is negligible everywhere over the photon energy region.

The situation with $\phi \to \gamma f_0 \to \gamma\pi^0\pi^0$ decay is not much different. As was shown in [1, 3, 17], the dominant background is the $\phi \to \pi^0\rho^0 \to \gamma\pi^0\pi^0$ process with $\mathrm{BR}(\phi \to \pi^0\rho^0 \to \gamma\pi^0\pi^0, \omega < 100\ \mathrm{MeV}) \approx 6.4 \times 10^{-7}$. The influence of this background process is negligible, provided $\mathrm{BR}(\phi \to \gamma f_0 \to \gamma\pi^0\pi^0,\ \omega < 100\ \mathrm{MeV}) \geq 5 \times 10^{-6}$.

The exact calculation of the interference patterns between the decays $\phi \to \gamma f_0 \to \gamma\pi^0\pi^0$ and $\phi \to \pi^0\rho \to \gamma\pi^0\pi^0$, which we present in this paper in Section 3, shows that the influence of the background in the decay $\phi \to \gamma\pi^0\pi^0$ for the obtained experimental data is negligible in the wide region of the $\pi^0\pi^0$ invariant mass, $m_{\pi\pi} > 670$ MeV, or in the photon energy region $\omega < 300$ MeV.

In Section 4, we discuss the mechanism of the scalar-meson production in the radiative decays and show that experimental data obtained in Novosibirsk give reasonable arguments in favor of the one-loop mechanism, $\phi \to K^+K^- \to \gamma a_0$ and $\phi \to$

*This article was submitted by the authors in English.

**e-mail: achasov@math.nsc.ru

***e-mail: gubin@math.nsc.ru

$K^+K^- \to \gamma f_0$, of these decays. In the same place, we also discuss distinctions between the four-quark, molecular, and two-quark models and explain why these data give evidence in favor of the four-quark nature of the scalar $a_0(980)$ and $f_0(980)$ mesons.

2. INTERFERENCE BETWEEN THE $\phi \to \gamma a_0 \to \gamma\pi^0\eta$ AND $\phi \to \pi^0\rho^0 \to \gamma\pi^0\eta$ DECAYS

As was shown in the papers [1, 3], the background process $e^+e^- \to \phi \to \pi^0\rho^0 \to \gamma\pi^0\eta$ is dominant between the other background processes. The amplitudes of the processes $e^+e^- \to \rho^0(\omega) \to \eta\rho^0(\omega) \to \gamma\pi^0\eta$ are much less than the amplitudes of the $e^+e^- \to \rho^0(\omega) \to \pi^0\omega(\rho^0) \to \gamma\pi^0\eta$ processes. In turn, the amplitudes of the $e^+e^- \to \rho^0(\omega) \to \pi^0\omega(\rho^0) \to \gamma\pi^0\eta$ processes are much less than the amplitudes of the $e^+e^- \to \phi \to \pi^0\rho^0 \to \gamma\pi^0\eta$ processes. The amplitude of the $e^+e^- \to \phi \to \eta\phi \to \gamma\pi^0\eta$ process is also much less than the amplitude of $e^+e^- \to \phi \to \pi^0\rho^0 \to \gamma\pi^0\eta$ process.

The amplitude of the background process $\phi(p) \to \pi^0\rho^0 \to \gamma(q)\pi^0(k_1)\eta(k_2)$ is

$$M_B = \frac{g_{\phi\rho\pi}g_{\rho\eta\gamma}}{D_\rho(p-k_1)}\phi_\alpha k_{1\mu}p_\nu\epsilon_\delta \times (p-k_1)_\omega q_\epsilon \epsilon_{\alpha\beta\mu\nu}\epsilon_{\beta\delta\omega\epsilon}, \quad (1)$$

where ϕ_α and ϵ_δ are the polarization vectors of the ϕ meson and photon. The inverse propagator of the ρ meson D_ρ is defined below. For the amplitude of the signal $\phi \to \gamma a_0 \to \gamma\pi^0\eta$, we use the model suggested in [1], in which the one-loop mechanism of the decay $\phi \to K^+K^- \to \gamma a_0$ is considered:

$$M_a = g(m)\frac{g_{a_0K^+K^-}g_{a_0\pi\eta}}{D_{a_0}(m)}\left((\phi\epsilon) - \frac{(\phi q)(\epsilon p)}{(pq)}\right), \quad (2)$$

where $m^2 = (k_1+k_2)^2$ and the function $g(m)$ is determined in [1, 3]. The mass spectrum is

$$\frac{d\Gamma(\phi \to \gamma\pi\eta)}{dm} = \frac{d\Gamma_{a_0}}{dm} + \frac{d\Gamma_{\rm back}(m)}{dm} \pm \frac{d\Gamma_{\rm int}(m)}{dm}, \quad (3)$$

where the mass spectrum for the signal is

$$\frac{d\Gamma_{a_0}}{dm} = \frac{2}{\pi}\frac{m^2\Gamma(\phi \to \gamma a_0(m))\Gamma(a_0(m) \to \pi\eta)}{|D_{a_0}(m)|^2} = \frac{2|g(m)|^2 p_{\pi\eta}(m_\phi^2 - m^2)}{3(4\pi)^3 m_\phi^3}\left|\frac{g_{a_0K^+K^-}g_{a_0\pi\eta}}{D_{a_0}(m)}\right|^2. \quad (4)$$

Accordingly, the mass spectrum for the background process $\phi \to \pi^0\rho \to \gamma\pi^0\eta$ is

$$\frac{d\Gamma_{\rm back}(m)}{dm} = \frac{(m_\phi^2 - m^2)p_{\pi\eta}}{128\pi^3 m_\phi^3}\int\limits_{-1}^{1} dx A_{\rm back}(m,x), \quad (5)$$

where

$$A_{\rm back}(m,x) = \frac{1}{3}\sum|M_B|^2 = \frac{1}{24}(m_\eta^4 m_\pi^4 + 2m^2m_\eta^2m_\pi^2\tilde m_\rho^2 - 2m_\eta^4m_\pi^2\tilde m_\rho^2 - 2m_\eta^2m_\pi^4\tilde m_\rho^2 + 2m^4\tilde m_\rho^4 - 2m^2m_\eta^2\tilde m_\rho^4 + 2m_\eta^4\tilde m_\rho^4 - 2m^2m_\pi^2\tilde m_\rho^4 + 4m_\eta^2m_\pi^2\tilde m_\rho^4 + m_\pi^4\tilde m_\rho^4 + 2m^2\tilde m_\rho^6 - 2m_\eta^2\tilde m_\rho^6 - 2m_\pi^2\tilde m_\rho^6 + \tilde m_\rho^8 - 2m_\eta^4m_\pi^2m_\phi^2 - 2m^2m_\eta^2m_\phi^2\tilde m_\rho^2 + 2m_\eta^2m_\pi^2m_\phi^2\tilde m_\rho^2 - 2m^2m_\phi^2\tilde m_\rho^4 + 2m_\eta^2m_\phi^2\tilde m_\rho^4 - 2m_\phi^2\tilde m_\rho^6 + m_\eta^4m_\phi^4 + m_\phi^4\tilde m_\rho^4)\left|\frac{g_{\phi\rho\pi}g_{\rho\eta\gamma}}{D_\rho(\tilde m_\rho)}\right|^2 \quad (6)$$

and

$$\tilde m_\rho^2 = m_\eta^2 + \frac{(m^2 + m_\eta^2 - m_\pi^2)(m_\phi^2 - m^2)}{2m^2} - \frac{(m_\phi^2 - m^2)x}{m}p_{\pi\eta}, \quad (7)$$

$$p_{\pi\eta} = \frac{\sqrt{(m^2 - (m_\eta - m_\pi)^2)(m^2 - (m_\eta + m_\pi)^2)}}{2m}.$$

The interference between the background-process amplitude and the signal amplitude is written in the following way:

$$\frac{d\Gamma_{\rm int}(m)}{dm} = \frac{(m_\phi^2 - m^2)p_{\pi\eta}}{128\pi^3 m_\phi^3}\int\limits_{-1}^{1} dx A_{\rm int}(m,x), \quad (8)$$

where

$$A_{\rm int}(m,x) = \frac{2}{3}{\rm Re}\sum M_aM_B^* = \frac{1}{3}\left((m^2 - m_\phi^2)\tilde m_\rho^2 + \frac{m_\phi^2(\tilde m_\rho^2 - m_\eta^2)^2}{m_\phi^2 - m^2}\right) \times {\rm Re}\left\{\frac{g(m)g_{a_0K^+K^-}g_{a_0\pi\eta}g_{\phi\rho\pi}g_{\rho\eta\gamma}}{D_\rho^*(\tilde m_\rho)D_{a_0}(m)}\right\}. \quad (9)$$

The inverse propagator of the a_0 meson, $D_{a_0}(m)$, is presented in the papers [1, 3]. The inverse propagator of the ρ meson has the following expression:

$$D_\rho(m) = m_\rho^2 - m^2 - im^2\frac{g_{\rho\pi\pi}^2}{48\pi}\left(1 - \frac{4m_\pi^2}{m^2}\right)^{3/2}. \quad (10)$$

We use the coupling constant $g_{\phi K^+K^-} = 4.68 \pm 0.05$ obtained form the decay $\phi \to K^+K^-$ [18] and

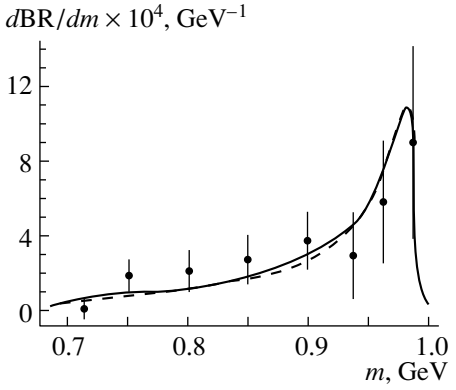

Fig. 1. Fitting of $d\mathrm{BR}(\phi \to \gamma\pi\eta)/dm \times 10^4$ with the background is shown with the solid curve and the signal contribution is shown with the dashed curve.

the coupling constant $g_{\rho\eta\gamma} = 0.572 \pm 0.08$ GeV^{-1} obtained from the decay $\rho \to \eta\gamma$ [19], with the help of the following expressions:

$$\Gamma(\phi \to K^+K^-) \tag{11}$$
$$= \frac{g^2_{\phi K^+K^-}}{48\pi} m_\phi \left(1 - \frac{4m_K^2}{m_\phi^2}\right)^{3/2},$$
$$\Gamma(\rho \to \eta\gamma) = \frac{g^2_{\rho\eta\gamma}}{96\pi m_\rho^3}(m_\rho^2 - m_\eta^2)^3.$$

The coupling constant $g_{\phi\rho\pi} = 0.811 \pm 0.081$ GeV^{-1} is obtained using the data on the decay $\phi \to \rho\pi \to \pi^+\pi^-\pi^0$ [18] with the help of the formulas from the paper [20].

The fit of the experimental data from the SND detector [9], taking into account the relation $g_{a_0\pi\eta} = 0.85 g_{a_0K^+K^-}$ resulting from the $q^2\bar{q}^2$ model [1], chooses the constructive interference and gives

$$m_{a_0} = 985.51 \pm 0.8 \text{ MeV}, \tag{12}$$
$$g_{a_0K^+K^-} = 2.747 \pm 0.428 \text{ GeV},$$
$$\frac{g^2_{a_0K^+K^-}}{4\pi} = 0.6 \pm 0.015 \text{ GeV}^2,$$
$$\chi^2/\mathrm{NDF} = 3.1/6.$$

The total branching ratio, taking into account the interference, is $\mathrm{BR}(\phi \to (\gamma a_0 + \pi^0\rho) \to \gamma\pi\eta) = (0.79 \pm 0.2) \times 10^{-4}$; the branching ratio of the signal is $\mathrm{BR}(\phi \to \gamma a_0 \to \gamma\pi\eta) = (0.75 \pm 0.2) \times 10^{-4}$; and the branching ratio of the background is $\mathrm{BR}(\phi \to \pi^0\rho^0 \to \gamma\pi^0\eta) = 3.43 \times 10^{-6}$. So, the integral part of the interference is negligible. The influence of the interference on the mass spectrum of the $\pi\eta$ system is also negligible (see Fig. 1).

The difference of the obtained parameters (12) from the parameters found in [9], which are $m_{a_0} = 994^{+33}_{-8}$ MeV, $g^2_{a_0K^+K^-}/4\pi = 1.05^{+0.36}_{-0.25}$ GeV^2, is due to the fact that in [9] a more refined fitting was performed considering the event distribution inside of each bin. Notice that this difference is less than two standard deviations.

Let us specifically emphasize that the value $g^2_{a_0K^+K^-}/4\pi = 0.6 \pm 0.015$ GeV^2 obtained by us on no account points to the possibility of the $K\bar{K}$ molecule description [2] of the a_0 meson. In the $K\bar{K}$-molecule model, the imaginary part of the K^+K^- loop is dominant because the real part of the K^+K^- loop is suppressed by the wave function of the molecule [4] (see also Section 4). Due to this fact, we have $\mathrm{BR}(\phi \to \gamma a_0 \to \gamma\pi\eta) \approx 1.5 \times 10^{-5}$ [4] in the $K\bar{K}$-molecule model at the same coupling constant and $m_{a_0} = 985$ MeV, which is almost six times less than the experimental value $\mathrm{BR}(\phi \to \gamma\pi\eta) = (0.88 \pm 0.14 \pm 0.09) \times 10^{-4}$ [9]. The divergence is five standard deviations! Besides, in the case of molecule, the bump in the spectrum of the $\pi\eta$ system is much narrower than the experimentally observed one (see [4], see also Section 4).

3. INTERFERENCE BETWEEN THE $\phi \to \gamma f_0 \to \gamma\pi^0\pi^0$ AND $\phi \to \pi^0\rho \to \gamma\pi^0\pi^0$ DECAYS

When analyzing the $\phi \to \gamma f_0 \to \gamma\pi^0\pi^0$ decay, one should take into account the mixing of the f_0 meson with the isosinglet scalar states. The whole formalism of the mixing of two scalar f_0 and σ mesons was considered in [3]. In this paper, we consider only expressions in regard to the interference with the background reactions.

As was shown in [1, 3], the dominant background is the $e^+e^- \to \phi \to \pi^0\rho \to \gamma\pi^0\pi^0$ reaction. The amplitude of the $e^+e^- \to \rho \to \pi^0\omega \to \gamma\pi^0\pi^0$ reaction is much less than the amplitude of the $e^+e^- \to \phi \to \pi^0\rho \to \gamma\pi^0\pi^0$ reaction. In turn, the amplitude of the $e^+e^- \to \omega \to \pi^0\rho \to \gamma\pi^0\pi^0$ reaction is much less than the amplitude of the $e^+e^- \to \rho \to \pi^0\omega \to \gamma\pi^0\pi^0$ reaction.

The amplitude of the background decay $\phi(p) \to \pi^0\rho \to \gamma(q)\pi^0(k_1)\pi^0(k_2)$ is written in the following way:

$$M_{\mathrm{back}} = g_{\phi\rho\pi^0} g_{\rho\pi^0\gamma} \phi_\alpha p_\nu \epsilon_{\delta} q_\epsilon \epsilon_{\alpha\beta\mu\nu} \epsilon_{\beta\delta\omega\epsilon} \tag{13}$$
$$\times \left(\frac{k_{1\mu}k_{2\omega}}{D_\rho(q+k_2)} + \frac{k_{2\mu}k_{1\omega}}{D_\rho(q+k_1)}\right).$$

The amplitude of the signal $\phi \to \gamma(f_0 + \sigma) \to \gamma\pi^0\pi^0$ takes into account the mixing of f_0 and σ mesons (see [3]),

$$M_{f_0} = g(m)e^{i\delta_B}\left((\phi\epsilon) - \frac{(\phi q)(\epsilon p)}{(pq)}\right) \times \left(\sum_{R,R'} g_{RK^+K^-}G^{-1}_{RR'}g_{R'\pi^0\pi^0}\right), \quad (14)$$

where $R, R' = f_0, \sigma$. The matrix of inverse propagators $G_{RR'}$ is defined in [3]. The phase of the signal amplitude is formed by the phase of the triangle diagram ($\phi \to K^+K^- \to \gamma R$) and by the phase of $\pi\pi$ scattering. In turn, the phase of $\pi\pi$ scattering is defined by the phase of the f_0–σ complex and by the phase of the elastic background of $\pi\pi$ scattering, δ_B (see details in [6, 3, 13]).

The mass spectrum of the process is

$$\frac{d\Gamma(\phi \to \gamma\pi^0\pi^0)}{dm} = \frac{d\Gamma_{f_0}}{dm} + \frac{d\Gamma_{\rm back}(m)}{dm} \pm \frac{d\Gamma_{\rm int}(m)}{dm}, \quad (15)$$

where the mass spectrum of the signal has the form

$$\frac{d\Gamma_{f_0}}{dm} = \frac{|g(m)|^2\sqrt{m^2-4m_\pi^2}(m_\phi^2-m^2)}{3(4\pi)^3m_\phi^3} \times \left|\sum_{R,R'} g_{RK^+K^-}G^{-1}_{RR'}g_{R'\pi^0\pi^0}\right|^2. \quad (16)$$

The mass spectrum for the background process $\phi \to \pi^0\rho \to \gamma\pi^0\pi^0$ is

$$\frac{d\Gamma_{\rm back}(m)}{dm} = \frac{1}{2}\frac{(m_\phi^2-m^2)\sqrt{m^2-4m_\pi^2}}{256\pi^3m_\phi^3} \times \int_{-1}^{1} dx A_{\rm back}(m,x), \quad (17)$$

where

$$A_{\rm back}(m,x) = \frac{1}{3}\sum \left|M_{\rm back}\right|^2 \quad (18)$$
$$= \frac{1}{24}g^2_{\phi\rho\pi^0}g^2_{\rho\pi^0\gamma}\{(m_\pi^8 + 2m^2m_\pi^4\tilde m_\rho^2 - 4m_\pi^6\tilde m_\rho^2 + 2m^4\tilde m_\rho^4 - 4m^2m_\pi^2\tilde m_\rho^4 + 6m_\pi^4\tilde m_\rho^4 + 2m^2\tilde m_\rho^6 - 4m_\pi^2\tilde m_\rho^6 + \tilde m_\rho^8 - 2m_\pi^6m_\phi^2 - 2m^2m_\pi^2\tilde m_\rho^2m_\phi^2 + 2m_\pi^4\tilde m_\rho^2m_\phi^2 - 2m^2\tilde m_\rho^4m_\phi^2 + 2m_\pi^2\tilde m_\rho^4m_\phi^2 - 2\tilde m_\rho^6m_\phi^2 + m_\pi^4m_\phi^4 + \tilde m_\rho^4m_\phi^4) \times \left(\frac{1}{|D_\rho(\tilde m_\rho)|^2} + \frac{1}{|D_\rho(\tilde m_\rho^*)|^2}\right) + (m_\phi^2-m^2) \times (m^2 - 2m_\pi^2 + 2\tilde m_\rho^2 - m_\phi^2)(2m^2m_\pi^2 + 2m_\pi^2m_\phi^2 - m^4)\frac{1}{|D_\rho(\tilde m_\rho^*)|^2} + 2\mathrm{Re}\left(\frac{1}{D_\rho(m_\rho)D_\rho^*(\tilde m_\rho^*)}\right)(m_\pi^8 - m^6\tilde m_\rho^2 + 2m^4m_\pi^2\tilde m_\rho^2 + 2m^2m_\pi^4\tilde m_\rho^2 - 4m_\pi^6\tilde m_\rho^2 - 4m^2m_\pi^2\tilde m_\rho^4 + 6m_\pi^4\tilde m_\rho^4 + 2m^2\tilde m_\rho^6 - 4m_\pi^2\tilde m_\rho^6 + \tilde m_\rho^8 + m^2m_\pi^4m_\phi^2 - 2m_\pi^6m_\phi^2 + 2m^4\tilde m_\rho^2m_\phi^2 - 4m^2m_\pi^2\tilde m_\rho^2m_\phi^2 + 2m_\pi^4\tilde m_\rho^2m_\phi^2 - m^2\tilde m_\rho^4m_\phi^2 + 2m_\pi^2\tilde m_\rho^4m_\phi^2 - 2\tilde m_\rho^6m_\phi^2 - m_\pi^4m_\phi^4 - m^2\tilde m_\rho^2m_\phi^4 + 2m_\pi^2\tilde m_\rho^2m_\phi^4 + \tilde m_\rho^4m_\phi^4)\}$$

and

$$\tilde m_\rho^2 = m_\pi^2 + \frac{(m_\phi^2-m^2)}{2}\left(1 - x\sqrt{1-\frac{4m_\pi^2}{m^2}}\right), \quad (19)$$
$$\tilde m_\rho^{*2} = m_\phi^2 + 2m_\pi^2 - m^2 - \tilde m_\rho^2.$$

The interference between the amplitudes of the background process and the signal has the form

$$\frac{d\Gamma_{\rm int}(m)}{dm} = \frac{1}{\sqrt{2}}\frac{\sqrt{m^2-4m_\pi^2}}{256\pi^3m_\phi^3}\int_{-1}^{1} dx A_{\rm int}(m,x), \quad (20)$$

where

$$A_{\rm int}(m,x) = \frac{2}{3}\mathrm{Re}\sum M_f M^*_{\rm back} \quad (21)$$
$$= \frac{1}{3}\mathrm{Re}\Bigg\{g(m)e^{i\delta_B}g_{\phi\rho\pi^0}g_{\rho\pi^0\gamma} \times \left(\sum_{R,R'} g_{RK^+K^-}G^{-1}_{RR'}g_{R'\pi^0\pi^0}\right) \times \left(\frac{(\tilde m_\rho^2 - m_\pi^2)^2m_\phi^2 - (m_\phi^2-m^2)^2\tilde m_\rho^2}{D_\rho^*(\tilde m_\rho)} + \frac{(\tilde m_\rho^{*2} - m_\pi^2)^2m_\phi^2 - (m_\phi^2-m^2)^2\tilde m_\rho^{*2}}{D_\rho^*(\tilde m_\rho^*)}\right)\Bigg\}.$$

The factor $1/2$ in (17) and the factor $1/\sqrt{2}$ in (20) take into account the identity of pions. In (16), the identity of pions is taken into account by the definition of the coupling constant $g_{R\pi^0\pi^0} = g_{R\pi^+\pi^-}/\sqrt{2}$. For the fitting of the experimental data, we use the model of $\pi\pi$ scattering considered in [3]. The phase of the elastic background of $\pi\pi$ scattering is taken in the form $\delta_B = b\sqrt{m^2-4m_\pi^2}$, where b is a constant. We fit simultaneously the phase of $\pi\pi$ scattering and the experimental data on the decay $\phi \to \gamma\pi^0\pi^0$.

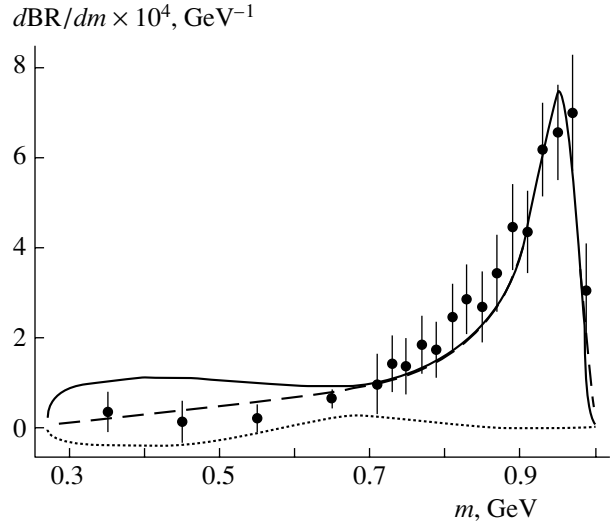

Fig. 2. Fitting of $d\mathrm{BR}(\phi \to \gamma\pi^0\pi^0)/dm \times 10^4$ with the background is shown with the solid curve, and the signal contribution is shown with the dashed curve. The dotted curve is the interference term. The data are from the SND detector.

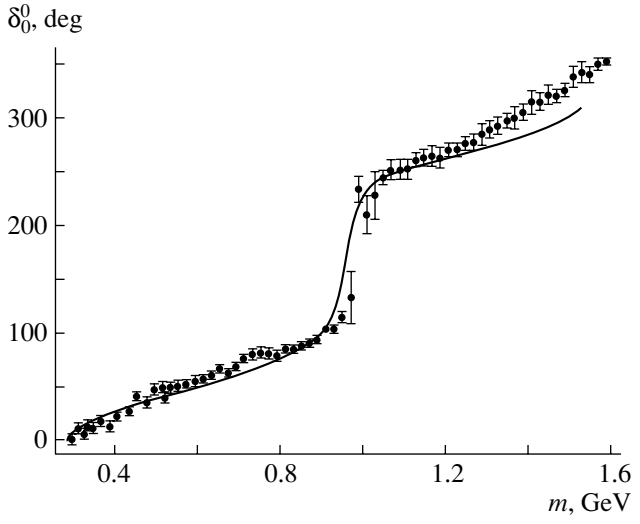

Fig. 3. Fitting of the phase δ_0^0 of $\pi\pi$ scattering.

The value $g_{\rho\pi^0\gamma} = 0.295 \pm 0.037$ GeV^{-1} is obtained from the data on the $\rho \to \pi^0\gamma$ decay [19] with the help of the following expression:

$$\Gamma(\rho \to \pi^0\gamma) = \frac{g^2_{\rho\pi^0\gamma}}{96\pi m_\rho^3}(m_\rho^2 - m_\pi^2)^3. \qquad (22)$$

The fit of the experimental data [10], obtained using the total statistics of SND detector, and the data on the $\pi\pi$ scattering phase [21–25] give the constructive interference and the following parameters:

$$\begin{gathered} g_{f_0K^+K^-} = 4.021 \pm 0.011 \text{ GeV}, \qquad (23) \\ g_{f_0\pi^0\pi^0} = 1.494 \pm 0.021 \text{ GeV}, \\ m_{f_0} = 0.996 \pm 0.0013 \text{ GeV}, \quad g_{\sigma K^+K^-} = 0, \\ g_{\sigma\pi^0\pi^0} = 2.58 \pm 0.02 \text{ GeV}, \\ m_\sigma = 1.505 \pm 0.012 \text{ GeV}, \\ b = 75 \pm 2.1 \ (1^\circ/\text{GeV}), \\ C = 0.622 \pm 0.04 \text{ GeV}^2, \\ g^2_{f_0K^+K^-}/4\pi = 1.29 \pm 0.017 \text{ GeV}^2. \end{gathered}$$

The constant C takes into account effectively the contribution of multiparticle intermediate states in the $f_0 \leftrightarrow \sigma$ transition in the $G_{RR'}$ matrix (see [3]), and incorporates the subtraction constant for the $R \to (0^-0^-) \to R'$ transition. We treat this constant as a free parameter.

The total branching ratio, with interference being taken into account, is $\mathrm{BR}(\phi \to (\gamma f_0 + \pi^0\rho) \to \gamma\pi^0\pi^0) = (1.26 \pm 0.29) \times 10^{-4}$; the branching ratio of the signal is $\mathrm{BR}(\phi \to \gamma f_0 \to \gamma\pi^0\pi^0) = (1.01 \pm 0.23) \times 10^{-4}$; the branching ratio of the background is $\mathrm{BR}(\phi \to \pi^0\rho^0 \to \gamma\pi^0\pi^0) = 0.18 \times 10^{-4}$. The results of fitting are shown in Figs. 2 and 3, where the mass distribution $d\mathrm{BR}/dm$ and the scalar isoscalar phase $\delta^{I=0}_{S=0}$ are depicted.

Note, that for our aim the phase in the region $m_{\pi\pi} < 1.1$ GeV is important.

The authors in the paper [10] fit the data taking into account the background reaction $\phi \to \pi^0\rho^0 \to \gamma\pi^0\pi^0$. The parameters found are $m_{f_0} = 0.9698 \pm 0.0045$ GeV, $g^2_{f_0K^+K^-}/4\pi = 2.47^{+0.73}_{-0.51}$ GeV^2, and $g^2_{f_0\pi^+\pi^-}/4\pi = 0.54^{+0.09}_{-0.08}$ GeV^2 [10]. They are different from the parameters found in our fitting. The difference is due to the fact that we perform the simultaneous fitting of the data on the decay $\phi \to \gamma\pi^0\pi^0$ and the data on the S-wave phase of $\pi\pi$ scattering, taking into account the mixing of f_0 and σ mesons.

Besides, in the paper [10], the interference between the background and signal is found from the fitting; meanwhile, in our paper, the interference is calculated. The branching ratio of the background $\mathrm{BR}(\phi \to \pi^0\rho^0 \to \gamma\pi^0\pi^0) = 0.12 \times 10^{-4}$ used in [10] is taken from the paper [17], in which the coupling constant $g_{\rho^0\pi^0\gamma}$ is less by 25% than the one resulting from the experiment. In our paper, the background is calculated on the basis of the experiment and is accordingly larger, $\mathrm{BR}(\phi \to \pi^0\rho^0 \to \gamma\pi^0\pi^0) = 0.18 \times 10^{-4}$. Note that in [10], in contrast to us, the fitting is performed taking into account the event distribution inside each bin.

The fitting of the experimental data of the CMD-2 detector [11] and the data on the $\pi\pi$ scattering phase

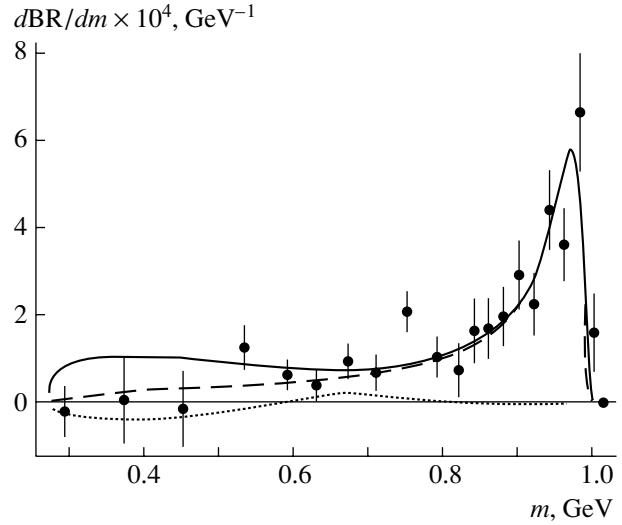

Fig. 4. Fitting of $d\mathrm{BR}(\phi \to \gamma\pi^0\pi^0)/dm \times 10^4$ with the background is shown with the solid curve, and the signal contribution is shown with the dashed curve. The dotted curve is the interference term. The data are from the CMD-2 detector.

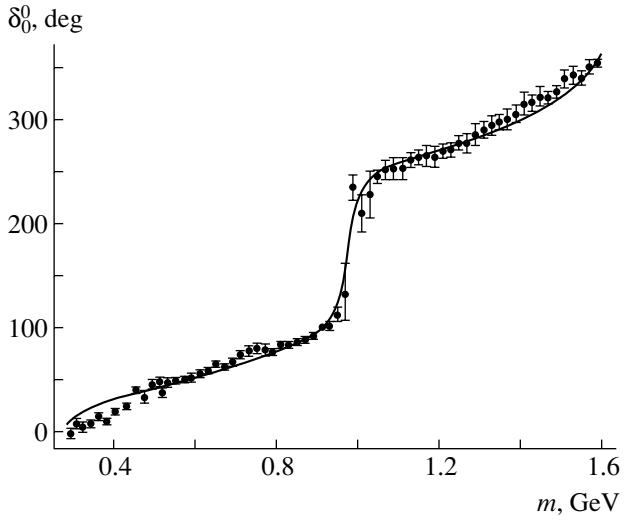

Fig. 5. Fitting of the phase δ_0^0 of $\pi\pi$ scattering.

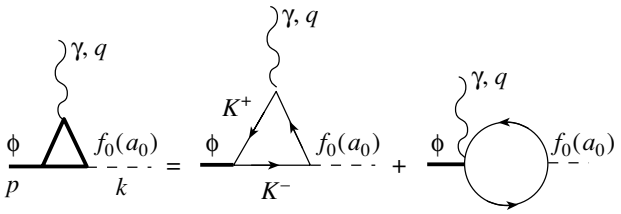

Fig. 6. Diagrams of the K^+K^--loop model.

[21–25] gives the constructive interference and the following parameters:

$$g_{f_0K^+K^-} = 3.874 \pm 0.17 \text{ GeV}, \qquad (24)$$
$$g_{f_0\pi^0\pi^0} = 0.536 \pm 0.03 \text{ GeV},$$
$$m_{f_0} = 1.0019 \pm 0.002 \text{ GeV}, \quad g_{\sigma K^+K^-} = 0,$$
$$g_{\sigma\pi^0\pi^0} = 2.61 \pm 0.1 \text{ GeV},$$
$$m_\sigma = 1.585 \pm 0.015 \text{ GeV},$$
$$b = 70.7 \pm 2.0(1^\circ/\text{GeV}),$$
$$C = -0.593 \pm 0.06 \text{ GeV}^2,$$
$$g^2_{f_0K^+K^-}/4\pi = 1.19 \pm 0.03 \text{ GeV}^2.$$

The total branching ratio taking into account the interference is $\mathrm{BR}(\phi \to (\gamma f_0 + \pi^0\rho) \to \gamma\pi^0\pi^0) = (0.98 \pm 0.21) \times 10^{-4}$, the branching ratio of the signal is $\mathrm{BR}(\phi \to \gamma f_0 \to \gamma\pi^0\pi^0) = (0.74 \pm 0.2) \times 10^{-4}$, and the branching ratio of the background is $\mathrm{BR}(\phi \to \pi^0\rho^0 \to \gamma\pi^0\pi^0) = 0.18 \times 10^{-4}$. The results of fitting are shown in Figs. 4 and 5.

The parameters found in [11], which are $m_{f_0} = 0.969 \pm 0.005$ GeV, $g^2_{f_0K^+K^-}/4\pi = 1.49 \pm 0.36$ GeV^2, and $g^2_{f_0\pi^+\pi^-}/4\pi = 0.4 \pm 0.06$ GeV^2, are different from the parameters found in our fitting. The difference is due to the fact that we perform the simultaneous fitting of the data on the decay $\phi \to \gamma\pi^0\pi^0$ and the data on the S-wave phase of the $\pi\pi$ scattering, taking into account the mixing of f_0 and σ mesons and taking into account the background reaction $\phi \to \pi^0\rho^0 \to \gamma\pi^0\pi^0$.

One can see from Figs. 2 and 4 that the influence of the background process on the spectrum of the $\phi \to \gamma\pi^0\pi^0$ decay is negligible in the wide region of the $\pi^0\pi^0$ invariant mass, $m_{\pi\pi} > 670$ MeV, or when photon energy is less than 300 MeV.

In the meantime, the difference from the experimental data is observed in the region $m_{\pi\pi} < 670$ MeV. We suppose this difference is due to the fact that in the experimental processing of the $e^+e^- \to \gamma\pi^0\pi^0$ events the background events $e^+e^- \to \omega\pi^0 \to \gamma\pi^0\pi^0$ are excluded with the help of the invariant mass cutting and simulation. In so doing, part of the $e^+e^- \to \phi \to \pi^0\rho \to \gamma\pi^0\pi^0$ events are excluded as well.

It should be noted that the SND and CMD-2 data on the branching ratios of the $\phi \to \gamma\pi^0\pi^0$ decay are quite consistent. In the meantime, the SND and CMD-2 data on the shapes of the spectra of the $\pi^0\pi^0$ invariant mass are rather different. The CMD-2 shape is noticeably narrower (compare Figs. 2 and 4). This difference reflects on the coupling constant $g_{f_0\pi^0\pi^0}$ and the constant C, which are quite different [see Eqs. (23) and (24)]. In all probability, this difference will disappear when the CMD-2 group processes the total statistics.

4. CONCLUSION

The experimental data give evidence not only in favor of the four-quark model but also in favor of the dynamical model suggested in [1], in which the discussed decays proceed through the kaon loop, $\phi \to K^+K^- \to \gamma f_0(a_0)$.

Indeed, according to the gauge-invariance condition, the transition amplitude $\phi \to \gamma f_0(a_0)$ is proportional to the electromagnetic tensor $F_{\mu\nu}$ (in our case to the electric field). Since there are no pole terms in our case, the function $g(m)$ in (2) and (14) is proportional to the energy of photon $\omega = (m_\phi^2 - m^2)/2m_\phi$ in the soft photon region. To describe the experimental spectra, the function $|g(m)|^2$ should be smooth (almost constant) in the range $m \leq 0.99$ GeV [see Eqs. (4) and (16)]. Stopping the function ω^2 at $\omega_0 = 30$ MeV, using the form factor of the form $1/(1 + R^2\omega^2)$, requires $R \approx 100$ GeV^{-1}. It seems to be incredible to explain the formation of such a huge radius in hadron physics. Based on the large, by hadron physics standard, $R \approx 10$ GeV^{-1}, one can obtain an effective maximum of the mass spectra under discussion only near 900 MeV. In the meantime, the K^+K^- loop (see Fig. 6) gives the natural description to this threshold effect (see Fig. 7).

To demonstrate the threshold character of this effect we present Figs. 8 and 9, in which the function $|g(m)|^2$ is shown in the case when K^+ meson mass is 25 and 50 MeV less than in reality. One can see from Figs. 8 and 9 that the function $|g(m)|^2$ is suppressed by the ω^2 low in the region 950–1020 and 900–1020 MeV, respectively. In the mass spectrum this suppression is increased by one more power of ω (see Eqs. 4 and 16), so that we cannot see the resonance in the region 980–995 MeV. The maximum in the spectrum is effectively shifted to the region 935–950 and 880–900 MeV, respectively. In truth this means that $a_0(980)$ and $f_0(980)$ resonances are seen in the radiative decays of the ϕ meson owing to the K^+K^--intermediate state, otherwise the maxima in the spectra would be shifted to 900 MeV.

It is worth noting that the K^+K^--loop model is practically accepted by theorists (compare, for example, [26] with [27]; true there is an exception [28]). The authors of [28] use the amplitude of the $\phi \to \gamma(f_0 +$ background$) \to \gamma\pi^0\pi^0$ decay, which does not vanish when $\omega \to 0$, i.e., which does not satisfy the gauge invariance condition. This amplitude is not adequate to the physical problem since the mass spectrum under discussion should have the behavior ω^3 at $\omega \to 0$ and not ω as in [28]. With the same result, one can study the electromagnetic form factor of the π meson in the

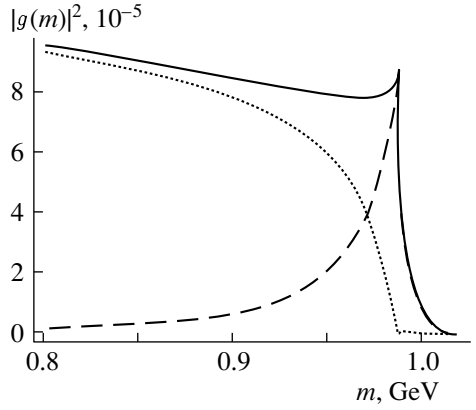

Fig. 7. The function $|g(m)|^2$ is drawn with the solid curve. The contribution of the imaginary part is drawn with the dashed curve. The contribution of the real part is drawn with the dotted curve.

$e^+e^- \to \pi^+\pi^-$ reaction near the threshold considering that the cross section of the process is proportional to the momentum of the π meson while the cross section is proportional to the momentum in the third power. After our criticism in hep-ph/0101024, the authors, correcting some typos and undoing some references in [28], inserted a crazy common factor $F_{\text{thresh}}(\omega) = \sqrt{1 - \exp\{-(\omega/36\ \text{MeV})^2\}}$ in the $\phi \to \gamma(f_0 + \text{background}) \to \gamma\pi^0\pi^0$ amplitude without any explanations {see Eq. (39) in [28]} to provide the spectrum behavior ω^3 at $\omega \to 0$. But the real trouble is that the calculation in [28] is not gauge invariant. The calculation of the $\phi \to q\bar{q} \to \gamma f_0$ amplitude requires a gauge-invariant regularization (for example, the subtraction at $\omega = 0$) in spite of the integral convergence. A textbook example of such a kind is $\gamma\gamma \to e^+e^-(\text{or}\, q\bar{q}) \to \gamma\gamma$ scattering. The authors of the paper under discussion obtained $A_{\phi\to\gamma f_0} = (\text{in our symbols}) \quad g(m)(g_{f_0K^+K^-}/e) \neq 0$ at $\omega = (m_\phi^2 - m^2)/2m_\phi = 0$ ($A_{\phi\to\gamma f_0}$ does not depend on m at all); see Eq. (30) in [28]. This means that the authors created the false pole in the invariant amplitude free from kinematical singularities: $\left(eA_{\phi\to\gamma f_0}/\left(m_\phi^2 - m^2\right)\right)(\phi_\mu p_\nu - \phi_\nu p_\mu) \times \epsilon_\mu q_\nu - \epsilon_\nu q_\mu$; compare with Eq. (9) in [28]. So, once again, the calculation of [28] is not adequate to the physical problem!

It was noted already in [1] that the imaginary part of the K^+K^- loop is calculated practically in a model-independent way making use of the coupling constants $g_{\phi K^+K^-}$ and $g_{a_0(f_0)K^+K^-}$ due to Low's theorem [29] for photons with energy $\omega < 100$ MeV, which is soft by the standard of strong interaction. In the same paper, it was noted that the real part of the loop (with accuracy up to 20% in the width

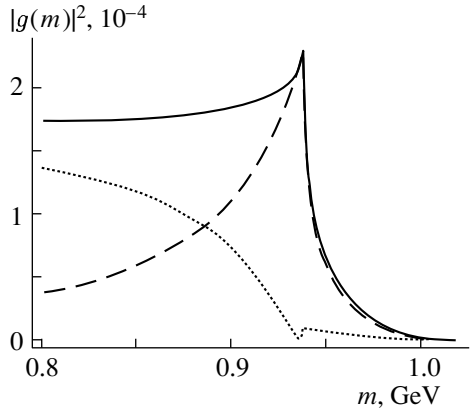

Fig. 8. The function $|g(m)|^2$ for $m_K = 469$ MeV is drawn with the solid curve. The contribution of the imaginary part is drawn with the dashed curve. The contribution of the real part is drawn with the dotted curve.

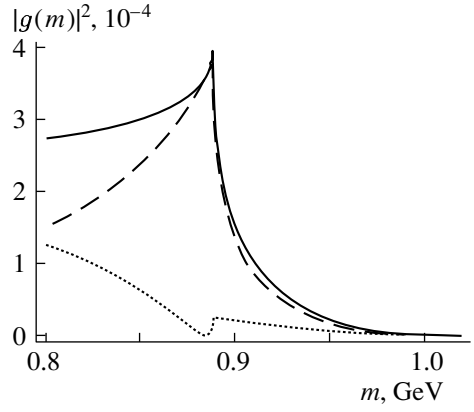

Fig. 9. The function $|g(m)|^2$ for $m_K = 444$ MeV is drawn with the solid curve. The contribution of the imaginary part is drawn with the dashed curve. The contribution of the real part is drawn with the dotted curve.

of the $\phi \to \gamma f_0(a_0)$ decay) is hardly different for the pointlike particle and the compact hadron with form factor which has the cutting radius in the momentum space about the mass of the ρ meson ($m_\rho = 0.77$ GeV). In contrast to the four-quark state which is the compact hadron [12], the bound $K\bar{K}$ state is the extended state with the spatial radius $R \sim 1/\sqrt{m_K\varepsilon}$, where ε is the binding energy. The corresponding form factor in the momentum space has a radius of the order of $\sqrt{m_K\varepsilon} \approx 100$ MeV for $\varepsilon = 20$ MeV. The more detailed calculation [2] gives for the radius in the momentum space the value $p_0 = 140$ MeV. As a result, the real part of the loop of the bound state is negligible [4]. It leads to a branching ratio much less than the experimental one, as was noted above. Besides, the spectrum is much narrower in the $K\bar{K}$-molecule case that contradicts the experiment; see the behavior of the imaginary part contribution in Fig. 7 and in corresponding figures in [4]. Unfortunately, in the interesting paper [30], the potential in the momentum space was taken as the momentum distribution in the molecule instead of the wave function in the momentum space. But the momentum distribution radius of the potential is 5–8 times as large as the one of the wave function, which the reason for the misleading conclusion on the possibility of explaining the Novosibirsk results in the molecule case.

Of course, the two-quark state is as compact as the four-quark one. The question arises, Why is the branching ratio in the two-quark model suppressed in comparison with the branching ratio in the four-quark model? There are two reasons. First, the coupling constant of two-quark states with the $K\bar{K}$ channel is noticeably less [3, 13], and, second, there is the Okubo–Zweig–Iizuka (OZI) rule that is more important really.

If the isovector $a_0(980)$ meson is the two-quark state, it has no strange quarks. Hence [1, 3, 15], the decay $\phi \to \gamma a_0$ should be suppressed according to the OZI rule. On the intermediate-state level, the OZI rule is formulated as compensation of the different intermediate states [31–33]. In our case, these states are $K\bar{K}$, $K\bar{K}^* + \bar{K}K^*$, $K^*\bar{K}^*$, and so on. Since, due to the kinematical reason, the real intermediate state is the only K^+K^- state, the compensation in the imaginary part is impossible and it destroys the OZI rule. The compensation should be in the real part of the amplitude only. As a result, the $\phi \to \gamma a_0$ decay in the two-quark model is mainly due to the imaginary part of the amplitude and is much less intensive than in the four-quark model [1, 3]. Besides, in the two-quark model, the $a_0(980)$ meson should appear in the $\phi \to \gamma a_0$ decay as a noticeably narrower resonance than in other processes (see the behavior of the imaginary part contribution in Fig. 7).

As regards the isoscalar $f_0(980)$ state, there are two possibilities in the two-quark model. If the $f_0(980)$ meson does not contain strange quarks, all the above-mentioned arguments about suppression of the $\phi \to \gamma a_0$ decay and the spectrum shape are also valid for the $\phi \to \gamma f_0$ decay. Generally speaking, there could be the strong OZI violation for the isoscalar $q\bar{q}$ states (mixing of the $u\bar{u}$, $d\bar{d}$, and $s\bar{s}$ states) with regard to the strong mixing of the quark and gluon degree of freedom which is due to the nonperturbative effects of QCD [34]. But an almost exact degeneration of the masses of the isoscalar $f_0(980)$ and isovector $a_0(980)$ mesons excludes such a possibility. Note also, the experiment points directly

to the weak coupling of $f_0(980)$ meson with gluons, $\mathrm{BR}(J/\psi \to \gamma f_0 \to \gamma\pi\pi) < 1.4 \times 10^{-5}$ [35].

If the $f_0(980)$ meson is close to the $s\bar{s}$ state [15, 36], there is no suppression due to the OZI rule. Nevertheless, if $a_0(980)$ and $f_0(980)$ mesons are the members of the same multiplet, the $\phi \to \gamma f_0$ branching ratio, $\mathrm{BR}(\phi \to \gamma\pi^0\pi^0) = (1/3)\mathrm{BR}(\phi \to \gamma\pi\pi) \approx 1.8 \times 10^{-5}$, is significantly less than that in the four-quark model due to the relation between the coupling constants with the $K\bar{K}$, $\pi\eta$ and $K\bar{K}$, $\pi\pi$ channels inherited in the two-quark model (see [1, 3]). Besides, in this case there is no natural explanation of the f_0 and a_0 mass degeneration.

Only in the case when the nature of the $f_0(980)$ meson is in no way related to the nature of the $a_0(980)$ meson (which, for example, is the four-quark state) could the branching ratio of the experimentally observed $\phi \to \gamma f_0$ be explained by the $s\bar{s}$ nature of the $f_0(980)$ meson. But, from the theoretical point of view, such a possibility seems awful [15].

ACKNOWLEDGMENTS

We gratefully acknowledge discussions with V.P. Druzhinin, A.A. Kozhevnikov, G.N. Shestakov, and Z.K. Silagadze.

This work was supported in part by a joint grant from INTAS and the Russian Foundation for Basic Research (no. IR-97-232) and by the Russian Foundation for Basic Research (project no. 02-02-16061).

REFERENCES

1. N. N. Achasov and V. N. Ivanchenko, Nucl. Phys. B **315**, 465 (1989).
2. F. E. Close, N. Isgur, and S. Kumano, Nucl. Phys. B **389**, 513 (1993).
3. N. N. Achasov and V. V. Gubin, Yad. Fiz. **61**, 274 (1998) [Phys. At. Nucl. **61**, 224 (1998)]; Phys. Rev. D **56**, 4084 (1997).
4. N. N. Achasov, V. V. Gubin, and V. I. Shevchenko, Yad. Fiz. **60**, 89 (1997) [Phys. At. Nucl. **60**, 81 (1997)]; Phys. Rev. D **56**, 203 (1997).
5. J. L. Lucio and M. Napsuciale, in *Contribution to the 3rd Workshop on Physics and Detectors for DAPHNE (DAPHNE 99), Frascati, Italy, 1999*; hep-ph/0001136.
6. N. N. Achasov and V. V. Gubin, Yad. Fiz. **61**, 1473 (1998) [Phys. At. Nucl. **61**, 1367 (1998)]; Phys. Rev. D **57**, 1987 (1998).
7. M. N. Achasov *et al.*, Phys. Lett. B **438**, 441 (1998).
8. M. N. Achasov *et al.*, Phys. Lett. B **440**, 442 (1998); hep-ex/9807016.
9. M. N. Achasov *et al.*, Phys. Lett. B **479**, 53 (2000); hep-ex/0003031.
10. M. N. Achasov *et al.*, Phys. Lett. B **485**, 349 (2000); hep-ex/0005017.
11. R. R. Akhmetshin *et al.*, Phys. Lett. B **462**, 380 (1999).
12. R. L. Jaffe, Phys. Rev. D **15**, 267 (1977); **15**, 281 (1977).
13. N. N. Achasov, S. A. Devyanin, and G. N. Shestakov, Usp. Fiz. Nauk **142**, 361 (1984) [Sov. Phys. Usp. **27**, 161 (1984)]; Z. Phys. C **22**, 53 (1984); Yad. Fiz. **32**, 1098 (1980) [Sov. J. Nucl. Phys. **32**, 566 (1980)].
14. N. N. Achasov and G. N. Shestakov, Usp. Fiz. Nauk **161** (6), 53 (1991) [Sov. Phys. Usp. **34**, 471 (1991)]; Z. Phys. C **41**, 309 (1988).
15. N. N. Achasov, Usp. Fiz. Nauk **168**, 1257 (1998) [Phys. Usp. **41**, 1149 (1998)]; hep-ph/9904223; Nucl. Phys. A **675**, 279c (2000).
16. O. Black, A. Fariborz, F. Sannino, and J. Schechter, Phys. Rev. D **59**, 074026 (1999).
17. A. Bramon, A. Grau, and G. Pancheri, Phys. Lett. B **289**, 97 (1992); **283**, 416 (1992).
18. Particle Data Group (D. E. Groom *et al.*), Eur. Phys. J. C **15**, 1 (2000).
19. S. I. Dolinsky *et al.*, Z. Phys. C **42**, 511 (1989).
20. N. N. Achasov *et al.*, Int. J. Mod. Phys. A **7**, 3187 (1992).
21. B. Hyams *et al.*, Nucl. Phys. B **64**, 134 (1973).
22. P. Estabrooks and A. D. Martin, Nucl. Phys. B **79**, 301 (1974).
23. A. D. Martin, E. N. Ozmutlu, and E. J. Squires, Nucl. Phys. B **121**, 514 (1977).
24. V. Srinivasan *et al.*, Phys. Rev. D **12**, 681 (1975).
25. L. Rosselet *et al.*, Phys. Rev. D **15**, 574 (1977).
26. E. Marco, S. Hirenzaki, E. Oset, and H. Toki, Phys. Lett. B **470**, 20 (1999).
27. A. Bramon *et al.*, hep-ph/0008188.
28. A. V. Anisovich, V. V. Anisovich, and V. A. Nikonov, hep-ph/0011191.
29. F. E. Low, Phys. Rev. **110**, 574 (1958).
30. V. E. Markushin, Eur. Phys. J. A **8**, 389 (2000).
31. H. Lipkin, Nucl. Phys. B **291**, 720 (1987).
32. P. Geiger and N. Isgur, Phys. Rev. D **44**, 799 (1991).
33. N. N. Achasov and A. A. Kozhevnikov, Phys. Rev. D **49**, 275 (1994).
34. A. I. Vainshtein, V. I. Zakharov, V. A. Novikov, and M. A. Shifman, Fiz. Élem. Chastits At. Yadra **13**, 542 (1982) [Sov. J. Part. Nucl. **13**, 224 (1982)].
35. G. Eigen, in *Proceedings of the XXIV International Conference on High Energy Physics, Munich, 1988,* Ed. by R. Kotthaus and J. H. Kuhn (Springer-Verlag, Berlin, 1988), p. 590.
36. N. A. Törnqvist, Z. Phys. C **68**, 647 (1995).

Physics of Atomic Nuclei, Vol. 65, No. 8, 2002, pp. 1537–1544. Translated from Yadernaya Fizika, Vol. 65, No. 8, 2002, pp. 1575–1582.

ELEMENTARY PARTICLES AND FIELDS
Theory

Pair Production of Doubly Heavy Diquarks

V. V. Braguta, V. V. Kiselev, and A. E. Chalov

Institute for High Energy Physics, Protvino, Moscow oblast, 142284 Russia

Received February 26, 2001; in final form, August 20, 2001

Abstract—The differential and total cross sections for the pair production of doubly heavy diquarks are calculated analytically within the diquark model. The cases of electron–positron and quark–antiquark annihilation are considered. The ratios of the total cross sections to the corresponding cross sections for annihilation into two heavy quarks are estimated numerically. © *2002 MAIK "Nauka/Interperiodica".*

1. INTRODUCTION

High luminosities of B factories and hadron colliders make it possible to observe experimentally the doubly heavy baryons $\Xi_{QQ'}$ and $\Omega_{QQ'}$. This possibility generates interest in theoretically studying such particles—in particular, in analyzing their spectra either on the basis of model potentials [1] or on the basis of QCD sum rules [2], their lifetimes and inclusive decay modes [3], the production mechanisms in deep-inelastic collisions, and the rate of their production at accelerators [4].

In the present study, we show that the cross section for pair production is rather large only in the energy region close to the reaction threshold.

The method that we use in our calculations provides a reliable approximation for doubly heavy baryons, because the dimension of a heavy diquark is much less than the radius of light-quark confinement in the $QQ'q$ system. We believe that, first, it is necessary to calculate the cross section for the production of heavy diquarks, whereupon one can apply models describing their fragmentation into a baryon [5].

In [6], the differential and total cross sections for exclusive meson-pair production in e^+e^- annihilation were obtained within the constituent quark model. These calculations were performed for the reaction whose energy is close to the threshold value, in which case pairs of both pseudoscalar and vector particles appeared in the final state. By using the same procedure, we consider the processes $e^+e^- \to \mathfrak{d}\bar{\mathfrak{d}}$ and $q\bar{q} \to \mathfrak{d}\bar{\mathfrak{d}}$, where $\mathfrak{d}$ and $\bar{\mathfrak{d}}$ are, respectively, a diquark and an antidiquark (in the calculations, we neglect the masses of annihilating particles).

We have calculated the differential and total cross sections for the exclusive production of diquark pairs occurring in axial–axial, axial–scalar, and scalar–scalar states and consisting of nonidentical quarks. We also consider annihilation into two axial vector diquarks containing identical quarks. Processes involving the production of diquarks in pseudoscalar and vector states do not contribute to the leading order of $1/m$ expansion; since such processes are higher order effects, we do not discuss them here. If we assume that the product diquarks fragment into doubly heavy baryons, the resulting formulas can be used in calculating the cross sections for the pair production of baryons.

The ensuing exposition is organized as follows. In Section 2, we describe the fundamentals of the constituent quark model. In Sections 3 and 4, we present the matrix elements and the differential and total cross sections for e^+e^- and $q\bar{q}$ annihilation into diquark pairs. In Section 5, we give relevant numerical estimates. In the Conclusion, we summarize the basic results of our study.

2. FUNDAMENTALS OF THE MODEL

In this study, we rely on the constituent quark model [6], which involves only quark masses and leptonic constants for input parameters.

Accordingly, the mass of the diquark $\mathfrak{d} = (Q_1Q_2)$ is the sum of the masses of the quarks constituting it; that is,

$$M = m_1 + m_2.$$

Their 4-momenta can be written as

$$k_{Q_1} = \frac{m_1}{M}P + q,$$

$$k_{Q_2} = \frac{m_2}{M}P - q,$$

where P is the diquark 4-momentum and q is the 4-momentum of the relative motion of the quarks.

In order to represent a state of a diquark containing two nonidentical quarks, the principle of superposition of wave packets characterized by the momentum

1063-7788/02/6508-1537$22.00

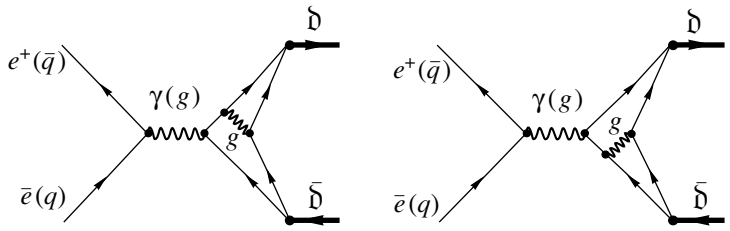

Fig. 1. Diagrams describing $e^+e^-(q\bar{q})$ annihilation into a pair of doubly heavy diquarks through one photon (gluon).

distributions $\Psi(q)$ is used in Fock space. Thus, we have

$$|S_d^i\rangle = \frac{\epsilon_{ijk}}{\sqrt{2}}\int\frac{d^3q}{(2\pi)^3}\Psi_s(q) \tag{1}$$
$$\times\sum_{\lambda_1\lambda_2}\frac{(\Psi^\dagger_{\lambda_1}\hat{C}\gamma_5\Psi_{\lambda_2})^*}{\sqrt{2}}\hat{a}^{j+}_{\lambda_1}\hat{b}^{k+}_{\lambda_2}|0\rangle$$

for a scalar diquark and

$$|A_d^i\rangle = \frac{\epsilon_{ijk}}{\sqrt{2}}\int\frac{d^3q}{(2\pi)^3}\Psi_a(q) \tag{2}$$
$$\times\sum_{\lambda_1\lambda_2}\frac{(\Psi^\dagger_{\lambda_1}\hat{C}\gamma_\mu\Psi_{\lambda_2})^*}{\sqrt{2}}e_\mu\hat{a}^{j+}_{\lambda_1}\hat{b}^{k+}_{\lambda_2}|0\rangle$$

for an axial diquark. In these expressions, $\hat{C}$ is the charge conjugation matrix; i and j are color indices; $\hat{e} = e_\mu\gamma_\mu$, where e_μ is the polarization vector of the axial diquark; $\hat{a}^+$ and $\hat{b}^+$ are the quark creation operators; Ψ_a and Ψ_s are the wave functions for the orbital motion of the quarks in the axial and in the scalar diquark, respectively; and Ψ_λ stands for the bispinors of the quarks constituting a diquark. From formulas (1) and (2), it can easily be seen that, in Fock space, these wave functions are normalized as

$$\langle S_d^i(\mathbf{P})|S_d^j(\mathbf{P}')\rangle = (2\pi)^3\delta_{ij}\delta(\mathbf{P}-\mathbf{P}'), \tag{3}$$
$$\langle A_d^i(\mathbf{P},\lambda)|A_d^j(\mathbf{P}',\lambda')\rangle = (2\pi)^3\delta_{ij}\delta_{\lambda\lambda'}\delta(\mathbf{P}-\mathbf{P}'), \tag{4}$$

where λ and λ' are the diquark polarization indices.

In the case of two heavy identical quarks, it is necessary to take into account the Pauli exclusion principle. Therefore, the above formulas for the wave functions must be divided by $\sqrt{2}$ and antisymmetrized with respect to permutations of the operators $\hat{a}^+$ and $\hat{b}^+$ in order to preserve normalization.

The quark propagator can be represented as

$$S(k) = (k_\mu\gamma_\mu + m)D(k),$$

where

$$D^{-1}(k) = k^2 - m^2.$$

3. AMPLITUDES AND CROSS SECTIONS FOR e^+e^- ANNIHILATION

In this section, we consider electron–positron annihilation followed by the production of a diquark–antidiquark pair. The diagrams corresponding to this process in the leading order are shown in Fig. 1. Their color factor is

$$\mathrm{Color}_{ij} = -\frac{2}{3}\delta_{ij}\,,$$

where i and j are diquark and antidiquark color indices.

3.1. Annihilation into a Pair of Scalar Diquarks

The matrix element for the pair production of scalar diquarks has the form

$$\mathcal{M}_{ss} = -i\frac{64\pi^2}{3}\frac{f_{ss}}{s^2}\delta_{ij}|\Psi_s(0)|^2(P'_\mu - P_\mu)l_\mu, \tag{5}$$

where

$$f_{ss} = M\left(\alpha_s\left(\frac{m_1^2}{M^2}s\right)\frac{q_2}{m_1^2}\right. \tag{6}$$
$$\left.+\,\alpha_s\left(\frac{m_2^2}{M^2}s\right)\frac{q_1}{m_2^2}\right)\alpha_{\mathrm{em}}(s) - \frac{2M^3}{s}$$
$$\times\left(\alpha_s\left(\frac{m_1^2}{M^2}s\right)\frac{q_2m_2}{m_1^3} + \alpha_s\left(\frac{m_2^2}{M^2}s\right)\frac{q_1m_1}{m_2^3}\right)\alpha_{\mathrm{em}}(s)\,,$$

and where we have introduced the following notation: l_μ is the vector leptonic current; $\Psi_s(0)$ is the wave function for the relative motion of the quarks in the scalar diquark at the origin in its rest frame; P' and P are the 4-momenta of the scalar diquark and the scalar antidiquark; q_1 and q_2 are the electric charges of the quarks Q_1 and Q_2, respectively.

After some simple algebra, we find that the differential cross section can be represented as

$$\frac{d\sigma_{ss}}{d\cos\theta} = 64\pi^3\frac{f_{ss}^2}{3s^3}|\Psi_s(0)|^4 \tag{7}$$
$$\times\left(1-\frac{4M^2}{s}\right)^{3/2}(1-\cos^2\theta),$$

where θ is the angle between the 3-momenta of the incoming lepton and the outgoing diquark.

From (7), we obtain the total cross section for the exclusive pair production of heavy scalar diquarks in e^+e^- annihilation, that is,

$$\sigma_{ss} = 256\pi^3 \frac{f_{ss}^2}{9s^3}|\Psi_s(0)|^4 \left(1 - \frac{4M^2}{s}\right)^{3/2}. \quad (8)$$

3.2. Annihilation into a Scalar and an Axial Diquark

For the production of a pair of diquarks in a scalar and an axial state, the matrix element can be represented as

$$\mathcal{M}_{as} = -\frac{128\pi^2}{3s^3}\delta_{ij} f_{as} \Psi_s^*(0)\Psi_a(0)\epsilon_{\mu\alpha\beta\gamma} e_\alpha P_\beta q_\gamma l_\mu, \quad (9)$$

where

$$f_{as} = M^3 \left(\alpha_s\left(\frac{m_1^2}{M^2}s\right)\frac{q_2}{m_1^3} - \alpha_s\left(\frac{m_2^2}{M^2}s\right)\frac{q_1}{m_2^3}\right)\alpha_{\rm em}(s),$$

$\Psi_a(0)$ is the wave function for the relative motion of the quarks in the axial diquark at the origin in its rest frame, and $q = P + P'$.

Upon performing similar algebraic calculations, we obtain the differential cross section in the form

$$\frac{d\sigma_{as}}{d\cos\theta} = 64\pi^3 \frac{f_{as}^2}{3s^4}|\Psi_s(0)\Psi_a(0)|^2 \quad (10)$$
$$\times \left(1 - \frac{4M^2}{s}\right)^{3/2}(2 - \sin^2\theta).$$

Accordingly, the total cross section for the exclusive production of heavy scalar and axial diquarks in e^+e^- annihilation is given by

$$\sigma_{as} = 512\pi^3 \frac{f_{as}^2}{9s^4}|\Psi_s(0)\Psi_a(0)|^2 \left(1 - \frac{4M^2}{s}\right)^{3/2}. \quad (11)$$

In all the formulas given in this section, we neglect the difference of the masses of the axial and scalar diquark.

3.3. Annihilation into a Pair of Axial Diquarks

For the pair production of heavy axial diquarks in e^+e^- annihilation, the matrix element has the form

$$\mathcal{M}_{aa} = -i\frac{128\pi^2}{3s^3}\delta_{ij}|\Psi_a(0)|^2 \quad (12)$$
$$\times \left(f_{aa}^{[1]}(P'_\mu - P_\mu)(e'^* e) + f_{aa}^{[2]}((e'^* q)e_\mu - (eq)e'^*_\mu)\right) l_\mu,$$

where $f_{aa}^{[1]}$ and $f_{aa}^{[2]}$ are defined as

$$f_{aa}^{[1]} = M^3 \left(\alpha_s\left(\frac{m_1^2}{M^2}s\right)\frac{q_2 m_2}{m_1^3} \right. \quad (13)$$
$$\left. + \alpha_s\left(\frac{m_2^2}{M^2}s\right)\frac{q_1 m_1}{m_2^3}\right)\alpha_{\rm em}(s),$$
$$f_{aa}^{[2]} = M^4 \left(\alpha_s\left(\frac{m_1^2}{M^2}s\right)\frac{q_2}{m_1^3} \right. \quad (14)$$
$$\left. + \alpha_s\left(\frac{m_1^2}{M^2}s\right)\frac{q_1}{m_2^3}\right)\alpha_{\rm em}(s).$$

For the differential cross section, we obtain the expression

$$\frac{d\sigma_{aa}}{d\cos\theta} = \frac{512\pi^3}{3s^5}|\Psi_a(0)|^4 \left(1 - \frac{4M^2}{s}\right)^{3/2}$$
$$\times (\mathcal{A} - \mathcal{B}\cos^2\theta),$$

where we have introduced (in order to simplify the representation) the quantities $\mathcal{A}$ and $\mathcal{B}$ defined as

$$\mathcal{A} = (f_{aa}^{[1]})^2(8 + (\eta - 2)^2)$$
$$- 2f_{aa}^{[1]} f_{aa}^{[2]}\eta(\eta - 2) + (f_{aa}^{[2]})^2(\eta^2 + 2\eta),$$

$$\mathcal{B} = (f_{aa}^{[1]})^2(8 + (\eta - 2)^2)$$
$$- 2f_{aa}^{[1]} f_{aa}^{[2]}\eta(\eta - 2) + (f_{aa}^{[2]})^2(\eta^2 - 2\eta)$$

and where $\eta = s/M^2$ is a quantity that depends only on the velocity of the final diquarks.

From the above relations, we find that the total cross section for the exclusive pair production of heavy axial diquarks in e^+e^- annihilation can be represented as

$$\sigma_{aa} = \frac{1024\pi^3}{9s^5}|\Psi_a(0)|^4 \left(1 - \frac{4M^2}{s}\right)^{3/2}(3\mathcal{A} - \mathcal{B}). \quad (15)$$

It can easily be seen from this formula that, at high energies, the cross section in question behaves as $\sigma_{aa} \sim 1/s^3$.

3.4. Diquark Involving Two Identical Quarks

In the case of the production of a diquark containing two identical quarks, the above formula must be modified. Obviously, we must consider only axial diquarks because a scalar diquark consisting of two identical quarks cannot exist by virtue of the Pauli exclusion principle.

Accordingly, all the above formulas for annihilation in two axial diquarks remain valid if we take into account a correction in the form factors $f_{aa}^{[1]}$ and $f_{aa}^{[2]}$, whereupon they become

$$f_{aa}^{[1]} = 2q\alpha_s(M^2)M\alpha_{\rm em}(s), \quad (16)$$
$$f_{aa}^{[2]} = 4q\alpha_s(M^2)M\alpha_{\rm em}(s), \quad (17)$$

where q is the quark charge.

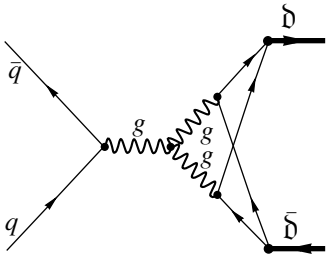

Fig. 2. Diagram describing $q\bar{q}$ annihilation into diquarks through the vertex of three-gluon interaction.

4. AMPLITUDES AND CROSS SECTIONS FOR $q\bar{q}$ ANNIHILATION

In this section, we consider $q\bar{q}$ annihilation followed by the production of a diquark–antidiquark pair. In the leading order, diagrams corresponding to this process are shown in Figs. 1–3. It should be noted that the diagram in Fig. 2 does not contribute in our approximation, since the quarks are on the mass shell.

The color factor of the diagrams in Fig. 1 is

$$\mathrm{Color}^{[1]}_{(ij)(lm)} = \frac{1}{3}t^a_{ij}t^a_{lm},$$

where m and l are the color indices of the annihilating quark and antiquark, respectively. It can easily be seen that $\mathrm{Color}^{[1]}_{(ij)(lm)}$ corresponds to an octet state.

The color factor of the diagrams in Fig. 3,

$$\mathrm{Color}^{[2]}_{(ij)(lm)} = \frac{5}{12}t^a_{ij}t^a_{lm} - \frac{1}{9}\delta_{ij}\delta_{lm},$$

is a mixture of the octet and the singlet color state.

4.1. Annihilation into a Pair of Scalar Diquarks

For the pair exclusive production of scalar diquarks, the matrix element has the form

$$\mathcal{M}_{ss} = \frac{32\pi^2 i}{s^2}|\Psi_s(0)|^2\left(\tilde{f}^{[1]}_{ss}\frac{2t^a_{if}t^a_{lm}}{3}P'_\mu - \tilde{f}^{[2]}_{ss}\left(\frac{5t^a_{if}t^a_{lm}}{6} - \frac{2\delta_{if}\delta_{lm}}{9}\right)\frac{(p,P'-P)}{s}P_\mu\right)l_\mu, \tag{18}$$

where

$$\tilde{f}^{[1]}_{ss} = M\left(\frac{\alpha_s\left(\frac{m_1^2}{M^2}s\right)}{m_1^2} + \frac{\alpha_s\left(\frac{m_2^2}{M^2}s\right)}{m_2^2}\right)\alpha_s(s) - \frac{2M^3}{s}\left(\alpha_s\left(\frac{m_1^2}{M^2}s\right)\frac{m_2}{m_1^3} + \alpha_s\left(\frac{m_2^2}{M^2}s\right)\frac{m_1}{m_2^3}\right)\alpha_s(s), \tag{19}$$

$$\tilde{f}^{[2]}_{ss} = \frac{M^5}{m_1^3m_2^3}\alpha_s\left(\frac{m_1^2}{M^2}s\right)\alpha_s\left(\frac{m_2^2}{M^2}s\right) \tag{20}$$

and p is the 4-momentum of the annihilating quark.

After some simple algebra, we obtain the differential cross section in the form

$$\frac{d\sigma_{ss}}{d\cos\theta} = \frac{8\pi^3}{81s^3}|\Psi_s(0)|^4 \times\left(\left(2\tilde{f}^{[1]}_{ss} + \frac{5}{4}\tilde{f}^{[2]}_{ss}\sqrt{1-\frac{4M^2}{s}}\cos\theta\right)^2 + \frac{(\tilde{f}^{[2]}_{ss})^2}{2}\left(1-\frac{4M^2}{s}\right)\cos^2\theta\right)\times\left(1-\frac{4M^2}{s}\right)^{3/2}(1-\cos^2\theta). \tag{21}$$

From (21), we find that the total cross section for the exclusive pair production of heavy scalar diquarks in $q\bar{q}$ annihilation can be represented as

$$\sigma_{ss} = \frac{8\pi^3}{81s^3}|\Psi_s(0)|^4\left(1-\frac{4M^2}{s}\right)^{3/2}\times\left(\frac{16}{3}(\tilde{f}^{[1]}_{ss})^2 + \frac{11}{20}\left(1-\frac{4M^2}{s}\right)(\tilde{f}^{[2]}_{ss})^2\right). \tag{22}$$

4.2. Annihilation into a Scalar and an Axial Diquark

For the production of a diquark pair in a scalar and an axial state, the matrix element can be written as

$$\mathcal{M}_{as} = \frac{32\pi^2}{s^3}\Psi^*_s(0)\Psi_a(0)\times\left(-\tilde{f}^{[1]}_{as}\frac{2t^a_{if}t^a_{lm}}{3}\epsilon_{\mu\alpha\beta\gamma}P_\beta e_\alpha q_\gamma - \tilde{f}^{[2]}_{as}\left(\frac{5t^a_{if}t^a_{lm}}{6} - \frac{2\delta_{if}\delta_{lm}}{9}\right)\epsilon_{\mu\nu\alpha\beta}q_\alpha e_\beta p_\nu\right)l_\mu, \tag{23}$$

where

$$\tilde{f}^{[1]}_{as} = M^3\left(\frac{\alpha_s\left(\frac{m_1^2}{M^2}s\right)}{m_1^3} - \frac{\alpha_s\left(\frac{m_2^2}{M^2}s\right)}{m_2^3}\right)\alpha_s(s), \tag{24}$$

$$\tilde{f}^{[2]}_{as} = \alpha_s\left(\frac{m_1^2}{M^2}s\right)\alpha_s\left(\frac{m_2^2}{M^2}s\right)\frac{M^5(m_2-m_1)}{m_1^3m_2^3}. \tag{25}$$

For the differential cross section $d\sigma_{as}/d\cos\theta$, we obtain the expression

$$\frac{d\sigma_{as}}{d\cos\theta} = \frac{64\pi^3}{81s^4}|\Psi_s(0)\Psi_a(0)|^2\sqrt{1-\frac{4M^2}{s}} \times\left(\frac{(\tilde{f}^{[1]}_{as})^2}{2}\left(1-\frac{4M^2}{s}\right)(1+\cos^2\theta) + \frac{33(\tilde{f}^{[2]}_{as})^2}{16}\right. \tag{26}$$

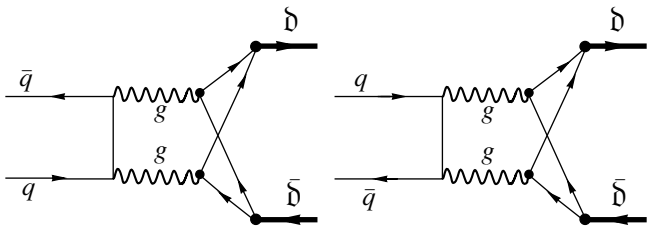

Fig. 3. Diagrams for the two-gluon annihilation of light quarks into a pair of doubly heavy diquarks.

$$\times\left(1+\frac{s-4M^2}{8M^2}\sin^2\theta\right)+\frac{5}{2}\tilde{f}^{[1]}_{as}\tilde{f}^{[2]}_{as}\sqrt{1-\frac{4M^2}{s}}\cos\theta\Bigg).$$

Accordingly, the total cross section for the exclusive production of a heavy scalar and a heavy axial diquark in $q\bar{q}$ annihilation is given by

$$\sigma_{as}=\frac{64\pi^3}{243s^4}|\Psi_s(0)\Psi_a(0)|^2\sqrt{1-\frac{4M^2}{s}} \quad (27)$$
$$\times\left(4(\tilde{f}^{[1]}_{as})^2\left(1-\frac{4M^2}{s}\right)+\frac{33(\tilde{f}^{[2]}_{as})^2}{8}\left(2+\frac{s}{4M^2}\right)\right).$$

In these calculations, we have also neglected the difference of the axial- and the scalar-diquark mass.

4.3. Annihilation into a Pair of Axial Diquarks

For the pair production of heavy axial diquarks in $q\bar{q}$ annihilation, the matrix element has the form

$$\mathcal{M}_{aa}=\frac{32\pi^2 i}{3}\frac{\alpha_s(4m_1^2)\alpha_s(4m_2^2)}{m_1^3m_2^3s^3}M^5|\Psi_a(0)|^2 \quad (28)$$
$$\times\Big\{\big((-Pe'^*)((pP')(le)+(lP')(pe))\big)+(-P'e)$$
$$\times\big((Pp)(le'^*)+(lP)(pe'^*)\big)+(ee'^*)\big((lP)(pP')$$
$$+(lP')(pP)\big)+\frac{s}{2}\big((pe)(le'^*)+(le)(pe'^*)\big)$$
$$\times\left(t^a_{if}t^a_{lm}-\frac{4}{15}\delta_{if}\delta_{lm}\right)+\Big(\tilde{f}^{[2]}_{aa}\big((el)(Pe'^*)$$
$$-(P'e)(e'^*l)\big)+\tilde{f}^{[1]}_{aa}(Pl)(ee'^*)\Big)(t^a_{if}t^a_{lm})\Big\}.$$

Accordingly, the differential cross section is given by

$$\frac{d\sigma_{aa}}{d\cos\theta}=\frac{200\pi^3}{81}\alpha_s^2(4m_1^2) \quad (29)$$
$$\times\alpha_s^2(4m_2^2)\frac{M^{10}}{m_1^6m_2^6s^7}|\Psi_a(0)|^4\sqrt{1-\frac{4M^2}{s}}$$
$$\times(a_4\cos^4\theta+a_3\cos^3\theta+a_2\cos^2\theta+a_1\cos\theta+a_0).$$

From here, it follows that the total cross section for the exclusive pair production of heavy axial diquarks in $q\bar{q}$ annihilation can be written as

$$\sigma_{aa}=\frac{200\pi^3}{81}\alpha_s^2(4m_1^2)\alpha_s^2(4m_2^2)\frac{M^{10}}{m_1^6m_2^6s^7} \quad (30)$$
$$\times|\Psi_a(0)|^4\sqrt{1-\frac{4M^2}{s}}\left(\frac{2}{5}a_4+\frac{2}{3}a_2+2a_0\right),$$

where the following notation has been introduced in order to simplify the presentation:

$$\tilde{f}^{[1]}_{aa}=-\frac{\alpha_s(s)}{\alpha_s(4m_1^2)\alpha_s(4m_2^2)}\frac{8m_1^3m_2^3}{5M^2}$$
$$\times\left(\frac{\alpha_s(4m_1^2)m_2}{m_1^3}+\frac{\alpha_s(4m_2^2)m_1}{m_2^3}\right),$$
$$\tilde{f}^{[2]}_{aa}=\frac{\alpha_s(s)}{\alpha_s(4m_1^2)\alpha_s(4m_2^2)}\frac{4m_1^3m_2^3}{5M}$$
$$\times\left(\frac{\alpha_s(4m_1^2)}{m_1^3}+\frac{\alpha_s(4m_2^2)}{m_2^3}\right),$$
$$a_4=\frac{99}{400}s^2(s-4M^2)^2,$$
$$a_3=\frac{1}{8}\frac{s^3}{M^2}\left(2\tilde{f}^{[2]}_{aa}s+\tilde{f}^{[1]}_{aa}(6M^2+s)\right)\left(1-4\frac{M^2}{s}\right)^{3/2},$$
$$a_2=\frac{1}{16M^4}s(s-4M^2)\Big\{4\tilde{f}^{[1]}_{aa}\tilde{f}^{[2]}_{aa}s(s-2M^2)$$
$$+(\tilde{f}^{[1]}_{aa})^2(12M^4-4M^2s+s^2)$$
$$+s\left(\frac{33}{25}(12M^6-M^4s)+4(\tilde{f}^{[2]}_{aa})^2(s-2M^2)\right)\Big\},$$
$$a_1=-\frac{s^2}{8M^2}\sqrt{1-4\frac{M^2}{s}}\left(2\tilde{f}^{[2]}_{aa}s(s+4M^2)\right.$$
$$\left.+\tilde{f}^{[1]}_{aa}(-24M^4+2M^2s+s^2)\right),$$
$$a_0=-\frac{s}{16M^4}\left(4\tilde{f}^{[1]}_{aa}\tilde{f}^{[2]}_{aa}s\left(8M^4-6M^2s+s^2\right)\right.$$
$$+(\tilde{f}^{[1]}_{aa})^2\left(-48M^6+28M^4s-8M^2s^2+s^3\right)$$
$$+2s\left(\frac{33}{25}M^4s(4M^2+s)\right.$$
$$\left.\left.+\tilde{f}^{[2]}_{aa}(-16M^4-4M^2s+2s^2)\right)\right).$$

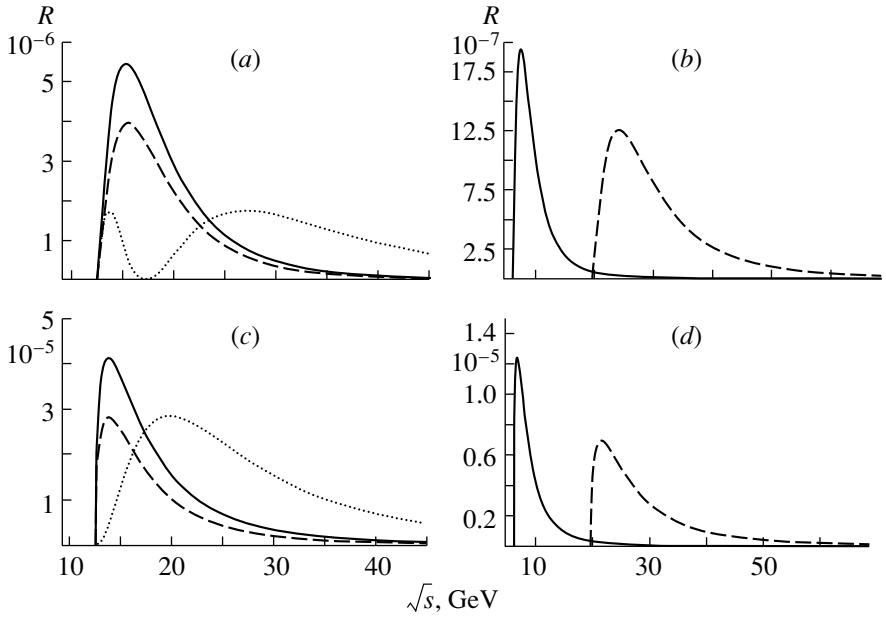

Fig. 4. (*a*) Ratio of the total cross sections for the exclusive production of pairs of *bc* diquarks to the cross section for $c\bar{c}$-pair production in e^+e^- annihilation versus the c.m. particle energy, the cases of the production of two axial diquarks [$R = \sigma_{aa}(s)/\sigma_{c\bar{c}}(s)$], an axial and a scalar diquark [$R = 15\sigma_{as}(s)/\sigma_{c\bar{c}}(s)$], and two scalar diquarks [$R = 400\sigma_{ss}(s)/\sigma_{c\bar{c}}(s)$] being represented by the solid, the dashed, and the dotted curve, respectively. (*b*) Ratio of the total cross section for the exclusive production of pairs of *bb* diquarks to the cross section for $b\bar{b}$-pair production and ratio of the cross section for the exclusive production of pairs of *cc* diquarks to the cross section for $c\bar{c}$-pair production in e^+e^- annihilation versus the c.m. particle energy, the cases of the production of cc diquarks [$R = \sigma_{cc}(s)/\sigma_{c\bar{c}}(s)$] and *bb* diquarks [$R = 30\sigma_{bb}(s)/\sigma_{b\bar{b}}(s)$] being represented by the solid and the dashed curve, respectively. (*c*) Ratio of the total cross section for the exclusive production of pairs of *bc* diquarks to the cross section for $c\bar{c}$-pair production in $q\bar{q}$ annihilation versus the c.m. particle energy, the cases of the production of two axial diquarks [$R = \sigma_{aa}(s)/\sigma_{c\bar{c}}(s)$], an axial and a scalar diquark [$R = 5\sigma_{as}(s)/\sigma_{c\bar{c}}(s)$], and two scalar diquarks [$R = 100\sigma_{ss}(s)/\sigma_{c\bar{c}}(s)$] being represented by the solid, the dashed, and the dotted curve, respectively. (*d*) Ratio of the total cross section for the exclusive production of pairs of *bb* diquarks to the cross section for $b\bar{b}$-pair production and ratio of the total cross section for the exclusive production of pairs of *cc* diquarks to the cross section for $c\bar{c}$-pair production in $q\bar{q}$ annihilation versus the c.m. particle energy, the cases of the production of *cc* diquarks [$R = \sigma_{cc}(s)/\sigma_{c\bar{c}}(s)$] and *bb* diquarks [$R = 30\sigma_{bb}(s)/\sigma_{b\bar{b}}(s)$] being represented by the solid and the dashed curve, respectively.

4.4. Diquark Involving Two Identical Quarks

In this section, we consider $q\bar{q}$ annihilation into a pair of diquarks consisting of two identical heavy quarks. As in the case of e^+e^- annihilation, the calculation must be performed only for the production of two axial vector states.

The amplitude can be written as

$$\mathcal{M}_{aa} = \frac{512\pi^2 i}{3}\frac{\alpha_s^2(M^2)}{Ms^3}|\Psi_a(0)|^2 \qquad (31)$$
$$\times\Big\{\big((-Pe'^*)\big((pP')(le)+(lP')(pe)\big)$$
$$+(-P'e)\big((Pp)(le'^*)+(lP)(pe'^*)\big)$$
$$+(ee'^*)\big((lP)(pP')+(lP')(pP)\big)$$
$$+\frac{s}{2}\big((pe)(le'^*)+(le)(pe'^*)\big)\Big\}$$
$$\times\left(t^a_{if}t^a_{lm}-\frac{4}{15}\delta_{if}\delta_{lm}\right)\Big\{\tilde{f}^{[2]}_{aa}\big((el)(Pe'^*)$$
$$-(P'e)(e'^*l)\big)+\tilde{f}^{[1]}_{aa}(Pl)(ee'^*)\Big)\left(t^a_{if}t^a_{lm}\right)\Big\}.$$

The expression for the differential cross section has the form

$$\frac{d\sigma_{aa}}{d\cos\theta} = 2^{11}\frac{25\pi^3}{81}\frac{\alpha_s^4(M^2)}{M^2s^7} \qquad (32)$$
$$\times|\Psi_a(0)|^4\sqrt{1-\frac{4M^2}{s}}$$
$$\times(a_4\cos^4\theta+a_3\cos^3\theta+a_2\cos^2\theta+a_1\cos\theta+a_0).$$

The total cross section for exclusive production as a function of energy is given by

$$\sigma_{aa} = 2^{11}\frac{25\pi^3}{81}\frac{\alpha_s^4(M^2)}{M^2s^7}|\Psi_a(0)|^4 \qquad (33)$$
$$\times\sqrt{1-\frac{4M^2}{s}}\left(\frac{2}{5}a_4+\frac{2}{3}a_2+2a_0\right),$$

where we have used the notation

$$\tilde{f}_{aa}^{[1]} = -\frac{\alpha_s(s)}{\alpha_s(M^2)}\frac{M^2}{5}, \quad (34)$$

$$\tilde{f}_{aa}^{[2]} = \frac{\alpha_s(s)}{\alpha_s(M^2)}\frac{M^2}{5}. \quad (35)$$

5. NUMERICAL ESTIMATES

The energy dependences of the ratios of the cross sections for the exclusive production of heavy-diquark pairs to the cross section for the production of the relevant two heavy quarks in e^+e^- annihilation,

$$\sigma(e^+e^- \to Q\bar{Q}) = \frac{4\pi\alpha_{\rm em}^2 q_Q^2}{s}\sqrt{1-\frac{4m_Q^2}{s}}\left(1+\frac{2m_Q^2}{s}\right),$$

are shown in Figs. 4*a* and 4*b*.

The corresponding energy dependences of the ratios of the cross sections for the exclusive production of heavy-diquark pairs to the cross section for the production of two heavy quarks in $q\bar{q}$ annihilation,

$$\sigma(q\bar{q} \to Q\bar{Q}) = \frac{8\pi\alpha_s^2}{27s}\sqrt{1-\frac{4m_Q^2}{s}}\left(1+\frac{2m_Q^2}{s}\right),$$

are given in Figs. 4*c* and 4*d*.

Figures 4*a* and 4*c* show the results for the case of diquarks involving different quarks, while Figs. 4*b* and 4*d* correspond to the case of diquarks containing identical quarks. In the calculations, we have used the following values of the quark masses and $\Lambda_{\rm QCD}$:

$$m_c = 1.55\ \text{GeV},$$
$$m_b = 4.9\ \text{GeV},$$
$$\Lambda_{\rm QCD} = 0.2\ \text{GeV}.$$

The values of the wave functions for the diquarks at the origin is the diquark rest frame were calculated in [1].

The displayed graphs give reason to believe that, at B factories, the production of cc diquarks will be dominant in relation to other doubly heavy diquarks and that, at a sufficiently high luminosity, it will be possible to obtain a few thousand pairs of doubly charmed baryons.

We also note that, in the process of $q\bar{q}$ annihilation in inelastic hadron collisions, the pair production of cc baryons constitutes about 10^{-5} of the charm yield at $\sqrt{s} < 100$ GeV.

At threshold energies, diquarks can be produced as discrete units. However, a consideration of an exotic bound diquark–antidiquark state ($\mathfrak{d}\bar{\mathfrak{d}}$) assumes the simulation of its wave function and spectral features. Here, the contribution of Coulomb-like interactions of two nonlocal objects will be significant. The contribution of such exotic hadrons is considerable in a narrow energy region near the production threshold, $\delta E \sim \alpha_s^2 m_{\mathfrak{d}} \sim 0.1$ GeV. Therefore, the foregoing consideration is valid slightly above the threshold energy, $E > 2m + \delta E$.

6. CONCLUSION

The exclusive pair production of doubly heavy diquarks in axial–axial, scalar–scalar, and axial–scalar states has been considered on the basis of the constituent quark model. Also, the matrix elements and the differential and total cross sections for e^+e^- and $q\bar{q}$ annihilation have been presented, and calculations have been performed for the pair production of diquarks involving two identical heavy quarks. The formulas obtained here can be used in calculating the cross sections for electron–positron annihilation and inelastic proton–antiproton collisions followed by the production of doubly heavy baryons, provided that one assumes diquark fragmentation into a baryon.

On the basis of the expressions that we have obtained for cross sections, it can be concluded that the yield of pairs of doubly heavy baryons can be as high as 10^3 events per year in e^+e^- annihilation implemented at B factories of luminosity $\mathcal{L} = 10^{34}$ cm^{-2} s^{-1}, 10^3 events per year in hadronic experiments with a fixed target at a luminosity of $\mathcal{L} = 10^{31}$ cm^{-2}s^{-1} (HERAB), and 10^6 events per year in the CHARM experiment employing extracted beams of the Tevatron at FNAL.

ACKNOWLEDGMENTS

We are grateful to A.K. Likhoded for stimulating discussions and valuable comments.

This work was supported by the Russian Foundation for Basic Research (project nos. 99-02-16558 and 00-15-96645) and by the Ministry for Higher Education of the Russian Federation (grant no. E00-3.3-62).

REFERENCES

1. S. S. Gershtein, V. V. Kiselev, A. K. Likhoded, and A. I. Onishchenko, Preprint No. 98-66, IHEP (Institute of High-Energy Physics, Protvino, 1998); hep-ph/9811212; Heavy Ion Phys. **9**, 133 (1999); Mod. Phys. Lett. A **14**, 135 (1999); S. S. Gershteĭn, V. V. Kiselev, A. K. Likhoded, and A. I. Onishchenko, Yad. Fiz. **63**, 334 (2000) [Phys. At. Nucl. **63**, 274 (2000)]; D. Ebert, R. N. Faustov, V. O. Galkin, *et al.*, Z. Phys. C **76**, 111 (1997); J. G. Körner, M. Krämer, and D. Pirjol, Prog. Part. Nucl. Phys. **33**, 787 (1994); R. Roncaglia, D. B. Lichtenberg, and E. Predazzi, Phys. Rev. D **52**, 1722 (1995).

2. V. V. Kiselev and A. I. Onishchenko, Nucl. Phys. B **581**, 432 (2000); V. V. Kiselev and A. E. Kovalsky, hep-ph/0005019; E. Bagan, M. Chabab, and S. Narison, Phys. Lett. B **306**, 350 (1993); E. Bagan *et al.*, Z. Phys. C **64**, 57 (1994).
3. V. V. Kiselev, A. K. Likhoded, and A. I. Onishchenko, Phys. Rev. D **60**, 014007 (1999); Yad. Fiz. **62**, 2095 (1999) [Phys. At. Nucl. **62**, 1940 (1999)]; Eur. Phys. J. C **16**, 461 (2000); B. Guberina, B. Melic, and H. Stefancic, Eur. Phys. J. C **9**, 213 (1999).
4. A. V. Berezhnoy, V. V. Kiselev, A. K. Likhoded, and A. I. Onishchenko, Phys. Rev. D **57**, 4385 (1998); A. V. Berezhnoy, V. V. Kiselev, and A. K. Likhoded, Z. Phys. A **356**, 89 (1996); A. V. Berezhnoĭ, V. V. Kiselev, and A. K. Likhoded, Yad. Fiz. **59**, 909 (1996) [Phys. At. Nucl. **59**, 870 (1996)]; S. P. Baranov, Phys. Rev. D **56**, 3046 (1997); V. V. Kiselev, A. K. Likhoded, and M. V. Shevlyagin, Phys. Lett. B **332**, 411 (1994); A. Falk *et al.*, Phys. Rev. D **49**, 555 (1994).
5. V. V. Kiselev and A. É. Koval'sky, Yad. Fiz. **63**, 1728 (2000) [Phys. At. Nucl. **63**, 1640 (2000)]; V. V. Kiselev, Yad. Fiz. **62**, 335 (1999) [Phys. At. Nucl. **62**, 300 (1999)]; V. V. Kiselev, Phys. Rev. D **58**, 054008 (1998).
6. V. V. Kiselev, Int. J. Mod. Phys. A **10**, 465 (1995).

Translated by A. Isaakyan

Physics of Atomic Nuclei, Vol. 65, No. 8, 2002, pp. 1545–1552. From Yadernaya Fizika, Vol. 65, No. 8, 2002, pp. 1583–1590.

ELEMENTARY PARTICLES AND FIELDS
Theory

Determination of Hadronic Partial Widths for Scalar–Isoscalar Resonances $f_0(980)$, $f_0(1300)$, $f_0(1500)$, $f_0(1750)$ and the Broad State $f_0(1530^{+90}_{-250})$*

V. V. Anisovich, V. A. Nikonov, and A. V. Sarantsev

Petersburg Nuclear Physics Institute, Russian Academy of Sciences, Gatchina, 188350 Russia

Received March 22, 2001; in final form, November 29, 2001

Abstract—Recently [see V.V. Anisovich *et al.*, Yad. Fiz. **63**, 1489 (2000)], the K-matrix solutions for the wave $IJ^{PC} = 00^{++}$ were obtained in the mass region 450–1900 MeV, where four resonances $f_0(980)$, $f_0(1300)$, $f_0(1500)$, $f_0(1750)$ and the broad state $f_0(1530^{+90}_{-250})$ are located. Based on these solutions, partial widths are determined for scalar–isoscalar states decaying into the channels $\pi\pi$, $K\bar{K}$, $\eta\eta$, $\eta\eta'$, $\pi\pi\pi\pi$ and corresponding decay couplings. © *2002 MAIK "Nauka/Interperiodica".*

1. INTRODUCTION

In [1], the combined K-matrix analysis was performed for the meson partial waves $IJ^{PC} = 00^{++}$, 10^{++}, 02^{++}, 12^{++} on the basis of GAMS data on $\pi^- p \to \pi^0\pi^0 n$, $\eta\eta n$, $\eta\eta' n$ [2], BNL data on $\pi^- p \to K\bar{K}n$ [3], and Crystal Barrel data on $p\bar{p}$ (at rest) $\to \pi^0\pi^0\pi^0$, $\pi^0\eta\eta$, $\pi^0\pi^0\eta$ [4]. The positions of amplitude poles (physical resonances) were determined together with the positions of the K-matrix poles (bare states) and bare-state couplings to the two-meson channels. The nonet classification of the bare $q\bar{q}$ states was suggested, and the possibilities for the location of the lightest scalar glueball in the mass region 1200–1700 MeV were discussed.

The K-matrix technique has an advantage of taking account of the unitarity condition constraints and, in this way, of a correct incorporation of threshold singularities into the scattering amplitude. Since the search for resonances is always related to the investigation of analytical structure of the amplitude in the complex-mass plane by using data at real masses, it is important to perform analytical continuation of the amplitude into the lower half-plane of the complex mass, with correctly taken singularities on the real axis.

However, the K-matrix amplitude does not include resonance parameters in an explicit form, so additional calculations are needed to determine masses and couplings of real resonances. In paper [1], the pole positions have been found for the considered partial wave amplitudes (i.e., masses and total widths of resonances were found), but more complicated calculation of couplings has not been done yet. The decay coupling constants are to be determined as residues of the pole singularities of the multichannel amplitude. In the present paper, we calculate coupling constants to the channels $\pi\pi$, $K\bar{K}$, $\eta\eta$, $\eta\eta'$, and $\pi\pi\pi\pi$ for the resonances $f_0(980)$, $f_0(1300)$, $f_0(1500)$, $f_0(1750)$, $f_0(1530^{+90}_{-250})$. This procedure provided us with partial widths for the decays of these resonances. The choice of the scalar–isoscalar sector for primary study follows from the interest in pursuing the destiny of the lightest scalar glueball after its mixing with neighboring states; one needs knowledge of the couplings $f_0 \to \pi\pi$, $K\bar{K}$, $\eta\eta$, $\eta\eta'$ for all resonances over the mass region 1000–1800 MeV.

The paper is organized as follows.

In Section 2, the coupling constants are presented for the decays $f_0 \to \pi\pi$, $K\bar{K}$, $\eta\eta, \eta\eta'$, $\pi\pi\pi\pi$, and partial widths for the mesons $f_0(1300)$, $f_0(1500)$, $f_0(1750)$, and $f_0(1530^{+90}_{-250})$ are determined.

In Section 3 the resonance $f_0(980)$ is considered in detail: the results of the analysis [1] tell us that standard formulas for the description of resonances, such as Breit–Wigner or Flatté ones, in the case of $f_0(980)$ are unable to give simultaneously the values of the decay coupling constants and the position of the amplitude pole. We suggest an alternative form of resonance amplitude for $f_0(980)$ in which the important role is played by the prompt transition $\pi\pi \to K\bar{K}$. In this section another low-mass state, namely, the σ meson, is also discussed.

The results are summarized in the Conclusion.

*This article was submitted by the authors in English.

1063-7788/02/6508-1545$22.00

Table 1. Partial widths of scalar–isoscalar resonances (in MeV) in hadronic channels $\pi\pi$, $K\bar{K}$, $\eta\eta$, $\eta\eta'$, and $\pi\pi\pi\pi$ for different K-matrix solutions of [1]

	$\pi\pi$	$K\bar{K}$	$\eta\eta$	$\eta\eta'$	$\pi\pi\pi\pi$	Pole position	Solution
$f_0(980)$	71	13	–	–	6	$1006 - i45$	I
	56	10	–	–	2	$1020 - i34$	II-1
	64	12	–	–	3	$1015 - i39.5$	II-2
$f_0(1300)$	75	13	8	–	180	$1303 - i138$	I
	38	2	2	–	192	$1311 - i117$	II-1
	39	2	2	–	193	$1304 - i118$	II-2
$f_0(1500)$	33	8	3.7	0.3	73	$1496 - i59$	I
	39	6	4	0.1	77	$1500 - i63$	II-1
	39	6	4	0.1	77	$1505 - i63$	II-2
$f_0(1750)$	45	28	6	4	29	$1775 - i56$	I
	66	1.5	5	2.5	89	$1814 - i82$	II-1
	64	1.5	5	2.5	87	$1809 - i80$	II-2
$f_0(1530^{+90}_{-250})$	406	186	45	2	881	$1670 - i760$	I
	393	204	40	1	452	$1470 - i545$	II-1
	387	202	39	1	451	$1420 - i540$	II-2

2. DECAY COUPLINGS AND PARTIAL DECAY WIDTHS

We determine the coupling constants and partial decay widths using the following procedure. The 00^{++} amplitude for the transition $a \to b$,

$$A_{a\to b}(s), \quad a,b = \pi\pi, K\bar{K}, \eta\eta, \eta\eta', \pi\pi\pi\pi, \qquad (1)$$

is considered as a function of the invariant energy squared s in the complex-s plane near the pole related to the resonance n. In the vicinity of the pole, the amplitude reads

$$A_{a\to b}(s) = \frac{g_a^{(n)} g_b^{(n)}}{\mu_n^2 - s} e^{i\theta_{ab}^{(n)}} + B_{ab}. \qquad (2)$$

Here, μ_n is the resonance complex mass $\mu_n = M_n - i\Gamma_n/2$; $g_a^{(n)}$ and $g_b^{(n)}$ are the couplings for the transitions $f_0 \to a$ and $f_0 \to b$. The factor $\exp(i\theta_{ab}^{(n)})$ is due to a background contribution which can be the nonresonance terms or tails of neighboring resonances. We also write down in (2) the nonpole background term B_{ab}.

The partial width for the decay $f_0 \to a$ is determined as a product of the coupling constant squared, $g_a^{(n)2}$, and phase space, $\rho_a(s)$, averaged over resonance density:

$$\Gamma_a(n) = C_n \int\limits_{s>s_{\rm th}} \frac{ds}{\pi} \frac{g_a^{(n)2}\rho_a(s)}{({\rm Re}\mu_n^2 - s)^2 + ({\rm Im}\mu_n^2)^2}. \qquad (3)$$

Following [1], we write down the phase-space factor as follows:

$$\rho_a(s) = \frac{2k_a}{\sqrt{s}}, \qquad (4)$$

where k_a is the relative momentum of mesons in the decay channel (for example, for the $\pi\pi$ channel $\rho_{\pi\pi}(s) = \sqrt{(s-4m_\pi^2)/s}$). For the $\pi\pi\pi\pi$ channel, the phase-space factor was chosen in [1] to be the same as for the two-ρ-meson state at $s < 1$ GeV^2 or be equal to 1 at $s \geq 1$ GeV^2. The integration over s in (3) is carried out in the region above the a-channel threshold, $s > s_{\rm th}$ (for the $\pi\pi$ channel it is $s > 4m_\pi^2$). The resonance density factor, $\left(({\rm Re}\mu_n^2 - s)^2 + ({\rm Im}\mu_n^2)^2\right)^{-1}$, guarantees rapid convergence of the integral (3). The normalization constant C_n is determined by the requirement that the sum of all hadronic partial widths is equal to the total width of the resonance:

$$\Gamma(n) = \sum_a \Gamma_a(n). \qquad (5)$$

Table 2. Coupling constants squared (in GeV^2) of scalar–isoscalar resonances to hadronic channels $\pi\pi$, $K\bar{K}$, $\eta\eta$, $\eta\eta'$, and $\pi\pi\pi\pi$ for different K-matrix solutions of [1]

Resonance	$\pi\pi$	$K\bar{K}$	$\eta\eta$	$\eta\eta'$	$\pi\pi\pi\pi$	Solution
$f_0(980)$	0.076	0.180	0.075	–	0.009	I
	0.076	0.186	0.072	–	0.004	II-1
	0.076	0.186	0.072	–	0.004	II-2
$f_0(1300)$	0.050	0.015	0.012	–	0.124	I
	0.026	0.002	0.003	–	0.132	II-1
	0.026	0.002	0.003	–	0.132	II-2
$f_0(1500)$	0.032	0.010	0.005	0.012	0.070	I
	0.038	0.009	0.007	0.006	0.074	II-1
	0.038	0.009	0.007	0.006	0.074	II-2
$f_0(1750)$	0.039	0.029	0.007	0.030	0.025	I
	0.086	0.003	0.009	0.028	0.117	II-1
	0.086	0.003	0.009	0.028	0.117	II-2
$f_0(1530^{+90}_{-250})$	0.329	0.229	0.061	0.022	0.764	I
	0.304	0.271	0.062	0.016	0.382	II-1
	0.304	0.271	0.062	0.016	0.382	II-2

In paper [1], three solutions for the wave $IJ^{PC} = 00^{++}$ have been found; they are labeled as I, II-1, and II-2 (see Tables 4 and 5 in [1]). In practice, solutions II-1 and II-2 give the same physical parameters of resonances, though they differ from parameters found for the K-matrix elements. In particular, in solution II-2, the state $f_0^{\mathrm{bare}}(1600)$ may be identified as a gluonium, for the decay couplings satisfy all the requirements inherent to glueball state; in solution II-1, such a state is $f_0^{\mathrm{bare}}(1230)$. For solution I, the same bare state, $f_0^{\mathrm{bare}}(1230)$, should be considered as a gluonium.

In Table 1, we show the values of partial widths for the resonances $f_0(980)$, $f_0(1300)$, $f_0(1500)$, $f_0(1750)$ and broad state $f_0(1530^{+90}_{-250})$. Partial widths for $f_0(1300)$, $f_0(1500)$, $f_0(1750)$, $f_0(1530^{+90}_{-250})$ are calculated within standard formulas for the Breit–Wigner resonances (3), (4), and (5). The resonance $f_0(980)$, being located near the strong $K\bar{K}$ threshold, needs a special consideration that is presented below.

The decay coupling constants squared, $g_a^{(n)2}$, are shown in Table 2 for $a = \pi\pi, K\bar{K}, \eta\eta, \eta\eta', \pi\pi\pi\pi$. The couplings are determined with the normalization of the amplitude used in [1]: for example, we write the $\pi\pi$-scattering amplitude (2) as $A_{\pi\pi\to\pi\pi}(s) = (\eta_0^0 \exp(2i\delta_0^0) - 1)/2i\rho_{\pi\pi}(s)$, where η_0^0 and δ_0^0 are the inelasticity parameter and phase shift for the 00^{++} $\pi\pi$ wave. The coupling constants $g_a^{(n)}$ are found by calculating the residues of the amplitudes $\pi\pi \to \pi\pi$, $K\bar{K}$, $\eta\eta$, $\eta\eta'$, $\pi\pi\pi\pi$. Also, we check the factorization property for the pole terms by calculating residues for other reactions, such as $K\bar{K} \to K\bar{K}$.

The position of poles in the complex-M plane ($M \equiv \sqrt{s}$) is illustrated by Fig. 1. The complex-M area, where the K-matrix fit [1] may reliably reproduce analyticity of the amplitude, is inside a semicircle depicted by dashed line. The poles which are a subject of the K-matrix analysis and correspond to $f_0(980)$, $f_0(1300)$, $f_0(1500)$, $f_0(1750)$, $f_0(1530^{+90}_{-250})$ are located on the third, fourth, fifth, and sixth sheets of the complex-M plane. The resonance $f_0(980)$ is located near the strong $K\bar{K}$ threshold; therefore, two poles are related to $f_0(980)$: the nearest one is on the third sheet ($M \simeq 1014 - i39$ MeV), and a remote pole is on the fourth sheet ($M \simeq 936 - i238$ MeV). Coupling constants for $f_0(980)$ are determined as residues of the nearest pole (on the third sheet). The $\eta\eta'$ threshold is weak for $f_0(1500)$, and because of that μ_n^2 for the positions of poles on the fifth and sixth sheets are practically the same (note that couplings related to these poles nearly coincide).

The K-matrix fit [1] has been carried out in a broad mass interval, $450 \le M \le 1900$ MeV. This very fact

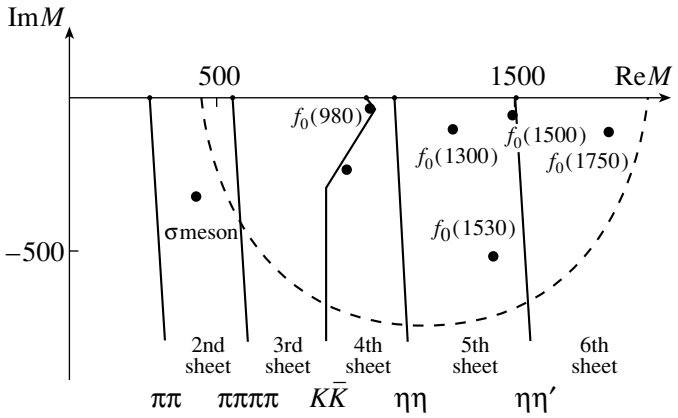

Fig. 1. Pole positions (closed circles) in the complex-M plane ($M \equiv \sqrt{s}$). Solid lines stand for cuts related to the threshold singularities ($\pi\pi$, $\pi\pi\pi\pi$, $K\bar{K}$, $\eta\eta$, and $\eta\eta'$). Two poles, which correspond to $f_0(980)$, are shown: on the third and fourth sheets. On the fifth sheet the poles for $f_0(1300)$, $f_0(1500)$, and broad state $f_0(1530^{+90}_{-250})$ are located (for the broad state the pole stands at $1420 - i540$ MeV, which is the mass for solution II-2 of the fit [1]). On the sixth sheet, there is a pole for $f_0(1750)$. The dashed semicircle restricts the area where the K-matrix fit [1], which was carried out on the real axis in the interval $450 \leq M \leq 1900$ MeV, can give a reliable reconstruction of analytical amplitude.

allows us to believe that we deal with a successfully reconstructed analytical amplitude which goes rather deeply into the lower half-plane M, and this area is restricted by the dashed line in Fig. 1. It is of crucial importance that the pole of the broad state $f_0(1530^{+90}_{-250})$ is inside this area, for this broad state plays a key role in a mixing of $q\bar{q}$ mesons with the lightest glueball (see [5, 6] for details).

3. THE LOW-MASS MESONS: $f_0(980)$ AND σ

The two low-mass mesons, $f_0(980)$ and σ meson, need special consideration and comments.

The analysis [1] shows us that $f_0(980)$ cannot be described either by the standard Breit–Wigner formula or its modification for the case of the nearly located strong $K\bar{K}$ threshold, that is, the Flatté formula [7]. Here, we suggest another resonance formula for $f_0(980)$ which agrees with the results of [1].

In the compilation of Particle Data Group [8], the σ meson is denoted as $f_0(400-1200)$ that reflects a cumulative result obtained in a number of papers where the mass of σ was found in this region or even higher. However, the analysis [1] definitely demonstrates the absence of poles in the 0^{++} amplitude at $600 \leq \mathrm{Re}M \leq 1200$ MeV, with an exception of poles for $f_0(980)$—we will discuss the situation with σ meson in this section later on.

3.1. Description of $f_0(980)$

For $f_0(980)$, the K-matrix fit [1] gives us the position of the pole and coupling constant values (see Tables 1 and 2). These parameters are sufficient to reconstruct the Breit–Wigner resonance amplitude. However, in case of $f_0(980)$, there exists a strong $K\bar{K}$ threshold near the pole, so the resonance term in the amplitude (2) should be suggested not as the Breit–Wigner pole but in a more complicated form. For the $\pi\pi \to \pi\pi$ and $K\bar{K} \to K\bar{K}$ transitions near $f_0(980)$, the following resonance terms can be written instead of the Breit–Wigner pole term $R_n^{(ab)} = g_a^{(n)} g_b^{(n)}/(\mu_n^2 - s)$ entering Eq. (2):

$$R_{f_0(980)}^{(\pi\pi,\pi\pi)} = \left(G^2 + i\frac{\sqrt{s-4m_K^2}}{m_0} F \right) \frac{1}{D}, \quad (6)$$

$$R_{f_0(980)}^{(K\bar{K},K\bar{K})} = \left(G_{K\bar{K}}^2 + iF \right) \frac{1}{D},$$

where

$$F = 2GG_{K\bar{K}} f + f^2(m_0^2 - s), \quad (7)$$

$$D = m_0^2 - s - iG^2 - i\frac{\sqrt{s-4m_K^2}}{m_0} \left(G_{K\bar{K}}^2 + iF \right).$$

Here, m_0 is the input mass of $f_0(980)$, G and $G_{K\bar{K}}$ are coupling constants to pion channels ($\pi\pi + \pi\pi\pi\pi$) and $K\bar{K}$. The dimensionless constant f stands for the prompt transition $K\bar{K} \to \pi\pi$: the value f/m_0 is the "transition" length which is analogous to the scattering length of the low-energy hadronic interaction. The constants m_0, G, $G_{K\bar{K}}$, f are parameters which are to be chosen to reproduce the $f_0(980)$ characteristics (position of pole $s \simeq (1.015 - i0.040)^2$ GeV^2 and couplings to the channels $\pi\pi$ and $K\bar{K}$, $g_{\pi\pi}^2 \simeq 0.076$ GeV^2 and $g_{K\bar{K}}^2 \simeq 0.184$ GeV^2—see Tables 1 and 2).

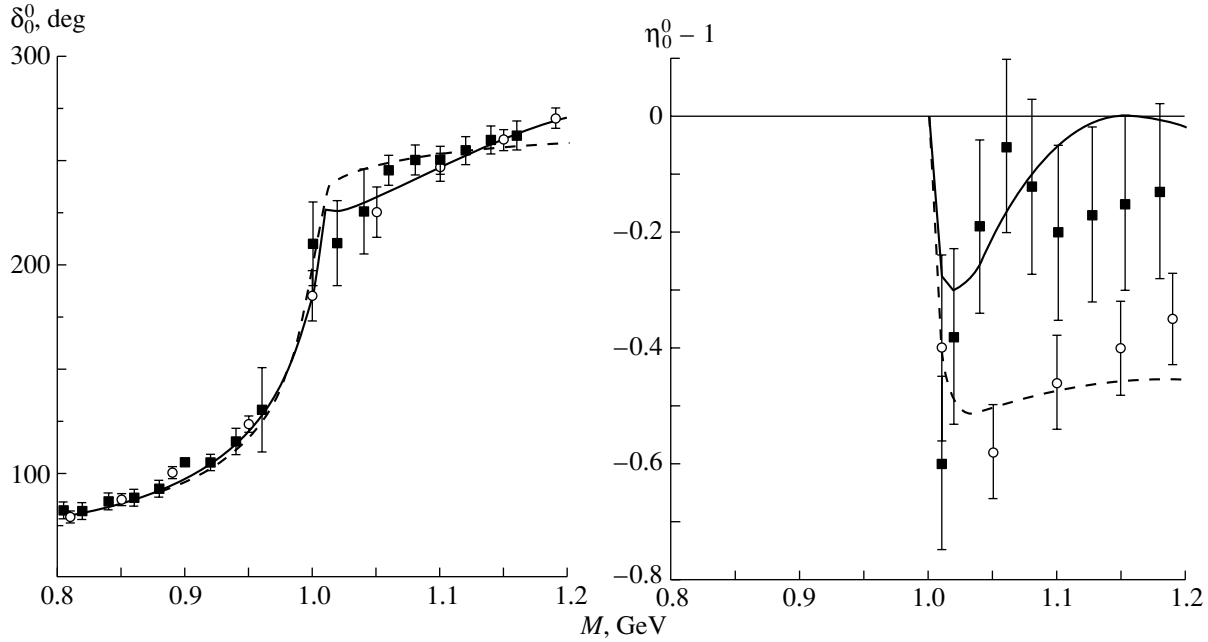

Fig. 2. Reaction $\pi\pi \to \pi\pi$: description of δ_0^0 and η_0^0 in the region of $f_0(980)$. Solid and dashed curves correspond to the parameter sets A and B, respectively. Data are taken from [9] (full squares) and [10] (open circles).

The $\pi\pi$-scattering amplitude in the $f_0(980)$ region is now defined as

$$A_{\pi\pi\to\pi\pi} = e^{i\theta} R_{f_0(980)}^{(\pi\pi,\pi\pi)} + e^{i\frac{\theta}{2}} \sin\frac{\theta}{2}, \qquad (8)$$

where θ is a parameter of the reaction. This formula may be compared with Eq. (2): the background term in (8) is fixed by the requirement that the $\pi\pi$-scattering amplitude below the $K\bar{K}$ threshold has the standard form, $\exp(i\delta)\sin\delta$, where δ is the phase shift in the $IJ^{PC} = 00^{++}$.

At $f \to 0$ the resonance factors (6) turn into the Flatté formula [7], which is used rather often for the description of $f_0(980)$. Still, it happened that the position of the pole (complex mass value) and the amplitude residue in the pole, which have been determined in [1] and shown in Tables 1 and 2, do not obey the Flatté formula but require $f \neq 0$.

We obtained two sets of parameters, with sufficiently correct values of the $f_0(980)$ pole position and couplings. They are equal (in GeV) to

$$\begin{aligned} \text{Solution } A: \quad & m_0 = 1.000, \quad f = 0.516, \qquad (9)\\ & G = 0.386, \quad G_{K\bar{K}} = 0.447,\\ \text{Solution } B: \quad & m_0 = 0.952, \quad f = -0.478,\\ & G = 0.257, \quad G_{K\bar{K}} = 0.388. \end{aligned}$$

The above parameters provide us with a reasonable description of the $\pi\pi$-scattering amplitude. The phase shift δ_0^0 and inelasticity parameter η_0^0 are shown in Fig. 2; the angle θ for the background term in Solutions A and B, determined as

$$\theta = \theta_1 + \left(\frac{\sqrt{s}}{m_0} - 1\right)\theta_2, \qquad (10)$$

is numerically equal to

$$\begin{aligned} \text{Solution } A: \quad & \theta_1 = 189^\circ, \quad \theta_2 = 146^\circ, \qquad (11)\\ \text{Solution } B: \quad & \theta_1 = 147^\circ, \quad \theta_2 = 57^\circ. \end{aligned}$$

Solutions A and B give significantly different predictions for η_0^0; however, the existing data [9, 10] do not allow us to discriminate between them.

Partial widths of $f_0(980)$ are calculated with an expression similar to (3), with the replacement of the integrand denominator as follows:

$$(\mathrm{Re}\mu_n^2 - s)^2 + (\mathrm{Im}\mu_n^2)^2 \to |D|^2. \qquad (12)$$

For both sets of parameters (9), the calculated partial widths are close to each other. For example, using solution II-2 and the A set of parameters, we have $\Gamma_{\pi\pi} = 62$ MeV, $\Gamma_{K\bar{K}} = 14$ MeV, while for solution II-2 and the B set of the parameters one has $\Gamma_{\pi\pi} = 66$ MeV, $\Gamma_{K\bar{K}} = 10$ MeV. The values of partial widths for $f_0(980)$ averaged over solutions A and B are presented in Table 1.

The total hadron width of $f_0(980)$ is defined in the same way as for the other f_0 mesons, namely, by using the position of pole in the complex-M plane: the imaginary part of the mass is equal to a half-width of the resonance. For the Breit–Wigner resonance, this

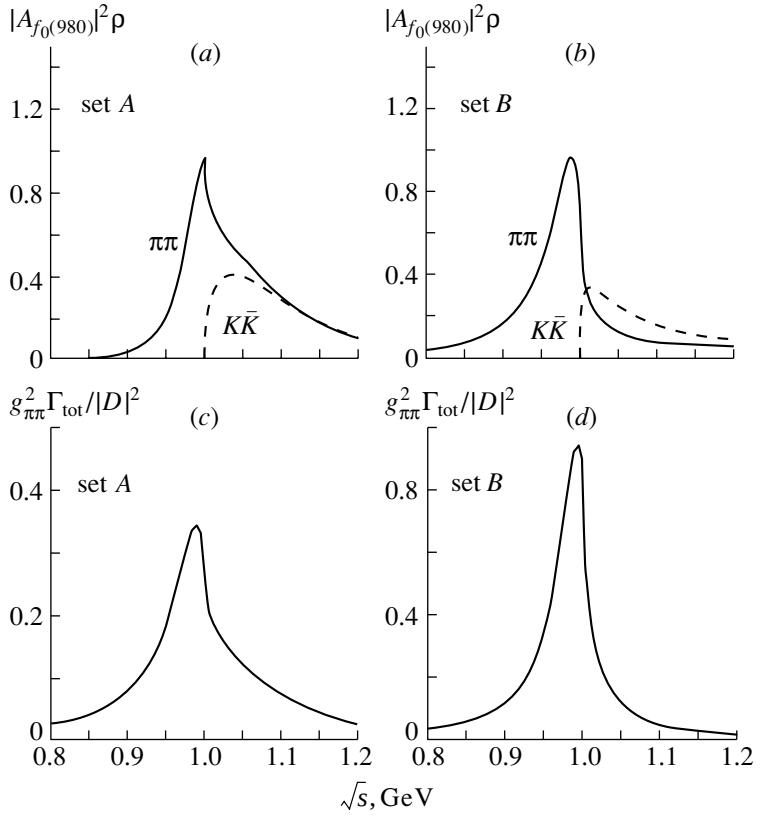

Fig. 3. The magnitudes $|A^{(\pi\pi,\pi\pi)}_{f_0(980)}|^2\rho_\pi(s)$ (solid curve), $|A^{(K\bar{K},K\bar{K})}_{f_0(980)}|^2\rho_K(s)$ (dashed curve), and $g^2_{\pi\pi}\Gamma_{\rm tot}/|D(s)|^2$ (where $g^2_{\pi\pi}\Gamma_{\rm tot} = 0.006$ GeV^2) for the parameter sets A and B. Visible peaks in the $\pi\pi$ spectra (a, b) have the total widths ~60 MeV (set A) and ~45 MeV (set B); visible total widths of the peaks are (c, d) ~55 MeV (set A) and ~45 MeV (set B).

definition is in accordance with what is observed from the resonance spectrum (provided there is no interference with the background). If the resonance is located in the vicinity of a strong threshold, the observed resonance width can differ significantly from what is given by the pole position. In Fig. 3, one can see the magnitudes $|R^{(\pi\pi,\pi\pi)}_{f_0(980)}|^2\rho_\pi(s)$, $|R^{(K\bar{K},K\bar{K})}_{f_0(980)}|^2\rho_K(s)$, and $g^2_{\pi\pi}\Gamma_{\rm tot}/|D(s)|^2$ for the parameter sets A and B: the width of peaks does vary, being less than the value determined by the complex mass of the resonance.

The only objective characteristic of the total hadron width is the position of pole in the complex-M plane; due to this reason, we employ such a definition of total hadron width. Multiple variations of total width in the compilation [8] are just due to the absence of a proper definition of $\Gamma_{\rm tot}$ for resonances near the strong threshold.

3.2. The Light σ Meson

The light σ meson reveals itself as a pole on the second sheet: it is shown in Fig. 1 at $M = 431 - i325$ MeV (or, in terms of s, which is a more appropriate variable for light particles, at $s = (4 - i14)m^2_\pi$), which corresponds to the magnitude obtained in [11]. Although this pole does not appear in the area of complex M, where the K-matrix fit [1] reconstructs the amplitude rather reliably, it still deserves detailed comments.

The situation with the σ meson is as follows. The K-matrix representation allows us to reconstruct correctly the analytical structure of the partial amplitude in the physical region, at $s \geq 4m^2_\pi$, by taking account of the threshold and pole singularities. The singularities related to forces (or left singularities, at $s \leq 0$) are not included directly in the K-matrix machinery. This does not allow us to be quite sure about the results of the K-matrix approach at $s \lesssim 4m^2_\pi$. Concerning the low-mass region, an important result of the K-matrix fit [1] is the absence of the pole singularity in the 00^{++} amplitude at 500–800 MeV. Here, the $\pi\pi$-scattering phase δ^0_0 increases smoothly, reaching 90° at 800–900 MeV. A straightforward explanation of such a behavior of δ^0_0 could consist in the existence of a broad resonance, with the mass about 600–900 MeV and width ~800 MeV (for example, see discussion in [12, 13] and references therein). However, as was stressed above, the K-

Resonance	$\Gamma_{\pi\pi}$	$\Gamma_{K\bar{K}}$	$\Gamma_{\eta\eta}$	$\Gamma_{\eta\eta'}$	$\Gamma_{\pi\pi\pi\pi}$	$\Gamma_{\rm tot}/2$
$f_0(980)$	64 ± 8	12 ± 1	–	–	4 ± 2	40 ± 5
$f_0(1300)$	52 ± 12	6 ± 3	5 ± 2	–	177 ± 10	120 ± 10
$f_0(1500)$	37 ± 2	6 ± 2	4 ± 1	0.2 ± 0.1	77 ± 6	62 ± 3
$f_0(1750)$	64^{+15}_{-30}	11^{+17}_{-9}	5 ± 1	3 ± 1	77^{+30}_{-60}	80^{+20}_{-40}
$f_0(1530^{+90}_{-250})$	390 ± 15	200 ± 10	40 ± 5	1 ± 1	529^{+260}_{-125}	580^{+120}_{-200}

matrix amplitude does not contain pole singularities at $500 \le {\rm Re}M \le 900$ MeV: the K-matrix amplitude has a low-mass pole only, which is located near the $\pi\pi$ threshold or below it. In [1], the presence of the pole near the $\pi\pi$ threshold was not emphasized, since the K-matrix solution does not guarantee a reliable reconstruction of the amplitude at $s \sim 4m_\pi^2$. In [11], in order to restore analytical structure at $s \sim 4m_\pi^2$, the left-hand-side singularities were accounted for on the basis of the dispersion relation N/D method. The $\pi\pi$ scattering N/D amplitude was represented at $M \le 900$ MeV being sewed with the K-matrix solution [1] at $450 \le M \le 900$ MeV. The N/D amplitude reconstructed in this way has a pole near the $\pi\pi$ threshold, thus proving that qualitatively the results of [1] are also valid for the region $s \sim 4m_\pi^2$. The σ meson pole of the N/D amplitude [11] is shown in Fig. 1.

It is worth mentioning that the low-mass location of the σ-meson pole was also obtained in a set of papers, where the low-energy $\pi\pi$ amplitude has been investigated by taking into account the left-hand cut as a set of meson exchanges. These papers include (i) dispersion relation approach, $s \simeq (0.2 - i22.5)m_\pi^2$ [14]; (ii) meson-exchange models, $s \simeq (3.0 - i17.8)m_\pi^2$ [15], $s \simeq (0.5 - i13.2)m_\pi^2$ [16], $s \simeq (2.9 - i11.8)m_\pi^2$ [17]; (iii) linear σ model, $s \simeq (2.0 - i15.5)m_\pi^2$ [18]. At the same time, in [19–24] the pole position was found in the region of higher s, at $s > 7m_\pi^2$, which reflects the ambiguities of approaches which treat the left-hand cut as a known quantity.

As to finding the location of the σ meson on the basis of the available experimental data, one should make a general remark. Since the width of the σ meson is rather large, it is necessary to fit to data in an energy interval which is much larger than the total width of the σ meson. For example, to speak about a σ meson with a mass $M_\sigma \sim 900$ MeV and half-width $\Gamma/2 \simeq 400$ MeV, one should fit to data in the interval $300 \lesssim M \lesssim 1400$ MeV and at the same time take a correct account of the nearest singularities, which are poles corresponding to $f_0(980)$, $f_0(1300)$, and presumably $f_0(1500)$ as well as threshold singularities $\pi\pi$, $K\bar{K}$, $\eta\eta'$, and $\pi\pi\pi\pi$. Concerning $\pi\pi\pi\pi$, one should have in mind that the contribution of this channel is significant starting from 1300 MeV, so this channel is absolutely necessary. Such demands towards the fit of experimental data have been fulfilled in no paper under discussion, with an exception for [1, 10].

4. CONCLUSION

We have obtained partial decay widths for five scalar–isoscalar states $f_0(980)$, $f_0(1300)$, $f_0(1500)$, $f_0(1750)$, $f_0(1530^{+90}_{-250})$ by calculating the decay couplings as residues of pole singularities in the K-matrix amplitude [1]: positions of poles in the complex-M plane are shown in Fig. 1. The pole which corresponds to the light σ meson is also shown in Fig. 1: it was not included in the K-matrix calculation procedure directly, being close to the left-hand cut; the discussion of its status can be found in [11] and references therein.

The results of our calculations of partial decay widths are presented in the table above (the magnitudes are given in MeV).

The values shown for partial widths as well as decay coupling constants of Table 2 need some comments.

The comparison of the hadron decays $f_0(980) \to K\bar{K}$ and $f_0(980) \to \pi\pi$ points to a large $s\bar{s}$ component in $f_0(980)$. The analysis of radiative decays $\phi(1020) \to \gamma f_0(980)$ and $f_0(980) \to \gamma\gamma$ [25] shows also that the $s\bar{s}$ component in $f_0(980)$ is large: with the $f_0(980)$ flavor wave function written as $n\bar{n}\cos\varphi + s\bar{s}\sin\varphi$, the radiative decay widths give either $\varphi \simeq -48^\circ$ or $\varphi \simeq 86^\circ$ (solution with negative φ is more preferable). When the decay processes are switched off, $f_0(980)$ transforms into $f_0^{\rm bare}(720 \pm 100)$, with $\varphi_{\rm bare} \simeq -70^\circ$ (corresponding pole trajectory in the complex-M plane is shown in Fig. 10 of [1]). We see that the decay processes and related change of the state do not diminish the $s\bar{s}$ component strongly.

An opposite situation takes place with $f_0(1750)$. After switching off the decay channels, this resonance transforms into $f_0^{\rm bare}(1810 \pm 30)$, which is dominantly $s\bar{s}$: $\varphi_{\rm bare} \simeq 90^\circ$ for solution I and $\varphi_{\rm bare} \simeq$

-60° for solution II. However, partial decay widths of $f_0(1750)$ (or decay coupling constants given in Table 2) unambiguously prove that the $s\bar{s}$ component in $f_0(1750)$ decreased strongly due to a mixing with other states after the onset of the decay processes. It is possible to guess that this $s\bar{s}$ component has flown into the broad state $f_0(1530^{+90}_{-250})$: the ratio $\Gamma_{K\bar{K}}/\Gamma_{\pi\pi}$ for $f_0(1530^{+90}_{-250})$ does not contradict such an assumption. Such a scenario looks rather intriguing, in particular when taking account of the fact that the broad state $f_0(1530^{+90}_{-250})$, according to [1], is a descendant of a pure glueball (see also [5, 26, 27]). However, the study of the mixing of $q\bar{q}$ state with the glueball is beyond the frame of this article; it will be investigated elsewhere.

For $f_0(980)$, the obtained magnitudes for the complex mass and decay couplings g^2_π and g^2_K demonstrate a failure of the Flatté formula. We suggest an alternative description of $f_0(980)$ which explores, as an addition to the pole term, the amplitude for the prompt transition $\pi\pi \to K\bar{K}$.

ACKNOWLEDGMENTS

The authors are indebted to D.V. Bugg, L.G. Dakhno, and L. Montanet for illuminative discussions of problems related to scalar–isoscalar resonances. The work was supported by the Russian Foundation for Basic Research, project no. 01-02-17861.

REFERENCES

1. V. V. Anisovich, A. A. Kondashov, and Yu. D. Prokoshkin, Yad. Fiz. **63**, 1489 (2000) [Phys. At. Nucl. **63**, 1410 (2000)].
2. D. Alde *et al.*, Z. Phys. C **66**, 375 (1995); Yu. D. Prokoshkin *et al.*, Dokl. Akad. Nauk **342**, 473 (1995) [Phys. Dokl. **40**, 266 (1995)]; A. A. Kondashov *et al.*, Preprint No. 95-137, IHEP (Institute of High-Energy Physics, Protvino, 1995); F. Binon *et al.*, Nuovo Cimento A **78**, 313 (1983); **80**, 363 (1984).
3. S. J. Lindenbaum and R. S. Longacre, Phys. Lett. B **274**, 492 (1992); A. Etkin *et al.*, Phys. Rev. D **25**, 1786 (1982).
4. V. V. Anisovich *et al.*, Phys. Lett. B **323**, 233 (1994); C. Amsler *et al.*, Phys. Lett. B **342**, 433 (1995); **355**, 425 (1995).
5. A. V. Anisovich, V. V. Anisovich, and A. V. Sarantsev, Z. Phys. A **359**, 173 (1997); Phys. Lett. B **395**, 123 (1997).
6. V. V. Anisovich, D. V. Bugg, and A. V. Sarantsev, Phys. Rev. D **58**, 111503 (1998); Yad. Fiz. **62**, 1322 (1999) [Phys. At. Nucl. **62**, 1247 (1999)].
7. S. M. Flatté, Phys. Lett. B **63B**, 224 (1976).
8. Particle Data Group, Eur. Phys. J. C **15**, 1 (2000).
9. G. Grayer *et al.*, Nucl. Phys. B **75**, 189 (1974); W. Ochs, PhD Thesis (Münich University, 1974).
10. V. V. Anisovich and A. V. Sarantsev, Phys. Lett. B **382**, 429 (1996).
11. V. V. Anisovich and V. A. Nikonov, Eur. Phys. J. A **8**, 401 (2000).
12. L. Montanet, Nucl. Phys. B (Proc. Suppl.) **86**, 381 (2000).
13. M. R. Pennington, *Riddle of the Scalars: Where is the σ?,* Frascati Phys., Ser. XV, 95 (1999).
14. J. L. Basdevant, C. D. Frogatt, and J. L. Petersen, Phys. Lett. B **41B**, 178 (1972).
15. J. L. Basdevant and J. Zinn-Justin, Phys. Rev. D **3**, 1865 (1971); D. Iagolnitzer, J. Justin, and J. B. Zuber, Nucl. Phys. B **60**, 233 (1973).
16. B. S. Zou and D. V. Bugg, Phys. Rev. D **48**, 3948 (1993); **50**, 591 (1994).
17. G. Janssen, B. C. Pearce, K. Holinde, and J. Speth, Phys. Rev. D **52**, 2690 (1995).
18. N. N. Achasov and G. N. Shestakov, Phys. Rev. D **49**, 5779 (1994).
19. S. D. Protopopescu *et al.*, Phys. Rev. D **7**, 1279 (1973).
20. P. Estabrooks, Phys. Rev. D **19**, 2678 (1979).
21. K. L. Au, D. Morgan, and M. R. Pennington, Phys. Rev. D **35**, 1633 (1987).
22. S. Ishida *et al.*, Prog. Theor. Phys. **98**, 1005 (1997).
23. N. A. Törnqvist and M. Roos, Phys. Rev. Lett. **76**, 1575 (1996).
24. M. Locher, V. E. Markushin, and H. Q. Zheng, Eur. Phys. J. C **4**, 317 (1998).
25. A. V. Anisovich, V. V. Anisovich, and V. A. Nikonov, Eur. Phys. J. A **12**, 103 (2001).
26. A. V. Anisovich and A. V. Sarantsev, Phys. Lett. B **413**, 137 (1997).
27. V. V. Anisovich, Usp. Fiz. Nauk **168**, 481 (1998) [Phys. Usp. **41**, 419 (1998)].

Physics of Atomic Nuclei, Vol. 65, No. 8, 2002, pp. 1553–1559. From Yadernaya Fizika, Vol. 65, No. 8, 2002, pp. 1591–1597.

ELEMENTARY PARTICLES AND FIELDS
Theory

Darboux Transformations for a System of Coupled Discrete Schrödinger Equations[1)*]

A. A. Suzko[2)]**

Joint Institute for Nuclear Research, Dubna, Moscow oblast, 141980 Russia

Received June 6, 2001

Abstract—Darboux transformations and a factorization procedure are presented for a system of coupled finite-difference Schrödinger equations. The conformity between generalized Darboux transformations and the factorization method is established. Factorization chains and consequences of Darboux transformations are obtained for a system of coupled discrete Schrödinger equations. The proposed approach permits constructing a new series of potential matrices with known spectral characteristics for which coupled-channel discrete Schrödinger equations have exact solutions. © *2002 MAIK "Nauka/Interperiodica".*

1. INTRODUCTION

Darboux transformations [1], the factorization technique [2, 3], the supersymmetry method [4], and Bargmann transformations [5] in quantum mechanics are closely related to one another [6–11]. The supersymmetry method is based on the factorization procedure, while Bargmann transformations can be obtained by means of a superposition of Darboux transformations, which in turn are related to formulas of the Schrödinger factorization method. The Darboux and Bargmann transformations are widely applicable to quantum-mechanical problems [12–15], as well as to nonlinear integrable systems [16–19]. If these methods are generalized to a number of wave-function components larger than one, the sphere of possible applications of these methods increases considerably to include multidimensional, few-particle, and multiparticle objects.

A matrix generalization of Darboux transformations (without thresholds) was described in [20]. Matrix Darboux and Bargmann transformations with thresholds were considered in [21–23] and, in a more general form, in [10] for the case of variable values of energy and angular momentum and in [8] for Schrödinger equations with a right-hand side. The foundation for developing algebraic transformations in finite differences for coupled-channel and two-dimensional cases was laid by Berezanskii [24], who developed the theory of orthogonal polynomials for the infinite Jacobi matrix. It is known [24–27] that spectral problems for finite-difference equations have much in common with the theory of orthogonal polynomials and that the latter is related to the method of Darboux transformations [28–30].

In the present paper, matrix discrete Darboux transformations are constructed for a coupled system of discrete Schrödinger equations. The relationships are established between Darboux transformations, the factorization method, and the supersymmetry method. The factorization method is based on generalizing, to a system of m coupled-channel discrete Schrödinger equations, Christoffel [28] and Geronimus [29] single-channel transformations, which are discrete analogs of Darboux transformations for differential equations. Under the corresponding generalized transformations, the spectrum of a given Hamiltonian changes in a simple controllable way, namely, by removing or adding a bound state without modifying other energy levels of the spectrum. This approach also allows one to construct completely isospectral operators if the spectra of two Hamiltonians H and $\bar{H}$ coincide. The generalized Darboux transformations can be applied repeatedly to obtain new matrix potentials and corresponding solutions. Therefore, the approach provides a powerful tool for performing spectral transformations with desired controllable modifications of the bound spectrum. Factorization chains for a system of coupled discrete Schrödinger equations are generated. The derived generalized transformations reduce to simpler ones for a single discrete Schrödinger equation.

*This article was submitted by the author in English.

[1)]Talk presented at the 23rd International Colloquium on Group Theoretical Methods in Physics, Dubna, July 31–August 5, 2000 (see Yad. Fiz. **64**, No. 12 (2001) [Phys. At. Nucl. **64**, No. 12 (2001)].

[2)]Institute of Radiation Physics and Chemistry Problems, Byelorussian Academy of Sciences, Minsk, Belarus.

**e-mail: suzko@thsun1.jinr.ru

1063-7788/02/6508-1553$22.00

2. MATRIX DARBOUX TRANSFORMATION AND FACTORIZATION METHOD

Let us consider the discrete Schrödinger equation in the Hermitian form

$$(H\Psi)_n = A(n)\Psi(n-1) + A(n+1)\Psi(n+1) + V(n)\Psi(n) = \lambda\Psi(n), \quad (1)$$

where $A(n)$ and $V(n)$ are $m \times m$ real symmetric discrete potential matrices, a solution $\Psi(n)$ can be either a column vector or a matrix, and λ is a spectral parameter. In the ordinary one-channel case considered (at $m = 1$), $A(n)$ and $V(n)$ are discrete potential coefficients. Here, we use the language of nonrelativistic quantum mechanics. In principle, the discrete index n can vary either from $-\infty$ to ∞ (this corresponds to the problem on a line) or from 0 to ∞ (the problem on a half-line); when $0 \le n \le N$, it is a special class of restricted problems. For the sake of definiteness, we consider the case on the half-line $-1 \le n < \infty$. If we set $\Psi(-1) = 0$, the action of the Schrödinger discrete operator H on the vector $\Psi = \{\Psi(0), \Psi(1), \Psi(2), ..., \Psi(n), ...\}^\dagger$ is represented by the action of the Jacobi block matrix J on Ψ:

$$(J\Psi)_n = \begin{pmatrix} V_0 & A_1 & 0 & 0 & 0 & ... & 0 \\ A_1 & V_1 & A_2 & 0 & 0 & ... & 0 \\ 0 & 0 & 0 & . & . & . & 0 \\ . & . & . & 0 & A_n & V_n & A_{n+1} \\ . & . & . & . & . & . & . \end{pmatrix} \times \begin{pmatrix} \Psi(0) \\ \Psi(1) \\ ... \\ \Psi(n) \\ ... \end{pmatrix} = \lambda \begin{pmatrix} \Psi(0) \\ \Psi(1) \\ ... \\ \Psi(n) \\ ... \end{pmatrix}. \quad (2)$$

From the Jacobi block matrix (2), which is tridiagonal in the variable n, it is seen that matrix solutions $\Psi(n)$ are connected at the neighboring points n and $n \pm 1$. It follows that, if the matrix coefficients $A(n)$ and $V(n)$ are known and if two boundary conditions are given at one end of the tested interval $-1 \le n \le N$, one can obtain solutions on the whole interval by moving in subsequent steps from that end.

For the system of Eqs. (1), let us define auxiliary matrix solutions $\Phi(\lambda, n)$ satisfying the boundary conditions

$$\Phi(\lambda, -1) = 0, \quad \Phi(\lambda, 0) = 1; \quad (3)$$

that is, $\Phi_{ms}(-1) = 0$ and $\Phi_{ms}(0) = \delta_{ms}$. Since the matrix Eq. (1) is tridiagonal in the coordinate variable n and owing to the boundary conditions (3), the matrix solutions $\Phi(\lambda, n)$ in the spectral parameter λ are polynomials of the nth degree with matrix coefficients that can be orthogonalized in their spectral measure [24].

The aim of this section is to give Darboux transformations and a factorization procedure for the system of coupled Eqs. (1) and to apply them to construct new potential matrices $\widetilde{V}(n)$ and $\widetilde{A}(n)$, along with the corresponding polynomial matrix solutions $\widetilde{\Phi}(n)$, by using the solutions $\Phi(n)$ of (1) appropriate for the known old potentials $V(n)$ and $A(n)$. Our next purpose is to create factorization chains with consequences of the Darboux transformations.

We define the discrete Darboux transformation operator $\hat{L}$ in the general form

$$\hat{L}\widetilde{\Phi}(\lambda, n) = \Phi(\lambda, n) = T(n)\widetilde{\Phi}(\lambda, n) - C(n-1)\widetilde{\Phi}(\lambda, n-1) \quad (4)$$

with some unknown matrix coefficients $T(n)$ and $C(n-1)$, which have to be defined. It is some analog of the Geronimus transformation [29] for polynomials $P(\lambda, n)$,

$$P(\lambda, n) = \widetilde{P}(\lambda, n) + C(n-1)\widetilde{P}(\lambda, n-1), \quad (5)$$

which satisfy, instead of (1), the three-term recurrence relation taken in the non-Hermitian form

$$a_n P(\lambda, n-1) + v_n P(\lambda, n) + P(\lambda, n+1) = \lambda P(\lambda, n). \quad (6)$$

We choose the symmetric form (2) of the discrete Schrödinger Eqs. (1) to have opportunities of establishing connections with formulas of the spectral inverse problem [15, 30] which is usually formulated for self-adjoint Hamiltonians. The next complication, in contrast to (5) and (6), is that we are dealing with the matrix Eqs. (1) and (4). The matrices of the solutions $\Phi(\lambda, n)$ and $\widetilde{\Phi}(\lambda, n)$ are polynomials in λ of the same degree but with different matrix coefficients. Since Darboux transformations can be applied repeatedly, we will consider a chain of transformations (4). Iteration of (4) leads to a family of orthogonal polynomial matrices $\Phi_t(\lambda, n)$ depending on a discrete parameter $t = 0, \pm 1, \pm 2, ...$ with the shift $t + 1 \to t$ defined as

$$\hat{L}_t\Phi_{t+1}(\lambda, n) = \Phi_t(\lambda, n) = T_t(n)\Phi_{t+1}(\lambda, n) - C_t(n-1)\Phi_{t+1}(\lambda, n-1). \quad (7)$$

The inverse transformation $\hat{R}_t$ from polynomial matrices $\Phi_t(n)$ to $\Phi_{t+1}(n)$ can be defined as

$$(\lambda - \mu_t)^{-1}\hat{R}_t\Phi_t(\lambda, n) = \Phi_{t+1}(\lambda, n) \quad (8)$$

$$= (\lambda - \mu_t)^{-1}[K_t(n+1)\Phi_t(\lambda, n+1) - N_t(n)\Phi_t(\lambda, n)],$$

where $K_t(n+1)$ and $N_t(n)$ are also unknown matrix coefficients and μ_t is a spectral parameter. Transformation (8) can be considered as a matrix generalization of the Christoffel transformation [28]

$$P_{t+1}(\lambda, n) = (\lambda - \mu_t)^{-1}[P_t(\lambda, n+1) + N_t(n)P_t(\lambda, n)]. \quad (9)$$

Geronimus and Christoffel transformations for discrete Eq. (6) play a role of Darboux transformations for ordinary differential equations.

2.1. Construction of an Initial Hamiltonian H_t in a Factorized Form

Let us find the conditions for potential matrices $V_t(n)$, $A_t(n)$ and $V_{t+1}(n)$, $A_{t+1}(n)$ under which the corresponding matrix functions $\Phi_t(\lambda, n)$ and $\Phi_{t+1}(\lambda, n)$ defined by (7) and (8) satisfy the system of Eqs. (1). For this purpose, we transform relation (7) by substituting $\Phi_{t+1}(n)$ and $\Phi_{t+1}(n-1)$ from (8),

$$\Phi_t(n) = (\lambda - \mu_t)^{-1}[T_t(n)K_t(n+1)\Phi_t(n+1) - T_t(n)N_t(n)\Phi_t(n) - C_t(n-1)K_t(n)\Phi_t(n) + C_t(n-1)N_t(n-1)\Phi_t(n-1)]. \quad (10)$$

Rewriting (10) as

$$(\lambda - \mu_t)\Phi_t(n) = T_t(n)K_t(n+1)\Phi_t(n+1) - [T_t(n)N_t(n) + C_t(n-1)K_t(n)]\Phi_t(n) + C_t(n-1)N_t(n-1)\Phi_t(n-1) \quad (11)$$

and performing a comparison with the Schrödinger Eqs. (1), we immediately have

$$T_t(n)K_t(n+1) = A_t(n+1), \quad (12)$$

$$C_t(n-1)N_t(n-1) = A_t(n) \quad (13)$$

and

$$V_t(n) = \mu_t - [T_t(n)N_t(n) + C_t(n-1)K_t(n)]. \quad (14)$$

It is understood that this procedure corresponds to factorization of an initial Hamiltonian H_t,

$$H_t = \hat{L}_t\hat{R}_t + \mu_t. \quad (15)$$

Now, it is necessary to find the matrix coefficients T_t, C_t, K_t, and N_t. If we require that $\Phi_t(\lambda, n) \neq 0 \ \forall n$ in the limit $\lambda \to \mu_t$, then it follows from (8) that

$$N_t(n)\Psi_t(n) = K_t(n+1)\Psi_t(n+1), \quad (16)$$

where $\Psi_t(n) = \Phi(\mu_t, n)M_t$, M_t being a matrix constant independent of n. Expressing $T_t(n)$ from (12) and $N_t(n)$ from (16) as

$$T_t(n) = A_t(n+1)K_t^{-1}(n+1), \quad (17)$$

$$N_t(n) = K_t(n+1)\Psi_t(n+1)\Psi_t^{-1}(n) \quad (18)$$

and taking into account (18) in (13), we obtain

$$C_t(n-1) = A_t(n)N_t^{-1}(n-1) = A_t(n)\Psi_t(n-1)\Psi_t^{-1}(n)K_t^{-1}(n). \quad (19)$$

One can see from (17)–(19) that, of four sought matrices T_t, N_t, C_t, and K_t in generalized Darboux transformations (7) and (8), three are expressed in terms of the known solutions $\Psi_t(n)$, the potentials $A_t(n)$, and one unknown matrix $K_t(n)$, which is still to be determined. Substituting (17)–(19) into (14), we find that the potential matrix satisfies the relation

$$V_t(n) = \mu_t - [A_t(n+1)\Psi_t(n+1)\Psi_t^{-1}(n) + A_t(n)\Psi_t(n-1)\Psi_t^{-1}(n)]. \quad (20)$$

From (20), it immediately follows that

$$A_t(n)\Psi_t(n-1) + V_t(n)\Psi_t(n) + A_t(n+1)\Psi_t(n+1) = \mu_t\Psi_t(n); \quad (21)$$

that is, $\Psi_t(n)$ is a solution of the finite-difference Eq. (1) for some fixed eigenvalue μ_t. Fulfillment of the condition $\Psi_t(n) \neq 0$ at all n implies that μ_t is the lowest eigenvalue. If we take into account (17) and (19) for $T_t(n)$ and $C_t(n-1)$, the matrix function $\Phi_t(\lambda, n)$ at arbitrary λ determined by (7) is recognized as

$$\Phi_t(n) = A_t(n+1)K_t^{-1}(n+1)\Phi_{t+1}(n) - A_t(n)\Psi_t(n-1)\Psi_t^{-1}(n)K_t^{-1}(n)\Phi_{t+1}(n-1) \equiv \hat{L}_t\Phi_{t+1}(n). \quad (22)$$

At the same time, the matrix function $\Phi_{t+1}(n)$ specified by (8) with $N_t(n)$ from (18) is written as

$$\Phi_{t+1}(n) = (\lambda - \mu_t)^{-1}K_t(n+1)[\Phi_t(n+1) - \Psi_t(n+1)\Psi_t^{-1}(n)\Phi_t(n)] \equiv (\lambda - \mu_t)^{-1}\hat{R}_t\Phi_t(n). \quad (23)$$

As a result, the Darboux transformations (7) and (8) for general solutions Φ_t and Φ_{t+1} reduce to relations (22) and (23), respectively, expressed in terms of the solutions $\Psi_t(n)$ and the potentials $A_t(n)$. As one can see from (20), the initial potential $V_t(n)$ is also represented in terms of $\Psi_t(n)$ and $A_t(n)$.

It is convenient to introduce the $m \times m$ matrices

$$W_t(n) = \Psi_t(n-1)\Psi_t^{-1}(n), \quad (24)$$

which can naturally be called superpotential ones by analogy with supersymmetric quantum mechanics [23]. Then, Eqs. (20), (22), and (23) can be rewritten as

$$V_t(n) = \mu_t - A_t(n+1)W_t^{-1}(n+1) - A_t(n)W_t(n), \quad (25)$$

$$\Phi_t(n) = A_t(n+1)K_t^{-1}(n+1)\Phi_{t+1}(n) \quad (26)$$

$$- A_t(n)W_t(n)K_t^{-1}(n)\Phi_{t+1}(n-1) \equiv \hat{L}_t\Phi_{t+1}(n),$$

$$\Phi_{t+1}(n) = (\lambda-\mu_t)^{-1}K_t(n+1)[\Phi_t(n+1) \quad (27)$$
$$- W_t^{-1}(n+1)\Phi_t(n)] \equiv (\lambda-\mu_t)^{-1}\hat{R}_t\Phi_t(n).$$

As the result of generalized Darboux transformations, the original Hamiltonian H_t is represented in the factorized form (15), while the potential matrix V_t and general solutions Φ_t and Φ_{t+1} are expressed in terms of the discrete superpotential matrices $W_t(n)$, which are related to the factorization solutions $\Psi_t(n)$ fixed by the spectral parameter μ_t.

In the next section, we determine, for the potential matrices V_{t+1} and A_{t+1}, conditions under which the functions specified by relations (23) or (27) will satisfy the system of discrete Schrödinger Eqs. (1).

2.2. Construction of H_{t+1} in a Factorized Form

Let us now seek the partner Hamiltonian H_{t+1} to H_t determined by (15) as

$$H_{t+1} = \hat{R}_t\hat{L}_t + \mu_t. \quad (28)$$

For this purpose, we perform transformations similar to the previous ones with the difference that, now, (26) is inserted into (27). As a result, we obtain

$$(\lambda-\mu_t)\Phi_{t+1}(n) = K_t(n+1)A_t(n+2) \quad (29)$$
$$\times K_t^{-1}(n+2)\Phi_{t+1}(n+1) - K_t(n+1)$$
$$\times \left\{W_t^{-1}(n+1)A_t(n+1) + A_t(n+1)W_t(n+1)\right\}$$
$$\times K_t^{-1}(n+1)\Phi_{t+1}(n) + K_t(n+1)W_t^{-1}(n+1)$$
$$\times A_t(n)W_t(n)K_t^{-1}(n)\Phi_{t+1}(n-1).$$

In accordance with the Schrödinger Eqs. (1), we have

$$A_{t+1}(n+1) = K_t(n+1)A_t(n+2)K_t^{-1}(n+2); \quad (30)$$

$$A_{t+1}(n) = K_t(n+1)W_t^{-1}(n+1) \quad (31)$$
$$\times A_t(n)W_t(n)K_t^{-1}(n);$$

$$V_{t+1}(n) = \mu_t - K_t(n+1)\left\{W_t^{-1}(n+1) \quad (32)\right.$$
$$\left.\times A_t(n+1) + A_t(n+1)W_t(n+1)\right\}K_t^{-1}(n+1)$$
$$= \mu_t - K_t(n+1)\left\{\Psi_t(n+1)\Psi_t^{-1}(n)A_t(n+1)\right.$$
$$\left.+ A_t(n+1)\Psi_t(n)\Psi_t^{-1}(n+1)\right\}K_t^{-1}(n+1).$$

According to (25) for $V_t(n)$, the potential $V_{t+1}(n)$ can be represented as

$$V_{t+1}(n) = K_t(n+1)\left\{A_t^{-1}(n+1)V_t(n) \quad (33)\right.$$
$$\left.\times A_t(n+1) + A_t^{-1}(n+1)A_t(n)W_t(n)A_t(n+1)\right.$$
$$\left.- A_t(n+1)W_t(n+1)\right\}K_t^{-1}(n+1)$$

or in the alternative form

$$V_{t+1}(n) = K_t(n+1)\{V_t(n+1) \quad (34)$$
$$+ A_t(n+2)W_t^{-1}(n+2)$$
$$- W_t^{-1}(n+1)A_t(n+1)\}K_t^{-1}(n+1).$$

In fact, we have already obtained the matrix discrete Darboux transformations with the relationships between old and new potentials (30)–(34) and solutions (26) and (27). Nevertheless, the formulas contain yet unknown matrix functions $K_t(n)$.

To determine $K_t(n)$, we express $A_{t+1}(n)$ from (30) and (31) and equate the right-hand sides of them. As a result, we obtain

$$K_t(n)A_t(n+1)K_t^{-1}(n+1) \quad (35)$$
$$= K_t(n+1)W_t^{-1}(n+1)A_t(n)W_t(n)K_t^{-1}(n).$$

We further introduce $\mathcal{B}_t(n)$ as

$$\mathcal{B}_t(n) = A_t(n+1)K_t^{-1}(n+1)K_t(n) \quad (36)$$

and perform transformations by multiplying (35) by $K_t^{-1}(n)$ from the left and by $K_t(n)$ from the right. Then, $\mathcal{B}_t(n)$ is expressed in terms of the known potentials A_t and superpotentials W_t:

$$\mathcal{B}_t(n)\mathcal{B}_t(n) = A_t(n+1) \quad (37)$$
$$\times W_t^{-1}(n+1)A_t(n)W_t(n).$$

Now, (36) gives the recurrence formulas for determining $K_t(n)$. By using definition (36) in (30) and (37) in (31), we can represent $A_{t+1}(n)$ and $A_{t+1}(n+1)$ in the same symmetric form; that is,

$$A_{t+1}(n) = K_t(n)\mathcal{B}_t(n)K_t^{-1}(n), \quad (38)$$
$$A_{t+1}(n+1) = K_t(n+1)\mathcal{B}_t(n+1)K_t^{-1}(n+1).$$

According to (37) and (24), the potentials $A_{t+1}(n)$ in (38) are defined as

$$A_{t+1}(n) = K_t(n)\left(A_t(n+1)W_t^{-1}(n+1)\right. \quad (39)$$
$$\left.\times A_t(n)W_t(n)\right)^{1/2}K_t^{-1}(n)$$
$$= K_t(n)\left(A_t(n+1)\ \Psi_t(n+1)\Psi_t^{-1}(n)\right.$$
$$\left.\times A_t(n)\Psi_t(n-1)\Psi_t^{-1}(n)\right)^{1/2}K_t^{-1}(n).$$

Relations (24)–(27) and (32)–(39) provide a complete description of Darboux transformations for the system of coupled discrete Eqs. (1). As a result, whenever the system of Eqs. (1) is exactly solvable or solutions are known numerically, the Darboux transformations give new Hamiltonians with potentials determined by (32) and (39) and solutions (27), which are determined analytically or numerically in terms of the known old solutions. Moreover, the successive application of these transformations allows us to generate a hierarchy

of new potentials and corresponding solutions. As one can see from (24), (20), (32), and (39), the potentials $V_t(n)$, $V_{t+1}(n)$, and $A_{t+1}(n)$ are singular when $\det \Psi_t(n)$ has zeros. To avoid this situation, the matrix $\Psi_t(n) = \{\psi_t^1(n), \psi_t^2(n), ..., \psi_t^M(n)\}$ has to be chosen in such a way that the columns $\psi_t^i(n)$ of Ψ_t are linearly independent.

Before completing this subsection, it should be noted that, as the result of Darboux transformations, the factorization of Hamiltonians H_t and H_{t+1} was obtained. In the next section, the connection between Darboux transformations and the factorization method will be established in the opposite direction: from the factorization of Hamiltonians to generalized Darboux transformations.

3. FACTORIZATION CHAIN AND INTERTWINING RELATIONS

Summarizing all the above, we can say that the operators $\hat{R}_t$ and $\hat{L}_t$ of Darboux transformations constitute the generalized factorization of the second-order Hamiltonians H_t and H_{t+1} for the system of coupled Eqs. (1) as products of the first-order operators

$$\hat{L}_t\hat{R}_t = H_t - \mu_t, \quad \hat{R}_t\hat{L}_t = H_{t+1} - \mu_t. \tag{40}$$

Consequences of the factorization procedure are the following:

(i) Relations (40) can be rewritten as the factorization chain

$$\hat{R}_t\hat{L}_t + \mu_t = \hat{L}_{t+1}\hat{R}_{t+1} + \mu_{t+1}. \tag{41}$$

As in the single-channel case, one can also show that

(ii) The factorization relations (40) are equivalent to the intertwining relations

$$\hat{R}_t H_t = H_{t+1}\hat{R}_t, \quad \hat{L}_t H_{t+1} = H_t\hat{L}_t. \tag{42}$$

Let us assume that $\widetilde{\Psi}_t$ and $\widetilde{\Psi}_{t+1}$ are matrix (or vector) solutions of (1) corresponding to H_t and H_{t+1} with the eigenvalues ν_t and ν_{t+1}, respectively; that is,

$$H_t\widetilde{\Psi}_t = \nu_t\widetilde{\Psi}_t, \tag{43}$$

$$H_{t+1}\widetilde{\Psi}_{t+1} = \nu_{t+1}\widetilde{\Psi}_{t+1}. \tag{44}$$

Applying the operator $\hat{R}_t$ to Eq. (43) and using (40), we deduce the simple relations

$$\hat{R}_t H_t\widetilde{\Psi}_t = \hat{R}_t(\hat{L}_t\hat{R}_t + \mu_t)\widetilde{\Psi}_t = H_{t+1}\hat{R}_t\widetilde{\Psi}_t. \tag{45}$$

Then, owing to $\hat{R}_t\mu_t = \mu_t\hat{R}_t$, we arrive at the first equation from (42). In the same manner, applying $\hat{L}_t$ to (44) and using (40), we can easily obtain the second equation from (42):

$$\hat{L}_t H_{t+1}\widetilde{\Psi}_{t+1} \tag{46}$$
$$= \hat{L}_t(\hat{R}_t\hat{L}_t + \mu_t)\widetilde{\Psi}_{t+1} = H_t\hat{L}_t\widetilde{\Psi}_{t+1}.$$

If $\hat{L}_t$ and $\hat{R}_t$ are taken as in (26) and (27), the factorization chain (41) leads to the set of finite-difference equations

$$\mu_t - K_t(n+1)\big\{W_t^{-1}(n+1)A_t(n+1) \tag{47}$$
$$+ A_t(n+1)W_t(n+1)\big\}K_t^{-1}(n+1) = \mu_{t+1}$$
$$- \big\{A_{t+1}(n+1)W_{t+1}^{-1}(n+1) + A_{t+1}(n)W_{t+1}(n)\big\}$$

and to relations (30) and (31) connecting A_t and A_{t+1} with each other, whence relations (39) follow. From (40) and (47), relations (33) or (34) between V_t and V_{t+1} follow too. The factorization-chain conditions (47), (39), and (33) [or (34)] are the generalization to the coupled system of m equations of the factorization-chain conditions for the discrete Schrödinger equation with $m = 1$ [3, 25].

One can easily see that the operators $\hat{R}_t$ and $\hat{L}_t$ provide transformations from the solutions of H_t to the solutions of H_{t+1}, and vice versa, from the solutions of H_{t+1} to solutions of H_t. From (40) and (44), it indeed follows that

$$\hat{R}_t\hat{L}_t\widetilde{\Psi}_{t+1} = (H_{t+1} - \mu_t)\widetilde{\Psi}_{t+1} \tag{48}$$
$$= (\nu_{t+1} - \mu_t)\widetilde{\Psi}_{t+1}.$$

Applying $\hat{L}_t$ to it and using (46) and (40), we get

$$\hat{L}_t\hat{R}_t\hat{L}_t\widetilde{\Psi}_{t+1} = (H_t - \mu_t)\hat{L}_t\widetilde{\Psi}_{t+1}$$
$$= (\nu_{t+1} - \mu_t)\hat{L}_t\widetilde{\Psi}_{t+1};$$

i.e., $H_t\hat{L}_t\widetilde{\Psi}_{t+1} = \nu_{t+1}\hat{L}_t\widetilde{\Psi}_{t+1}$. A comparison of the latter with (43) gives

$$\widetilde{\Psi}_t = \hat{L}_t\widetilde{\Psi}_{t+1}, \tag{49}$$

and ν_{t+1} is the energy eigenvalue of not only H_{t+1} but also H_t, $\nu_{t+1} = \nu_t$, except for the case where $\hat{L}_t\widetilde{\Psi}_{t+1} = 0$. At last, setting $\hat{L}_t\widetilde{\Psi}_{t+1} = \widetilde{\Psi}_t$ in (48) yields

$$\widetilde{\Psi}_{t+1} = (\nu_{t+1} - \mu_t)^{-1}\hat{R}_t\widetilde{\Psi}_t. \tag{50}$$

At the operator level, relations (49) and (50) obtained from the factorization of H_t and H_{t+1} coincide with the Darboux transformations (26) and (27).

Here, it should be noted that (42) ambiguously determines the relations between $\widetilde{\Psi}_t$ and $\widetilde{\Psi}_{t+1}$. Actually, it is easy to obtain from (42) the relations

$$\widetilde{\Psi}_{t+1} = \hat{R}_t\widetilde{\Psi}_t, \ \ \widetilde{\Psi}_t = (\lambda - \mu_t)^{-1}\hat{L}_t\widetilde{\Psi}_{t+1} \tag{51}$$

instead of (49) and (50). Indeed, if we start from

$$\hat{L}_t\hat{R}_t\widetilde{\Psi}_t = (H_t - \mu_t)\widetilde{\Psi}_t = (\nu_t - \mu_t)\widetilde{\Psi}_t \tag{52}$$

and apply $\hat{R}_t$ to it

$$\hat{R}_t(\hat{L}_t\hat{R}_t)\widetilde{\Psi}_t = (H_{t+1} - \mu_t)\hat{R}_t\widetilde{\Psi}_t = (\nu_t - \mu_t)\hat{R}_t\widetilde{\Psi}_t,$$

we have

$$H_{t+1}\hat{R}_t\widetilde{\Psi}_t = \nu_t\hat{R}_t\widetilde{\Psi}_t. \quad (53)$$

A comparison of this with (44) leads to the first equation in (51) and to the coincidence of H_t eigenvalues with H_{t+1} ones, $\nu_{t+1} = \nu_t$, except for the case where $\hat{R}_t\widetilde{\Psi}_t = 0$. The substitution of $\widetilde{\Psi}_{t+1} = \hat{R}_t\widetilde{\Psi}_t$ into (52) yields the second equation in (51).

It is evident now that the spectrum of H_t coincides with the spectrum of H_{t+1} except for the cases where $\hat{R}_t\widetilde{\Psi}_t = 0$ or $\hat{L}_t\widetilde{\Psi}_{t+1} = 0$. Let us consider these cases.

(i) Whenever $\hat{R}_t\widetilde{\Psi}_t = 0$ holds for a bound state $\widetilde{\Psi}_t$ of H_t, then the use of (52) yields

$$\hat{L}_t\hat{R}_t\widetilde{\Psi}_t = (H_t - \mu_t)\widetilde{\Psi}_t = (\nu_t - \mu_t)\widetilde{\Psi}_t = 0,$$

which implies that $\nu_t = \mu_t$ and $\widetilde{\Psi}_t$ coincides with the bound-state function Ψ_t, determining the Darboux transformations specified by Eqs. (22) and (23). In this case, H_{t+1} has no bound state with $\nu_{t+1} = \mu_t$. The spectrum of H_{t+1} contains one level less than that of H_t; i.e., the procedure of Darboux transformations removes one level from the spectrum of H_t. The procedure corresponds to the undressing one for the single-channel case. If $\mu_t = \nu_t^{\min}$ is chosen and if Ψ_t is a ground-state wave function, then Darboux transformations remove the lowest level.

(ii) Whenever $\hat{L}_t\widetilde{\Psi}_{t+1} = 0$ holds for a bound state $\widetilde{\Psi}_{t+1}$ of H_{t+1}, then the use of (48) leads to

$$\hat{R}_t\hat{L}_t\widetilde{\Psi}_{t+1} = (H_{t+1} - \mu_t)\widetilde{\Psi}_{t+1}$$
$$= (\nu_{t+1} - \mu_t)\widetilde{\Psi}_{t+1} = 0.$$

This implies that the eigenvalue of $\widetilde{\Psi}_{t+1}$ is $\nu_{t+1} = \mu_t$, and this level is absent from the spectrum of H_t (since $\widetilde{\Psi}_t = \hat{L}_t\widetilde{\Psi}_{t+1} = 0$). In this case, $\mu_t < \nu_t^{\min}$, and Ψ_t in (22) and (23) is not a bound-state matrix function of H_t, but it is a general solution of (1) with H_t at the energy $\lambda = \mu_t$. This means that the spectrum of H_{t+1} contains one level more than that of H_t. The procedure corresponds to the dressing one for the single-channel case. The term "dressing" was introduced by Zakharov and Shabat [31]. There also exists a situation where $\mu_t < \nu_t^{\min}$, but where neither H_t nor H_{t+1} has bound states at μ_t and the spectra of H_t and H_{t+1} coincide exactly; i.e., H_t and H_{t+1} are completely isospectral operators. In quantum mechanics, this case is known as broken supersymmetry.

Thus, with this section and with due regard for the preceding section, where the factorization of the Hamiltonians was obtained as the result of Darboux transformations, one can conclude that the factorization method and Darboux transformations for the system of discrete coupled equations are equivalent to each other.

ACKNOWLEDGMENTS

I am grateful to Dr. Yu. Karpeshina and Dr. I.A. Amirchanov for stimulating discussions.

The work was supported by the Russian Foundation for Basic Research (project no. F99R-162).

REFERENCES

1. G. Darboux, C. R. Acad. Sci. **94**, 1456 (1882).
2. E. Schrödinger, Proc. R. Ir. Acad. A, Math. Phys. Sci. **46**, 9, 183 (1940).
3. L. Infeld and T. E. Hull, Rev. Mod. Phys. **23**, 21 (1951).
4. E. Witten, Nucl. Phys. B **188**, 513 (1981).
5. V. Bargmann, Phys. Rev. **75**, 301 (1949); Rev. Mod. Phys. **21**, 488 (1949).
6. M. M. Nieto, Phys. Lett. B **145B**, 208 (1984); C. V. Sukumar, J. Phys. A **18**, 2937 (1985).
7. B. F. Samsonov, J. Phys. A **28**, 6989 (1995); J. Math. Phys. (N.Y.) **39**, 967 (1998).
8. A. A. Suzko, Int. J. Mod. Phys. A **12**, 277 (1997).
9. A. A. Suzko, Phys. Scr. **31**, 447 (1985).
10. A. A. Suzko, Phys. Scr. **34**, 5 (1986).
11. A. A. Suzko, Fiz. Élem. Chastits At. Yadra **24**, 1133 (1993) [Phys. Part. Nucl. **24**, 485 (1993)]; *Lecture Notes in Physics,* Ed. by H. von Geramb (Springer-Verlag, Berlin, 1993), Vol. 427, p. 67.
12. K. Chadan and P. C. Sabatier, *Inverse Problems in Quantum Scattering Theory* (Springer-Verlag, Berlin, 1989, 2nd ed.; Mir, Moscow, 1980, translation of 1st ed.).
13. *Lecture Notes in Physics* (Springer-Verlag, Berlin, 1993), Vol. 427.
14. *Lecture Notes in Physics* (Springer-Verlag, Berlin, 1997), Vol. 488.
15. B. N. Zakhariev and A. A. Suzko, *Direct and Inverse Problems. Potentials in Quantum Scattering* (Springer-Verlag, Berlin, 1990).
16. S. Novikov, S. V. Manakov, L. P. Pitaevskii, and V. E. Zakharov, *Theory of Solitons: the Inverse Scattering Method* (Nauka, Moscow, 1980; Consultants Bureau, New York, 1984).
17. F. Calogero and A. Degasperis, *Spectral Transformation and Solitons* (North-Holland, Amsterdam, 1982; Mir, Moscow, 1985).
18. V. B. Matveev and M. A. Salle, *Darboux Transformations and Solitons* (Springer-Verlag, Berlin, 1991), Springer Series in Nonlinear Dynamics.
19. V. B. Matveev and M. A. Salle, Lett. Math. Phys. **3**, 425 (1979).
20. Z. S. Agranovich and V. A. Marchenko, *Inversion Problem of Scattering Theory* (Kharkov State Univ. Press, Kharkov, 1960; Gordon and Breach, New York, 1963).
21. M. Humi, J. Phys. A **18**, 1085 (1985).
22. A. A. Suz'ko, Yad. Fiz. **55**, 2446 (1992) [Sov. J. Nucl. Phys. **55**, 1359 (1992)].
23. J. M. Sparenberg and D. Baye, Phys. Rev. Lett. **79**, 3802 (1997).

24. Yu. M. Berezanskii, *Expansion in Eigenfunctions of Self-Adjoint Operators* (Naukova Dumka, Kiev, 1965; American Mathematical Society, Providence, 1968).
25. V. Spiridonov and A. Zhedanov, Methods Appl. Anal. **2**, 369 (1995); J. Phys. A **30**, 8727 (1997).
26. K. M. Case and M. Kac, J. Math. Phys. (N.Y.) **14**, 594 (1973); K. M. Case, J. Math. Phys. (N.Y.) **15**, 2166 (1974).
27. F. Gesztezy and B. Simon, in *Proceedings of the International Conference "Mathematical Results in Quantum Mechanics," Prague, 1998*.
28. T. S. Chihara, *Introduction to Orthogonal Polynomials* (Gordon and Breach, New York, 1978); G. Szegö, *Orthogonal Polynomials* (American Mathematical Society, New York, 1959, 4th ed.; Inostrannaya Literatura, Moscow, 1975).
29. Ya. I. Geronimus, Izv. Akad. Nauk SSSR, Ser. Fiz. **4**, 215 (1940).
30. A. A. Suzko, in *Proceedings of the Seminar "Symmetries and Integrable Systems," Dubna, 1999,* Ed. by A. N. Sissakian, p. 258; Preprint ESI-665 (1999).
31. V. E. Zakharov and A. B. Shabat, Funct. Anal. Appl. **8**, 226 (1974); **13**, 166 (1979).

Physics of Atomic Nuclei, Vol. 65, No. 8, 2002, pp. 1560–1562. Translated from Yadernaya Fizika, Vol. 65, No. 8, 2002, pp. 1598–1600.

LETTERS TO THE EDITOR

Possibilities of Investigating Pionic Degrees of Freedom in Nuclei by Using Quasielastic Pion Knockout by High-Energy Electrons

V. G. Neudatchin, N. P. Yudin, and L. L. Sviridova

Institute of Nuclear Physics, Moscow State University, Vorob'evy gory, Moscow, 119899 Russia

Received November 8, 2001

The exclusive reactions of quasielastic proton knockout from a nucleus by a proton, $(p, 2p)$, or by an electron, (e, ep), of energy of about a few hundred MeV have been studied by many authors [1]. Such reactions make it possible to determine reliably the momentum distributions of protons in orbitals of given binding energy E_{bind}. In contrast to conventional photon–proton reactions, (γ, p), the above reactions allow one to explore the entire range of momenta of a virtual proton in the nucleus involved from zero value. The virtual-proton momentum can be determined by using the coincidence technique and the energy–momentum conservation law (this is a great advantage of the processes being discussed)

$$E_0 = E_1 + E_2 + E_{\text{bind}}, \qquad (1)$$
$$\mathbf{p}_0 + \mathbf{q} = \mathbf{p}_1 + \mathbf{p}_2,$$

where $\mathbf{q}$ is the momentum of the knock-on virtual particle, the rest of the notation being obvious. The energy resolution of the relevant experiment is $\Delta E \approx 1$ MeV. The quasielastic knockout of composite particles (clusters) from a nucleus, which have pronounced features, is also of considerable interest [2]. Similar investigations are being performed in atomic, molecular, and solid-state physics by using $(e, 2e)$ reactions [3, 4] at beam energies of a few keV for gas targets and of 20 to 50 keV for solid films, the energy resolutions being $\Delta E \approx 0.1$ eV and $\Delta E \approx 0.5$ eV, respectively.

In the present article, we call the attention of researchers to the possibility of studying pionic degrees of freedom in nuclei by using $(e, e\pi)$ reactions of quasielastic pion knockout from a nucleus by an electron of energy of about a few GeV.

The problem of injecting pions into the ground state of a nucleus has been discussed in the literature since the appearance of the articles of Migdal and his disciples [5, 6]. In Migdal's concept, this injection is indirect: the pion condensate is in fact the condensate of configurations of the Δ-*particle–nucleon-hole* type, the interaction in this condensate being mediated by pion exchange. However, the estimates presented in [6, 7] revealed that the actual density ρ_{nucl} of nucleons in a nucleus is two to three times less than that required for the formation of the condensate. In the past decade, Preparata and his clleagues [8] found an important new mechanism of pion injection into the ground state. This mechanism is associated with Dicke superradiation [9], which has been known in physics for several decades. This phenomenon is based on a coherent emission of photons by identical atoms. The intensity of such photon emission is proportional to $N^2/4$, where N is the number of atoms. This gives rise to a superstrong interaction of the photon field with the atoms (there is no such interaction in the case of an individual atom). This concept was extended in [8] to the nucleon system. In this case, N (Δ) corresponds to the ground (excited) state of an atom, while the pion field corresponds to the photon field. The estimates given by Preparata and his collaborates show that, although as great an amount of energy as 300 MeV is required for exciting Δ particle, the strong interaction between the $N-\pi-\Delta$ subsystems effectively increases the binding energy ΔE by about 10 MeV/nucleon. The coherence region where this interaction occurs comprises some 70 nucleons. According to [8], this new mechanism of pion-condensate generation results in that, even at the actual nucleon density, a nucleus appears to be in a superradiation state with respect to the pion mode, where the momentum q is determined from the formula

$$\sqrt{q^2 + m_\pi^2} = m_\Delta - m_N, \quad q \approx 0.3\ \text{GeV}. \qquad (2)$$

The number per nucleon of collective pions of the same type i (π^+, π^-, or π_0) in an $N = Z$ nucleus that have the above momentum $\mathbf{q}$ ($n_{i,\text{coll}}/A$) is about 0.1 [8]. This is greater than the respective number of pions with momenta, for example, in the range $\mathbf{k} = (1 \pm 0.2)\mathbf{q}$ in the virtual pion cloud of an individual nucleon (we mean here the P-wave pion state in the channel $p \to n\pi^+$ or $n \to p\pi^-$ [10, 11]).

This raises the question of experimentally verifying the occurrence of this mechanism in a nucleus. To provide an answer to this question, we propose investigating quasielastic pion knockout from a nucleus.

1063-7788/02/6508-1560$22.00

It turns out that the momentum distribution of pions knocked out from a free nucleon differs substantially from the momentum distribution of pions knocked out from a nucleus (according to the Preparata mechanism). Let us dwell on this point at some length. For the sake of simplicity, we assume that the domain of coherence for collective pions extends over the entire nucleus and that the radial pion wave function has the simplest standing-wave (p-wave) form (we consider here the case where the A nucleus involved does not change parity upon pion knockout, implying transitions like $0^+ \to 1^+$ and $1^+ \to 1^+$) [8]

$$\Phi(\mathbf{r}) = cj_1(\mathbf{q}\cdot\mathbf{r}) \text{ for } |\mathbf{r}| \le R \qquad (3)$$
$$\Phi(\mathbf{r}) = 0 \text{ for } |\mathbf{r}| > R,$$

where R is the radius of the nucleus corresponding to $A = 70$ and $N = Z$ and the constant c is determined by the normalization of the wave function to the above value $n_{i,\mathrm{coll}}$ common to all i ($c = 0.027$). At a large number of pions, the function in (3) can be interpreted as a classical field.

Making the Fourier transformation, we derive the momentum distribution shown in the figure (it is normalized to one nucleon; to obtain the momentum distribution for an A nucleus, it should be multiplied by A). It has a pronounced peak at $k = q$, which means that this momentum distribution is close to that for a plane wave and that it differs substantially from the momentum distribution that we reconstructed [10] for pions in a nucleon (dashed curve) on the basis of experimental data from [11] by employing the concept of quasielastic knockout in the physics of pion electroproduction. Our analysis revealed that this experiment was performed in quasielastic kinematics (there, the square of the virtual-photon mass was as large as 1 to 3 GeV^2). In that analysis, performed in the laboratory frame, we relied on the relativistic pole approximation, taking into account the Z diagram. The momentum distribution is isotropic (independent of the direction of the momentum $\mathbf{q}$) because it is an average over the magnetic quantum numbers of a pion in the p orbit in a nucleus.

Of crucial importance is the fact that the recoil momentum due to the knockout of collective pions is transferred to the nucleus as a discrete unit. Since $A = 70$–80, the recoil energy $E_{\mathrm{rec}} \approx \mathbf{q}^2/2AM_N$ is very small (the resolution in the experiments being discussed is sufficiently high: $\Delta E \approx 10$ MeV). This physics conforms well to the pattern where a pion in a nucleus is described by the simplest single-particle wave function (3), where spatial pion–nucleon correlations are neglected and where the recoil nucleus involves no internal excitations (in experiments characterized by a resolution of $\Delta E \approx 10$ MeV, this radical oversimplification is relaxed, since many excited states of the final nucleus are summed via a kind of a sum rule).

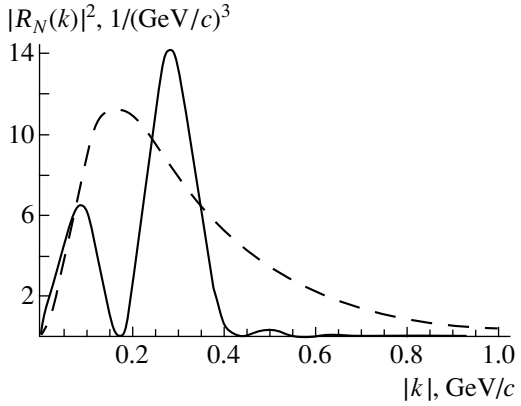

Momentum distribution of pions (solid curve) for the case of collective pions in the $A = 70$–80 nucleus (Preparata model) and (dashed curve) for the case of pions in a free nucleon [10].

On the other hand, the knockout of a virtual pion having a high momentum $\mathbf{q} = 0.3$ GeV/c (the main peak is shown by the solid curve in the figure) from the meson cloud of an individual nucleon results in the transfer of the kinetic energy $E_{\mathrm{ind}} \approx \mathbf{q}^2/2M_N \approx 50$ MeV to only one nucleon (we mean here numerous and loosely bound nucleons of the external shell). In a double-coincidence experiment, such an event looks as follows: the final spectator nucleus receives not only the recoil momentum $-\mathbf{q}$ but also an excitation energy of about 50 MeV. Thus, we conclude that, at a resolution of 10 MeV, the knockout of a "collective" pion is clearly distinguished from the knockout of an "individual" pion not only by the form of the momentum distribution but also by the recoil energy (there is an analogy here with the Mössbauer effect).

It is worthwhile to study experimentally, with a resolution of $\Delta E \approx 10$ MeV, the $(e, e'\pi^-)$ process on an $A \approx 70$–80 odd–odd nucleus having a large number (about 30 to 40) of nucleons in the external shell (of course, more neutrons than protons) and a high level density in the external shell at low excitation energies (summation over these levels is to be performed according to the above sum rule). A clear-cut maximum in the momentum distribution at $k \approx 0.3$ GeV/c (see solid curve in the figure)—it is associated with the aforementioned plane wave—would be the main signal indicating the presence of collective pions in a nucleus, provided that the coincidence scheme is tuned, to within the experimental resolution ΔE, to zero excitation energy E^* of the recoil nucleus. At $E^* \approx 50$ MeV, there must not be such a peak. Note that small values of k in the figure are not informative because, in this domain, one can hardly

decide whether the recoil momentum is transferred to a nucleon or the nucleus as a discrete unit.

The expressions for the cross sections involving the above momentum distributions are presented in [10]. These expressions correspond to the plane-wave approximation. A transition to distorted waves has virtually no effect on the shape of the above main peak, but this reduces the cross section by a factor of 3 to 5. It should be noted that the energy of knock-on pions must be greater than 1 GeV for Δ-isobar production in the final state to be ruled out (otherwise the proposed description would be drastically complicated).

Information about the quasielastic pion knockout in $(\pi, 2\pi)$ processes at these energies (the respective experimental studies have begun [12], but the energies of knock-on pions are still comparatively small) may be of interest for the above consideration because such processes have a large cross section due to strong interactions and receive a contribution from the π^0 collective component; however, pions in this reaction are knocked out mainly from the surface region of the nucleus since high-energy pions are substantially absorbed by nuclei [13]. This point can be taken into account by using distorted waves for initial or final pions, whereupon the interpretation of experimental data becomes less clear. It can also be included (see above) in the quantitative description of $(e, e\pi)$ processes, which are much less sensitive to the distortion of pion waves (because they involve one pion wave instead of three). It is worth noting that pion knockout from a nucleus in (γ, π) processes is being extensively studied, but it does not furnish direct information about the momentum distributions of pions because the interference of amplitudes associated with several diagrams is operative in that case [14].

In conclusion, we note that the cross section for the quasielastic knockout of Δ isobars by the electrons or protons of energy about 1 GeV provides a good means for testing a high concentration of Δ isobars in a nucleus. The quasielastic knockout of Δ isobars can easily be identified in triple-coincidence experiments involving, for example, the production of a correlated $p\pi$ pair.

ACKNOWLEDGMENTS

We are grateful to A.A. Ogloblin and B. Slovinskii for their interest in this study.

This work was supported in part by the Russian Foundation for Basic Research (project no. 00-02-16117).

REFERENCES

1. S. S. Volkov, A. A. Vorob'ev, O. A. Domchenkov, *et al.*, Yad. Fiz. **52**, 1339 (1990) [Sov. J. Nucl. Phys. **52**, 848 (1990)]; A. A. Vorob'ev, Yu. V. Dotsenko, A. A. Lobodenko, *et al.*, Yad. Fiz. **58**, 1923 (1995) [Phys. At. Nucl. **58**, 1817 (1995)]; D. G. Ireland and G. van der Steenhoven, Phys. Rev. C **49**, 2182 (1994); D. Debruyne, J. Ryckebush, W. van Nespen, and S. Janssen, Phys. Rev. C **62**, 024611 (2000).
2. V. G. Neudatchin, A. A. Sakharuk, W. W. Kurowsky, and Yu. M. Tchuvil'sky, Yad. Fiz. **58**, 1234 (1995) [Phys. At. Nucl. **58**, 1155 (1995)]; Yu. M. Tchuvil'sky, V. V. Kurovsky, A. A. Sakharuk, and V. G. Neudatchin, Phys. Rev. C **51**, 784 (1995).
3. V. G. Neudachin, Yu. V. Popov, and Yu. F. Smirnov, Usp. Fiz. Nauk **169**, 1111 (1999).
4. E. Weigold and I. McCarthy, *Electron Momentum Spectroscopy* (Kluwer, New York, 1999).
5. A. B. Migdal, Zh. Éksp. Teor. Fiz. **61**, 2209 (1971) [Sov. Phys. JETP **34**, 1184 (1972)]; A. B. Migdal, Rev. Mod. Phys. **50**, 107 (1978).
6. A. B. Migdal, D. N. Voskresenskiĭ, É. E. Sapershteĭn, and M. A. Troitskiĭ, *Pionic Degree of Freedom in Nuclear Matter* (Nauka, Moscow, 1991).
7. Yu. B. Ivanov, J. Knoll, H. van Hees, and D. N. Voskresensky, Yad. Fiz. **64**, 711 (2001) [Phys. At. Nucl. **64**, 652 (2001)].
8. R. Alzetta, G. Liberti, and G. Preparata, Nucl. Phys. A **585**, 307c (1995); R. Alzetta, T. Bubba, R. Le Perra, *et al.*, Nuovo Cimento A **112**, 762 (1999); R. Alzetta, G. Liberti, and G. Preparata, Nuovo Cimento A **112**, 1609 (1999).
9. A. V. Andreev, V. I. Emel'yanov, and Yu. A. Il'inskiĭ, *Coherent Phenomena in Optics* (Nauka, Moscow, 1988).
10. V. G. Neudatchin, N. P. Yudin, and L. L. Sviridova, Yad. Fiz. **60**, 2020 (1997) [Phys. At. Nucl. **60**, 1848 (1997)]; Yad. Fiz. **64**, 1680 (2001) [Phys. At. Nucl. **64**, 1600 (2001)].
11. P. Brauel, T. Canzler, D. Cords, *et al.*, Z. Phys. C **3**, 101 (1979).
12. F. Bonutti, P. Camerini, E. Fragiacomo, *et al.*, Phys. Rev. C **55**, 2999 (1997); B. Slovinski, in *Proceedings of the XIV International Seminar on High Energy Physics Problems, 1998*, Ed. by A. M. Baldin and V. V. Burov, (JINR, 2000), Vol. II, p. 194.
13. S. Khallaf and A. Ebrahim, Phys. Rev. C **62**, 024603 (2000); S. Jena and S. Swain, Phys. Rev. C **55**, 3015 (1997); M. H. Cha and Y. J. Kim, Phys. Rev. C **54**, 429 (1996).
14. M. Guidal, J.-M. Laget, and M. Vanderhaeghen, Nucl. Phys. A **627**, 645 (1997); V. G. Neudatchin, L. L. Sviridova, and N. P. Yudin, Yad. Fiz. **65**, 594 (2002) [Phys. At. Nucl. **65**, 567 (2002)].

Translated by R. Rogalyov